HAKONE X

10th International Symposium on High Pressure Low Temperature Plasma Chemistry

CONTRIBUTED PAPERS

Cooperated with The Third Polish-Japanese Hakone Group Symposium on Non-thermal Plasma Processing of Water and Air

---

Saga University
Saga, Japan

September 4th-8th, 2006

HAKONE X

Program of the 10th International Symposium on High Pressure Low Temperature Plasma Chemistry

Organized by : The Local Organizing Committee of the Hakone X

Cooperated with : Saga University
Saga Prefecture
Saga City
The Institute of Electrical Engineers of Japan (IEEJ)
The Japan Ozone Association (JOA)
The Japan Society of Applied Physics (JSAP)
The Institute of Engineers on Electrical Discharges in Japan (IEEDJ)

Editor: Saga University

The Local Organizing Committee greatly appreciates the sponsorship
of the following companies.

Densoken Ltd.

Fuji Electric Systems Co., Ltd.

Lesca Corporation

Meidensha Corporation

Mitsubishi Electric Corporation

Seicho-Corporation

Taiyo, Ltd.

Ushio Incorporation

Yamato Create Corporation

Yaskawa Electric Corporation

Professor Iwo Pollo, Lublin University of Technology, Polland
RESEARCHER AND TEACHER (1927 – 2005)

IWO POLLO - RESEARCHER AND TEACHER (1927 – 2005)

Iwo Pollo was born in 1927 in Delatyń (former eastern Poland, now Ukraine). After completing chemical studies he became a scientific worker of the Silesian University of Technology, developing investigations in the area of chemical technology. He worked on the synthesis of nitrogen oxide in glow discharges developing the cooperation with the famous school of gas electrochemistry of Moscow University.

In 1975 he begun work in Lublin as a professor of the newly formed technical university (presently Lublin University of Technology), where he set up the Department of Chemical Technology, which he chaired for over twenty years. He developed studies on plasma processes (ozone synthesis, purification of gases), and the significant scientific achievements of his group resulting in many publications and a dozen or so Ph.D. dissertations gained international acknowledgment. Having considerable standing among the academic community, Professor Iwo Pollo held many important posts in the Lublin University of Technology, during 1984-1990 he was its Vice-Rector, and during 1993-1996 its Rector. During the crucial days of Polish history he was not only an efficient manager of a large educational institution, but also a caring protector of its workers, trying to help especially those who suffered from the severity of the martial law forced in the 1980-ies.

Professor Iwo Pollo, being an outstanding organizer of scientific researches, acted in many institutions, such as the Committee of Chemical Sciences of Polish Academy of Sciences (PAS), Subcommittee of Plasma Chemistry of International Union of Pure and Applied Chemistry (IUPAC), Polish Group of International Ozone Association (IOA). He was chairman of the Plasma Chemistry Commission of Polish Chemical Society and Low Temperature Plasma Chemistry Commission of PAS. He fruitfully cooperated with many scientific institutions in France, Germany, Italy, Japan, Soviet Union, and Switzerland. He was a member of editorial boards and organizer of many scientific conferences, the International Symposium on High Pressure Low Temperature Plasma Chemistry HAKONE being one of them. And the tenth HAKONE meeting is taking place now, when he is not with us any more. Already 17 years have passed from the second such conference organized in Poland by Professor Iwo Pollo as its chairman. Due to his efforts, fruitful cooperation and exchange of Polish scientists with many distinguished groups carrying out studies on plasma processes in numerous countries developed, with the important share of Japan scientists.

Professor Iwo Pollo carried out numerous original studies on the chemical processes proceeding in non-equilibrium plasma, such as ozone synthesis or nitrogen oxide synthesis. He developed also the theory of these processes. However, his broad range of interests and great erudition were especially impressive. He knew perfectly the history of chemistry and chemical technology development and he could quote many interesting and not very known facts. He always paid great attention to passing over his knowledge to younger scientific workers and students, and this he did with great talent. He was an understanding teacher and caring tutor of young people. Despite his broad knowledge and high academic position, he was an extremely modest person, open and favorably inclined towards all who addressed him with their problems. One could always count on his good advice and help. These rare features of character distinguished him among the academic community. This is how he is remembered by his numerous students and friends.

(Noted by Dr. Krzysztof Schmidt-Szalowski, professor of Warsaw University of Technology)

Hakone X program

Monday, September 4

15:00 Registration
18:30 Welcome reception at Hotel Saga Hagakure (Hagakure-so) where is the conference site

Tuesday, September 5

08:40 Official Opening of the Symposium and the memorial address for late professor Iwo Pollo of the Lublin University of Technology, Poland
(by President of Saga University, Dr. Akira Hasegawa, Prof. Chobei Yamabe and Prof. Krzysztof Schmidt-Szalowski)

Chair: Dr. Kirill.V. Kozlov

Invited lecture 1

09:00 IL-01 *The special invited lecture of Hakone X in honor of Dr. Michel Lecuiller*:
Biological Applications of Atmospheric Pressure Dielectric Darrier Discharges
B. Dodet, E. Odic, S. Salamitou, A. Goldman, M. Goldman ---------- 355

Oral session A

Chair: Prof. Hans.-Erich Wagner

Topic 1 : Fundamental aspects of high pressure discharges(1)

09:20 1O-01 **20 Years of HAKONE: From Basic Plasma Chemistry to Billion Dollar Markets**
Ulrich Kogelschatz ---------- 5

09:40 1O-06 **Transition from atmospheric pressure Townsend discharge (APTD) to filamentary discharge in N_2/O - containing mixtures** ---------- 21
N. Gherardi, N. Naudé, Et. Es-sebbar, I. Enache, H. Caquineau, F. Massines

10:00 1O-03 **High Frequency Discharges in Ar/O_2 Mixture**
M. Laan, J. Raud and J. Aarik ---------- 9

10:20 Coffee break

Oral session B

Chair: Dr. Ulirich Kogelschatz

Topics 5 Ozone generation and applications(1) and Topics 7 Environmental applications(1)

10:35 5O-01 **Ozone Formation in DC Corona Discharge Fed by Carbon Dioxide in Flowing Regime**
J. Országh, J. D. Skalný, Š. Matejčík, N. J. Mason and A. Stoica ----------148

10:55 5O-02 **Ozone Generating Method using a Catalysis Electrode in Barrier Discharge**
A. Murai, T. Nakajima ---------- 152

11:15 5O-03 **Narrow Gap Discharge for Ozone Generation**
N. Wada, Y. Tanimura, M. Tanaka and M. Kuzumoto ---------- 156

11:35 5O-04 **Analysis of Non-Equilibrium Phenomena Occurring during an Ozone Generation Process Part I. Conception of Equilibrium Processes Electrosinthesis Ozone**
J. Ozonek and S. Fijalkowski ---------- 160

11:55 7O-01 **Non-thermal Plasma Reactors Power Systems' Designing and Efficiency**
H. D. Stryczewska and T. Janowski ---------- 197

12:15 7O-14 **Effects of Gliding Arc Discharges on *Erwinia carotovora atroseptic*a 1526**
M. Moreau, N. Orange, J. L. Brisset ---------- 246

12:35 - 14:00 Lunch

14:00 - 15:35 **Poster session 1**

15:35 - 15:50 Coffee break

Oral session C

Chair: Prof. Tairou Ito

Topics 7: Environmental applications(2)

15:50 7O-02 **Dilute Trichloroethylene Decomposition in Air by the Nonthermal Plasma, Byproducts and Carbon Balance**
T. Oda, K. Ono and R. Ono ---------- 201

16:10 7O-03 **Thermal Decomposition of Mineral Oxides Treated in an Immersed Arc-plasma**
Z. Kolacinski, L. Szymanski ---------- 207

16:30 7O-04 **Properties of a Heterogeneous System of Solid Particles in Gliding-Discharge Plasma**
K. Schmidt-Szalowski, K. Krawczyk, M. Mlotek ---------- 213

16:50 7O-05 **Increase of NO Removal Efficiency by Glow Like Discharge**
Y. Yoshioka and T. Shoyama ---------- 217

17:10 7O-06 **Treatment of NOx by the Barrier Discharge Reactor**
M. Fujii and T. Fujii ---------- 375

17:30 end of session
18:00 Meeting of the International Organizing and Scientific Committee

Wednesday, September 6

Chair: Prof. Jerzy Mizeraczyk

Invited lecture 2

08:40 IL-02 *The special invited lecture of Hakone X in honor of Dr. Michel Lecuiller* : **Saga Synchrotron Light and its Application for Advanced Science/technology and Regional Development**
M. Kamada, K. Takahashi, J. Azuma, H. Sugiyama, S. Tokudomi, T. Tanaka, and H. Ogawa
---------- 306

Oral session D

Chair: Prof. Jean-Louis Brisset

Topic 7 *Environmental applications(3)*

09:00 7O-07 **Phenol Oxidation by Pulsed Streamer Discharge in Water**
M. Dors, E. Metel, M. Kocik, J. Mikielewicz, J. Mizeraczyk ---------- 221

09:20 7O-08 **Research on Waste Water Purification by Ozone and Photocatalyst Treatment**
Y. Suda, H. Kawasaki, T. Ohshima and Y. Yagyu ---------- 225

09:40 7O-09 **Inactivation of Escherichia coli by Pulsed Corona Discharge in Water**
T. Vykouk, M. Clupek and P. Lukes ---------- 229

10:00 7O-10 **Plasma Water Treatment by Micro Discharge Channels at Atmospheric Pressure**
K. Yasuoka, A. Yamatake, H. Katayama and S. Ishii ---------- 234

10:20 - 10:35 Coffee break

Oral session E

Chair: Prof. Matti Laan

Topics 1, 2, 4 *Fundamental aspects of high pressure discharges, Modeling and diagnostics, Molecular synthesis and decomposition*

10:35 1O-04 **Investigation of Fine Structure of Surface Discharge in Air at Atmospheric Pressure**
M.V. Sokolova, K.V. Kozlov, S.A.Krivov, P.A. Tatarenko and V.G. Samoilovich ---------- 13

10:55 1O-05 **Measurement of Gas Temperature During Streamer Discharge Propagation in Atmospheric Air**
T. Namihira, T. Tokuichi, H. Tamaribuchi, D. Wang, S. Katsuki and H. Akiyama ---------- 17

11:15 4O-01 **Radiation Kinetics and Chemical Reactivity of Barrier Discharges in Humid Argon**
K.V. Kozlov, E. Odic, P.A. Tatarenko, B. Dodet, G..S. Fedoseev, M.J. Kirkpatrick, V.G.. Samoilovich and M. Ganciu ---------- 124

11:35 4O-02 **Treatment of Tetrafluoride with Gas Discharges**
G. J. Pietsch1 and A. B. Saveliev ---------- 128

11:55 2O-01 **Nucleation in Atmospheric Pressure Electrical Discharges**
J.P. Borra ---------- 55

12:15 The title will be announced later
Lucjan Pawłowski

12:35 - 14:00 Lunch

14:00 - 15:35 **Poster session 2**

15:35 Coffee break

Oral session F

Chair: Prof. Gerhard J. Pietsch

Topic 1,7,9 ***Fundamental aspects of high pressure discharges, Environmental applications(4), Miscellaneous***

15:50 1O-07 **Electrical and Optical Properties of AC Microdischarges in Porous Ceramics**
K. Hensel, M. Janda, M. Lestinsky, Z. Machala, V. Martisovits, P. Tardiveau and A. Mizuno ---------- 41

16:10 7O-11 **The Effects of Pulsed Streamer Discharge on a Marine Red Algae, Porphyra Yezoensys**
Z. Li, X. Lin, T. Ohno, T. Namihira, S. Katsuki, and H. Akiyama---------- 238

16:30 7O-12 **Removal of Acetone and Isopropyl Alcohol by Non-thermal Plasmas : Kinetic Studies using a Photo-triggered Discharge**
O. Sarroukh, F. Jorand, L. Magne, S. Pasquiers, C. Postel

16:50 7O-15 **Surface Biological Decontamination using Gliding Discharges in Humid Air at Atmospheric Pressure: Impact of the Treatment Distance**
C. Bourgeois, J. M. Herry, D. Hilaire, J. L. Brisset M. Naitali

17:10 9O-02 **PBG fiber for Low Gas Concentration Measurement**
J. Pawłat, T. Sugiyama, T. Matsuo, T. Ueda ---------- 359

17:30 end of session

18:30 Conference Dinner

Thursday, September 7

Chair: Prof. Jan D. Skalny

Invited lecture 3

08:40 IL-03 *The special invited lecture of Hakone X in honor of Dr. Michel Lecuiller* : **How do we Prepare Cross Section Sets for Molecules from Electron Swarm Data?**
Yoshiharu Nakamura ---------- 1

Oral session G

Chair: Prof. Nicolas Gherardi

Topic 2: *Modeling and diagnostics*

09:00 2O-02 **Measurements of OH Radical Density in $N_2/O_2/H_2O$ Streamer Corona Discharges by Laser-induced Fluorescence Imaging Spectroscopy**
K. Sasaki, T. Yoshida, and N. Takada ---------- 59

09:20 2O-03 **Measurement of OH Radicals in DC Streamer Corona Discharges by Laser-Induced Fluorescence**
S. Kanazawa, F. Mitsugi, T. Ohkubo, Y. Nomoto, M. Kocik J. Mizeraczyk and J.-S. Chang ---------- 63

09:40 2O-04 **Influence of Penning Ionization for Glow-like Discharge Formation in Dielectric Barrier Discharge In Ar-based Gas**
F. Tochikubo, Y. Matsushita and S. Uchida ---------- 67

10:00 2O-05 **Collisional-Radiative Model for Diffuse Dielectric Barrier Discharge in Neon at Atmospheric Pressure**
Z. Navrátil, D. Trunec and H.-E. Wagner ---------- 71

10:20 - 10:35 Coffee break

Oral session H

Chair: Prof. Henryka D. Stryczewska

Topic 2, 6, 7: Fundamental aspects of high pressure discharges, Modeling and diagnostics, Generation of radiation in high pressure discharges, Environmental applications

10:35 2O-06 **Evolution of Axial and Radial Distributions of the Electric Field in the Microdischarge of Barrier Discharge in Air**
K.V. Kozlov, H.-E. Wagner, T. Hoder and R. Brandenburg ---------- 75

10:55 2O-07 **Improvement of Plasma Parameters of Coplanar Barrier Discharge using Different Emitting Layers**
J. Čech, P. Sťahel A. Brablec and M. Černák ---------- 79

11:15 2O-08 **Stabilization of Atmospheric Pressure Discharge**
H. Matsuura, and Y. Sasada ---------- 83

11:35 6O-02 **Application of XeI Excimer Radiation for Excitation of Phosphors**
M. M. Guivan, A. Brablec, J. Janca, P. St'ahel, P. Slavicek and A. N. Malinin ---------- 184

11:55 7O-13 **On the Hydrogen Enrichment of an Air-methane Mixture in a Rotating Discharge Reactor**
E. El Ahmar, A. Khacef and J. M. Cormier ---------- 242

12:15 7O-16 **High Dense Ozone Generation and the Supply System for Agricultural Soil Sterilization**
K. Ebihara, T. Ikegami, M. Takayama, H. Ishida,
T. Sakai, Y. Gyoutoku, H. D.Stryczewska ---------- 247

12:35 - 14:00 Lunch

14:00 - 15:35 **Poster session 3**

15:35 - 15:50 Coffee break

Oral session I

Chair: Prof. Kenji Ebihara

Topic 8: Surface processing and technology (cleaning, etching and modification, equipment)

15:50 8O-01 **Powder Treatments using Atmospheric Pressure Glow Plasma ＜Silica coating on PLGA powder for DDS＞**
M. Kogoma, K. Yamaguchi and K. Tanaka ---------- 310

16:10 8O-03 **Silicon-fluoric Films Deposited in DBD under Atmospheric Pressure**
Z. R anek-Boroch, M. Wojucki, A. Ilik, A. Kosinski ---------- 318

16:30 8O-04 **Patterned DBD Pretreatment at Ambient Pressure for Low Temperature Wafer Bonding**
M. Eichler, B. Michel, M. Thomas, C. Ruddy, H. Reinecke,
M. Reiche, M. Gabriel and C.-P. Klages ---------- 322

16:50 8O-05 **Germ Reduction of Heat Sensitive Materials by using Atmospheric Pressure Plasma sources**
R. Brandenburg, J. Ehlbeck, U. Krohmann, M. Stieber,
Th. von Woedtke, J. Zeymer, K. Rackow and K.-D. Weltmann ---------- 326

17:10 Closing remarks by LOC Chairperson

Friday, September 8

09:00 One day technical tour for Nagasaki City by bus with free.
We will return to Saga City about 18:00.

Poster presentation 1: (20 papers)

Tuesday , September 5 (14:00 - 15:35)

Chair: Prof. Yoshio Yoshioka

1P-01
Discharge Characteristic of CNT Covered Electrode
N. Okayama, S. Ono ---------- 25

1P-07
Electron and Gas Temperature Evaluation of a He Atmospheric Pressure, DC Hollow-cathode Micro Plasma by a Procedure Based on Trace Rare Gases Optical Emission Spectroscopy
T. Nakano, H. Akashi, H. Imaizumi and T. Kitajima ---------- 51

2P-01
Visualization of the Flow in a Pulsed Positive Discharge in Water
J. Mikielewicz, J. Podliński, M. Dors, E. Metel, M. Kocik, J. Mizeraczyk ---------- 87

5P-03
Air Cleaning Test by Corona Reactor with Water
K. Ohara, T. Fujii, Y. Arao and M. Rea ---------- 371

5P-06
Improvement of Ozone Generation Efficiency using Parallel Surface Discharge Type Ozonizer
K. Fujii, S. Ihara and C. Yamabe ---------- 180

7P-10
Phenol Oxidation by DC Gas Phase Corona Discharge to the Water Surface
M. Kocik, M. Dors, E. Metel, J. Mikielewicz, J. Mizeraczyk ---------- 284

7P-11
The role of iron ions in the phenol oxidation in water by gas phase DC corona discharge
J. Mizeraczyk, M. Dors, E. Metel, M. Kocik, J. Mikielewicz ---------- 288

7P-14
Application of Gliding Arc Plasma in Humid Air to the Treatment of Thiourea
E. B. Tsagou-Sobze, D. Moussa, A. Doubla, E. Hnatiuc, J. L. Brisset ---------- 297

8P-01
Modification of Polymeric Surface Exposed to Discharge Plasma
Yong Zhu, Masahisa Otsubo, Chikahisa Honda1 and Youl-Moon Sung ---------- 330

8P-02
An Atmospheric Non-thermal DC Plasma Jet and Microwave Plasma Jet for Surface Cleaning of PET Films
Youl-Moon SUNG

8P-03
Deposition of Thin Films at Higher Substrate Temperatures in Atmospheric Pressure Glow Discharge
D. Trunec, M. Šíra, P. Stahel, V. Buršíková, D. Franta ---------- 331

8P-04
Thick Film Deposition of Photo-catalytic Oxide Films by TPCVD
Y. Ando, S. Tobe and H. Tahara ---------- 335

8P-05
Organic Thin Films Deposited by PLD Method in Nitrogen Atmosphere
T. Tomemori, Sang-Moo Park, K. Ebihara, T. Ikegami ---------- 339

8P-06
Effect of Electric and Magnetic Fields on Separate PLD Method
S. Yamaguchi, Sang-Moo Park, K. Ebihara, T. Ikegami ---------- 343

8P-07
Application of Surface Barrier Discharge for Deposition of Protective Coatings at Atmospheric Pressure
P. Sťahel, V. Buršíková , Z. Navrátil, P. Kloc, A. Brablec, M. Šíra and J. Janča ---------- 347

8P-08
Coating on the Inside of Microfluidic Systems with DBD Based Atmospheric Pressure PA-CVD
M. Eichler, C. Berger, M. Thomas and C.-P. Klages ---------- 351

8P-09
Silicon Based Thin Film Deposited from Hexamethyldisiloxane in an Atmospheric Pressure Townsend Discharge
T. Paulmier, N. Gherardi, L. Maechler, I. Enache, H. Caquineau, F. Massines ---------- 314

9P-02
Development of a Type of Compact Nanosecond Pulse Generator
Quan Zhaochun, Liu Zhongjie, Li Zhi, Gao Yanhui, Xie Xiongjie, Zhang Yuanfang, Guan Genzhi
---------- 363

9P-03
Breaking of Ice using Pulsed Power
S. Ihara, Y. Miyazaki, C. Yamabe, S. Ushio ---------- 367

Poster presentation 2: (18 papers)

Wednesday, September 6 (14:00 - 15:35)

Chair: Prof. Haruo Itoh

1P-02
Plasma Processing of Propane at Hyper-atmospheric Pressure: Experiment and Modeling
S. L. Hill, J. C. Whitehead and K. Zhang ---------- 29

1P-03
Synchronization and Development of Positive Surface Streamer Discharges in Air, Nitrogen and Oxygen
Y. Kashiwagi and H. Itoh ---------- 33

1P-04
The Effect of Temperature on Corona Characteristics and its Revelation
C. Shixiu, C.Cixuan, X. Guangrun, S. Youlin, C. Xuegou ---------- 37

1P-06
Some Peculiarities of the Barrier Discharge in Pure Argon
K. V. Kozlov, P. A. Tatarenko, V. G. Samoilovich ---------- 47

2P-02
Diagnostics of He Atmospheric Pressure Glow Plasma: Measurement of Metastable He ($2s^1S$, $2s^3S$) with Atomic Resonance Absorption Spectroscopy
K. Tanaka, Y. Yanagawa, and M. Kogoma ---------- 91

2P-03
Diagnostics of Organics Compounds Degradation by Optical Emission Spectroscopy
J. Prochazkova, Z. Stara and F. Krcma ---------- 95

2P-04
Acoustic Spectra Characteristics of Micro Discharge
T. Nakamiya, D. Sasahara, K. Ebihara, T. Ikegami and R. Tsuda ---------- 99

2P-05
The Analysis of Influence of Essential Parameters on Ozone Electrosynthesis Course in Simulating Approach
K. Jaholkowski, J. Ozonek and S. Fijalkowski ---------- 103

2P-06
RF Microdischarge Generated by Plasma Pencil at Atmospheric Pressure
Brablec A., Slavicek P., Kadlecova J., Smekal P., Vanek P

2P-07
Five Limb Transformer as a Power System of Arc Discharge Reactor
H. D. Stryczewska, G. Komarzyniec and T. Janowski ---------- 107

2P-08
Efficient use of Plasma Ozonisers in the Water-based Absorption of NOx
J. Jaroszyńska-Wolińska ---------- 111

2P-09
Observation of Laser-induced Streamer Corona Discharge in a Corona Radical Shower System
S. Kanazawa, F. Mitsugi, T. Ohkubo, Y. Nomoto, M. Kocik, J. Mizeraczyk and J.-S. Chang ---------- 116

2P-10
Evolution of Axial and Radial Distributions of Electric Field in the Microdischarge of Barrier Discharge in Air
K.V. Kozlov, H.-E. Wagner, T. Hoder and R. Brandenburg

2P-11
Characteristics of a Novel Partial Discharge in Water
W. Guan, S. Ihara, C. Yamabe ---------- 120

4P-02
Loss Processes of $N_2(A^3\Sigma_u^+)$ by Benzene
S.Suzuki, T.Suzuki and H.Itoh ---------- 132

4P-03
CO_2 reforming of CH4 in a Non Thermal Plasma Reactor at Atmospheric Pressure
F. Ouni, A. Khacef, J. M. Cormier ---------- 136

4P-04
Generation of Nitric Oxide by Pulsed Arc Discharge
S. Sakai, T. Namihira, D. Wang, T. Kiyan, H. Akiyama, K.Okamoto, N. Teshima and K. Toda ---------- 140

4P-05
Destruction of VOCs in the Air by Barrier Discharge
M.Wronski, B.Polednik ---------- 144

7P-15
Decreased Ozone Concentration During Ozone Generation Using 99.99% Pure Oxygen as the Feed Gas
M. Taguchi, T. Takano, H. Itoh ---------- 298

Poster presentation 3: (19 papers)

Thursday, September 7 (14:00 - 15:35)

Chair: Prof. Kogoma Masuhiro

5P-01
Influence of Ozone Generation on the Thickness of Discharge Electrode at Saw Tooth Plate Electrode Type of Electrostatic Precipitator
Y. Takagi, T. Takahashi, Y. Ehara, K. Yasumoto, A. Zukeran ---------- 164

5P-02
Analysis of Non-equibrium Phenomena Occurring During an Ozone Generation Process part II. Analysis of Electrosynthesis of Ozone Processes in the Range of Irreversibility and Non-equilibrium
S. Fijalkowski and J. Ozonek ---------- 168

5P-04
Development of Ozone Generator using Parallel Driving of Piezoelectric Transformers
K. Teranishi, S. Suzuki and H. Itoh ---------- 172

5P-05
Research on the power factor characteristics of ozonizer
L. ZhongJie, Q. Zhaochun, G. Genzhi, Z. Yuanfang ---------- 176

6P-02
Investigation of DBD Power Supplier Optimization
G.Zvereva , M.Maaspuro ---------- 188

6P-03
Design and Development of the 1 kJ Nd:glass Laser Facility for Basic Research on Quantum Engineering
S. K. Hong, K. H. Ko, K. T .Lee, J. T. Jin, M.S. Kim, D. H. Yun, J. J. Goo, L. Li and C. H. Lim
---------- 189

6P-04
Electric Characteristics of Rare Gases Barrier Discharges
G. Zvereva, G. Volkova, G. Gerasimov ---------- 193

7P-01
Plasma Water Purification by Dielectric Barrier Discharge in Mixed State of Liquid and Gas
H. Katayama, K. Yasuoka, S. Ishii ---------- 251

7P-02
SPME analysis of VOC destruction products – Atmospheric pressure discharge
H. Grossmannova, M. Ciganek, J. Prochazkova and F. Krcma ---------- 255

7P-03
Removal of COD and Color using Electrical Discharge in Foaming Column
J. Pawłat, S. Ihara ---------- 259

7P-04
Conversion of Nitrous Oxide by Pulsed Corona Discharge
K. Schmidt-Szałowski and K. Krawczyk ---------- 263

7P-06
CO Oxidation using Atmospheric Nonthermal Plasma-driven Catalysis
H. H. Kim, S. Tsubota, M. Date, A. Ogata, and S. Futamura ---------- 267

7P-07
Conversion of Propane by Pulsed Dielectric Barrier Discharges in Air
O. Aubry, A. Khacef, and J. M. Cormier ---------- 272

7P-08
Oxydation of Soot Particulates in Dielectric Barrier Discharges
J. Grundmann, S. Müller, R.-J. Zahn, A. Quade and H. Steffen ---------- 397

7P-09
Biological Effects of DC Discharges in Atmospheric Air with Water
Z. Machala, I. Jedlovsky, K. Hensel, V. Martisovits, V. Foltin ---------- 277

7P-12
Fundamental Research of Water Treatment using a Pulsed Power Technology
S. Nakazaki, S. Ihara and C. Yamabe ---------- 292

7P-13
Post-discharge Phenomena in a Gliding Arc Treatment of an Azo Dye
D. Moussa, G. Kamgang, J. L. Brisset, E. Hnatiuc ---------- 296

7P-16
Decolorlzation of Indigo Carmine Solution Using Discharge on Surface of a Gas-Layer in Water
T. Miichi ----------302

(Notice)
The shadow color as shown below means oral presentation.

List of titles of papers

Topic 1 (Fundamental aspects of high pressure discharges) ----------14 papers

IL-03
How do we prepare cross section sets for molecules from electron swarm data?
Yoshiharu Nakamura

1O-01
20 Years of HAKONE: From Basic Plasma Chemistry to Billion Dollar Markets
Ulrich Kogelschatz

1O-03
High Frequency discharges in Ar/O_2 Mixture
M. Laan, J. Raud and J. Aarik

1O-04
Investigation of Fine Structure of Surface Discharge in Air at Atmospheric Pressure
M.V. Sokolova, K.V. Kozlov, S.A.Krivov, P.A. Tatarenko and V.G. Samoilovich

1O-05
Measurement of Gas Temperature during Streamer Discharge Propagation in Atmospheric Air
T. Namihira, T. Tokuichi, H. Tamaribuchi, D. Wang, S. Katsuki and H. Akiyama

1O-06
Transition from atmospheric pressure Townsend discharge (APTD) to filamentary discharge in N_2/O - containing mixtures
N. Gherardi, N. Naudé, Et. Es-sebbar, I. Enache, H. Caquineau, F. Massines

1O-07
Electrical and Optical Properties of AC Microdischarges in Porous Ceramics
K. Hensel, M. Janda, M. Lestinsky, Z. Machala, V. Martisovits,
P. Tardiveau and A. Mizuno

1P-01
Discharge characteristic of CNT covered electrode
N. Okayama, S. Ono

1P-02
Plasma processing of propane at hyper-atmospheric pressure: Experiment and modelling
S. L. Hill, J. C. Whitehead and K. Zhang

1P-03
Synchronization and development of positive surface streamer discharges in Air, Nitrogen and Oxygen
Y. Kashiwagi and H. Itoh

1P-04
The effect of temperature on corona characteristics and its revelation
C. Shixiu, C. Cixuan, X. Guangrun, S. Youlin, C. Xuegou

1P-06
Some peculiarities of the barrier discharge in pure argon
K. V. Kozlov, P. A. Tatarenko, V. G. Samoilovich

1P-07
Electron and gas temperature evaluation of a He atmospheric pressure, DC hollow-cathode micro plasma by a procedure based on trace rare gases optical emission spectroscopy
T. Nakano, H. Akashi, H. Imaizumi and T. Kitajima

Topic 2 (Modeling and diagnostics) ---------- 19 papers

2O-01
Nucleation in Atmospheric Pressure Electrical Discharges
J.P. Borra

2O-02
Measurements of OH radical density in $N_2/O_2/H_2O$ streamer corona discharges by laser-induced fluorescence imaging spectroscopy
K. Sasaki, T. Yoshida, and N. Takada

2O-03
Measurement of OH Radicals in DC Streamer Corona Discharges by Laser-Induced Fluorescence
S. Kanazawa, F. Mitsugi, T. Ohkubo, Y. Nomoto, M. Kocik, J. Mizeraczyk and J.-S. Chang

2O-04
Influence of Penning Ionization for glow-like discharge formation in dielectric barrier discharge In Ar-based gas
F. Tochikubo, Y. Matsushita and S. Uchida

2O-05
Collisional-Radiative Model for Diffuse Dielectric Barrier Discharge in Neon at Atmospheric Pressure
Z. Navrátil, D. Trunec and H.-E. Wagner

2O-06
Evolution of axial and radial distributions of the electric field in the microdischarge of barrier discharge in air
K.V. Kozlov, H.-E. Wagner, T. Hoder and R. Brandenburg

2O-07
Improvement of plasma parameters of coplanar barrier discharge using different emitting layers
J. Čech, P. Sťahel A. Brablec and M. Černák

2O-08
Stabilization of atmospheric Pressure discharge
H. Matsuura, and Y. Sasada

2P-01
Visualization of the flow in a pulsed positive discharge in water
J. Mikielewicz, J. Podliński, M. Dors, E. Metel, M. Kocik, J. Mizeraczyk

2P-02
Diagnostics of He atmospheric pressure glow plasma: Measurement of metastable He ($2s^1S$, $2s^3S$) with atomic resonance absorption spectroscopy
K. Tanaka, Y. Yanagawa, and M. Kogoma

2P-03
Diagnostics of organics compounds degradation by optical emission spectroscopy
J. Prochazkova, Z. Stara and F. Krcma

2P-04
Acoustic spectra characteristics of micro discharge
T. Nakamiya, D. Sasahara, K. Ebihara, T. Ikegami and R. Tsuda

2P-05
The Analysis of influence of essential parameters on ozone electrosynthesis course in simulating Approach
K. Jaholkowski, J. Ozonek and S. Fijalkowski

2P-06
RF microdischarge generated by plasma pencil at atmospheric pressure
Brablec A., Slavicek P., Kadlecova J., Smekal P., Vanek P

2P-07
Five limb transformer as a power system of arc discharge reactor
H. D. Stryczewska, G. Komarzyniec and T. Janowski

2P-08
Efficient use of Plasma Ozonisers in the Water-based Absorption of NOx
J. Jaroszyńska-Wolińska

2P-09
Observation of laser-induced streamer corona discharge in a corona radical shower system
S. Kanazawa, F. Mitsugi, T. Ohkubo, Y. Nomoto, M. Kocik, J. Mizeraczyk and J.-S. Chang

2P-10
Evolution of axial and radial distributions of electric field in the microdischarge of barrier discharge in air
K.V. Kozlov, H.-E. Wagner, T. Hoder and R. Brandenburg

2P-11
Characteristics of a novel partial discharge in water
W. Guan, S. Ihara, C. Yamabe

Topic 3 (Ionization and ion-molecule reactions in non-thermal plasma) -----0 papers

Topic 4 (Molecular synthesis and decomposition) ----------6 papers

4O-01
Radiation Kinetics and Chemical Reactivity of Barrier Discharges in Humid Argon
K.V. Kozlov, E. Odic, P.A. Tatarenko, B. Dodet, G..S. Fedoseev,
M.J. Kirkpatrick, V.G.. Samoilovich and M. Ganciu

4O-02
Treatment of Tetrafluoride with Gas Discharges
G. J. Pietsch1 and A. B. Saveliev

4P-02
Loss processes of $N_2(A^3\Sigma_u^+)$ by benzene
S.Suzuki, T.Suzuki and H.Itoh

4P-03
CO_2 reforming of CH4 in a non thermal plasma reactor at atmospheric pressure
F. Ouni, A. Khacef, J. M. Cormier

4P-04
Generation of Nitric Oxide by Pulsed Arc Discharge
S. Sakai, T. Namihira, D. Wang, T. Kiyan, H. Akiyama, K.Okamoto, N. Teshima and K. Toda

4P-05
Destruction of VOCs in the air by barrier discharge
M.Wronski, B.Polednik

Topic 5 (Ozone generation and applications) ----------10 papers

5O-01
Ozone formation in DC corona discharge fed by carbon dioxide in flowing regime
J. Országh, J. D. Skalný, Š. Matejčík, N. J. Mason and A. Stoica

5O-02
Ozone generating method using a catalysis electrode in barrier discharge
A. Murai, T. Nakajima

5O-03
Narrow gap discharge for ozone generation
N. Wada, Y. Tanimura, M. Tanaka and M. Kuzumoto

5O-04
Analysis of non-equilibrium phenomena occurring during an ozone generation process Part I. Conception of equilibrium processes electrosinthesis ozone
J. Ozonek and S. Fijalkowski

5P-01
Influence of ozone generation on the thickness of discharge electrode at saw tooth plate electrode type of electrostatic precipitator
Y. Takagi, T. Takahashi, Y. Ehara, K. Yasumoto, A. Zukeran

5P-02
Analysis of non-equibrium phenomena occurring during an ozone generation process part II. Analysis of electrosynthesis of ozone processes in the range of irreversibility and non-equilibrium
S. Fijalkowski and J. Ozonek

5P-03
Air cleaning test by corona reactor with water
K.Ohara, T.Fujii, Y. Arao and M. Rea

5P-04
Development of ozone generator using parallel driving of piezoelectric transformers
K. Teranishi, S. Suzuki and H. Itoh

5P-05
Research on the power factor characteristics of ozonizer
L. ZhongJie, Q. Zhaochun, G. Genzhi, Z. Yuanfang,

5P-06
Improvement of ozone generation efficiency using parallel surface discharge type ozonizer
K. Fujii, S. Ihara and C. Yamabe

Topics 6 (Generation of radiation in high pressure discharges) ----------4papers

6O-02
Application of XeI excimer radiation for excitation of phosphors
M. M. Guivan, A. Brablec, J. Janca, P. St'ahel, P. Slavicek and A. N. Malinin

6P-02
Investigation of DBD power supplier optimization
G. Zvereva, M. Maaspuro

6P-03
Design and development of the 1 kJ Nd:glass laser facility for basic research on quantum engineering
S. K. Hong, K. H. Ko, K. T .Lee, J. T. Jin, M.S. Kim, D. H. Yun, J. J. Goo, L. Li and C. H. Lim

6P-04
Electric characteristics of rare gases barrier discharges
G. Zvereva, G. Volkova, G. Gerasimov

Topics 7 (Environmental applications) ---------- 33 papers

7O-01
Non-thermal plasma reactors power systems' designing and Efficiency
H. D. Stryczewska and T. Janowski

7O-02
Dilute trichloroethylene decomposition in air by the nonthermal plasma, byproducts and carbon balance
T. Oda, K. Ono and R. Ono

7O-03
Thermal decomposition of mineral oxides treated in an immersed arc-plasma
Z. Kolacinski, L. Szymanski

7O-04
Properties of a heterogeneous system of solid particles in gliding-discharge plasma
K. Schmidt-Szalowski, K. Krawczyk, M. Mlotek

7O-05
Increase of NO removal efficiency by glow like discharge
Y. Yoshioka and T. Shoyama

7O-06
Treatment of NOx by the barrier discharge reactor
M. Fujii and T. Fujii

7O-07
Phenol Oxidation by Pulsed Streamer Discharge in Water
M. Dors, E. Metel, M. Kocik, J. Mikielewicz, J. Mizeraczyk

7O-08
Research on Waste Water Purification by Ozone and Photocatalyst Treatment
Y. Suda, H. Kawasaki, T. Ohshima and Y. Yagyu

7O-09
Inactivation of Escherichia coli by pulsed corona discharge in water
T. Vykouk, M. Clupek and P. Lukes

7O-10
Plasma Water Treatment by Micro Discharge Channels at Atmospheric Pressure
K. Yasuoka, A. Yamatake, H. Katayama and S. Ishii

7O-11
The Effects of Pulsed Streamer Discharge on a Marine Red Algae, Porphyra Yezoensys
Z. Li, X. Lin, T. Ohno, T. Namihira, S. Katsuki, and H. Akiyama

7O-12
Removal of Acetone and Isopropyl Alcohol by Non-thermal Plasmas : Kinetic Studies using a Photo-triggered Discharge
O. Sarroukh, F. Jorand, L. Magne, S. Pasquiers, C. Postel

7O-13
On the hydrogen enrichment of an air-methane mixture in a rotating discharge reactor
E. El Ahmar, A. Khacef and J. M. Cormier

7O-14
Effects of gliding arc discharges on *Erwinia carotovora atroseptic*a 1526
M. Moreau, N. Orange, J. L. Brisset

7O-15
Surface Biological Decontamination using Gliding Discharges in Humid Air at Atmospheric Pressure: Impact of the Treatment Distance
C. Bourgeois, J. M. Herry, D. Hilaire, J. L. Brisset M. Naitali

7O-16
High dense ozone generation and the supply system for agricultural soil sterilization
K. Ebihara, T. Ikegami, M. Takayama, H. Ishida, T. Sakai, Y. Gyoutoku, H. D.Stryczewska

7O-17
The title will be announced later
Lucjan Pawłowski

7P-01
Plasma water purification by dielectric barrier discharge in mixed state of liquid and gas
H. Katayama, K. Yasuoka, S. Ishii

7P-02
SPME analysis of VOC destruction products – Atmospheric pressure discharge
H. Grossmannova, M. Ciganek, J. Prochazkova and F. Krcma

7P-03
Removal of COD and Color using electrical discharge in foaming column
J. Pawłat, S. Ihara

7P-04
Conversion of nitrous oxide by pulsed corona discharge
K. Schmidt-Szałowski and K. Krawczyk

7P-05
A hybrid plasma/catalytic reactor for tar removal from syngas
A.J.M. Pemen, J.J. Schmeits, R.A.B.P. Kerst, K. Yan, E.J.M. van Heesch, K.J. Ptasinski

7P-06
CO oxidation using atmospheric nonthermal plasma-driven catalysis
H. H. Kim, S. Tsubota, M. Date, A. Ogata, and S. Futamura

7P-07
Conversion of propane by pulsed dielectric barrier discharges in air
O. Aubry, A. Khacef, and J. M. Cormier

7P-08
Oxydation of soot particulates in dielectric barrier discharges
J. Grundmann, S. Müller, R.-J. Zahn, A. Quade and H. Steffen

7P-09
Biological effects of DC discharges in atmospheric air with water
Z. Machala, I. Jedlovsky, K. Hensel, V. Martisovits, V. Foltin

7P-10
Phenol oxidation by DC Gas phase corona discharge to the water surface
M. Kocik, M. Dors, E. Metel, J. Mikielewicz, J. Mizeraczyk

7P-11
The role of iron ions in the phenol oxidation in water by gas phase DC corona discharge
J. Mizeraczyk, M. Dors, E. Metel, M. Kocik, J. Mikielewicz

7P-12
Fundamental research of water treatment using a pulsed power technology
S. Nakazaki, S. Ihara and C. Yamabe

7P-13
Post-discharge phenomena in a gliding arc treatment of an azo dye
D. Moussa, G. Kamgang, J. L. Brisset, E. Hnatiuc

7P-14
Application of gliding arc plasma in humid air to the treatment of thiourea
E. B. Tsagou-Sobze, D. Moussa, A. Doubla, E. Hnatiuc, J. L. Brisset

7P-15
Decreased Ozone Concentration During Ozone Generation Using 99.99% Pure Oxygen as the Feed Gas
M. Taguchi, T. Takano, H. Itoh

7P-16
Decolorlzation of Indigo Carmine Solution Using Discharge on Surface of a Gas-Layer in Water
T. Miichi

Topics 8 (Surface processing and technology (Cleaning, coating, etching and modification, equipment) ----------14 papers

IL-02
Saga synchrotron light and its application for advanced science/technology and regional development
M. Kamada, K. Takahashi, J. Azuma, H. Sugiyama, S. Tokudomi, T. Tanaka, and H. Ogawa

8O-01
Powder treatments using atmospheric pressure glow plasma ＜Silica coating on PLGA powder for DDS＞
M. Kogoma, K. Yamaguchi and K. Tanaka

8O-03
Silicon-fluoric films deposited in DBD under atmospheric pressure
Z. R anek-Boroch, M. Wojucki, A. Ilik, A. Kosinski

8O-04
Patterned DBD Pretreatment at ambient pressure for low temperature wafer bonding
M. Eichler, B. Michel, M. Thomas, C. Ruddy, H. Reinecke,
M. Reiche, M. Gabriel and C.-P. Klages

8O-05
Germ reduction of heat sensitive materials by using atmospheric pressure plasma sources
R. Brandenburg, J. Ehlbeck, U. Krohmann, M. Stieber,
Th. von Woedtke, J. Zeymer, K. Rackow and K.-D. Weltmann

8P-01
Modification of polymeric surface exposed to discharge plasma
Y. Zhu, M. Otsubo, C. Honda1 and Youl-Moon Sung

8P-02
An atmospheric non-thermal DC plasma jet and microwave plasma jet for surface cleaning of PET films
Youl-Moon SUNG

8P-03
Deposition of thin films at higher substrate temperatures in atmospheric pressure glow discharge
D. Trunec, M. Šíra, P. Stahel, V. Buršíková, D. Franta

8P-04
Thick film deposition of photo-catalytic oxide films by TPCVD
Y. Ando, S. Tobe and H. Tahara

8P-05
Organic thin films deposited by PLD method in nitrogen atmosphere
T. Tomemori, Sang-Moo Park, K. Ebihara, T. Ikegami

8P-06
Effect of electric and magnetic fields on separate PLD method
S. Yamaguchi, Sang-Moo Park, K. Ebihara, T. Ikegami

8P-07
Application of Surface Barrier Discharge for deposition of protective coatings at atmospheric pressure
P. Sťahel, V. Buršíková , Z. Navrátil, P. Kloc, A. Brablec, M. Šíra and J. Janča

8P-08
Coating on the inside of microfluidic systems with DBD based atmospheric pressure PA-CVD
M. Eichler, C. Berger, M. Thomas and C.-P. Klages

8P-09
Silicon based thin film deposited from hexamethyldisiloxane in an Atmospheric Pressure Townsend Discharge
T. Paulmier, N. Gherardi, L. Maechler, I. Enache, H. Caquineau, F. Massines

Topics 9 (Miscellaneous) ----------4 papers

IL-01
Biological applications of atmospheric pressure dielectric barrier discharges
B. Dodet, E. Odic, S. Salamitou, A. Goldman, M. Goldman

9O-02
PBG fiber for low gas concentration measurement
J. Pawłat, T. Sugiyama, T. Matsuo, T. Ueda

9P-02
Development of a type of compact nanosecond pulse generator
Q. Zhaochun, L. Zhongjie, L. Zhi, G. Yanhui, X. Xiongjie, Z. Yuanfang, G. Genzhi

9P-03
Breaking of ice using pulsed power
S. Ihara, Y. Miyazaki, C. Yamabe, S. Ushio

(Notice)
The shadow color as shown below means oral presentation.

BIOLOGICAL APPLICATIONS OF ATMOSPHERIC PRESSURE DIELECTRIC BARRIER DISCHARGES

B. Dodet[1], E. Odic[1], S. Salamitou[2], A. Goldman[3], M. Goldman[3]

[1] *Départment Energie – Supélec, F-91192 Gif-sur-Yvette CEDEX, France*
[2] *Institut de Génétique et Microbiologie CNRS/Université Paris XI, F-91405 Orsay CEDEX, France*
[3] *Equipe DEE, LPGP, CNRS/Université Paris XI, Supélec, F-91192 Gif-sur-Yvette CEDEX, France*

ABSTRACT. A reduction of more than 4 orders of magnitude of survivors was obtained by exposing a *Bacillus Stearothermophilus* spores - contaminated surface to an atmospheric pressure DBD post-discharge for 20 minutes. The tested bacteria strain was. Decontamination mechanisms are investigated assuming that (i) inactivation is obtained when the bacteria DNA is fragmented, (ii) the protein coats are the main protection of the cell core DNA in the case of bacteria spores. The degradation of DNA (plasmid) and protein (RNAse A) samples submitted to the post-discharge is evaluated according to the operating conditions: gas composition, treatment time and sample state, i.e. hydrated or dried samples.

1. INTRODUCTION - CONTEXT

Among the possible alternatives to conventional wet heat treatment, non-thermal plasma technologies can be of interest for the purpose of surface decontamination. Such technologies in gases at pressures below atmospheric pressure (less than 10^3 Pa) have been successfully investigated [1] but in this paper, we will only focus on atmospheric pressure non-thermal plasmas obtained by dielectric barrier discharges in various gas mixtures. A surface decontamination process must be compliant with the following requirements: (i) high efficiency, (ii) low degradation of the treated surface, (iii) reasonable investment costs and (iv) low operating costs. The two last items are satisfied by working at atmospheric pressure. Except in the case of the APGD and jet plume [2,3], non-thermal plasma develops in filaments, with high current density, leading to a local degradation of the surface if directly submitted to the discharge. Furthermore, the treatment shall not be homogeneous. In the present work, there is no direct contact between the plasma and the surface and only the discharge products are transferred to the surface, thus avoiding cathodic sputtering. In such a treatment configuration, significant decontamination efficiencies have been obtained with different bacteria strains under different operating conditions. The present study is an attempt to investigate the inactivation mechanisms occurring during the plasma induced treatment of sporulated bacteria. For this purpose, DNA and protein degradation by the plasma process is studied, assuming that (i) inactivation is obtained when the bacteria DNA is fragmented, (ii) the protein coats are the main protection of the cell core DNA in the case of bacteria spores.

2. EXPERIMENTAL

2.1. Non-thermal plasma source

The non-thermal plasma is obtained by dielectric barrier discharges in a co-axial geometry reactor. The high voltage electrode consists of a metallic rod (2 mm diameter) centered in a Pyrex® tube (6 mm and 3 mm external and internal diameters respectively). A 24 mm length

copper tape covers the external surface of the tube and constitutes the grounded electrode. In this device, discharges propagate in the volume between the high voltage electrode and the internal face of the Pyrex® tube delimited in length by the outer grounded electrode. The DBD reactor is energized by an ac high voltage power supply at 28.5 kHz. Biological samples, placed in a separated box, are submitted to the discharge effluent, 3 cm from the tube outlet. Ozone and nitrogen oxides were detected in gas phase using absorption spectroscopy. H_2O_2 was measured in water droplets exposed to the discharge effluents using a spectrophotometric method. These chemical aspects won't be discussed in the paper. More details can be found in [4].

2.2. Bacteria inactivation evaluation

The bacteria were treated in 10 µL distilled water droplets deposited on sterile glass slides. The suspensions contain 2.10^6 bacteria/mL *Bacillus Stearothermophilus* spores (10 µL giving 2.10^4 bacteria). Droplets could be dried or not before treatment. After treatment, the bacteria on each slide are collected in 2 mL of distilled water. The suspensions obtained are serially diluted and then plated out (100 µL) on an agar surface (Petri dish). After incubation, (36h at 56°C), direct colony counting is done.

2.3. Biochemical techniques

Protein and DNA solutions were treated in 10 µL distilled water droplets (containing 10 µg and 1 µg respectively) deposited on sterile glass slides dried or not before treatment. After treatment, protein and DNA samples were collected respectively in 100 µl and 40 µL distilled water volumes.

Proteins were separated according to their molecular weight by electrophoresis (150V, 90 minutes) on sodium dodecyl sulphate-polyacrylamide gel (SDS-PAGE). Prior to electrophoresis, proteins were submitted to a denaturing treatment.

Agarose gel electrophoresis was used to separate DNA molecules according to their molecular weight and 3-D structure. After migration, the agarose gel was treated by ethidium bromide (DNA intercalant agent), allowing visualization of DNA migration bands exposed to UV illumination. In the case of high DNA degradation, a PCR (Polymerase Chain Reaction) was made on the treated samples to detect the presence of residual DNA molecules.

3. RESULTS –DISCUSION

3.1. Bacteria treatment

Using the set-up described in the experimental section, *B. Stearothermophilus* spores were submitted to an air discharge effluent under three different operating conditions: (a) dried spore samples submitted to a wet air discharge effluent (b) liquid spore samples (spores suspended in distilled water) submitted to a dry air discharge effluent (c) dried spore samples submitted to a dry air discharge effluent. Under conditions (a) and (b), the number of survivors was reduced of at least 4 orders of magnitude within 20 minute treatment time whereas the same treatment under conditions (c) led to a population reduction inferior to 90%. From these results, it can be stated that only wet samples (droplets or water film coming from condensation) can be effectively decontaminated using this plasma source. Focusing on the stable oxidative species which can be involved in the inactivation mechanism, two gaseous

products may be considered: ozone and nitrogen oxides (mainly NO_2). The biocidal effect of ozone is well known, and furthermore nitrogen oxide formation in presence of a wet film (or droplets) will lead to an acidification of the solution, through different mechanisms according to the experimental conditions: (i) in gas phase resulting from the OH produced by water dissociation in the discharge (wet air conditions only): $NO_2 + OH \rightarrow HNO_{3\ (g)}$ followed by a dissolution of the HNO_3 into the aqueous phase (Henry constant: 2.1×10^5 M/atm); (ii) in aqueous phase by dissolution of the formed NO_2 (dry and wet air conditions): $2\ NO_2 + H_2O_{\ (l)} \rightarrow HNO_{2\ (aq)} + HNO_{3\ (aq)}$ (Henry constant: 1×10^{-2} M/atm). As a matter of fact, after a 20 minute treatment time of distilled water droplets (pH 6), the pH reached a 1.8 value. Then, under conditions (a) and (b), reactions take place in an acidified liquid phase. This fact should be considered in the following investigations.

3.2. Investigations on DNA

Assuming that bacteria inactivation is obtained if its DNA is irreversibly damaged, a model DNA molecule (plasmid PET9SnI) has been directly submitted to the plasma process. DNA samples were treated with the same operating conditions that led to significant decontamination results on *B. Stearothermophilus* spores (wet samples and dry air discharge). After a 10 minute treatment time, plasmid was no longer detected by electrophoresis gel technique, showing an important degradation / fragmentation of DNA molecules. The same plasmid quantity incubated for 10 minutes in an acidic solution (HNO_3 solution pH 1.8) led to an intact migration band, showing that these pH conditions do not damage DNA molecules. Moreover, when acid formation is prevented by replacing N_2 by argon (no acidification of the wet samples), the migration band disappeared from 2 minute treatment time (Fig. 1 – lanes 6). Nevertheless, a 10 minute treatment time is necessary to obtain a degradation of the total amount of the nucleic acid chains in the sample, as assessed by a negative result of the PCR test. This confirms that oxidative species (O_3 and short lived species) produced by the Ar/O_2 (80/20) discharge are responsible for the DNA degradation.

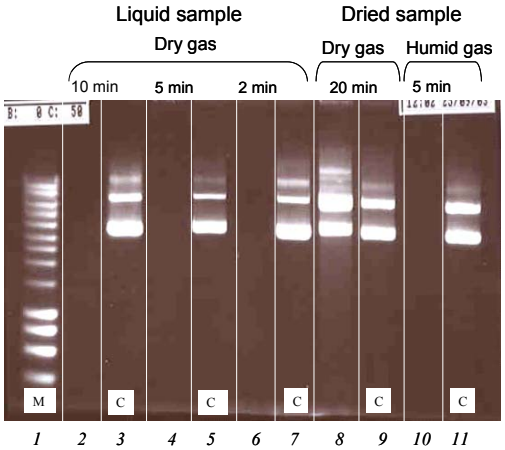

Lane 1: molecular weight marker (M)
Lanes 3, 5, 7, 9, 11: Controls (C)

Liquid sample / dry Ar/O_2 :
Lane 2: 10 minute treatment time
Lane 4: 5 minute treatment time
Lane 6: 2 minute treatment time

Dried sample / dry Ar/O_2 :
Lane 8: 20 minute treatment time

Dried sample / humid Ar/O_2 :
Lane 10: 5 minute treatment time

FIGURE 1. PET9SnI agarose gel electrophoresis of plasmid for different treatments.

Furthermore, the 260 nm absorption band (puric and pyrimidic bases characteristic UV absorption region) exhibited a strong decay correlated with treatment duration, indicating a progressive degradation of DNA bases. The treatment then leads to a fragmentation of the nucleic chain but also to its components (bases) destruction. Figure 1 also shows that, as for spore inactivation, DNA molecules are only significantly damaged when treated in an aqueous phase (droplet solution or condensed liquid film) as illustrated by lanes 8 and 10.

3.3. Investigations on proteins

During bacteria spores treatment, active species must first encounter the protein shell before reaching the DNA molecules in the spore core. The protein chosen to model the protein shell of the spore is the RNAse A. Investigations on the protein were only made on liquid samples and SDS-PAGE migration bands are shown in Figure 2. As for DNA, the incubation of proteins in an acidic solution (pH 1.8) (Figure 2 - lanes 5 and 6) didn't lead to degradation. Moreover, the same weak intensity migration bands were obtained after treatment whether in acidification conditions (air discharge lanes 2 and 4) or in Ar/O_2 conditions (lanes 7 and 8). It can then be stated that acid has a minor role in degradation mechanisms.

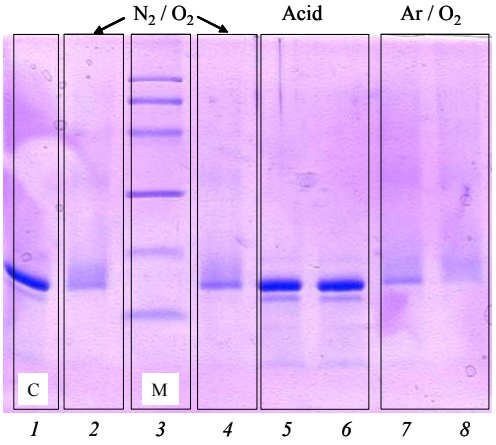

Lane 1: Control

Lane 3: molecular weight marker

Lane 2&4: N_2/O_2 discharge treatment

Lanes 5&6: Acid control

Lanes 7&8: Ar/O_2 discharge treatment

FIGURE 2. RNAse A SDS-PAGE for different treatments.

4. CONCLUSION

Degradation of macromolecules such as DNA and proteins, as well as bacteria spore inactivation require wet conditions at least on the sample. For bacteria spore inactivation, the association of acid with oxidizing species is needed whereas DNA and protein degradation only require oxidizing agents. It appears that mechanisms leading to the permeation of the protein shell of the spore are quite more complex than for the degradation of a simple model protein. Note that the pH dependence of the bacteria inactivation is specific to spores, since vegetative bacteria (e. g. *E. Coli*) can be inactivated under non acidic condition [5].

REFERENCES

[1] Villeger, S.; Cousty, S.; Ricard, A.; Sixou, M. (2003) Sterilization of E. Coli bacterium in a flowing N2-O2 post-discharge reactor, *J. Phys. D: Applied Phys*, 36, 60-62.

[2] Laroussi, M.; Alexeff, I.; Kang, L. (2000) Biological decontamination by non-thermal plasma, *IEEE trans. on Plasma Science*, 28-1, 184-188.

[3] Stoffels, E.; Flikweert, A. J.; Stoffels, W.; Wand Kroesen, G. M.W. (2002) *Plasma Sources Sci. Technol*. 11, 383.

[4] Dodet, B.; Odic, E.; Goldman, A.; Goldman, M.; Renard, D. (2005) Hydrogen Peroxide Formation by Discharges in Argon/Water Vapor Mixtures at Atmospheric Pressure *J. Adv. Oxid. Technol.*, 8-1, 91-97.

[5] Kirkpatrick, M. J.; Dodet, B.; Odic, E. (2006) Atmospheric Pressure Humid Argon DBD Plasma for the Application of Sterilization - Measurement and Simulation of Hydrogen, Oxygen, and Hydrogen Peroxide Formation, *5th Intern. Symp. on Non-Thermal Plasma technology for Pollution Control*, Oléron, France, paper 2C1.

SAGA SYNCHROTRON LIGHT AND ITS APPLICATION FOR ADVANCED SCIENCE/TECHNOLOGY AND REGIONAL DEVELOPEMENT

M. Kamada, K. Takahashi, J. Azuma, H. Sugiyama, S. Tokudomi, T. Tanaka, and H. Ogawa

Synchrotron Light Application Center,
Saga University
1 Honjo, 840-8502, JAPAN

ABSTRACT. Synchrotron Light (SL) source and beamlines have been constructed in Saga and are ready for users to conduct advanced science and technology. New frontier fields such as non-thermal process and advanced analyses on semiconductor surfaces will be promoted. The variety of SL applications is expected to activate and encourage the regional development as well.

1. INTRODUCTION

Since Synchrotron Light (SL) has many useful characteristics such as wide photon energy range from far-infrared to x-rays, high flux, high brilliance, small divergence, cleanness, polarization, short pulse, and so on, it is a powerful and promising tool for nano-technology, bio-technology, material engineering, environmental applications, and other future technologies and science. The Saga-SL, the first synchrotron light facility in Kyushu Island, has been constructed in Tosu city by Saga prefectural government. The accelerator complexes are consisted of a 250 MeV linac and an accelerator/storage ring, which have passed the inspection by the national government on December 15, 2005. The open ceremony and the memorial symposium have been held on February 17 and March 7 in 2006, respectively. The Saga-ring has the circumstance of 75.6 m, the storage electron energy of 1.4 GeV and the emittance of 25.5 nm-rad. The critical photon energy from bending magnets is about 1.9 KeV, while a wiggler of 5 T can provide hard x-rays with the critical energy of about 6.5 KeV. From the comparison with the spectral distribution of Spring-8 that is the biggest storage ring for SL in the world, the photon flux of Saga-LS is comparable with that of Spring-8 in the soft x-ray regions. The Saga-LS is therefore expected to be useful for wide variety of advanced science and technology applications as well as future developments in the Saga-Kyushu area.

2. BACKGROUND OF SAGA SYNCHROTRON LIGHT PROJECT

The Saga synchrotron light project has been planned and promoted by the close relation between Saga University and Saga Prefecture Government with supports from the Japanese National Government. There are several purposes of the Saga synchrotron light project. The first is the industrial application of SL. The second is to create a key station for collaboration of industry, academia and government. We expect to enhance and create new regional industries from the excellent center in Asia for advanced science and technology. The third

aim is to congregation of excellent talent and brains for world-class research and education. We expect to grow up many young persons' capability for future science and technology. We will also educate many public persons to have essential understanding of science and technology. Our intelligent synchrotron light center is based on the collaboration of many universities and Saga Prefecture Government, and the close collaboration between the Kyushu Synchrotron Light Research Center belonging to the Saga Prefecture Government and the Synchrotron Light Application Center of Saga University plays an important role. We have also good collaborations with domestic and foreign universities, and also partnerships with synchrotron light facilities in the world. We hope to create venture companies from the partnership with facilities in Saga university such as Venture Business Laboratory.

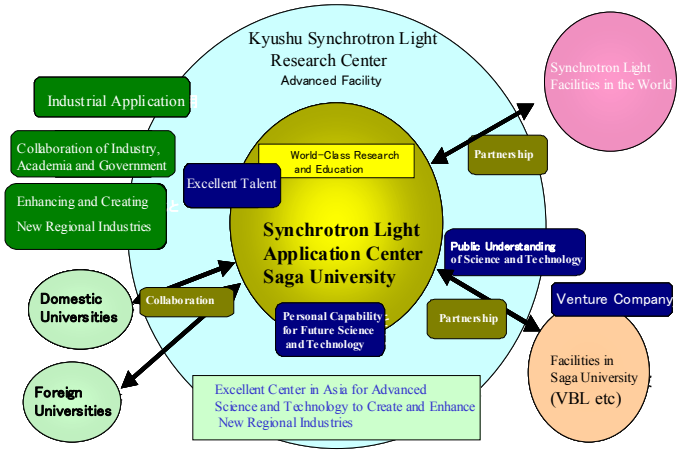

Intelligent Synchrotron Light Center Based on Collaboration
of National University and Prefecture Government

FIGURE 1. Schematic picture showing Saga synchrotron light project

3. BEAMLINES AND SL APPLICATIONS

3.1. Open Beamlines

There are three prefecture open beamlines and one university's beamline, which are ready for uses from industries, universities, and institutes, which may activate and encourage the regional development. One of the important roles of the open beamlines in Saga is to promote local developments and create new industries with using SL.

The beamline BL9 aims applications for material development. The Vacuum Ultra-Violet photons monochromatized with a Seya-Namioka monochromator, SL through a Be window, or SL introduced by two focusing mirrors can be used for irradiation to Chemical Vapor Deposition, so-called LIGA technology to micro-fabrication, and so on. The BL12 is used for soft x-rays applications to precise analyses. It is important in the industry application and advanced technology to analyze the electronic states and structures of new materials, the oxidation of semiconductor surfaces, the degradation of the organic compounds and so on. Therefore, the soft x-rays beamline BL12 makes it possible to measure X-ray Photoelectron Spectroscopy (XPS) and X-ray Absorption Fine Structure (XAFS) in solids and surfaces of many materials used in industries.

The BL12 working group has been organized three and a half years ago, consisting of active users from universities and companies. The performance requested from the users and the prefecture government is to achieve the wide energy range covering from 40 to 1,000 eV with medium resolution for XPS and XAFS measurements. The design ideas of the monochromator system are fully depending on the Synchrotron Light Application Center, Saga University. The XPS and XAFS analyzing system at the end station involves requirements and ideas from the working group.

The BL15 aims to use hard x-rays for various applications. The photons in the energy range from 2.1 to 14 KeV can be provided using a double crystal monochromator with Si crystals. Various measurements such as XAFS, diffraction, fluorescence, small-angle scattering, and imaging analyses can be conducted in this beamline.

3.2. University's Beamline

The Synchrotron Light Application Center of Saga University is interested in the new frontier fields such as non-thermal process and photo-CVD, advanced surface analyses, creation of combination system between semiconductors and bio-specimens, basic and application in environmental and material science, and so on. The center is also interested in the industrial application with SL as well. The useful and powerful methods with SL may produce wide variety of applications. Besides the open beamlines, Saga University has therefore constructed a soft x-rays beamline for advanced researches on nano-surface and interface of semiconductors as well as education.

There are two branches; the one is highly precisely adjusted for undulator radiation that is very intense as shown in Fig. 2, while another is constructed to use SL from a bending magnet. The plane view of the beamline is shown in Fig. 3. SL as well as laser can be used in these beamlines and the various combination experiments using SL and laser are expected. The schematic optical arrangement of the beamline is shown in Fig. 4, where the conceptual figure for the combinational experiment is also shown. This February the surface photo-voltage effect was observed in the university beamline, namely the Ga-3d photoelectron peak of GaAs was shifted clearly depending on the laser illumination. This study is expected to be applied for the investigation of the solar cells and electron emitters as well. Besides this beamline, the Saga University is proposing to construct other beamlines for semiconductor technology, protein engineering, environmental technology, material development, medical applications and so on.

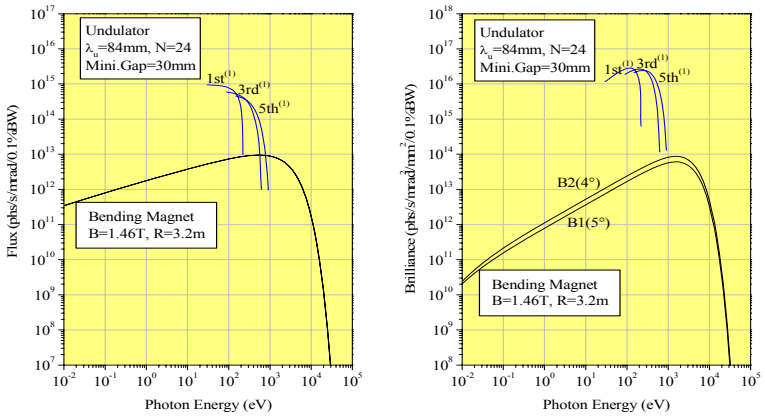

FIGURE 2. Photon flux and brilliance of SL from a planar undulator.

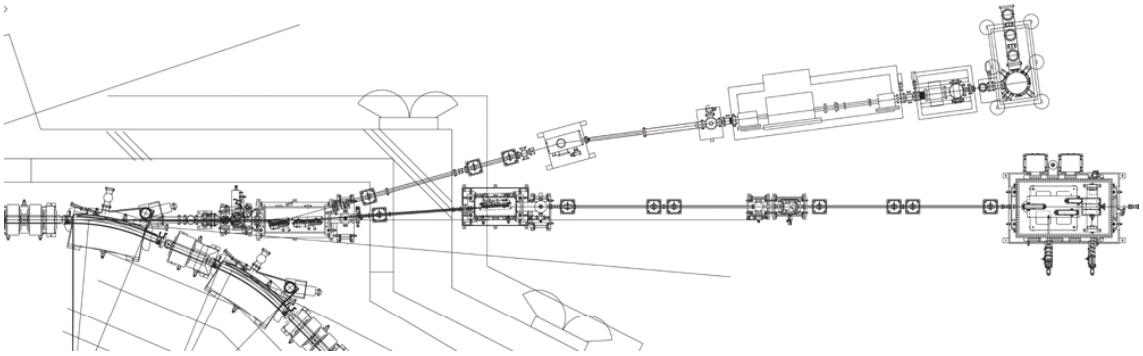

FIGURE 3. Plane view of the university beamline.

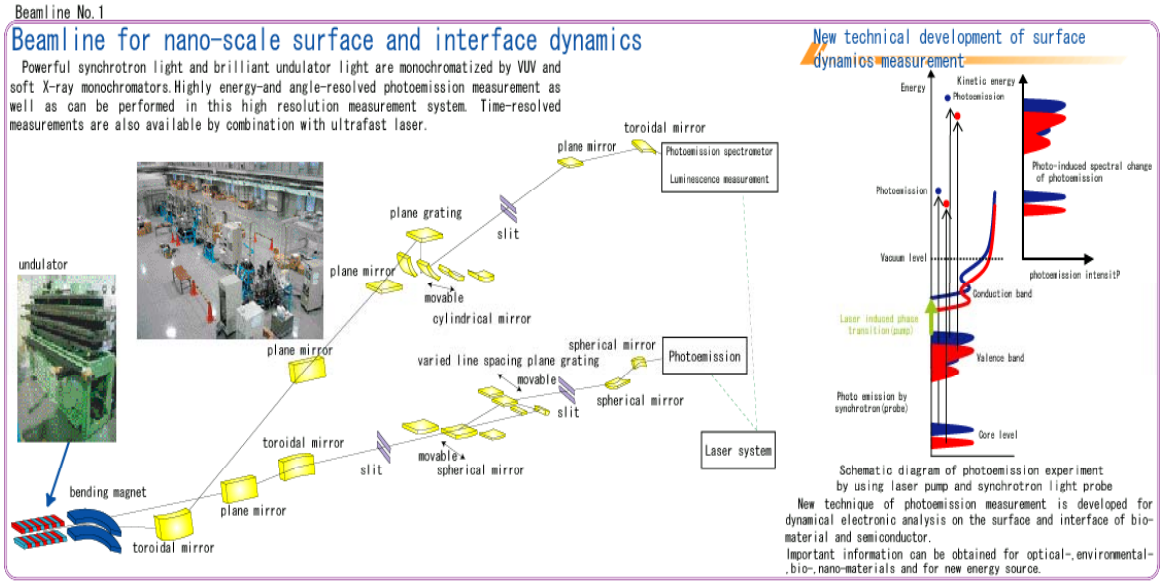

FIGURE 4. Schematic illustration of the university beamline. The conceptual figure for combinational experiments using SL and laser is also given.

ACKNOWLEDGMENTS

We would like to thank many scientists and engineers working in the existing synchrotron radiation facilities, universities, and companies for their kind and useful information about recent SL-related technologies.

REFERENCES

[1] Y. Kondo, J. Azuma, K. Takahashi, and M. Kamada, Proc.of 8th Int. Conf. on Synchrotron Radiation Instrumentation (2004) 627.
[2] M. Kamada et al. Proc. of Synchrotron Radiation Instrumentation 2006.
[3] K. Takahashi et al. Proc. of Synchrotron Radiation Instrumentation 2006.

number

HOW DO WE PREPARE CROSS SECTION SETS FOR MOLECULES FROM ELECTRON SWARM DATA?

Y. Nakamura

Department of Electrical and Electronics Engineering,
Faculty of Science and Technology, Keio University
3-14-1 Hiyoshi, Yokohama, 223-8522, JAPAN

ABSTRACT. Theoretical and experimental developments in the study on electron swarms in gases and sharp increase in PC power have made the so-called electron swarm study a reliable and realistic means for determining electron collision cross sections for atoms and molecules. The use of swarm parameters measured in dilute molecular gas mixtures with rare gas adds a new possibility to current swarm study. It can determine a set of electron collision cross sections for a molecule in low-energy range which is relevant to high-pressure plasma studies in particular.

1. INTRODUCTION

In order to understand the properties of weakly ionized plasmas in terms of electron collision cross sections for atoms and molecules, it is important to construct detailed models of the plasmas. And in order that the simulations based on these models are to have any reality, a whole set of cross sections for the elastic and inelastic collisions of electrons with atoms and molecules in the gas mixture must be accurate. Unfortunately many of the cross sections for molecules used in the current plasma technologies are not known and the need for a quantitative understanding of these plasmas put increasing demands on the availability and reliability of related cross sections in the range of low energies. Recent development in high pressure and low temperature plasmas will certainly increase demands on low energy cross section data for molecules, in particular rotational and vibrational excitation cross sections.

The nitrogen molecule, for example, is the most popular ambient gas and one of the most thoroughly studied molecules, but its rotational excitation cross sections are still not very well established [1]. Electron impact dissociation process commences at about 40 Td and because of efficient R-T process neutral gas heating occurs only through the rotational excitation by electron collisions in low *E/N*. The rotational excitation cross section in the resonance energy range is especially important [2].

2. ELECTRON SWARM STUDY USING RARE GAS-MOLECULAR GAS MIXTURES

When a small amount of molecular gas, say a few percent or less, is mixed into rare gas with the Ramsauer minimum (Ar for example), the electron swarm parameters in the mixture are greatly changed from those in pure rare gas. The electron drift velocity, for example, is usually increased by more than an order of magnitude in a narrow *E/N* region, and this brings about decrease in drift velocity in the higher *E/N* (the negative differential conductivity, NDC). The vibrational excitation cross section of the most molecules has a very sharp

threshold peak and this sharp inelastic cross section constricts the electron energy distribution function and results in the enhancement [3]. Some molecules have a resonance peak in higher energy range and this brings about another enhancement at higher *E/N* [4]. Because of the low concentration of the molecules in the mixture, the elastic momentum transfer cross section of the molecule will play only minor roles in the electron swarm parameters: this will be supported by the fact that the swarm parameters in the mixture are approaching to those in the pure rare gas in higher *E/N*.

This is the principle of our electron swarm study for determining the electron collision cross section set for the molecule by using electron swarm parameters measured in the dilute mixtures of the molecule with the Ramsauer gas as well as in the pure molecular gas. The principle consists of the following three steps [3].

Step 1: Modification of inelastic (vibrational excitation) cross sections in order that the calculated swarm parameters in the mixtures agree with the experimental data.

Step 2: Modification of the elastic momentum transfer cross section of the molecule so that the calculated swarm parameters in pure molecular gas agree with those measured, when the inelastic cross sections determined in Step 1.

Step 3: Modification of the electron attachment and electronic excitation cross sections for the molecule in order that the calculated and measured attachment and ionization coefficients agree.

Following these three steps we can determine a set of cross sections for the molecule, which is consistent with a number of electron swarm parameters in gases containing the molecule. The principle seems straightforward but it still demands weeks or even months of laborious trial-and-error modifications of cross sections.

3. TOOLS FOR EFFICIENT SWARM STUDY

We developed a Windows application for efficient determination of a set of cross sections from measured electron swarm parameters [5]. Figure 1 shows an example of the picture on the computer display. The picture consists of menu and tool bars and a view window. On the view window of the example there are four graphs: the cross section set, the drift velocity (the crosses, experimental), the product of the gas number density and the longitudinal diffusion coefficient(the crosses, experimental), and the percentage deviation between the experimental and computed drift velocity, clockwise from the top left. Any red cross section data points can be altered by mouse drag, and the effect of this cross section modification on the swarm parameters can be indicated on the remaining graphs in a few seconds by clicking a button in the tool bar. The Boltzmann two-term approximation is used in this application. The calculated electron energy distribution function can be shown on the cross section graph by a left-click at any calculated swarm data point. Overlap between the energy distribution function and the cross section indicates the possible energy range for modification.

A prototype of this application was constructed in 1994 [6], when, however, the PC power was not powerful enough. Now this application serves as a very powerful and efficient tool for our electron swarm study thanks to the recent PC power development. It also serves as an effective educational tool to understand the relationship between the microscopic collision processes and the macroscopic electron transports through gases by observing electron collision cross sections, energy distribution functions and electron swarm parameters on the same view window.

The Boltzmann code including the super-elastic collisions is now used in the newer version.

The Windows application explained so far is very effective but it still cannot solve an inherent problem of the reverse problems; the cross section uniqueness. The optimization algorithm is an alternative approach to the problem and Morgan et al [7] applies the simplex algorism to the electron swarm study. Hasegawa [8] found that successive application of simulated annealing and simplex algorisms improve speed and accuracy of the swarm study. We are continuing to develop another application using the optimization algorithms and the principle explained in the previous section.

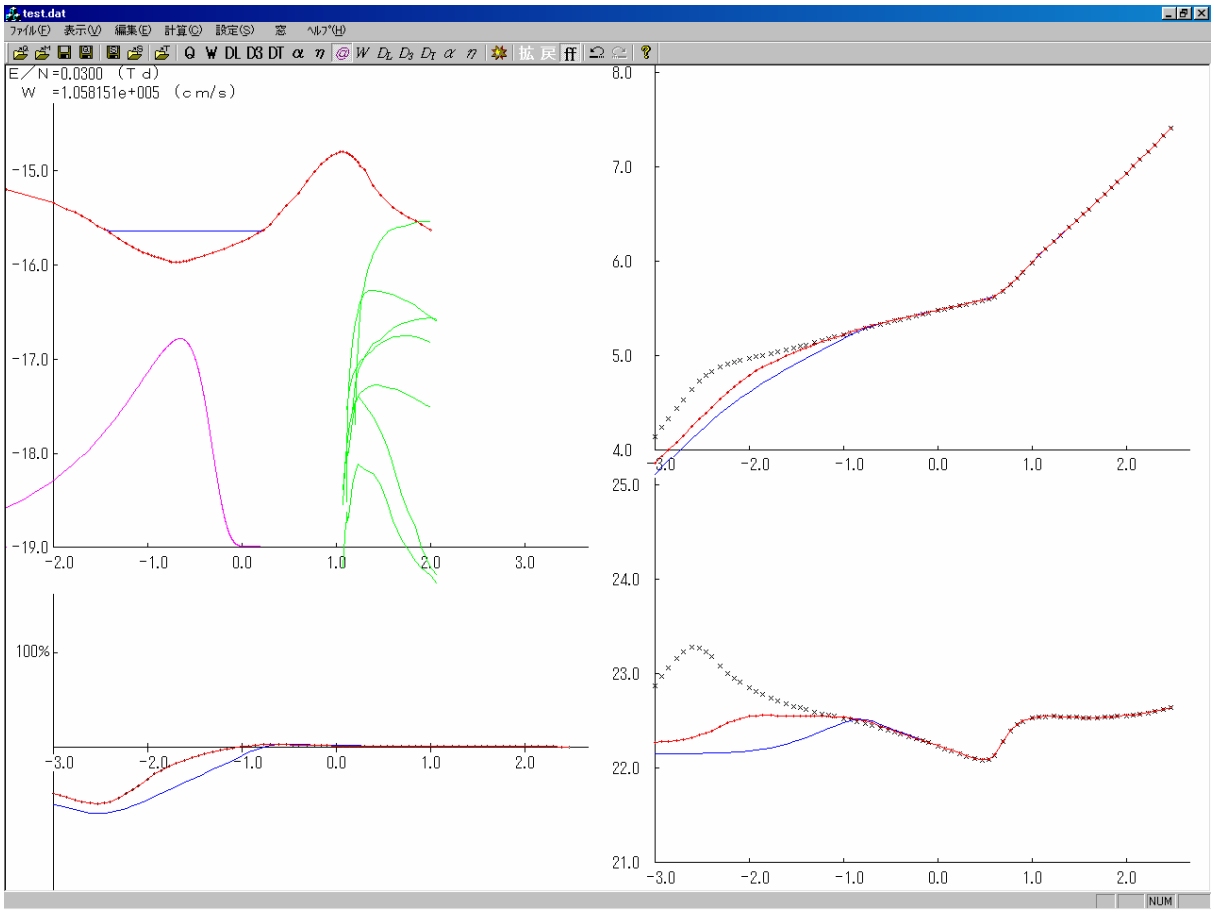

FIGURE 1. An example of the picture on the computer display of the application.

4. REFERENCE DATA AND CROSS SECTION DATA ACCUMULATED BY THE DECEASED PROFESSOR M. HAYASHI

The late Professor Makoto Hayashi collected and left a huge amount of reference data concerning about 70 atoms and molecules published in the 20th century. They are;

He, Ne, Ar [9], Kr, Xe [13], F, O, Li, Na, K, Rb, Cs, Cu, Hg, Cd, Ba, F_2 [14], Cl_2 [14], Br_2 [14], I_2 [14], H_2 [16], N_2 [12], O_2, CO, NO, HF [17], HCl [17], HBr [17], HI [17], O_3, CO_2 [10], COS, CS_2, H_2O [15], SO_2, NO_2, N_2O, H_2S, C_2H_2, H_2CO, NF_3, NH_3 [18], PH_3 [18], BCl_3, BF_3, CCl_4, CF_4, CH_4 [19], GeH_4, CH_3Br, CH_3Cl, CF_3Cl, CCl_2F_2, SiF_4, SiH_4, CH_3OH, C_2H_4, SF_6 [11], C_2F_6, C_2H_6, Si_2H_6, C_3H_6, C_2H_5OH, C_3F_8, C_3H_8, C_3H_7OH, C_6F_6, C_6H_6, c-C_4F_8, C_{60}.

The data concerning to only 18 out of 70 atoms and molecules were published from NIFS, but all the rest are left intact. The Investigating R&D Committee on Electron Interaction with

Atoms, Molecules, and Photons, IEE of Japan (Chairman, Prof. H. Itoh) is now transferring data into DOS-V format. The data will be published on the web through NIFS.

5. CONCLUSION

Deriving electron collision cross sections from electron swarm data, the electron swarm study, and the electron beam study are complementary each other. Advances in theory and experiment on electron swarm and in computer made the electron swarm study realistic and reliable.

REFERENCES

[1] Robertson, A.G. et al (1997). Rotational and vibrational excitation of nitrogen by electron impact. *Aust. J. Phys.*, 50, 441-472.
[2] Phelps, A.V., Pitchford, L.C. (1985). Anisotropic scattering of electrons by N_2 and its effect on electron transport. *Phys. Rev. A*, 2932-2949.
[3] Shishikura Y. et al (1997). Low-energy electron collision cross sections of ethane by electron swarm study. *J. Phys. D*, 30, 1610-1615.
[4] Kurachi, M., Nakamura, Y. (1988). Electron swarm parameters in SiH_4-Ar mixtures. J. Phys. D, 21, 602-606.
[5] The Investigating R&D Committee (2001). Dynamics of low energy electrons and ions and simulations II. *Technical Report of IEE of Japan*, No. 853
[6] Asano, K. (1994). Report of Final Year Project, Department of Electrical Engineering, Keio University
[7] Morgan, W.L. (1991). Use of numerical optimization algorithms to obtain cross sections from electron swarm data. Phys. Rev. A, 44, 1677-1681.
[8] Hasegawa, H. (2001). Study on application of numerical optimization algorithms on electron swarm study, Master's thesis, Keio University
[9] Hayashi, M. (2003). Bibliography of electron and photon cross sections with atoms and molecules published in the 20th century -Ar-. NIFS-DATA-72.
[10] Hayashi, M. (2003). Bibliography of electron and photon cross sections with atoms and molecules published in the 20th century –Carbon Dioxide-. NIFS-DATA-74.
[11] Hayashi, M. (2003). Bibliography of electron and photon cross sections with atoms and molecules published in the 20th century –Sulfer Hexafluoride-. NIFS-DATA-76.
[12] Hayashi, M. (2003). Bibliography of electron and photon cross sections with atoms and molecules published in the 20th century –Nitrogen Molecule-. NIFS-DATA-77.
[13] Hayashi, M. (2003). Bibliography of electron and photon cross sections with atoms and molecules published in the 20th century -Xenon-. NIFS-DATA-79.
[14] Hayashi, M. (2003). Bibliography of electron and photon cross sections with atoms and molecules published in the 20th century –Halogen Molecules-. NIFS-DATA-80.
[15] Hayashi, M. (2003). Bibliography of electron and photon cross sections with atoms and molecules published in the 20th century –Water Vapour-. NIFS-DATA-81.
[16] Hayashi, M. (2004). Bibliography of electron and photon cross sections with atoms and molecules published in the 20th century –Hydrogen molecules-. NIFS-DATA-82.
[17] Hayashi, M. (2004). Bibliography of electron and photon cross sections with atoms and molecules published in the 20th century –Hydrogen Halide Molecules-. NIFS-DATA-83.
[18] Hayashi, M. (2004). Bibliography of electron and photon cross sections with atoms and molecules published in the 20th century –Ammonia and Phosphin-. NIFS-DATA-87.
[19] Hayashi, M. (2004). Bibliography of electron and photon cross sections with atoms and molecules published in the 20th century -Methane-. NIFS-DATA-90.

20 YEARS OF HAKONE: FROM BASIC PLASMA CHEMISTRY TO BILLION DOLLAR MARKETS

U. Kogelschatz[1]

Retired from ABB Corporate Research, Baden, SWITZERLAND

Obere Parkstr. 8, 5212 Hausen, SWITZERLAND

ABSTRACT. The progress of atmospheric-pressure non-thermal plasma technology since the first HAKONE symposium in 1987 is summarized. Advances in the fundamental understanding of the discharge physics of corona and dielectric-barrier discharges led to a number of technical developments that resulted in improved industrial processes and novel products: improved ozone generation and advanced surface treatment, pollution control, silent discharge-driven SD CO_2 lasers, excimer-based ultraviolet sources and fluorescent lamps, and flat large-area plasma display panels (PDPs) using vacuum ultraviolet radiation from Xe_2^* excimers. The newly established markets surpass the original market of ozone generators by two orders of magnitude.

1. INTRODUCTION

The first meeting on High Pressure Low temperature Plasma Chemistry at Hakone (HAKONE I) in 1987 was mainly devoted to fundamental aspects of O_3 and NO_x formation in dielectric-barrier discharges (DBDs) and in corona discharges. Since then substantial progress has been made in the understanding and also in the numerical modeling of atmospheric-pressure non-equilibrium discharges. This resulted in improved industrial ozone generation and in a number of novel applications: Silent discharge-driven SD CO_2 lasers [1], excimer-based UV (ultraviolet) sources and fluorescent lamps [2], and flat large-area plasma display panels (PDPs) using VUV (vacuum ultraviolet) radiation from Xe_2^* excimers [3, 4]. Additional large-scale applications are evolving in pollution control devices [5] and for the treatment of surfaces, fibers, fabrics and powders. Recent investigations concentrate on biomedical applications including biological funtionalization and the sterilization and decontamination of surfaces. New types of corona discharges were developed in the form of pulsed streamer coronas that find applications in pollution control. More recently different types of miniature discharges in spatially confined geometries (microplasmas) gained considerable attention in the research community. They will find important industrial applications as well [6].

2. DISCHARGE PHYSICS

Non-equilibrium discharges at atmospheric pressure are characterized by high electron temperatures (10^4 -10^5 K) and low gas temperatures, in many cases close to room temperature. Most of the energy taken up by the electrons in the electric field is used for the production reactive species rather than for gas heating. This way fast chemical reactions can be initiated.

[1] Electronic address: u.kogelschatz@bluewin.ch

Atmospheric pressure operation has the advantage of high collision rates but is always endangered by spark or arc formation, which would lead to high gas temperatures. In dc corona discharges spark formation is prevented by confining the active ionization region to a minute region close to the specially shaped active electrode, in pulsed corona discharges by limiting the pulse duration. In dielectric-barrier discharges the dielectric barrier limits the transferred charge und thus prevents spark formation. At the time of HAKONE I it was known that the current in most DBDs at atmospheric pressure consists of many short-lived thin current filaments, called microdischarges. Through the pioneering work of S. Okazaki and her group at Sophia University in Tokyo [7] it was demonstrated that also apparently homogeneous discharges referred to as APGs (**A**tmospheric **P**ressure **G**low discharges) can be obtained in DBD configurations. Later, mainly through the work of F. Massines and her group at the University of Toulouse [8], it became apparent that these homogenous or diffuse DBDs can take the form of either a glow discharge or a more Townsend like discharge (APT). Also intermediate forms exhibiting self-organized regular (glow) discharge patterns have been obtained [9]. In the mean time many additional groups have entered the field and extensive experimental and theoretical studies have been carried out concerning the structure of DBDs in different gases, different electrode configurations and under various operating conditions. Much of the very extensive literature on the subject is reviewed in a recent book on *Non-Equilibrium Air Plasmas at Atmospheric Pressure* [10] and in several review articles [11,12,13,14].

Recently experimental details of individual microdischarges in DBDs with unprecedented spatial and temporal resolution were obtained by cross-correlation spectroscopy [15, 16], and also the interaction of adjacent microdischarges was investigated [17]. Advanced diagnostics was also applied to an electrode configuration combing ac corona and DBD features [18].

As far as the DBD electrode configuration is concerned the important contribution of S. Masuda and his group at the University of Tokyo by introducing surface discharges should be mentioned [19]. In a slightly modified version, referred to as coplanar DBD configuration, surface discharges are now widely used in plasma display panels, in compact ozone generators and for surface treatment.

As far as the theoretical description of DBDs is concerned two-dimenional modeling of microdischarges has been refined over the years [20, 21, 22, 4] and new models for homogeneous discharges were developed [23,24,25,26]. Also the numerical modeling of surface discharges has progressed [21,27,28].

3. PLASMA CHEMISTRY

In air the major active species produced by the discharge are $O_2^*(a^1\Delta_g)$, $O(^1D)$, $O(^3P)$, $N_2^*(A^3\Sigma_u^+)$, $N_2^*(B^3\Pi_g)$, and $N(^4S)$. If humidity is present important additional highly reactive species are formed: H, OH or HO_2. Reactions of these species have been studied extensively with respect to ozone formation, NO_x chemistry and pollution control. Many investigations have also been performed in rare gases and rare gas/halogen mixtures. Here the main aim was to understand and optimize the formation of excimers (excited dimers) that can be used in lamps and displays. The interaction of discharge born reactive species with surfaces and with precursors that can result in surface coatings is an additional field of current interest. When particles are formed or injected fast reactions with photons or electrons can be initiated in addition to reactions with active species [29].

4. APPLICATIONS AND MARKETS

DBDs and corona discharges have found many applications. Industrial ozone production, based on dry air or oxygen as a feed gas, has found new applications in pulp bleaching in addition to its classical use in water treatment. The wide spread "corona treatment" of polymer foils and other plastic parts today is mainly achieved with DBD configurations. In addition to adhesion and wettability enhancement new applications are evolving: etching, roughness control, thin film deposition, sterilization, bio-decontamination, functionalization for biological and medical applications. It has been shown that a uniform surface treatment can be achieved in homogeneous as well as in filamentary DBDs. Considerable progress with respect to specific power consumption in pollution control has been made with pulsed coronas and with DBDs. Rather large pilot facilities are under construction [5]. Excimer formation in DBDs found a number of novel applications in strong VUV and UV sources, as well in mercury-free fluorescent lamps and thin flat backlighting screens for LCDs (liquid crystal displays) [2,3,30]. The most surprising development was the market introduction of large flat plasma displays in which each pixel point is a miniature excimer-based fluorescent lamp with an internal phosphor coating. Production started in Miyasaki/Japan in 1996, 30 years after the invention of the plasma display by Donald Bitzer and Hiram Slottow [31]. Later, production facilities were also established in South Korea, Taiwan, Shanghai. Last year (2005) more than 7 million PDPs were sold, with a world market of 25 million panels anticipated by 2010. This market by far exceeds that of all other DBD applications.

REFERENCES

[1] Yagi, S., Kuzumoto, M., Nitta, T. (1989). Silent-discharge excited CO_2 laser, *Denshi Tokyo,* 28, 39-42.

[2] Kogelschatz, U. (2004). Excimer Lamps: History, discharge physics, and industrial applications, *Proc. SPIE,* 5483, 272-286.

[3] Kogelschatz, U., Eliasson, B., Egli, W. (1999). From ozone generators to flat television screens: History and future potential of dielectric barrier discharges, *Pure Appl. Chem.,* 71, 1819-1828.

[4] Boeuf, J.-P. (2003). Plasma display panels: physics, recent developments and key issues, *J. Phys. D: Appl Phys.,* 36, R53–R79.

[5] Kim, H.-H. (2004). Nonthermal plasma processing for air-pollution control: A historical review, current issues and future prospects, *Plasma Process. Polym.,* 1, 91-110.

[6] Becker, K.H., Schoenbach, K.H., Eden, J.G. (2006). Microplasmas and applications. *J. Phys. D: Appl. Phys.,* 39, R55-R70.

[7] Kanazawa S., Kogoma, M., Moriwaki, T., Okazaki, S. (1988). Stable glow at atmospheric pressure. *J. Phys. D: Appl. Phys.,* 21, 838–840.

[8] Massines, F., Rabehi, A., Decomps, P., Gadri, R.B., Ségur, P., Mayoux, C. (1998). Experimental and theoretical study of a glow discharge at atmospheric pressure controled by a dielectric barrier. *J. Appl. Phys.,* 83, 2950-2957.

[9] Breazeal, W., Flynn, K.M., Gwinn, E.G. (1995). Static and dynamic two-dimensional patterns in self-extinguishing discharge avalanches. *Phys. Rev.,* E52, 1503-1515.

[10] Becker, K.H., Kogelschatz, U., Schoenbach, K.H., Barker, R.J., Eds. (2004). *Non-Equilibrium Air Plasmas at Atmospheric Pressure* , Institute of Physics Publishing, Bristol, UK (now distributed by Taylor & Francis, CRC Press).

[11] Kogelschatz, U. (2002). Filamentary, patterned, and diffuse barrier discharges, *IEEE Trans. Plasma Sci.,* 30, 1400-1408.

[12] Kogelschatz, U. (2003). Dielectric-barrier discharges: Their history, discharge physics

and industrial applications, *Plasma Chem. Plasma Process.,* 23, 1–46.
[13] Wagner, H.-E., Brandenburg, R., Kozlov, K.V., Sonnenfeld, A., Michel, P., Behnke, J.F. (2003), The barrier discharge: basic properties and applications to surface treatment, *Vacuum,* 71, 417–436.
[14] Fridman, A., Chirokov, A., Gutsol, A. (2005). Non-thermal atmospheric pressure discharges, *J. Phys. D: Appl. Phys.,* 38, R1–R24.
[15] Kozlov, K.V., Wagner, H.-E., Brandenburg, R., Michel, P. (2001). Spatio-temporally resolved spectroscopic diagnostics of the barrier discharge in air at atmospheric pressure, *J. Phys. D: Appl. Phys.,* 34, 3164-3176.
[16] Kozlov, K.V., Brandenburg, R., Wagner, H.-E., Morozov, A.M., Michel, P. (2005). Investigation of the filamentary and diffuse mode of barrier discharges in N_2/O_2 mixtures at atmospheric pressure by cross-correlation spectroscopy, *J. Phys. D: Appl. Phys.,* 38, 518–529.
[17] Chirokov, A., Gutsol, A., Fridman, A., Sieber, K., Grace, J., Robinson, K. (2004). Analysis of two-dimensional microdischarge distribution in dielectric-barrier discharges**,** *Plasma Sources Sci. Technol.,* 13, 623–635.
[18] Radu, I., Bartnikas, R., Wertheimer, M.R. (2003). Dielectric barrier discharges in helium at atmospheric pressure: experiments and model in the needle-plane geometry, *J. Phys. D: Appl. Phys.,* 36, 1284–1291.
[19] Masuda, S., Akutsu, K., Kuroda, M., Awatsu, Y., Shibuya, Y. (1988). A ceramic-based ozonizer using high-frequency discharge, *IEEE Trans. Ind. Appl.,* 24, 223-231.
[20] Gibalov, V.I. Pietsch, G. (1994). Simulation of the formation and development of a microdischarge channel, *Russ. J. Phys. Chem.,* 68, 839–846.
[21] Gibalov, V.I., Pietsch, G.J. (2000). The development of dielectric barrier discharges in gas gaps and on surfaces, *J. Phys. D: Appl. Phys.,* 33, 2618–2636.
[22] Steinle, G., Neundorf, D., Hiller, W., Pietralla, M. (1999). Two-dimensional simulation of filaments in barrier discharges, *J. Phys. D: Appl. Phys.,* 32, 1350–1356.
[23] Tochikubo, F., Chiba, T., Watanabe, T. (1999)**.** Structure of low-frequency helium glow discharge at atmospheric pressure between parallel plate dielectric electrodes, *Jpn. J. Appl. Phys.*, 38, Part 1, 5244-5250.
[24] Massines, F., Ségur, P., Gherardi, N., Kamphan, C., Ricard, A. (2003). Physics and chemistry in a glow dielectric barrier discharge at atmospheric pressure: diagnostics and modelling, *Surface Coat. Technol.,* 174-175, 8–14.
[25] Golubovskii, Yu.B., Maiorov, V.A., Behnke, J., Behnke, J.F. (2003). Modelling of the homogeneous barrier discharge in helium at atmospheric pressure, *J. Phys. D: Appl. Phys.,* 36, 39–49.
[26] Golubovskii, Yu.B, Maiorov, V.A., Li, P., Lindmayer, M. (2006). Effect of the barrier material in a Townsend barrier discharge in nitrogen at atmospheric pressure, *J. Phys. D: Appl. Phys.,* 39, 1574-1583.
[27] Gibalov, V.I., Pietsch, G.J. (2004). Dynamics of dielectric barrier discharges in coplanar arrangements, *J. Phys. D: Appl. Phys.,* 37, 2082–2092.
[28] Gibalov, V.I., Pietsch, G.J. (2004). Properties of of dielectric barrier discharges in extended coplanar electrode systems, *J. Phys. D: Appl. Phys.,* 37, 2093-2100.
[29] Borra, J.-P. (2006). Nucleation and aerosol processing in atmospheric pressure electrical discharges: powders production, coatings and filtration, *J. Phys. D: Appl. Phys.,* 39, R19–R54.
[30] Park, H.-B., Lee, S.-E., Kim, G.J., Lee, Y.D., Choi, K.C. (2006). Effect of dual coplanar electrodes on mercury-free flat fluorescent lamps for liquid crystal display, *J. Display Technol*. 2, 60 – 67.
[31] Bitzer, D.L., Slottow, H.G. (1966). The plasma display panel - a digitally addressable display with inherent memory, *AFIPS Conf. Proc.,* 29, 541-547.

HIGH FREQUENCY DISCHARGE IN Ar/O_2 MIXTURE

M. Laan[1a], J. Raud[1] and J. Aarik[2]

[1] *University of Tartu, Institute of Experimental Physics and Technology, Tähe 4, 51010, Tartu, ESTONIA*
[2] *University of Tartu, Institute of Physics, Riia 142, 51014, Tartu, ESTONIA*

ABSTRACT. High frequency capacitively coupled plasma in Ar/O_2 mixture at 2-Torr pressure was studied. Spatial and electrical characteristics of plasma allowed treating the plasma as positive column of normal glow discharge, which is controlled by diffusion. Spectrum of plasma in 200-850 nm region was recorded as a function of electron density and fraction of O_2 in the mixture. The analysis showed that at low fraction of O_2, excited oxygen atoms are produced mainly by O_2 dissociation via metastable argon atoms.

1. INTRODUCTION

Our recent study [1] showed that properties of TiO_2 films produced by atomic layer deposition (ALD) method depend on oxygen precursors (H_2O or H_2O_2). The finding forced us to turn to plasma as an alternative source of active species of oxygen. From the viewpoint of plasma-assisted deposition the most promising seems to be metastable atoms, $O(^1D_2)$. In [2] was found by vacuum ultraviolet absorption spectroscopy that the highest efficiency of $O(^1D_2)$ production was achieved in Ar/O_2 plasma, which contained < 10% of O_2. Unfortunately, the direct measurement of $O(^1D_2)$ demands a complicated experimental device and it is hardly possible to match the method with the on-line control of ALD process.

Optical actinometry [3] is an indirect but readily available method, which decides about the production of oxygen atoms comparing the intensities of some characteristic spectral lines. In Ar/O_2 mixture there are three main reactions leading to excitation of oxygen atoms, O*. First, the excitation by electron impact with ground-state atoms, $O + e \rightarrow O^* + e$ (R1). Secondly, the dissociation of O_2 via electron impact, $O_2 + e \rightarrow O^* + O + e$ (R2). Thirdly, the dissociation of O_2 via argon metastable atoms, $O_2 + Ar_m \rightarrow O^* + O^{**}$ (R3). Among the products of reaction R3 a remarkable part is in $O(^1D_2)$ state [2].

The main goal of the present study was to record the spectrum of plasma as a function of electron concentration and on the basis of these data to determine, which of reactions R1-R3 is dominating in production of oxygen atoms at low fractions of O_2.

2. EXPERIMENTAL SETUP

The existing ALD device set restrictions both to the pressure range (2-10 Torr) and the geometry of the discharge chamber. Figure 1 gives a sketch of the discharge tube, which was the most suitable from the viewpoint of the application.

Capacitively coupled discharge was excited in a quartz tube which inner radius, *R*, was 0.65 mm. A generator of 40 MHz frequency and of 100 W output power was used. A mesh of 20-mm length, which enveloped the outer surface of the tube, was powered. The opposite

electrode was an aluminium cylinder, which was grounded via resistors. The distance between the electrodes, L, was 90 mm. The applied voltage, U, current, i, and the phase shift, Φ, between U and i, were measured by the help of oscilloscope.

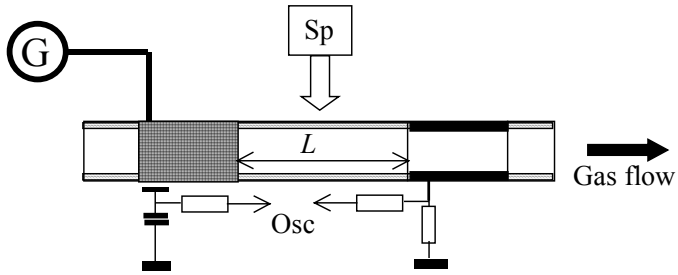

FIGURE 1. Sketch of the discharge tube

O_2 concentration, $[O_2]$, in Ar/O_2 mixture was changed from 0 to 20%. The measurements were carried out in a gas flow organised by a rotary pump and the total 2-Torr pressure was set using a needle valve.

The discharge spectrum was recorded in the direction perpendicular to the tube axis. The fibre spectrometer USB2000 (Ocean Optics), Sp, had 1.5 nm resolution and it recorded the spectrum in 200-850 nm range. The full spectrum was recorded during 50-100 ms. Intensity measurements were relative i.e. uncorrected for the spectral sensitivity of the recording system.

3. RESULTS AND DISCUSSION

3.1 Appearance and electrical characteristics

On the basis of discharge photos was found that between the electrodes the intensity of radiation did not depend on the distance from electrodes. The radial distribution of intensity in the tube, *I(r)*, was calculated using Abel inversion. At 2-Torr pressure the distribution *I(r)* was independent on gas composition and discharge current.

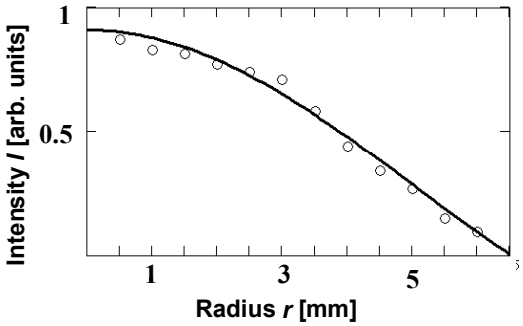

FIGURE 2. Radial distribution of intensity; points – experiment; line – Bessel function J0(2.4*r*/*R*).

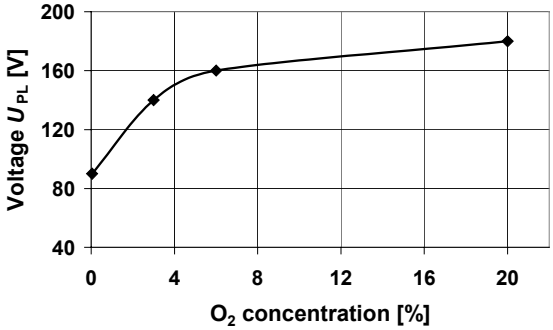

FIGURE 3. Plasma voltage as a function of O_2 concentration.

Figure 2 demonstrates that Bessel function, J0(2.4*r*/*R*), is a good fit of the distribution determined from the experiment. This result means that at 2-Torr pressure the main loss mechanism of charge carriers is diffusion i.e. the ionisation rate approximately equals to the diffusive loss rate, $\nu_i \approx \nu_d$. Using the procedure presented in [4] was found the value of the electron temperature in argon (i.e. 0% of $[O_2]$), $T_e \approx 1.4$ eV, as well as the reduced field in the plasma column, $E/p \approx 5$ V cm^{-1} Torr^{-1}.

For all mixtures used, the applied voltage, U, and the phase shift, ϕ, as functions of current, i, were recorded. The range of the power delivered to plasma, $P = Ui\cos\phi$, was 1-40 W. The

capacitance between powered and grounded electrodes was very small and thus the plasma current, i_{PL}, was equal to the recorded current. The knowledge of P and i_{PL} allowed calculating the voltage at the plasma column, U_{PL}. In the case of a fixed Ar/O_2 mixture, U_{PL} did not depend on plasma current. The last finding proves that the plasma between the electrodes may be treated as the positive column of the normal glow discharge. Figure 3 shows how U_{PL} increases with the growth of [O_2] in the mixture. It is noticeable that at 0% of [O_2] the value of the reduced field, $E/p = U_{PL}/pL$, coincides with the value given at the end of the previous paragraph. Further, using the curve in Figure 3 and supposing that used concentrations of O_2 did not change the electron mobility, the electron concentration was calculated.

3.2 Spectral characteristics

The dominating lines in the discharge spectrum belonged to argon and oxygen atoms. Comparatively intensive were also OH band at $\lambda \approx 308$ nm and lines of hydrogen, λ = 486, 656 nm. Starting from 2% of [O_2] in the mixture, the radiation of oxygen atoms at λ = 777 nm was the most intensive in the 'red' part of the spectrum.

The radiation of argon at λ = 750.4 nm (4p′-4s′ transition) is often used in the actinometry as a reference line characterising electrons belonging to 12-14 eV energy interval. This status of λ = 750.4 nm line is valid when the population of 4p′ state is not influenced by collisional quenching [5]. Our measurements showed that at 2-Torr pressure the dependence $I_{750} = f(n_e)$ was a linear one and the slope of the dependence did not depend on O_2 percentage. Thus, in our conditions λ = 750.4 nm line could be used as the reference line. Because of the recording direction of the spectrum the radiation at λ = 763.5 nm (4p-4s) was not influenced by self-absorption. At the same time appeared that the intensity I_{763} diminished with the growth of O_2 percentage. Consequently, 4p state is quenched by O_2.

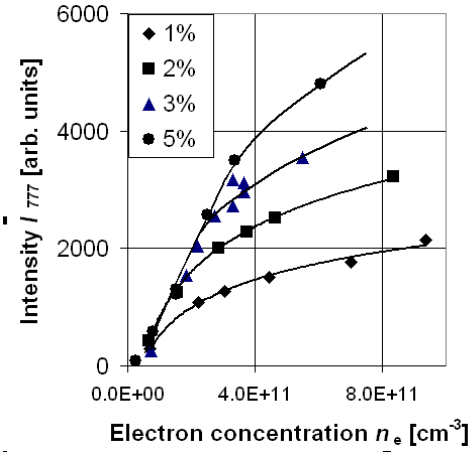

FIGURE 4. Intensity of λ = 777 nm oxygen line as a function of electron concentration; parameter – percentage of O_2; lines are drawn for clarity.

From the viewpoint of production of oxygen atoms by dissociative excitation via argon metastable atoms, Ar_m, the most informative should be the radiation at λ = 844.6 nm (3P-3S′) [2]. Unfortunately, the sensitivity of the spectrometer was very low in this part of the spectrum and the line was partially overlapped by the lines of argon. Therefore, we had to limit ourselves with the study of λ = 777 nm (5P-5S′) line. Figure 4 shows that dependencies $I_{777} = f(n_e)$ are non-linear: the growth of n_e brakes the increase of intensity.

Among the reactions R1-R3, which lead to the production of excited oxygen atoms only R3 is considerably influenced by n_e. As the concentration [Ar_m] increases due to the electron impact with the ground-state atoms and diminishes mainly due to the quenching by O_2 (rate coefficient k_{qO2}) and by n_e (rate coefficient k_{qe}), we can write for steady-state condition

$$[Ar_m] \propto \frac{[Ar]\, n_e}{k_{qO2}[O_2] + k_{qe} n_e}.$$

Neglecting the reaction R2, we can present the ratio of intensities as

$$I_{777} / I_{750} \propto [Ar_m]\,[O_2] + C1\frac{[O]}{[O_2]}$$

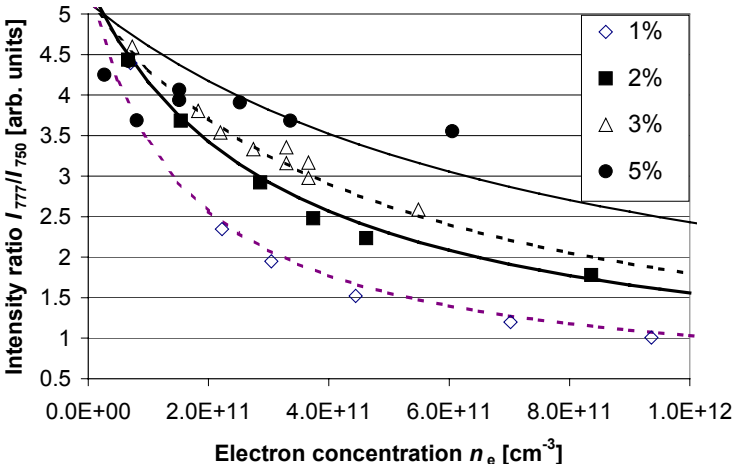

FIGURE 5. Intensity ratio I_{777}/I_{750} as a function of electron concentration; parameter – concentration of O_2; points – experiment; solid lines – calculations.

C1 contains the ratio of O(5P) excitation and quenching rate coefficients. Using literature data for k_{qO2} and k_{qe} the latter relationship was fitted with the dependence determined from the experiment.

Figure 5 gives the comparison of experiment and calculation. It appeared that at low concentrations of O_2 the reaction R3 is the main source of oxygen atoms and the role of R2 is totally negligible. This conclusion is valid at $[O_2]$ values < 5%. Growth of $[O_2]$ diminished the concentration of Ar_m and at 10% of $[O_2]$ in the mixture the ratio I_{777}/I_{750} did not depend on electron concentration.

4. CONCLUSIONS

We guess that the most important findings are

- present experimental conditions allow to use the radiation of argon at λ = 750 nm for actinometry;
- in the case of low O_2 fraction in Ar/O_2 mixture the dissociative excitation via argon metastable atoms is the main mechanism of excited oxygen atom production.

REFERENCES

[1] Jõgi, I., Aarik, J., Laan, M., Jun Lu, Kukli, K., Käämbre, H., Sajavaara, T., Uustare, T. (2006). Effect of preparation conditions on properties of atomic layer deposited TiO_2 films in Mo-TiO_2-Al stacks. *Thin Solid Films*, 510, 39-47

[2] Kitajima, T. and Nakano, T. (2006). Increased O(^{1}D) metastable density in highly Ar-diluted oxygen plasmas. *Appl. Phys. Lett.,* 88, 091501

[3] Jašik, J., Macko, P., Martišovitš, V., Lukac, P., Veis, P. (2004). Time resolved actinometric study of pulsed RF oxygen discharge. *Czech. J. Phys,* 54, 661-676

[4] Raizer, Y. P. (1991). In: *Gas Discharge Physics*, Berlin, Springer Verlag

[5] Francis, A., Czarnetzki, U., Döbele, H. F., Sadeghi, N. (1997). Quenching of the 750.4 nm argon actinometry line by H_2. *Appl. Phys. Lett.,* 71, 3796-3798

INVESTIGATION OF FINE STRUCTURE OF SURFACE DISCHARGE IN AIR AT ATMOSPHERIC PRESSURE

M.V. Sokolova[1], K.V. Kozlov[2], S.A.Krivov[1], P.A. Tatarenko[2] and V.G. Samoilovich[2]

[1] *Department of Electrophysics & HV Technique,*
Moscow Power Engineering Institute (Technical University),
Krasnokazarmennaya 14, 111250 Moscow, RUSSIA

[2] *Department of Chemistry,*
Moscow State University, Leninskie Gory 1, str.9, 119899 Moscow, RUSSIA

ABSTRACT. Fine structure of an electric discharge over the surface of a dielectric plate (ceramics of different composition and different surface structure) was investigated. The electrode system consisted of a small piece of metallic foil placed on one side of the dielectric plate of 1 mm thickness (the discharge electrode), while the back side of the plate was covered by another more extended metallic foil (high voltage electrode). . The aim of the present work was to investigate the influence of dielectric barrier material (ε value and surface structure) on the fine structure of the discharge. The experiments were carried out with an ac applied voltage (up to 2,6 kV r.m.s. and frequency 5-14 kHz). Besides current oscillography and high magnification photography the technique of cross-correlation spectroscopy (CCS) was applied for the first time in the world, to determine spatio-temporal structure of separate SDs. This method allowed to construct in a nanosecond time scale with spatial resolution of 0,1 mm spatio-temporal distributions of the SD luminosities for two the most intensive bands of the second positive (λ=337.1 nm) and the first negative (λ=391.5 nm) systems of nitrogen. These distributions were found to depend on the voltage amplitude as well as on the composition and surface structure of the dielectric barrier.

1. INTRODUCTION

The surface discharge (SD) which is a discharge in a thin gas layer near the surface of a solid dielectric is an object of many investigations in the recent years. It is well known by now that together with the applied voltage (its form and amplitude) the parameters of the solid dielectric – its material and its thickness – define the discharge characteristics. It has been shown in [1] that the structure of the solid dielectric surface plays an important role as well, the rough structure supporting a more intense discharge process. The aim of the present work was to use some additional experimental methods to investigate the fine structure of SD and its dependence on the solid dielectric surface structure. Together with taking oscillograms of current impulses of individual microdischarges (MD) and high magnification photography a spatio-temporally resolved spectroscopic diagnostics has been used for the first time to investigate the surface discharge. The results of such complex investigation are presented.

2. EXPERIMENTAL PROCEDURE

The electrode system (Figure 1) consisted of a small piece of metallic foil placed on one side of a dielectric plate of 1 mm thickness (the discharge electrode), while the back side of the plate was covered by another more extended metallic foil (high voltage electrode).

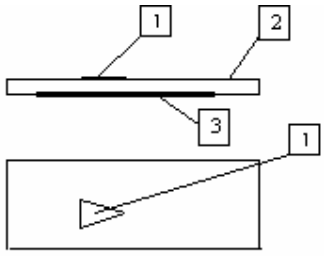

Figure 1. Electrode arrengement. 1 - discharge electrode, 2 - dielectric plate, 3 - yigh voltage electrode

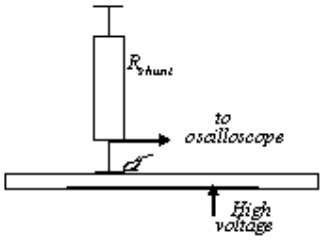

Figure 2 Electrical circuit

Dielectric plates (40x60 mm) of different kinds of ceramic (alumina and piroceramics) were used. The thickness of the plates is 1,2 mm. The ε values of the material is in the range 9.8-10. The piroceramic plates have different structure of their surface –one side rough and the other smooth, so it was possible to see the influence of the surface structure on the discharge keeping all other characteristics of the plate the same. The discharge foil electrode (1) has only a small part of its edge about 1.5 mm long open to develop the discharge. All other edges of the discharge and of the HV electrodes are covered by an epoxide layer to prevent the discharge formation. So it was possible to investigate the discharge in ambient air without much ozone formation.

An ac sinusoidal high voltage (f=5-14 kHz) was used. The initial voltage of the discharge depends on the material and in our case it was 1,1 kV (r.m.s.) for smooth piroceramics, 1,35 kV for rough one and 1.3 for alumina. To have an extended discharge area all investigations were carried out with 1.8 and 2.6 kV. To measure the current impulses a 11.8 Ohm shunt was constructed. The electric circuit is presented in Figure 2. The main features of cross-correlation spectroscopy (CCS) method used in the present work is described in details elsewhere [2,3].

3. EXPERIMENTAL RESULTS AND DISCUSSION

Figure 3. Enlarged photo of SD from the electrode tip.

An example of high magnification photography of the discharge over alumina is given that correspond to the applied voltage U = 2.1 kV (r.m.s.). Three distinct microdischarge channels are seen in the photo as a superposition of all discharges that developed from the electrode tip during the time of exposition. The radius of the electrode tip R = 500 μm, so the length of the channels is in the range (4–6) mm with approximately (500-600) μm between the points of their origin. So microdischarges stick to certain points at the electrode edge. An example of current impulse curve for positive polarity of the electrodeis also presented (Fig.4). An analysis of many oscillograms for different materials of the dielectric plate, different surface structure and different voltage values show practically the same form of the current curve: the front duration about 4-5 ns, length of the curve to half amplitude about 8-9 ns. Amplitudes of the current impulses depend on the dielectric material and its surface structure but it needs a special analysis. In a whole it can be said that the current values lay in the range from 5 to 35 mA.

The most interesting to our opinion are the spatio-temporal distributions of the SD

luminosities obtained for different conditions: different materials, different surface state of the dielectric barrier and different values of the applie voltage. In fig. 5-8 some examples of CCS pictures are given for alumina and λ=337.1 nm.

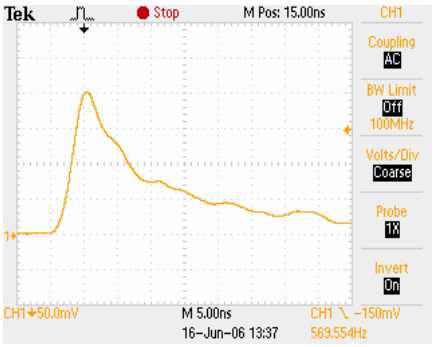

Figure 4. Current curve of a micro-discharge for U=1.8 kV. Dielectric – alumina.

At the right side of the figures there is placed a scale of the relative intensity of luminosity. As is seen the most intense light comes from the center of the MD channel. In all figures d is the distance from the electrode tip where d=0. We present here the first results of investigation of the luminosity of SD. Qualitative analysis of these results shows their surprising similarity to the spatial-temporal distributions of luminosity for traditional barrier discharge in nonsymmetrical case – "metal-glass". Two local maxima and clearly expressed minimum between them are seen in fig.5 when the dielectric is anode (the metallic electrode in this case is negative) and practically uniform distribution of luminosity for other polarity (dielectric – cathode (fig. 6).

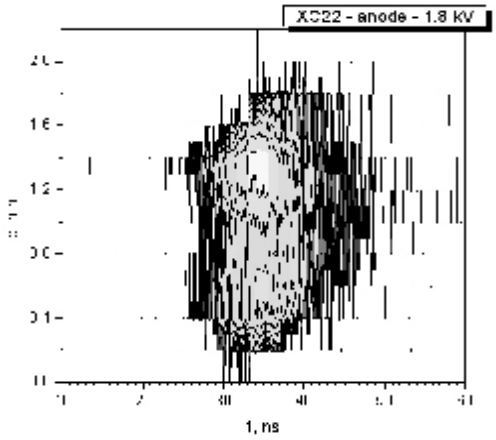

Figure 5. CCS –figure for dielectric-anode.

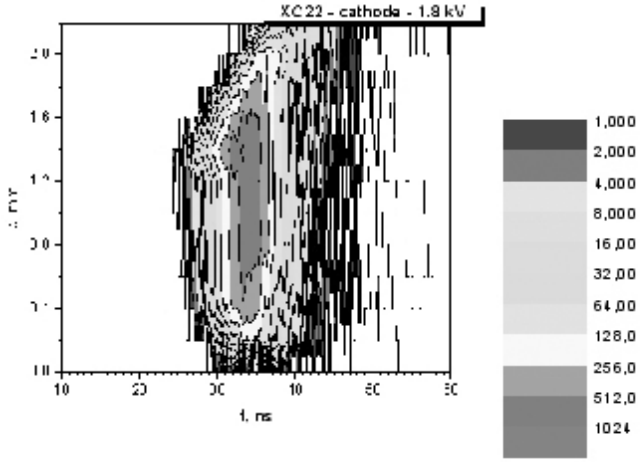

Figure 6. The same for dielectric-cathode.

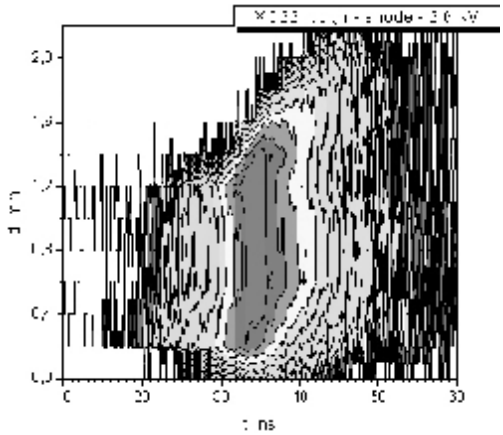

Figure 7. Dielectric – anode for U=2.6 kV.

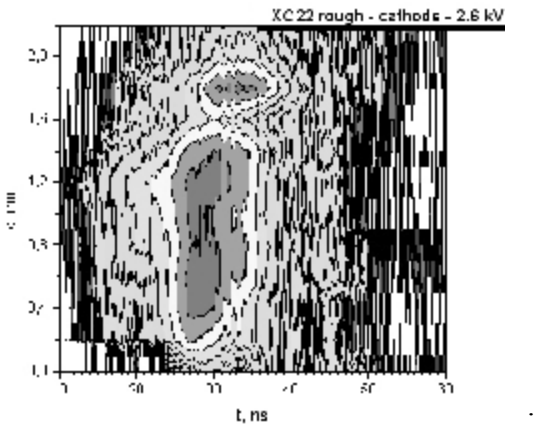

Figure 8. Dielectric – cathode for U = 2.6 kV.

With rising voltage amplitude the luminosity expands further from the second maximum for dielectric-anode (fig.7), while for other polarity a second maximum appears (fig.8). This last can be interpreted as an appearance of a second microdischarge. The most interesting fact is that this second microdischarge appears practically at the same time as the first one. So a qualitative physical model of the SD development with an increase of the applied voltage can be presented as follows: for a negative metal electrode the microdischarges just become longer as a result of the electron drift, while with a positive one (for the dielectric –cathode) a sequence of surface microdischarges appears. To some extend this model is confirmed by an increase of the mean current impulse amplitude and impulse duration with increasing voltage value when the metallic electrode is negative.

Comparison of CCS figures obtained for rough surface of piroceramics for U = 1.8 kV and the same for alumina (fig.5) shows a marked difference the luminosity for piroceramics being more intense and lasting for nearly 50 ns instead of 20 ns for alumina. As for different wave lengths (337.1 and 391.5 nm) there is also seen a difference in light intensity and in its duration when the dielectric-anode is piroceramics. The same characteristics obtained in the same conditions for smooth piroceramics are even more different as there has been not detected any luminosity for $\lambda = 391$ nm.

4. CONCLUSIONS

1. The obtained experimental data confirms the influence of the dielectric plate surface structure on discharge characteristics that has been shown in [1]. It especially concerns the spatio-temporal distributions of surface discharge luminosities.

2. The mean value of current impulse duration of a surface microdischarge in the conditions of our work does not exeed 10 ns, while the length of microdischarge channels are in the range from 1 to 6 mm.

4. REFERENCES

1. Sokolova M., Hulka L., Pietsch G.J. Plasma Processes and Polymers 2005, 2, 162-169.
2. Kozlov K.V., Tatarenko P.A. and Samoilovich V.G. "Some peculiarities of the barrier discharge in pure argon", these proceedings
3. Kozlov K., Shepeluk O. and Samoilovich V. Proc. 11-th Int. Conf. On Gas Discharges and their Application, Tokyo, Japan, pp. 142-145, 1995

Paper number

MEASUREMENT OF GAS TEMPERATURE DURING STREAMER DISCHARGE PROPAGATION IN ATMOSPHERIC AIR

T. Namihira, T. Tokuichi, H. Tamaribuchi, D. Wang, S. Katsuki and H. Akiyama

Department of Electrical and Computer Science,
Graduate School of Science and Technology, Kumamoto University
2-39-1 Kurokami, Kumamoto 860-8555, JAPAN

ABSTRACT. Pulsed power technology has been used in many applications such as control of NOx and SOx from exhaust gases, treatment of dioxins, removal of volatile organic compounds, generation of ozone, and laser excitation. In this situation, it is well known that the shorter pulse width of applied voltage to discharge reactor improves energy efficiency of the pollutant removal. However, it is still unclear why the shorter pulse brings less energy consumption to treat pollutant. In this paper, the gas temperatures during the propagations of 5 ns and 100 ns streamer discharges in atmospheric air gap were measured by analysis of optical emissions. As the experimental data, the gas temperature increases from 293 K to approximately 400 K during 100 ns streamer discharge propagation. On the other hand, the gas temperature rises during 5 ns streamer discharge propagation was less than 10 degree. From these results, it is obvious that the shorter pulse has less energy consumption for heating gas during discharge propagation. It means that the shorter pulse can consume energy for radical formations, which react with pollutant, efficiently and can improve the energy efficiency of pollutant removal.

1. INTRODUCTION

Recently pulsed power technology has been developed and applied to many applications such as exhaust gas treatment, ozone generation and laser excitation. Especially, the pollution control using non-thermal plasma produced by pulsed streamer discharges becomes one of promising method. Namihira et al have reported that the shorter pulse width of applied voltage to discharge reactor improves energy efficiency of NO removal and they have guessed that the propagation mechanism of pulsed streamer discharge bring it [1]. However, it is still unclear why the shorter pulse brings less energy consumption to treat pollutant. Normally, the heating of medium gas during discharge is thought as one of cause of energy loss. Therefore, in this work, the temperature of medium gas in discharge reactor was measured during streamer discharge propagation.

2. EXPERIMENTAL SET-UP AND PROCEDURE

Fig. 1 shows a schematic diagram of the gas temperature measurement system including the pulsed power generator, the discharge reactor, electrical parameter measurement devices and the optical emission spectroscopy system. In this paper, two Blumlein lines, having 100 ns or 5 ns of pulse width, were utilized as a pulsed power generator. The detail information of

Electronic address: namihira@cs.kumamoto-u.ac.jp

the Blumlein generators and the measurement of applied voltage and discharge current are in Ref. 2 and 3. The cylindrical coaxial electrode, having 0.5 mm of inner wire diameter, 76 mm of outer cylinder diameter and 10 mm long, was used to observe pulsed streamer discharges and was filled up with room air (RH 20 % at 293 K). In the optical emission spectroscopy system, the emissions from pulsed streamer discharges were corrected into a spectroscope equipped with 1,200 gr/mm grating (C5094S, Hamamatsu Photonics K.K., Japan) through a focus lens (A4869, Nikon Co, Japan). The temporal spectra of discharge emission from the spectroscope were recorded by a streak camera (C7700, Hamamatsu Photonics K.K., Japan). A delay generator (DG535, Stanford Research Systems, USA) synchronized the discharge application to the reactor and the triggering of the streak camera. In the experiments, the slit widths of the spectroscope and the streak camera were set with 30 μm and 100 μm, respectively. The focus lens focused at the vicinity of wire electrode of the discharge reactor.

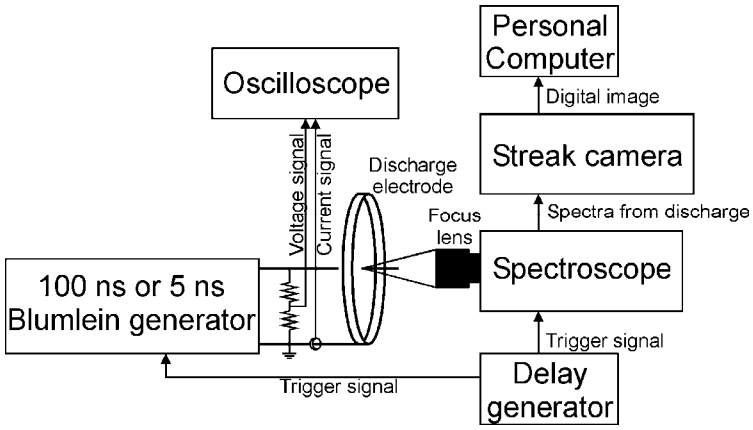

FIGURE 1. Schematic diagram of experimental set-up

3. EXPERIMENTAL RESULTS AND DISCUSSION

3.1. 100 ns streamer discharges

Fig. 2 shows the typical waveforms of the applied voltage to and the discharge current through the electrode during 100 ns pulsed streamer discharges. The streak image of the emission spectral from 100 ns streamer discharges is indicated in Fig. 3. It will be observed from Fig. 3 that three main discharge emissions from second positive system of N_2 were recorded and the discharge emissions last for about 100 ns. The integrated spectral calculated from Fig. 3 is shown in Fig. 4. From Fig. 4, it is obvious that three main wavelengths of 337.1, 375.5 and 380.4 nm are from the bands of [(*v', v''*)=(0, 0)], [(*v', v''*)=(1, 3)] and [(*v', v''*)=(0, 2)] of N_2 second positive system, respectively. In this paper, the medium gas temperature during the streamer discharge propagation was defined by the comparison measured spectral with synthesized spectral of [(*v', v''*)=(0, 2)] band of N_2 second positive system. Fig. 5 presents the synthesized spectral of [(*v', v''*)=(0, 2)] band of N_2 second positive system for the different N_2 temperature. The computed method of spectral synthesis was presented in Ref. 4. From Fig. 5, the emission intensity of shorter wavelength increased with increasing N_2 gas temperature. The measured and synthesized spectra are shown in Fig. 6. The synthesized spectra was in good agreement with the measured one, and the estimated rotational temperature (=gas temperature) of N_2 at the vicinity of wire electrode was about 400 K. This result is summarized like that the part of input energy into 100 ns streamer discharges was consumed for heating the medium gas approximately 100 degree and it cause directly loss of energy.

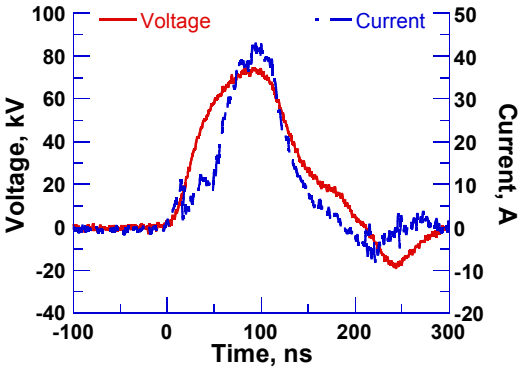

FIGURE 2. Typical waveforms of applied voltage and discharge current during 100 ns streamer discharge

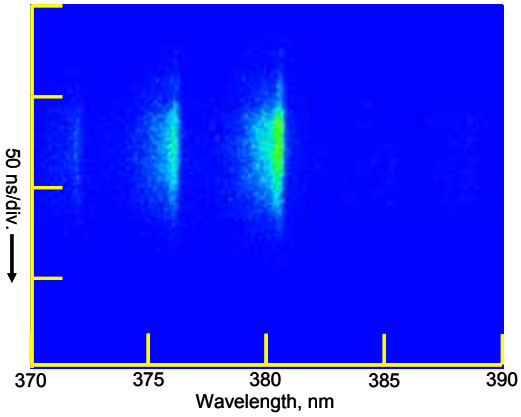

FIGURE 3. Streak image of discharge emission spectral during 100 ns streamer discharge.

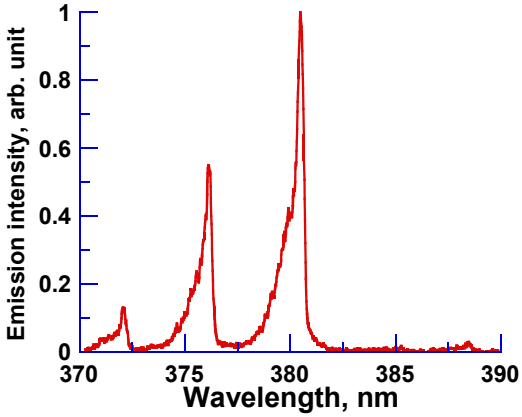

FIGURE 4. Integrated spectral of 100 ns streamer discharge emission.

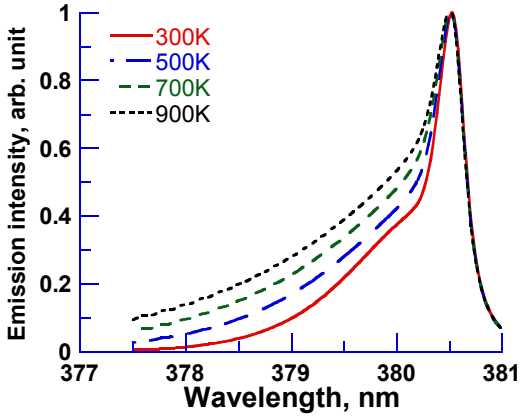

FIGURE 5. Simulated spectra of [(v', v'')=(0, 2)] band of N_2 2nd positive system for different N_2 temperature.

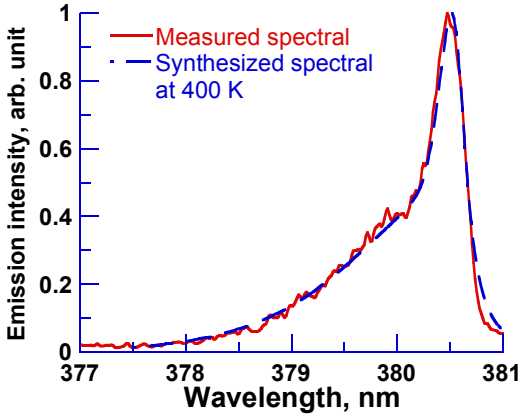

FIGURE 6. Comparison of measured and synthesized spectra.

3.2. 5 ns streamer discharges

Fig. 7 shows the typical waveforms of the applied voltage to and the discharge current through the electrode in the case of application of 5 ns pulsed streamer discharges. The streak image of the emission spectral from 5 ns streamer discharges is indicated in Fig. 8. It will be observed from Fig. 8 that three main discharge emissions from second positive system of N_2 were recorded as same to that of 100 ns streamer discharges and the discharge emissions last for about 10 ns. The integrated spectral calculated from Fig. 8 is shown in Fig. 9. From Fig. 9, it is also obvious as same to that of 100 ns that three main wavelengths from N_2 second positive system were observed. Likewise to the case of 100 ns streamer discharges, the

measured and synthesized spectra are shown in Fig. 10. The synthesized spectral was in good agreement with the measured one, and the estimated rotational temperature of N_2 at the vicinity of wire electrode was about 300 K. From this result, no energy consumption for heating medium gas was confirmed. By the comparison of the gas temperatures during 100 ns and 5 ns streamer discharges, it is clear that the shorter pulse width has advantage of less energy loss caused by heating gas.

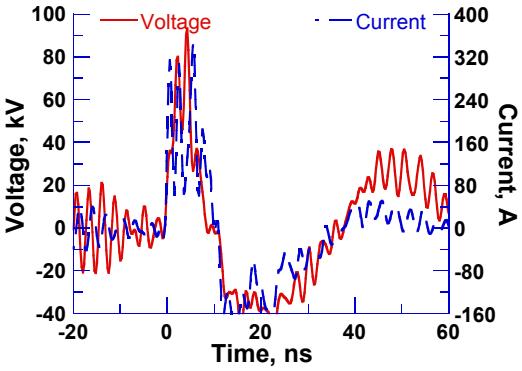

FIGURE 7. Typical waveforms of applied voltage and discharge current during 5 ns streamer discharge

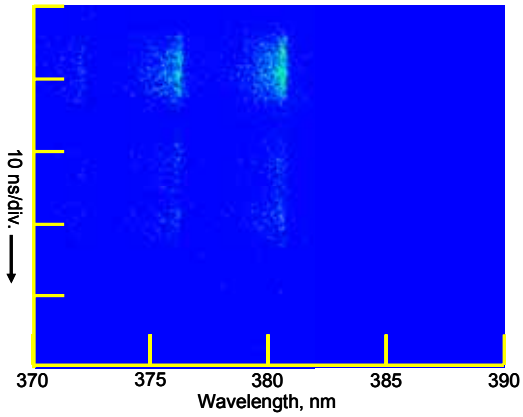

FIGURE 8. Streak image of discharge emission spectral during 5 ns streamer discharge.

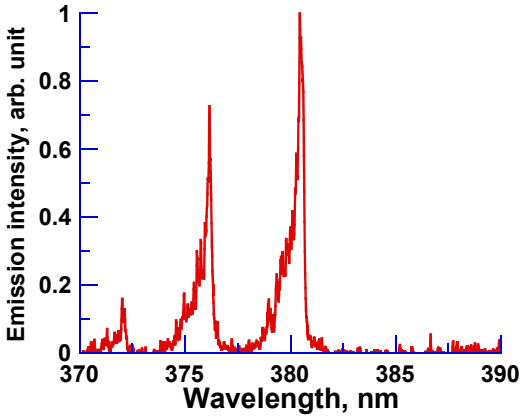

FIGURE 9. Integrated spectral of 5 ns streamer discharge emission.

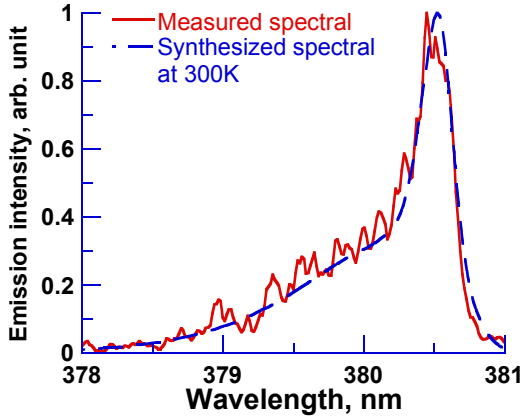

FIGURE 10. Comparison of measured and synthesized spectra.

4. CONCLUSIONS

In this work, the medium gas temperatures during 100 ns and 5 ns pulsed streamer discharges were calculated by comparison the measured and the synthesized discharge emission spectra. As the results, the gas temperature rise up to about 400 K during 100 ns streamer discharges. On the other side, 5 ns pulsed streamer discharge has no energy consumption for heating gas. Finally, it is clear that the higher energy efficiency of pollution control using the shorter pulsed power could be led by less energy loss to heat flux.

REFERENCES

[1] T. Namihira, S. Tsukamoto, D. Wang, S. Katsuki, R. Hackam, H. Akiyama, Y. Uchida and M. Koike, "Improvement of NO_X removal efficiency using short width pulsed power", IEEE Transactions on Plasma Science, Vol.28, No.2, pp.434-442, 2000.

[2] D. Wang, M. Jikuya, S. Yoshida, T. Namihira, S. Katsuki and H. Akiyama, "Observation of pulsed streamer discharges in atmospheric air using sub-microsecond pulse generator", 15th IEEE International Pulsed Power Conference, Monterey, USA, 2005. (In print)

[3] D. Wang, S. Yoshida, M. Jikuya, T. Namihira, S. Katsuki and H. Akiyama, "Observation of pulsed streamer discharges in atmospheric air using nano-second pulse generator", 15th IEEE International Pulsed Power Conference, Monterey, USA, 2005. (In print)

[4] K. Nishijima and Y. Mizuta, "An accurate diagnostic method with emission spectroscopy on vibrational temperature and its application for DC-glow discharge plasma in N_2 gas", Transactions on IEE Japan, Vol.110-A, No.11, pp.767-772, 1990.

TRANSITION FROM ATMOSPHERIC PRESSURE TOWNSEND DISCHARGE (APTD) TO FILAMENTARY DISCHARGE IN N_2/O-CONTAINING MIXTURES

N. Gherardi*, N. Naudé, Et. Es-sebbar, I. Enache, H. Caquineau, F. Massines

Laboratoire de Génie Electrique de Toulouse, Université Paul Sabatier,
118 route de Narbonne, 31062 Toulouse Cedex 09, FRANCE

ABSTRACT. In this paper, we have studied the influence of small admixtures of nitrous oxide (N_2O) and oxygen (O_2) on the behavior of an Atmospheric Pressure Townsend Discharge in nitrogen (N_2) atmosphere.

1. INTRODUCTION

Dielectric barrier discharges have tremendous popularity for atmospheric pressure applications including thin-film coating, sterilization, treatment of flue and toxic gases, aerodynamic flow control, and energy-efficient lighting devices. Depending on the gas, electrical parameters, and electrode configuration, these discharges can operate in a diffuse or filamentary mode. The goal of this work is to help to the understanding of the processes which control the transition between the two modes. In particular, in nitrogen atmospheres, the Atmospheric Pressure Townsend Discharge (diffuse mode of the DBD) turns into microdischarges when the flow rate of reactive gas increases. This limitation largely depends on the nature of the additive. In the case of oxydizing gases, the maximum concentration is only few hundreds of ppm for O_2 [1]. This limitation has been attributed to the destruction of the energetic long-lived metastable states of nitrogen, which are needed to enhance electron emission at the cathode before breakdown. However, in the case of N_2O, the maximum concentration which can be added keeping a Townsend discharge is much more than 1000 ppm. In order to study this difference, we have followed very carefully the transition from the Townsend to the filamentary mode in the two mixtures through electrical measurements.

2. EXPERIMENTAL SET-UP

The experimental set-up has already been described in previous publications [2]. The discharge area is 12 cm^2. The gap distance is adjusted to 1 mm by space holder made of glass. The flowing gas, which consists of nitrogen (N_2) with small admixtures of oxygen (O_2) or nitrous oxide (N_2O), is injected directly inside the discharge through a gas diffuser. The total gas flow is 1 slpm, which results in a mean gas velocity of 14 $cm.s^{-1}$. The voltage applied to the electrodes is measured by means of a high voltage probe. The current is measured through a 50 Ω resistor in series with the electrodes. The discharge current and the voltage really applied to the gas are calculated from these two measurements [2].

* Electronic address : gherardi@lget.ups-tlse.fr

3. RESULTS AND DISCUSSION

3.1. N_2/O_2 mixtures

The influence of small admixtures of oxygen on the discharge current and gas voltage of the Atmospheric Pressure Townsend Discharge (APTD) is detailed in figure 1. As observed by Brandenburg *et al.* [1], up to 100 ppm of O_2 in N_2, the breakdown occurs sooner, which implies a lower breakdown voltage. This is coherent with the fact that the inverse current peak (observed just after the polarity change of the gas voltage) increases for the same O_2 concentrations. In pure N_2, this inverse peak is due to electrons generated in between two discharges, when the field is low enough to "trap" them in the gas volume. These electrons come from collisions of metastable molecules with the charged dielectric surface [3]. Then these two results (increase of inverse current peak and decrease of breakdown voltage) would suggest that the metastable flux on the surface increases for low (tens of ppm) amount of O_2.

For higher concentrations, the breakdown voltage increases again and the inverse current peak decreases drastically, and even disappears for 500 ppm of O_2 added. This can be explained by a strong destruction of $N_2(A^3\Sigma_u^+)$ nitrogen metastables [1,4].

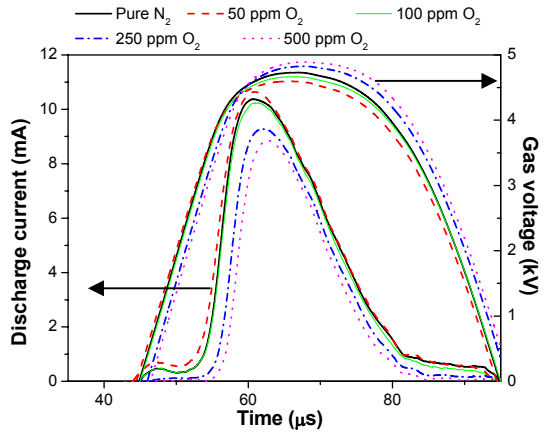

FIGURE 1. Discharge current and gas voltage for different concentrations of O_2 (V_a=15kV$_{pk-pk}$-f=10kHz)

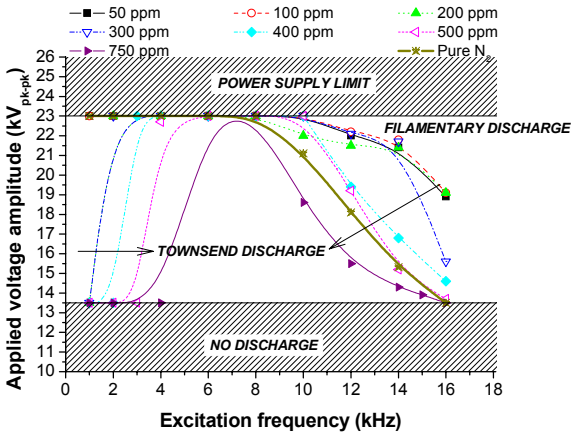

FIGURE 2. Working domains of the APTD for different concentrations of O_2 in N_2

The working domains (in terms of excitation frequency and voltage amplitude that can be applied to the electrodes keeping an APTD) for different O_2 concentrations added in N_2 are shown in figure 2. At a given frequency, the working domain has got two limits. The lower limit corresponds to the applied voltage necessary to extend the discharge over the entire electrode surface. For the gas velocity considered here, it is constant all over the frequency range, and whatever the O_2 concentration. The upper limit is either 23 kV$_{pk-pk}$, which is the maximum voltage used for these experiments (power supply limit) or the applied voltage at which instabilities appear on the discharge current and so which defines the transition to filamentary discharge.

Once again the behavior is different for low and large amounts of O_2. For oxygen amounts lower than 200 ppm, the working domain is larger than in pure N_2, confirming that a process compensates the nitrogen metastable destruction. For higher concentrations, filamentary discharge can be observed at low frequency and the voltage limit at high frequency decreases as well. Thus, for 750 ppm of oxygen added in N_2, the working domain is especially reduced and centered around 8 kHz. It has to be noted here that it is possible to obtain a Townsend

discharge with as much as 1000 ppm of oxygen added in the discharge. However, the working domain is so tiny that it has not been represented in figure 2. Actually, the behavior observed with 1000 ppm is very interesting. It is summarized in figures 3 and 4: at a given frequency, the higher the voltage amplitude (and so the dissipated power), the easier it is to get a Townsend discharge. Hence, at 6 kHz (figure 3), when the discharge is almost purely filamentary at 19,5 kV_{pk-pk}, it tends to be stable for 24,3 kV_{pk-pk} applied on the electrodes (power supply limit). At 8 kHz, it is even possible to get a Townsend discharge for 23 kV_{pk-pk} applied on the electrodes, when a lower voltage amplitude leads to oscillations on the discharge current (figure 4). It is interesting to note that these oscillations were observed by Brandenburg *et al.* [1] during their study on the influence of oxygen on the discharge mechanisms. In this study, these oscillations were appearing from 480 ppm only. This difference is probably related to the dissipated power inside the two apparatus: the maximum current density was about 0.1 $mA.cm^2$ at 6,95 kHz in their case, when it is 1.4 $mA.cm^2$ at 8 kHz on the example represented in figure 4 (V_a = 23 kV_{pk-pk}), which corresponds to 28 W/cm^3. Hence, the power dissipated in the discharge has clearly an effect on the discharge stability. One explanation could be the fact that detachment processes are very sensitive to the discharge temperature [3]. Indeed, in our discharge configuration, 28W/cm^3 dissipated in the discharge leads to a gas temperature elevation of 200°C [2].

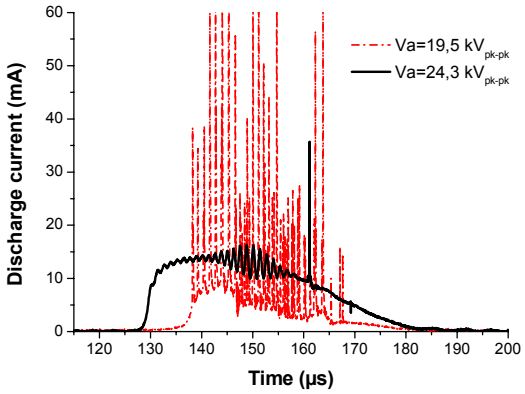

FIGURE 3. Discharge current for different applied voltage amplitudes (O_2=1000 ppm, f=6 kHz)

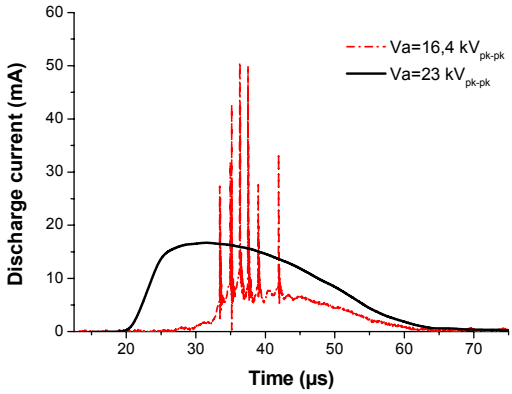

FIGURE 4. Discharge current for different applied voltage amplitudes (O_2=1000 ppm, f=8 kHz)

3.2. N_2/N_2O mixtures

The influence of small admixtures of nitrous oxide on the discharge current and gas voltage time dependences is very similar to the one of oxygen, except for the absolute concentrations values. Indeed, the decrease of the breakdown voltage (here also associated with an increase of the inverse current peak) is observed for amounts of N_2O in N_2 lower than 350 ppm. For higher value, the breakdown voltage decreases like in the O_2 case, and the inverse peak is no more observable.

Concerning the working domains (figure 5), the high frequency behaviour is here also very similar to what is observed with O_2: for amounts lower than 1000 ppm, the domain is larger than in pure N_2, showing that here also something compensates the nitrogen metastable destruction. Indeed, N_2O is also an efficient quencher of $N_2(A^3\Sigma_u^+)$ [4], and the reactive products generated by a N_2/N_2O discharge should not be really different from the ones produced by N_2/O_2 discharge. Actually, this is interesting to notice that the high frequency limit is similar in N_2/O_2 and N_2/N_2O mixtures for N_2O concentrations twice as large as in O_2

case (see figure 6). Nevertheless, the low frequency behaviour is completely different than in N_2/O_2 mixtures: it is always possible to get a Townsend discharge at low power.

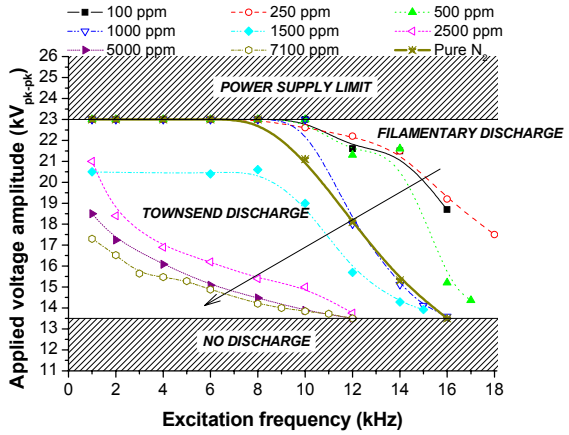

FIGURE 5. Working domains of the APTD for different concentrations of N_2O in N_2

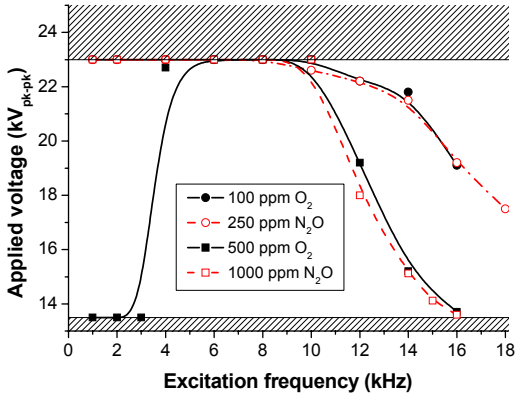

FIGURE 6. Comparison between working domains in N_2/N_2O and N_2/O_2

Another different feature is that it is possible to inject very large amount of N_2O keeping a stable Townsend discharge: APTD can be generated with more than 7000 ppm of N_2O in N_2 (figure 5). Actually, a stable discharge could even be obtained in pure N_2O, with electrical characteristics (discharge current and gas voltage time dependence) very close to N_2 ones.

4. CONCLUSION

For very small admixtures (<200 ppm for O_2 and <1400 ppm for N_2O), O_2 and N_2O have a similar influence on the APTD behavior. For higher reactive concentrations, the two behaviors depend on the discharge power: at low power, O_2 leads very easily to discharge destabilization when N_2O has much less influence; at high power, N_2O and O_2 have a similar effect, which can be related to the fact that for high discharge power, the dissociation products are the same in both cases. However that may be, N_2O is much easier to use than O_2 as oxidizing gas.

REFERENCES

[1] Brandenburg R., Maiorov V.A., Golubovskii Yu B., Wagner H-E., Behnke J., Behnke J.F. (2005). Diffuse barrier discharges in nitrogen with small admixtures of oxygen: discharge mechanism and transition to the filamentary regime. *J. Phys. D: Appl. Phys.*, 38, 2187-2197

[2] Naudé N., Gherardi N., Es-sebbar Et., Cambronne J-P., Massines F. (2004). Electrical model of an Atmospheric Pressure Townsend Discharge: application to the determination of the gas temperature. *HAKONE IX, Padova, Italy*

[3] Massines F., Ségur P., Gherardi N., Khamphan C., Ricard A. (2003). Physics and chemistry in a glow dielectric barrier discharge at atmospheric pressure: diagnostics and modeling. *Surf. Coat. Technol.*, 174-175, 8-14.

[4] Kossyi I.A., Kostinsky A. Yu, Matveyev A.A., Silakov V.P. (1992) Kinetic scheme of the non-equilibrium discharge in nitrogen-oxygen mixtures. *Plasma Sources Sci. Technol.*, 1, 207-220

Paper number

ELECTRICAL AND OPTICAL PROPERTIES OF AC MICRODISCHARGES IN POROUS CERAMICS

K. Hensel[1], M. Janda[1], M. Lestinsky[1], Z. Machala[1], V. Martisovits[1], P. Tardiveau[2] and A. Mizuno[3]

[1] *Department of Astronomy, Earth Physics and Meteorology, Faculty of Mathematics, Physics and Informatics, Comenius University 84248 Bratislava, SLOVAKIA (hensel@fmph.uniba.sk)*
[2] *Laboratoire de Physique des Gaz et des Plasmas, Université Paris-Sud, 91400 Orsay, FRANCE*
[3] *Department of Ecological Engineering, Toyohashi University of Technology 441858 Toyohashi, JAPAN*

ABSTRACT. Generation of microdischarges inside porous ceramics by AC high voltage has been investigated. Electrical and optical measurements were performed to explore the physical properties of the microdischarges. The effect of pore size, discharge power and gas mixture on the discharge properties and development is described.

1. INTRODUCTION

Research of various types of non-thermal plasmas (i.e. plasmas with electron temperature elevated with respect to the gas temperature) generated by electrical discharges at atmospheric pressure has received a fast development in the last two decades. The environmental applications of such non-thermal plasmas are based on their plasma-chemical effects, where generated electrons, ions, excited species and radicals initiate processes that occur neither in classical chemistry, nor in thermal plasmas. Streamer and pulsed coronas, and various types of dielectric or ferroelectric barrier discharges are mostly used. They are typical with nonequilibrium character and a large amount of thin filamentary channels, called microdischarges. The microdischarges produce a large density of energetic electrons and free radicals at relatively low energy consumption; therefore they represent a potential method for car exhaust cleaning [1-3]. The exhaust cleaning effect can be even enhanced when the discharge plasma is combined with catalysts. The catalyst, typically of ferroelectric bed type or pellets or of honeycomb structure, can be placed either behind the plasma zone or directly in it. In comparison with plasma-only flue gas treatment systems, the plasma-assisted catalysis performs 0-order kinetics (thanks to the heterogeneous catalytic surface reactions), excellent carbon balance, and minimal aerosol production [4-7]. The pressure drop on the catalyst appearing at high gas flow rates and a small volume of the generated plasma associated with the pellet bed type plasma reactors leads to a more prospective use of porous materials, such as honeycomb catalysts or porous ceramics.

In the recent years, there appeared a few pioneering works dealing with the generation of microdischarges in narrow cavities and capillaries of porous dielectric materials with the aim to investigate their physical properties and use them for the removal of volatile organic compounds and nitrogen oxides [8-10]. Unlike most of pulsed discharges that need a special high voltage power supplies generating pulses with a rise time of some tens of nanoseconds in

order to efficiently produce radicals and oxidants, microdischarges can be generated even with an AC or a DC high voltage power supply [11-13]. This fact substantially enlarges the possibilities of the microdischarge use in porous materials because high investment costs for the construction of a pulsed power supply are reduced.

The objective of the paper was to investigate the physical properties of the microdischarges generated inside porous ceramics by AC high voltage power supply. In the previous works we described the properties of the microdischarges generated using DC power [11, 13]. The methods of the investigations in the presented work consisted of electric and optical measurements focused on determining the optimal conditions of the discharge generation with main respect to the pore size.

2. EXPERIMENTAL SET-UP

The experimental set-up consisting of a discharge reactor and electric and optical circuits is depicted in *Figure 1*. A porous ceramics was placed between two stainless steel mesh electrodes. The ceramics were sintered from alumina or fused silica and their diameter and thickness were 31 and 7 mm, respectively. The pore size of the ceramics was 2, 10, 30, 80 (alumina) and 50, 120, 200 μm (silica). The ceramics was set inside the quartz cylinder sealed by silicon stoppers at the both ends. The discharge reactor was placed in a Faraday cage to reduce induced noise signals and correctly measure voltage and current waveforms.

AC regulated high voltage power supply connected via a 5 MΩ series resistor limiting the total discharge current was used to excite the discharge reactor. The total power including the power losses in the electrical circuit was measured by digital multimeter Metex 3860M. The voltage at the reactor was measured by a high voltage probe Tektronix P6015A and the discharge current was measured using a current probe Pearson Electronics 2877 (1V/A) linked to the digitizing oscilloscope Tektronix TDS1012 (100 MHz, 1 GS/s).

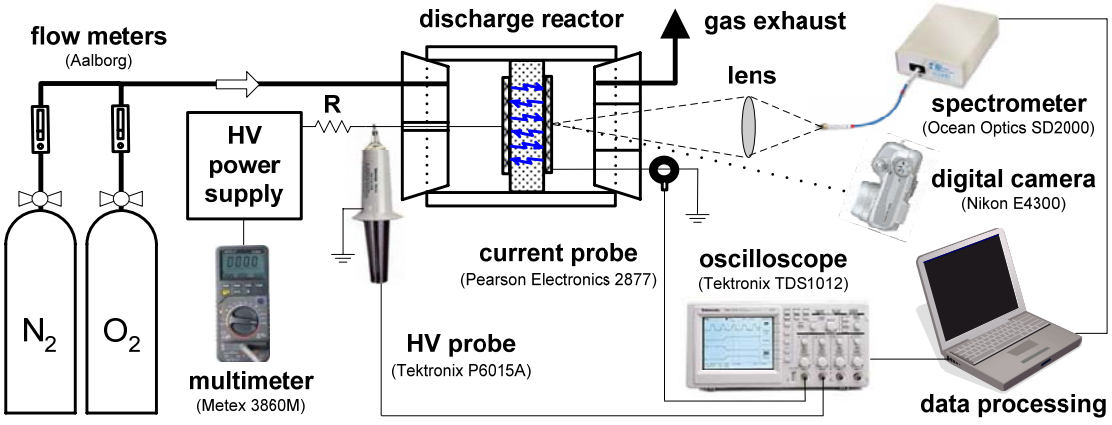

FIGURE 1. Experimental set-up.

Emission spectroscopy optical system consisted of a dual fiber-optic compact spectrometer Ocean Optics SD2000 with CCD detector used for fast scanning in the UV and VIS-NIR region (200-500 and 400-1050 nm). The photographs of discharge were taken by the digital camera Nikon E4300 with manually adjustable aperture and exposure time.

All experiments were carried out in atmospheric pressure nitrogen, oxygen or air at room temperature. The pressure drop across the discharge reactor was measured by the digital manometer PCE P-30.

3. RESULTS AND DISCUSSION

The effect of the pore size, discharge power, and gas mixture on the properties and development of the discharge was investigated by means of electrical and optical measurements. The pore size of the used ceramics was a critical parameter for selecting a total gas flow rate. The smaller the pore size, the bigger was the pressure drop across the reactor. *Figure 2* shows the dependence of the pressure drop on the gas flow rate for various pore sizes. For the tests, we have used the gas flow rate of 0.4 l/min, as the pressure drop at this flow rate was almost negligible (< 200 Pa) for all ceramics, except for the one with 2 μm pores.

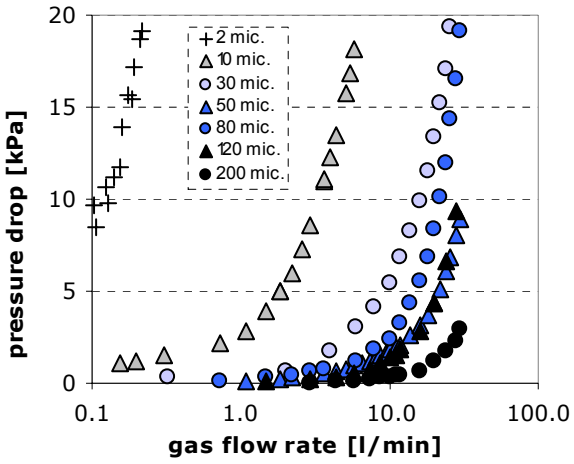

FIGURE 2. Pressure drop across the reactor as a function of gas flow for various pore sizes.

Generation of microdischarges inside the ceramics was possible only at the specific discharge power depending on the pore size of the ceramics. In the previous studies, we reported that at a small applied voltage, the surface discharge development over the surface of the ceramics could be observed. It mainly occurred with the ceramics of the smallest pore size. By the increase of the applied voltage, however, a gradual change of the discharge mode was observed. At a certain voltage, the surface discharge "leaked into" the ceramics and the microdischarges inside the material were formed. *Figure 3* represents the instant values of the applied voltage and the total power in the moment of the surface discharge transition to microdischarges related to the pore size. As the figure shows, the voltage and the power at the onset of the microdischarges decreases with the pore size. *Figure 4* displays the total power-to-voltage (P-U) characteristics of the microdischarges. For better readability of the figure, the results of three ceramics are presented only. The P-U characteristics of the surface discharge for all ceramics were almost identical. After the transition to microdischarges, the slope of the P-U characteristics increased. The slope of the characteristics increased with the pore size. The results presented in the *Figure 3* and *4* are in the agreement with those obtained for microdischarges generated by DC power [11-13].

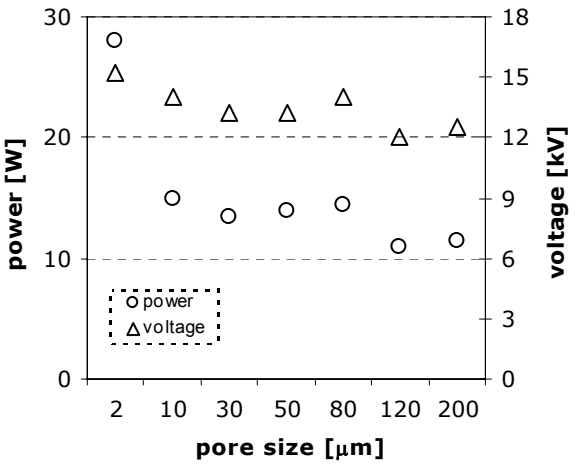

FIGURE 3. Total power and applied voltage in the moment of transition to microdischarges.

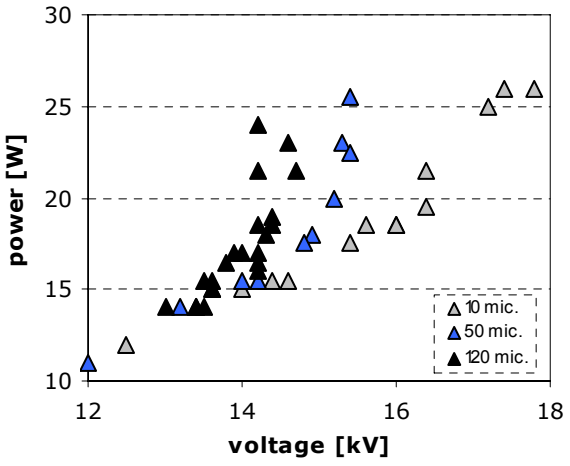

FIGURE 4. Total power as a function of discharge voltage for the selected pore size (in air).

We also recorded waveforms of both the applied voltage and the current pulses. *Figure 5* presents the waveforms obtained for 30 μm ceramics at the various timescales. The discharges occurred in both negative and positive polarities of the applied high voltage. The amplitude of the current pulses increases with the applied voltage and the power and reached several tenths of amps (*Fig. 6*). For a given power, the maximal amplitude of the current pulses was observed with 50 and 80 μm pore size ceramics (*Fig. 7*).

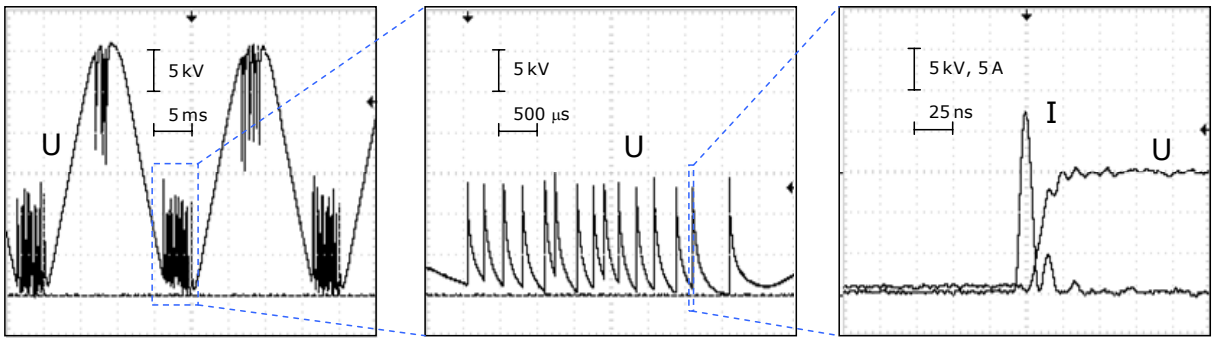

FIGURE 5. Voltage and current waveforms of the discharge in porous ceramics at the different timescales (pore size 30 μm, U = 16.2 kV, P = 23 W, air).

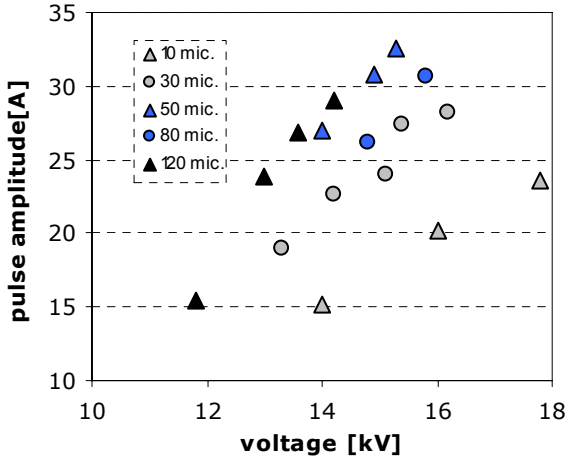

FIGURE 6. Current pulse amplitude as a function of applied voltage (in air).

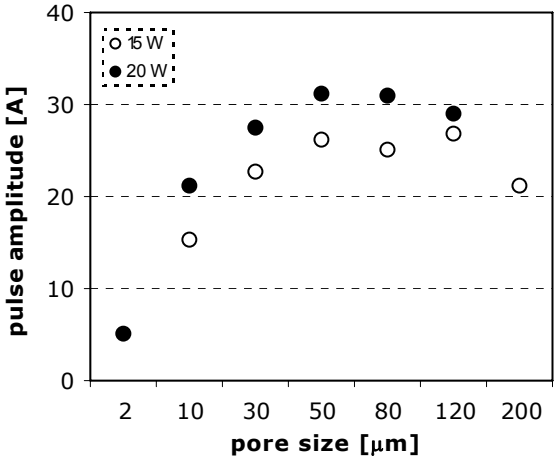

FIGURE 7. Current pulse amplitude as a function of pore size for a different power (in air).

The optical characteristics of the discharge were recorded simultaneously with their electric characteristics. *Figures 8-10* presents three sequences of photographs visualizing the effect of the power, the gas and the pore size on the discharge character and spatial development. All photographs were taken with the same exposition time. The light emission of a single microdischarge channel was not constant in time, as well as, the spatial distribution of the channels randomly changed, too. The figures show that the light intensity increased with the discharge voltage and the power. It is also evident, that the increase of the oxygen contents in the gas mixture resulted into redistribution of the microdischarge channels inside the ceramics. In oxygen rich mixtures, the channels concentrated mainly around the outer circumference of the mesh electrodes and almost no emission from the center the ceramics was observed. On the other hand, in nitrogen the light emission was relatively homogenously distributed over the whole surface of the ceramics. The oxygen contents cause the number of discharge channels decreased resulting in a decrease of the discharge power for a given voltage.

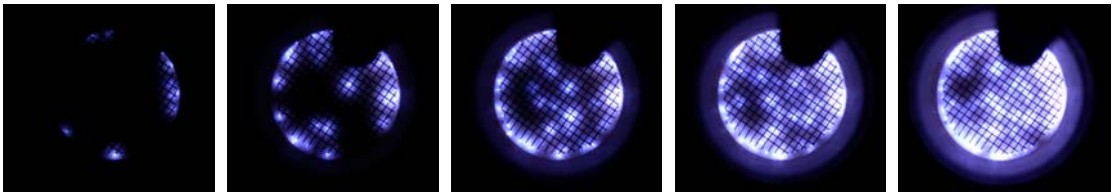

FIGURE 8. The effect of power (left to right): 17, 19, 21, 23, 26 W (pore size 80 μm, exposure time 1s, f-number f/3.5, air).

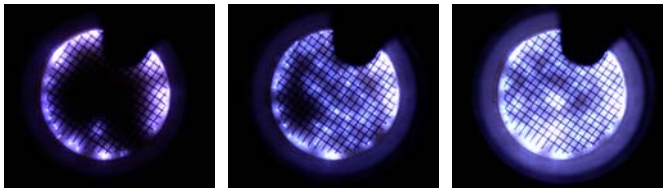

FIGURE 9. The effect of gas (left to right): O_2, air, N_2 (pore size 80 μm, exposure time 1s, f-number f/3.5, P = 22 W).

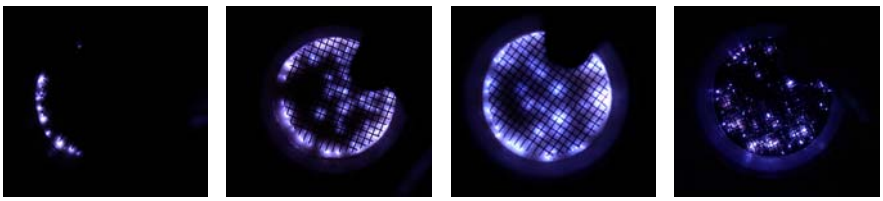

FIGURE 10. The effect of pore size (left to right): 10, 30, 80, 120 μm (exposure time 1s, f-number f/3.5, P = 20 W, air).

The emission spectroscopy was employed as a powerful technique of plasma diagnostics to give us valuable information on excited atomic and molecular states and the insight in ongoing plasma chemistry. *Figure 11* presents the emission spectra of microdischarges in VIS-NIR region taken at the constant power in various gas mixtures. In nitrogen and air, two principal systems of bands have been observed. The 2nd positive system of N_2 in the violet region corresponding to the transition $C^3\Pi_u - B^3\Pi_g$ of N_2 excited states, and the 1st positive system of N_2 in the visible orange-red region corresponding to the transition $B^3\Pi_g - A^3\Sigma_u^+$.

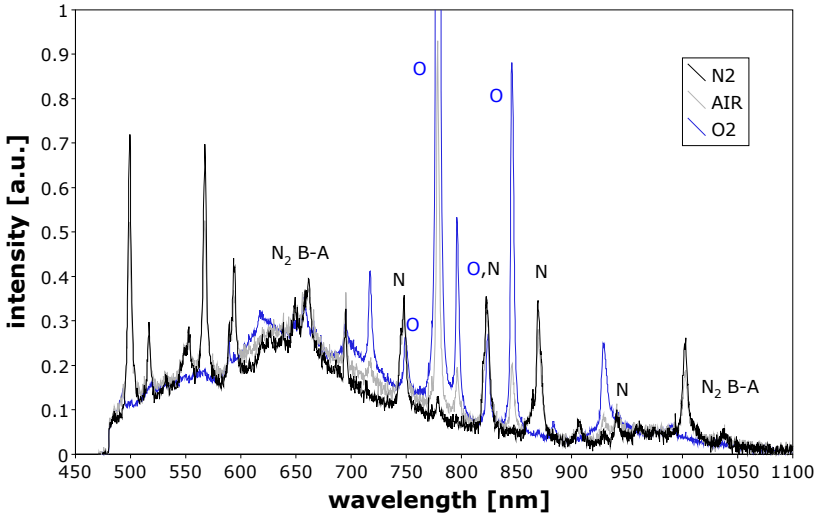

FIGURE 11. Emission spectra of microdischarges in VIS in various gas mixtures (pore size 80 μm, P = 30 W).

Significant changes in emission spectra depending on the O_2 content and many other unidentified bands have been observed (502, 518, 568, 695, 718, 795 nm, etc.). They may belong to the bands of Fe (electrodes) and/or to various atomic spectra of N, O, NO, O_3, etc. Their interpretation, however, needs further investigation.

4. CONCLUSIONS

Electrical and optical properties of microdischarges generated inside the porous ceramics by AC high voltage power have been investigated. The effect of the pore size, discharge power and gas mixture on the discharge properties and development was described. It was found the onset voltage of the microdischarges decreases with the pore size, while that the slope of P-U characteristics slope increases with the pore size. Amplitude of the current pulses increased with the applied voltage. The maximal amplitude was observed for 50 and 80 μm pore size ceramics. In nitrogen, the light emission was relatively homogenously distributed over the whole surface of the ceramics, while in oxygen the microdischarges concentrated mainly at the circumference of the ceramics and a decrease of the discharge power was observed. Emission spectroscopy also showed significant changes in emission spectra depending on the O_2 content. In total, the optimal generation of the microdischarges and their distribution in the ceramics was observed namely for 30-80 μm pore sizes. The discharge formation inside porous ceramics presents a novel way to generate large volume stable atmospheric pressure plasmas in hybrid plasma–catalyst reactors and can be effectively used for flue gas treatment.

ACKNOWLEDGMENTS

The research has been supported by Science and Technology Assistance Agency Grant APVT 20-032404, and by Slovak Grant Agency VEGA 1/3041/06.

REFERENCES

[1] Oda T, Kato T, Takahashi T, Shimizu K (1998) *IEEE Trans. Industry Appl. 34*, 268-272.
[2] Yamamoto T, Okubo M, Nagaoka T, Hayakawa K (2002) *IEEE Trans. Ind. Appl. 38*, 1168-1173.
[3] Kim H-H, Prieto G, Takashima K, Katsura S, Mizuno A (2002) *J. Electrostat. 55*, 25-41.
[4] Hammer T. (2002) *Plasma Sources Sci. Technol. 11*, 1.
[5] Holzer F, Roland U, Kopinke F-D (2002) *Appl. Catal. B: Environ. 38*, 163-181.
[6] Kim H-H (2004) *Plasma Process. Polym. 1*, 91-110.
[7] Penetrante BM, Hsiao MC, Bardsley JN et al. (1997) *Plasma Sources Sci. Technol. 6*, 251-259.
[8] Gherardi N, Gouda G, Gat E, Ricard A, Massines F (2000) *Plasma Sources Sci. Technol. 9*, 340-346.
[9] Blin-Simiand N, Tardiveau P, Risacher A, Jorand F, Pasquiers S (2005) *Plasma Proc. Polym. 2*, 256-262.
[10] Jidenko N, Petit M, Borra J-P (2006) *J. Phys. D: Appl. Phys. 39*, 281-293.
[11] Hensel K, Katsura S, Mizuno A (2005) *IEEE Trans. Plasma Sci., 33*, 574- 575.
[12] Sawada J, Matsui Y, Hensel K, Koyamoto I, Takashima K, Katsura S, Mizuno A(2004) *"Microdischarge in Porous Ceramics for Exhaust Gas Cleaning*", 5th International Conference on Applied Electrostatics ICAES 2004, Shanghai, November 2-5, 128-131.
[13] Hensel K, Matsui Y, Katsura S, Mizuno A (2004) *Czech. J. Phys., 54*, C683-C689.

DISCHARGE CHARACTERISTIC OF CNT COVERED ELECTRODE

N. Okayama, S. Ono

Musashi Instutute of Technology, Tamatsutsumi 1-28-1, Setagaya-ku, Tokyo, 158-0087, JAPAN

ABSTRACT. We have tried to obtain stable plasma using carbon nanotube (CNT) covered electrode under atmospheric pressure. The counter electrode was used metal pipe. RF power of 13.56MHz was applied to these electrodes to produce atmospheric pressure plasma. The CNT was synthesized on the nickel substrate by alcohol catalyst CVD. The produced plasma was observed by a zoom microscope and was diagnosed by spectroscopic method. The electron temperature and electron density of the plasma produced with CNT electrode were much higher than the plasma produced with the metal electrode.

1. INTRODUCTION

In recent years, the CNT is a material which attracts attention all over the world. The CNT has a tube structure which rounded the graphene sheet of sp2 carbon bond in diameter of several nanometers. As a feature of CNT, there are a large aspect ratio, thermal conductivity, field emission, mechanical strength etc. From these features, there are applications of a field emission display, an electronic device, etc. and research and development have carried out in various fields.

On the other hand, since the atmospheric pressure discharge plasma has unnecessary vacuum apparatus and can process a material in large amount and high speed compared with low-pressure plasma, it has a big advantage when applying to an industrial process.

The application of atmospheric pressure plasma production is employed the advantage that the aspect ratio of CNT is large. This is considered that an electron emission is high and discharge is produced easily, in order that the energy may concentrate to the tip of CNT if a voltage is applied since the CNT is nanosize. From this characteristic, the synthesized CNT is used for an electrode, and application of the discharge electrode in atmospheric pressure discharge is considered.

In this paper, the plasma stabilized under atmospheric pressure using the CNT covered electrode is produced, and analysis of CNT and diagnosis of plasma are performed.

2. EXPERIMENTAL APPARATUS AND METHOD

2.1 Hot filament CVD method

Figure 1 shows the schematic diagram of the experimental set-up used. The CNT was synthesized on the Ni substrate (20mm×20mm, thickness 0.2mm) by alcohol catalyst CVD. The Ni also plays the role of a catalyst. The methanol was used as a source of carbon. The tungsten wire (0.2 mm in diameter, 150mm in length) was used as a filament. The distance between the Ni substrate and the filament was 3mm.

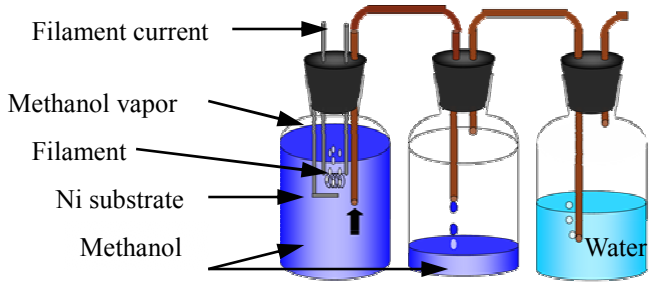

FIGURE 1. The schematic of hot filament alcohol catalyst CVD method.

As the experimental method, a glass bottle in the filament is filled with methanol. When the filament is applied the current and temperature is raised, methanol is evaporated. Then methanol accumulates on the upper part of a bottle. After a filament is surfaced from a liquid level, the current is raised and the filament is made red heat. Thereby, the methanol is decomposed and the CNT is synthesized on the substrate.

Filament current was changed and synthesis time was 60mins. The product on the Ni substrate was analyzed by a scanning electron microscope (SEM) and Raman spectroscopy.

2.2 A plasma production under atmospheric pressure

The plasma was produced using CNT covered electrode in atmospheric pressure. Another counter electrode was used the metal pipe (0.5mm in inner diameter, 0.8mm outer diameter) and was passed the argon gas of 0.5 l/min inside. It is for being comparatively easy to discharge and preventing oxidization of an electrode surface as a reason for using argon gas.

The Ni substrate was connected to the ground. The metal pipe was connected to 13.56MHz RF power supply through the matching box. The distance between electrodes in experiment is constant 3mm. The emission spectroscopy and the digital camera were investigated the plasma state when the substrates with CNT and without CNT were used.

The gas temperature of plasma is determined from nitrogen rotation temperature. Since a small amount of nitrogen molecules are contained in the plasma produced under atmospheric pressure. The rotation temperature (It is almost equal to gas temperature) is estimated using the fitting method. Since the strong continuous spectra were observed with the emission spectroscopy, the electron temperature of plasma is calculated using the intensity ratio of the continuous spectra and line spectra of argon plasma. For argon plasma, the intensity ratio of the continuous spectra and line spectra is given

$$\frac{I_l}{I_c}(\lambda) = Cr\frac{A_{21}g_2}{U_i}\frac{\lambda_c{}^2}{\Delta\lambda\lambda_l T_e}\frac{1}{\xi}\exp\left(\frac{E_i - E_2}{kT_e}\right) \qquad (1)$$

where A_{21}: Einstein A coefficient, g_2: degeneracy, U_i: partition function, E_i: ionization potential, E_2: energy of level 2 and Cr: 2.005×10^{-5}, respectively.

3. RESULT

3.1 Analysis of the product

Figure 2 shows the SEM image of the Ni substrate deposit. The tube diameter of CNT in the filament power in 50W was 20 to 50 nm, and the tube diameter in 75W was about 200nm.

The Ni substrate deposits were analyzed by the Raman spectroscopy. The Raman peak appeared in the vicinity of 1590cm^{-1} is called G band. The peak appeared in the vicinity of 1350cm^{-1} is called D band. The feature peaks of CNT are appeared in the vicinity of Raman shift 100-500cm^{-1}. These peaks are called the radial breathing mode that diameter of the tube expand and contract in total symmetry.

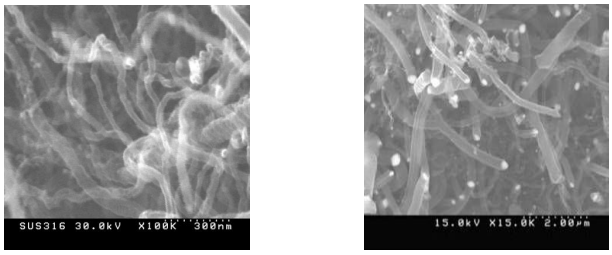

FIGURE 2. SEM images of the product. (a) filament power 50W, (b) filament power 75W.

3.2 Plasma production using CNT covered electrode

Each discharge states in a Ni, a graphite and a CNT electrode are observed. The experiment was performed in the RF electric power 16W, the argon flow 0.5m/l, and 3mm of distance between electrodes. In the case of a CNT electrode, very strong emission was observed compared with other electrodes.

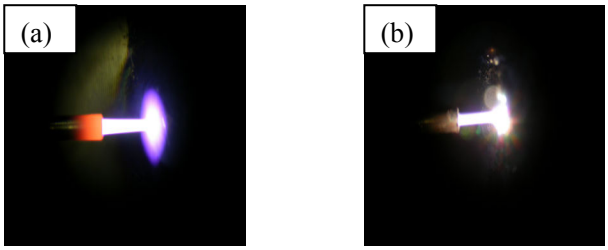

FIGURE 3. Photomacrograph of a Ni electrode (a) and a CNT covered electrode (b)

Figure 3 shows the photomacrograph of Ni electrode (a) and CNT covered electrode (b) as lower electrode. In the case of a metal pipe electrode, this tip is observed red heat, it is thought a strong electric field against the produced is required for this. In the case of a CNT electrode, since plasma is easy to be produced, an electrode is not red heat. From these, a CNT covered electrode has great effect on the discharge.

3.3 Plasma characteristics

The electron temperature and gas temperature of plasma in CNT and Ni electrode were measured. RF power dependence property of the gas temperature in Ni and CNT electrode is shown in a figure 4(a). The gas temperature of CNT covered electrode was about 3000K and was higher than Ni electrode. In both electrodes, the gas temperature by RF power hardly changed. In the case of the CNT electrode, it is attributed to the fact that the electron density is high as a reason the gas temperature becomes high. Since CNT has high electron emission capability, the electron density in plasma becomes high. Therefore, it is considered that energy exchange of an electron and a molecule increases in high electron density, and gas temperature is high. From the emission spectrum of plasma using CNT covered electrode, the continuous spectrum which is the feature of high-density plasma is observed, and it is very stronger than the line spectrum of argon. RF power dependence property of the electron temperature in Ni and CNT electrode is shown in a figure 4(b). The electron temperature of CNT covered electrode was about 25000K was higher than Ni electrode. In high-density plasma, the rate of recombination loss becomes large and this is considered to be an element of an electron temperature rise.

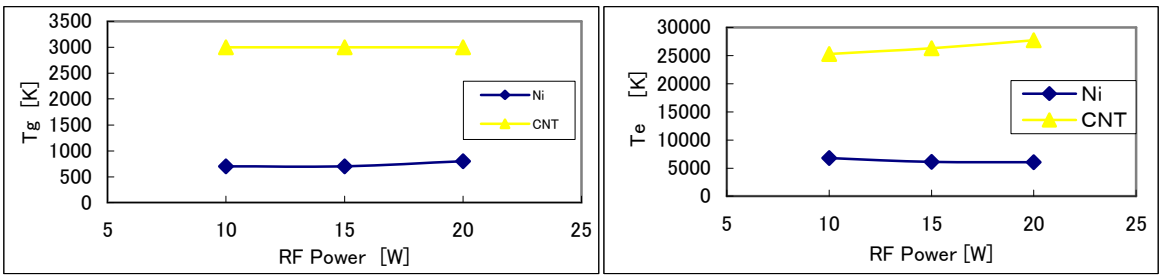

FIGURE 4. RF power dependence of gas temperature (a) and electron temperature (b)

4. SUMMARY

The discharge experiment using a CNT covered electrode was performed under atmospheric pressure. The following results were obtained.

(1) The CNT was synthesized on the Ni substrate by the hot filament CVD method.

(2) Atmospheric pressure discharge plasma was generable using the CNT covered electrode.

(3) The electron temperature and the electron density of the plasma produced in this process were much higher than the plasma produced in the metal electrode.

REFERENCES

[1] S. Teii. (1997). Fundamental Plasma Engineering. Uchidarokakudou Ltd.

[2] Y. Hirose, Private communication

[3] S. Maruyama et.al., (2002). Chem. Phys. Lett., 360, 229

[4] Y. Matsuo, (2005). Master thesis, Musashi Institute of trchnology

PLASMA PROCESSING OF PROPANE AT HYPER-ATMOSPHERIC PRESSURE: EXPERIMENT AND MODELLING

Sarah L. Hill[1], J. Christopher Whitehead[1a] and Kui Zhang[1]

[1] School of *Chemistry,*
Faculty of Engineering and Physical Sciences, The University of Manchester,
Manchester, M13 9PL, UK

ABSTRACT. To make non-equilibrium plasma technology more appealing to industry it would be advantageous to process gases at high pressure. Propane destruction in air using a packed-bed, non-thermal plasma reactor has been studied at both 1 and 3 bar pressure. Propane conversions of 23% and 13% were achieved at 1 and 3 bar respectively. Calculating an energy efficiency parameter from the experimental data showed that it is more efficient to work at 3 bar pressure; when the pressure is tripled, the energy density required for 50% conversion only doubles. Modelling was carried out to assess the destruction pathways and their pressure dependencies. The reactions were predominately found to occur through the peroxy radical, $C_3H_7O_2$.

1. INTRODUCTION

There have been very few studies on the effect of hyper-atmospheric pressure on non-thermal plasma processing. However, literature on electrical breakdown of gases at high pressure is available. Generally it is documented that increasing gas pressure leads to an increase in the voltage required for breakdown [1], [2]. Unfortunately none of these high pressure investigations include the study of dielectric barrier discharges (DBDs). Eliasson and Kogelschatz [3] have studied DBD operation at high pressure and show that an increase in pressure from 1 to 5 bar does not effect the charge created in a DBD. However they do not comment on chemical changes at high pressure.

2. EXPERIMENTAL

A schematic diagram of the arrangement is shown in Figure 1. A packed bed DBD was used for these experiments. The reactor consisted of a glass tube with 24 mm internal diameter and two electrodes 12 mm apart through which the gas could pass. Barium titanate beads (3.5 mm diameter) were used to pack the space between the electrodes. An AC voltage at a frequency between 10.25 and 13.25 kHz is applied between the two electrodes. The carrier gas used was pure air (N_2 80%, O_2 20%, BOC) and along with propane gas (100 ppm, Air Products) was introduced into the system using mass flow controllers (MKS flow control systems); the flow rate was varied from 0.5 L min^{-1} to 2 L min^{-1}. A valve was placed in the exit tube of the reactor to regulate the pressure; a pressure gauge (MKS pressure sensor) was placed immediately after the

[a] Electronic address: Christopher.whitehead@manchester.ac.uk

reactor to monitor the pressure which was varied from 1 bar to 3 bar. The products were monitored on-line by infrared spectroscopy using a long-path gas cell (2.76m, Venus Series) and a FTIR spectrometer (Shimadzu FTIR-8300). Stainless steel, Teflon and PTFE tubing, valves, and fittings of 1/4in. internal diameter were used to handle the gases as appropriate.

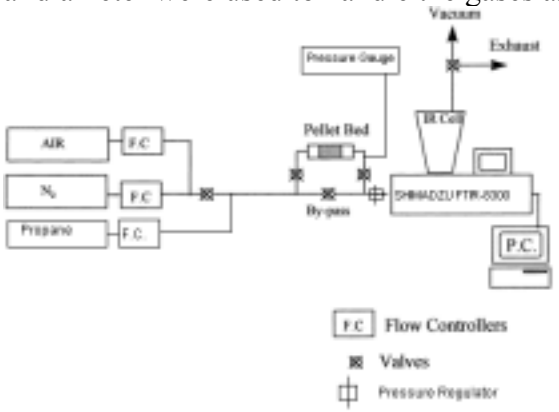

FIGURE 1. Schematic diagram of the arrangement used to study the removal of propane from a nitrogen/oxygen gas stream using a DBD reactor at elevated pressure

Flow Rate ($lmin^{-1}$)	Pressure	Conv. of Propane	NO_2 (ppm)	NO (ppm)	Total NOx (ppm)	NO_2/NO Ratio
0.5	1 Bar	42 %	339	309	648	1.10
	3 Bar	29 %	348	206	564	1.69
1	1 Bar	23 %	202	159	361	1.27
	3 Bar	13 %	216	37	253	5.84
2	1 Bar	17 %	158	84	242	1.88
	3 Bar	7 %	158	15	173	10.53

TABLE 1. Experimental results for the conversion of 100 ppm propane in air with a DBD reactor with 12 mm electrode distance, varying flow rate and pressure

3. RESULTS AND DISCUSSION

3.1 Experimental Results

Table 1 shows that residence time affects the conversion of propane, the shorter the residence time (i.e. a faster flow rate) the smaller the conversion. A pressure effect is also observed, at elevated pressure (3 bar) the conversion of propane is reduced. This is due to a combination of factors which change at high pressure such as, a change in the electrical properties of the discharge, altered reaction rates and a change in plasma species composition. These alterations are also responsible for the changes observed in the total NOx production and NOx ratio (NO_2:NO). The results show that the total NOx produced is reduced at 3 bar and the NOx ratio increases dramatically, indicating higher NO_2 concentrations than NO concentrations at high pressure.

3.1.1 Energy Efficiency

The energy efficiency parameter, β [4], can be calculated using, $[X] = [X]_0 \exp -\rho_E / \beta$ (where [X] is concentration of propane, $[X]_0$ is initial concentration of propane and ρ_E is the energy density) to allow a better comparison between work at 1 and 3 bar pressure. The β parameters were found to be 183 JL^{-1} and 377 JL^{-1} for 1 and 3 bar respectively. Using these results the

theoretical energy density required to convert 50% of propane can be calculated, this was found to be 127 JL^{-1} at 1 bar and 261 JL^{-1} at 3 bar pressure with a flow rate of 1 $Lmin^{-1}$. When the pressure is tripled the energy density required to convert 50% only doubles, thus the number of propane molecules processed is greater at 3 bar than 1 bar, thus making high pressure operation more efficient.

3.2 Modelling Results

Using CHEMKIN II a propane destruction model was created to support the experimental work and to investigate breakdown pathways of the propane molecules. Table 2 shows the obtained results.

Flow rate ($lmin^{-1}$)	Pressure	Conv. Of Propane	NO_2 (ppm)	NO (ppm)	Total NOx (ppm)	NO_2/NO Ratio
0.5	1 Bar	37 %	187	508	695	0.37
	3 Bar	15 %	435	3	438	145
1	1 Bar	23 %	191	155	346	1.23
	3 Bar	10 %	217	3	220	72.3
2	1 Bar	14.5 %	132	41	173	3.22
	3 Bar	6 %	110	3	113	36.6

TABLE 2. Modelling results for the conversion of 100 ppm propane in air with a DBD reactor with 12 mm electrode distance, varying flow rate and pressure

The outcome of the model, with respect to the destruction of propane, shows it proceeds via the peroxy radical, $C_3H_7O_2$, which decomposes via R1.

$$C_3H_7O_2 => CH_3CHO + CH_3O \quad (1)$$

A common finding in the literature is that decomposition of propane occurs via oxidative steps, [5], [6], [7].

Using the model, reaction profiles were produced to clearly show the interaction between NO, NO_2 and ozone (O_3), see Figures 3 and 4. The interaction is O_3 dominated due to the residence times involved in these reactions. As the production of O_3 is a three body reaction the concentration is greatly enhanced at 3 bar pressure allowing any NO created to be directly converted to NO_2 via;

$$NO + O_3 => NO_2 + O_2 \quad (2)$$

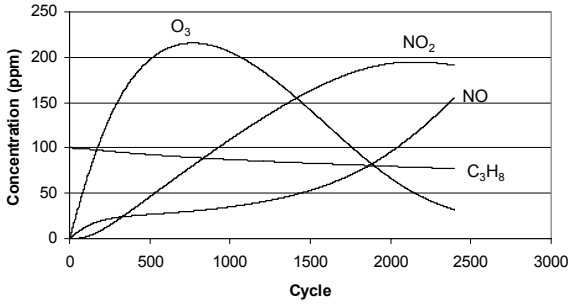

FIGURE 3. NOx reaction profile showing the inter-conversion of NO and NO_2 and the relationship with O_3 at 1 bar and 1 $lmin^{-1}$

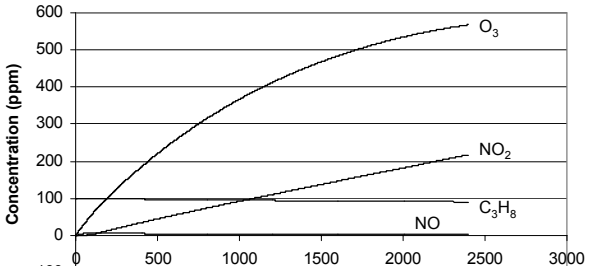

FIGURE 4. NOx reaction profile showing the inter-conversion of NO and NO_2 and the relationship with O_3 at 3 bar and 1 $lmin^{-1}$

The model shows good agreement with propane destruction experimental data however discrepancies within the model are apparent with respect to the NOx results. The model greatly underestimates the production of NO, this maybe explained due to surface reactions. The model only takes account of gas phase reactions whereas O species on the $BaTiO_3$ beads are known to occur [8]. It is conceivable that these surfaces could aid reactions which convert NO_2 back to NO which would not be included in the CHEMKIN-II model.

4. CONCLUSION

The mechanism by which propane is destroyed in a DBD is a well documented oxidative process. The results of our experiment and modelling suggest a similar pathway of destruction as in other literature, via a peroxy radical. The NOx chemistry within a DBD is not well understood. Our findings show it is difficult to produce a model which successfully reproduces experimental data at a variety of different parameters, for example residence time and pressure. This leads to the conclusion that there are more than gas phase reactions responsible for the inter-conversion of NO and NO_2, surface reactions on the dielectric are suspected to influence the NOx ratio especially at slow flow rates and elevated pressures.

ACKNOWLEDGEMENTS

The support of this work by the UK Engineering and Physical Sciences Research Council and by Plasma Clean Ltd. is gratefully acknowledged.

REFERENCES

1. Blair, D.T.A., *Breakdown Voltage Characteristics*, in *Electrical Breakdown of Gases*, J.M. Meek and J.D. Craggs, Editors. 1978, John Wiley & Sons. p. 533-654.
2. Craggs, J.D., *High-frequency Breakdown of Gases*, in *Electrical Breakdown of Gases*, J.M. Meek and J.D. Craggs, Editors. 1978, John Wiley & Sons. p. 689-716.
3. Eliasson, B. and U. Kogelschatz, *Modeling and applications of silent discharge plasmas.* IEEE Transactions on Plasma Science, 1991. **19**(2): p. 309-323.
4. Fitzsimmons, C., et al., *The chemistry of dichloromethane destruction in atmospheric-pressure gas streams by a dielectric packed-bed plasma reactor.* J. Phys. Chem. A, 2000. **104**: p. 6032-6038.
5. Shin, H.-H. and W.-S. Yoon, *Effect of hydrocarbons on the promotion of NO-NO2 conversion in nonthermal plasma DeNOx treatment.* Society of Automotive Engineers, [Special Publication] SP, 2000. **SP-1566**(Non-Thermal Plasma): p. 103-110.
6. Park, K.-S., et al., *Effect of various hydrocarbons on the plasma DeNOx process.* Society of Automotive Engineers, [Special Publication] SP, 2001. **SP-1639**(Non-Thermal Plasma Emission Control Systems): p. 59-67.
7. Dorai, R. and M.J. Kushner, *Effect of multiple pulses on the plasma chemistry during the remediation of NOx using dielectric barrier discharges.* Journal of Physics D: Applied Physics, 2001(4): p. 574-583.
8. Futamura, S., A. Zhang, and T. Yamamoto, *Behavior of N2 and nitrogen oxides in nonthermal plasma chemical processing of hazardous air pollutants.* Ieee Transactions on Industry Applications, 2000. **36**(6): p. 1507-1514.

SYNCHRONIZATION AND DEVELOPMENT OF POSITIVE SURFACE STREAMER DISCHARGES IN AIR, NITROGEN AND OXYGEN

Y. Kashiwagi[1] and H. Itoh[2]

[1] *Department of Electrical and Electronic Engineering,*
Kisarazu National College of Technology
2-11-1 Kiyomidai-Higashi, Kisarazu, Chiba, 292-0041, Japan
[2] *Department of Electrical, Electronics and Computer Engineering,*
Faculty of Engineering, Chiba Institute of Technology
2-17-1 Tsudanuma, Narashino, Chiba, 275-0016, Japan

ABSTRACT. *Investigation is carried out for synchronous generation of surface streamer discharges from two electrodes and development of the streamers in air, nitrogen and oxygen. It is found that light emitted from the first streamer causes the photoelectron emission and/or the photoionization in the vicinity of the opposing electrode, triggering synchronous discharge of the second streamer. The wavelength of the light contributing to this phenomenon is shorter than 250 nm, ultraviolet and vacuum ultraviolet region. Short time lags of the streamers are observed when the surrounding air is humid. The streamers elongate in nitrogen in comparison with in air. In contrast, the streamers shorten in oxygen compared to in air. Differences are also found clearly in the current waveforms of the surface streamers. The peak value and the decay time of the current waveforms are influenced by gas molecules.*

1. INTRODUCTION

In 1778, Lichtenberg published a historic document on the dust figure method. After that, many investigations on surface discharge phenomena have been studied. In 1919, Pederson described about synchronization of surface streamers for the first time [1]. It is well known that the surface streamers develop and spread in a regular radial pattern from one electrode on an insulator plate. Recently, this phenomenon has been studied by Chiba et al. [2], who reported that the radial spread of streamers would be caused by the synchronous generations of all the streamer branches. Tanaka et al. [3] modeled the dynamic behaviour of the surface streamers and found that, in addition to electron multiplication by collisional ionization in the area of the forefront of the streamer, it is also necessary to account for photoelectron emission from the surface of the insulator and photoionization in the discharge area. Observed phenomena can be reproduced by the simulation only when photoelectron emission and photoionization are included.

But there remain some debates over the mechanism of streamer development, in particular the supply of initial electrons. This paper reports on detailed investigations of the surface streamer discharges in air (humid and dry), nitrogen and oxygen.

2. EXPERIMENTAL SETUP AND PROCEDURE

The experimental setup for this study is illustrated in Figure 1. A standard lightning impulse voltage of about +24 kV with 1.2/50 μs waveform was applied to the parallel-connected electrodes (A). Two sphere metallic electrodes of 30 mm diameter were placed on an insulator plate 300mm square and 10mm thick made of acrylic resin (B). The electrode mounted on the back of the insulator plate was an aluminium plate 500mm square and 10mm thick (C) and was grounded via a resistor (D) in a shielding box or CT. The terminal of the resistor or CT and the output terminal of a voltage divider (G) were monitored by a digital waveform recording system. The current and the voltage were simultaneously recorded by this system. Furthermore, the dust figures were obtained on the insulator plate using photocopier toner. A 40mm high shading plate (H) was used to intercept the discharge light passing through the region between the parallel electrodes. Optical filters were also used in the same manner as the shading plate to investigate the wavelength dependence of synchronization probabilities. All optical filters were of the long wave path type with 50% cutoff wavelengths of 115, 164, 260, 280, 300, 320, 395 and 590 nm. According to demand, the experiments were carried out in oxygen and nitrogen. In this case, the electrodes and the insulator were covered by a chamber (I) of 300mm square and height 100mm made of acrylic resin. The gases were flowed into the chamber from a gas cylinder at a constant flow rate.

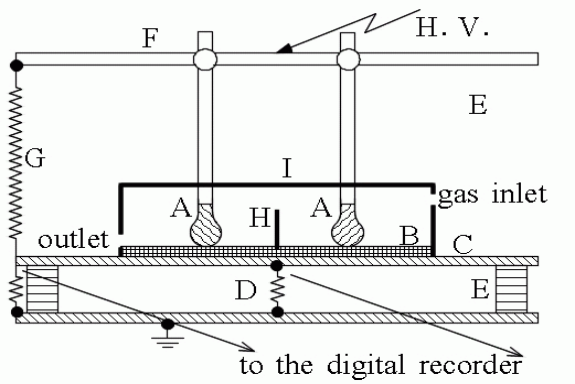

FIGURE1. Experimental setup

A: Spherical electrode,
B: Acrylic resin insulator,
C: Back electrode, D: Current shunt,
E: Insulators, F: Metallic bars,
G: Voltage divider,
H: Shading plate or optical filter,
I: Chamber for gas charging.

3. RESULTS AND DISCUSSIONS

3.1. Effect of Optical Filters

Figure 2 shows the variation in the synchronization probability in air with cutoff wavelength utilizing the optical filters in place [4]. The probabilities are almost 0% until the filter with 400 nm cutoff. However, the value remarkably increases as cutoff wavelength becomes shorter through 300, 250 and 165 nm. The probability with filtering at 115 nm is 100% over 100 measurements. The plot at 700 nm represents the result for the shading plate in place, showing asynchronous generation. In contrast, the plot at 0 represents the result without shading plate or filter, showing completely synchronous generation. The results suggest that the discharge light including UV and VUV emitted from the streamer is capable of being a source of initial electrons for the successive surface discharges.

3.2. Effect of Humidity

Figure 3 shows the time lags of the first and the second streamers in humid air and dry conditions. Here, the time lags are defined as the time between the origin of the applied voltage waveform and the peak of the current pulse. Dry condition means that the insulator was dried by a hair dryer. On the other hand, humid air means that the relative humidity of surrounding air was above 90% and no drying treatment was done. Humidity is effective for decrease of the time lag of the streamer. When the time lags of both the first and the second streamer are minimized, the time lags are approximately equal and are judged as both the streamers were synchronized. Therefore, the synchronization probability increases as the humidity increases. Humidity effect [5][6] have also proposed by Gosho report on the time lags in SF_6 [7] and the same mechanism might be applied on an insulator plate.

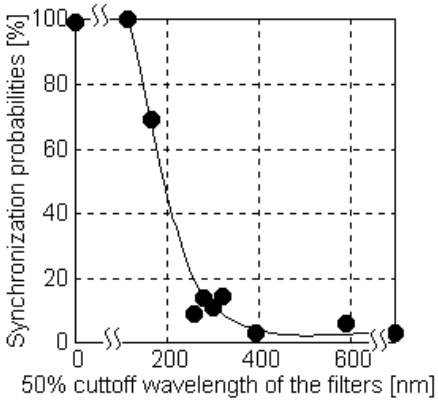

FIGURE 2. Synchronization probabilities as a function of cutoff wavelength.

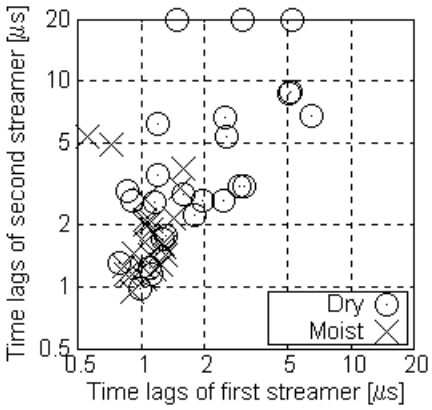

FIGURE3. Time lags of the first and the second streamers.

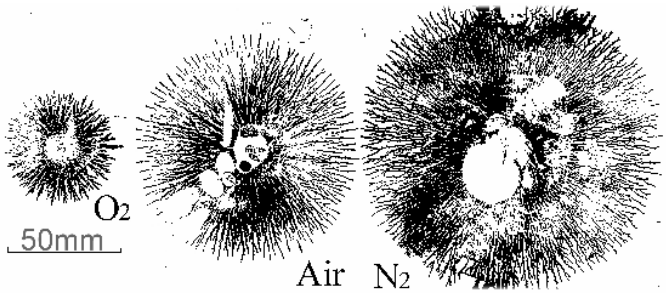

FIGURE 4. Dust figures for the gases.

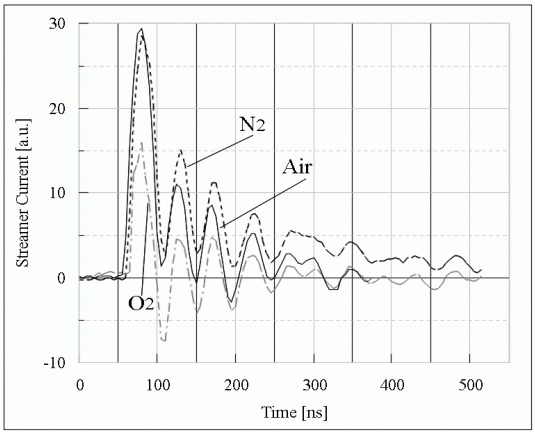

FIGURE 5. Current wave forms for the gases.

3.3. Effect of Types of Gases

Figure 4 shows the dust figures of the streamers in oxygen, air and nitrogen. The applied voltage was almost the same but the diameters are clearly different as Przibram reported [8] in 1920. It is considered that, because nitrogen is not only incapable of

attaching electrons but also producing active species and photons, the streamer in nitrogen grows larger than that in air. On the other hand, because oxygen is electronegative, the electron attachment inhibits the growth of the streamer in oxygen. Since air is a mixture of oxygen and nitrogen, the diameter of air is also intermediate.

Figure 5 shows the current waveforms for oxygen, air and nitrogen corresponding respectively to the dust figures in Figure 4. In oxygen, the current pulse with the lowest peak decreases rapidly, but in the nitrogen the higher peak is found and the values decrease slowly, maybe for the reason above.

4. CONCLUSION

The results suggest that the photon energy required to supply initial electrons sufficient to trigger the surface streamers on an acrylic resin insulator is at least 5 eV, and more enhancements are found at 8 eV and 10 eV. This is considered to be due to the existence of a number of photoabsorption windows for oxygen in this vacuum ultraviolet (VUV) region. The diameter of the dust figure and the decay time of the streamer current are influenced by the types of the gases. Humidity is effective for the decrease of the time lag of the surface streamer in the same manner as in a gaseous discharge.

These phenomena are involved with photoemission from an insulator surface, photoabsorption and photoionization of the surrounding gases. Therefore, on supplying the initial electrons, these problems are strongly related to the dielectric barrier discharge, the micro discharge, plasma display and other trends on plasma physics and industrial applications.

ACKNOWLEDGMENTS

The authors would like to thank Mr.ASANUMA Takuya, Mr.TAKAGI Tetsuya and Mr.TOBINAGA Kazuma of Kisarazu college for assistance with the experiments.

REFERENCES

[1] Pedersen, P. O. (1919). On the Lichtenberg Figures Part I. A Preliminary Investigation. Andr, Fred, Host & Son, Kobenhavn.

[2] Chiba, M., Hidaka, K. and Kouno, T. (1992). Paper of the Technical Meeting on Electrical Discharge, IEEJ ED-92-114. (in Japanese)

[3] Tanaka, M., Murooka, Y. and Hidaka, K. (1987) Nanosecond surface discharge development using the computer simulation method. J. Appl. Phys., 61, 9, 4471-4478

[4] Kashiwagi, Y. and Itoh, H. (2006) Synchronization of positive surface streamers triggered by vacuum ultraviolet in atmosphere. J. Phys. D: Appl. Phys., 39, 113-118.

[5] Aints, M., Haljastea, A. and Roots, L. (2002) Photoionizing radiation of positive corona in moist air. HAKONE VIII, P5.1, 282-285

[6] Naidis.G.V. (2006) On photoionization produced by discharges in air. Plasma Sources Sci. Technol., 15, 253-255.

[7] Gosho, Y. (1974) Anomalous Decrease of Time Lag of Breakdown of Gaps in Gases by Mixing Water Vapor", T. IEE Japan, 94-A, 9. (in Japanese)

[8] Przibram, K. (1920) Phys. Z., 21,480.

THE EFFECT OF TEMPERATURE ON CORONA CHARACTERISTICS AND ITS REVELATION*

Chen Shixiu[1], Chen Cixuan[1], Xie Guangrun[1], Sun Youlin[2], Chen Xuegou[1]

[1]*School of Electrical Engineering, Wuhan University*
[2]*School of Physics Science & Technology, Wuhan University*
Wuhan Hubei,430072 China

ABSTRACT. Because temperature affects corona characteristics greatly, it is important to find out how dose the corona characteristics vary with temperature. To understand the characteristics of onset voltage and breakdown voltage of both positive and negative corona varying with temperature, both the experiment results and theoretic analyses are reported in this paper.

1. INTRODUCTION

Temperature of flue gas to be treated by ESP may be much higher than the room temperature, which depends on the kinds of industrial furnaces and technology. Because temperature greatly affects both corona characteristics of both onset voltage and breakdown voltage, to get higher dust collection efficiency, operating voltage should be lower than but close to the breakdown voltage. In this case, how to determine the suitable corona polarity to get a higher voltage is very important. Early on we have found out the corona characteristics of both onset voltage and breakdown voltage varying with temperature under positive corona and negative corona, respectively [1], the remainder work, why dose the characteristics of both positive corona and negative corona vary with temperature, is reported in this paper.

2. EXPERIMENTAL RESULTS AND ANALYSES

The characteristics of onset voltage and breakdown voltage of both positive and negative corona under one atmospheric pressure versus temperature are illustrated in Fig.1.

2.1 Onset voltage

a. It can be seen from fig.1 that from 280k to 873k, the onset voltage of negative corona is always lower than that of positive corona, which indicates that the explanation of why the onset voltage of negative corona is lower than that of positive corona at room temperature holds true in this temperature range [2].

b. The onset voltage of both positive and negative corona drop slowly along with temperature increasing.

---

* The Project supported by the Natural Science Foundation of China（58977295）.

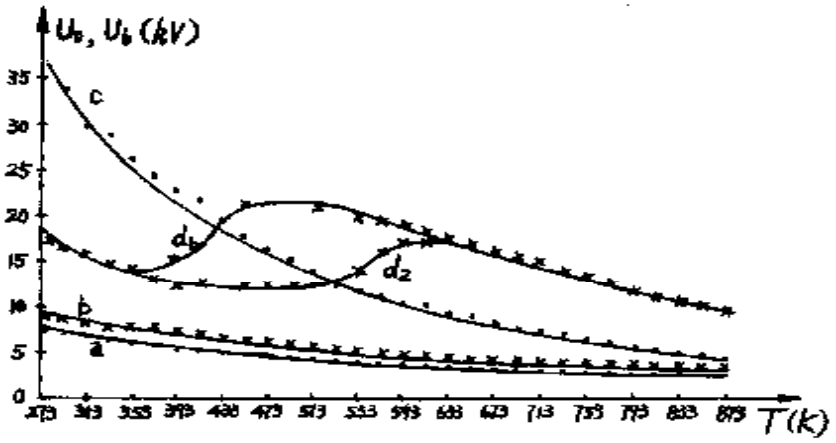

Curve a: onset voltage of positive corona, Curve b: onset voltage of negative corona, Curve c: breakdown voltage of negative corona, Curve d_1, d_2: breakdown voltage of positive corona.

FIGURE 1. Onset voltage and breakdown voltage versus temperature

If onset voltage is known when temperature is T_0, then the onset voltage at temperature T can be forecasted by Eq.(1)

$$U_T = (T_0 / T) U_0 \qquad (1)$$

Table 1 shows the experimental data、 calculated data and relative errors ($\Delta = \left| \frac{U' - U}{U'} \right| \times 100\,\%$) of onset voltage for both positive corona and negative corona at different temperature.

TABLE 1. Experimental data and calculated data of onset voltage

T(k)	Positive corona			Negative corona		
	Experimental Data U(kV)	Calculated Data U'(kV)	Δ	Experimental Data U(kV)	Calculated Data U'(kV)	Δ
280	9.2	10.05	10.4	7.5	7.88	4.8
373	7.6	7.54	0.8	5.5	5.92	7.1
473	6.2	5.95	4.2	4.8	4.67	2.8
573	5.0	4.91	1.8	4.0	3.85	3.9
673	4.1	4.18	1.9	3.3	3.28	0.6
773	3.8	3.64	4.4	2.9	2.86	1.4
873	3.2	3.22	0.6	2.6	2.53	2.8

It can be seen from table 1 that the calculated data coincide with the experimental data quite well.

2.2 Breakdown voltage of negative corona

Curve 1 in Fig.2 shows the electric field excited by applied voltage between the needle-plate electrodes. The space charge resulted from ionization will distort markedly the electric field shown by curve 1, at this moment, the distribution of electric field in gas is shown by curve 2. Along with the raising of applied voltage, the ionization region stretches

towards the anode electrode gradually, electric field is shown by curve 3. If applied voltage is high enough to result in a new electron avalanche at the boundary of the ionization region, which would eventually lead to a streamer, breakdown will follow in the gap.

Assuming that E_0 and E_1 are field strength at the boundary of the ionization region excited by applied voltage and the space charge respectively, so $E_0 = cU$. Since direction of vector E_1 at the boundary of the ionization region is the same as that of vector E_0, the vector sum at the boundary is E_0+E1[3]. In this case, to ionize a gas molecule, the following condition should be meet

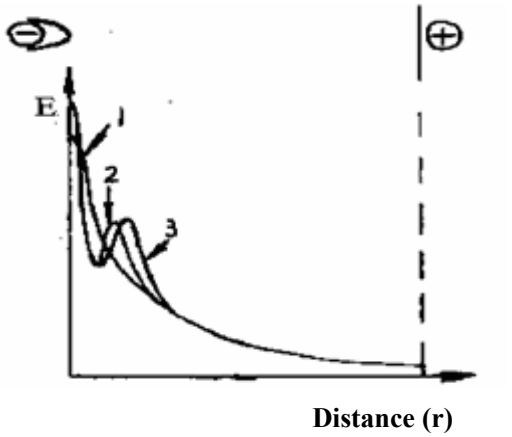

FIGURE 2. Sketch of electric field in needle-plate gap

$$e(|cU| + E_1)\bar{\lambda}_e \geq eU_i \qquad (2)$$

Suppose that a gas molecule could be ionized as long as the electron energy equals the ionization energy of a gas molecule, which implies that the ionization probability equals to 1. So, Eq. (2) can be rewritten as

$$|cU|\bar{\lambda}_e = U_i - E_1\bar{\lambda}_e \qquad (3)$$

When temperature is at T_0 and T respectively, the corresponding mean free path of electron is $\bar{\lambda}_{e0}$ and $\bar{\lambda}_{eT}$, breakdown voltage U_0 and U_T, field strength excited by the space charge E_{10} and E_{1T}, respectively. Then substitute these two sets of data into Eq. (3) respectively, and divide one set of data by another set, hence

$$\frac{|U_0|\bar{\lambda}_{e0}}{|U_T|\bar{\lambda}_{eT}} = \frac{(U_i - E_{10}\bar{\lambda}_{e0)}}{(U_i - E_{1T}\bar{\lambda}_{eT})} \qquad (4)$$

where the $\bar{\lambda}_{e0}$ and $\bar{\lambda}_{eT}$ can be calculated from $\bar{\lambda}_e = kT / p\pi r^2$, radius of a gas molecule can be taken as 1.75×10^{-10}m, the ionization potential of a gas molecule can be taken as 15.6V[1]. It can be seen from Eq.(4) that if breakdown voltage U_0 at temperature T_0 has been known, to find out the breakdown voltage U_T at temperature T, the E_{10} and E_{1T} should be find out at first. Known to all, the space charge may distort the applied electric field, but the ability for space charge to distort the field for a gap is limited to a certain value. So we can assume when close to the critical breakdown voltages at different temperature, the field strength at the boundary of the ionization region excited by the space charge should be equal. That is, $E_{10}=E_{1T}=E_{1i}=\bar{E}$.

From experiment data of breakdown voltage at different temperature, $E_{10}=E_{1T}=E_{1i}$ can be calculated to be about $\bar{E}$ =100kV/cm, then Eq. (4) can be gives

$$|U_T| = \delta U_0(U_i - \bar{E}\bar{\lambda}_{eT})/(U_i - \bar{E}\bar{\lambda}_{e0}) \qquad (5)$$

δ is relative density of gas. Eq.(5) shows that the breakdown voltage is only a function of mean free path of electron, in other words, is only a function of gas density.

2.3 Breakdown voltage of positive corona

It can be seen from Fig.1, that breakdown voltage of positive corona drops along with the temperature increasing and is lower than that of negative corona in the range of 280k~333k. Experiments on breakdown voltage repeated 5 times show that the range about from 333k to 633k is a transition range in which the breakdown voltage of positive corona some times lower than, but some times higher than that of negative corona. In 633k≤T≤873k, breakdown voltage of positive corona drops along with the temperature increasing but it is higher than that of negative corona.

Why is the breakdown voltage of positive corona higher than that of negative corona in the range of 633k≤T≤873k. Because the mean free path of an electron at temperature 673K is almost twice of that of an electron at 373K, therefore an electron can accumulate bigger energy at higher temperature; after collisions of these bigger energy electrons with neutral particles, the latter will emit a mount of photons when they transit to some lower energy levels or base energy level. Under this condition, it seems that glow corona occurs in positive corona, which means that photon ionization plays more important role. Because photon ionization can take place in the outside of corona region, and in which electric strength is weaker than in corona region; as a result, electrons will attach more easily to the neutral particles to form negative ions, these negative ions drift towards positive electrode and forms a swarm of negative ions in adjacent region of positive electrode, which will make the electric field in corona region more uniform; but in negative corona case, negative ions can not make the electric field more uniform; eventually, breakdown voltage of positive corona is higher than that of negative corona.

3. CONCLUSIONS AND SUGGESTION

(1) Experimental results and theoretical analyses show that onset voltage and breakdown voltage of both positive and negative corona (except in range of 333k<T<633k for positive corona) varying with temperature are due to the decrease of gas density, or the increase of mean free path of electron.

(2) In application of ESP, if temperature of flue gas is higher than 533K, it is better to use positive corona, because the breakdown voltage of positive corona is higher than that of negative corona.

(3) It is possible to make breakdown voltage of positive corona higher than that of negative corona in temperature range lower than 353K if ultraviolet light irradiates the space between electrodes, further experiment study should be continued.

REFERENCE

[1]Shixiu Chen, et al. .The Effect of Gas Density on Corona Characteristics, 10th International Symposium on High Voltage Engineering: 235-238, Montreal, Canada, 1997.

[2]Zhu Deheng, Yian Zhang, High voltage insulation, Tsinghua University Press House, 1992.2.

[3]E. Kuffel, W. S. Zaengl, High-voltage engineering fundamentals, Pergamon Press Ltd., 1984.

SOME PECULIARITIES OF THE BARRIER DISCHARGE IN PURE ARGON

K.V. Kozlov [a], P.A. Tatarenko and V.G. Samoilovich

Department of Chemistry, Moscow State University, Leninskie Gory 1, str.3, 119899 Moscow, RUSSIA

ABSTRACT. Microdischarges of the dielectric barrier discharge in a symmetric electrode arrangement ("glass-glass") in pure argon at atmospheric pressure were investigated by cross-correlation spectroscopy. In the emission spectrum of the discharge, spectral bands of the second positive system of nitrogen as well as of OH-radical were observed besides the peaks of argon. The following three spectral indicators were used to record the spatio-temporal distributions of the microdischarge luminosity: Ar*(4p), λ=727.3 nm; $N_2(C^3\Pi_u)$, λ=337 nm; and $OH(A^2\Sigma^+)$, λ=309 nm. The radiation kinetics of these species is discussed briefly.

1. INTRODUCTION

This experimental research was originally aimed at establishing the mechanism of the barrier discharge (BD) development in pure argon at ambient pressure. However, some preliminary experiments showed that even visible shape of the discharge as well as its electrical characteristics depended strongly on the concentrations of the impurities in the ppm range. That is why an investigation of the influence of impurities upon the BD mechanism became second objective of this work. Electrical measurements and the technique of cross-correlation spectroscopy (CCS, see [1,2]) were used as basic diagnostic tools.

2. EXPERIMENTAL SET-UP AND PROCEDURE

The main idea of the method of cross-correlation spectroscopy (CCS) is to replace a direct measurement of the single pulse luminosity of a repetitive light pulse emitter by a statistically averaged determination of the correlation function between two optical signals, both originating from the same source. The first one of these signals (so-called "synchronizing signal") is used to define a relative time scale, the second one ("main signal") has to be detected with a probability at least one order of magnitude lower, than that one of the synchronizing signal. The measured quantity is actually a time delay between these two signals, and the recorded quantity is a probability density function for the light pulse intensity evolution. If the repetitive light pulses reproduce each other sufficiently exactly, and if the synchronizing signal detection is adjusted in such a way as to occur always at the same moment of a single light pulse evolution, then the recorded probability density function is proportional to the light intensity *I(t)* of the source under consideration. A detailed description of the theoretical foundations of CCS technique is given in the book [1].

The CCS-setup is shown schematically in fig.1. By means of a quartz lens, the discharge zone is imaged onto the optical slit. By appropriate adjustment and movement of this slit, the discharge area can be scanned in vertical direction (resolution not worse than 0.1 mm). Thus localized radiation (MAIN signal) is resolved spectrally by a monochromator and detected by the high-gain photo-multiplier (PMT 1) operated in a single photon counting mode.

[a] Electronic address: kozlov@kge.msu.ru

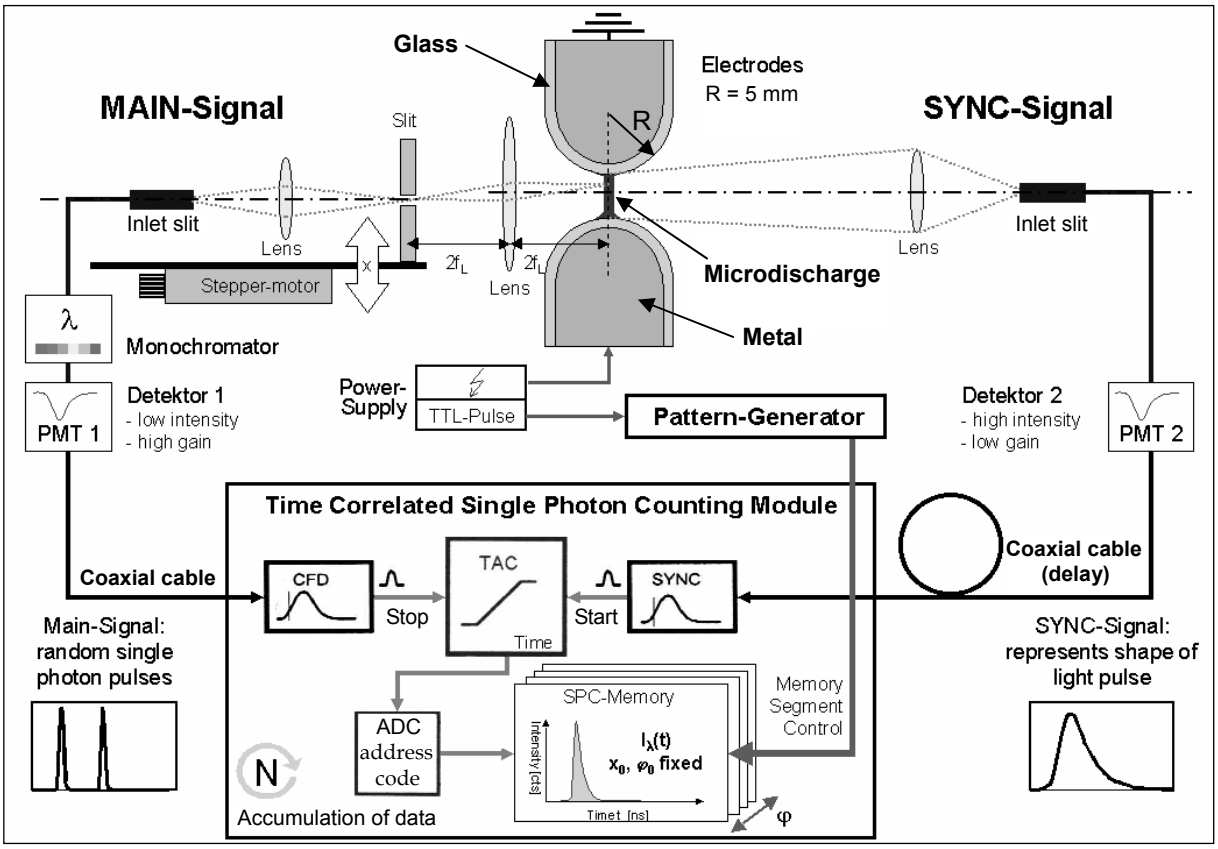

FIGURE 1. General scheme of the discharge cell and a diagram of the CCS-apparatus.
Abbreviations: PMT – photomultiplier tube, SYNC – synchronization, CFD – constant fraction discriminator, TAC – time-to-amplitude converter, ADC – analogue-to-digital converter, SPC – single photon counting.

The second detector (PMT 2) provided the synchronizing (SYNC) signal necessary for the CCS measurements (see [1,2] for the details).

For the CCS-measurements, we used the instrument "Fluor-99" manufactured by the company "NPO Spektroskopiya" from Belarus and equipped with the special photo-multipliers [3], combined with the monochromator "MDR-2". The basic components of this instrument are two discriminators (CFD and SYNC), a time-to-amplitude converter (TAC), an analogue-to-digital converter (ADC) and a memory. The time gate of the TAC of the instrument "Fluor-99" enable the variation of the time scale from 50 ns up to 40 μs corresponding to 1024 channels for data recording.

In order to localize filamentary BD (a sequence of microdischarges, MDs) to a definite position, we used special semi-spherical glass electrodes with the radius of curvature of 5 mm. The discharge gap width (distance between the electrode tips, see fig.1) was about 1 mm. Feeding voltage frequency was varied within the range 4-7 kHz. To investigate individual MDs, the voltage amplitude was adjusted so as to maintain the DBD in a mode corresponding to 1 MD per half cycle. Under these experimental conditions, the discharge demonstrated perfect localization and extremely high stability.

3. RESULTS AND DISCUSSION

Emission spectrum of the BD in pure argon was found to consist of the peaks of Ar*, the bands of OH* radical, and the bands of molecular nitrogen (2^{nd} positive system), although the concentrations of H_2O and N_2 in argon were about 3 ppm and 10 ppm, respectively [4]. The most intensive lines corresponding to these species (λ=727.3 nm for Ar*, λ=309 nm for OH*,

and λ=337 nm for N_2*,) were chosen as their spectral indicators. Spatio-temporal distributions of radiation intensity for thus selected wavelengths within the MD channels were determined by means of the technique of CCS with the resolution of 0.1 mm over spatial coordinates and of 0.05 ns over time. Some results of these measurements are shown in fig.2.

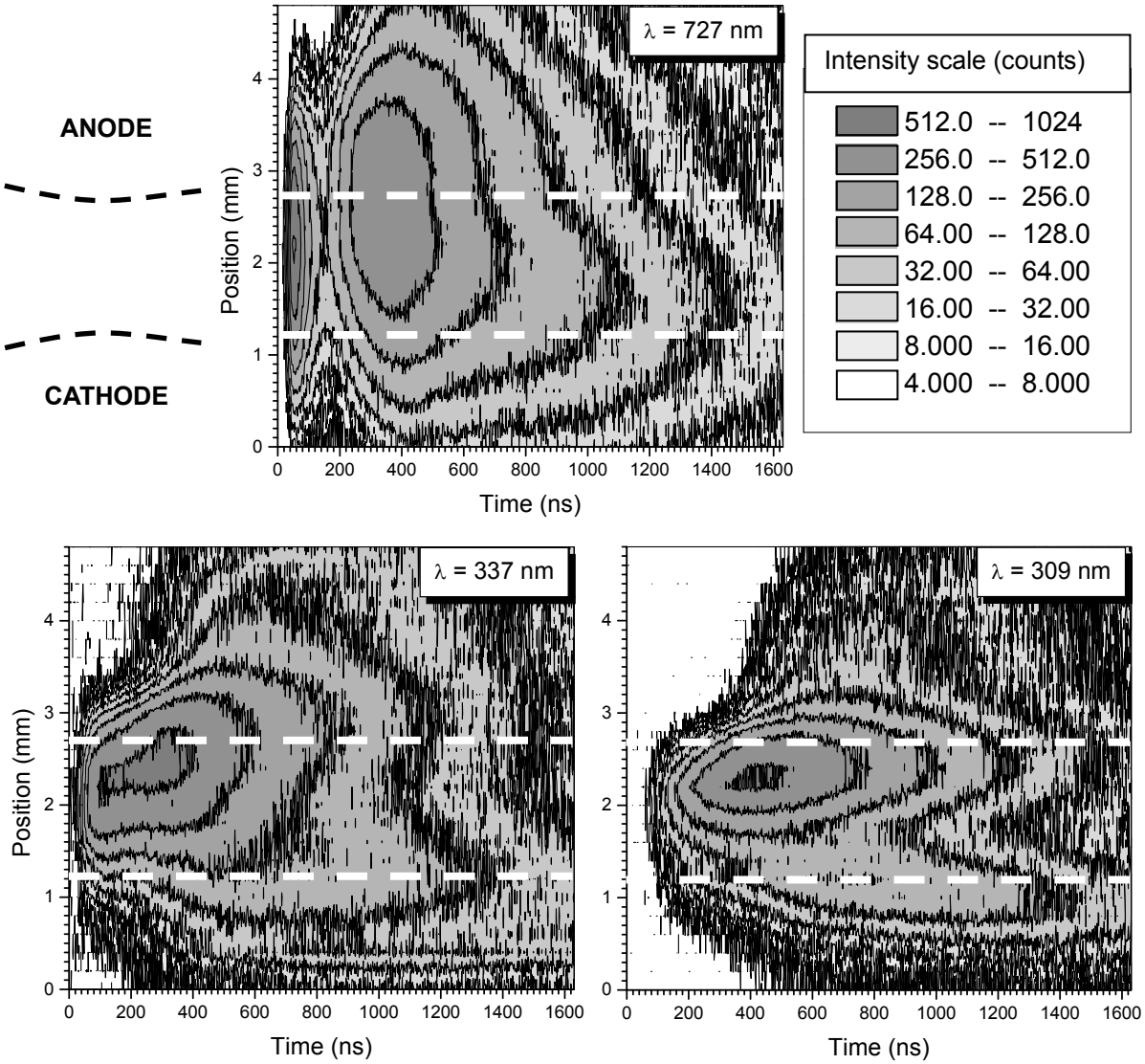

FIGURE 2. Spatio-temporal distributions of the luminosity for three selected spectral indicators. Experimental conditions: flowing argon at p=1.1 bar; the distance between the electrode tips (denoted on the figures by the white dashed lines) d = 1.5 mm; voltage frequency f = 5.1 kHz..

The following peculiarities of the luminosity distributions presented in fig.2 should be noted. First, there are two distinct periods of the MD activity corresponding to the local maximums of radiation intensity of Ar* (40-60 ns and 300-500 ns, see upper plot in fig.2). This is an evidence for a double-step mechanism of electrical breakdown. Second, there are considerable differences in the luminosity distributions for different spectral indicators. This can be regarded as an evidence for complex radiation kinetics within the MD channel.

The phenomenon of a double-step electrical breakdown in argon was observed earlier in the BD for discharge gap width of 4 mm [5], and in a long gap for the spark breakdown [6]. The authors [6] explained the mechanism of second breakdown by the dominant role of the metastable excited states of Ar. The metastables of Ar can be also an additional (indirect)

source of the radiating species OH* and N_2*. The latter assumption accounts for the complicated nature of radiation kinetics.

In the case of a closed system, the properties of BD were found to change gradually. After 2-3 hours of the BD operation without gas flow, the second intensity maximum for Ar* disappeared (see fig.2), and the light pulse duration for all three spectral indicators decreased considerably. Furthermore, the burning voltage was increasing continuously during this initial period, in contrast to the case of an open flowing system with argon flow rates greater than 10 l/h when no changes in discharge operation were observed (see fig.3). For the gas flow rates less than 10 l/hour, an increase in burning voltage was found to occur as well, although it was lower than in the case of a closed system.

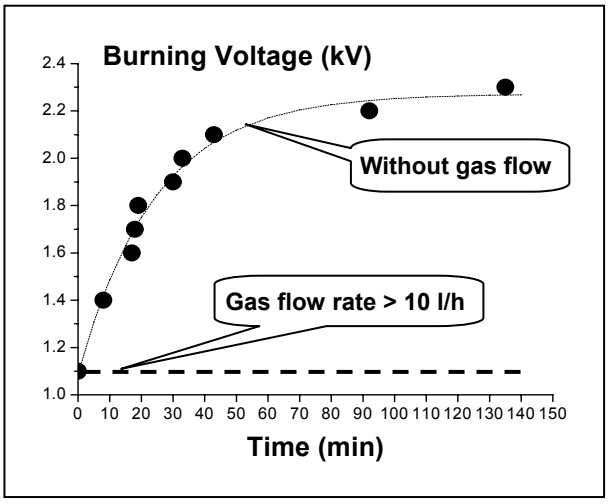

The described above changes of the BD properties in a closed system can be explained by the effect of accumulation of some impurities (molecular gases) in the discharge area. Such impurities (N_2, O_2, H_2O, CO_2 etc.) are present in argon in a ppm-range. These molecules are effective quenchers of the radiating species as well as of the metastable excited states of Ar. Hence, an increase in their concentrations within the MD channel accounts for the experimentally observed shortening of the light pulses and disappearance of the second intensity maximum for Ar*.

FIGURE 3. Evolution of burning voltage in the barrier discharge in pure argon. d = 1 mm; f = 6 kHz.

On the other hand, a local increase in the concentrations of molecular admixtures in the discharge area can be expected to affect the process of electrical breakdown in argon due to their influence on electron energy distribution function. The greater the content of molecular admixtures in argon, the lower the electron energy. In order to compensate this effect and to sustain the BD operation, certain increase of the electric field strength (consequently, of the burning voltage of the BD) appears to be necessary.

REFERENCES

[1] Becker W. Advanced Time-Correlated Single Photon Counting Techniques. Springer-Verlag Berlin Heidelberg, 2005.

[2] Kozlov K.V., Wagner H.-E., Brandenburg R., Michel P. Spatio-temporally resolved spectroscopic diagnostics of the barrier discharge in air at atmospheric pressure. J. Phys. D: Appl. Phys., 2001, v. 34, No. 21, p. 3164-3176.

[3] Vetokhin S.S., Ermalitski F.A., Melnikov S.M., Sukhanin S.V. Functional Materials, 1996, v.3, p.556-561.

[4] Kozlov K.V., Tatarenko P.A., Chernov S.V., Samoilovich V.G. Spatio-temporal structure of the microdischarge in argon at atmospheric pressure. Proc. 4 Int. Symp. on Theoretical and Applied Plasma Chemistry, Ivanovo, Russia, 2005, ISBN 5-9616-0087-4, v.2, p. 553-556 (in Russian).

[5] Heuser C. Zur Ozonerzeugung in Elektrischen Gasentladungen. Thesis RWTH Aachen (Germany), 1985 (in German).

[6] Aleksandrov N.L., Bazelyan E.M., Gorunov A.Yu., Kochetov I.V. A non-thermal mechanism of spark breakdown in Ar. J.Phys.D: Appl. Phys., 1999, v.32, p.2636-2644.

Paper number

ELECTRON AND GAS TEMPERATURE EVALUATION OF A HE ATMOSPHERIC PRESSURE, DC HOLLOW-CATHODE MICRO PLASMA BY A PROCEDURE BASED ON TRACE RARE GASES OPTICAL EMISSION SPECTROSCOPY

T. Nakano[1], H. Akashi[2], H. Imaizumi[1] and T. Kitajima[1]

[1] *Department of Electrical and Electronic Engineering,*
School of Electrical and Computer Engineering, National Defense Academy
1-10-20 Hashirimizu, Yokosuka, 239-8686, JAPAN
[2] *Department of Applied Physics,*
School of Applied Science, National Defense Academy
1-10-20 Hashirimizu, Yokosuka, 239-8686, JAPAN

ABSTRACT. The evaluation of electron and gas temperatures (T_e and T_g) in a positive column of a He DC hollow-cathode micro plasma using the optical emission intensity of trace rare gases is presented. The T_e and T_g are evaluated with the ratio of the emission intensity from the Ar $2p_1$ level to that from the Xe $2p_5$ level and also the ratio of the intensity from the Ar $2p_1$ level to that from the Ar $2p_5$ level. The electron energy distribution and T_g are also evaluated using non-Maxwellian electron energy distribution functions (EEDFs) and compared those evaluated assuming Maxwellian EEDFs.

1. INTRODUCTION

Hollow-cathode micro plasmas have drawn much attention because of their potential applications such as vacuum ultraviolet light emission and material processing. When optimizing the characteristics of the plasmas for these applications, it is essential to know the electron and gas temperatures (T_e and T_g) of the plasmas. The T_e and T_g in micro plasmas have been measured by laser Thomson scattering [1]. This measurement is, however, not so easy and requires a high-energy laser and a special spectroscopic instrument for extreme reduction of stray light. The measurement of the T_e and T_g in micro plasmas should be made preferably by simple and easy procedures.

In the present study, the evaluation of the T_e and T_g in a positive column of a DC hollow-cathode micro plasma through He at atmospheric pressure by a procedure based on trace-rare-gas optical emission spectroscopy (TRG-OES) is presented [2]. The physical validity of the T_e and T_g evaluation by this procedure is discussed by Monte Carlo simulation (MCS) of electron swarms in atmospheric pressure He. A comparison is made between the electron energy distribution functions (EEDFs) evaluated by the TRG-OES-based procedure and those computed by MCS, which confirms the physical validity of the T_e and T_g evaluated by the procedure proposed in this study. Moreover, an attempt is made that the electron energy distribution and T_g is evaluated using the non-Maxwellian EEDFs obtained from the Boltzmann equation solutions by 6-term approximation.

2. EXPERIMENTAL

Schematic representation of a DC hollow-cathode micro plasma source and an optical emission measurement system used in the present study is shown in Fig. 1. A 1-mm-thick cupper disk with a 0.1-mm diam. aperture made in its center or a 0.1-mm ID stainless steel tube is served as a hollow-cathode. After evacuating a vacuum chamber to 1.3 Pa, trace-rare-gas-added He is fed to the chamber through the hollow cathode. The trace rare gases (Ar, Kr, and He) are added 5 ppm to He. Typical conditions of micro plasma generation are 10-30 mA of the discharge current, 350-400 V of the anode-cathode voltage and 100-300 sccm of the gas flow rate. Optical emission of the micro plasma is sampled in the middle of a 3-mm gap between electrodes, from the direction perpendicular to the symmetrical axis of the electrodes. Thus, a positive column of the plasma is diagnosed in the present study. The optical emission is focused onto the entrance slit of a monochromator with a lens. The emission intensity of the lines from the level of Ar $2p_1$ (at 750.4 nm), $2p_5$ (at 751.4 nm) and Xe $2p_5$ (at 828.0 nm) is measured using a photomultiplier equipped to the monochromator and saved to a PC via an A/D converter. Despite of a small concentration (5 ppm) of trace rare gases, the three lines were found to be recorded clearly.

The reduced electric field in a positive column of the micro plasma is evaluated from the T_g determined by the TRG-OES-based procedure and the electric field in the positive column. The electrode potential variations caused by slight (±0.1 mm), periodic changes in an electrode gap are measured. Assuming that the electric field is unaltered when the electrode gap is varied, the electric field is calculated to be the ratio of the electrode potential variation to the electrode gap change. The reduced electric field is obtained by dividing the electric field by the He number density calculated with T_g.

MCS of electron swarms in He is done by the null-collision method[3]. The set of cross sections provided by Kinema Research & Software[4] is employed. The computed swarms are sampled by the pulse Townsend method in order to obtain transport coefficients and EEDFs.

3. RESULTS AND DISCUSSION

The evaluation of T_e and T_g is based on TRG-OES[5]. In this method, T_e is determined by comparing the measured intensity of the optical emission lines from trace rare gas atoms with that computed by a simple model for the excitation and de-excitation of the atoms. Because a DC hollow-cathode micro plasma is generated at atmospheric pressure, the model for computing the rare gas line intensity is modified slightly to take account of the collisional quenching of excited species by He atoms.

In the present study, the ratio of the emission line intensity from the Ar $2p_1$ level to that from the Xe $2p_5$ level (Ar $2p_1$/Xe $2p_5$) and also the ratio of the emission line intensity from the Ar $2p_1$ level to that from the Ar $2p_5$ level (Ar $2p_1$/Ar $2p_5$) are employed to determine T_e and T_g simultaneously. These ratios are computed as a function of T_e and T_g. Because of different quenching rate coefficients and threshold energies of optical emission for these levels, the T_e and T_g dependence of the Ar $2p_1$/Xe $2p_5$ intensity ratio are different from that of the Ar $2p_1$/Ar $2p_5$ intensity ratio. As a consequence, T_g-T_e relations drawn under constant intensity ratios for Ar $2p_1$/Xe $2p_5$ are different from those for Ar $2p_1$/Ar $2p_5$. Thus, T_e and T_g can be determined simultaneously by seeking a pair of T_e and T_g which gives the computed ratios of Ar $2p_1$/Xe $2p_5$ and Ar $2p_1$/Ar $2p_5$ that are equal to those measured[2]. For an example, the Ar $2p_1$/Xe $2p_5$ and Ar $2p_1$/Ar $2p_5$ intensity ratios were measured to be 1.25 and 6.52, respectively, for the plasma generated at a flow rate of 200 sccm and a discharge current of 20 mA. From these ratios, the T_e and T_g of the plasma are evaluated to be 1.25 eV and 665 K, respectively, as

shown in Fig. 2. The evaluated T_e is comparable to those reported previously for the micro plasmas generated in similar conditions[1].

Comparison of an EEDF deduced from the TRG-OES-based evaluation of T_e with that computed by MCS is made to ensure further the physical validity of the T_e and T_g evaluation. An evaluated EEDF in a positive column of the micro plasma, which is a Maxwellian EEDF with an average T_e (1.1 eV) of four TRG-OES measurements, is shown in Fig. 3 together with the EEDFs computed by MCS. The EEDFs are computed with 4.0, 4.5 and 5.0 Td of reduced electric field. Comparison of the EEDFs in Fig. 3 clearly indicates that the MCS-computed EEDF at 4.5 Td exhibits the same exponential decay with electron energy as that of the Maxwellian EEDF determined by the TRG-OES-based procedure. The reduced electric field in the positive column is, meanwhile, deduced to be 4.9 Td from a measured electric field in the positive column (6.3×10^4 V/m) and an average of the four T_g measurements (570 K) when the plasma is generated at 20 mA and 200 sccm.

In general, by TRG-OES, T_e is evaluated from the exponential decay in an EEDF above the electron energy where electronic excitation processes begin taking place[5]. In particular, the intensity ratios of Ar $2p_1$/Xe $2p_5$ and Ar $2p_1$/Ar $2p_5$ are determined predominantly by the EEDF shape above ≈9 eV because of the weak stepwise excitation via metastable levels to Ar $2p_1$, $2p_5$ and Xe $2p_5$ levels from which radiative transition occurs. Consequently, the MCS-computed EEDF at 4.5 Td corresponds to the Maxwellian EEDF deduced from the TRG-OES-based procedure. The satisfactory agreement of the reduced electric field employed by MCS (4.5 Td) with the field determined experimentally from the measured electric field and the T_g evaluated by the TRG-OES-based procedure (4.9 Td) is strong evidence that this procedure provides physically valid T_e and T_g in a positive column of the DC hollow-cathode micro plasma in He. It should be noted that this procedure is available when the electron density of plasma is lower than $\approx10^{19}$ m^{-3}, i.e. the condition that the physical validity of the computation model for the TRG line intensity is confirmed.

The procedure proposed in the present study determines a non-Maxwellian EEDF using the intensity ratios of Ar $2p_1$/Xe $2p_5$ and Ar $2p_1$/Ar $2p_5$ if non-Maxwellian EEDFs are employed to compute the intensity of the above lines. To demonstrate this, the EEDFs are obtained from Boltzmann equation solutions by 6-term approximation because the EEDFs computed by MCS exhibit a large statistical error when they decrease to about 10^{-6}. As the parameter

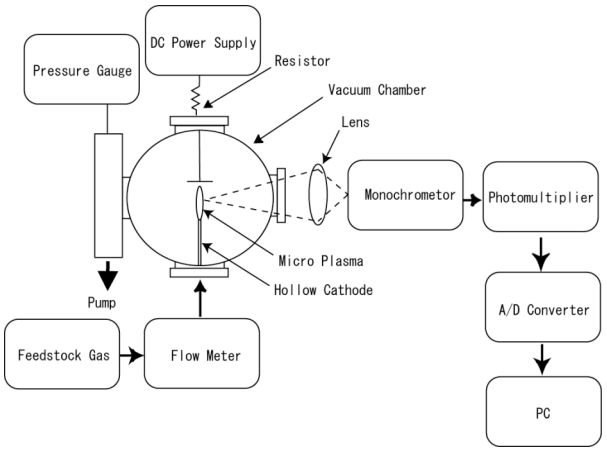

FIGURE 1. Schematic representation of a DC hollow-cathode micro plasma source and an optical emission measurement system.

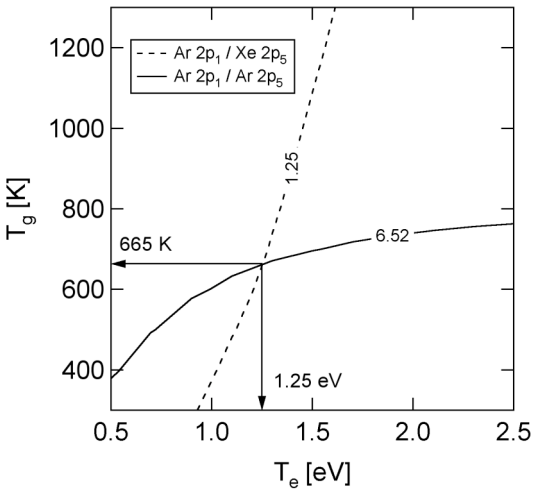

FIGURE 2. T_g-T_e relations drawn under constant emission intensity ratios for Ar $2p_1$/Xe $2p_5$ and Ar $2p_1$/Ar $2p_5$.

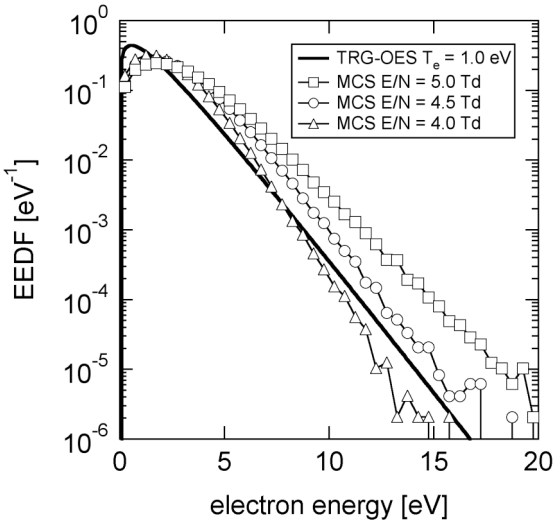

FIGURE 3. Comparison of the EEDF evaluated by the TRG-OES-based procedure with the EEDF computed by Monte Carlo simulation.

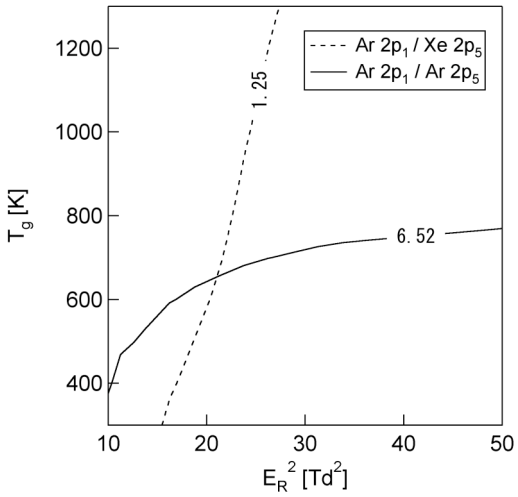

FIGURE 4. T_g-E_R^2 relations drawn under constant emission intensity ratios for Ar $2p_1$/Xe $2p_5$ and Ar $2p_1$/Ar $2p_5$.

characterizing the shape of an EEDF, the reduced electric field (E_R) is employed. Thus, the intensity ratios of Ar $2p_1$/Xe $2p_5$ and Ar $2p_1$/Ar $2p_5$ are computed as a function of E_R^2 ($\propto T_e$) and T_g. Using this result, T_g-E_R^2 relations are drawn as shown in Fig. 4, where the relations drawn under the same intensity ratios as used in Fig. 2 are indicated. A root mean square of E_R^2 and a T_g average of the four TRG-OES measurements were found to be 4.2 Td and 560K, respectively. The T_g evaluated by non-Maxwellian EEDFs is in excellent agreement with the T_g evaluated by Maxwellian EEDFs. The fair agreement of the E_R evaluated by the non-Maxwellian EEDFs with the E_R determined by the electric field and TRG-OES measurements support the physical validity of the electron energy distribution and T_g evaluated by the procedure proposed in the present study.

4. CONCLUSIONS

The evaluation of T_e and T_g in a positive column of a He DC hollow-cathode micro plasma using the optical emission intensity of trace rare gases is presented and demonstrated. The physically valid T_e and T_g is found to be evaluated from the discussion based on the MCS-computed electron energy distribution. The use of non-maxwellian EEDFs in the procedure presented here is also confirmed to provide the physically valid T_g and electron energy distribution in the plasma.

REFERENCES

[1] Y. Noguchi et al, *J. Appl. Phys.,* Vol.91, 613 (2002).
[2] H. Imaizumi et al, *Proc. 2005 Annual Conference of Fundamentals and Materials Society IEE Japan*, p. 333 (2005) [in Japanese].
[3] H. R. Skullerud, *Brit. J. Appl. Phys.*, Vol.1, 1567 (1968).
[4] Kinema Research & Software, http://www.kinema.com/download.htm
[5] V. M. Donnelly, *J. Phys. D: Appl.Phys.*, Vol.37, R217 (2004).

NUCLEATION IN ATMOSPHERIC PRESSURE ELECTRICAL DISCHARGES

J.P. Borra

Laboratoire de Physique des Gaz et des Plasmas,
Supélec, 3 Rue Joliot Curie, Plateau du Moulon, 91192 Gif sur Yvette, France
Tél : 00 33 1 69 85 17 91, jp.borra@pgp.u-psud.fr

ABSTRACT. This paper deals with the production of nano-particles in Atmospheric Pressure Electrical Discharges (APED). Two mechanisms of particle production are depicted in APED (e.g. for dc corona, streamer and spark filamentary discharges, as well as for ac filamentary and homogeneous Dielectric Barrier Discharges): when filamentary discharges interact with the surface of electrodes or dielectrics, and when both filamentary and homogeneous Dielectric Barrier Discharges induce reactions with gaseous precursors in volume. In both cases, condensable gaseous species are produced, leading to nano-sized particles by physical and chemical routes of nucleation and to fine powders production and thin films deposition.

1. INTRODUCTION

This work focuses on sub-micrometer aerosol production in Dielectric Barrier Discharges by nucleation of locally saturated vapour produced when filamentary discharges reach the surface in Dielectric Barrier Discharges in air at atmospheric pressure. A gas velocity threshold has to be overcomes for particle detection independently of the energy per filament. The comparison of aerosol frequency (part/s) at constant surface energy fluxes, related to constant charge per filament with different surface temperatures allows us to discuss two hypotheses for vapours production either by sublimation by Joule effect and/or ion sputtering. Then, the competition between production and collection in this plane-to-plane DBD arrangement is shown by air flow-rate variation. The interest of this nano-particles production process lies on the control of both surface temperature and related vapour flux to avoid agglomeration of nanoparticles formed in high concentrations by classical nucleation processes (flames and/or spark generator). Actually, this vapour flux is directly linked to unitary characteristics of filament (via geometry) and to impulse discharge current (via filaments frequency controlled by surfaces polarisation/depolarisation regulated by voltage, signal frequency, relative humidity and gas temperature).

2. SET-UP AND DIAGNOSTICS

Two parallel planes of alumina and separated by 1 mm are polarized by 3 cm long brass electrodes, thanks to a 60 kHz sinusoidal power supply. The dry air flow velocity between the planes is controlled between 0.8 and 5 $m.s^{-1}$. Current and voltage are measured with an oscilloscope (LeCroy LC374A, 500 Mhz, 2 Gs/s) [1]. The particles size and concentration are measured with CPC (3022 TSI), diffusion battery and Electrical Low Pressure Impactor.

3. RESULTS AND DISCUSSION

3.1. dc confined corona and ac homogeneous Glow Discharge at Atmospheric Pressure

Neither the first confined one produced with asymmetric centimetre gaps, nor the second homogeneous one filling the whole gap of ac millimetre plane-to-plane Dielectric Barrier Discharges, leads to nucleated nano-particles in clean dry gases. However, with gaseous impurities like acetic acid from sealing silicon paste, a decreasing concentration of nucleated particles formed by plasma-gas interaction is detected up to the end of desorption. Similar gas-to-particle conversion may also occur permanently when using an unexpected VOC source from compressed air devices [2], as detailed in Figure 1.

This chemical route of nucleation from gas-phase reactions is similar in flame and in plasmas. In both cases, (i) condensable species are formed by gas-phase reactions between a gaseous precursor and reactive species formed in APED (e-, photon, excited species, radicals and ions, O_3, NO_x, HNO_x), and (ii) the nucleated aerosol grows by simultaneous condensation and coagulation. The formation of nucleated particles in non-thermal APED is thus used for gas-phase pollution control and thin film deposition.

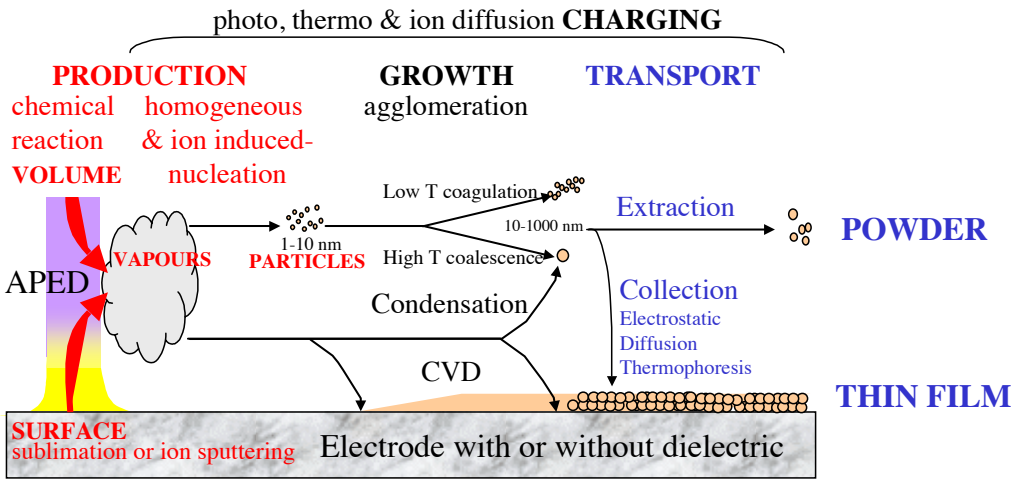

FIGURE 1. Mechanisms of vapour and particle production (nucleation) and subsequent growth, charging and resulting transport with eventual electro-collection in APED

3.2. Atmospheric Pressure Filamentary Discharges (APFD)

When filamentary discharges develop at atmospheric pressure, particles can be detected at the reactor outlet. The weak energies per filament with short duration (20 ns) on small surfaces ($\sim 10^{-2}$ mm^2) correspond to high surface energy flux of the same order of magnitude than in spark ($> 10^9$ W.m^{-2}), in spite of lower local surface energy (10^2 J.m^{-2}). This tends to show that with "small filaments", either the kinetic energy of ions reaching the plane is still higher that the minimum kinetic energy required for ion sputtering (from 10 eV to keV [3]) and/or the temperature at the feet of the filament is above sublimation temperature of the surface. Whatever the vapour generation processes are, nanometer sized particles produced (90% under 30 nm) confirms that the nucleation of vapour is still efficient in silent discharges as already demonstrated in different geometries and depicted in figure 1.

For a given surface temperature and a constant number of filaments per second, a gas flow velocity threshold (around 2 m.s^{-1}) has to be overcome for particle detection. Under this velocity threshold, there is no aerosol whatever the electrode temperature is, probably related

to longer transit time of charged particles in the polarised gap enabling charging, and electro-thermal collection of particles. Indeed, between the production of vapour and the detection, there are at least five processes.

Once created, nano-particles can grow by heterogeneous nucleation and coagulation (cf. figure 1). Then ions produced by the discharge can charge the particles leading to a possible electro-precipitation on surfaces. Above this velocity threshold, particles have less time to grow up, to get charged and to be collected thus the entrainment force becomes sufficient to extract particles.

Moreover, this competition between production and collection of particles is confirmed because at a given flow velocity, the number of particles detected per filament still depends on the number of filaments with constant surface temperature. Thus, both production of particle detailed above and post-production collection depend on the number of filaments per second influencing charging efficiency, electric field and electro-precipitation in the gap.

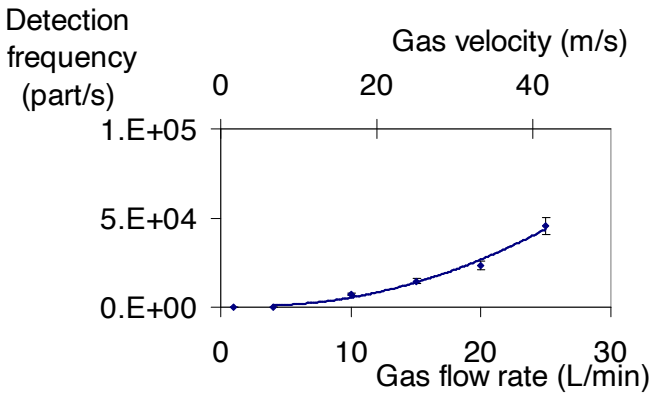

FIGURE 2. Mechanisms of vapour and particle production (nucleation) and subsequent growth, charging and resulting transport with eventual electro-collection in APED

4. CONCLUSION

Nano-particles are formed in all APFilamentary Discharge by nucleation of vapours from FD-surface interaction, whatever the geometry, the electrode material (metal or metal oxides), the polarity, the clean dry gas, as well as the related energy and distribution of FD in time and space are. If vapours are formed by evaporation in hotter non-thermal sparks FD, the mechanism of vapour production by streamers FD, the local recollection by thermophoresis and electro-collection of charged species deserved further investigation. Indeed, initial photo-ionisation and ion-induced nucleation as well as post-production photo-charging have not yet been studied in APFD, whereas a large stroke of progression still exists to optimise the out-coming mass flux of particles per FD. However, when electro-deposition is prevented in dc and ac APFD with short transit time or with high ac frequency (10-100 kHz) APFD in DBD, tuning surface energy density in spots of streamers and sparks FD and gas flow rate, enables to control the vapour flux from each FD (with voltage in asymmetric gap and with gap length in plane-to-plane ac APFD in DBD) and the related concentration and growth by coagulation for the production of powders with tailored size.

Unagglomerated nano-particles (< 10 nm) can be produced with low energy FD in dc and ac APFD in mono-point-to-plane. For higher surface energy densities in dc sparks FD and for

multi-source ac APFD in DBD in plane-to-plane ac DBD in N_2, particle size resulting from coagulation can be controlled with higher electrode area, as well as with the number of FD per unit surface and time by varying the voltage and the frequency. Indeed, coagulation leads to unimodal self-preserving size-distribution (mean diameter from 30 to 200 nm).

Despite low mass production per APFD, increased number of FD per unit surface and time can be achieved in multiple dc point-to-plane systems (up to 50.10^6 FD $s^{-1}.m^{-2}$ i.e. 10^9 FD $s^{-1}.m^{-2}$) for the production of metal nano-particles in $mg.h^{-1}$. Even higher repetition rates can be reached with higher ac frequency and/or larger ac DBD reactors (up to 10^{11} FD $s^{-1}.m^{-2}$) for the production of metal oxide nano-particles in $g.h^{-1}$. Thus, higher production rate can be reached at atmospheric pressure than with low pressure laser system (10-20 $mg.h^{-1}$). Nanograms per spark can be scaled-up to $g.h^{-1}$ at atmospheric pressure, as with other vacuum coating processes (1 to 100 g. h^{-1}).

As APFD may be promoted with any electrode or dielectric material (metal, metal oxide, polymer), particles of any required composition can be achieved, with mass production cost from $ng.J^{-1}$ with streamers FD to $mg.J^{-1}$ with hotter sparks FD in inert gases. Compared to low pressure Pulsed Laser Deposition, also developed for the conservation of the target composition, FD allow one to reach similar mass production cost with coagulation-controlled size-distributions at atmospheric pressure.

The interest of this particle production tool lies on the possible size adjustment through surface temperature controlling the vapour flux, the resulting nucleation rate (nanoparticle concentration) and the subsequent post-production coagulation. Silent discharges at atmospheric pressure could be used as nanoparticles production tool for coating 3D objects either by diffusion (cf. fig. 1) or by charging and electro-precipitation.

REFERENCES

[1] Jidenko N *et al*. (2006) Electrical characterization of microdischarges produced by dielectric barrier discharge in dry air at atmospheric pressure *J. Phys. D: Appl. Phys*. **39** No 2 281-293

[2] Borra JP et al. (1998). Electrical Discharge regimes and aerosol production in point-to-plane DC high-pressure cold plasmas: aerosol production by electrical discharges *J Aerosol Science* **29** No5/6, 661-674.

[3] Auciello et al. (1984). *Ion bombardment modification of surfaces*, Edited by Elsevier.

Paper number

MEASUREMENTS OF OH RADICAL DENSITY IN $N_2/O_2/H_2O$ STREAMER CORONA DISCHARGES BY LASER-INDUCED FLUORESCENCE IMAGING SPECTROSCOPY

K. Sasaki, T. Yoshida, and N. Takada

Department of Electrical Engineering and Computer Science, Nagoya University
Furo-cho, Chikusa-ku, Nagoya 464-8603, Japan

ABSTRACT. We measured the temporal variations of the distributions of OH radical density in streamer corona discharges in $N_2/O_2/H_2O$ mixture by laser-induced fluorescence imaging spectroscopy. The experimental results indicated that OH radicals were produced by electron impact dissociation of H_2O and were lost by chemical reactions in the gas phase. The kinetics of OH radicals was examined by rate equation analysis including 34 chemical reactions, which also gave us an estimation of the absolute OH radical density. According to the rate equation analysis, H_2 and H_2O_2 are the major reaction products at the final stage of the discharge.

1. INTRODUCTION

Since OH radical has a higher oxidation potential than O, O_3 and H_2O_2 [1], it is useful in sterilization of food and medical instruments, the removal of gaseous pollutants such as NO_x, SO_x, and volatile organic compounds (VOCs), and cleaning up waste water. By generating nonthermal plasmas in air with water vapor at atmospheric pressure, OH radicals can be produced at a low gas temperature without vacuum equipment. In this work, we measured two-dimensional distributions of OH radical density in streamer corona discharges in $N_2/O_2/H_2O$ mixture at 200 Torr by laser-induced fluorescence (LIF) imaging spectroscopy with the intension of investigating the dynamics and kinetics of OH radicals. We also carried out rate equation analysis including 34 chemical reactions, which gave us insights into reaction kinetics of OH radicals and an estimation of the absolute OH radical density.

2. EXPERIMENTAL PROCEDURE

Figure 1 shows the experimental apparatus. A vacuum chamber was evacuated below $5x10^{-4}$ Torr using a turbomolecular pump. After the evacuation, the chamber was filled with a mixture of water vapor, O_2, and N_2. All the experimental results shown in this paper were obtained at a total gas pressure of 200 Torr with no gas flow. Streamer corona discharges were produced by applying pulsed high voltages between a tungsten needle electrode and a stainless-steel planar electrode installed in the vacuum chamber. The diameters of the needle and planar electrodes were 0.5 and 60 mm, respectively. The tip of the needle electrode was tapered. The distance between the needle and planar electrodes was 15 mm. Pulsed high voltages with a positive polarity were applied to the needle electrode by discharging a capacitor through a CMOS switch. The repetition rate of the discharge was 10 Hz. The applied voltage was measured using a high-voltage probe at the needle electrode, and the

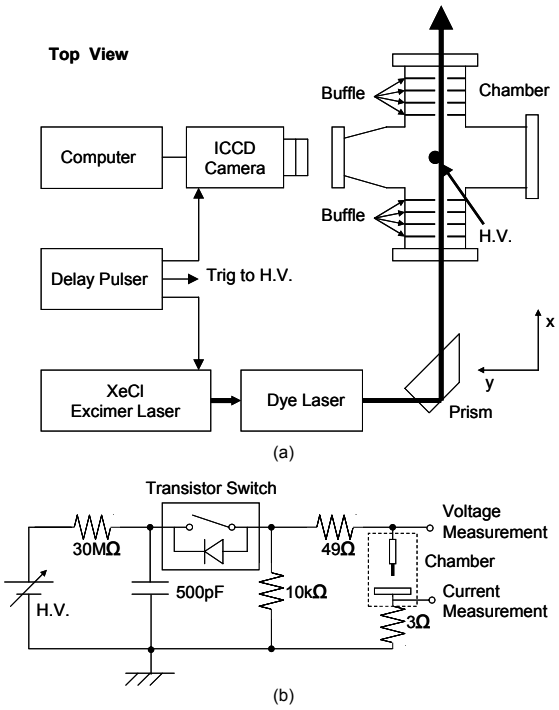

FIGURE 1 Schematic of the experimental apparatus (a) and discharge circuit (b).

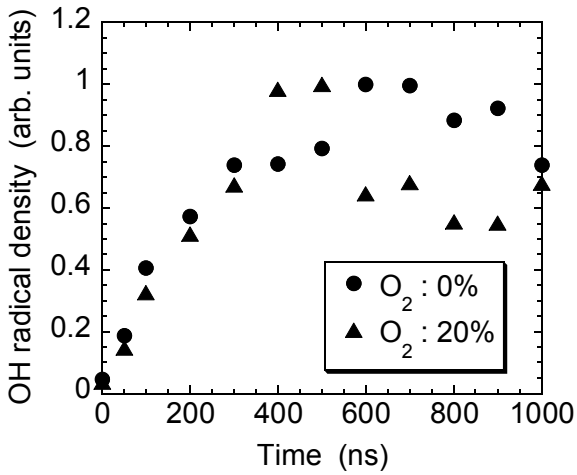

FIGURE 2 Temporal evolution of the OH radical density after the initiation of the discharge.

discharge current was measured by observing the voltage that appeared between a resistor of 3 Ω which was inserted between the planer electrode and the ground potential.

A dye laser pumped by a XeCl excimer laser generated tunable laser radiation at around 618 nm. A KDP crystal pumped by the tuned laser beam produced a second-harmonic radiation at around 309 nm. The shape of the 309 nm laser beam with an energy of 0.2-0.4 mJ/pulse and a duration of 18 ns was arranged to have a planar profile with a width of 15 mm and a thickness of 1 mm. The plane-shaped laser beam was introduced between the needle and planar electrodes to excite OH radicals. The fluorescence emission from excited OH radicals was imaged onto a charge-coupled device camera with a gated image intensifier (ICCD camera) from the direction perpendicular to both the planar laser beam and the axis of the discharge. Since the image thus obtained included the LIF emission, the self-emission of the plasma, and the stray laser light, we obtained the spatial distribution of the OH radical density by subtracting the self-emission and the stray light components. The temporal variations of the density distributions were obtained by changing the delay time between the laser irradiation and the discharge pulse using a digital delay pulser. The excitation wavelength was determined experimentally from spectral analyses. In this experiment, the line at 308.99 nm was chosen for exciting OH radicals because of the high LIF intensity. This line corresponds to $Q_2(2)$ and $Q_2(3)$ branches (overlapping) in the $A^2\Sigma(v'=0)\leftarrow X^2\Pi(v''=0)$ transition [2].

A problem of LIF in a high gas pressure is collisional quenching of the laser-excited state, which reduces the LIF intensity significantly. Since the rate coefficient for collisional quenching of the $A^2\Sigma$ stare is different in N_2, O_2, and H_2O, the degree of the reduction in the LIF intensity is dependent on their partial pressures. In this work, the decrease in the LIF intensity due to collisional quenching was compensated by considering the rate coefficients reported in literature [3].

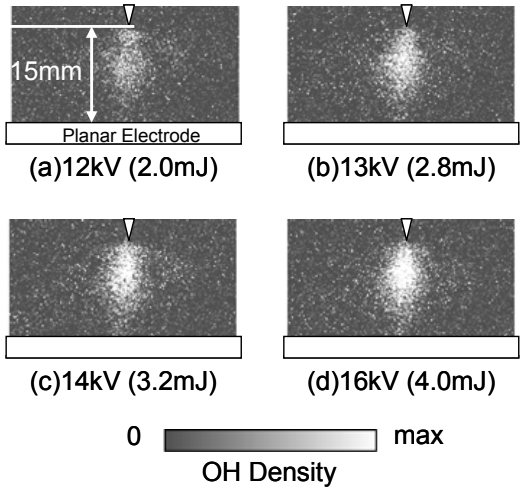

FIGURE 3 Distributions of OH radical density observed in $N_2/O_2(20\%)/H_2O(5\%)$ mixture at various discharge voltages. The delay time after the initiation of discharge was 10 μs.

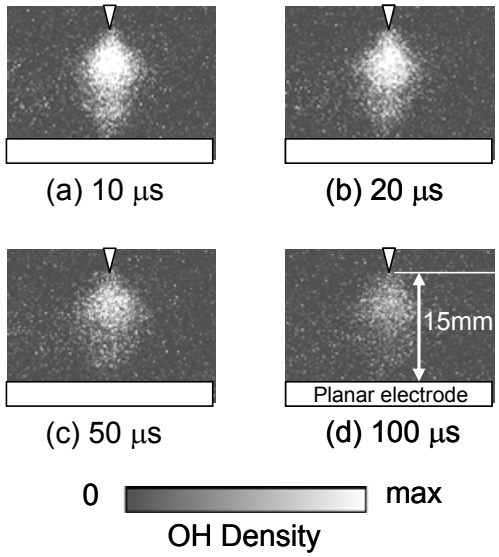

FIGURE 4 Distributions of OH radical density in $N_2/O_2(20\%)/H_2O(5\%)$ mixture at various delay times after the initiation of discharge.

3. EXPERIMENTAL RESULTS AND DISCUSSION

To investigate production processes of OH radicals, we measured the temporal evolution of OH radical density after the initiation of discharge. Figure 2 shows the temporal variations of OH radical density below the needle electrode in $N_2/H_2O(5\%)$ and $N_2O_2(20\%)/H_2O(5\%)$ mixtures. The maximum density under each condition was normalized to unity in Fig. 2. The increase period of the OH radical density corresponded to the duration of the discharge current. Since we can expect energetic electrons during the current pulse, this experimental result suggests that OH radicals are mainly produced by electron impact dissociation of H_2O, and reactions involving free radicals are not responsible to the production of OH radicals.

Figure 3 shows the two-dimensional distributions of OH radical density at 10 μs after the initiation of the discharge in $N_2/O_2(20\%)/H_2O(5\%)$ mixture at various applied voltages. The discharge energy, which was calculated by integrating the product between the discharge current and voltage, is also indicated. The OH radical density concentrated in the region below the needle electrode. This distribution was similar to the distribution of the streamer channel (namely the optical emission from the discharge), which also suggests the production of OH radicals by electron impact dissociation of H_2O.

The temporal decay of OH radical density was measured to examine loss processes of OH radicals. Figure 4 shows the two-dimensional distributions of OH radical density at 10, 20, 50, and 100 μs after the initiation of discharge in $N_2/O_2(20\%)/H_2O(5\%)$ mixture. The OH radical density decreased monotonically with time without changing the spatial distribution significantly. This indicates that the diffusion loss of OH radicals is negligible and the principal loss processes of OH radicals are chemical reactions in the gas phase. Figure 5 shows the temporal variations of the total number of OH radicals in $N_2/O_2(20\%)/H_2O$ mixture at various H_2O concentrations. The total amount of OH radicals just after the initiation of discharge was larger at a higher H_2O concentration. The temporal decrease in the total number of OH radicals was not approximated by exponential functions. The loss frequency of OH

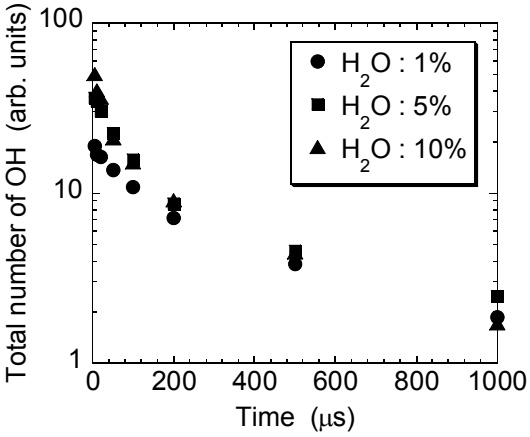

FIGURE 5 Temporal variation of the total number of OH radicals in the discharge space. The gas mixture was $N_2/O_2(20\%)/H_2O(5\%)$, and the discharge energies were 5.5, 4.9, and 4.0 mJ at H_2O percentages of 1%, 5%, and 10%, respectively.

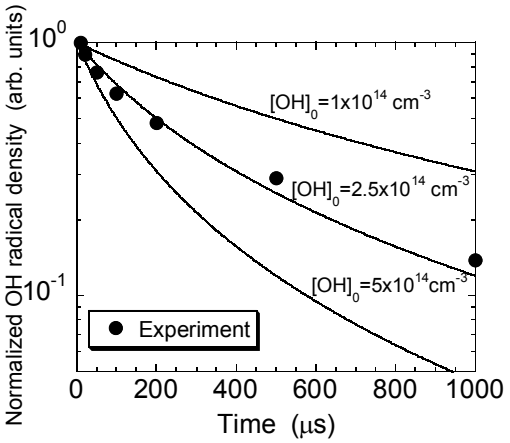

FIGURE 6 Temporal variations of the OH radical density obtained by rate equation analysis and experiment. The gas mixture was $N_2/H_2O(5\%)$. The discharge energy was 3.8 mJ.

radicals decreased with time. In addition, the decay at the beginning was steeper at a higher H_2O concentration (namely a higher OH radical density). These results suggest the importance of self association reaction among OH radicals in the loss processes.

4. RATE EQUATION ANALYSIS

The loss processes of OH radicals were also investigated by rate equation analysis including 34 chemical reactions among H_2O, OH, H, O, H_2, O_2, O_3, HO_2, and H_2O_2. Since the transport of OH radicals is negligible as shown in Fig. 4, the zero-dimensional analysis is sufficient to examine the kinetics of OH radicals. This rate equation analysis did not include electron impact processes, and it calculated only chemical kinetics after the disappearance of energetic electrons. The analysis was limited in N_2/H_2O discharge since we had no idea about the degree of dissociation of O_2 in $N_2/O_2/H_2O$ discharge. The temporal variations of species densities were calculated by solving the rate equations with the initial densities of OH and H. The initial OH and H densities were assumed to be equal since they are produced from H_2O by electron impact at the beginning of discharge.

Figure 6 shows the temporal variations of the normalized OH radical densities obtained by the rate equation analysis with various values of the initial OH density. $N_2/H_2O(5\%)$ mixture at 200 Torr was assumed. The closed circles are the experimental result (the total number of OH radicals) obtained at a discharge energy of 3.8 mJ. An agreement between the experiment and the analysis was obtained when we assumed the initial OH density of $2.5\text{x}10^{14}$ cm^{-3}. The degree of dissociation of H_2O corresponding to this absolute density is 0.08%. The rate equation analysis indicates that the final products of the N_2/H_2O discharge are H_2 and H_2O_2.

REFERENCES

[1] B. Sun, M. Sato and J. S. Clements, J. Electrostat. **39**, 189 (1997).
[2] J. Luque and D. R. Crosely, "LIFBASE: Database and Spectral Simulation Program (Version 1.9)", SRI International Report MP 99-099 (1999).
[3] F. Tochikubo and T. H. Teich, Jpn. J. Appl. Phys. **41**, 5792 (2000).
[4] F. Tochikubo, S. Uchida, and T. Watanabe, Jpn. J. Appl. Phys. **43**, 315 (2004).

Paper number

MEASUREMENT OF OH RADICALS IN DC STREAMER CORONA DISCHARGES BY LASER-INDUCED FLUORESCENCE

S. Kanazawa[1], F. Mitsugi[2], T. Ohkubo[1], Y. Nomoto[1], M. Kocik[3]
J. Mizeraczyk[3] and J.-S. Chang[4]

[1] *Department of Electrical and Electronic Engineering,*
Faculty of Engineering, Oita University
700 Dannoharu, Oita, 870-1192, JAPAN
[2] *Venture Business Laboratory, Oita University*
700 Dannoharu, Oita, 870-1192, JAPAN
[3] *Centre for Plasma and Laser Engineering,*
Institute of Fluid Flow Machinery, Polish Academy of Sciences
80-231,Gdańsk, POLAND
[4] *Department of Engineering Physics, McMaster University*
Hamilton, Ontario, L8S 4M1, CANADA

ABSTRACT. The LIF detection of the OH radicals was performed in a nozzle-to-plane electrode system having an electrode gap of 30 mm during the steady-state positive streamer corona discharge at atmospheric pressure. First, the time relationship between the regular streamer coronas, laser pulse, OH fluorescence and laser-induced streamer was measured. Next, the time dependence of OH radicals between the successive streamers was measured for the evaluation of OH dynamics. The two-dimensional OH distribution around the streamer corona region was also observed. The ground-state OH radicals were generated and stayed mainly in the region where streamers propagated between the electrodes.

1. INTRODUCTION

The DC streamer corona is one of the nonthermal plasmas used for pollution control. It is well known that hydroxyl (OH) radicals play an important role for the plasma chemical reactions occurred in the nonthermal plasma reactor. Therefore, the direct study of the radicals in nonthermal plasma reactors is of great interest. Laser-induced fluorescence (LIF) is a useful diagnostic method for *in-situ* observation of the phenomena during the nonthermal plasma processing of gaseous pollutants. Several researchers have succeeded in measuring the OH radicals using LIF technique in the pulsed corona discharges [1, 2] and dielectric-barrier discharges [3].

The DC streamer corona discharge consists of more of less regular self-repetitive current pulses (streamers) with the pulse duration up to several hundred nanoseconds and repetition frequency in the range of 1 to 100 kHz. While, the OH radicals generated by the discharges have time transient characteristics (i.e. there are generation period and decay period during/after the discharge), and the lifetime is very short. These complex phenomena make the measurement of OH radicals in the DC streamer corona difficult. However, it was found that OH radicals between these successive streamers can be measured by LIF method. We succeeded in the evaluation of OH dynamics in open air during the steady-state discharge condition [4]. In this paper, OH radical behavior in the nonthermal plasma reactor is presented. The influence of ozone on the OH LIF is also investigated.

2. EXPERIMENTAL SETUP

Figure 1 shows the schematic diagram of the experimental setup. For monitoring the ground-state OH radicals, the scheme with excitation at 282 nm [$A^2\Sigma^+(v'=1) \leftarrow X^2\Pi(v''=0)$] and detection at 309 nm [$A^2\Sigma^+(v'=0) \rightarrow X^2\Pi(v''=0)$] was used. The 282 nm laser beam was generated by a laser system consisted of XeF excimer laser (Lambda Physik, COMPex 150), dye laser (Lambda Physik, SCANmate) and BBO crystal. Excitation of OH was achieved via the $Q_1(1)+Q_{21}(1)$ line (281.92 nm). LIF signal emitted at 90 degree to the laser beam was imaged onto a gated ICCD camera (LaVision, Flame Star II or Andor, iStar). To remove the scattered laser light from the OH signal, the optical filter was attached to the lens of the ICCD camera. No time synchronization between the discharge and laser shot was made. This means that a laser pulse is irradiated at random between the discharge current pulses.

A stainless-steel pipe with a nozzle (1.0 mm in inner diameter, 1.5 mm in outer diameter) was used as the stressed electrode. As a grounded electrode, the plate electrode was used as shown in Fig. 1. DC high voltage with positive polarity was applied through a 10MΩ resistor to the nozzle electrode and the DC positive corona discharge was generated at room temperature under atmospheric pressure. Wet air flowed along the reactor with a flow rate of 3 L/min. An additional gas (argon or CO_2+air) was supplied to the discharge zone through the nozzle with a flow rate of 0.45 L/min.

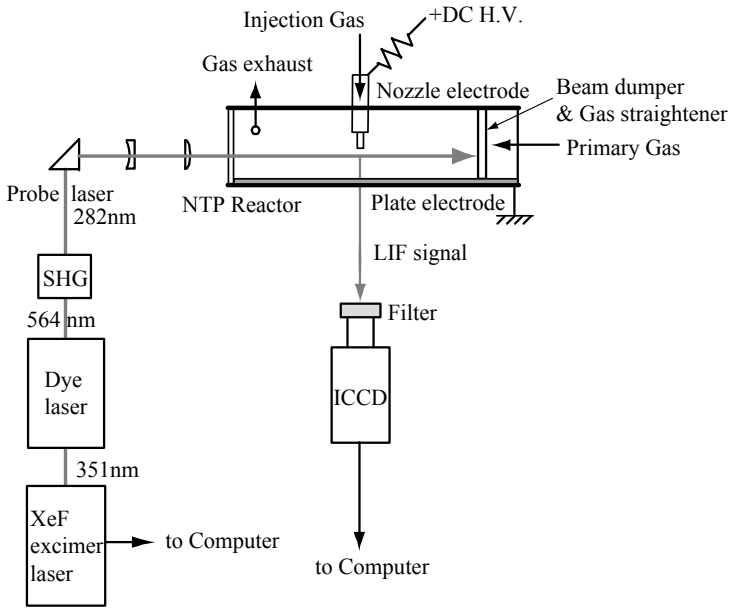

FIGURE 1. A schematic diagram of the experimental apparatus.

3. EXPERIMENTAL RESULTS AND DISCUSSIONS

During the steady-state discharge the ground-state OH radicals produced in the one streamer may be still present in the discharge region until the next streamers occur. Therefore, the measurement method based on no time synchronization between the streamer and laser pulse can be applied to the evaluation of steady-state DC streamer coronas. Figure 2 shows the schematic illustration of the time relationship between laser incidence, OH LIF signal and laser-induced streamer when the laser beam was irradiated between the successive streamers during the steady-state discharge. The LIF signal appears immediately after the laser pulse

and lasts over about 30-40 ns. If we average the signals, the steady-state measurement of OH LIF is possible. The similar scheme has been applied for NO measurement [5].

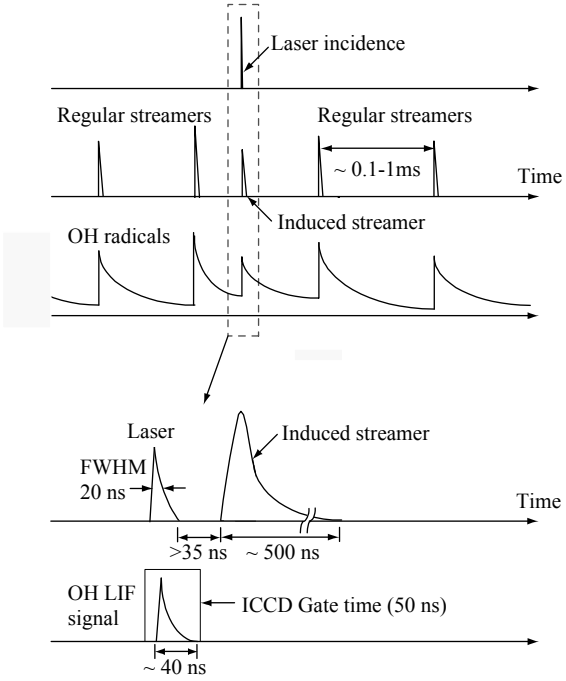

FIGURE 2. Time relationship between laser, streamer, OH radical, and LIF signal.

When the discharge was generated in the reactor by CO_2/air injection through the nozzle electrode, spread streamers were generated as shown in Fig. 3(a). Fig.3 (b) shows OH images in the reactor. In order to increase SN ratio of the image, the images shown in figure 3 are a sum of 10 captured images. The intensive part of the LIF signal corresponds to the region of streamers. After a time elapsed OH LIF signal was also observed outside the streamer region. The reason for this observation may be due to the ozone interference explained later.

Although the plasma chemical reaction is not simple, the principal reactions for producing OH radial are expected as follows:

$$H_2O + e \rightarrow H + OH + e \quad \text{(R1)}$$

$$O_2 + e \rightarrow O(^3P) + O(^1D) + e \quad \text{(R2)}$$

$$O(^1D) + H_2O \rightarrow 2OH. \quad \text{(R3)}$$

The produced OH is also reduced in the plasma. Moreover, it is noted that the effects of other reactions should be taken into account for explaining the OH behavior.

While, we found that the OH LIF signal was detected after the stop of the discharge. In this case, the OH LIF signal became weaker as a time elapsed. The detection time limit was almost equal to the gas residence time in the reactor. This may suggest that ozone, which has a long life time compared to other radicals such as O and OH, is related to the formation of OH radical under the UV irradiation (in this case, probe laser beam). In the discharge, it is well known that ozone is produced through the reaction

$$O + O_2 + M \rightarrow O_3 + M, \quad \text{(R4)}$$

where M is a third body. The UV laser dissociates ozone into $O(^1D)$ and O_2.

$$O_3 + h\nu\,(\lambda<310\text{ nm}) \rightarrow O(^1D) + O_2. \qquad \text{(R5)}$$

OH radical is produced by the reaction R3 and is also contributed to OH LIF signal. This ozone interference has been observed in LIF measurement using the pulsed corona discharge [6]. Therefore, the evaluation method of discharge-induced OH radicals should be considered in the next experiment.

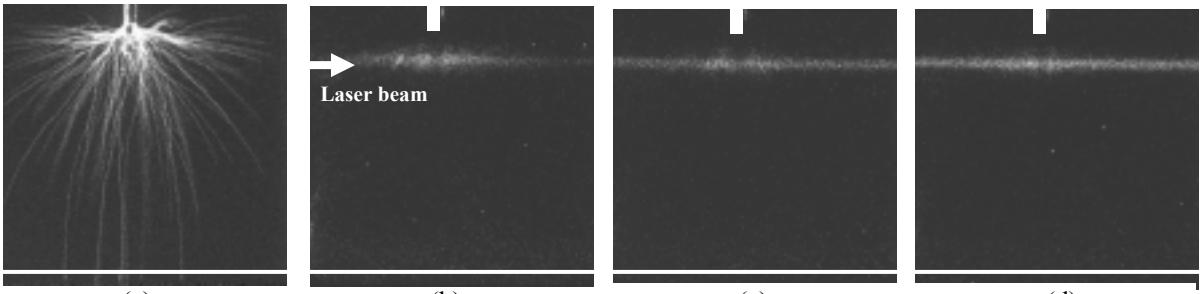

FIGURE 3. Comparison of (a) streamer (gate time 1 ms, sum of 5 images) and (b) OH LIF at t = 10 s, (c) OH LIF at t = 2 min, (c) OH LIF at t = 6 min after the start of the discharge (V=20 kV, I=50 μA, primary gas: wet air, 3 L/min., injection gas: CO_2, 0.15 L/min and air, 0.3 L/min, gate time 50 ns, sum of 10 images)

4. CONCLUSIONS

The LIF measurement method based on non-time synchronization between the streamer and laser pulse was applied to the evaluation of OH radicals during steady-state DC streamer coronas. The streamer discharge was composed of many branches, resulting in the profiles of OH radicals. Although the OH radical profile reflected on the path of the streamers between the electrodes, a weak OH LIF signal was observed outside the streamer region due to the ozone interference in OH LIF measurement.

REFERENCES

[1] Ono R., and Oda T. (2002). Measurement of hydroxyl radicals in pulsed corona discharge, *J. Electrostatics*, 55, 333-342.

[2] Tochikubo F., Uchida S., and Watanabe T. (2004). Study of decay characteristics of OH radical density in pulsed discharge in Ar/H_2O, *Jpn. J. Appl. Phys*., 43, 315-320.

[3] Sankaranarayanan R., Pashaie B., and Dhali S. K. (2000). Laser-induced fluorescence of OH radicals in a dielectric barrier discharge, *Appl. Phys. Let*t., 77, 2970-2972.

[4] Kanazawa S., Tanaka H., Kajiwara A., Ohkubo T., Nomoto Y., Kocik M. Mizeraczyk J., and Chang J. S. (2006). LIF imaging of OH radicals in DC positive streamer coronas, *Thin Solid Films*, In press.

[5] Kanazawa S., Sumi T., Shimamoto S., Ohkubo T., Nomoto Y., Kocik M., Mizeraczyk J., and Chang J.S. (2004). Diagnostics of NO oxidation process in a nonthermal plasma reactor: Features of DC streamer-corona discharge and NO LIF profile, *IEEE Trans. Plasma Sci*., 32, 25-31.

[6] Ono R., and Oda T. (2002). Dynamics of ozone and OH radicals generated by pulsed corona discharge in humid-air flow reactor measured by laser spectroscopy, *J. Appl. Phys*., 93, 2133-2138.

Paper number

INFLUENCE OF PENNING IONIZATION FOR GLOW-LIKE DISCHARGE FORMATION IN DIELECTRIC BARRIER DISCHARGE IN AR-BASED GAS

F. Tochikubo, Y. Matsushita and S. Uchida

Department of Electrical and Electronic Engineering,
Graduate Schools of Science and Engineering, Tokyo Metropolitan University
1-1, Minami-Osawa, Hachioji, Tokyo 192-0397, JAPAN

ABSTRACT. Influence of Penning ionization for glow-like discharge formation was investigated in Ar-C_2H_4 mixtures in medium pressure dielectric barrier discharge. First, Ar($1s_5$) density was investigated by laser absorption spectroscopy as a parameter of C_2H_4 ratio as well as the electrical measurement and visual observation of discharge figure. Effective ionization coefficient in Ar-C_2H_4 mixtures was evaluated by Boltzmann equation analysis. Finally, fluid simulation was carried out to evaluate the contribution of Penning effect.

1. INTRODUCTION

Atmospheric pressure glow discharge (APG) is a very attractive tool for material processing without vacuum components. Since Kanazawa *et al.* presented the APG formation in dielectric barrier discharge in helium [1], the APG in helium with DBD structure has been extensively studied [2-7]. Yokoyama *et al.* suggested that the low breakdown voltage of helium is important characteristics to form APG [2]. From microscopic viewpoint of electron swarm characteristics in helium, we indicated that relatively high ionization coefficient at low *E/N* region plays an essential role in maintaining APG at low applied voltage without filamentary discharges [5]. A part of the ionization coefficient in helium results from the Penning ionization between helium metastable atom and impurities such as nitrogen. When we use other gases for APG formation with similar mechanism to helium APG, ionization coefficient at low *E/N* region has to be enhanced by Penning ionization to reduce the breakdown voltage. This effect was demonstrated by Okazaki *et al.* in APG formation in argon with small amount of ketone addition [3]. Many of hydrocarbons such as ethylene, acetylene etc. have ionization potential lower than the excitation potential of Ar($1s_5$), 11.55 eV. Also fluorocarbons such as tetrafluoro-ethene has ionization potential lower than the excitation potential of Ar($1s_5$). Therefore, APG in argon with the small addition of these hydrocarbons or fluorocarbons can be the uniform plasma source for carbon deposition or etching.

In this work, we have investigated the discharge property of DBD in argon-hydrocarbon mixtures experimentally and theoretically. Small amount of ethylene is added to argon expecting Penning effect. As an experimental work, laser absorption spectroscopy was performed to measure the time-resolved Ar($1s_5$) density in addition to the electrical measurement and visual discharge observation. The experimental results are shown in Sec. 2. In Sec. 3, the ionization coefficient is examined in Ar-C_2H_4 mixture using Boltzmann

equation analysis. The discharge structure is theoretically investigated using one-dimensional fluid simulation in Sec. 4.

2. EXPERIMENT

2.1. Experimental setup

Experimental setup is shown in Fig. 1. The parallel plate electrodes with 4 cm diameter and 3 mm spacing are positioned in the center of the stainless-steel chamber. Both electrodes are made of aluminum, whose surfaces facing the discharge are covered with 0.5 mm thickness mica plate. Ar-C_2H_4 mixture gas is fed into the chamber through a mass-flow controller. The gas pressure ranges from 50 to 300 Torr in this experiment. The chamber and the lower electrode are grounded. Sinusoidal voltage with frequency of 100 kHz is applied to the upper electrode. The applied voltage and discharge current are measured by a high-voltage probe and the current probe, respectively.

The temporal variation of Ar($1s_5$) density was measured by a laser absorption spectroscopy using tunable diode laser (DL). The DL beam with diameter of about 3 mm was passing through the discharge region and was detected by a photo-diode. The transition from Ar($1s_5$) to Ar($2p_6$) in Paschen notation with central wavelength of 763.721 nm is used to detect Ar($1s_5$). The temporal variation of Ar($1s_5$) is monitored on the oscilloscope synchronizing with the current waveform.

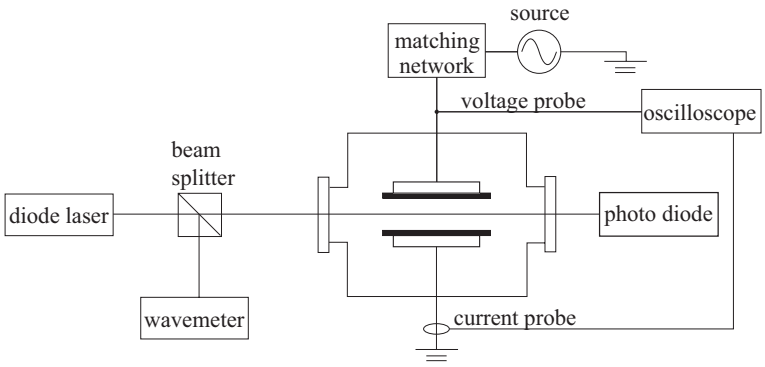

FIGURE 1. Experimental arrangement.

2.2. Experimental result

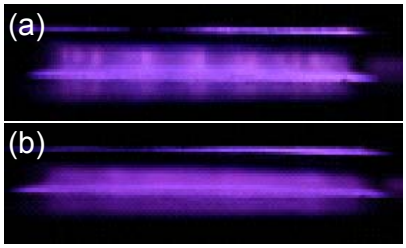

FIGURE 2. Gas discharge pictures in (a) 230 Torr Ar(100%) and (b) 300 Torr Ar/C_2H_4(0.1%).

In our experimental setup, complete glow-like discharge was obtained up to 200 Torr in pure argon. With additional increase of gas pressure, filamentary discharges were admixed in the glow-like discharge as shown in Fig. 2(a). The voltage and current waveforms in glow-like discharge mode are very similar to those observed in helium APG [5], that is, the current has a peak with about 1 μs width during each half cycle. When the filamentary discharges were admixed in the glow-like discharge due to the gas pressure increase, the many small but sharp noises appeared on the current waveform. The ethylene addition effectively contributes to the disappearance of the filamentary discharges as shown in Fig. 2(b). Therefore, Penning effect improves the glow-

like discharge formation. In our experimental setup, complete glow-like discharge was obtained up to 350 Torr in Ar/C_2H_4(0.01%). Temporal variation of relative Ar($1s_5$) density is shown in Fig. 3. The maximum density of Ar(1s5) is evaluated to be 10^{10} cm^{-3}. The Ar($1s_5$) density varies temporally coinciding with the current. This means that the generated Ar($1s_5$) is lost by the reaction with time constant much less than 1 μs. The major loss process of Ar($1s_5$) will be the reaction with Ar producing excimer or the reaction with C_2H_4 causing Penning effect. Let us assume that the Ar($1s_5$) production is proportional to current. Then the reaction rate coefficient between Ar($1s_5$) and C_2H_4 is estimated to be 10^{-10} cm^3s^{-1} using the rate equation for Ar($1s_5$).

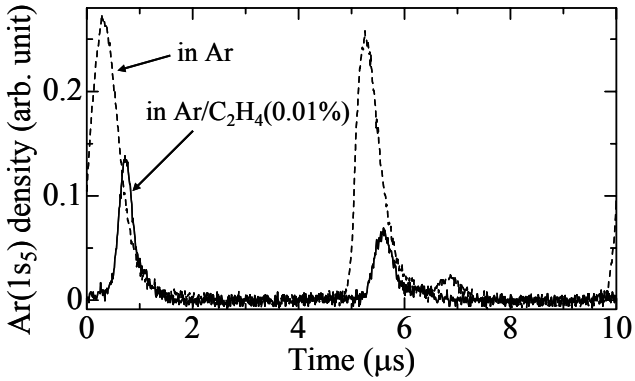

FIGURE 3. Temporal variation of Ar(1s5) density in Ar and Ar/C_2H_4(0.01%). As a discharge condition, the gas pressure is 300 Torr and the amplitude of applied voltage is 1500 V.

3. BOLTZMANN EQUATION ANALYSYS OF PENNING EFFECT

Boltzmann equation analysis of electrons in Ar-C_2H_4 mixtures was carried out to examine Penning effect by the conventional two-term approximation using cross sections for Ar [8-12] and C_2H_4 [13]. Figure 4 shows the calculated effective ionization coefficient with experimental data by Heylen[14]. Considering the reaction rate of Ar metastable atoms with C_2H_4, the calculated effective ionization coefficient is fitted to the experimental data. The results clearly show that small amount of C_2H_4 addition enhances the ionization coefficient at low E/N region. The calculated results in Ar/C_2H_4(0.03%) and Ar/C_2H_4(0.003%) are larger than the experimental ones at E/N less than 20 Td.

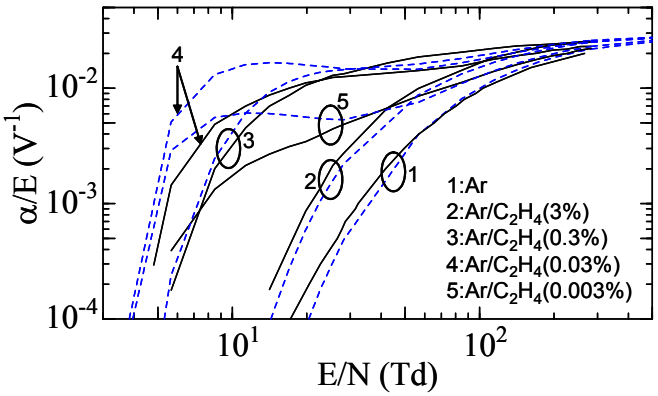

FIGURE 4. Effective ionization coefficient in Ar/C_2H_4 mixture. Dashed lines show the present Boltzmann analysis and solid lines show the experimental results by Heylen[14].

4. FLUID SIMULATION

Using the calculated electron swarm parameters in Ar-C_2H_4 mixtures, one dimensional fluid simulation is carried out using continuity equations for charged and excited species coupled with Poisson's equation. The simulation condition is same as that of our experiment. Figure 5 shows the spatiotemporal profiles of electron, Ar^+, Ar_2^+ and $C_2H_4^+$ in 250 Torr Ar/C_2H_4(0.1%) at driving frequency of 100 kHz and voltage amplitude of 1500 V. Sharp peaks of electrons at 1.2 μs and 6.2 μs result from the electron impact ionization at plasma-sheath boundary in front of instantaneous cathode. These peaks correspond to the current

peaks, which are typical in APG using DBD. The electron impact ionization generates Ar^+, which is immediately changed into Ar_2^+ under high gas pressure condition. Although the mixture ratio of C_2H_4 is only 0.1%, the $C_2H_4^+$ density is almost same as Ar_2^+ density in the plasma region, that is, the Penning ionization is relatively effective. In the present case, C_2H_4 addition causes the slight increase of plasma density, which causes the larger voltage drop compared with the case in pure Ar.

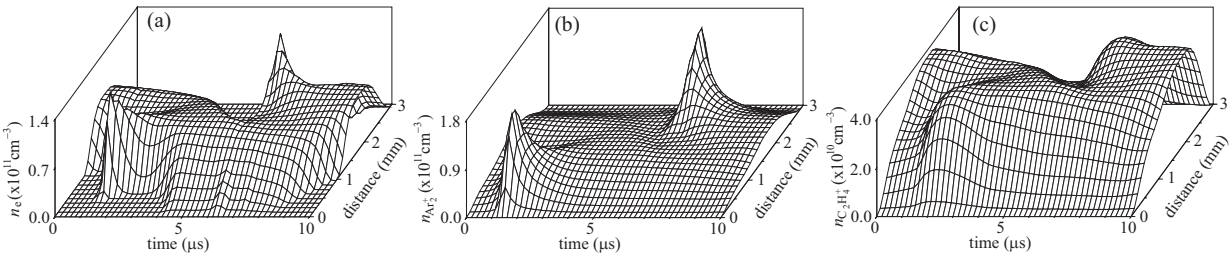

FIGURE 5. Calculated spatiotemporal density profiles of (a) electron, (b) Ar_2^+ and (c) $C_2H_4^+$ in 250 Torr Ar/C_2H_4(0.1%) at voltage amplitude of 1500 V.

ACKNOWLEDGMENTS

This work was partly supported by a Grant-in-Aid for Scientific Research from the Ministry of Education, Culture, Sports, Science and Technology.

REFERENCES

[1] S. Kanazawa, M. Kogoma, T. Moriwaki and S. Okazaki, *J. Phys. D,* 21, (1988) 838.
[2] T. Yokoyama, M. Kogoma, T. Moriwaki and S. Okazaki, *J. Phys. D,* 23, (1990) 1125.
[3] S. Okazaki, M. Kogoma, M. Uehara and Y. Kimura, *J. Phys. D,* 26, (1993) 889.
[4] F. Massines, A. Rabehi, P. Decomps, R. R. Gadri, P. Segur, and C. Mayoux, *J. Appl. Phys.,* 83, (1998) 2950.
[5] F. Tochikubo, T. Chiba and T. Watanabe, *Jpn. J. Appl. Phys.,* 38, (1999) 5244.
[6] Yu B.Golubovskii, V. A. Maiorov, J. Behnke and J. F. Behnke, *J. Phys. D,* 36 (2003) 39
[7] C. Anderson, M. Hur, P. Zhang, L. Mangolini and U. Kortshagena, *J. Appl. Phys,* 96 (2004) 1835
[8] M. Hayashi and S. Ushiroda, *J. Chem. Phys.*, 78 (1983) 2621.
[9] Y. Nakamura and M. Kurachi, *J. Phys. D*, 21 (1988) 718.
[10] A. Chutjian and D. C. Cartwright, *Phys. Rev. A*, 23 (1981) 2178.
[11] D. Rapp and P. Englander-Golden, *J. Chem. Phys.*, 43 (1965) 1464.
[12] D. Ton-That and M. R. Flannery, *Phys. Rev. A*, 15 (1977) 517.
[13] M. Hayashi, "Electron collision cross sections determined from beam and swarm data by Boltzmann analysis," in "Nonequilibrium Processes in Partially Ionized Gases," eds. M. Capitelli and J.N. Bardsley (Plenum Press, New York, 1990)
[14] A. E. D. Heylen, *J. Phys. D,* 3 (1970) 789.

Paper number

COLLISIONAL-RADIATIVE MODEL FOR DIFFUSE DIELECTRIC BARRIER DISCHARGE IN NEON AT ATMOSPHERIC PRESSURE

Z. Navrátil[1, 2], D. Trunec[1] and H.-E. Wagner[3]

[1] *Department of Physical Electronics, Faculty of Science, Masaryk University*
Kotlářská 2, Brno, 611 37, CZECH REPUBLIC
[2] *Department of General Physics, Faculty of Science, Masaryk University*
Kotlářská 2, Brno, 611 37, CZECH REPUBLIC
[3] *Institute of Physics, EMA University Greifswald,*
Domstrasse 10a, Greifswald, 174 89, GERMANY

ABSTRACT. A collisional-radiative model was applied to the study of the reduced electric field strength (*E/N*) in the column of the diffuse dielectric barrier discharge in neon. The calculated emission spectra were fitted by the least-squares method to the measured spectra with respect to the unknown parameter *E/N*. In the model the populations of thirty excited levels of neon atom were calculated. Various elementary collision processes were taken into account: electron impact excitation, deexcitation and ionization of neon atoms, emission and absorption of radiation, metastable-metastable collisions, metastable and radiative dimer production, Penning ionization, recombination etc. The Boltzmann kinetic equation for electron distribution function was solved for given *E/N* to determine the rates of electron collisions. Although differences between measured and calculated spectra were observed, the method allowed to estimate the reduced electric field strength to be 1 – 3 Td.

1. INTRODUCTION

Non-thermal discharges at atmospheric pressure belong to the most industrially interesting plasma sources. Among other discharges, especially dielectric barrier discharges, are studied. In some gases (helium, neon, nitrogen) a homogeneous kind of discharge, so called diffuse dielectric barrier discharge (DDBD) or atmospheric pressure glow discharge (APGD), can be generated. Whereas an attention has been paid to the study of DDBD in helium [1-5], the DDBD in neon has been studied rarely, e.g. [6, 7]. Since this discharge is operated at atmospheric pressure, it is even difficult to measure the physical basic quantities (as electric field strength, electron concentration etc.) in the discharge. Thus, in this paper we present a collisional-radiative model, which was developed for neon diffuse dielectric barrier discharge in order to determine the reduced electric field strength in the discharge from the optical emission spectra.

2. PRINCIPLE

2.1. Model

The overall scheme of the method is shown in figure 1. An electron distribution function (EDF) was determined for a given reduced electric field strength (*E/N)* by the solution of the stationary and local Boltzmann kinetic equation. As the homogeneous electric field was assumed, the EDF could be expanded in terms of Legendre polynomials of $\cos\theta$, where θ is

the angle between the velocity and the electric field strength. As inelastic collisions in the collision integral electron excitation and ionization collisions with the ground state atoms and electron excitation, deexcitation and ionization collisions with the atoms in $1s_2$–$1s_5$ states of $2p^5$ 3s configuration were taken into account.

Various elementary processes were incorporated in the rate equations for thirty excited levels of neon atom. Besides the above mentioned collisions processes as emission and absorption of radiation, metastable-metastable collisions, metastable and radiative dimer production in 3-body collisions, Penning ionization, 3-body ion conversion and 2-body recombination were taken into account. The built-up rate equations with the initial guess of populations of excited states were solved by a explicit fourth-order Runge-Kutta method until the steady state values of populations of excited states were reached.

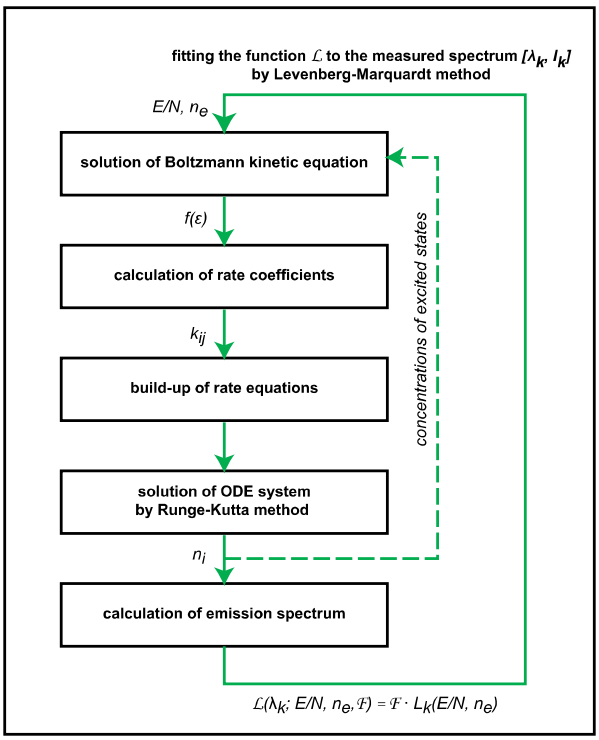

FIGURE 1. The overall scheme of the method used.

The calculated steady state populations were used to determine the optical emission spectrum in a distinct time and space of the developing discharge. This theoretical spectrum was compared with the measured time- and space- resolved spectrum by the least-squares method in order to find the *E/N* in this region. In this procedure a fast Marquardt-Levenberg method was applied.

2.2. Experimental set-up

The experiments were carried out with the apparatus for Cross-Correlation Spectroscopy as described in our previous work [7]. The discharge was generated between two parallel-plane metal electrodes, with the discharge gap of 5 mm. The electrodes were covered with 0.7 mm thick alumina layers. The discharge was driven by AC high voltage of frequency 10 kHz.

The temporally resolved optical emission spectra were measured by TRIAX 320 monochromator, equipped with sensitive Hamamatsu photomultiplier, and analyzed by single photon counting module (SPC-530, Becker and Hickl). The spatial resolution was achieved simply by an independent optical slit, which was movable in the discharge image. With this experimental set-up the intensities of 18 neon spectral lines of diffuse dielectric barrier discharge in neon were measured. See the reference [7] for other experimental details.

3. RESULTS AND DISCUSSION

The results of the fit to the spectra measured in the time of the intensity maximum about 1 mm far from the anode are listed in table 1. Since the dependence of the relative line intensities on the electron concentration n_e is rather slow, n_e could be assumed to be 10^{10} cm^{-3}. The example of the fitted spectrum and the *E/N* developments during the iterations of the

Marquardt-Levenberg algorithm are shown in figure 2. Substantial differences between the measured and calculated spectra were found out. Whereas in measured spectra the spectral lines at 703.24, 724.52 and 743.90 nm were the most intensive, in the calculated spectra the most intensive line was generally the line at 640.2 nm, originating from the state $2p_9$. These differences may be caused by overestimation of 3s states concentrations, leading to the enhancement of stepwise excitation of 3p states via 3s states, by memory effect due to the long effective life of 3s metastable and radiative states and perhaps by neglect of the forbidden electron impact transitions among 3s-3p states (which cross sections generally have a sharp maximum at low electron energies). The questionable is the influence of large errors of the used excitation cross sections, especially in the case of 3s-3p excitations, or of a slow discharge instability during the successive measurement of individual spectral lines.

Nevertheless, the reduced electric field strength in the discharge could be estimated from non-equal dependencies of line intensities on the electric field. As can be seen in figure 3, the lines originating from different upper states have also onset at different electric field. Therefore the lines at 703.24, 724.52 and 743.90 nm reach their highest relative values at the electric field, at which the increase of intensity of line at 640.2 nm, being intensive mainly due to the stepwise excitation, stagnates (in the normalized spectrum), and line at 585.25 nm, originating from the highest 3p level, is still weak. This requirement leads to the value of electric field strength of 2 – 3 Td, which is roughly in agreement with the estimates, based on the comparison of the discharges in neon [7] and in helium [1, 5].

TABLE 1. The results of collisional-radiative model fit applied to the spectra of DDBD measured in the time of current maximum 1 mm far from anode. The error estimates are calculated for confidence level of 68.3 %.

Spectrum	Time (μs)	*E/N* (Td)
1	32.5	1.1 ± 5.9
2	32.8	1.2 ± 6.0
3	33.1	2.5 ± 5.6

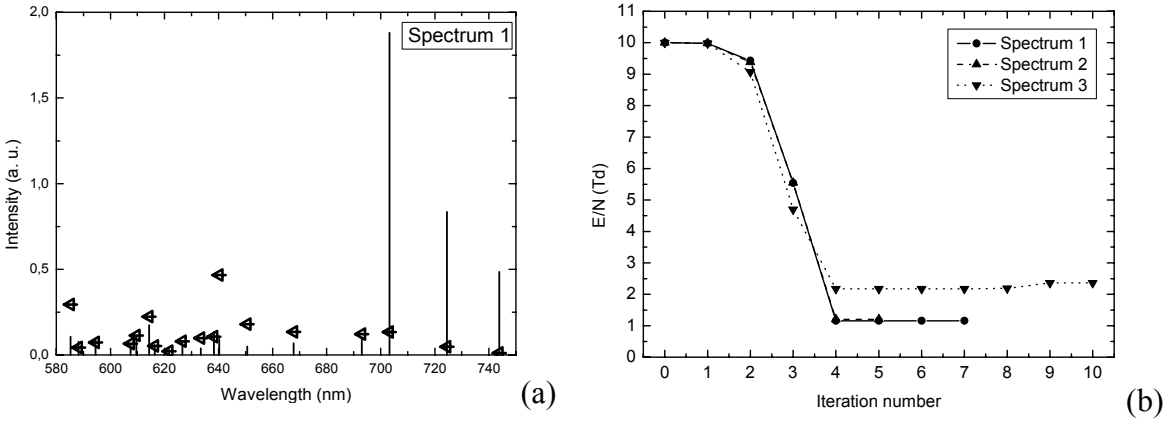

FIGURE 2. (a) Fit of the theoretical spectrum calculated by the model (displayed by arrows) to the experimental spectrum of DDBD, measured in the time of the intensity maximum 1 mm far from the anode (displayed by vertical abscissae). (b) Development of *E/N* during the iterations of Marquardt-Levenberg algorithm, carried out on several time- and space- resolved spectra, measured at the intensity maximum.

ACKNOWLEDGMENTS

The work was supported by research project MSM0021622411 of Ministry of Education of the Czech Republic and by grants No. 202/05/0777 and 202/06/1473 of Czech Science Foundation.

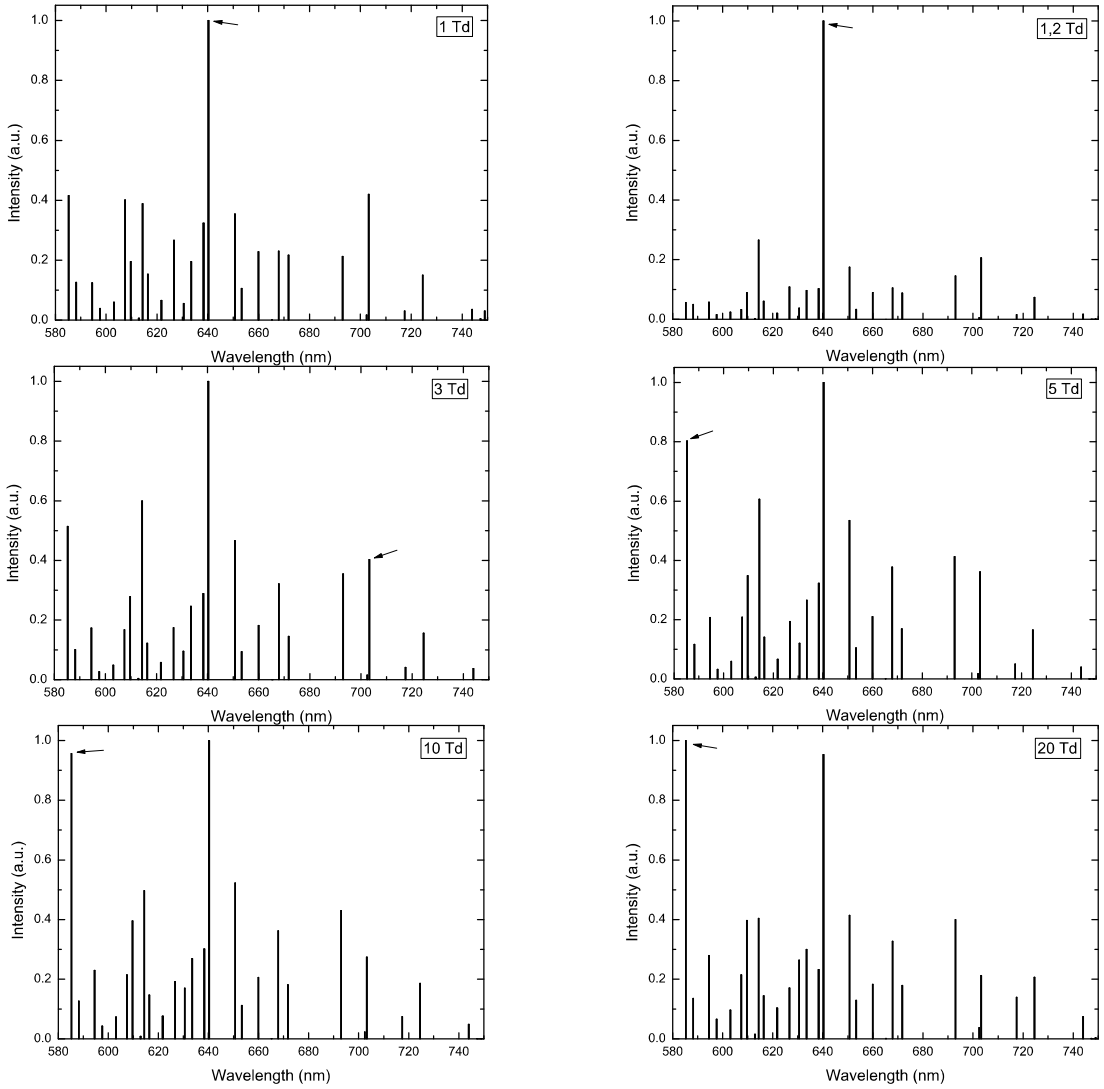

FIGURE 3. The theoretical spectra of the DDBD in neon, calculated by the model for various values of *E/N* and n_e 10^{10} cm^{-3}. The arrow denotes the most rapidly increasing line.

REFERENCES

[1] Massines, F. *et al*. (1998). Experimental and theoretical study of a glow discharge at atmospheric pressure controlled by dielectric barrier. *J. Appl. Phys.*, 83, 2950-2957.

[2] Ricard, A., *et al*. (1999). Kinetics of radiative species in helium pulsed discharge at atmospheric pressure. *Surf. & Coat. Technol.*, 112, 1-4.

[3] Golubovskii, Yu., *et al*. (2003). Modelling of the homogeneous barrier discharge in helium at atmospheric pressure. *J. Phys. D: Appl. Phys.,* 36, 39-49.

[4] Radu, I., *et al*. (2004). Dielectric barrier discharges in atmospheric pressure helium in cylinder-plane geometry: experiments and model. *J. Phys. D: Appl. Phys.*, 37, 449-462.

[5] Mangolini, *et al*. (2004). Effects of current limitation through the dielectric in atmospheric pressure glows in helium. *J. Phys. D: Appl. Phys.*, 37, 1021-1030.

[6] Trunec, D., *et al*. (2001). Atmospheric pressure glow discharge in neon. *J. Phys. D: Appl. Phys.*, 34, 1697.

[7] Navrátil, Z., *et al*. (2006). Comparative study of diffuse barrier discharges in neon and helium. *Plasma Sources Sci. Technol.*, 15, 8-17.

EVOLUTION OF AXIAL AND RADIAL DISTRIBUTIONS OF THE ELECTRIC FIELD IN THE MICRODISCHARGE OF BARRIER DISCHARGE IN AIR

K.V. Kozlov[1,2,a], H.-E. Wagner[1], T. Hoder[3] and R. Brandenburg[4]

[1] *Institute of Physics, Ernst-Moritz-Arndt University, Domstrasse 10a, D-17489 Greifswald, GERMANY*
[2] *Department of Chemistry, Moscow State University, Leninskie Gory 1, str.9, 119899 Moscow, RUSSIA*
[3] *Faculty of Science, Masaryk University, Kotlarska 2, CZ-61137 Brno, CZECH REPUBLIC*
[4] *Institute of Low Temperature Plasma Physics, F.-L.-Jahn-Strasse 19, D-17489 Greifswald, GERMANY*

ABSTRACT. The technique of spatially resolved cross-correlation spectroscopy was used to record two-dimensional luminosity distributions for selected spectral bands of molecular nitrogen (λ = 337.1 nm and λ = 391.5 nm) emitted by the microdischarges of barrier discharge in flowing synthetic air at atmospheric pressure. These experimental data enabled the quantitative estimate of electric field evolution in the microdischarge channel. The procedure of data processing included Abel transformation (assuming cylindrical symmetry), smoothing, differentiation over time and calculation of E/N(z,r,t) using calibration results.

1. INTRODUCTION

Systematic study of barrier discharges (BDs) using the technique of cross-correlation spectroscopy (CCS, see [1]) has been conducted at the university in Greifswald since 2000. Principal results of the CCS diagnostics to the BDs in air and in N_2/O_2 mixtures were published in the review papers [2,3]. Here, we report the results obtained in the course of two last years using the improved measurement technique and data processing procedure. The objective of this work was to reconstruct the evolution of axial and radial distributions of electric field within the microdischarge (MD) of the BD in air at atmospheric pressure from experimental data on spatially 2-dimensional radiation kinetics for two selected wavelengths (λ=337.1 nm of the 2nd positive and λ=391.5 nm of the 1st negative system of nitrogen).

2. EXPERIMENTAL SET-UP AND PROCEDURE

The experimental set-up and the CCS-method are described in detail in [4]. Here a brief review is given. In order to localise repetitive MDs, we used a discharge cell consisting of two semi-spherical electrodes (radius of curvature R = 2 mm, see fig.1-a), both covered with alumina. This electrode arrangement provided the possibility to observe not only the volume part of the MD, but also the surface discharges. The BD was operated by sinusoidal voltage at a frequency of 6 kHz. To investigate individual MDs, the voltage amplitude was adjusted so as to maintain the DBD in a mode corresponding to 1 MD per half cycle.

The CCS-setup is shown schematically in fig.1-b. By means of a quartz lens, the discharge zone was imaged onto the optical slit. By appropriate adjustment and movement of this slit, the discharge area could be scanned in vertical (z) and horizontal (r) directions (resolution not worse than 0.1 mm). Thus localized radiation (so-called MAIN signal) was resolved spectrally by a monochromator and then detected by the high-gain photo-multiplier (PMT) operated in a

[a] Electronic addresses: kozlov@physik.uni-greifswald.de

single photon counting mode. The second detector (PMT) provided the synchronizing (SYNC) signal necessary for the CCS measurements (see [4] for the details).

The measurements of the correlation functions and accumulation of the results were carried out by the Time Correlated Single Photon Counting (TC-SPC) board. The basic components of the TC-SPC instrument are two discriminators (DISC), a time-to-amplitude converter (TAC), an analogue-to-digital converter (ADC) and a memory (MEM).

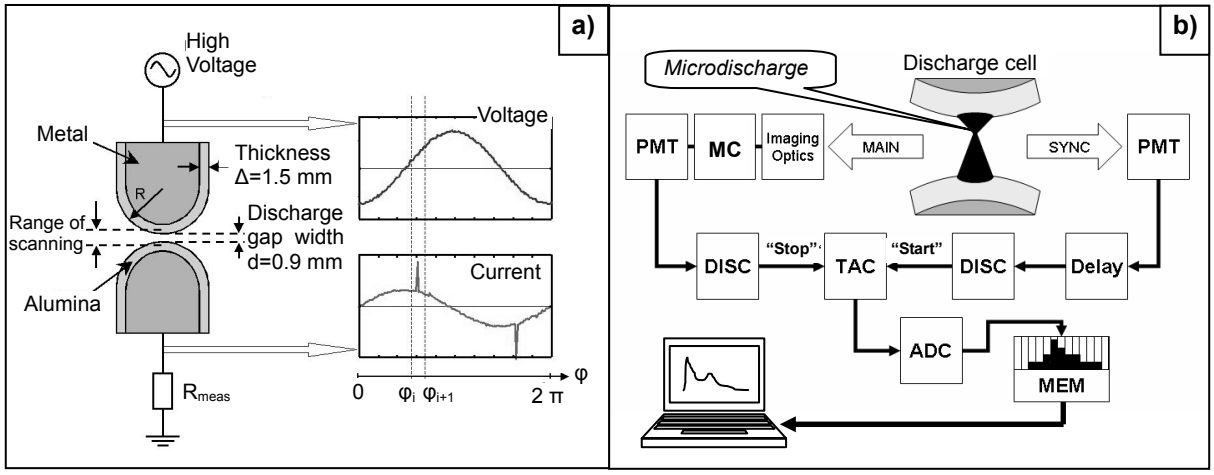

FIGURE 1. General scheme of the discharge cell with indicated range of optical scanning and typical examples of the oscillograms of voltage and current (a), and a diagram of the CCS-apparatus (b).
Abbreviations: PMT – photomultiplier tube, MC – monochromator, SYNC – synchronization signal, DISC – discriminator, TAC – time-to-amplitude converter, ADC – analogue-to-digital converter, MEM – memory.

All experiments were performed in the discharge cell shown in fig.1 with flowing synthetic air (20% O_2 + 80% N_2) at ambient pressure. The discharge gap width was chosen to be d = 0.9 mm. The spatio-temporal distributions of radiation intensity for the selected wavelengths within the MD channels were recorded by means of the technique of CCS with the resolution of 0.1 mm over spatial coordinates and of 0.05 ns over time.

3. RESULTS AND DISCUSSION

According to the results [5] based on the general kinetic scheme of a non-equilibrium discharge in nitrogen-oxygen mixtures, the following six elementary processes should be taken into account to describe the radiation kinetics for the second positive and first negative system of nitrogen (0-0 transitions) at atmospheric pressure.

Excitation of the molecules of nitrogen (in the ground state) by direct electron impact:

$$e + N_2(X^1\Sigma^+_g)_{v=0} \rightarrow N_2(C^3\pi_u)_{v'=0} + e \qquad (\Delta E = 11\ eV) \qquad (1)$$

$$e + N_2(X^1\Sigma^+_g)_{v=0} \rightarrow N_2^+(B^2\Sigma^+_u)_{v'=0} + 2e \qquad (\Delta E = 19\ eV) \qquad (2)$$

Spontaneous radiation of thus formed excited species:

$$N_2(C^3\pi_u)_{v'=0} \rightarrow N_2(B^3\pi_g)_{v''=0} + h\nu \qquad (\lambda = 337.1\ nm;\ \tau^C_o = 40\ ns) \qquad (3)$$

$$N_2^+(B^2\Sigma^+_u)_{v'=0} \rightarrow N_2^+(X^2\Sigma^+_u)_{v''=0} + h\nu \qquad (\lambda = 391.5\ nm;\ \tau^B_o = 60\ ns) \qquad (4)$$

Collisinal quenching of the excited species by the molecules of nitrogen and oxygen:

$$N_2(C^3\pi_u)_{v'=0} + N_2 / O_2 \rightarrow \text{Products} \qquad (5)$$

$$N_2^+(B^2\Sigma^+_u)_{v'=0} + N_2 / O_2 \rightarrow \text{Products} \qquad (6)$$

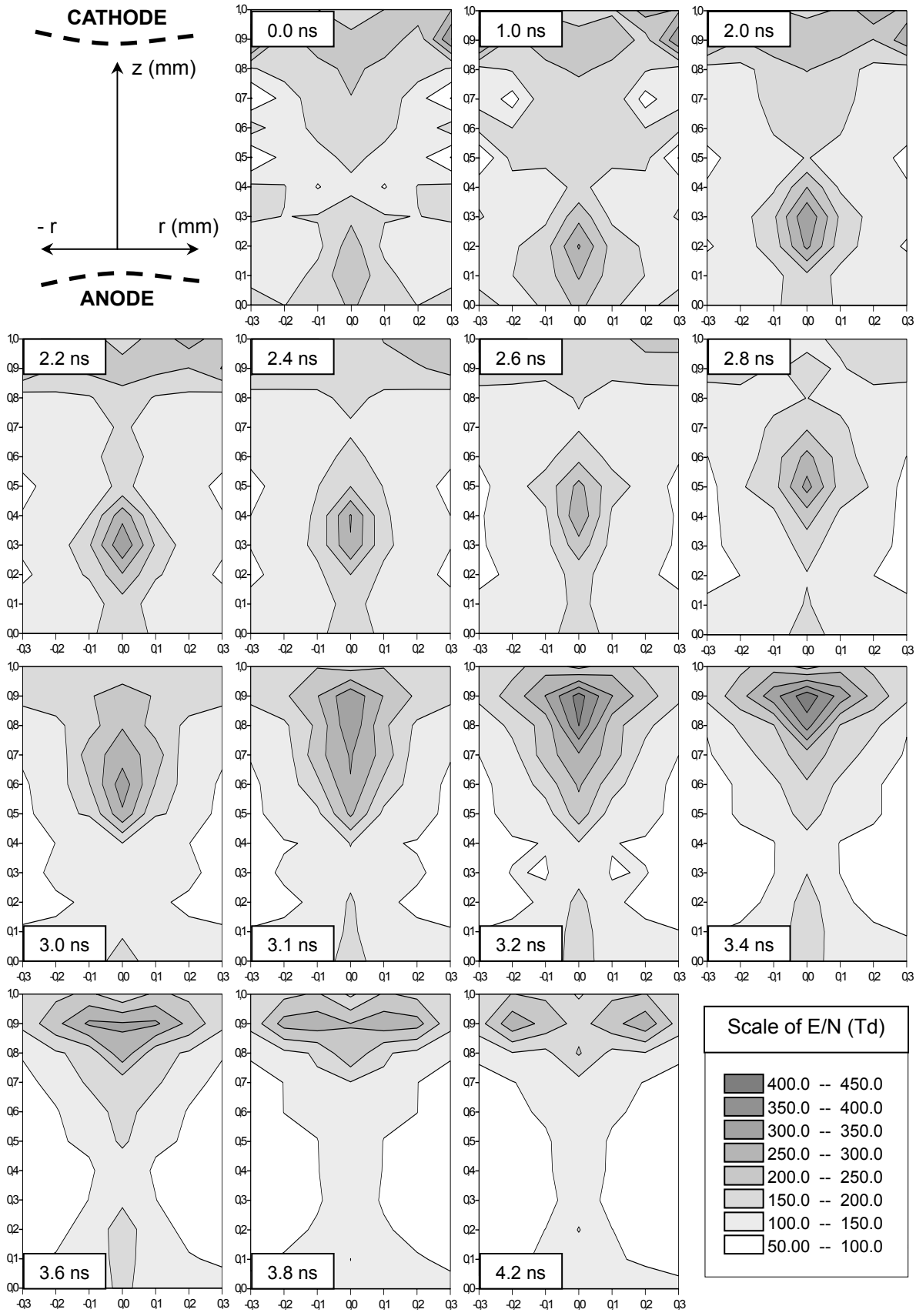

FIGURE 2. Evolution of electric field within the microdischarge channel. Experimental conditions: flowing synthetic air at p=1.03 bar; gap width (distance between the electrode tips) d=0.9 mm; voltage frequency 6 kHz.

Within the frame of this kinetic model, the ratio of the rate constants of the reactions (1,2) is a sole function of the reduced field strength, i.e $k_2/k_1=k_2/k_1(E/N)$, and it can be calculated from the measured radiation intensities for the selected wavelengths at any point (z,r,t). The corresponding formulas are given in [4,5].

The procedure of data processing consisted of the following basic steps: Abel inversion, numerical smoothing over time, numerical differentiation over time, evaluation of reduced field strength E/N(z,r,t). Several special algorithms and computer programs were developed to realize this procedure, taking into account some peculiarities of experimental data arrays (statistical nature of the measurement results and a priori estimates of their accuracy). To evaluate reduced field strength E/N(z,r,t) from the calculated rate constant ratio k_2/k_1 (z,r,t), we used the calibration curve $k_2/k_1(E/N)$ that was obtained experimentally in [6].

An example of thus computed results is presented in fig.2. The propagation of the cathode-directed ionizing wave with amplitude of up to 450 Td is clearly seen there. It is interesting to mention that when this ionizing wave reaches the cathode surface, it does not stop but continues its movement in radial direction from the MD axis. Therefore, the surface part of the MD on the cathode can be regarded as a natural continuation of the volume part of the MD. It should be noted also that an estimate of the size of local field enhancement which can be derived from fig.2, is limited in fact by the resolution of the apparatus (0.1 mm).

Qualitatively, the axial development of electric field within the MD channel shown in fig.2 does not differ from the corresponding results in [4] obtained earlier within the frame of a spatially 1-dimensional approximation (i.e. assuming uniform radial distributions of radiation intensity for both selected wavelengths). However quantitatively, there is certain difference between the data being considered. For example, the maximal value of E/N (see fig.2) appears to be about two times higher than the corresponding maximum in [4].

4. CONCLUSION

The radial component of the luminosity distributions within the MD channel should be taken into account to provide a correct quantitative estimate of the reduced electric field strength E/N(z,r,t). This estimate reveals axial and radial development of electric field that can be considered as an ionizing wave starting from the anode and propagating to the cathode in a few ns, and then spreading out over the cathode surface from the center of the MD channel.

REFERENCES

[1] Becker W. Advanced Time-Correlated Single Photon Counting Techniques. Springer-Verlag Berlin Heidelberg, 2005.

[2] Wagner H.-E., Brandenburg R., Kozlov K.V. Progress in the Visualization of Filamentary Gas Discharges. Part 1: Milestones and Diagnostics of Dielectric-Barrier Discharges by Cross-Correlation Spectroscopy. J. Adv. Oxid. Technol., 2004, v.7, No. 1, p.11-19.

[3] Wagner H.-E., Brandenburg R., Kozlov K.V., Morozov A.M., Michel P. Cross-Correlation Spectroscopy Applied to the Investigation of Barrier Discharges in N_2/O_2 Mixtures at Atmospheric Pressure. Contrib. Plasma Phys., 2005, v.45, No. 5-6, p.338-347.

[4] Kozlov K.V., Wagner H.-E., Brandenburg R., Michel P. Spatio-temporally resolved spectroscopic diagnostics of the barrier discharge in air at atmospheric pressure. J. Phys. D: Appl. Phys., 2001, v. 34, No. 21, p. 3164-3176.

[5] Kozlov K.V., Brandenburg R., Wagner H.-E., Morozov A.M., Michel P. Investigation of the filamentary and diffuse mode of barrier discharge in N_2/O_2 mixtures at atmospheric pressure by cross-correlation spectroscopy. J.Phys.D: Appl. Phys., 2005, v.38, p.518-529.

[6] Paris P., Aints M., Valk F., Plank T., Haljaste A., Kozlov K.V., Wagner H.-E. Intensity ratio of spectral bands of nitrogen as a measure of electric field strength in plasmas. J. Phys. D: Appl. Phys., 2005, v. 38, p. 3894-3899.

Paper number

IMPROVEMENT OF PLASMA PARAMETERS OF COPLANAR BARRIER DISCHARGE USING DIFFERENT EMITTING LAYERS

J. Čech, P. Sťahel A. Brablec and M. Černák

Department of Physical Electronics, Masaryk University,
Kotlarska 2, 611 37 Brno, Czech Republic

ABSTRACT. Plasma parameters of one atmosphere coplanar barrier discharge (CBD) performed in pure N_2 atmosphere was investigated as a function of discharge power and different emitting layers (BaO, TiO_2 and Al_2O_3 doped with N ions) deposited on the surface of the bulk alumina dielectrics. The variations of the ignition voltages and extinction voltages as well as vibrational temperatures estimated from N_2 second positive system ($\Delta v = -2$) were studied.

1. INTRODUCTION

Dielectric barrier discharges (DBDs) became very useful in the field of in-line plasma processing at atmospheric pressure. DBDs can be used as sources of low temperature plasma for a variety of technical applications like surface modification, plasma deposition, sterilization, etc. [1,2]
The coplanar barrier discharge (CBD) [3] has following unique properties among others DBDs. The CBD generates a thin layer of non-equilibrium atmospheric pressure plasma being not in contact with metal electrodes [4,5]. That results in an increased lifetime of electrode system and decreased contamination of plasma from electrodes. Moreover, high power densities (up to 100 W/cm^3) can be achieved and noble gases such as helium, argon, etc. are not needed for CBD stabilisation [5]. The CBD has a unique structure where the diffuse part of the discharge can be emphasised while the filamentary part can be suppressed. This unique property can reduce one disadvantage of majority of barrier discharges -their inhomogeneity.
In this work the parameters of one atmosphere CBD plasma generated in pure nitrogen was investigated as a function of discharge power and different emitting layers (BaO, TiO_2 and Al_2O_3 doped with N ions) deposited on the surface of the bare alumina dielectric. The variations of the ignition voltages and extinction voltages as well as vibrational temperatures estimated from N_2 second positive system ($\Delta v = -2$) were studied.

2. EXPERIMENTAL

Discharge electrode used for spectroscopic or electric measurements and also for taking the pictures of discharge consisted of alumina (Al_2O_3) dielectric plate 0.5 mm thick with/or without different emitting layer created on the discharge side. On the uncoated side of dielectric plate the system of two coplanar electrodes was placed. Coplanar electrodes were 20 mm wide and distance between them was 2.4 mm in all cases. The electrode system was dipped in a transformator oil bath serving for electrode insulation and also for system cooling. The system was placed into the discharge chamber of size 80x80x30 mm that enabled one to use pure working gas atmosphere. For ignition and extinction voltage measurements spherical electrodes were used in order to obtain one filament discharge. The nitrogen flow rate of 6 slpm was kept in all cases. The plasma was driven by high voltage (HV) power supply with frequency 8.5 kHz. The surface of the dielectric plate was modified by means of deposition of BaO or TiO_2 thin layer or nitrogen implantation in order to change emitting properties of alumina.
Electrical parameters (voltage and current) were measured by means of digital oscilloscope HP 54820A Infinium (2 channel, 500 MHz/2 GSa). The power absorbed by plasma was then estimated from the current-voltage time evolution measurements.
The emission spectra were recorded by the JobinYvon monochromator, Triax 550 equipped with 1 200 gr/mm and liquid nitrogen cooled CCD detector.The vibrational temperature was then calculated from the bands of second positive system of nitrogen N2 (Δv = -2, heads (0-2, 1-3, 2-4 and 3-5). Discharge pictures were taken by digital camera.

3. EXPERIMENTAL

Fig. 1 shows images of the coplanar barrier discharge generated on the surface of different emitting layers taken with exposition time of 1/25 s. The discharge consists of two parts. The first, inter-electrode, part consists of many filaments, the second, above-electrode part, is consisted of diffuse plasma. The different emitting layers were able to change diffuse/ filamentary part ratio and also the character of the discharge itself.

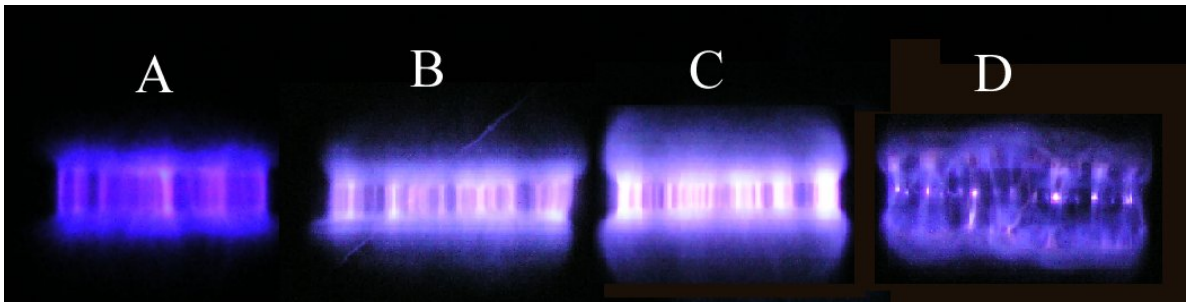

FIGURE 1. Effect of emitting layer on discharge. A-Al_2O_3 (bare),B- Al_2O_3+BaO, C- Al_2O_3+N_2,D- Al_2O_3+TiO_2

.

In the case of uncoated alumina both diffuse part and also filamentary part of discharge were not distinct (see part A). The discharge generated on the dielectric coated with BaO or on alumina with implanted nitrogen (see part B and C) exhibited enhanced above-electrode diffuse part. In the case of discharge generated on the surface of the alumina coated by TiO_2 a character of discharge completely changed. The diffuse and filamentary part mixed up and radiant points between the electrodes appeared (see part D).

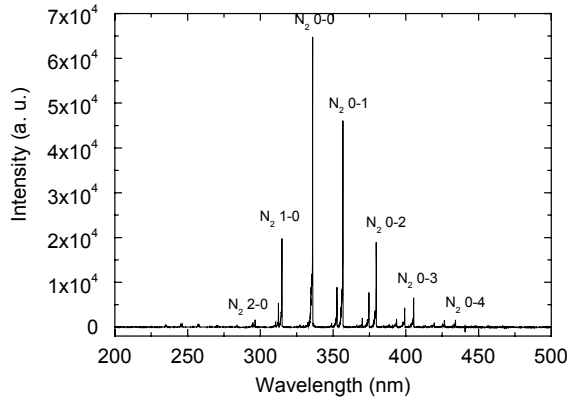

FIGURE 2. Typical spectrum of the coplanar barrier discharge in pure nitrogen.

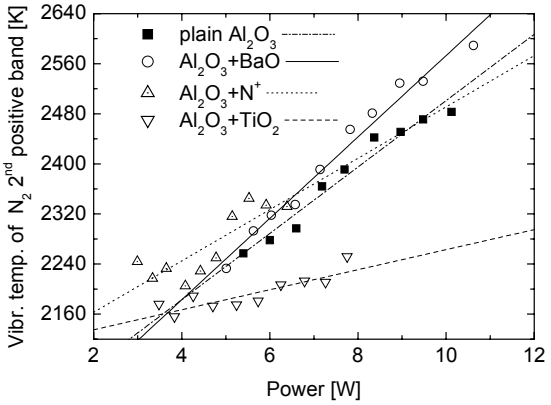

FIGURE 3. Vibrational temperature of CBD as a function of power for different emitting layers.

.

A typical spectrum of the coplanar barrier discharge is shown in Fig. 2. Above 500 nm only the second spectral order was observed. The spectra consisted of the molecular bands of second positive system of nitrogen ($C\ ^3\Pi_u \rightarrow B\ ^3\Pi_g$), The vibrational temperature was calculated from the bands of second positive system of nitrogen N_2 0-2, N_2 1-3 and N_2 2-4 for different power and different emitting layers with relative error lower then 10 %. In Fig. 3 the variation of the vibrational temperature as a function of power is shown. The error bars are not plotted to maintain lucidity of the plot. The vibrational temperature of nitrogen increases with increasing power for each emitting layers. The regression coefficients of linear fits of vibrational temperatures are given in table 1.

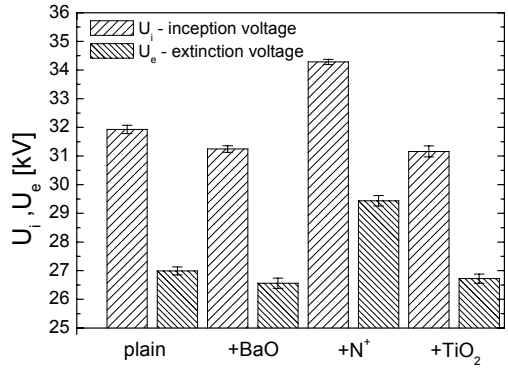

FIGURE 3. Variation of ignition and extinction voltages with respect to different emitting layers.

	a [K]	δa [K]	b [K.W^{-1}]	δb [K.W^{-1}]	R
Al_2O_3(bare)	1970	32	53	4	0.98
Al_2O_3+BaO	1922	26	65	3	0.99
Al_2O_3+N^+	2081	43	41	9	0.85
$Al_2O_3TiO_2$	2102	19	16	3	0.87

TABLE 1. Coefficients of N_2 vibrational temperature linear fits.

Moreover, using the different surface layer it was possible to modify the ignition and extinction voltages as well. Fig. 4 shows ignition and extinction voltages for four different emitting layers. Surface emitting layer affected not only the ignition/extinction voltage but also ignition to extinction voltage range.

4. CONCLUSION

The influence of different surface layers on the plasma properties and ignition and extinction voltage was proved. It was shown that vibrational temperature linearly increased with increasing input power and its slope is depending on the emitting layer. The power absorbed by discharge was calculated from voltage and current time evolution measurements. The emitting layers were able to change not only the plasma parameters as vibrational temperature, ignition and extinction voltages and discharge filament/diffuse ratio, but also the structure of the discharges as well.

ACKNOWLEDGMENTS

This research has been supported by the grant No. 202/05/0777, Grant Agency of Czech Republic and the Long-term intent project No. MSM0021622411, Ministry of Education, Czech Republic.

REFERENCES

[1] M. Simor, J. Rahel, P. Vojtek, A. Brablec, M. ·Cernak: *Appl. Phys. Lett.* 81 (2002) 2716-2718.
[2] M. Cernak, J. Rahel, D. Kovacik, M. Simor, A. Brablec, P. Slavicek: *Contrib. Plasma Phys.* 44 (2004) 504{507.
[3] M. ·Cernak: *International Patent Application* No. PCT/SK02/00008 (9 May 2002).
[4] J. R. Roth: *Industrial Plasma Engeneering* Vol II -*Applications to Non-Thermal Plasma Processing*. Institute of Physics Publishing, Bristol.
[5] B. Eliasson, U. Kogelschatz: *Appl. Phys. Lett. B* 46 (1998) 1685{94.

Paper number

STABILIZATION OF DC ATMOSPHERIC PRESSURE DISCHARGE

H. Matsuura[1], and Y. Sasada[1]

[1] *Department of Mechanical Engineering,*
Grduate School of Engineering,Osaka Prefecture University
1-1Gakuen-cho, Sakai Naka-ku, 599-8531, JAPAN

ABSTRACT. We have studied an atmospheric pressure discharge with a small hollow needle cathode and a plate anode. By controlling the the gap between electrodes, stable plasma is produced and ststained even without gas flow controll. From a simple heat conduction model, natural convection is found to play an important roll to keep cathode temperature low.

1.INTRODUCTION

Recently application of the glow discharge plasma under an atmospheric pressure has been collected attentions due to its non-thermal properties. An atmospheric pressure discharge plasma is expected not only to reduce processing cost such as pumping systems, but also to enhance plasma application including material processings which are not resistant to the vacuum condition. One example is the application in the bio-physical field. The production mechanism is, however, still complicated and necessary to be studied further.

About twenty years ago, atmospheric pressure glow discharge(APGD) was found firstly with rare gas and dielectric barrier AC discharge. [1] Since then, gas spices and discharge type have been extended. Even with DC condition, by using a needle type cathod, stable APGD production is reported in [2] and [3]. In these study, gas flow control seems to be important to obtain stablilized discharge.

We also design a simple plasma source with a small hollow needle cathode and a plate anode. By controlling the the gap between electrodes, stable plasma is produced and ststained even without gas flow controll. In the section 2, first experimental results are shown. A simple heat transfer modelling is shown in section 3.

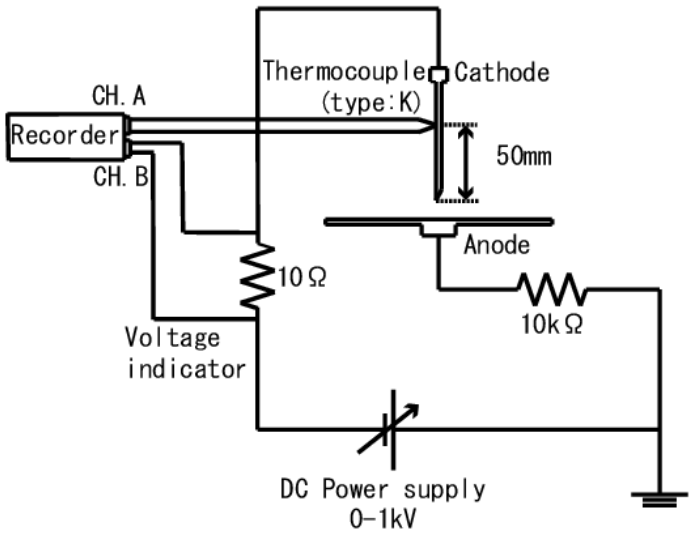

FIGURE 1. Experimental setup.(Both anode and cathode are made of stainless steel.)

[1] Electronic address: matsu@me.osakafu-u.ac.jp

2.EXPERIMENTAL SETUP AND RESULTS

The experimental setup is shown in Fig.1. A hollow needle with the diameter of about 1mm is used as a chathod. Anode is the circlar plane. Both electrodes are made of stainless steel (SUS). A DC high voltage up to 1[kV] is applied between these electrodes with a safety resistor of 10 [kilo-ohm] inserted in series. The distance between electrodes can be controlled manually. Dischage current is monitered with a pickup resister of 10 [ohm]. The cathode temperature is also monitered with a type-K thermocouple located at 5cm above of cathode tip.

In Fig.2, typical moniter signals are shown. By keeping an electrode distance of sub mm, DC high voltage is applied at 30[s]. The current of several 10 [mA] is observed to flow. However, this current seems to be sustained by field emission effect and no plasma is produced. Local electric field around the cathod tip is estimete to exceed 100 [MV/m] due to the sharp geometry.

Then at 150[s], we extend the gap between electrodes to 2[mm], and bright light emitted from electron impact excited atoms and molecules appears. The cathode moniter temperature begins to increase as shown in Fig.2, and reaches steady state of about 40 [deg.]. It is still not clear whether plasma production is a Corona type discharge or a Glow type one. At first, a needle cathode is heated up to the melting temperature and obtained plasma is somehow unstable. But soon plasma reaches a steady state and cathod temperature is kept low.

Though, in previous stuties of references [2] or [3], gas flowing condition in discharge region was a key issue to improve stability as a plasma source, our experiment has no direct control of a forced gas flow. Since there is a natural convection inside of cathode hole or outside of it, our cathode may be prevent from an Arc discharge. In the next section, we made a simple heat transfer modelling of a cathode which is set up vertically.

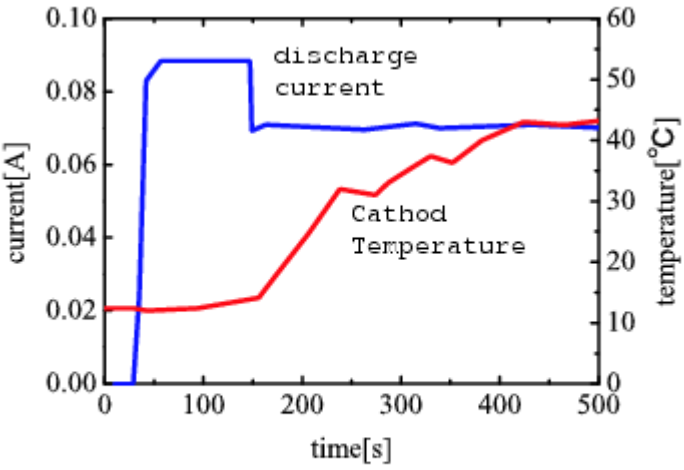

FIGURE 2. Time evolution of discharge current and Cathode temperature monitor.

3.1D HEAT TRANSFER MODEL OF THE VERTICAL CATHODE

Though a chathod used in our experiment is a tube with a hole, we used here cylinder model with lingth of L and radius of r_c. From the view point of heat transfer, this simplification may lead underestimate of natural convection effect.[4] We also assume here that a cathode receive plasma energy flux only at one edge ($z = 0$) and that heat transfer from a cathode side wall can be described as

$$q_k = q_{km}\frac{T - T_n}{T_m - T_n} \propto (T - T_n) \qquad (1)$$

where T_m and T_n are melting point of cathod material and background gas temperature, respectively. In our experimental condition, q_{km} is much larger than radiation heat flux estimated with Stefan-Boltzmann law, so hereafter we neglect radiation effect.

Using L and characteristic heat flux density $q_0 = \lambda\frac{T_m - T_n}{L}$, where λ is the heat conductivity of the cathod, coordinate z, conductive heat flux density q_c and temperature T are normalized as the following,

$$\tilde{z} = \frac{z}{L},\ \tilde{q} = \frac{q_c}{q_0},\ \tilde{T} = \frac{T - T_n}{T_m - T_n} \qquad (2)$$

Basic equations of our modelling becomes very simple.

$$\frac{d\tilde{q}}{d\tilde{z}} = -2C\tilde{T},\ \frac{d\tilde{T}}{d\tilde{z}} = -\tilde{q} \qquad (3)$$

Since parameter $C = \frac{L}{r_c}\frac{q_{km}}{q_0}$ is much larger than unity, analytical solutions of Eq.(3) become expnential type.

Figure 3 shows spatial profile along cathod axis of normalized temperature (solid line) and heat flux (broken line). The moniter tempeartue $T(L)$ and estimated $q_c(0)$ are used as boundary conditions. From this figure, we can see that q_c decays very rapidly due to natural convection and that T is kept low at almost whole positon.

We have very limited expereimental result with short cathod(2 [mm]). In this case, temperature becomes more then 100 [deg.]. Our modeling does not contradict with this observationt. But $T(0)$ seems to be smaller than melting point. This may be due to the limitation of our modelling.

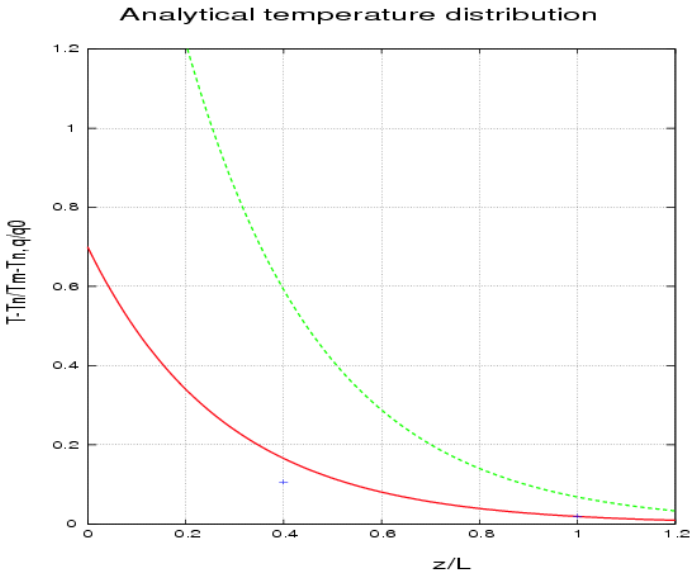

FIGURE 3. Spatial profile modeling of Normalized temperature (solid line) and heat flux (broken line).

REFERENCES

[1] Takkaki, K., Fujiwara, T., Tochikubo, F.(2003). *J. Plasma Fussion Res.,*79,1002-1008[in Japanese].

[2] Hattori, K., Ishii, Y., Tobari, H., Ando, A., Inutake, M.(2006). *Thin Solid Films*, 506-507, 440-443.

[3] Sankaran, R.M., Giapis, K.P.(2002).*J.Appl.Phys.*, 92, 2406-2411.

[4] Japanese Society of Mechanical Engineering.(1986). Chapter 2 Convective heat transfer In *JSME Data book: Heat transfer(4th Edition)* [in Japanese].

Paper number

VISUALIZATION OF THE FLOW IN A PULSED POSITIVE STREAMER DISCHARGE IN WATER

J. Mikielewicz, J. Podliński, M. Dors, E. Metel, M. Kocik, J. Mizeraczyk

Centre for Plasma and Laser Engineering
The Szewalski Institute of Fluid Flow Machinery, Polish Academy of Sciences
Fiszera 14, 80-231 Gdańsk, POLAND

Results of the laser visualization of the gas bubbles flow in a needle-to-cylinder pulsed streamer discharge reactor filled with distilled water are presented. It was observed that the discharge in water produced bubbles with a production rate proportional to the applied voltage. Large vortices generated during the streamer discharge distributed bubbles in the whole reactor volume, providing good mixing and distribution of active species, what is very important when water is polluted with organic compounds. The more needles were used, the larger number of bubbles were observed. The strength of the vortices increased with increasing applied voltage as well.

1. INTRODUCTION

The high voltage pulsed discharges in water have been investigated for many years due to its application [1-4]. The pulsed discharge in water is efficient in formation of chemically active species such as OH, H, O, H_2O_2 and O_3 (with or without air or oxygen bubbling), which cause degradation of organic compounds contained in water. Besides the chemically active species, the discharge generates ultraviolet radiation and shock waves, which also contribute to the organic compound degradation. The streamer discharge is accompanied with the bubbles formation. The size and the velocity of the bubbles [5, 6], and also rebounds of the bubbles as a function of hydrostatic pressure, electrical energy and nature of the liquid [7] can be measured. The bubbles are filled with the gas, which presumably contains the gaseous hydrogen, water vapor and oxygen.

The aim of our investigation was to show streamers and gas bubbles formation as well as motion of bubbles under the influence of electric field formed in the streamer discharge (point-to-cylinder electrode system) in the reactor with 1 and 3 needles in distilled water. The gas bubbles were used as tracers for the laser visualization of their flow.

2. EXPERIMENTAL SET-UP

The experimental setup consisted of a reactor, DC power supply with a rotating spark gap switch, CuBr laser, optics for the laser beam formation, CCD camera for laser visualization of the bubbles and their flow and a photo-camera for visualization of the streamers (Fig. 1).

The pulsed positive discharge was generated between a stressed stainless steel needle

Electronic address: mdors@imp.gda.pl

electrode(s) and a grounded brass cylinder electrode. Two needles arrangements were used: the first was equipped with one needle electrode, and the second - with three needle electrodes. The non-active part of the needle was covered with an insulator. The needle-cylinder spacing was 45 mm. The electrodes were placed in a glass parallelpiped reactor (36 mm wide, 144 mm long and 120 mm high), which was filled with distilled water. The conductivity of the water was 4 μS/cm.

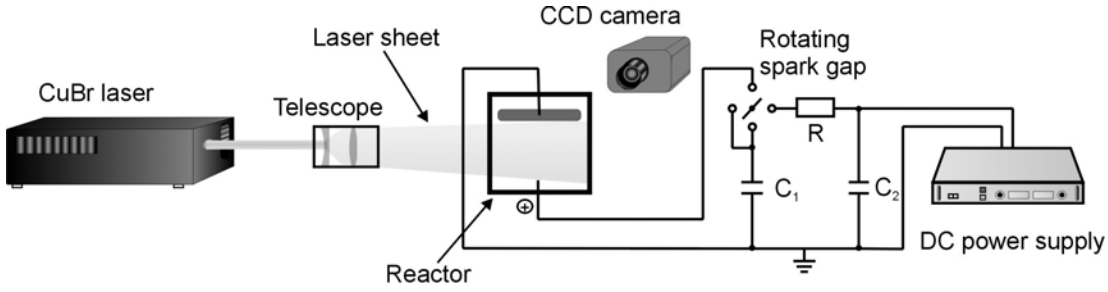

FIGURE 1. Experimental set-up.

The positive high voltage pulses were applied to the needle electrode(s) from a discharge capacitor C_1 (2 nF). The capacitor was charged from a DC power supply through a resistor R (10 kΩ) and a capacitor C_2 (22 nF). The amplitudes of the voltage and current pulse were up to 31 kV and 3 A respectively, with a pulse width up to 800 μs. The pulse repetition rate of 50 Hz was determined by the rotation velocity of a rotating spark gap switch.

A CuBr laser was used for the visualization of the flow in the reactor. The laser beam emitted by the CuBr laser was transferred into a laser sheet by a cylindrical telescope. Images of the bubbles moving in the water were recorded by a CCD camera in the form of movies. The visualization of the bubbles flow in the water was performed in a few horizontal and vertical positions of the laser sheet, crossing the reactor.

3. RESULTS AND DISCUSSION

During the discharge in the water the gas bubbles were formed. According to our results the bubbles contain gaseous hydrogen, and presumably oxygen and water vapor. The bubbles were produced near the needle electrode(s) and due to buoyant and electrohydrodynamic forces the bubbles were moved upward towards the cylindrical electrode. An initiation of the bubbles production was observed at the voltage of 18 kV (for 1 and 3 needles).

The movement of the bubbles, easily seen with the naked eye, was recorded with the video camera.In this paper we present selected single images of the bubble positions during the discharge in the water, extracted from the corresponding movies, with the sketches of the bubble flow trajectories deduced from the observation of the full movie. Each arrow represents the direction of the bubbles motion. Movies were recorded at the discharge voltage up to 31 kV, with the pulse current of up to 3 A.

Fig. 2a shows the bubble flow trajectories in the vertical plane along the reactor passing through 1 needle. It is seen that the bubbles flow stream was flowing from the needle vicinity to the grounded electrode, and then at the left and the right side it started to circulate, forming bubble flow vortices. The vortices cause the water mixing in the reactor volume and transport the bubbles back towards the discharge region. Above the cylindrical electrode small vortices were observed.

The bubbles flow trajectories in the reactor with 3 needles in the vertical plane along the reactor passing through the needles are shown in Fig. 2b. It is seen that three bubbles flow patterns corresponding to each needle electrode were formed. The bubbles streams moving

from the needle electrode to the cylindrical electrode were relatively strong. After coming to the cylindrical electrode the bubble stream turned and went downwards, forming vortices on both sides of each discharge. The downward bubble streams were weaker compared to the upward bubble stream. The vortices were smaller than in the reactor with 1 needle. It could be caused by a different currents (the discharge current of 0.2 and 0.4 A for 1 and 3 needles at voltage of 25 kV, respectively) and a small spacing between the needle electrodes. They cause a relatively strong mixing of the water in the whole reactor volume.

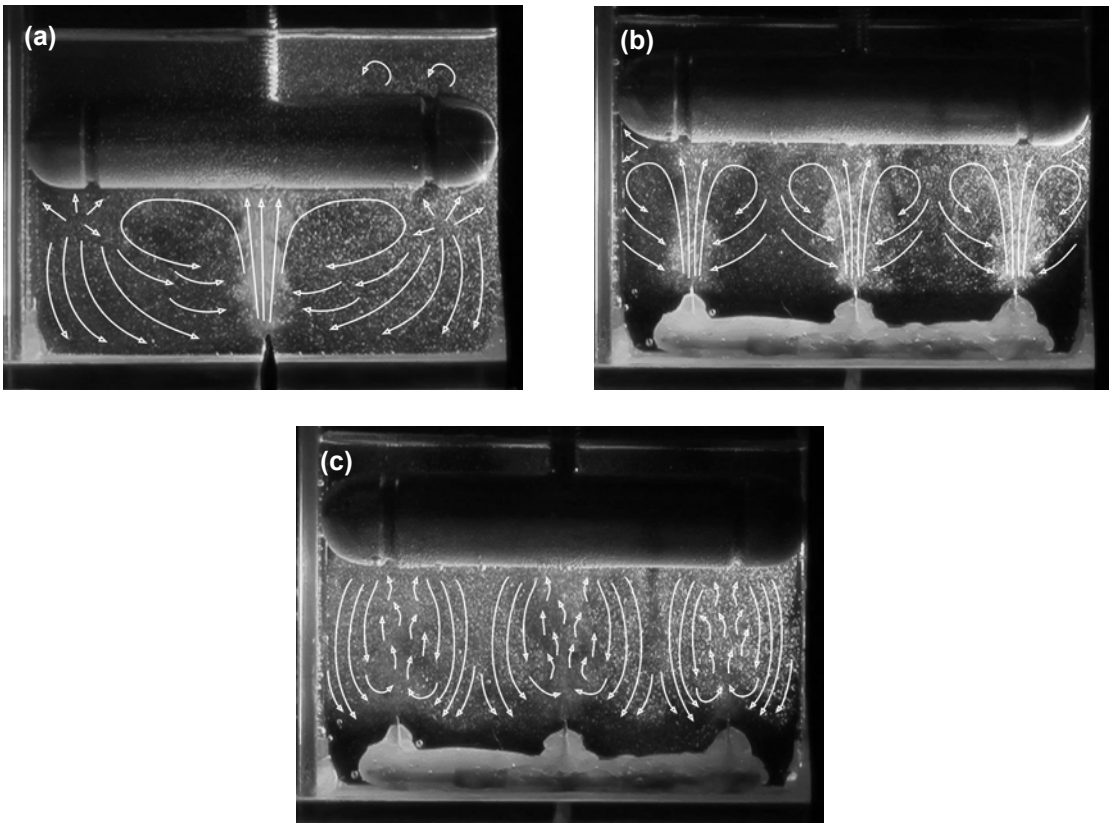

FIGURE 2. Bubbles flow trajectories in the vertical plane along the reactor with 1 and 3 needles. The laser sheet passed through needles (a), (b) and behind needles (c). The discharge voltage up to 31 kV, the discharge current up to 3 A.

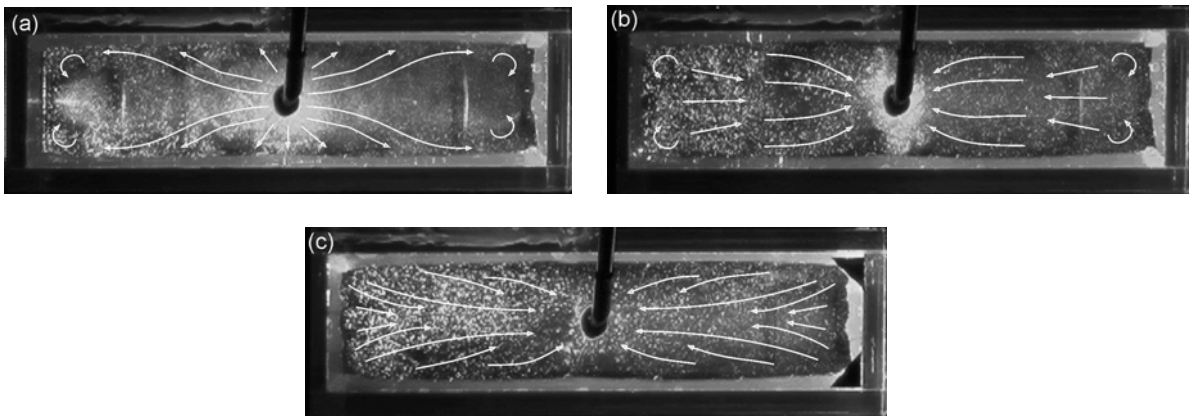

FIGURE 3. Bubbles flow trajectories in the horizontal plane of the reactor with 1 needle: (a) the laser sheet under the cylindrical electrode, (b) the laser sheet in the middle of the needle-cylinder spacing, (c) the laser sheet passing through the needle. The discharge voltage up to 31 kV, the discharge current up to 3 A.

In the vertical plane along the reactor behind the needles, motion of the bubbles in the discharge direction was low (Fig. 2c). It is worth noting that the bubbles motion between the streams directed downward was stronger than in the plane passing through the needles.

In the horizontal plane close the cylindrical electrode in the 1-needle reactor the bubbles pushed up from the needle electrode were dispersed symmetrically to the reactor walls (Fig. 3). In the corners of the reactor small horizontal vortices were observed. For 3–needle reactor the horizontal movement of the bubbles around each needle electrode in the plane 1 looks similarly to that of 1–needle reactor.

4. CONCLUSIONS

The experiment was focused on the formation and movement of the bubbles in the streamer discharge in the reactor filled with distilled water.

We observed that the bubble flow from the needle tip towards the cylindrical electrode is the stronger stream. Under the cylindrical electrode vortices appear, which transport scattered bubbles back towards the discharge region(s) and they cause mixing the water in the whole reactor volume. During the discharge the whole reactor volume is filled with the bubbles and some of them was going out to the water surface.

We found that the bubbles production and the streamer size increased with increasing applied voltage, regardless of the needle electrode numbers. However, in 3–needle reactor more gas bubbles were produced than in the reactor with single needle, probably due to higher currents (0.4 A and 0.2 A for 3 and 1 needle(s) at the voltage of 25 kV, respectively) and higher number of the generated streamers.

ACKNOWLEDGMENTS

This work was supported by the Ministry of Science and Information Society Technologies under programme PB 1280/T10/2004/27 and by the Institute of Fluid Flow Machinery, Polish Academy of Sciences under programme IMP PAN O3Z3T2.

REFERENCES

[1]Sugiarto A.T., Ito S., Ohshima T., Sato M., Skalny J.D. (2003). *J. Electrostat.* 58, 135-145.
[2]Grymonpre, D.R., Sharma, A.K., Finney, W.C., Locke, B.R. (2001). *Chem. Eng. J.*, 82, 189-207.
[3]Sunka, P., Babicky, V., Clupek, M., Lukes, P., Simek, M., Schmidt, J., Cernak, M. (1999). *Plasma Sources Sci. Technol.*, 8, 258–265.
[1]Locke, B.R., Sato, M., Sunka, P., Hoffmann, M.R., Chang, J.S. (2006). *Ind. Eng. Chem. Res.*, 45, 882-905.
[5]Tsouris, C., Shin, W., Yiacoumi, S., DePaoli, D.W. (2000). *J. Colloid and Interface Science,* 229, 335-345.
[6]Sato, M., Hatori, T., Saito, M. (1997). *IEEE Trans. Ind. Appl.*, 33, 1527-1534.
[7]Jomni, F., Aitken, F., Denat, A. *(1999). J. Electrostat.,* 47, 49-59.
[8]Sun, B., Sato, M., Harano, A., Clements, J.S. (1998). *J. Electrostat.*, 43, 115-126.

Paper

DIAGNOSTICS OF He ATMOSPHERIC PRESSURE GLOW PLASMA: MEASUREMENT OF METASTABLE He ($2s^1S$, $2s^3S$) WITH ATOMIC RESONANCE ABSORPTION SPECTROSCOPY

Kunihito Tanaka, Yoshihisa Yanagawa and Masuhiro Kogoma

Department of Chemistry,
Faculty of Science and Technology, Sophia University
7-1 Kioi-cho, Chiyoda-ku, Tokyo 102-8554, JAPAN

ABSTRACT. The single and triplet metastable helium ($2s^1S$, $2s^3S$) atoms in the He atmospheric pressure glow plasma obtained from a RF dielectric barrier discharge were detected by the atomic resonance absorption spectroscopy. Their densities were estimated to be about 10^{11}~10^{12} cm^{-3} and the density of triplet He^m was several times bigger than that of singlet He^m. While their absorbances indicated almost linear relationship with the discharge power, they were increased by increasing the He flow rate. This dependence was occurred by the variation of the impurity, such as N_2, concentration. And the both metastables seemed to disappear in several tens nanoseconds.

1. INTRODUCTION

The generation mechanism of the helium (He) atmospheric pressure glow (APG) plasma has been investigated by some researchers [1-5]. However, almost these studies are carried out with the computer simulation, and there are few studies of experimental measurement such as density and energy distribution of electron, excited gas molecule density and so on.

The dielectric barrier discharge (DBD) at atmospheric pressure is a simple system to obtain a low temperature non-equilibrium plasma. The electron charge on the dielectric surfaces limits the increasing of the gas voltage and avoids the transition of plasma to arc. On the other hands, it is considered that some active species always remain in the plasma and that they construct the easy space to generate a discharge. The metastable He (He^m) behavior in He APG plasma is supposed to play an important role in the APG plasma generation mechanism because of its high energy level and long life time. However, this supposition has not been confirmed clearly, and there is a computer simulation result that indicates short life times of the metastables [3].

In this study, we measured the absorbance of He^m in He APG plasma with atomic resonance absorption spectroscopic (ARAS) technique to reveal the relation between some plasma parameters and the absorbances.

2. EXPERIMENTAL

A general dielectric barrier discharge plasma reactor shown in figure 1 was used for He APG plasma deposition. The dielectrics were quartz plate, whose size was 200 × 200 × 2 mm. The electrode size and the discharge gap were 200 × 20 mm and 2 mm,

TABLE 1. Discharge conditions.

Discharge frequency / MHz	13.56
Discharge power / W	100 - 600
He flow rate / slm	1 - 10
Discharge volume / mm^3	8000

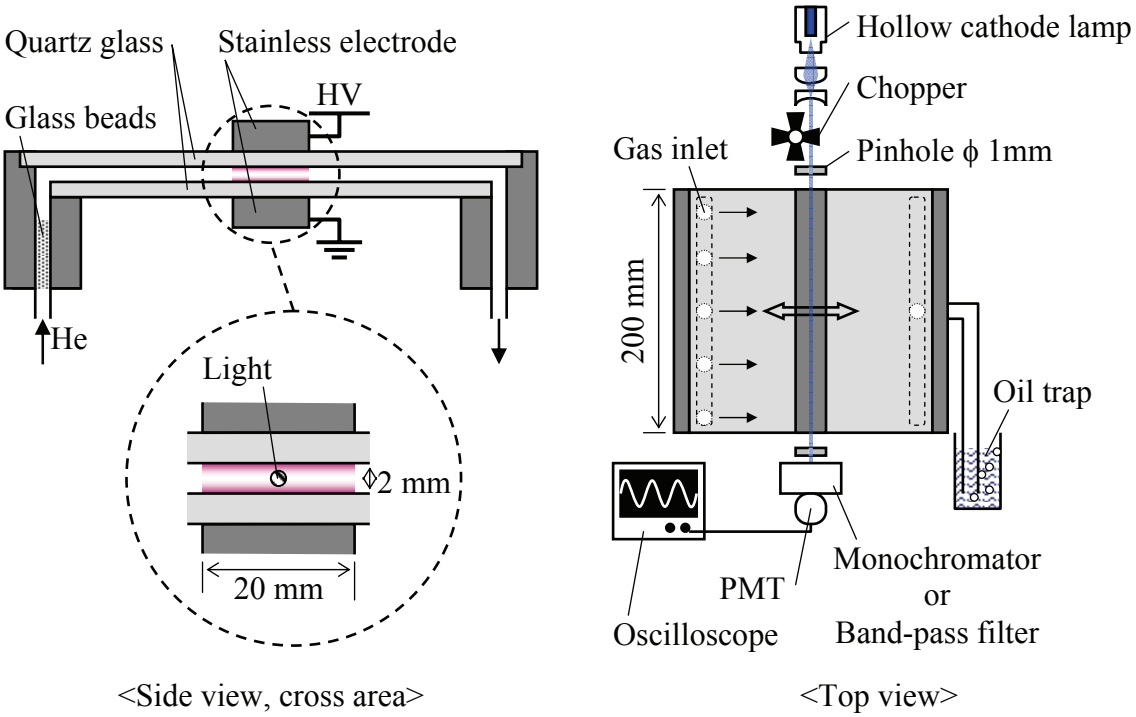

Figure 1. Schematic diagram of the plasma reactor and ARAS system.

respectively. The flux of He gas introduced from 5 ports was made uniform via glass beads (ϕ 1mm) as much as possible. The exhaust He pass through the silicone oil trap to prevent the air back-diffusion. The discharge conditions are shown in table 1.

A hollow cathode (HC) lamp (L233-14HEU, Hamamatsu) fed with He gas was used as a light source; the wavelengths, 501.5 nm and 388.8 nm were used for the measurement of singlet and triplet He^m, respectively. Other emissions near around those wavelengths were not detected from the HC lamp. The monochromator (focal length, 200 mm; grating, 1200 mm^{-1}) and the band-pass filter (FWHM, 10 nm) were used for the time integrated and time resolved absorbance, respectively. The emission signals were measured with the photon multiplier tube (R928, Hamamatsu) and the oscilloscope (54616B, Agilent technologies).

3. RESULTS AND DISCUSSION

The both metastables were detected by ARAS system and the variations of their absorbances as functions of the discharge power and He flow rate are shown in figure 2. Although we didn't measured the line width of the light source, from the general line width (about 10 GHz) of HC lamp, the maximum densities of singlet and triplet He^m are calculated to about 10^{11} and 10^{12} cm^{-3}, respectively. The absorbance indicated almost linear relationship with the discharge power. Moreover, they were increased by increasing the He flow rate as show in figure 3, which is the same result of singlet metastable in figure 2. Since the high gas flow rate means decreasing the residence time of gas molecules in the plasma zone, the density of the active species usually decrease or show a steady value as increasing the gas flow rate. We supposed that the reason for this result was the influence of the impurity.

Since the optical emissions attributed nitrogen molecules were detected in the He APG plasma, we supposed that the main impurity is N_2 (air). Since the emission intensities

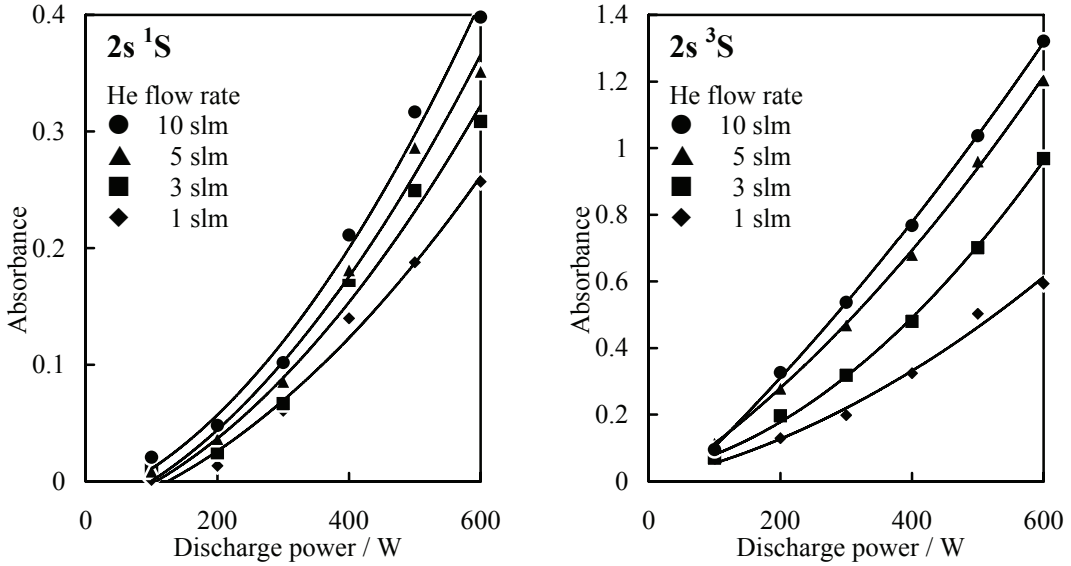

Figure 2. The variation of the absorbance of each metastable as a function of the discharge power. The marks show different He flow rates. The light source was pass through the center of the plasma zone; the position was 10 mm.

attributed N_2 were decreased by setting an oil trap to the exhaust, some air back-diffused into the plasma zone. Although the results of figures 2-6 were obtained with the oil trap, the emissions attributed N_2 were not disappeared completely. Moreover, those intensities were decreased by increasing the He flow rate as shown in figure 4 and showed same values in spite of using higher purity (99.95% → 99.9999%) He gas. Therefore, we supposed that the main impurity source is N_2 (air) absorbed on the inner surface of gas piping.

Figure 5 shows the absorbance profiles of singlet He^m as a function of the position in the plasma zone. The absorbance of triplet He^m showed same profiles. The variation of the absorbance in the plasma zone was caused by the unevenness of the plasma reactor (discharge gap or electrode surface). So the absorbance in the plasma zone seemed almost same value.

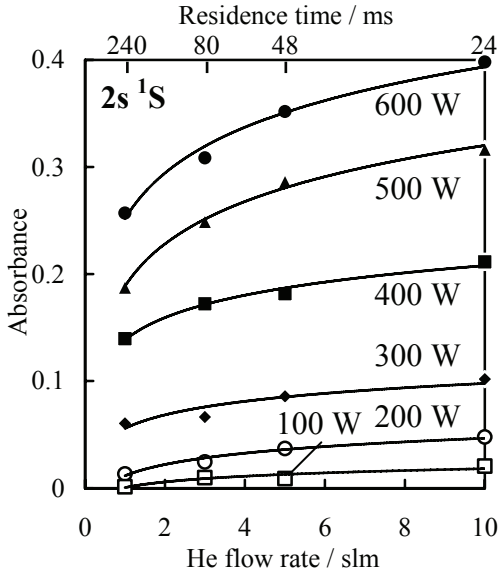

Figure 3. The variation of the absorbance of singlet metastable as a function of the He flow rate. The marks show different discharge powers.

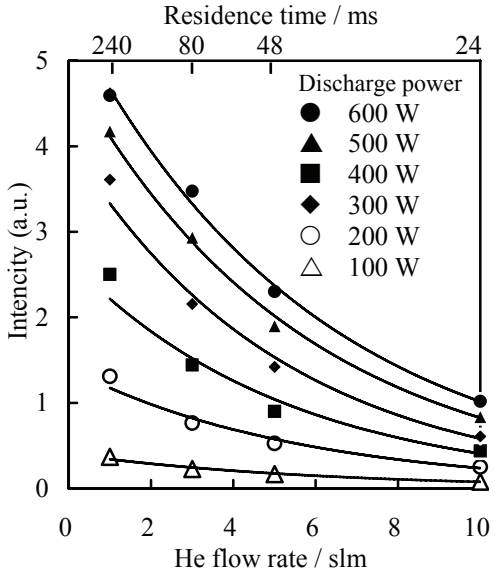

Figure 4. The variation of the intensity of nitrogen ion, N_2^+ ($B\ ^2\Sigma_u \rightarrow X\ ^2\Sigma_u$, 391.4 nm) as a function of the He flow rate.

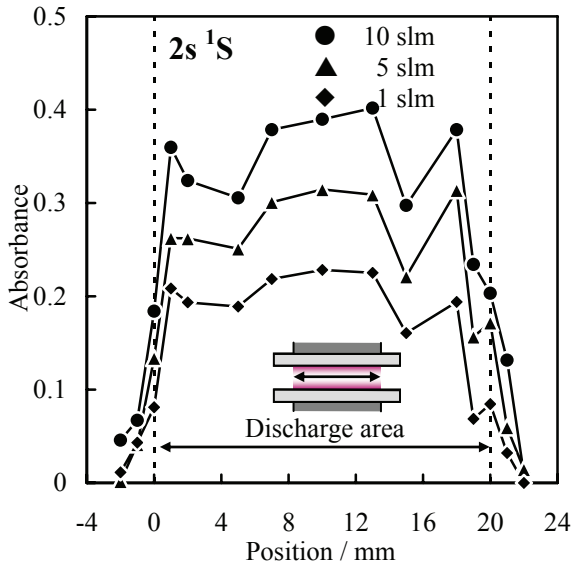

Figure 5. The absorbance profiles as a function of the position in the plasma zone. The discharge power was 500 W.

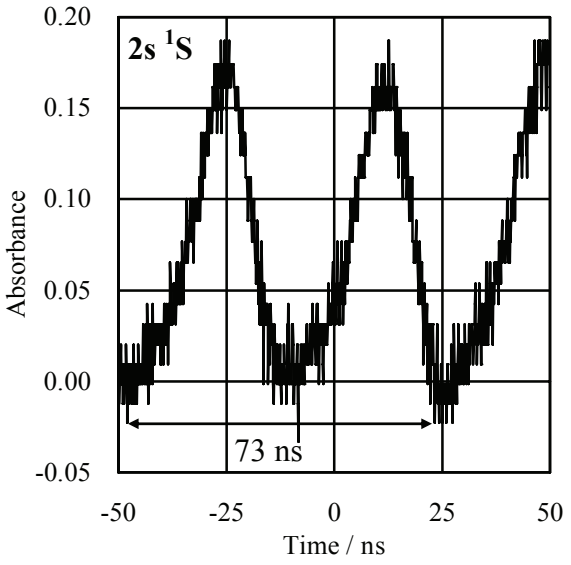

Figure 6. An example of the time resolved absorbance. The discharge power was 300 W and the He flow rate was 5 slm.

And the generation and decay rate were faster than several tens milliseconds. Although the time resolved absorbance measurement was not compliant, an example result shown in figure 6 suggested that those rates were about several tens nanoseconds.

4. CONCLUSION

It was suggested that the life times of singlet and triplet He^m were shorter than our estimation. Thus, we considered that it is necessary to measure other active species, such as He_2^+, that were indicated from some computer simulation result to have an important role.

REFERENCES

[1] Massines, F., Rabehi, A., Decomps, P., Ben Gadri, R., Segur, P., Mayoux, C. (1998) Experimental and theoretical study of a glow discharge at atmospheric pressure controlled by dielectric barrier. *J. App. Phys.*, 83 (6), 2950-2957.

[2] Massines, F., Segur, P., Gherardi, N., Khamphan, C., Ricard, A. (2003) Physics and chemistry in a glow dielectric barrier discharge at atmospheric pressure: diagnostics and modelling. *Surface and Coatings Technology*, 174-175, 8-14.

[3] Tochikubo, F., Chiba, T., Watanabe, T. (1999) Structure of low-frequency helium glow discharge at atmospheric pressure between parallel plate dielectric electrodes. *Jpn. J. Appl. Phys. Part 1*, 38, 9A, 5244-5250.

[4] Honda, Y., Tochikubo, F., Uchida, S. (2002) Initial growth process of barrier discharge in atmospheric pressure helium for glow discharge formation. *Jpn. J. Appl. Phys. Part 2*, 41, 11A, 1256-1258.

[5] Tachibana, K., Kishimoto, Y., Sakai, O. (2005) Measurement of metastable $He^*(2^3S_1)$ density in dielectric barrier discharges with two different configurations operating at around atmospheric pressure. *J. App. Phys.*, 97, 123301.

DIAGNOSTICS OF ORGANICS COMPOUNDS DEGRADATION BY OPTICAL EMISSION SPECTROSCOPY

J. Prochazkova, Z. Stara and F. Krcma

Faculty of Chemistry, Brno University of Technology,
Purkynova 118, Brno, CZECH REPUBLIC

ABSTRACT. The study is focused on the investigation of the DC diaphragm discharge in water solutions of various organic compounds, especially organic dyes. This type of the discharge is created in a small pin-hole in the dielectric diaphragm located between two high voltage electrodes. Various reactive species such as radicals and ions produced by the discharge are precursors for consequent chemical reactions.
The degradation processes were studied in water solutions of selected organic dyes (Direct Blue 106 and Solvent Yellow 94). The spectroscopic observations were carried out in these solutions and the influence of experimental conditions on the emission intensity of selected species (OH radicals, hydrogen and oxygen atoms etc.) was studied. Dissociation of studied organic compounds by the discharge was dependent mainly on the applied high voltage and on the initial solution conductivity (i.e. electrolyte concentration), respectively.

1. INTRODUCTION

Discharges generated in liquids have a special position among the plasma sources. The common discharge configurations are point-to plane [1] and coaxial [2], several experiments were done in a diaphragm (electrode-less) configuration. This work focuses on the diaphragm discharge created using the non-pulsed DC high voltage with the tension of about 2 kV. Besides the study of these discharges from the electrical point of view [3], chemical processes are the second main research field [4]. In water solutions, various chemical active species are produced by the discharge, for example radicals, hydrogen peroxide, ozone etc. [1]. These active species initiate many further chemical reactions. Therefore the processes taking place in such discharges can be applied in the fields of water treatment, surface treatment etc. [2]. The reaction mechanisms in the electrical discharges in liquids are not fully understood yet because many different active species are created [5]. The OES can give basic direct information about these processes.

2. EXPERIMENTAL

A simplified scheme of the used batch discharge reactor is shown in Figure 1. It consists of two parts - a „negative part" with an anode (negative streamers are created) and a „positive part" with the cathode (positive streamers are created). Two planar stainless steel electrodes are installed in the distance of 4 cm symmetrically with respect to the PET dielectric diaphragm (the thickness of 0.25 mm) with a small pin-hole in its centre (initial diameter of 0.25 mm). To generate high voltage and to create the discharge, a non-pulsed DC high

voltage source is used. To ensure homogeneous conditions in the whole volume of the liquid, a mechanical mixing system is used. Details of the reactor construction can be found in [6].

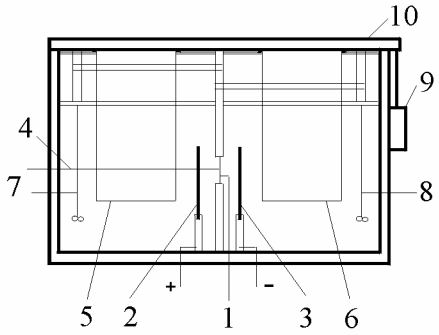

FIGURE 1. A scheme of the discharge reactor: 1 – dielectric diaphragm, 2 – anode, 3 – cathode, 4 – quartz optical fibre, 5, 6 – cooling boxes, 7, 8 – stirrers, 9 – safety switch, 10 – cap.

The $NaNO_3$ and KNO_3 salts were used as the electrolytes. They were solved in the demineralized water to obtain the initial conductivity in the range of 150–850 $\mu S \cdot cm^{-1}$.

The destruction was studied using water solutions of selected organic dyes (Direct Blue 106 and Solvent Yellow 94). As the organic dyes are not electrolytes we have to add a specific amount of the NaCl electrolyte to obtain the defined conductivity of the solution, optimal for the stable discharge operating. Organic dyes and NaCl were solved in the demineralized water to obtain the initial conductivity, again in the range of 150–850 $\mu S \cdot cm^{-1}$.

At these conditions, the plasma is created in a relatively small volume of a few mm^3 around the pin-hole. Due to this fact, one end of the quartz optical fibre (thickness of 0.7 mm) was installed at the distance of 5 mm from the diaphragm. The other end of this fibre was connected by an optical cable to the spectrometer Jobin Yvon Triax 550 with a CCD detector. The spectra were recorded for each measured element separately: for O emission spectrum in the range of 770–780 nm and using, for H^{α} emission spectrum in the range of 650–660 nm, for H^{β} spectrum in the range of 480–490 nm and for H^{γ} spectrum in the range of 430–440 nm. The integration time was 1–100 s dependent on the line intensities.

Our diaphragm discharge is not fully stable and it has a quasi-pulsed character [7]. Due to the strong UV radiation and generation of high reactive species as free atoms and OH radicals, the pin-hole is corroded by the discharge. The pin-hole diameter enhances and it also becomes irregular in its shape in the dependence on the discharge power, solution conductivity and other experimental parameters. To eliminate these disturbing effects, we used the integral intensity of OH radical (307.30–308.79 nm) as a normalization constant for the spectral observations.

The OH radical spectrum was used also for the calculation of the discharge rotational temperature. The rotational line intensities from 0-0 transition of the OH (A-X) system (lines J = 5/2, 9/2, 11/2, 3/2) and the constants given by NIST [8] were used for the rotational temperature calculation. The spectra of other species (both atomic and molecular) have not been recorded with sufficient intensity.

3. RESULTS AND DISCUSSION

The initial conductivity of the solution is one of the most important parameters for the discharges in liquids. This parameter was studied for two nitrate salts. Figure 2 shows the evaluation of the emission intensity for the hydrogen atomic line H^{α} as a function of the initial conductivity. It is obvious that the dependences have a more or less linearly

increasing character for both salts and with the same slope. The first point for KNO_3 is probably irregular due to the instability of the discharge. The atomic hydrogen line intensity is about ten times higher then intensity of the oxygen line (see Figures 2, 3). Dependencies of both line intensities on the solution conductivity are more or less the same.

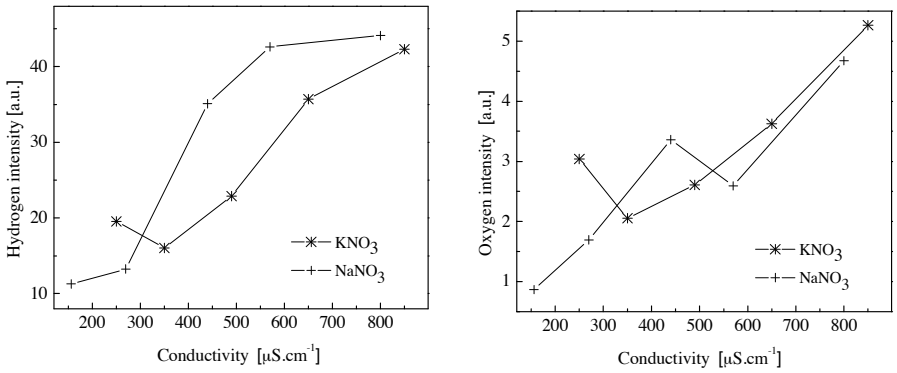

FIGURES 2, 3. Emission intensity dependences of hydrogen and oxygen atoms on the initial conductivity for two different nitrate electrolytes (discharge power of 170 W).

The rotational temperature calculated from the OH radical spectrum slightly depends on the initial solution conductivity, too, as it is demonstrated in Figure 4 for $NaNO_3$ salt. The dependence is not as significant as it was presented above for the atomic line intensities but the temperature slightly increases with the increasing solution conductivity. Similar dependence of rotational temperature on the solution conductivity was obtained also for the other nitrate salt (the rotational temperature for the NaCl salt was in the range 700–800 K).

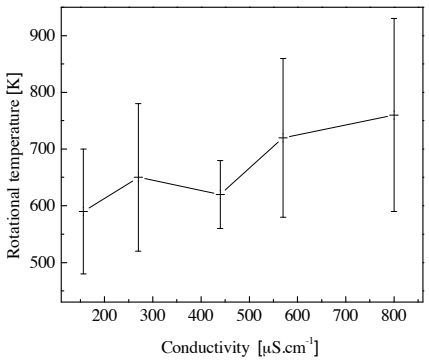

FIGURE 4. Rotational temperature calculated from the OH radical spectrum as a function of the initial conductivity of $NaNO_3$ solution (discharge power of 170 W).

Table 1 summarizes the normalized intensities of the detected hydrogen lines for all used dye solutions. The hydrogen H^{α}, H^{β}, H^{γ} line intensities are strongly dependent on the kind of the organic dye. In the case of H^{α} in Direct Blue 106, it is about one half of the intensity compared to the solution of the Solvent Yellow 94. The hydrogen H^{β} intensity is also dependent on the organic dye and this dependence is more or less the same for both organic dyes. In the last column of Table 1, the rotational temperatures are added. This discharge parameter does not show any significant dependence on the used organic dyes and its value is approximately 1400 K.

TABLE 1. The comparison of the normalised atomic line intensities of observed elements and the rotational temperature for different organic dyes (electrolyte: NaCl – the concentration of 4 mM, experimental conditions: solution initial conductivity 300 $\mu S \cdot cm^{-1}$, discharge current 110 mA, discharge power of 170 W).

	Emission intensity [a.u.]			**Rotational temperature [K]**
	H^{α}	H^{β}	H^{γ}	
Direct Blue 106	2610	680	50	1490 ± 280
Solvent Yellow 94	1400	230	20	1400 ± 140

4. CONCLUSIONS

This work is focused on the optical emission spectroscopy observations of the DC non-pulsed diaphragm discharge in various water solutions of organic dyes and alkaline electrolytes. This effect together with the small discharge volume significantly complicates the comparison of the optical emission spectra among different experiments (the spectra normalization to the integral OH intensity is applied to eliminate disturbing effects).

We studied intensities of detected hydrogen lines for all used dye solutions. The hydrogen H^{α}, H^{β}, H^{γ} line intensities are strongly dependent on the kind of the organic dye. The atomic line intensities of hydrogen and oxygen increase with the increasing conductivity in nitrate salt electrolytes. The rotational temperature calculated from the OH radical spectrum slightly increases with the increasing initial solution conductivity and it is dependent on the inorganic salt kind. In the case NaCl (with organic dyes), the rotational temperature is about 1440 K, but in the case of $NaNO_3$ the rotational temperature about 700 K.

ACKNOWLEDGEMENTS

This work was supported by the Czech Science Foundation, contract No. 202/03/H162.

REFERENCES

[1] Joshi, A.A., Locke, B.R., Arce, P., Finney, W.C. (1995), J. Hazard Mater., 41, 3.
[2] Šunka, P., Babický, V., Člupek, M., Lukeš, P., Šimek, M., Schmidt, J., Černák, M. (1999), Plasma Source Sci. Tech., 8, 258.
[3] Lukeš, P., Člupek, M., Babický, V., et al. (2005), Generarion of ozone by pulsed corona discharge over water surface in hybrid gas-liquid electrical discharge reactor, J. Phys. D-Appl. Phys. 38 (3), 409-416.
[4] Lukeš, P., Člupek, M., Babický, V., et al. (2003), Acta Phys. Slovaca 53, 423.
[5] Lukeš, P. (2001), Water treatment by pulsed streamer corona discharge, Ph.D. Thesis, Institute of Plasma Physics, Prague.
[6] Stará, Z. (2006), Study of chemical processes in electrical discharges in liquids, Ph.D. Thesis, Brno University of Technology, Brno.
[7] Stará, Z., Krčma, F. (2005), Acta Phys. Slovaca 55, 515.
[8] Talrose, V., Yermakov, A.N., Usov, A.A., et al., UV/Visible Spectra. In. Linstrom, P.J., W.G. Mallard, NIST Chemistry WebBook, (on-line).

Acoustic Spectra Characteristics of Micro Discharge

Toshiyuki Nakamiya[1], Daiki Sasahara[2], Kenji Ebihara[3], Tomoaki Ikegami[3] and Ryoichi Tuda[1]

[1]*Department of Information science,*
Kyushu Tokai University,
9-1-1 Toroku, Kumamoto 862-8652, JAPAN
[2]*Power Device Division, Semiconductor Group,*
Mitsubishi Electric Company,
1-1-1 Imajyuku higashi, Fukuoka, 819-0192, JAPAN
[3]*Graduate School of Science and Technology,*
Kumamoto University,
2-39-1 Kurokami, Kumamoto 860-0082, JAPAN

ABSTRACT. When the high voltage (5kV, f=10kHz) is applied to the mesh type electrode, the discharge current flows and the sound signal are generated. The current, voltage waveforms of micro discharge and the sound signal detected by the condenser microphone are stored in the memory recorder. Continuous Wavelet Transform (CWT) is applied to discriminate the sound signal of the micro discharge and the dominant frequency components are studied. CWT result of sound signal shows that the dominant frequency components appear over 20kHz. In addition, the energy distribution of acoustic spectra is examined, when the frequency of power supply is increased from 10kHz to 30kHz with applied voltage of 5kV.

1. INTRODUCTION

The micro discharge is observed between electrodes, when the ozone is generated by the dielectric barrier discharge (DBD). Physics of DBD is based on the initial avalanche-to-streamer transition that is followed by the formation of micro discharge and their arrangement in the specific pattern[1]. It was shown recently that DBD can exhibit two major discharge modes: filamentary mode and homogeneous or glow mode. The filamentary mode is a topic for active investigations in the past several years. Most industrial DBD applications utilize filamentary mode. However, for a homogeneous treatment of surfaces, or for the deposition of thin films, the glow discharge mode has obvious advantages over the filamentary mode[2]. Unfortunately the DBD glow discharge is very unstable and prone to spontaneous transition to more stable filamentary mode. The electric discharge sound may be considered the utilization of the monitor of the DBD glow discharge, the effective ozone generation. We also proposed the procedure to detect the tracking phenomenon using the sound signal due to the micro discharge[3]. The fundamental experiments are carried to discriminate the dominant frequency components of the sound signal generated by the micro discharge. In addition, the energy distribution of the sound signal over the time-frequency plane is examined using CWT. CWT has better accuracy and precision than those obtained with the other time-frequency analysis method such as short-time Fourier transform.

[1]Electronic address: nakamiya@ktmail.ktokai-u.ac.jp

2. EXPERIMENTAL PROCEDURES

The DBD were generated using the electrode in order to understand the fundamental relationship between the micro discharge and the acoustic properties. The mesh type electrode was prepared to cause the DBD. A lot of holes (20μm diameters) had been opened in the mesh type electrode. The cover glass (22mm x 4mm, Thickness: 0.15mm) was held between mesh electrode (30mm x 50mm) of the 2 sheets, and the gap length of mesh type electrode was 0.8mm. One of the electrode was connected to the high voltage terminal through the resistance 200kΩ. Other terminal was grounded. The high voltage (4～6kV:peak to peak voltage, 10～30kHz) was produced by the impulse high frequency and high voltage power supply. The sound signal was generated by the discharge of the electrode. The current, voltage waveforms of micro discharge and the acoustic signal detected by the condenser microphone were stored in the memory Hi-coder 8855(Hioki). The sampling frequency was 1 MHz and the measurement time was 1 second. Data analysis was performed using MATLAB with the Wavelet toolbox (The Mathworks, Inc.).

3. CONTINUOUS WAVELET TRANSFORM (CWT)

The wavelet transform converts a signal from time domain to the time-scale domain. The wavelet transform of a continuous signal is defined at time *b* and scale *a* as:

$$\hat{f}(a,b)=\frac{1}{\sqrt{a}}\int_{-\infty}^{\infty}\frac{1}{2\sqrt{\pi}\sigma}e^{-\frac{(t-b)^2}{\sigma^2 a^2}}\cos\left(\frac{t-b}{a}\right)f(t)dt \qquad (1)$$

where the sound signal $f(t)$ is transformed by the mother wavelet. The real part of gabor function is used as a mother wavelet (σ=8). The squared magnitude of the CWT, $\left|\hat{f}(a,b)\right|^2$ is called scalogram and can be used to obtained the energy distribution of the sound signal over the entire time-scale plane. The time-scale expression can be transformed to an equivalent time- frequency expression[4],[5].

4. RESULTS AND DISCUSSION

4.1 Atmospheric pressure

The voltage was applied to the mesh type electrode in atmospheric pressure. Figure 1 (a) shows the voltage and the current waveforms with applied voltage of 5kV and the frequency of 10kHz. The discharge current flows at 1.5μs and 9.2μs. The maximum current value is

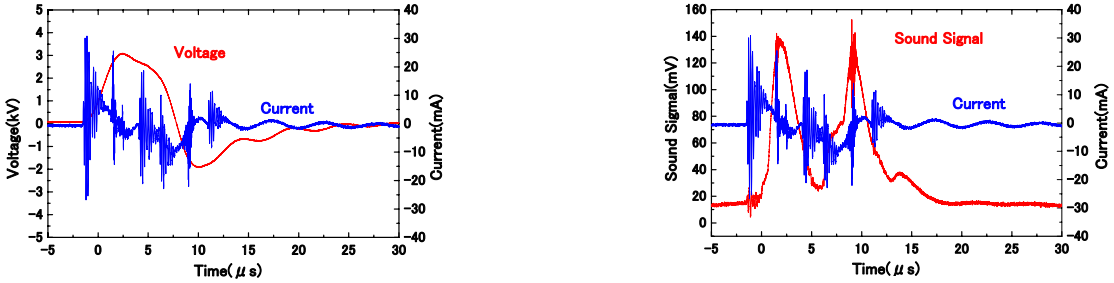

(a) (b)

FIGURE 1. Voltage and current waveforms, and (b) Sound signal and Current waveforms with applied voltage of 5kV(f=10kHz).

30mA and the current waveform is pulse-like. The luminescence has begun at the edge of the mesh type electrode. Light is not emitted from the whole electrode. The measurement result of sound and current waveforms are shown in Fig.1 (b). The sound signal is observed in the form superimposed on the drift signal, and the maximum value of the amplitude is 67mV.

Figure 2 shows the analyzing result of the acoustic signal by CWT with applied voltage of 5kV to the electrode. The frequency components over 20kHz appear at 1.5μs and 9.1μs. These values by CWT are fairly good agreement with the time of discharge current by DBD. The dominant frequency components at the time of 1.5μs contain from 20kHz to 108kHz. The sound signal at the time of 9.1μs has the wide frequency components from 20kHz to 150kHz. This figure shows the five peaks and the maximum peak appear at 9.1μs and 35kHz of the time-frequency plane.

The frequency of high voltage power supply increases to 30kHz and the applied voltage keeps the value of 5kV. The CWT scalogram of sound signal is shown in Fig.3. The frequency components over 20kHz appear at 2.5μs and 8.6μs. At the time of 2.5μs, the dominant

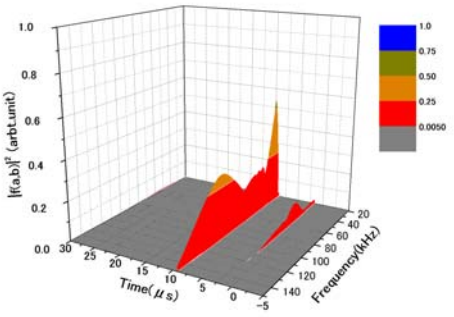

FIGURE 2. Time-frequency representation of sound signal using CWT scalogram with applied voltage of 5kV(f=10kHz).

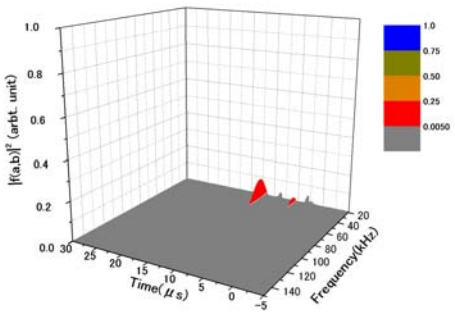

FIGURE 3. Time-frequency representation of sound signal using CWT scalogram with applied voltage of 5kV(f=30kHz).

frequency components are contained between 20kHz and 30kHz at 2.5μs. The dominant frequency components are contained between 20kHz and 45kHz at 8.6μs. The scalogram shows the energy distribution of the acoustic spectra over the time-frequency plane. The peak value of the sound energy of 30kHz(frequency of applied voltage) becomes smaller than that of 10kHz.

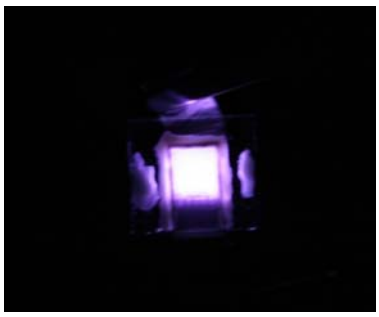

FIGURE 4. Photograph of DBD by the mesh type electrode with applied voltage of 5kV(f=30kHz). Light is uniformly emitted from the whole electrode.

Figure 4 shows the photograph of the light emission from the mesh type electrode with applied voltage of 5kV(f=30kHz). The whole electrode uniformly emits the light. When the frequency of power supply increases from 10kHz to 30kHz with the applied voltage of 5kV, the peak values of the sound energy decrease and the brightness of the light emission increase.

4.2 Ar atmosphere

The high voltage of 4kV is applied to the mesh type electrode in Argon (Ar) atmosphere. The frequency of the impulse power supply is 10kHz. Figure 5 shows the time-frequency representation of sound signal. The frequency components over 30kHz appear between 0.86μs and 1.9μs. The sound signal at the time of 1.4μs has the wide frequency components from 35kHz over 85kHz. The peak value of the sound energy is shown at 1.4μs and 55kHz of the time-frequency plane.

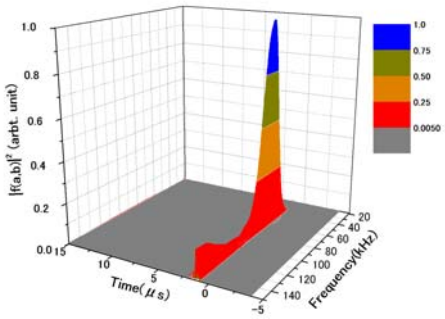

FIGURE 5. Time-frequency representation of sound signal using CWT scalogram with applied voltage of 4kV(f=10kHz, Ar atmosphere).

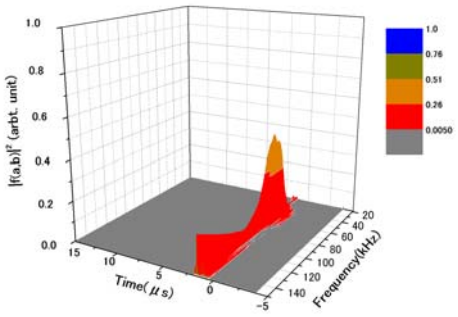

FIGURE 6. Time-frequency representation of sound signal using CWT scalogram of with applied voltage of 5kV(f=10kHz, Ar atmosphere).

When the applied voltage of the electrode increase to the value of 5kV, time-frequency representation of sound signal is shown in Fig.6. The frequency components over 20kHz appear between 0.95μs and 2.1μs. The dominant frequency components are contained between 45kHz and 85kHz at 1μs. The peak value of the sound energy at the case of 4kV is smaller than that of 5kV. The light emission by DBD is uniformly emitted from the whole electrode. When the applied voltage to the electrode increase from 4kV to 5kV at the power supply frequency of 10kHz, the peak values of the sound energy decrease and the brightness of the light emission increase.

5. CONCLUSIONS

The experiments are carried to examine the micro discharges using the acoustic spectra. CWT is applied to discriminate the sound signal of the micro discharge and the dominant frequency components are studied. The following results are obtained.

1. At the case of high voltage (5kV, f=10kHz) is applied to the mesh type electrode, the discharge current flow at 1.5μs and 9.2μs. CWT scalogram of sound signal shows that the frequency components over 20kHz appear at 1.5μs and 9.1μs.
2. When the frequency of power supply increases from 10kHz to 30kHz with the applied voltage of 5kV, the peak values of the sound energy decrease and the light emission becomes more brightness.

REFERENCES

[1] Chirokov A., Gutsol A., Fridman A., Sieber K. D., Grace J. M., Robinson K. S. (2004). Analysis of two-dimensional microdischarge distribution in dielectric-barrier discharges. *Plasma Sources Sci. Technol.*, 13, 623-635.

[2] Martin S., Massines F., Gherardi N., Jimenez C. (2004). Atmospheric pressure PE-CVD of silicon based coatings using a glow dielectric barrier discharge. *Surface and coatings Technology*, 177-178, 693-698.

[3] Nakamiya T.,Tanaka T., Ebihara K., Ikegami T. and Tsuda R. (2004)Acoustic Signal Analysis in the Partial Discharge by Short Time Fourier Transformation. *The Papers of Technical Meeting on Plasma Science and Technology, IEE Japan,* PST-04-80, 45-49.

[4] Charles K. C. (1992). *An Introduction to Wavelets*, ACADEMIC PRESS, Orland, USA.

[5] Abry P. (1997) *Ondelettes et turbulence. Multirésolutions, algorithmes de décomposition, invariance d'échelles*, Diderot Editeur, Paris.

THE ANALYSIS OF THE INFLUENCE OF ESSENTIAL PARAMETERS ON OZONE ELECTROSYNTHESIS COURSE IN SIMULATING APPROACH

K. Jaholkowski[1], J. Ozonek[2] and S. Fijalkowski[3]

[1] *Department of Electrical Machines, Lublin University of Technology, POLAND*
[2] *Institute of Environmental Protection Engineering, Lublin University of Technology, POLAND*
[3] *Department of Technical Thermodynamics, Lublin University of Technology, POLAND*

ABSTRACT The influence of basic electrical and geometrical parameters in simulating investigations on electric parameters of discharge set-up was presented. Moreover the influence of discharge gap, thickness and kind of dielectric and intensity of electric field was analyzed

1. INTRODUCTION

Nowadays, for the protection of the environment, ozone is produced in industrial plasmachemical reactors (being the main unit of production lines) during electrical discharges in the substrate gas, as a direct result of electric energy conversion in a physico-chemical transformation.

In this context the ozonizer should be treated – in respect of electricity – as a system of capacitances connected in series, namely the capacitance of the dielectric layer and the capacitance of the discharge gap. Two characteristic operation phases may be distinguished in this system's operation: a phase when the source of voltage is connected to the ozonizer's system, but in the area of the gap no microcanals appear – the system reveals the features of capacitances connected in series, and the second phase, which starts at the moment of the appearance of first discharge microcanals in the gap, then the system's features partly change - the electrical features of the gap partly change while the dielectric capacitance remains [1– 3].

Model investigations of the first phase, taking into account the property of dielectric, the size of discharge gap and the intensity of electric field in work were presented.

2. THE BASIC PARAMETERS OF THE OZONE ELECTROSYNTHESIS PROCESS

Barrier discharges in gas during course of ozone synthesis are characteristic in that during the occurrence discharge temperature of gas little differs from the temperature of surroundings.

With regard to electrodes configuration of the ozonizer, barrier discharges can be divided into volume, built-up from many of microchannels (fig. 1a), surface discharge, in this case discharge microchannels create on the surface of dielectric (fig. 1b) and with packing in discharge gap (fig. 1c) [4].

The main parameters of process are: electric parameters - frequency of the alternating current f, supplied voltage U, active power in the discharges zone P; physico-geometrical parameters - electric permeability of dielectric ε_d, capacity of dielectric C_d, and capacity of

discharge gap C_g, and also the parameters of ozone synthesis process - the kind of the substrate gas (oxygen, air), the speed of gas flow w_{av}, temperature of reaction environment T_p.

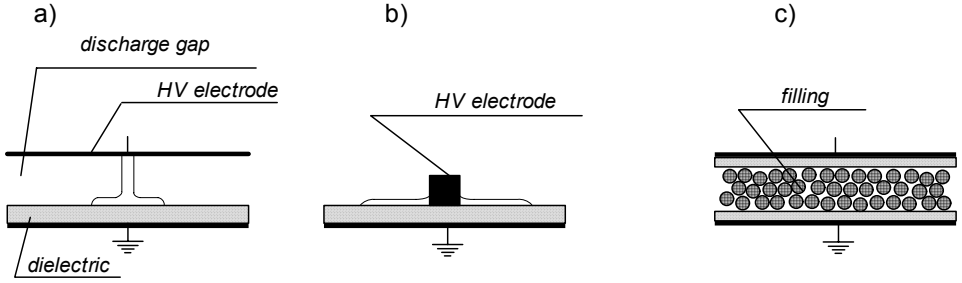

FIG. 1. Configuration set-up of electrodes in barrier discharge
a) volume, b) surface, c) with packing

The presented parameters concern initiating and sustains ozone synthesis course. They influence on level of driving energy of process.

Essential parameter characterizing barrier discharge is the quantity of electric charge transferred during discharge $\dot{Q}$. The efficiency of electrochemical process is proportional to this quantity.

In the case of barrier discharges among two metal electrodes are placed two dielectrics, one is dielectric solid, the other flowing gas. Such system keeps the property of condenser in the range of voltage and the electric field strength till to the moment of crossing of ignition voltage. After exceeding the ignition voltage the discharge gap alters its electric properties, it becomes the area of discharge and the resistance character with characteristic non - linear profile.

The shape of electrodes in discharge system is responsible for electric field line. In the case of regular shape and even space the electric field has the character of homogeneous field. The average value of field strength can be definite:

$$E_0 = \frac{U}{d} \tag{1}$$

where: d -distance between electrodes, U - applied voltage to electrodes .

In the case of the system with non-heterogeneous field the value of field strength is determined by value E_0 and the coefficient of inhomogeneity of electric field. The value of the coefficient decides about maximum intensity of electric field and the value of ignition voltage. The quantity of coefficient inhomogeneity field is connected with intensity of electric field potential through scalar potential of inter-electrode space:

$$E_0 = -\,grad\,\varphi \quad \text{; where: } \varphi \text{ - field potential} \tag{2}$$

The problem is to obtain the solution of Poisson equation:

$$\nabla^2 \varphi = \rho / \varepsilon \tag{3}$$

where: the ρ - the volumetric density of charge, ε - the dielectric permeability

In the case of the absence of spatial charge this equation becomes to Laplace equation in the form:

$$\nabla^2 \varphi = 0 \tag{4}$$

The solution to equation (4) can be obtained in several ways: analytic, numeric, graphic or experimental. One of the numeric method is a finite element method, depending on division of solution area on finished number of geometrical units elements of determined properties and conferment this units the definite physical properties (approximation distribution φ).

3. SIMULATING INVESTIGATIONS

The numerical analysis (according to the finite element method) was carried out using the QuickField program, for the following assumption: the discharge geometry, kind of dielectric and the voltage of breakdown. The investigation area was divided into triangular elements and the condensation of mesh points was chosen in dependence on prediction concentration of field line (fig. 2).

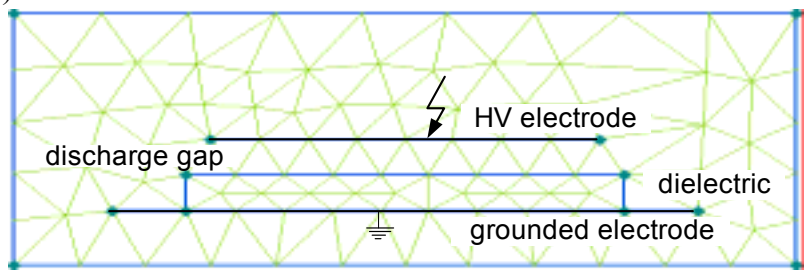

FIGURE 2. View of simulation area of volume discharge set-up of with generated mesh of finite element method

The obtained results of equipotential lines distribution of volume set-up discharge in tested area are presented in fig. 3.

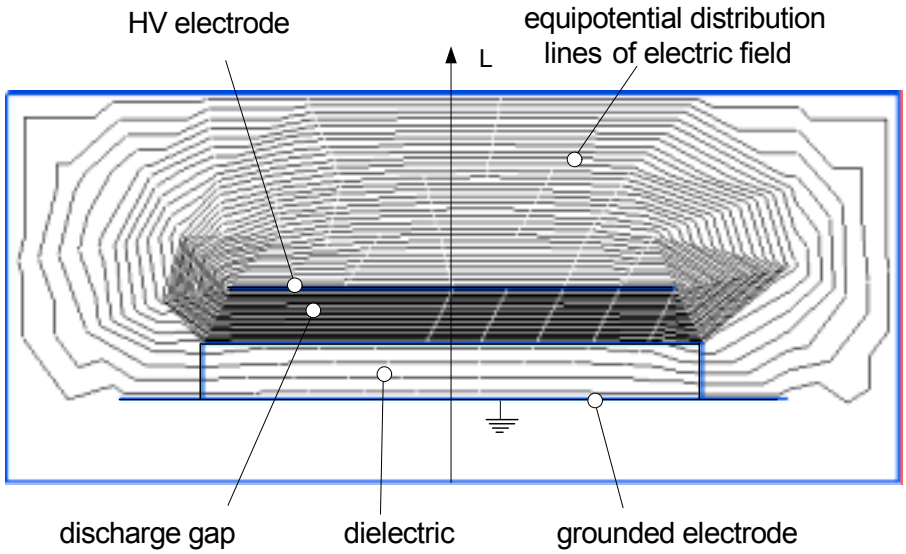

FIGURE 3. View of equipotential distribution lines of volume discharge set-up

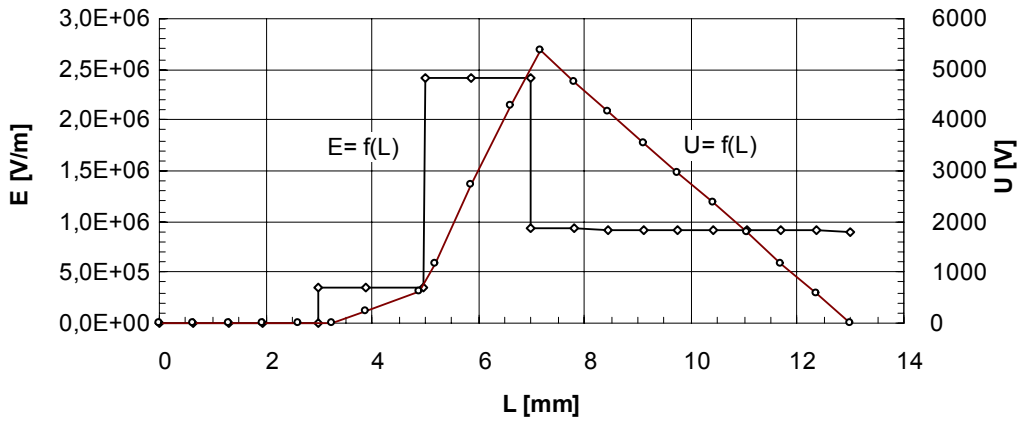

FIGURE 4. Distribution of electric field intensity and the potential along axis of barrier discharge symmetry for discharge gap d = 2 mm and the thickness of dielectric g = 2 mm

In fig. 4 the distribution of electric field intensity is shown. Fig. 5 shows the distribution of electric field tension along axis of symmetry of configuration the barrier discharge in dependence of discharge gap.

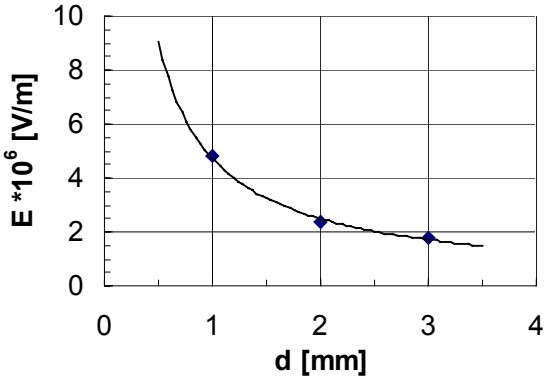

FIGURE 5. Distribution of electric field intensity along axis of symmetry of configuration the barrier discharge in dependence from size of discharge gap for dielectric thickness g = 1 mm

CONCLUSIONS

The conducted simulating investigation allows coming to the following conclusions:

- in discharge gap the density of equipotential lines is large, which testifies about considerable difference of potentials among dielectric and the high-voltage electrode, intensity increases near the edge of high-voltage electrode with simultaneous change of the course of line the φ = const,
- in homogeneous field the value of intensity of electric field in dielectric is constancy and dependent from his dielectric permeability, in the system arranged in series the intensity of field in individual layers of dielectric is inversely proportional to dielectric permeability
- in parallel arrangement of electrodes on value the intensity of electric field influences the size of discharge gap and the kind of dielectric, during the growth of discharge gap the intensity of field diminishes.

Having the possibility of suitable configuration of the discharge system it is possible to influence the parameters connected with construction of ozone generator as well as electric parameters of its work. The obtained results can be useful for project of ozonizer configuration discharge gap.

REFERENCES

[1] Kogelschatz U., Eliasson B., (1995). *Ozone generation and applications*, in: Handbook of Electrostatic Processes, ed. By J.S. Chang, A.J. Kelly, J.M., Crowley, Marcel Dekker, Inc, 581-605.

[2] Ozonek J., Wronski M., Pollo I., (2000). Ozone synthesis – mechanism and technology, *Polish Journal of Chemical Technology*, 2, 19-24.

[3] Ozonek J., Pollo I., (1998). *Ozone synthesis in ozonizers with multilayer electrodes*, Pol. J. Appl. Chem., 42, 113-118.

[4] Jaholkowski K., Ozonek J., (2005). Evaluation of electric parameters characteristic for plasmachemical reactors used in environmental protection, *Polish Journal of Applied Chemistry*, 49, 123-130.

FIVE LIMB TRANSFORMER AS A POWER SYSTEM OF ARC DISCHARGE REACTOR

H. D. Stryczewska, G. Komarzyniec and T. Janowski

Institute of Electrical Engineering and Electrotechnologies,
Faculty of Electrical Engineering and Computer Science, Lublin University of Technology,
Lublin, 20-618, POLAND

ABSTRACT. Arc discharge plasma reactors require power supply systems that permit the arc ignition and then perform cyclic and non-equilibrium operation of the discharge after ignition while presenting stable and reliable operation. Transformers of special construction are the basic elements of all power systems of arc discharge plasma reactors. Paper presents the 5-limb transformer as a power supply system for the arc plasma reactor and results of its laboratory investigation. Investigations showed that voltage induced in the external columns of the 5-limb transformer could be used for arc discharge ignition.

1. INTRODUCTION

The plasma reactors with arc discharges at non-equilibrium state, like gliding arc, are especially suitable for purification of big volume of exhaust gases emitted to the atmosphere during various technological processes. To increase their capability, they can be connected in series or parallel to the gas flow and can operate at three-phase power system.

Power systems of arc discharge reactor with special transformers due to their magnetic circuit nonlinearity can integrate in one device all basic functions required by arc plasma reactor, i.e. preliminary ionization of the inter-electrode zone, ignition and discharge maintaining during the plasma reactor operation cycle as well as limiting the short circuit current after arc extinguish. Gliding arc discharge reactors can be constructed as two- or multi- electrode systems. Figure 1a presents the construction of three-electrode reactor with additional ignition electrode. Other possible electrodes' configurations are given in Figure 1b.

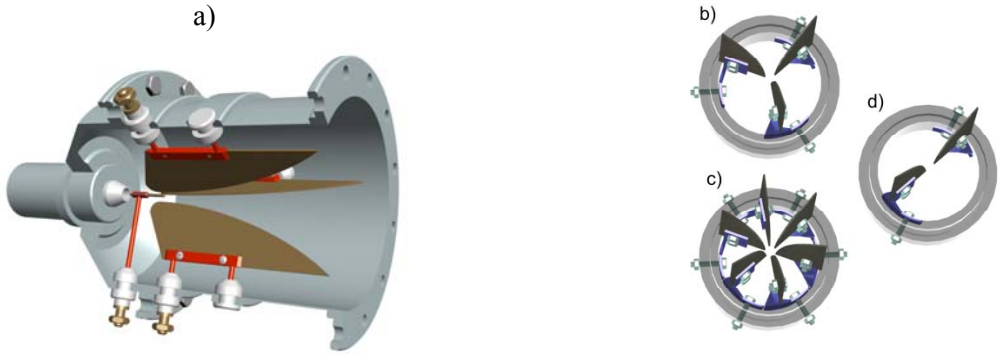

Figure. 1. Plasma reactor with gliding arc discharge (a), different electrode arrangements (b, c, d)

In the three electrode configuration flat, knife shaped, working electrodes are arranged every 120 degrees in the plasma reactor discharge chamber. This plasma reactor requires

Electronic address: h.stryczewska@pollub.pl

three-phase system power supply system. To assure necessary non-thermal plasma conditions, working electrodes should be energized with voltage of about 1-2 kV and current value lower than 10 A. Such values of voltage and current are not typical for arc discharge and the produced plasma is at non-equilibrium state similar to glow discharge rather than to arc discharge plasma. Moreover, the interelectrode voltage lower than 2 kV, at the conditions of high gas flow velocity (5-20 m/s), is not sufficient for discharge ignition and therefore it is necessary to introduce the additional ignition electrode to the zone in which the discharge starts to move through electrodes.

Typical voltage –current characteristic of the gliding arc discharge, presented in Figure 2, shows that voltage required for the discharge ignition (10,5 kV) is more than sixth times greater than for the discharge sustaining (1,5 kV) at nominal current (2 A) and explains how the power supply system characteristics should be constructed to fulfill the plasma reactor requirements.

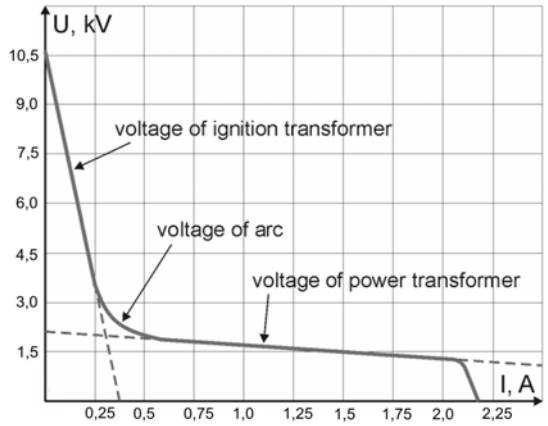

Figure 2. Current-voltage characteristics

The discharge ignition starts between ignition electrode and the working one. At the moment of ignition the simultaneous quick drop of ignitron electrode voltage occurs, what means that the current-voltage characteristic of the ignition transformer should be very soft.

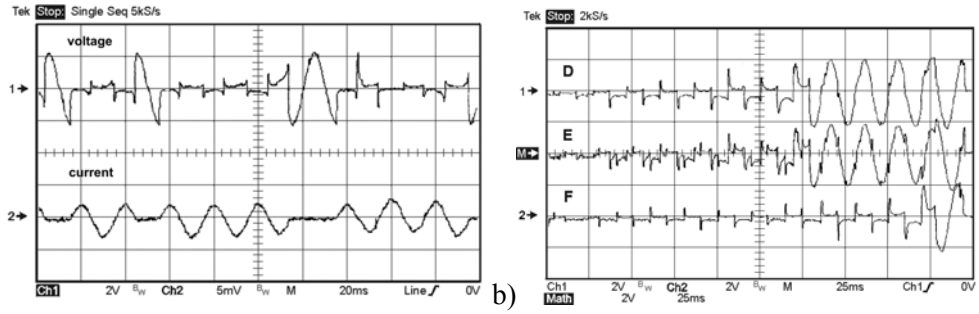

Figure 3. Inter-electrode voltage courses of the gliding discharge in two (a), and triple-electrode, (b), plasma reactor

Developing arc discharge after ignition is maintained by energy provided from working electrodes operating at the much lower than ignition voltage. Therefore, the operation cycle of plasma reactor can be divided into three phases: (I) the discharge ignition, (II) discharge development (most important phase of plasma reactor work) and (III) phase of discharge extinction. All electrodes (working and ignition) are participating in the phase of discharge ignition while during the discharge development only working electrodes take part in the reactor operation. Working plasma reactor with gliding arc discharge is strongly non-linear resistive energy receiver with discharge resistance being the function of time, temperature and

velocity of the plasma gas. Moreover, the multi-electrode reactor loads power supply asymmetrically. Figure 3 presents voltage and current courses representative for two- and three-electrode configuration of the gliding arc discharge reactor. Usually, current has close to sine form, while interelectrode voltage is considerably distorted.

2. POWER SUPPLY SYSTEM WITH 5-LIMB TRANSFORMER

Power supply systems of arc discharge reactors with specially constructed transformers that utilize the nonlinear *B-H* characteristic of their magnetic cores, are very simple, reliable and low cost, specially suitable for industrial application. Investigated 5-limb transformer's core is built of four wound and cut magnetic cores presented in Figure 4. Primary windings of the transformer are put on the three internal columns. There are connected in the star with zero wire and linked to the three-phase four-wired system. On the same internal columns the secondary windings are put and connected in star. The terminals of secondary windings are connected to working electrodes of plasma reactor. On the external columns of the transformer there are additional windings placed. The windings are connected together in series. Their terminals are connected to the ignition electrode and to the neutral point of winding star of transformer's secondary windings (Figure 4 b). The transformer working point is chosen on the linear part of magnetizing characteristics below the saturation point of the *B-H* curve. The magnetizing transformer current contains higher odd harmonics, i.e. 3, 5, 7, 9, ..., which are essential to generate sinusoidal magnetic flux in the transformer core.

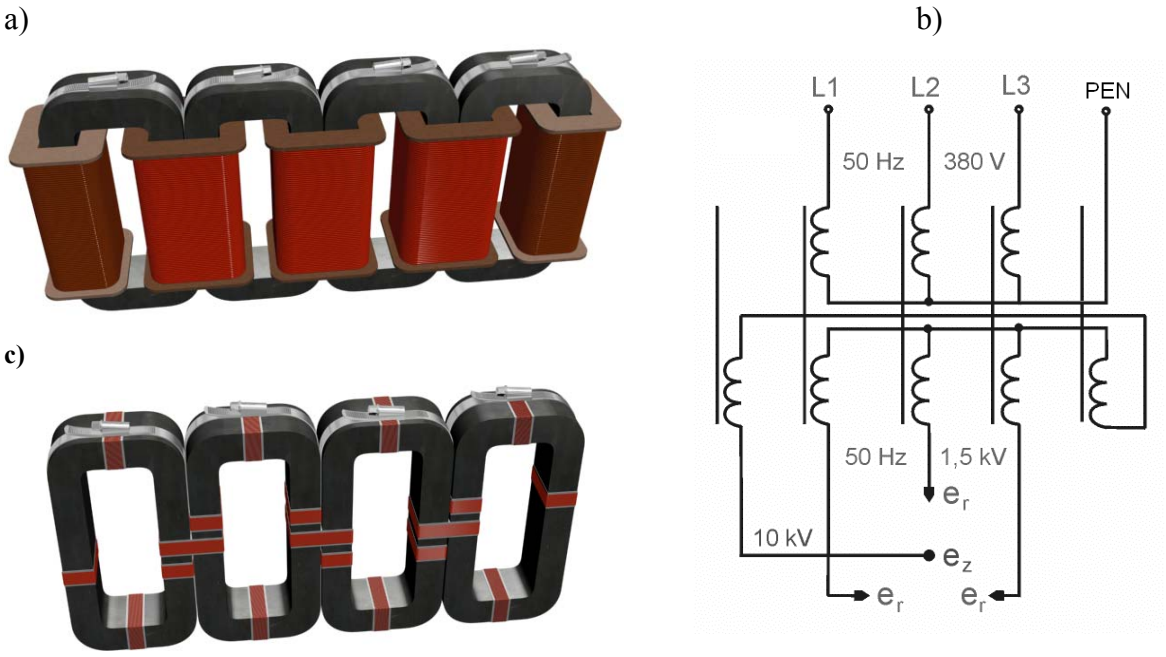

Figure 4. The 5-limb transformer core (a), windings connection (b), and measuring coils arrangement (c)

2.1. Results of measurements

To investigate the magnetic flux distribution in the 5-limb core under three-phase sinusoidal magnetization and for no-load, short-circuit and load conditions, there are measuring coils put on yokes and columns of the model of magnetic core arranged like it is presented in Figure 4c. Figure 5a shows voltage courses induced under sine excitation in the internal columns 1, 2 and 3, of the investigated transformer for no-load conditions, while voltages induced in the external yokes of the core (measuring coils 4, 5, 6 and 7) are presented in Figure 5b. Voltages 1, 2 and 3 are sinusoidal, they form three-phase system with

value insufficient for discharge ignition but able to support the discharge elongating between operating electrodes. Voltages 4 and 7, measured on the external yokes, are distorted by odd harmonics, mainly third and fifth. As it was mentioned, the voltage –current characteristic of ignition windings (4, 7) put on the yokes should be soft enough to limit the current after ignition the discharge. The softness of ignition characteristic can be adjusted by introducing air-gaps into the yokes of 5-limb core.

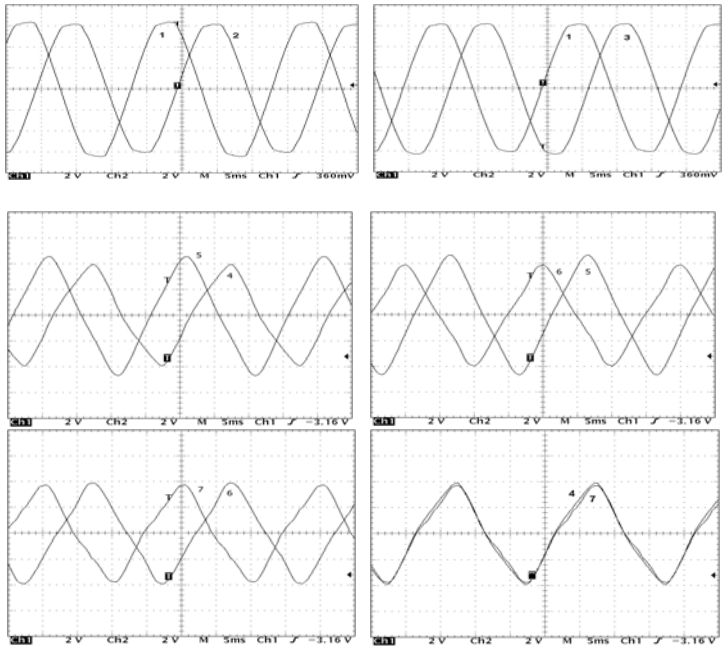

Figure 5. The courses of voltages induced in the measuring windings 1, 2, 3 (a) and 4, 5, 6 and 7(b)

Depending on number of primary, secondary and ignition windings, the 5-limb transformer structure enables to design power supply system for multielectrode and multistage arc plasma reactors.

3. CONCLUSIONS

Power systems with 5-limb transformers can fulfill requirements of arc discharge plasma reactors, both during the ignition phase and the discharge development. The important issue is to obtain the soft current-voltage characteristics of the ignition windings put on the external columns of 5-limb transformer that can be achieve by introducing air-gap into the yokes of the transformer core. Thanks to proposed solution, the operating windings can be designed for several times lower voltage than ignition and transformer's core dimensions can be considerably reduced. Further benefits of this solution are the tightness and simplicity of construction and the possibility to power multi-electrode and multi-stage arc plasma reactor.

REFERENCES

[1] H. Lesueur, A. Czernichowski, J. Chapelle, *French Patent* 2639172.
[2] Stryczewska H.D. (2000), *Polish Patent* 317110,
[3] G. Komarzyniec, H. D. Stryczewska, (2003), Transformer Supply System of Plasma Reactor, *ELMECO'4* Conference, Nałęczów, Poland

EFFICIENT USE OF PLASMA OZONISERS IN THE WATER-BASED ABSORPTION OF NO_X

J. Jaroszyńska-Wolińska

Department of Civil Engineering , Lublin University of Technology,
Nadbystrzycka 40, 20-618 Lublin, Poland,
e-mail: jwtchem@akropolis.pol.lublin.pl

ABSTRACT. The paper investigates a method to improve the efficiency of NO_x removal from a gas stream through oxidation and water absorbtion. Oxidation is carried out by applying the output from a conventional dielectric barrier discharge industrial ozoniser type and process efficiency is characterized by the ratio (moles of NO_x removed) / (moles of O_3 consumed). Experimental data is based upon ceramic bead packed absorbtion reactors and simulated gas streams containing NO mixed with either N_2 or air. It was found that if a two-stage process is used in which oxygen in air is applied as a first stage oxidiser and the ozone/oxygen mix from the commercial ozoniser is applied as a second stage, the speed and overall process efficiency increase significantly despite the far slower reaction rate of oxygen in comparison with ozone.

1. INTRODUCTION

The problem of removal of the serious pollutant NO_x from industrial flue gases is environmentally important. However, it is commercially difficult because of the cost of current removal methods and the wide variety of emission sources. These problems motivate development of an energy and chemicals efficient, widely applicable, end-of–pipe exhaust NO_x abatement technology. Ozone produced by industrial plasma systems (ozonisers) coupled with simple water and oxygen based processing steps, appear to offer technically feasible and commercially interesting solutions.

The work proposes a scheme for the removal of nitrogen oxide from a polluted gas stream. Such scheme comprises a two-stage oxidation process coupled with water absorbtion over both stages. The two-stage oxidation comprises, firstly, admixture of the NO_x exhaust with oxygen and, secondly, mixing of the resulting gas stream with an ozone/oxygen gas mix of the type generated by conventional industrial dielectric barrier discharge plasma ozonisers. Both stages are done in the presence of liquid water via ceramic bead packed absorbtion columns through which water runs from the top and through which the gas streams are bubbled from the base.

The two-stage oxidation process is shown to significantly enhance overall NO_x removal process efficiency defined by the ratio (moles of NO_x removed from the gas stream by water absorbtion) / (moles of O_3 consumed) over the single stage process where the ozone/oxygen mix output from commercial ozonisers is immediately applied to the polluted gas stream. This increase in process efficiency of ozone usage is believed to be potentially commercially significant in view of the huge volumes of current industrial NO_x gas streams and the cost of ozone generation.

Experimental data is based upon ceramic bead packed absorbtion reactors for which a technological parameter based criterion equation has been previously derived for the experimental conditions [1].

2. EXPERIMENTAL METHODS

Experimentation was undertaken using the apparatus schematically shown in Figure 1. A two-stage reactor comprises two cylinders packed with ceramic beads with water flow running counter to gas flow. NO gas is controllably diluted with nitrogen to replicate typical industrial exhaust gas stream concentrations. Air can be controllably added to the NO/N_2 flow. The gas mixture is fed into the base of a vertical glass cylinder of internal diameter 38 mm packed with hollow rod-shaped ceramic beads of length 8 mm, external diameter 8 mm and wall thickness 1.5 mm. The length of each of the ceramic bead beds is 580 mm.

The gas stream exits the first cylinder at the top and is then fed into the base of a second duplicate vertical cylinder through which it flows to exit at the top, at which point analysis of the gas by spectrophotometric methods is carried out. A stream of ordinary tap water is fed into the top of the first cylinder, spreads over the cylinder cross-section and percolates through the ceramic beads to exit at the base. The water is then fed into the top of the second cylinder to flow in similar fashion down that tube and exits finally at its base. Accordingly, the water flow is at all times counter to the gas flow.

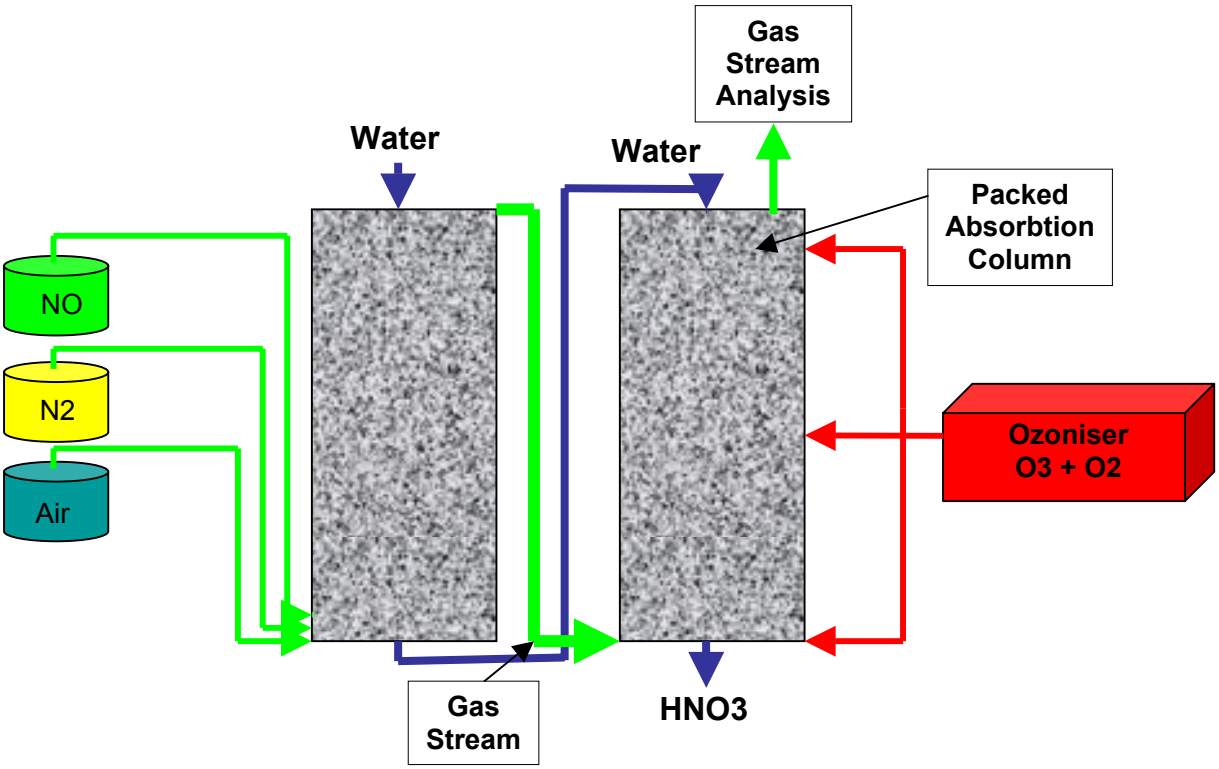

Figure 1. Scheme of NO_x reduction by the application of a two-stage oxidation process

The output from a small scale ozoniser of design similar to that of conventional industrial systems and using ambient air as feedstock gas is fed into the second cylinder at three points along its major axis – the base, midway and 0.10 m from the top. The ozoniser comprises two cylindrical electrodes of different diameter with common major axis, one cylinder sitting inside the other. The inner high voltage electrode is coated with a glass dielectric and a 50 Hz frequency voltage applied across the discharge gap between the inner and outer cylinders. This is the classical dielectric barrier or silent discharge plasma generation configuration and results in plasma being generated from oxygen in the ambient air throughout the region of the discharge gap. Discharge gaps of 1, 1.5 and 2 mm can be set with the applied voltage varying

from 4.0 – 7.5 kV. Such configurations generate a mix of ozone and oxygen with the ozone comprising a few percent only by volume of the system output. The low conversion efficiency of such air driven ozone generation systems motivates the maximisation of process efficiency.

The process of nitrogen oxide oxidation with ozone culminates in the formation of N_2O_5 which is readily absorbed in water generating the industrially useful by-product, nitric acid. The mechanism of NO_x removal by oxidation is complex and not understood. A simple first approximation of the process can be described by the following reactions:

$$NO + O_3 \rightarrow NO_2 + O_2 \quad (1)$$

$$NO_2 + O_3 \rightarrow NO_3 + O_2 \quad (2)$$

$$NO_2 + NO_3 \rightarrow N_2O_5 \quad (3)$$

$$2\,NO_2 + O_3 \rightarrow N_2O_5 + O_2 \quad (4)$$

$$N_2O_5 + H_2O \rightarrow 2\,HNO_3 \quad (5)$$

This rapid process comprises many stages, and the issue is to recognize the scheme of individual reaction mechanisms and to determine their competitiveness. This would constitute the basis of a global model of the process and facilitate determination of optimal conditions for its running.

The percentage of NO removed from the gas stream as a function of the molar ratio of ozone to NO was measured with the concentration of NO (mol/m^3) as a parameter. This was firstly done with only NO and nitrogen in the initial gas stream (Figure 2):

Figure 2. NO Removal rate vs. O_3-to-NO molar ratio (single-stage process)

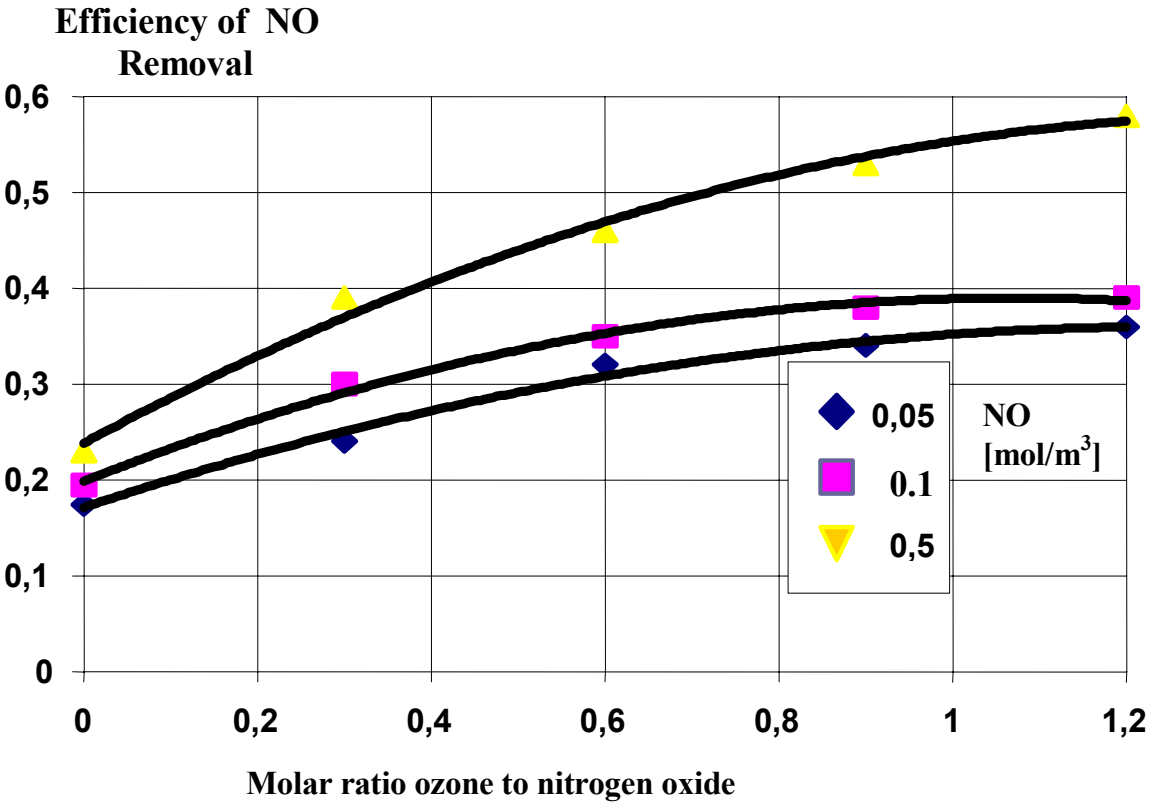

The experiment was then repeated but with air replacing nitrogen in the initial gas stream to deliver the same total flow rate (Figure 3):

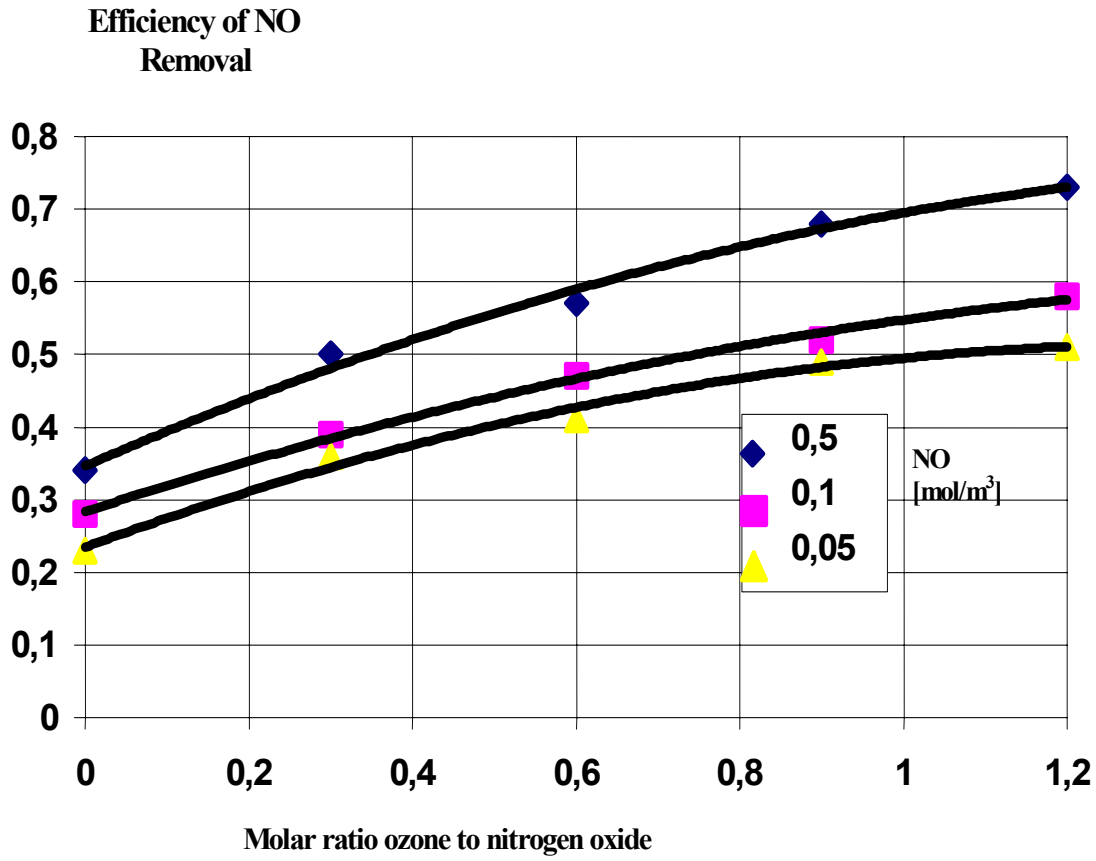

Figure 3. NO Removal rate vs. O_3-to-NO molar ratio (with preliminary oxidation by oxygen in air – two-stage process)

It is seen that the efficiency of the NO removal process defined as (moles of NO_x absorbed by water)/(moles of O_3 consumed) is significantly enhanced by the addition of oxygen in air to the gas stream flowing through the first stage reactor:

NO concentration (mol/m^3)	Maximum increase in NO removal by use of two-stage process
0.05	42%
0.1	53%
0.5	28%

3. DISCUSSION AND CONCLUSIONS

The presented work deals with nitrogen monoxide removal from a gas stream by means of oxidation and absorbtion in liquid water. Oxidation is carried out by application of the oxygen/ozone mix output from the non-thermal equilibrium plasma of a conventional industrial type ozoniser (single-stage process) or, alternatively, by serial application of, firstly, oxygen in air and, secondly, of the ozoniser output (two-stage process). The objective is to investigate parameters that determine process efficiency as defined by the ratio (moles of NO_x removed from the gas stream by water absorbtion) / (moles of O_3 consumed). The two-stage oxidation process is shown to enhance overall NO_x removal process efficiency by 28-53%

over the single stage process where the ozone/oxygen mix output from industrial-style ozonisers is applied alone to the polluted gas steam. This increase in process efficiency of ozone usage is believed to be potentially commercially significant in view of the huge volumes of current industrial NO_x gas streams and the cost of ozone generation.

The paper shows that, although ozone is a highly powerful and commercially attractive oxidiser, very effective in the removal of NO_x, its single stage application to a NO_x contaminated gas stream results in a relatively low and wasteful process efficiency in overall NO_x removal. The application of a preliminary process step whereby oxygen in air is applied to the NO_x gas stream results, despite the vastly slower reaction rate of O_2 relative to O_3, in significantly enhanced overall process efficiency, an apparently surprising result at first glance.

The complete oxidation process chain of NO to N_2O_5 is complex and not understood. However, the paper suggests that if a typical ozone/oxygen mix output from commercial ozonisers containing only a very few % of ozone is allowed early access to the reaction chain, the ozone is rapidly consumed in the initial oxidation reactions. The remaining oxidation reactions required to complete the transition to N_2O_5 must then be carried out by oxygen alone resulting in a slow and inefficient process.

In contrast, if a two-stage process is used in which oxygen alone is the first stage oxidiser and the ozone/oxygen mix from the commercial ozoniser is applied as a second stage, the speed and overall process efficiency increase significantly. Detailed knowledge of reaction paths and kinetics, not yet available, is required to explain these phenomena, but forcing the oxygen to carry out initial oxidation processes while preserving ozone for later processes, rather than sacrificing it early in the reaction chain, appears to increase the overall speed of NO_x oxidation to N_2O_5 and overall process efficiency.

ACKNOWLEDGEMENTS

The research has been supported by *The Ministry of Scientific Research and Information Technology of Poland* within the frame of the Polish research project 4T 09B03425 covering the period 2003-2006.

REFERENCES

1. Jaroszyńska-Wolińska J., (2002) Ozone application to a two-stage NO removal from waste gases, *Polish Journal of Chemical Technology,* 4 , 2, 5-7.

2. Jaroszynska-Wolińska J., Wroński., Ozonek., Pollo I.,.(2002). Efficiency of an ozone synthesis process realized in ozonizers of various high–voltage inner electrode designs, *Proc.Int.Symp. on High Pressure Low Temperature Plasma Chemistry, Hakone VIII, Estonia,* 2, 210-214.

3. Jaroszyńska-Wolińska J., Wroński M.,(2002). The influence of high voltage electrode design on Electrical parameters of the ozone generator, *Polish Journal of Chemical Technology,* 4 , 2, 8-11.

Paper number

OBSERVATION OF LASER-INDUCED STREAMER CORONA DISCHARGE IN A CORONA RADICAL SHOWER SYSTEM

S. Kanazawa[1], F. Mitsugi[2], T. Ohkubo[1], Y. Nomoto[1], M. Kocik[3], J. Mizeraczyk[3] and J.-S. Chang[4]

[1] *Department of Electrical and Electronic Engineering, Faculty of Engineering, Oita University 700 Dannoharu, Oita, 870-1192, JAPAN*
[2] *Venture Business Laboratory, Oita University 700 Dannoharu, Oita, 870-1192, JAPAN*
[3] *Centre for Plasma and Laser Engineering, Institute of Fluid Flow Machinery, Polish Academy of Sciences 80-231,Gdańsk, POLAND*
[4] *Department of Engineering Physics, McMaster University Hamilton, Ontario, L8S 4M1, CANADA*

ABSTRACT. Positive DC corona streamers play an important role for treatment of harmful gases. We have developed a generation technique of laser-induced streamer and its observation system to understand dynamics of streamer. In this paper, we studied the properties of the streamers such as the propagation and branching phenomena in a corona radical shower system. Time evolution and time-resolved characteristics for the laser-induced streamers were observed using an intensified charge coupled device (ICCD) camera.

1. INTRODUCTION

Recently, a corona radical shower system using positive DC corona streamers has been proved to be one of the most efficient nonthermal plasma processing for treatment of harmful gases. It is necessary to understand the characteristics of the streamer discharge and to control the streamers in theoretical and practical point of view.

We have investigated time-accumulated observation, laser-induced fluorescence (LIF) measurements and the electrical properties for the positive DC corona streamers in the previous studies [1]. The positive DC corona streamer is self-repetitive with current pulse, which has the pulse time duration of several hundred nanoseconds and the repetition frequency of 1-100 kHz. Because the time interval between the current pulses fluctuates, it has been considered that time-resolved analysis for the streamer may be difficult in spite of the recent progress of the observation system using an intensified charge coupled device (ICCD) camera.

In recent years, however, we have developed a generation technique of time-controlled streamer, which is called laser-induced streamer and the time-resolved observation system using the ICCD camera [2]. The irradiation of the UV pulsed laser in the electrode gap during the operation of normal streamer discharge can generate the laser-induced streamer between individual normal streamers. Because the laser-induced streamer generates immediately after the laser irradiation, it can be distinguished from normal streamers. Therefore, we found that the laser-induced streamer was available to understand dynamics of streamer discharge.

In this study, we investigated the properties of the streamers such as the propagation and branching phenomena for the laser-induced streamers in the corona radical shower reactor.

Time evolution and time-resolved characteristics for the laser-induced streamers were observed using the ICCD camera.

2. EXPERIMENTAL SETUP

Figure 1 shows a schematic diagram of the corona radical shower reactor with the ICCD (LaVision, Flame Star II) camera observation system. The corona radical shower reactor consists of a pipe with nozzles-to-plates electrode system. The gap distance from the nozzle to the plate is 50 mm. This system is set inside the acrylic box (100 x 120 x 700 mm) with a quartz window through which streamers can be observed as the side view images by the ICCD camera. Positive DC high voltage is applied to the stressed electrode. NO(100 ppm)/air mixture gas is flowed along the reactor through the gas straightener with a flow rate of 3 L/min. There is no additional gas flow from the nozzles. In order to generate laser-induced streamers, the pulsed laser sheet (1 mm-thickness and 25 mm-height) is irradiated between the stressed electrode and the lower grounded plate in the reactor. The wavelength λ of the pulsed laser sheet is 226 nm and the energy is 1.3 mJ.

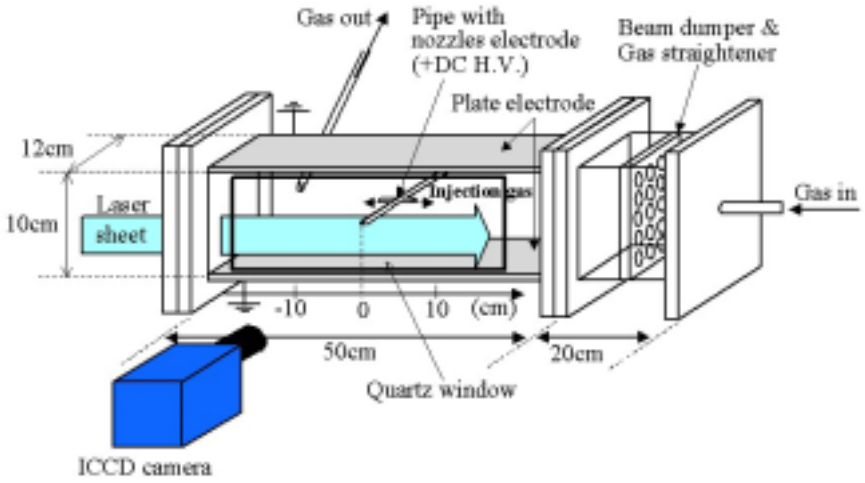

FIGURE 1. A schematic diagram of the corona radical shower reactor and the ICCD camera.

3. EXPERIMENTAL RESULTS AND DISCUSSIONS

3.1. Observation of normal positive DC streamer corona

Figure 2 shows typical images (side view) of normal positive DC streamer corona generated at various applied voltage between a pipe with nozzles-to-plates electrode gap in NO(100 ppm)/air mixture taken with a long ICCD exposure time of 0.6 ms. At low applied voltage (19-22 kV), relatively short streamers are formed around the nozzles. Streamers reach to the both plate electrodes at around 24 kV. Completely bridged streamers are observed when the applied voltage is 27-30 kV. It was revealed that the development of streamers in the direction from nozzle to plate became dominant compared to that in the direction parallel to the plate with increasing of the applied voltage. Therefore, the average discharge current also increases with the increase of the applied voltage. These results are time-accumulated characteristics for the normal streamers.

3.2. Time-resolved observation for laser-induced streamers

Figure 3 shows time evolution images of laser-induced streamers generated at a pipe with

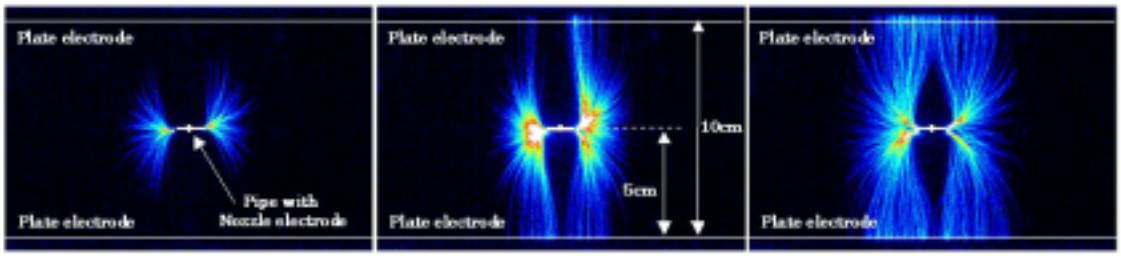

(a) 19 kV, 20μA (b) 24 kV, 70μA (c) 30kV, 135μA

FIGURE 2. Images of normal positive DC corona streamers taken with a long ICCD exposure time of 0.6 ms. The images (a), (b) and (c) correspond to streamers generated at the applied voltage of 19, 24 and 30 kV, respectively. Each image is an average of 100 images.

nozzles-to-plates electrode gap in NO (100 ppm)/air mixture. The applied voltage was 30 kV, which was sufficient to get the well-developed streamers in the normal case as mentioned above (see Figure 2(c)). The ICCD camera was opened when the laser-induced streamer generated. In this figure, the ICCD exposure time is varied from 50 to 500 ns. Although each image actually presents different laser-induced streamers, similar appearance was observed because of the good reproducibility. As can be seen in the figure, the laser-induced streamer propagates from the nozzles to the upper and lower plates with generating branches. The average diameter of the branches is approximately 150 μm. The average evolution velocity of the laser-induced streamer from the nozzle to the plate estimated from the images is about 2.5 x 10^5 m/s.

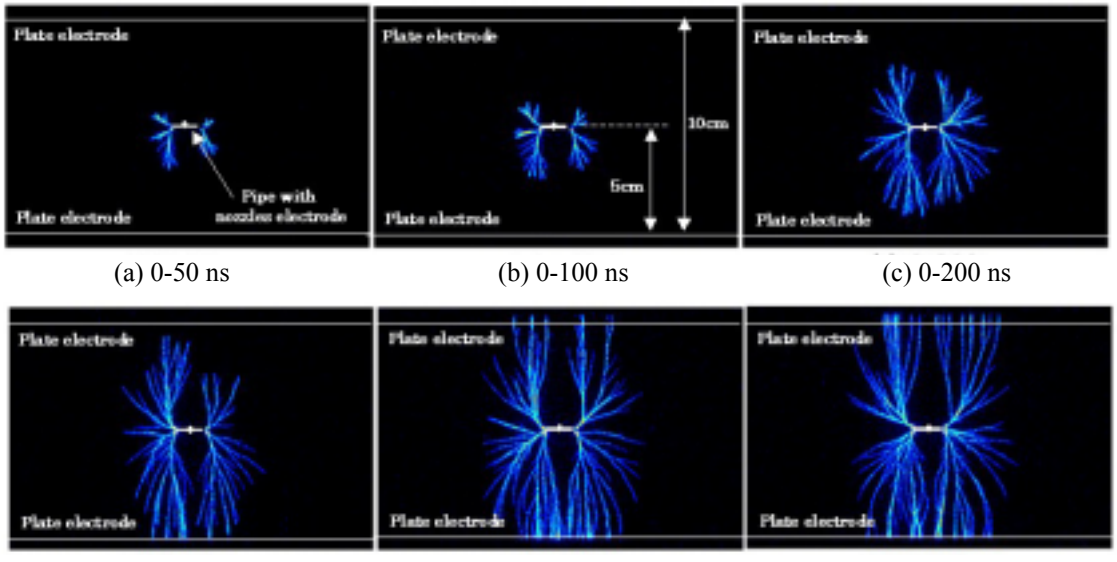

(a) 0-50 ns (b) 0-100 ns (c) 0-200 ns

(d) 0-300 ns (e) 0-400 ns (f) 0-500 ns

FIGURE 3. Time evolution images of laser-induced streamers at the applied voltage of 30 kV. Laser wave-length is λ=226 nm and the laser energy is 1.3 mJ. The ICCD exposure time was varied from 50 to 500 ns. Each image is a result of a single laser shot.

To analyze the laser-induced streamer in detail, the ICCD exposure time was fixed at 50 ns and the delay time (after inception of laser-induced streamers) was varied. Figure 4 shows time-resolved images of laser-induced streamers generated at a pipe with nozzles-to-plates electrode gap and at the applied voltage of 30 kV in NO(100 ppm)/air mixture. Since the light emitted from the laser-induced streamers during such short exposure time is very faint, each image is an average of 100 images of the individual streamers. It is found from the figure that the laser-induced streamers propagating toward the plates (so-called vertical streamers) are

faster than those propagating parallel to the plates (lateral streamers). As for the both streamers, the velocity is not constant along their pathways. In the case of the vertical streamers, the velocity changes from about 3.5 x 10^5 m/s near the nozzles (see Figure (a)) to about 1.3-1.5 x 10^5 m/s in the middle of the gap (see Figure (c)) and near the plates (see Figure (d)). On the other hand, the velocity of the lateral streamers changes from about 1.7 x 10^5 m/s near the nozzles (see Figure (a)) to about 1.3 x 10^5 m/s in the middle of the gap (see Figure (c)). From figure 3 and figure 4, the time-resolved developing behavior of the laser-induced streamer was revealed.

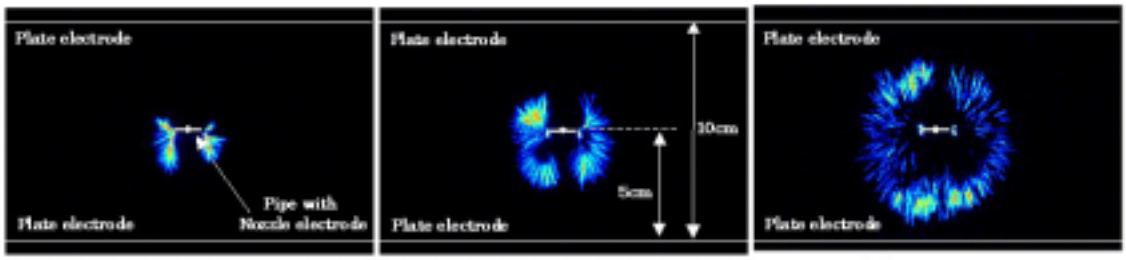

(a) 0-50 ns (b) 50-100 ns (c) 150-200 ns

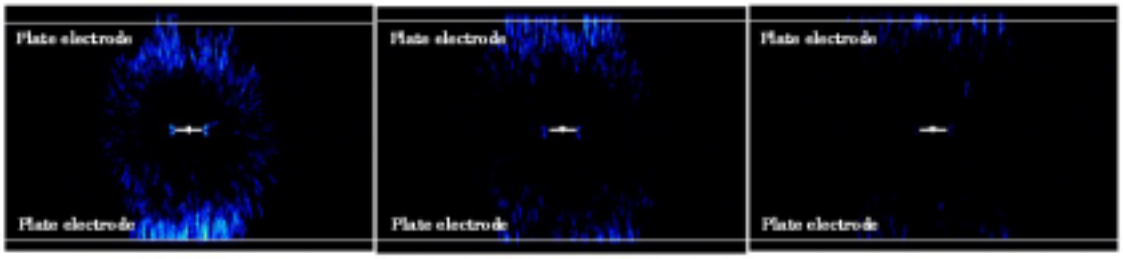

(d) 250-300 ns (e) 350-400 ns (f) 450-500 ns

FIGURE 4. Time-resolved images of laser-induced streamers generated at the applied voltage of 30 kV. Laser wavelength is λ=226 nm and the laser energy is 1.3 mJ. The ICCD exposure time was fixed at 50 ns and the delay time was varied. Each image is an average of 100 images.

4. CONCLUSIONS

From the investigation on time-resolved observation for laser-induced streamers in the corona radical shower reactor, it was revealed that the laser-induced streamers propagating from the nozzle to the plates (vertical streamers) are faster than those propagating parallel to the plates (lateral streamers). The velocity of vertical streamer changes from about 3.5 x 10^5 m/s near the nozzles to about 1.3-1.5 x 10^5 m/s in the middle of the gap and near the plates. The velocity of the lateral streamers changes from about 1.7 x 10^5 m/s near the nozzles to about 1.3 x 10^5 m/s in the middle of the gap. It is considered that the laser-induced streamer can be available to understand the dynamics for the normal streamer corona discharge.

REFERENCES

[1] Kanazawa, S., Sumi, T., Sato, N., Ohkubo, T., Nomoto, Y., Kocik, M., Mizeraczyk, J., Chang, J.S. (2005). Wide-range two-dimensional imaging of NO density profiles by LIF technique in a corona radical shower reactor. *IEEE Trans. Ind. Appl.*, 41, 200-205.

[2] Ohkubo, T., Kanazawa, S., Nomoto, Y., Kocik, M., Mizeraczyk. (2005). Characteristics of DC corona streamers induced by UV laser irradiation in non-thermal plasma. *J. Adv. Oxid. Technol.*, 8, 218-225.

CHARACTERISTICS OF A NOVEL PARTIAL DISCHARGE IN WATER

Weimin Guan, Satshi Ihara, Chobei Yamabe, Saburo Satoh*

Department of Electrical and Electronic Engineering,
Faculty of Science and Engineering, Saga University, Saga 840-8502, Japan.
** Joint Research and Development Center, Saga 840-8502, Japan.*
E-mail :04641002@edu.cc.saga-u.ac.jp

ABSTRACT. Discharges in liquid media can generate high electrical field, ultraviolet rays, as well as various chemically active species which can be utilized for sterilization and decompositions of toxin and bacteria in water. In order to obtain continuous and stable discharge in water, barrier discharge was produced. The electrical and optical characteristics of the barrier discharge in water are discussed. The mechanism and possible application of barrier discharge in water are also prospected.

1. INTRODUCTION

Water discharge techniques of sterilization have some principal merits as compared with conventionally used methods. Continuous and stable discharge in water is able to produce high energy electrons, ultraviolet emission, shock waves, ozone and other chemically active species which are effective for sterilization and water purifications. To apply water discharge techniques in above fields we need to deliver electrical energy through discharge in water more efficiently. In this experiment, we attempted to produce the barrier discharge in water. To determine characteristics of the discharge, electrical and optical measurements were performed. The investigation of active species produced the barrier discharge in water also had been done.

2. EXPERIMENT

The schematic diagram of the experimental is shown in Fig. 1. We applied pulsed voltage to the reactor with a power source switched by hydrogen thyratron. We can obtain 20 kV to 40 kV output while the FWHM is about 1μs. (See Fig. 2) The barrier discharge reactor was constructed with an inner glass tube (ϕ18 mm, length: 80mm), which was covered by stainless mesh (ϕ0.23mm, 32mesh/cm^2, length: 60mm). High voltage (H.V.) was applied through a H.V. cable, which immerse in the center of inner glass tube. The H.V. electrode located at the middle of inner glass tube at length of 2mm. All of the setup of reactor was settled in a cylinder outer glass container. The active volume of the discharge reached 700mm^2 approximately. The photograph of discharge was taken by a digital camera (Shutter time: three second.). The emission spectra was observed by a spectroscope and analyzed with a computer.

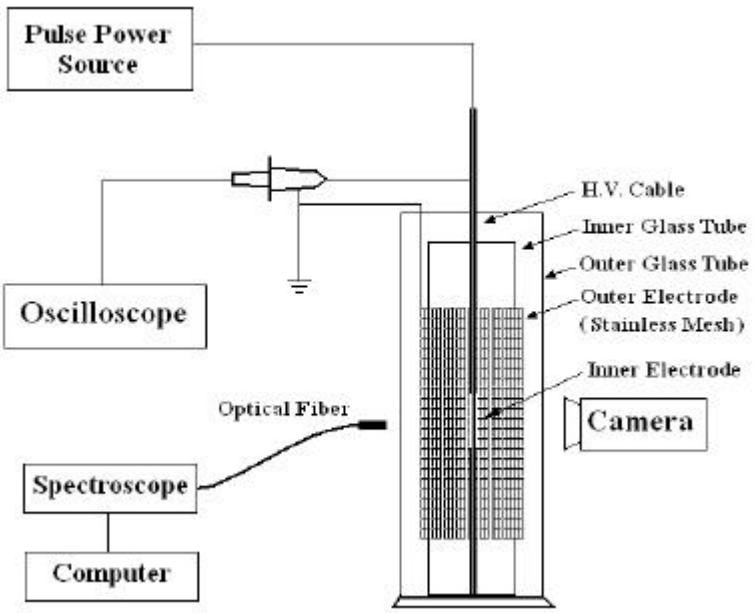

FIGURE 1. Schematic diagram of the experimental setup.

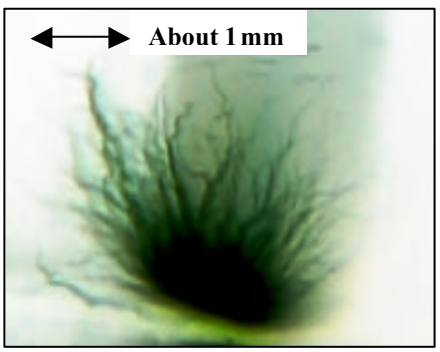

FIGURE 3. Image of the barrier discharge occurred in water.

3. RESULTS AND DISCUSSION

Based on the obtained results of optical observation and the electrical measurement during the discharge progressing process (see Fig. 2), we considered that there are three stages in the conduction process prior to breakdown for non-uniform field geometries. The first stage is characterized by a resistive current at low electric field. The second stage consist of a rapid rise in the injection current associated with increasing electric field due to dark current through the gap. The transition from the resistive to the dark current stage occurs when the stress of applied electric field reduces the barrier. This transition point is polarity dependent. In the third stage, at high electric field the current reaches charge saturation prior to breakdown. The process of final breakdown also shows a distinct polarity dependence. Such strong polarity dependence indicates breakdown occurs in the gaseous phase. This is supported by the images of discharge channel regions forming at the current injection point.

Digital camera photograph shows that the discharge has a lot of diffuse channels across the discharge gap. (See Fig.3) The performed investigations of these optical photographs indicate that the discharge has its own micro and macro structures. Optical emission spectrum of the discharge confirmed that the main part of the spectral characteristics radiation lies in the region from 300nm to 800 nm, and the radiation spectrum has linear character while the applied voltage increasing. Especially, the radiation of hydrogen α line at 656 nm was the

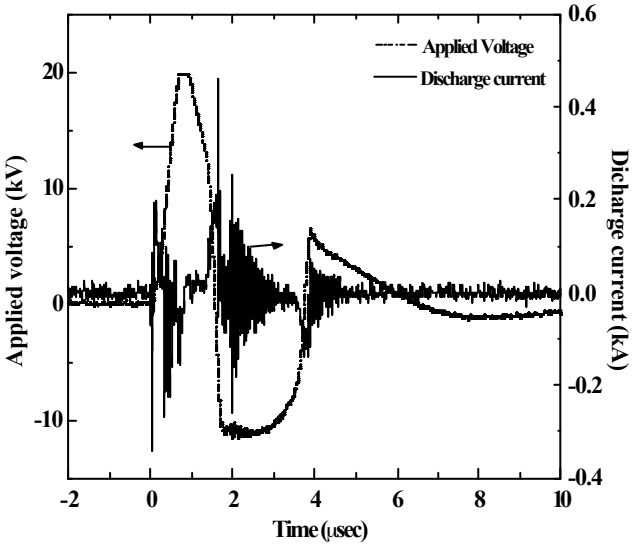

FIGURE 2. Voltage and current waveforms of barrier discharge in water.

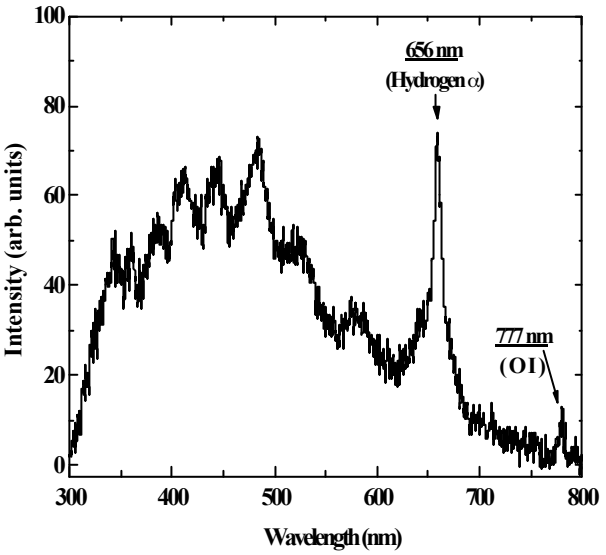

FIGURE 4. Optical emission spectrum from the barrier discharge in water.

characteristic peak of the spectrum (See Fig.4), while oxygen atomic I radiation at 777 nm was also observed. These results evident that water was decomposed during the barrier discharge, and active species were generated as byproducts.

The byproducts were supposed to be hydrogen gas and excited oxygen atom. From the measurement of hydrogen peroxide it was confirmed that hydrogen peroxide was generated in the inner glass tube. The concentration was about 5 mg/L at ten minutes after the discharge termination and reduced to 2mg/L at twenty minutes after the discharge termination.

4. CONCLUSION AND PROSPECT

We had generated barrier discharge in water and observe the electrical and optical characteristics of discharge in present work. Such discharge can be stably maintained to produce active radicals which are available for sterilization and decompositions of toxin and bacteria in water.

OH radical has large oxidation ability, however, its lifetime is approximately 10^{-4} times shorter than O radical. Therefore the quantitative observation of OH radical produced in water discharge remains difficulty.

While on the other hand, we noticed that barrier discharge in water are result in an erosion of electrodes material in water. In the future, we are going to perform further experiments aiming to study the biological effect of these particles produced by barrier discharge in water.

REFERENCE

[1] E.M.Veldhuizen, Electrical Discharges for Environmental Purposes: Fundamentals and Applications, Nova Science Publishers, Huntington, NY, 2000.
[2] S. Katsuki, D. Takano, T. Namihira and H. Akiyama, "Repetitive operation of water-filled Blumlein generator", American Institute of Physics, Review of Scientific Instruments, Vol.72, No.6, pp.2759-2763, 2001.6.
[3] J.S.Clements, M.Sato, R.H.Davis, Preliminary investigation of pre-breakdown phenomena and chemical reactions using a pulsed high voltage discharge in liquid water, IEEE Trans.Ind.Appl, IA-23 (2) pp.224 –235,1987.
[4] B.Sun, M.Sato, J.S.Clements, Optical study of active species produced by a pulsed streamer corona discharge in water, J.Electrostat, 39 (3) pp.189 –202, 1997
[5] I.V. Lisitsyn, H. Nomiyama, S. Katsuki and H. Akiyama, "Thermal processes in a streamer discharge in water", IEEE Transactions on Dielectrics and Electrical Insulation, Vol.6, No.3, pp.351-356, 1999.6.

RADIATION KINETICS AND CHEMICAL REACTIVITY OF BARRIER DISCHARGES IN HUMID ARGON

K.V. Kozlov[1,a], E. Odic[2], P.A. Tatarenko[1], B. Dodet[2], G.S. Fedoseev[1], M.J. Kirkpatrick[2], V.G.. Samoilovich[1] and M. Ganciu[3]

[1] *Department of Chemistry, Moscow State University, Leninskie Gory 1, str.3, 119899 Moscow, RUSSIA*
[2] *Départment Energie – Supélec, Plateau de Moulon, 3 rue Joliot-Curie, F-91192 Gif-sur-Yvette CEDEX, FRANCE*
[3] *Universite Paris XI – LPGP – Bat210, F-91405 Orsay CEDEX, FRANCE*

ABSTRACT. The technique of spatially resolved cross-correlation spectroscopy was used to record two-dimensional luminosity distributions for the selected spectral bands of molecular nitrogen (λ=337.1 nm), OH-radical (λ=308 nm), and two spectral lines of excited Ar (λ=750.4 nm and λ=763.5 nm) emitted by the microdischarges of the barrier discharge in flowing humid argon at atmospheric pressure. Concentrations of two stable reaction products of H_2O decomposition (H_2 and O_2) in argon plasma were determined experimentally as functions of humidity. Comparison of these results with the corresponding measurements of radiation kinetics permitted a detailed analysis of the influence of the discharge mechanism on its chemical reactivity in humid argon to be accomplished.

1. INTRODUCTION

Barrier discharges (BDs) in humid argon can be regarded not only as prospective plasma chemical reactors for H_2O_2 synthesis [1], but also as useful UV-radiation sources [2]. The objective of this research was to carry out a complete plasma diagnostics (including electrical measurements, spatially resolved kinetic spectroscopy, and chemical analysis of the stable reaction products) of the BD in humid argon, in order to improve understanding of the discharge development mechanism and to determine its influence upon the kinetics of the decomposition of H_2O molecules. The technique of cross-correlation spectroscopy (CCS) was a basic tool to investigate radiation kinetics, and the method of gas chromatography was used to determine the concentration of reaction products (H_2 and O_2) in the gas phase.

2. EXPERIMENTAL SET-UP AND PROCEDURE

The experimental set-up for spatially resolved spectroscopic measurements and the CCS-method are described in detail elsewhere [3,4]. In order to localize repetitive microdischarges (MDs) at a fixed position, a discharge cell consisting of two semi-spherical electrodes (radius of curvature R = 7.5 mm, see fig.1-a), both covered with glass was used. This electrode arrangement provided the possibility to observe not only the bulk volume portion of the MD, but also its surface components. The BD was operated by sinusoidal voltage at a frequency of 5 kHz. The discharge gap width (the distance between the electrode tips) was equal to 1.9 mm. The spatio-temporal distributions of radiation intensity for the selected wavelengths within the MD channels were recorded by means of the technique of CCS with spatial and temporal resolutions of 0.1 mm and 0.05 ns, respectively.

[a] Electronic address: kozlov@kge.msu.ru

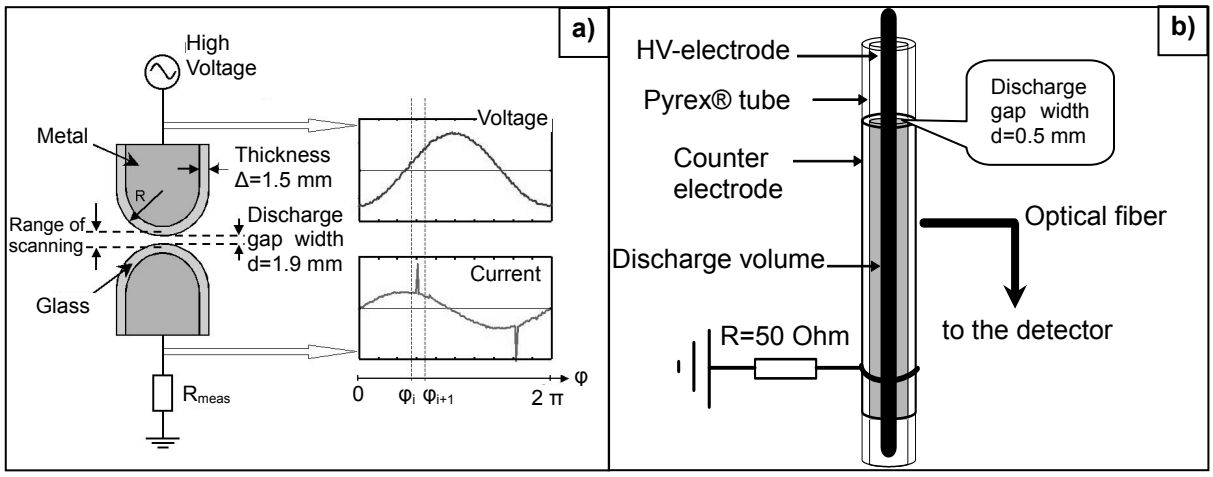

FIGURE 1. a) General scheme of the discharge cell used for spatially resolved CCS-measurements with the indicated range of optical scanning and typical examples of the oscillograms of voltage and current; b) Sketch of the discharge cell used for the investigations of chemical reactivity and for time-space integrated spectroscopic measurements. See explanations in the text.

The reactor used for the experiments on H_2O decomposition and for the time-space integrated spectroscopic measurements, was based on a coaxial electrode arrangement (see fig.1-b). The inner electrode was a stainless steel rod of 2 mm diameter, centered in a Pyrex tube (inner diameter 3 mm), wrapped with a copper foil (45 mm length). The inner electrode was energized using a 28.6 kHz high voltage power supply. The copper foil was connected to ground through a 50 Ω resistor for discharge current measurements. The reactor was fed with humid argon with variable water vapor content (1.8-23 g/m^3). The flow rate ranged from 0.2 to 2 L/min. The input power range was: 0.5-3 W.

3. RESULTS AND DISCUSSION

In the emission spectrum of the BD in flowing humid argon, the spectral bands of the second positive system of nitrogen as well as of OH-radical were observed along with the peaks of argon. The following four spectral indicators were selected to record the spatio-temporal distributions of the MD luminosity: Ar(I), E_{exc}= 13.48 eV, λ = 750.4 nm; Ar(I), E_{exc}= 13.17 eV, λ = 763.5 nm; $N_2(C^3\Pi_u)$, E_{exc}= 11.0 eV, λ = 337 nm; and $OH(A^2\Sigma^+)$, E_{exc}= 9.1 eV, λ = 308 nm. The CCS-measurements were carried out for several different levels of relative humidity in the range 3-95%. Some results of these experiments are shown in fig.2.

Generally, spatial distributions of light intensity of the radiating species being considered are determined by the corresponding distributions of electric field strength and electron density within the MD channel. However, these functional dependences are different for different spectral indicators, and the following simple rule may be used to provide a qualitative interpretation of experimental results: the greater the threshold energy E_{exc} of a spectral indicator, the stronger the dependence of its excitation rate (consequently, of its radiation intensity) upon electric field strength [3]. Using this rule to analyze the luminosity distributions shown in fig.2 and taking into account the values E_{exc} listed above, we can assume that the structure of the MD channel is similar to that one found earlier for the BD in air [3]. There are two active zones near the electrodes, and electric field is higher near the cathode, while electron density is greater near the anode.

The influence of argon humidity on the radiation kinetics within the MD channel can be considered as a superposition of the following two effects: (i) the dependence of collisional quenching rate of the radiating species upon H_2O concentration and, (ii) the influence of water vapour on electron energy distribution. Since the rate of collisional quenching of the radiating species by H_2O molecules is proportional to the humidity, an increase in water vapour content

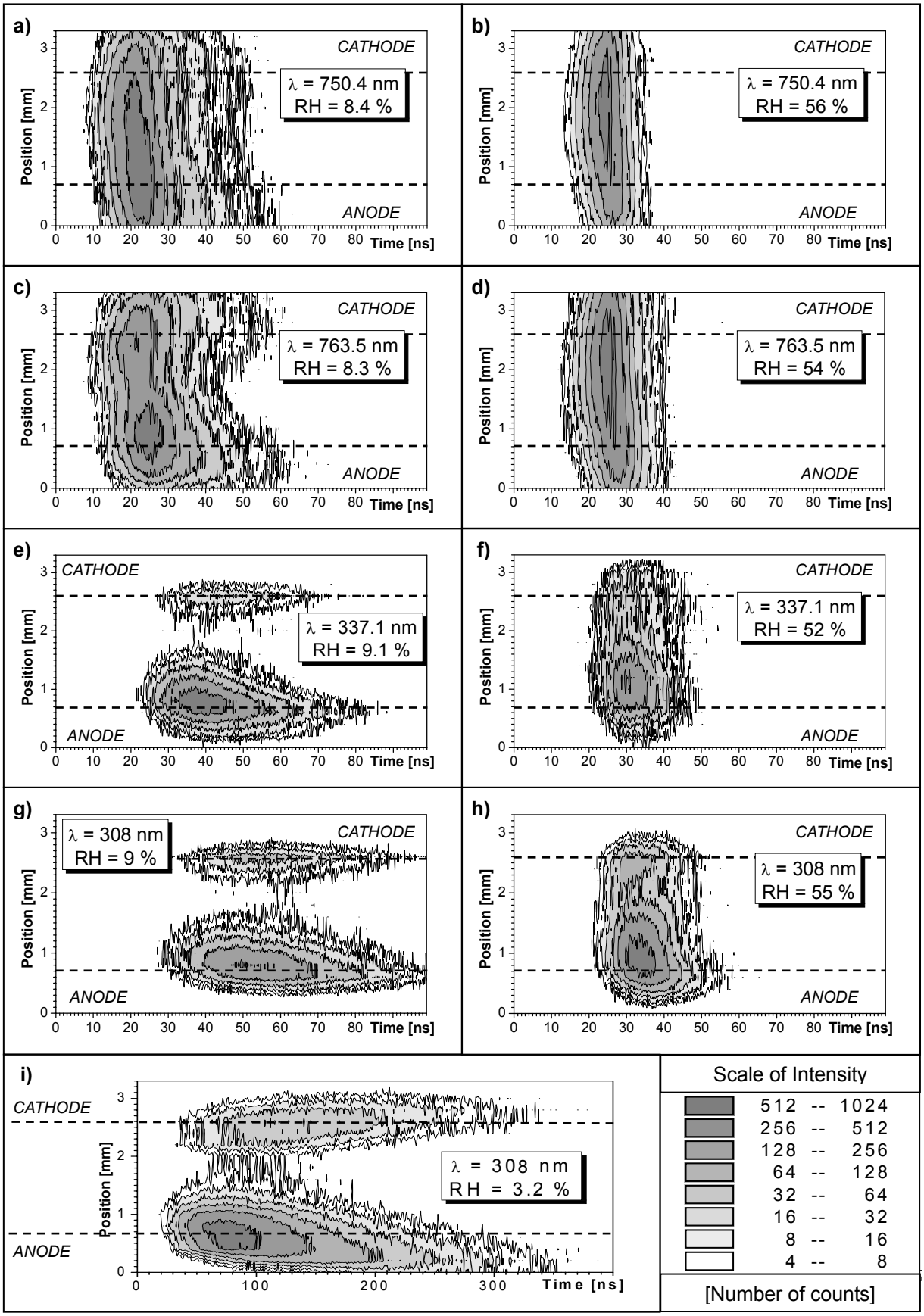

FIGURE 2. Spatio-temporal distributions of the MD luminosity for the selected wavelengths. Experimental conditions: p=1.05 bar; d=1.9 mm; gas flow rate 8 l/h; voltage frequency 5 kHz. RH denotes relative humidity.

results in a noticeable shortening of light emission duration for all spectral indicators being considered (compare the left and right columns of the plots (a-f) in fig.2, and the plots (g,h,i)).

An addition of molecular gas admixture to argon plasma results in a decrease in electron energy [4]. This effect can explain the difference between the luminosity distributions shown in fig.2-c,d. For relative humidity (RH) of 54%, the electron energy is lower than for RH=8.3% and therefore the local intensity maximum near the anode on fig.2-c is not seen in fig.2-d. This influence of humidity on electron energy is also clearly seen from the results on chemical reactivity measurements presented in fig.3.

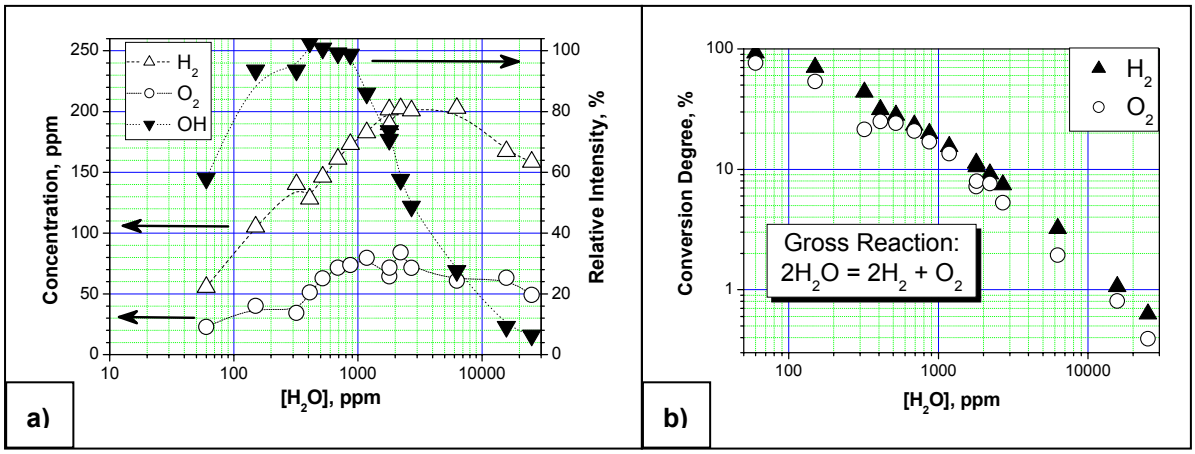

FIGURE 3. Dependences of the reaction product yields and light emission intensity for λ = 308 nm (a), and of the corresponding chemical conversion degrees (b) upon the humidity of argon.

The shapes of the curves for reaction product concentrations (fig.3-a) are determined by the following two kinetic effects of humidity acting in opposite directions. First, the dissociation rate of H_2O molecules is proportional to the concentration of water vapour. Second, the rate constant of this process decreases with the humidity due to the decrease in electron energy. For the H_2O concentrations greater than 1000 ppm, the second effect begins to dominate and the concentration curves for H_2 and O_2 fall down. The shape of the curve for integral emission intensity of the radicals $OH(A^2\Sigma^+)$ at λ = 308 nm (see fig.3-a) can be explained in a similar way. However in the latter case, the influence of collisional quenching of the radiating species by H_2O molecules should be taken into account. This influence results in a shift of the maximum to a lower humidity as compared to the curves for H_2 and O_2. The dependence of the conversion degrees of H_2O to H_2 and O_2 on the humidity (see fig.3-b) demonstrates that an increase in water content in argon exerts a profound negative influence on the chemical reactivity of the BD in the entire concentration range of water vapour.

REFERENCES

[1] Dodet B., Odic E., Goldman A., Goldman M., Renard D. Hydrogen Peroxide Formation by Discharges in Argon/Water Vapor Mixtures at Atmpspheric Pressure. J. Adv. Oxid. Technol., 2005, v.8, No.1, p.91-97.

[2] Hibert C., Gaurand I., Motret O., Pouvesle J.M. [OH(X)] measurements by resonant absorption spectroscopy in a pulsed dielectric barrier discharge. J. Appl. Phys., 1999, v.85, No.10, p.7070-7075.

[3] Kozlov K.V., Wagner H.-E., Brandenburg R., Michel P. Spatio-temporally resolved spectroscopic diagnostics of the barrier discharge in air at atmospheric pressure. J. Phys. D: Appl. Phys., 2001, v. 34, No. 21, p. 3164-3176.

[4] Kozlov K.V., Tatarenko P.A., Samoilovich V.G.. Some peculiarities of the barrier discharge in pure argon. These Proceedings.

TREATMENT OF TETRAFLUORIDE WITH GAS DISCHARGES

G. J. Pietsch[1] and A. B. Saveliev

[1]*Electrical Engineering & Gas Discharge Technology, RWTH Aachen University, 52056 Aachen GERMANY*
[2]*Now with Philips Automotive Lighting, 52068 Aachen, GERMANY*

ABSTRACT. Waste gases from semiconductor industry contain perfluorocarbons (PFCs), which cause global warming and should be removed. One of the possibilities to do this is treatment by non-thermal plasmas, such as dielectric barrier discharges (DBDs). The PFCs molecules are rather stable. The feasibility of conversion of CF_4 as a sample for PFCs by DBDs at different conditions as well as by heating and by electric arc is discussed.

1. INTRODUCTION

Perfluorocarbons (PFCs) are widely used in semiconductor industry for etching purposes. They are not completely consumed during semiconductor production, leaving residues. Carbon tetrafluoride (CF_4) is the most important one; its Global Warming Potential (GWP) is 6,500. CF_4 was used as sample gas for PFCs to find out optimal conditions for its destruction.

CF_4 is a rather stable compound. Its dissociation is possible e.g. by direct electron collisions and thermally. In order to remove CF_4 fragments, bonding substances such as SiO_2 or CaO are used.

Most plasma chemical processes, e.g. ozone synthesis, can be described by an exponential function.

$$C = C_\infty - (C_\infty - C_0) \cdot \exp\left(-\frac{P/Q}{\beta}\right) \tag{1}$$

with C_0 the initial concentration of the substance to be decomposed, C_∞ the final minimum achievable "equilibrium" concentration and C the actual one at the outlet of the reactor. P/Q is the specific energy (power P over gas flow rate Q). β, the energy consumption factor, is the energy density necessary to reduce the concentration (related to the minimum achievable one) by 63 %. β and C_∞ characterize the decomposition/conversion of the pollutant. In order to simplify the representation, the Destruction Removal Efficiency, $DRE = (C_0 - C)/C_0 \cdot 100$ % is used. With equation (1) it follows

$$DRE = DRE_{\max} \cdot \left(1 - \exp\left(-\frac{P/Q}{\beta}\right)\right). \tag{2}$$

The residual PFCs remaining after etching are usually flushed with a cheap non-oxidising gas, usually nitrogen. In most of our experiments nitrogen/CF_4 mixtures 100:1 were used.

2. EXPERIMENTAL SET-UP

The experimental set-up consists of gas mixture system, reactor with power supply and measuring devices. Three types of reactors were used, one working with DBDs, the second with a heating coil (heat reactor) and the third with arc heating. The gas at the outlet of the reactors was analysed with a FTIR spectrometer equipped with a 10 cm single-pass gas cell.

The DBD reactor consists of a quartz glass tube of 10 mm diameter with wall thickness 1.4 mm as dielectric. High voltage of up to 15 kV at 15 kHz is applied to a metal rod in the tube centre. The counter electrode is a coil winded around the tube. Another reactor with a tube from alumina of 25 mm diameter with wall thickness 2.5 mm was used as well. The discharge gap was filled with glass pieces or CaO. Temperature was controlled by thermocouples on the tube surface. As the reactor was operated with comparative high power, the system heated itself. In some experiments the tube was heat insulated to increase the operating temperature.

The heat reactor consists of a quartz glass tube wrapped with a heating winding. The model gas was passed through the tube filled with quartz glass pieces. In order to avoid heat losses the tube was placed between two chamotte bricks. The temperature is measured with a thermocouple inside the tube.

The arc reactor was equipped with electrodes from Cu-W alloy. The electrodes are placed in a quartz glass tube with inner diameter of 7.2 mm. The electrode holders as well as the outer surface of the quartz tube are water-cooled. The gap between the electrodes was up to 1 cm. The device was supplied with a stabilized current source of 5 or 10 A. The arc voltage varied between 25 and 50 V, the power was changed between about 100 and 500 W. The tested gas mixture passed through the quartz glass tube from top to bottom.

3. DESTRUCTION OF CF_4 IN BARRIER DISCHARGES

The destruction removal efficiency (DRE) of CF_4 in nitrogen by DBDs depending on specific energy is shown in Fig. 1. With glass wool in the reactor a DRE of 95 % is reached. The dissociation products of CF_4 react with the substances in the reactor. CO_2 and SiF_4 has been detected in quantities nearly equivalent to the amount of decomposed CF_4. Small quantities of CO and COF_2 have been detected at the outlet of the reactor as well.

The energy demand to remove CF_4 from nitrogen is relative large (Fig. 1), e.g. in order to reach a DRE of 95 % 1.25 kW·h is needed to treat 10 L gas. Only a small part of this energy is used for CF_4 dissociation; the main part converts to heat. Addition of water vapour (up to 2 vol. %), oxygen (up to 20 vol. %), change of filling material (glass wool, glass beads, quartz glass pieces or CaO) and variation in temperature (from 125 to 450°C) do not change the energy consumption considerably. The β values derived from experimental results (using equation 1 or 2) are in the same order of magnitude (between 30 and 50).

Furthermore, if the CF_4 content in the gas mixture is increased, the efficiency of CF_4 conversion decreases. Replacing the carrier gas nitrogen by a noble gas, the energy consumption decreases (Fig. 2); the nature of carrier gas does not influence the composition of the reaction products.

The experimental results can be explained looking at the mechanism of CF_4 decomposition. As CF_4 is a chemical rather stable gas, the “active” particles (e.g. oxygen atoms, hydroxyl radicals, excited nitrogen molecules) appearing in DBDs, do not react with CF_4 at moderate temperatures (up to some 100 °C). Electron impact dissociates CF_4 if the electron energy is high enough (the dissociation energy of CF_4 is 12.5 eV). The majority of electrons in nitrogen containing non-thermal plasmas have energies in the order of 1 eV [1]. The reason is, inelastic collisions of electrons of comparative low energy with diatomic molecules lead to vibrational and rotational excitation. As result electrons loose energy. The size of the CF_4 molecule and its degree of freedom are larger than those of nitrogen so that more possibilities for rotational or vibrational excitations exist than in nitrogen. Taking into account that only a small part of electrons reach the dissociation energy of CF_4, increasing the CF_4 concentration in the carrier gas will decrease the mean electron energy in the discharge. This fact explains the different efficiencies of CF_4 decomposition for different initial concentrations.

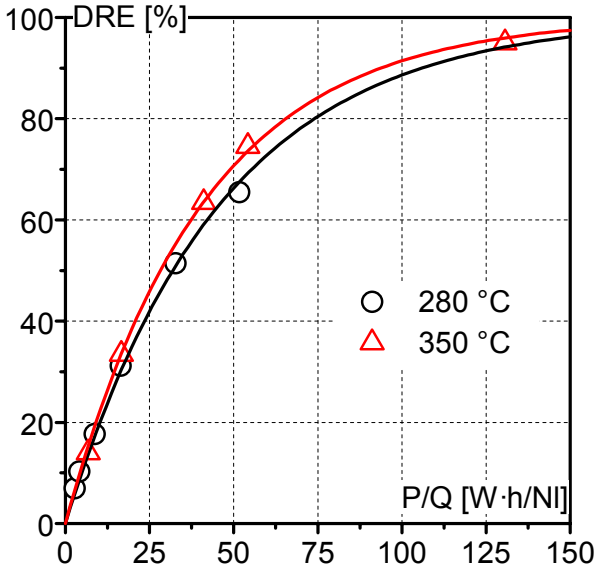

FIGURE 1. CF_4 decomposition in a DBD reactor filled with glass wool for two operating temperatures (initial CF_4 concentration 1 vol. %, carrier gas – nitrogen).

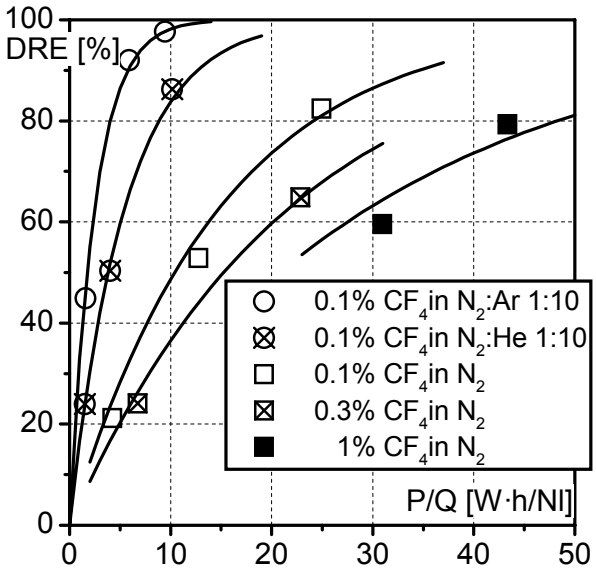

FIGURE 2. Decomposition of CF_4 in a DBD reactor filled with quartz glass beads with different carrier gases.

The electron energy in non-thermal noble gas plasmas is higher than in molecular gases [1]. The reason is that electrons collide mainly elastically in noble gases. The electron energy distribution function (EEDF) in argon at relevant field strength has a broad maximum in the region between 5 and 8 eV. Because of this, a certain amount of electrons with high energy are available, which are able to dissociate CF_4. The dissociation products (F, CF_3, CF_2 etc.) can recombine or react with other substances present in the reactor like glass, CaO, water vapour. The following sum reaction of CF_4 with SiO_2 is valid

$$CF_4 + SiO_2 = SiF_4\uparrow + CO_2\uparrow.$$

In the presence of water vapour the reaction products with H_2O are

$$CF_4 + 2\,H_2O = 2\,HF\uparrow + CO_2\uparrow.$$

The kind of the reaction partner has only a small influence on the performance of the process.

4. DESTRUCTION OF CF_4 AT HIGH TEMPERATURE

A CF_4-N_2 mixture with 1 vol. % CF_4 at a relative low flow rate of 0.09 slm was passed through the heated quartz glass tube. In Fig. 3 the temporal development of the CF_4 and SiF_4 concentration at the outlet of the reactor together with its temperature are shown. Up to about 800 °C no reactions are observed. At higher temperature CF_4 reacts quantitatively to SiF_4. The part of molecules, which have enough energy to dissociate CF_4 is rather low up to temperatures of about 1100 °C.

5. DESTRUCTION OF CF_4 IN ARCS

In order to increase the temperature a water-cooled arc reactor was used for further experiments. To provide reaction partners for the dissociation products of CF_4, a humidified gas mixture was used, a $CF_4/H_2O/N_2$ mixture with 1 vol. % CF_4 and 2 to 2.5 vol. % H_2O at 1 slm. The distance between the electrodes was varied during the experiment. The final width of the discharge gap was approximately 1 cm. The main conversion products of CF_4 in humid nitrogen are CO_2 and HF. Small amounts of CO were found as well.

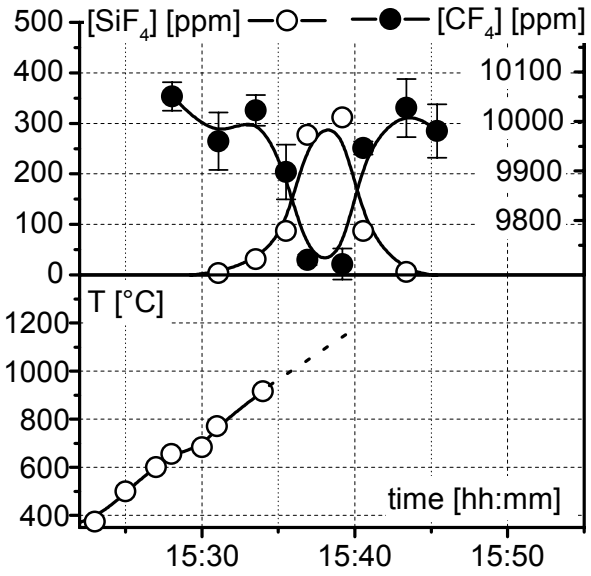

FIGURE 3. Temporal development of CF_4, SiF_4 concentrations and temperature.

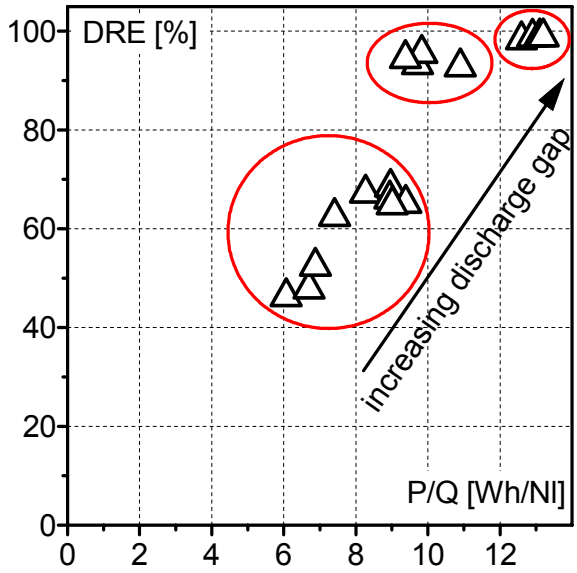

FIGURE 4. DRE over energy density from experiments with the arc arrangement.

The DRE, depending on energy density, is shown in Fig. 4. The groups of points inside each group belong to a certain value of the electrode gap. The measuring points on the right hand side belong to the largest gap. As the experimental conditions differ (e.g. bypass situation), a kinetic curve cannot be drawn. DRE values of about 99 % are reached even at moderate energy densities of about 12 to 13 Wh/Nl.

6. CONCLUSIONS

CF_4 does not react with radicals and excited particles generated in DBDs, however, high-energy electrons are able to dissociate it. In the presence of SiO_2, SiF_4 and CO_2 will be generated in dry carrier gases. In the presence of humidity HF and CO_2 appear.

If nitrogen is used as carrier gas, the energy consumption factor β is in the order of 30 to 50 Wh/Nl. The β value is hardly influenced by temperature (up to 450 °C), kind of the filling material of the reactor and kind of the dielectric barrier material.

An improvement of the energy consumption factor β down to 3 to 9 Wh/Nl is reached if noble gases are used as carrier gas in DBDs. In noble gases the electron energy is higher than in molecular gases improving CF_4 dissociation.

Thermal decomposition of CF_4 at temperatures above 1000 °C is possible. Using electric arc the removal efficiency is comparable to that reached with dielectric barrier discharges in noble gases.

ACKNOWLEDGMENT

The authors gratefully acknowledge the financial support of the European Community under the “Competitive and Sustainable Growth” program (Project No. GIST-CT-2001-50138, project coordinator: Ecozone Technologies, Israel).

REFERENCE

[1] Tas, M. A.; Veldhuizen, E. M. v.; Rütgers, W. R. (1997). Plasma excitation processes in flue gas simulated with Monte Carlo electron dynamics. *J. Phys. D: Appl. Phys.* 30, 1636–1645

Paper number

LOSS PROCESSES OF $N_2(A^3\Sigma_u^+)$ BY BENZENE

S. Suzuki[1], T. Suzuki[2] and H. Itoh[2]

[1] *Education Center, Faculty of Engineering,*
Chiba Institute of Technology, 2-1-1 Shibazono, Narashino,
Chiba, 275-0023, JAPAN
[2] *Department of Electrical, Electronics and Computer Engineering,*
Faculty of Engineering, Chiba Institute of Technology,
Tsudanuma, Narashino 275-0016, JAPAN

ABSTRACT. Experimental investigation is carried out on the destruction processes of metastable nitrogen molecules $N_2(A^3\Sigma_u^+)$ using a theoretical procedure that is possible to take into account the reflection of metastables at the boundary. The obtained quenching rate coefficient of $N_2(A^3\Sigma_u^+)$ by benzene (C_6H_6) is 3.3×10^{-10} cm^3/s.

1. INTRODUCTION

Benzene is typical one of volatile organic compounds (VOCs) and is widely used in the solvent and the organic chemical industry. It is also contained in the fuel typically of internal combustion engine. In addition, benzene is a carcinogen. Therefore, the decomposition of benzene is strongly desired for the harmful air pollutant. The discharge plasma has been adopted for a decomposition method of benzene by many researchers [1-3]. McCorkle *et al* [1] investigated using the DC glow discharge in the noble gas diluted by benzene and they proposed the decomposition method using the glow discharge. Sato *et al* [2] reported that benzene was decomposed by the electron collision in the DC glow discharge in air. Goto *et al* [3] also described a similar report using the barrier discharge and was suggested that benzene was resolved with N atom. Recently, Kim *et al* [4] have reported that the metastable nitrogen molecule $N_2(A^3\Sigma_u^+)$ was a main factor in the decomposition process of benzene.

Nitrogen is main constituent of air. If the discharge plasma is adopted for the decomposition and recombination of air pollutant, it is necessary to understand the reaction process between the pollutant and the active nitrogen [5,6].

It has already been reported the quenching rate coefficient of $N_2(A^3\Sigma_u^+)$ by air pollution gas, for example, fluorocarbons, CO and NO by us [7,8]. This paper describes the results of observed effective lifetime of $N_2(A^3\Sigma_u^+)$ in pure N_2 gas and determined the diffusion coefficient of $N_2(A^3\Sigma_u^+)$, the collisional quenching rate coefficient of $N_2(A^3\Sigma_u^+)$ by N_2 and the reflection coefficient of $N_2(A^3\Sigma_u^+)$ that are reflected at the electrodes. Furthermore the measurement of the effective lifetime of $N_2(A^3\Sigma_u^+)$ in N_2/0.0001%(1ppm)C_6H_6 mixture gas is carried out to determine the quenching rate coefficient of $N_2(A^3\Sigma_u^+)$ by benzene.

2. EXPERIMENTAL APPARATUS AND METHOD

A schematic of apparatus used the study is shown in Fig. 1. A vacuum chamber was evacuated down to pressures around 10^{-8} Torr by a turbo molecular pump. A pair of gold plated plane parallel electrodes was mounted on the central part of chamber and a stabilized DC high voltage was applied to the anode. The UV light driven by the pulse lighting of period about 3 Hz was irradiated on the cathode through a quartz window and holes at the central part of anode. It was observed the transient ionization current by a fast current amplifier after turning off the UV light. A typical transient current waveform is shown in Fig. 2. This is drawn in the semilogarithmic graph as averaging of 64 times measurement. At the turning off the UV light, a stepwise decrease in the current I_p is found first from the total current I. This component is multiplification current by collisional ionization of electron of primary photoemission current by UV light and the secondary electron emission current caused by the positive ions and photon so called first γ action. Then, it was followed by a gradually decreasing current $i_m(t)$ with initial amplitude I_m and a time constant τ_m due to the decay of the electrons released by metastables striking the surface, so-called γ_m process [9,10,11]. By using both the observed currents I and I_m, the ratio I_m/I and τ_m, the effective lifetime τ_1 of $N_2(A^3\Sigma_u^+)$ was given [7] by

$$\tau_1 = \tau_m \left(1 - \frac{I_m}{I} \right). \qquad (1)$$

The effective lifetime τ_1 is calculated from the analysis [7,8,12] which can take account of the reflection of $N_2(A^3\Sigma_u^+)$ on the surface of electrodes. It consists of the diffusion term and

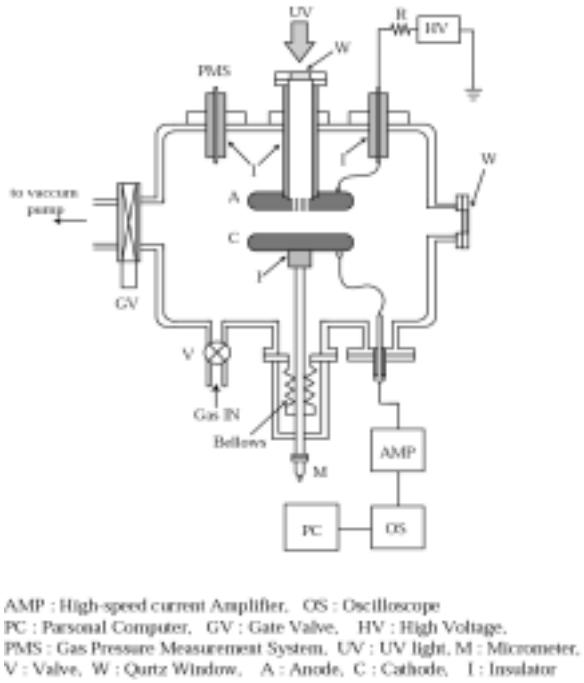

FIGURE 1. A schematic of the experimental apparatus.

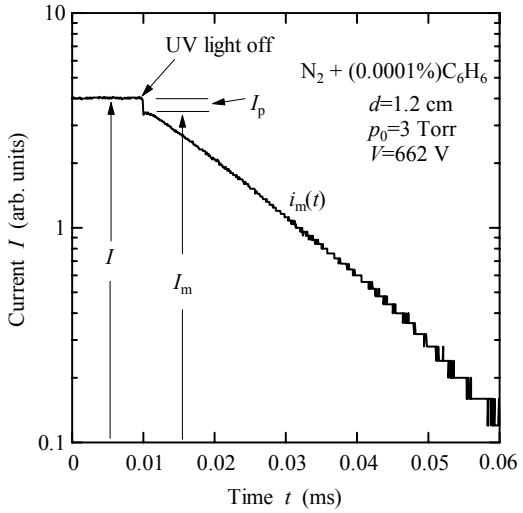

FIGURE 2. A typical transient current waveform.

the collisional quenching term by means of N_2 and C_6H_6 as follows,

$$\frac{1}{\tau_1} = D_{m1}\frac{{\mu_1}^2}{d^2}\frac{1}{p_0} + (ak + bk')N_1 p_0 . \qquad (2)$$

Here, D_{m1} (=$D_m \cdot p_0/p_1$) cm^2s^{-1} is the diffusion coefficient of $N_2(A^3\Sigma_u^+)$ at 0°C under p_1 Torr, k cm^3s^{-1} is the collisional quenching rate coefficient of $N_2(A^3\Sigma_u^+)$ by N_2, k' cm^3s^{-1} is the collisional quenching rate coefficient of $N_2(A^3\Sigma_u^+)$ by C_6H_6, N_1 cm^{-3} is the density of gas molecules at 0°C under p_1 Torr, d cm is the gap length, a and b (=1 - a) are the number of gas molecule of the fraction of N_2 and C_6H_6 against the total number of gas molecules in the chamber. p_0 is the reduced gas pressure at 0°C. p_1 is taken to be 1 Torr. μ_1 is the first order constant that describes the density function of the metastables, that is to say, the first root of Fourier Radiation series given by the reflection coefficient R of metastable nitrogen molecules at the surface of electrode.

3. EXPERIMENTAL RESULTS

Figure 3 shows the obtained relationship between the effective lifetime τ_1 and the gas pressure p_0 with the gap length as the parameter in N_2 gas. The experimental data is plotted with the error bar of the standard deviation and in log-log scale the values increases approximately with a slope of unity against the gas pressure. The broken lines are given by the curve fitting procedure using the present results based on the theory [12]. Solid lines are the experimental value reported previously [7, 13] and are agree well each other. From this curves, the collisional quenching rate coefficient k of $N_2(A^3\Sigma_u^+)$ by $N_2(X^1\Sigma_g^+)$ is decided. However it shows the broken line for a value that is smaller approximately 37% than the previous values [7][13]. In the recommended value in nitrogen of us, the diffusion coefficient D_{m1} of $N_2(A^3\Sigma_u^+)$ and the collisional quenching rate coefficient k are determined 157 cm^2s^{-1}

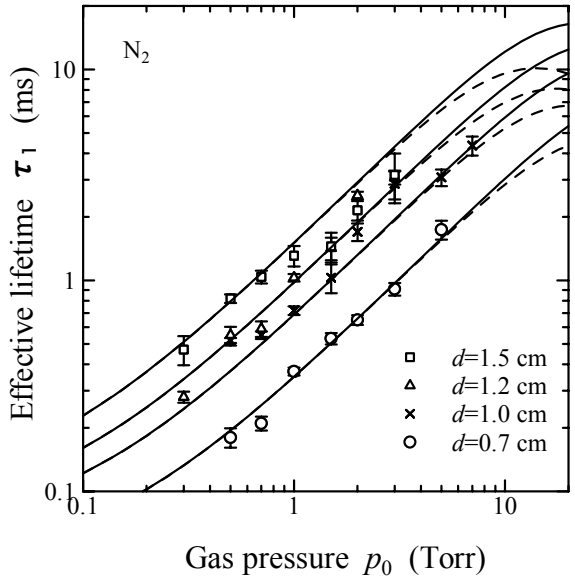

FIGURE 3. Effective lifetime τ_1 as a function of gas pressure p_0 for N_2.

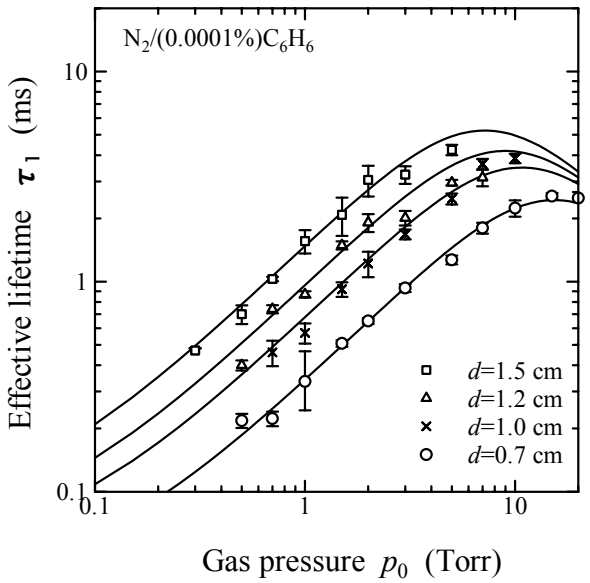

FIGURE 4. Effective lifetime τ_1 as a function of gas pressure p_0 for $N_2/(0.0001\%)C_6H_6$.

[13] and 3.7×10^{-17} cm^3s^{-1} [7], respectively. From this figure, it is estimated that the reflection coefficient R of $N_2(A^3\Sigma_u^+)$ at the electrodes is 0.28.

Similarly, the results on N_2/0.0001%C_6H_6 mixture gases are shown in Fig. 4. Though the deviation is found in the experimental value of the effective lifetime τ_1. However it increases almost proportionally against the gas pressure and decrease the gradient of the curves gradually. From this curve, the diffusion coefficient D_{m1}, the collisional quenching rate coefficient k' of $N_2(A^3\Sigma_u^+)$ by C_6H_6 and the reflection coefficient R are 157 cm^2s^{-1}, 3.3×10^{-10} cm^3s^{-1} and 0.16, respectively. It is understood that the value of k' is almost same with the one reported by Meyer *et al* [14].

4. CONCLUSIONS

The collisional quenching rate coefficient of $N_2(A^3\Sigma_u^+)$ by C_6H_6 is determined. The value is ensured the same order of O_2.

REFERENCES

[1] D.L.McCorkle, W.Ding, Cheng-Yu Ma and L.A.Pinnaduwage (1999). *J. Phys. D: Appl. Phys.,* 32, 46-54.

[2] K.Satoh, S.Hayashi, N.Kudoh, H.Itoh, H.Tagashira and M.Shimozuma (2002). *T. IEE Japan,* 122-A, 5, 479-484. [in Japanese]

[3] N.Goto, H.Kurimoto, S.Kudo and Y.Watanabe (2003). *IEEJ Trans. FM,* 123, 9, 900-906. [in Japanese]

[4] K.Kim, F.Tochikubo, S.Uchida and T.Watanabe (2006). *The 2006 Annual Meeting Record I.E.E. Japan,* 1-068. [in Japanese]

[5] A.N.Wright and C.A.Winkler (1968). Active Nitrogen, Academic Press.

[6] J.T.Herron (1999). *J. Phys. Chem. Ref. Data,* 28, 5, 1453-1483.

[7] S.Suzuki, H.Itoh, H.Sekizawa and N.Ikuta (1993). *J. Phys. Soc. Jpn.,* 62, 8, 2692-2697.

[8] S.Suzuki, H.Itoh, H.Sekizawa and N.Ikuta (1997). *Jpn. J. Appl. Phys.,* 36, 4744-4746.

[9] J.P.Molnar (1951). *Phys. Rev.,* 83, 933-940.

[10] J.P.Molnar (1951). *Phys. Rev.,* 83, 940-952.

[11] S.C.Haydon and O.M.Williams (1973). *J. Phys. B: Atom. Mol. Phys.,* 6, 227-231.

[12] S.Suzuki, H.Itoh, N.Ikuta and H.Sekizawa (1992). *J. Phys. D: Appl. Phys.,* 25, 1568-1573.

[13] S.Suzuki, H.Itoh, N.Ikuta and H.Sekizawa (2000). *Jpn. J. Appl. Phys.,* 39, 1333-1337.

[14] J.A.Meyer, D.H.Klosterboer and D.W.Setser (1971). *J. Chem. Phys.,* 55, 2084-2091.

CO_2 REFORMING OF CH_4 IN A NON THERMAL PLASMA REACTOR AT ATMOSPHERIC PRESSURE

F. Ouni, A. Khacef, J. M. Cormier

GREMI-Polytech'Orléans, 14 rue d'Issoudun, BP 6744, 45067 Orléans Cedex 2, France
e-mail: fakhreddine.ouni@univ-orleans.fr

ABSTRACT

Hydrogen-rich gas can be efficiently produced in compact plasma reformers by the conversion of a variety of hydrocarbon fuels including natural gas and gasoline. This article describes a first approach in non thermal plasma reforming of methane with carbon dioxide. Experiments have been carried out in a compact device operating at low consumed power (100 - 200 W). Experiments demonstrated clearly the plasma ability to convert CO_2 and CH_4. A high level of hydrogen was obtained ($[H_2]$ up to 25 %). System efficiency was investigated as a term of both CO_2 and CH_4 conversion and syngas production

1 INTRODUCTION

The evolution of pollution problem and the increase of greenhouse gases emission (especially CO_2) required serious solutions [1]. Transforming CO_2 into recoverable products has become a major focus of researchers [2] and CH_4 reforming with CO_2 has become the object of several fundamental researches [3]. The reforming process could be described by the main following reaction:

$$CH_4 + CO_2 \leftrightarrow 2H_2 + 2CO \qquad \Delta H^0 = 247.0\,\text{kJ mol}^{-1} \qquad (1)$$

which is strongly endothermic and in conventional technology it requires high temperature (873 - 1223 K) [4] .

Recently, due to their compactness, efficiency and energetic low cost, non thermal plasma reformers overcome conventional technology drawback and give an attractive alternative for CO_2 and CH_4 transformation.

In this paper, we present a methane dry reforming process initiated by a 50 Hz AC discharge at room temperature and atmospheric pressure. The effect of the feeding reactor parameters was investigated. System efficiency was evaluated as a term of reactants conversion and syngas production.

2 EXPERIMENTAL

2.1. The non thermal plasma reactor

The plasma reactor [5] has a cylindrical configuration (figure 1). This geometry was chosen because of its simplicity. Reactor body was a Pyrex tube (220 mm length, 32 mm external diameter) inserted between two stainless covers. Pyrex was used to enable us to visualize plasma evolution and to perform spectroscopy measurements. The plasma reactor consists of two graphite vertical electrodes with an adjustable gap. The discharge column is a plasma string, with a visible diameter less than one millimeter stabilized in the gas flow between electrodes (figure 1). The power supply device used in these experiments consists of a leakages fluxes transformer made by Aupem SEFLI Company, details are given in ref [6]. Current and voltage measurements were achieved using a Hall Effect probe and voltage divider (ratio of 0.01), respectively. The output signals were transmitted to a transient digitizer (Tektronix TDS 3034B) interfaced with a personnel computer. The mean electrical power, $P = \frac{1}{T}\int u(t)\,i(t)\,dt$, is obtained by averaging results over a large number of discharges.

2.1 Diagram of the experimental setup

Figure 2 shows the diagram of experimental setup. All experiments were conducted at atmospheric pressure and room temperature. CO_2 and CH_4 are mixed, before injection in the plasma reactor. The gaseous products were analysed online and quantified using two techniques: micro gas chromatography (µGC, Varian CP2003-P) and Fourier Transform Infra Red spectroscopy (FTIR, Nicolet Magna-IR 550 series II). The µGC analyzer was equipped with Molsieve 5Å and PoraPlot Q columns. Both columns were equipped with thermal conductivity detector (TCD) calibrated with standards of known composition. The major gas components identified were H_2, CO, and no transformed CH_4 and CO_2. Small amounts of C_2 hydrocarbons (C_2H_2, C_2H_4, and C_2H_6) have been detected with concentrations lower than 5% in all cases studied.

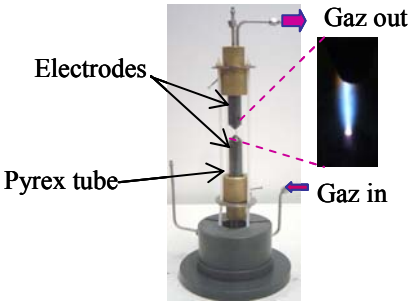

FIGURE 1: Schematic of the plasma reactor and photography of the produced discharge.

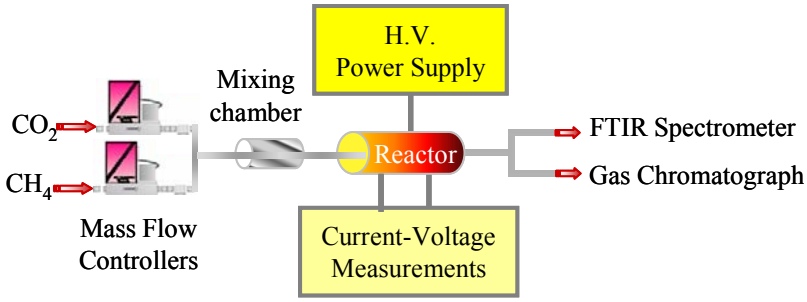

FIGURE 2: Synoptic of the experimental setup.

3 RESULTS AND DISCUSSION

3.1 Chemical analysis

As shown in figure 3 the products identified in the reactor outlet are: CO, light C_2 hydrocarbons (C_2H_2, C_2H_4) and non transformed CH_4 and CO_2. H_2 can't be identified via FTIR, Thus it was identified and quantified by gas chromatography.

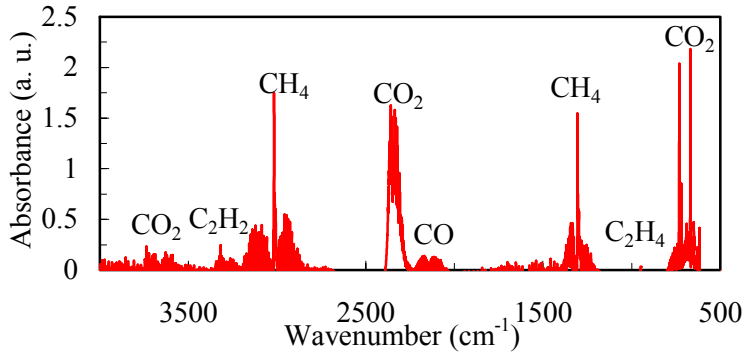

FIGURE 3: Typical FTIR spectrum obtained by plasma processing of CO_2-CH_4 (50% - 50%) mixture (Average electrical power: 180 W & Flow rate: 5 l/min).

3.2 Feeding parameters influence on the H_2 and CO distribution

Figure 4 shows an example of H_2, CO, outlet reactor concentrations as a function of the inlet $[CO_2]/[CH_4]$ with the total flow rate as a parameter. Results showed that CO and H_2 concentrations depended strongly on the feeding reactor parameters. Outlet syngas

concentration decreases with the increasing the inlet flow rate. It could be explained by the decrease of the reactant residence time in the reactive zone. We note that the maximum syngaz production was obtained for the inlet $[CO_2]/[CH_4]$ of about 1.5. Besides in the major studied cases CO concentration seems to be higher than H_2 concentration. This phenomenon could be attributed to the simultaneous water-gas shift (WGS) reaction (2) as demonstrated in catalytic process by R Martinez and al in ref [7].

$$CO_2 + H_2 \leftrightarrow CO + H_2O \qquad (2)$$

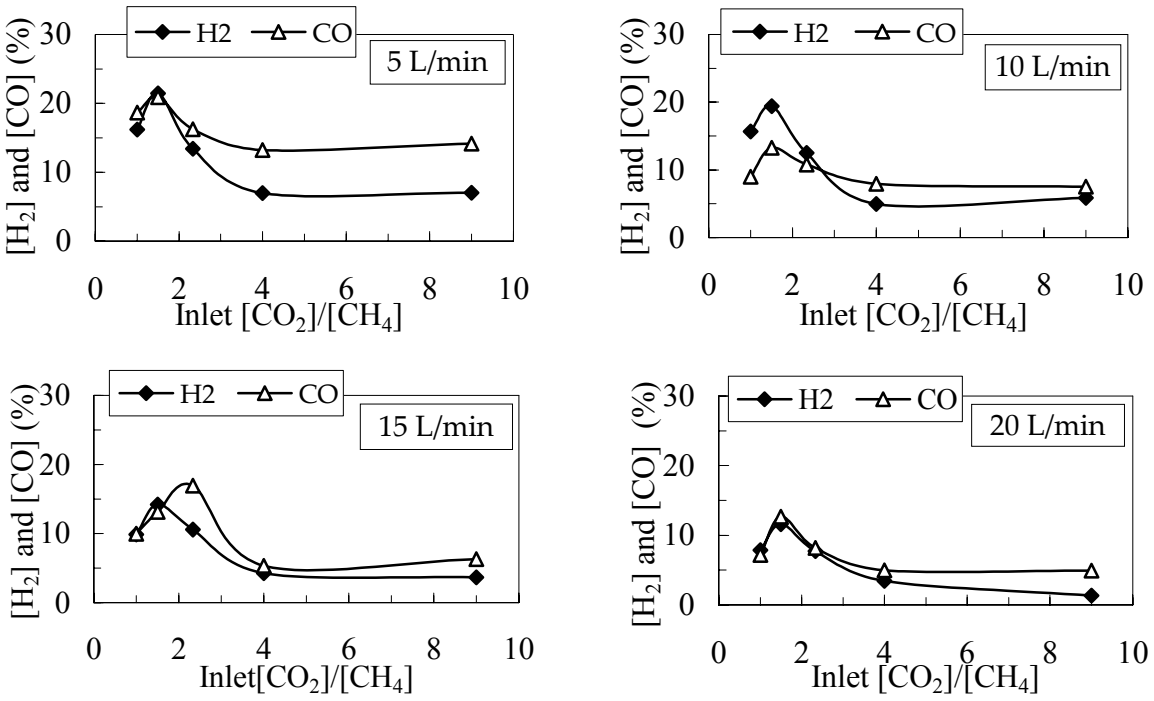

FIGURE 4: Evolution of H_2 and CO concentrations as a function of the feeding reactor parameters (Average electrical power: 180 W).

3.3 Feeding parameters influence on CH_4 and CO_2 conversion

CO_2 and CH_4 conversion rate were calculated respectively using the following expressions:

$$\tau_{CO_2} = \frac{[CO_2]_i - [CO_2]_f}{[CO_2]_i}, \qquad \tau_{CH4} = \frac{[CH_4]_i - [CH_4]_f}{[CH_4]_i}$$

where, brackets design concentrations and the subscripts i and f design initial and final states, respectively.

Figure 5 describes the evolution of both CO_2 and CH_4 conversion. The concept reactor leads to convert a large amount of reactants. Conversion rate is up to 60 %. Both CO_2 and CH_4 conversion rate are strongly influenced by the feeding reactor parameters. As it shown on figure 4, maximum conversion was obtained under an inlet $[CO_2]/[CH_4]$ ranging between 1 and 1.5 and an inlet flow rate of about 5 L/min.

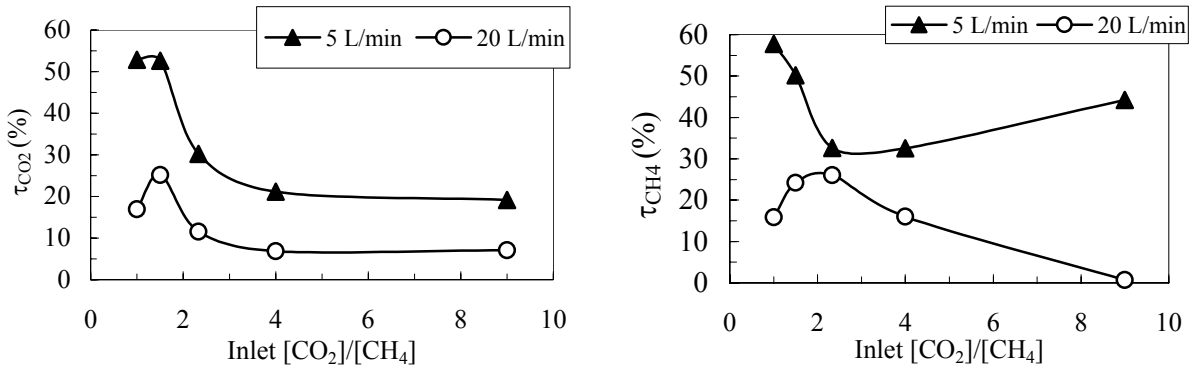

FIGURE 5: CO_2 and CH_4 conversion rate evolution as a function of the feeding reactor parameters (Average electrical power: 180 W)

Chemical analysis demonstrated clearly the ability of non thermal plasma for initiating chemical reactions and converting CO_2 and CH_4 into recoverable products. Bodrov and Apel'baum [8] propose a mechanism which demonstrated different produced species in dry methane reforming reaction in non thermal plasma. This proposed mechanism will be used to modulate chemical process in our operator conditions.

CONCLUSION

This series of experiments is a first approach to convert CO_2 and CH_4 into syngas and recoverable products in non thermal plasma. The concept plasma reactor demonstrated its ability to initiate chemical reaction. A high level of conversion was obtained (up to 60 % for both CH_4 and CO_2). Therefore more work is required to improve the plasma reactor efficiency and then both conversion and syngas yield.

REFERENCES

[1] Manahan, S. (1994). Environmental Chemistry, *Lewis Publishers: Boca Raton, FL, 6th ed*., 338.

[2] Verykios, X.E. (2003). Catalytic dry reforming of natural gas for the production of chemicals and hydrogen. *Int. J. Hydrogen Energ*., 28,1045–1063.

[3] Kurz, G., Teuner, S.(1990). *Erdol. Kohle.* 43, 171.

[4] Chubb, T.A. (1980). Characteristics of CO_2-CH_4 reforming-methanation cycle relevant to the solchem thermochemical power system. *Solar Energ.,* 24, 341.

[5] Ouni, F., Cormier, J.M., Khacef , A., (2006).Modeling of a nitrogen glow discharge at atmospheric pressure. *Proceeding of 5th International Symposium of Non-Thermal Plasma Technology, CD Rom INSTPT 5.*

[6] Martinie, O. (2000). Caractérisation physique et chimique de décharge hors équilibre. *PhD thesis, Orleans University*.

[7] Martınez, R., Romero, E., Guimon, C., Bilbao, R. (2004). CO_2 reforming of methane over coprecipitated Ni–Al catalysts modified with lanthanum., *App. Catal. A: General*, 274, 139–149.

[8] Bodrov, I. M., Apel'baum, L. O. (1967). *Kinet. Katal.* 8, 379.

Paper number

GENERATION OF NITRIC OXIDE BY PULSED ARC DISCHARGE

S. Sakai[1], T. Namihira[1], D. Wang[1], T. Kiyan[1], H. Akiyama[1], K.Okamoto[2], N. Teshima[3] and K. Toda[4]

1 Graduate School of Science and Technology, Kumamoto University, 2-39-1 Kurokami, Kumamoto 860-8555, Japan, sakai@st.cs.kumamoto-u.ac.jp

2 Department of Intensive and Critical Care Medicine, Shinshu University School of Medicine, 3-1-1 Asahi, Matsumoto city, Nagano 390-8621, Japan

3 Department of Applied Chemistry, Aichi Institute of Technology, 1247 Yachigusa, Yakusa Cho, Toyota city, Aichi 470-0392, Japan

4 Department of Environmental Science, Kumamoto University, 2-39-1 Kurokami, Kumamoto 860-8555, Japan,

ABSTRACT. Recently, Nitric oxide (NO) is increasingly being used in medical treatments for some illness related lung. Currently a system of NO inhalation has a gas cylinder of N_2 mixed with a high concentration of NO. This method is potentially risky due to the possibility of accidental leak of NO from the cylinder. Therefore, an on-site generation of NO would be highly desirable for patient, who is suffering lung disease, and medical doctors. In this paper, the dependences of NO generation using pulsed arc discharge on polarity of charging voltage into the discharge capacitor, a discharge capacitance value and a pulse repetition rate have been reported. As the results, it is obvious that the positive charging voltage into capacitor and the smaller capacitance value of discharge capacitor are suitable condition for NO generation by pulsed arc discharge.

1. INTRODUCTION

In 1987, Palmar et al found that nitric oxide (NO) works as an endothelium-derivered relaxing factor (EDRF) [1]. NO has been widely used in medical applications since then. Recently, inhaled NO (iNO) has been becoming a sufficient treatment for high blood pressure, acute respiratory distress syndrome and some lung diseases. Fig. 1 shows a patient under medical treatment for ARDS with all accessory equipments of iNO system including gas cylinders of N_2 mixed with NO, O_2 and air, a gas analyzer which detects NO and nitric dioxide (NO_2), a humidifier and water trap [2]. Present iNO systems consist of a gas cylinder of N_2 mixed with a high concentration of NO. The concentration of NO in the gas cylinder is typically between about 500 ppm [3] to 800 ppm [4]. However, this arrangement is potentially risky due to the possibility of accidental leak of NO from the gas cylinder. The presence of NO in air leads to the formation of NO_2, which is well known to be harmful to human being. Therefore, an on-site generation of NO would be of interest to the medical doctors and be desirable for the patients who struggle with the diseases related a lung.

Recently, Namihira et al have reported the production of NO using pulsed arc discharge [5-8] and the development of a trial NO production system for medical applications [9, 10]. In

the present work, the dependence of NO generation on polarity of charging voltage into the discharge capacitor, capacitance value of discharge capacitor and pulse repetition rate have been studied to miniaturize of the NO production system.

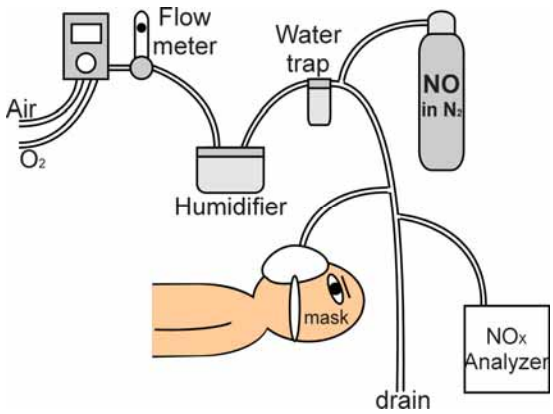

FIGURE 1. NO supply system for patients with ARDS

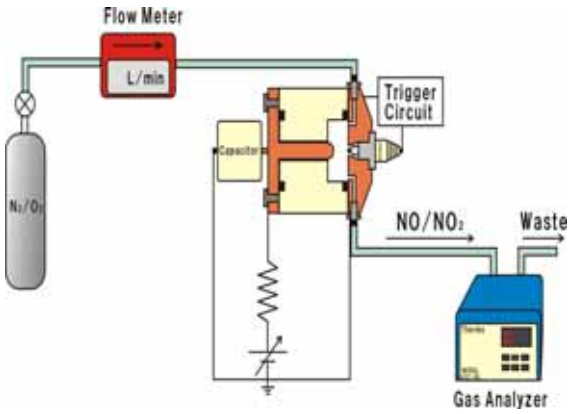

FIGURE 2. Experimental set-up

2. EXPERIMENTAL SETUP AND RESULTS

Fig. 2 shows experimental setup for NO generation including the pulsed arc discharge reactor, a charging capacitor (0.1 to 4.0 nF), a dc power supply (HDV-20K30SX, Pulse Electronic Engineering Co., Japan), a limiting resistor (2 to 10 MΩ), and a spark plug connected to a trigger pulse circuit. In the experiment, a rod to plate electrode geometry was utilized as a discharge reactor. The outer diameter of and the length of the discharge reactor were 60 mm and 100 mm, respectively. The rod and the plate electrodes were made of brass. The brass rod ending with a hemisphere had a diameter of 10 mm. The gap distance between the rod and the plate electrodes was fixed at 5 mm. The charging voltage to the capacitor was fixed at 13 kV, which is about 80 % value of self-breakdown voltage of the discharge reactor. The pulsed arc discharge between the rod and the plate electrodes were initiated by the UV radiation from the discharge between the spark plug and the plate electrode [11]. The applied voltage to the rod electrode was measured using a voltage divider (EP-50K, Pulse Electronic Engineering Co., Japan), which was connected between the rod (High voltage side) and the plate (Ground side) electrodes. The current through the discharge reactor was measured using a current transformer (Pearson current monitor Model 2878, Pearson Electronics, USA), which was located the return current to ground. In the experiment, a dry air was fed into the discharge reactor with 300 mL/min of the gas flow rate. In this paper, the dependences of NO generation on the polarity of charging voltage, the capacitance value of charging capacitor and the pulse repetition rate were investigated to find the best discharge condition.

3. EXPERIMENTAL RESULTS

Fig. 3 shows the typical waveforms of the applied voltage to and the discharge current into the discharge reactor during the pulsed arc discharge in the case of using 2 nF capacitor. It will be observed from Fig. 3 that the applied voltage and the discharge current waveforms show damped oscillations. Fig. 4 shows the concentrations of NO and NO_2 as a function of the pulse repetition rate for both of positive and negative charging voltages. In this experiment, 1 nF of capacitor was used for both cases. The measurement at 0 pps was taken when the pulsed arc discharge was not applied to the mixture of N_2 and O_2. From Fig. 4, the concentrations of NO and NO_2 are in direct proportion to the pulse repetition rate since the

input power into the discharge increased with increasing the pulse repetition rate. Fig. 5 shows the dependences of the NO proportion calculated from $NO/(NO+NO_2)$ on the pulse repetition rate for the both of positive and negative charging voltage. It will be observed from Fig. 5 that the NO proportion increased with increasing the pulse repetition rate and saturated over 25 pps of the pulse repetition rate. At the same pulse repetition rate, the higher NO proportion was given by the positive charging voltage. For the medical applications, 100 % of NO proportion would be required. Therefore, the charging voltage with positive polarity was chosen for NO generation in this paper. Fig. 6 shows the concentration of NO as a function of the pulse repetition rate for the different capacitances. The concentrations of NO and NO_2 (not shown for brevity) increased linearly with increasing the pulse repetition rate due to increasing the input energy into the discharge. Likewise, the concentrations of NO and NO_2 increased with increasing capacitance at a fixed pulse repetition rate. Fig. 7 shows the dependence of NO concentrations on the averaged consumption power of the dc supply for different capacitances. The consumption power (P, in Watts) was calculated from

$$P = \frac{1}{2} \times C \times V^2 \times f \quad (1),$$

where C, V and f are the capacitance value (in F) of capacitor, the charging voltage (in V) to the capacitor and the pulse repetition rate (in pps). It will be observed from Fig. 7 that for a given concentration of NO, the power requirement decreased with decreasing capacitance. This could be due to the faster rise time of the discharge current in the case of smaller capacitor. Therefore, a smaller capacitance led to higher energy efficiency for NO production. Fig. 8 shows the NO proportion as a function of the input power into the pulsed arc discharge for the different capacitances. From Fig. 8, the NO proportion increased with increasing the input power and saturated at 84 % over 2.0 W for different capacitance value.

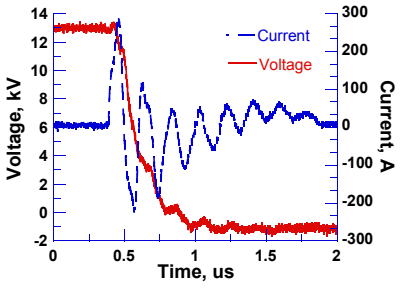

FIGURE 3. Waveforms of applied voltage and discharge current.

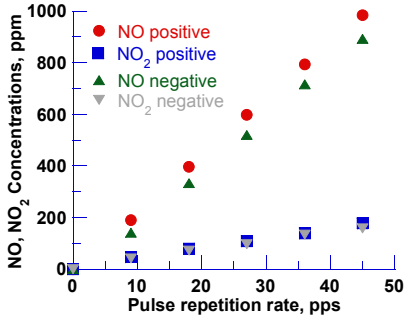

FIGURE 4. Concentrations of NO and NO_2 as a function of pulse repetition rate for both of positive and negative charging voltages.

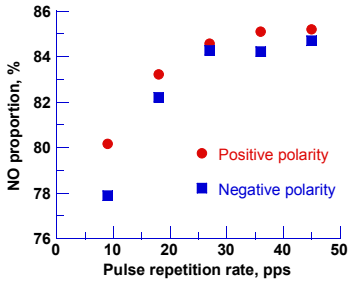

FIGURE 5. Dependence of NO proportion on pulse repetition rate calculated from Fig. 4.

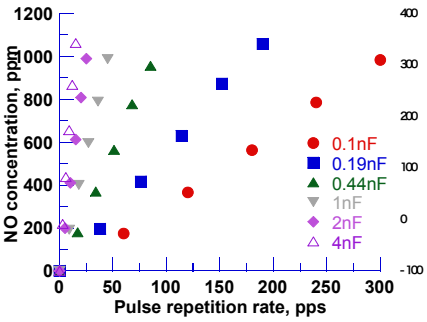

FIGURE 6. Dependence of NO concentration on pulse repetition rate for different capacitance.

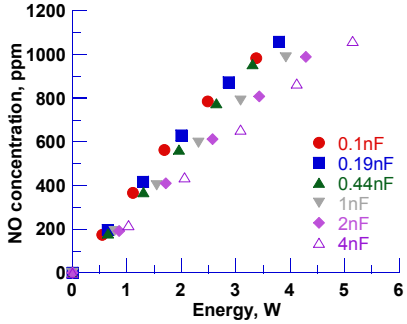

FIGURE 7. Dependence of NO concentration on input power for different capacitance.

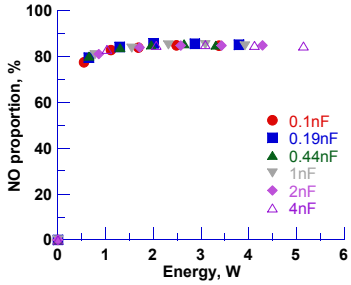

FIGURE 8. NO proportion as a function of input power for difference capacitance.

4. CONCLUSIONS

Production of nitric oxide using pulsed arc discharge for medical application was studied in this paper. The results are as follows:

1) Concentrations of NO and NO_2 increase linearly with the pulse repetition rate (=input power into discharge).
2) At same pulse repetition rate (=input power), positive polarity of charging voltage give higher concentration of NO.
3) Smaller discharge capacitor consumes lower energy for NO generation.

*This study was supported by Industrial Technology Research Grant Program in ’05 from New Energy and Industrial Technology Development Organization (NEDO) of Japan.

REFERENCES

[1] R.M. Palmer, A.G. Ferrige and S. Moncada, “Nitric oxide release accounts for the biological activity of endothelium-derived relaxing factor”, Nature, Vol.327, pp. 524-556, 1987
[2] NO research association, “Basic and clinical of NO research”, vol.2, pp. 21-28, 1996 (In Japanese)
[3] O. Stenqvist, B. Kjelltoft and S. Lundin, “Evaluation of a new system for ventilatory administration of nitric oxide”, Acta Anaesthesiologica Scandinavica, Vol.37, pp. 687-691, 1993
[4] I. Kukita, K. Okamoto, T. Sato, Y. Shibata, K. Shiihara and K. Kikuta, “Evaluation of Mapleson systems for administration of inhaled nitric oxide”, Journal of Anesthesia, Vol.10, pp. 44-48, 1996
[5] T. Namihira, S. Tsukamoto, D. Wang, S. Katsuki, H. Akiyama, R. Hackam and K. Okamoto, “ Production of nitric monoxide in dry air using pulsed discharge”, 12th IEEE International Pulsed Power Conference, Monterey, USA, Vol.2, pp. 1313-1316, 1999
[6] T. Namihira, S. Tsukamoto, D. Wang, S. Katsuki, R. Hackam, K. Okamoto and H. Akiyama, “Production of nitric monoxide using pulsed discharges for a medical application”, IEEE Transactions on Plasma Science, Vol.28, No.1, pp. 109-114, 2000
[7] T. Namihira, K. Shinozaki, H. Hori, S. Tsukamoto, S. Katsuki, H. Akiyama, K. Okamoto and R. Hackam, “Production of NO for medical applications using pulsed power technology”, 2nd International Symposium on Nonthermal Medical/Biological Treatments Using Electromagnetic Fields and Ionized Gases, Portsmouth, USA, Symposium Record Abstracts, p. 35, 2001
[8] T. Namihira. S. Katsuki, R. Hackam, H. Akiyama and K. Okamoto, ”Production of nitric oxide using a pulsed arc discharge”, IEEE Transactions on Plasma Science, Vol.30, No.5, pp. 1993-1998. 2002
[9] T. Namihira, D. Wang, S. Katsuki, H. Akiyama and K. Okamoto, “Development of NO generator for medical applications”, IEEJ Transactions on Electronics, Vol.124-C, No.1, pp.215-216, 2004. (In Japanese)
[10] T. Namihira, D. Wang, S. Katsuki, H. Akiyama and K. Okamoto, “Development of NO production system for medical applications”, 15th International Conference on Gas Discharges and Their Applications, Toulouse, France, vol.2, pp.725-728, 2004.
[11] S.L. Moran and L.W. Hardesty, “High-repetition-rate hydrogen spark gap”, IEEE Transactions on Electron Devices, Vol.38, No.4, pp.726-730, 1991.

DESTRUCTION OF VOCS IN AIR BY BARRIER DISCHARGE

M.Wronski, B.Polednik

Department of Civil Engineering,
Lublin University of Technology
Nadbystrzycka 40, Lublin, 20-618, POLAND

ABSTRACT. The results of experimental investigations of VOCs decomposition in dielectric barrier discharge are given. Gas flow rate changed from 20 to 300 dcm^3/h. Concentrations of VOC were varied from 50 to 500 ppm. The degree of VOCs decomposition depends on kind of compound, gas flow rate, applying voltage reached 65 -96 %. An analysis of gas composition at the reactor inlet and outlet has been performed with a gas chromatography. The VOCs had been decomposed to carbon dioxide and water, mainly.

1. INTRODUCTION

Many various industrial processes generate Volatile Organic Compounds (VOCs). Waste gases and off-air from chemical processing, plastic manufacturing and processing, mechanical engineering, electronic, paper printing, paint manufacturing and other industries can contain some amounts of VOCs like aromatic hydrocarbons, esters or alcohols considered as pollutants. About 50% of VOCs is due to the painting industry, printing industry, metal degreasing and other activities employing organic solvents. To avoid a risk to exceed a threshold or explosion limits, the concentration of solvent vapours in the circulating air is kept low and can never be higher than a half of the flammability limit at working conditions. These industrial ventilation streams are classified as high volume – low concentration (HVLC) gas streams.

Several processes are used to lower the emission of VOCs: catalytic decomposition, absorption on active coal and biological degradation methods. Except the condensation, all other processes should be less or more completed by a final combustion of concentrated vapours or an incineration of diluted ones. The catalytic incinerators can be easily poisoned by sticking varnish droplets. The commonly used thermal incinerators are also very expensive: one has to heat the gas up to about 850^oC to mineralize all organic compounds. A fuel addition is necessary and even with an obligatory heat recovery, the cost of installation is high [1].Gas phase hazardous organic wastes can be destroyed by oxidation to non-hazardous compounds, such as carbon dioxide and water.

The application of non-thermal plasma for VOCs decomposition has been widely studied in the last few years [2,3]. However, chemical mechanisms of VOCs decomposition in low temperature plasma are not yet well understood, especially those concerned in the treatment of aromatic hydrocarbons where a large number of reaction mechanism are possible. Non-thermal plasma processing is an emerging technology for the decomposition of Volatile Organic Compounds (VOCs) in atmospheric-pressure gas streams. The presence of high energy electrons (5-10 eV) and reactive chemical species cause activation of chemical reactions. In non-equilibrium plasma most of electrical energy (up to 99.9%) goes into the production of energetic electrons, rather than into gas heating [5]. The most effective way of oxidizing organics is to use highly reactive species, i.e. reactant with a high oxidizing potential, such as OH, O, H, O_3, and H_2O_2. The hydroxyl radical is especially known to play an important role in oxidative degradation of organic compounds [6]. O-atoms are the active

species for degradation of VOCs and it is clear that it will be limited by the amount of high energy electrons.

$$O_2 + e = 2O + e \quad (1)$$

In presence of water, the reactive species are O-atoms and OH radicals in addition to free electrons and a part of the O-atoms produced are used to dissociate water:

$$H_2O + e = H + OH + e \quad (2)$$
$$H_2O + O(1D) = 2OH \quad (3)$$

EXPERIMENTAL

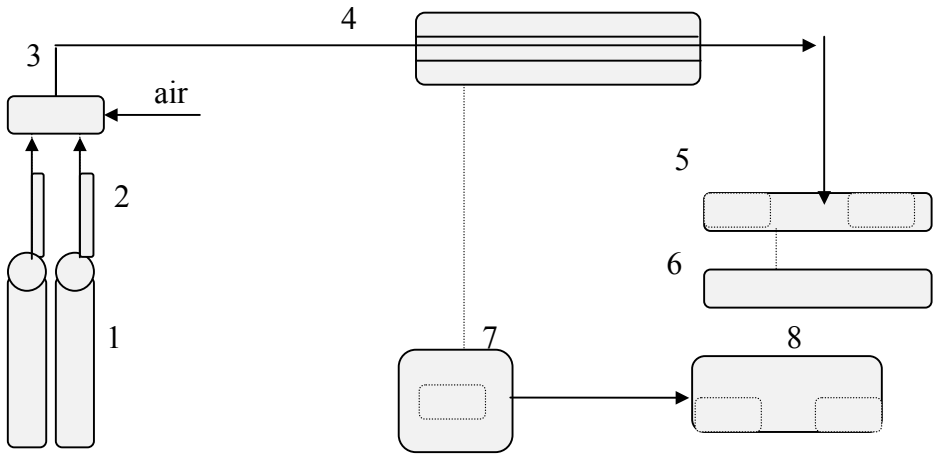

FIGURE 1. Experimental set-up: 1- synthetic air bottles, 2- rotameters, 3- bubbling system, 4-reactor, 5 – mass spectrometer, 6 – gas analyzer, 7 – HV feeder, 8 – computer

All the experiments were performed in a flow-through configuration. A general view of the experimental system is presented in Figure 1 (high voltage power supply up to 20 kV, oscilloscope, gas mixer unit, flow gas controller, dielectric barrier discharge reactor , gas chromatograph and gas analyzer IMR 3000P). The experimental variables were the applied voltage, the gas flow rate (20 to 300 dm^3/h) and the organic compound vapour (concentrations of VOC were varied from 50 to 500 ppm). The coaxial reactor was constructed of the 316 stainless steel tube (diameter 50 mm and length 500 mm). The distance between the grounded electrode and dielectric material was 3.0 mm. Electrodes were made from glass or quartz. As carrier gas synthetic air ($20\%O_2+80\%N_2$) were used. Bubbling method was used to set VOC and water in the gas stream. In part of experiments the polluted gas was slightly wet (up to 30% of relative humidity) and it had an ambient temperature. The gas flow rate was verified by rotameter and power of discharge by Lissajous figure. No other energy sources were applied. An analysis of gas composition at the reactor inlet and outlet were performed with a gas chromatography. Waste gas analyzer IMR 3000P with chemical cells for determination balance of products was used, too.

RESULTS

Figures 2-4 present typical results of investigation into an effect of various parameters on the process of the VOCs decomposition in dielectric barrier discharges. The degree of decomposition achieved depended on the magnitude of voltage, concentration of individual compound, water vapour presence, gas flow rate and the chemical nature of the vapour. The maximum percentage decomposition was achieved with a minimum flow rate and maximum voltage for all organic compounds.

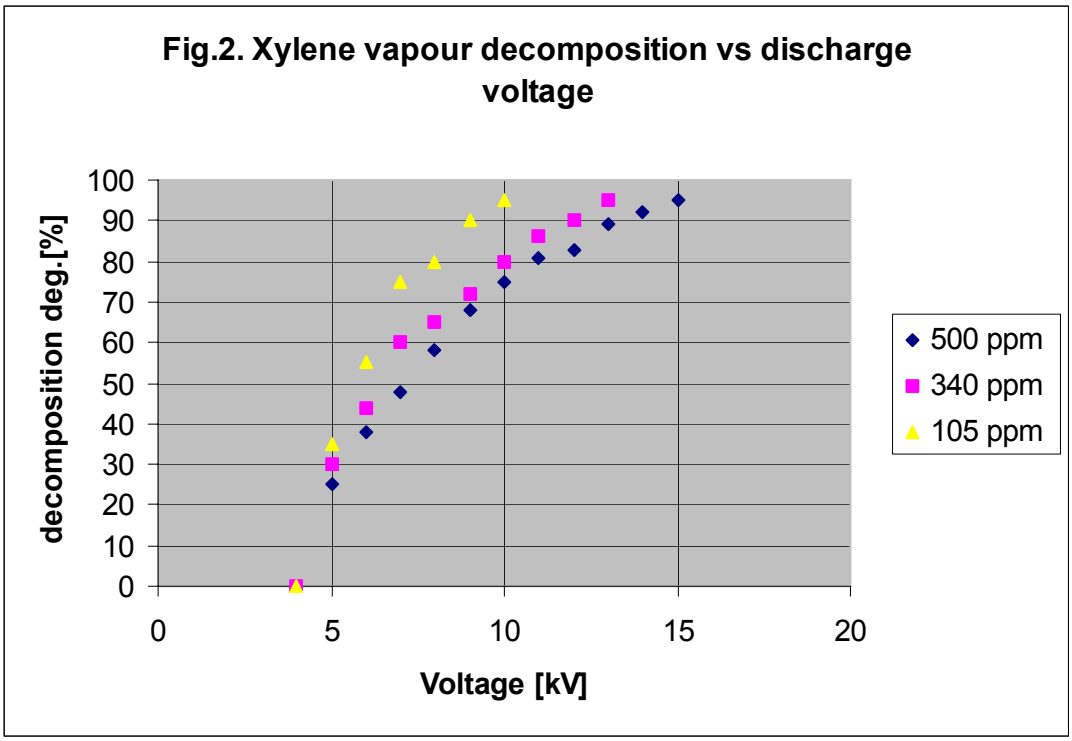

FIGURE 2. Figure shows a dependency of xylene decomposition efficiency vs voltage discharge in synthetic air ($20\%O_2+80\%N_2$) for various start concentrations. For 95% efficiency of xylene decomposition 10.0 kV (for 105 ppm), 13.5 kV (for 340 ppm), and 15.0 kV (for 500 ppm) are necessary.

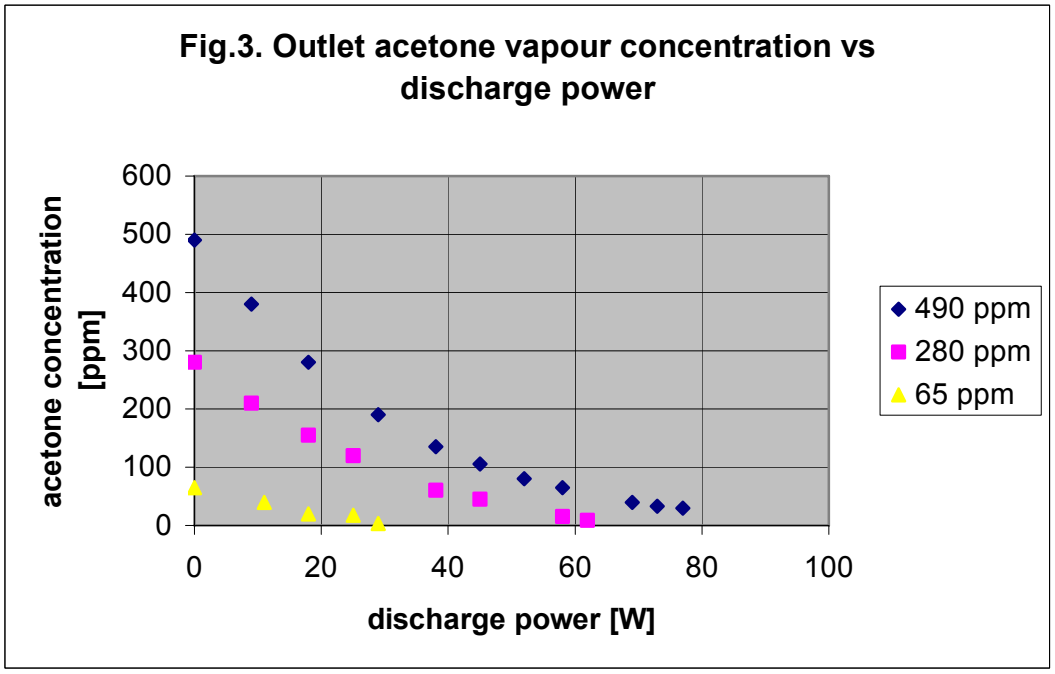

FIGURE 3. Figure shows that energetic cost of plasma treatment of acetone synthetic air ($20\%O_2+80\%N_2$) for various start concentrations. Higher a start concentrations for a rate decomposition more than 90% need much more power discharge, but for the other hand energy efficiency significant rises with VOC concentration. For an acetone conversion rate R=50 :

- 12W/32ppm = 0.375 W/ppm (for start concentration 65 ppm)
- 20W/140ppm = 0.143 W/ppm (for start concentration 280 ppm)
- 24W/250ppm = 0.096 W/ppm (for start concentration 500ppm), is needed.

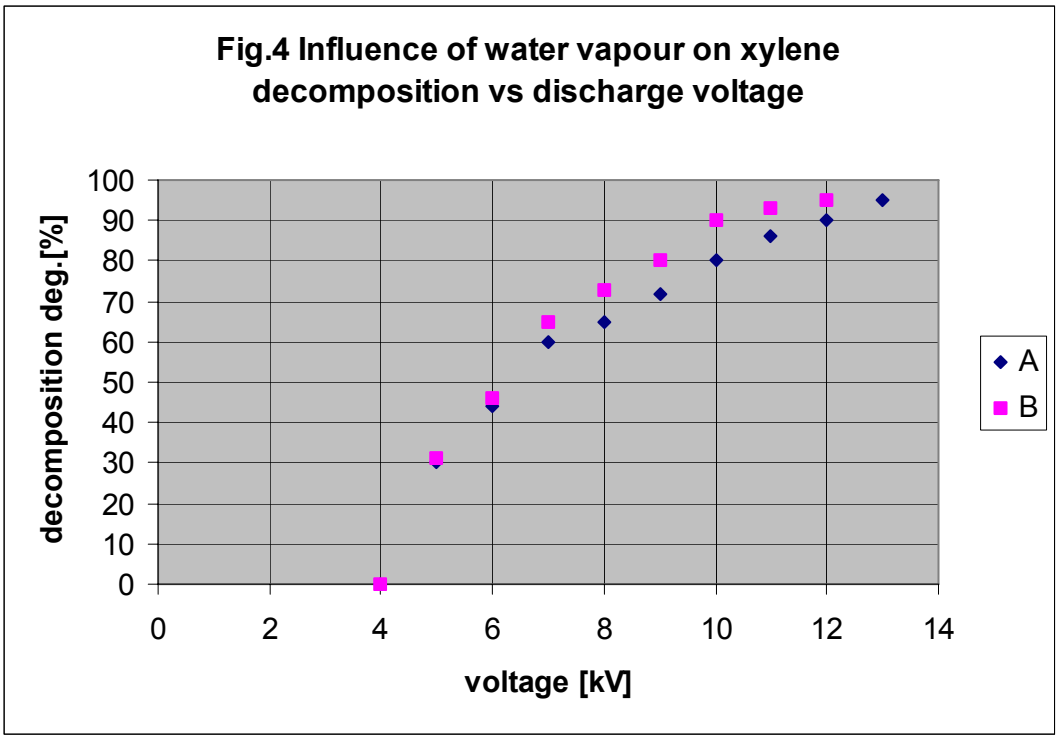

FIGURE 4. Figure shows a influence of water vapour on xylene decomposition efficiency vs voltage discharge, **A** - synthetic air (20%O_2+80%N_2) + 340 ppm of xylene**, B** – air (40% of relative humidity) + 340 ppm of xylene . Temperature 293K.

CONCLUSIONS

In dielectric barrier discharge (DBD) gas phase hazardous organic wastes can be decomposed by oxidation to non-hazardous compounds, such as carbon dioxide and water. Degree of the VOC decomposition mainly depends on the amount of energy supplied into a gas. Along with the growing feeding voltage, the degree efficiency of the VOCs decomposition increases and depends on chemical nature of individual organic compound and gas flow rate. Presence of water vapour increases the degree of the VOCs decomposition.

ACKNOWLEDGMENT

This work was supported by Ministry of Scientific Research and Information Technology (Poland) Grant PB1118/T09/2003/25

RFERENCES

[1] Paur H.R.(1992) *Non-Thermal Plasma Techniques for Pollution Control*, eds. B.M.Penetrante and S.E. Schulthesis, Berlin, Springer-Verlag, pp.277-289.
[2] Oda T., Takahashi T., Tada K.(1999) *IEEE Trans. on Industrial. Aplication*, 35-2, p.373
[3] Vertriest R., Morent R,, Dewulf J., Leys C. and van Langenhove H.(2003) *Plasma Source and Science Technology*, 12, pp.412-416.
[4] Yamamoto T. at al(1992)*IEEE Trans*., vol 28, nr 3, pp. 528-534.
[5] Harkness J.B.L., Fridman A.A.(1999) *NCASI Technical Bulletin*, No. 797.
[6] Sun B., Sato M, Clements J.S.(1999) *Journal of Applied Physics*, 32, pp.1908-1915.

Paper number

OZONE FORMATION IN DC CORONA DISCHARGE FED BY CARBON DIOXIDE IN FLOWING REGIME

J. Országh[1], J. D. Skalný[1], Š. Matejčík[1], N. J. Mason[2] and A. Stoica[3]

[1] *Department of Experimental Physics,*
Faculty of Mathematics, Physics and Informatics, Comenius University
Mlynská dolina F-2, 842 48 Bratislava, SLOVAKIA
[2] *Department of Physics and Astronomy,*
The Open University
Walton Hall, MK7 6AA Milton Keynes, UNITED KINGDOM
[3] *Department of Physics,*
Ovidius University
Av Mamaia 124, 8700 Constanta, ROMANIA

ABSTRACT. The mechanism of ozone formation in DC corona discharges of both polarities fed by pure carbon dioxide was studied. The influence of ozone concentration on discharge parameters in flowing regime, especially onset voltage, breakdown voltage and the current-voltage (CV) characteristics was investigated. The ozone concentration was measured by UV absorption spectrometry.

1. INTRODUCTION

Ozone is widely used gas especially in various industrial processes (paper and fabric production) and its disinfective and germicidal impacts are also often utilized. These are important arguments why it is necessary to study the process of generation and destruction of this gas. Moreover the basic research in the field of astrophysics is also focused to atmospheres of planets where ozone can be present. The study of plasma initiated chemical processes in the discharges fed by gasses present in the atmosphere of these planets can be sometimes applied for the interpretation of effects observed in atmosphere of planets [1-3]. Carbon dioxide is the typical representative of such gases. The concentration of CO_2 is very low in atmosphere of Earth, anyway as a good infrared absorber in the Earth atmosphere, the concentration of CO_2 considerably affects phenomena known as a greenhouse effect. In contrast the content of carbon dioxide in Martian atmosphere is absolutely dominant. Hence the dissociation of CO_2 could be a source for oxygen and ozone production in Martian atmosphere [4]. The idea to use such conversion of CO_2 an electrical discharge was appeared recently [3]. Several studies of CO_2 decomposition in corona discharges have been published over the last two decades both in pure carbon oxide and/or its mixtures with other gases, predominately air.

Recently we have presented study of products contained in pure CO_2 and mixtures CO_2 + O_2 treated by negative corona discharge with particular emphasis on the production of ozone [5]. The discharge current in pure CO_2 was found to be highly sensitive to the presence of trace concentrations of molecular oxygen and to changes in the flow speed through the discharge. The ozone concentration increases monotonically with increasing content of oxygen in the mixture with carbon dioxide whereas the CO concentration exhibits a flat maximum for oxygen concentrations around of 4%. The remarkable sensitivity of the

discharge current on the flow rate has been ascribed to changes in concentration of ozone produced in the discharge.

The goal of presented contribution is to study an effect of ozone formation in DC corona discharge fed by pure CO_2 on the properties of the discharges both in positive and negative polarities**.**

2. EXPERIMENT

The experimental apparatus scheme is shown in the figure 1. Two cells containing identical coaxial cylindrical electrodes systems (stainless steel inner electrode of diameter 125 μm and stainless steel outer electrode of diameter 16 mm), were used in experiments. Active part length of the discharge tube was 10 cm. DC corona discharge was generated in one of the tubes; the second has been used as a comparative tube. Both were placed into cell compartment of Shimadzu UV spectrometer, which was employed for measurement of the optical transmittance of gas treated in cell containing the active discharge electrodes. The transmittance value was recorded simultaneously with discharge voltage and current by PC. Using Lambert-Beer formula the ozone concentration in the discharge gap was calculated. The flow rate of the gas was kept constant by mass flow controller in the range 5 – 200 cm^3/min. Glassman high voltage power supply unit was used to feed the system of discharge electrodes. The measured data of discharge current and the voltage on electrodes have been measured by two multimeters and acquisited by PC. First the onset voltage of corona discharge was detected by jumped appearance of the discharge current of order 0.1 μA. In next the current-voltage characteristic was measured and for each voltage value the transmittance T was registered after stabilisation of the discharge current. Experiments have been carried out at ambient temperature and atmospheric pressure.

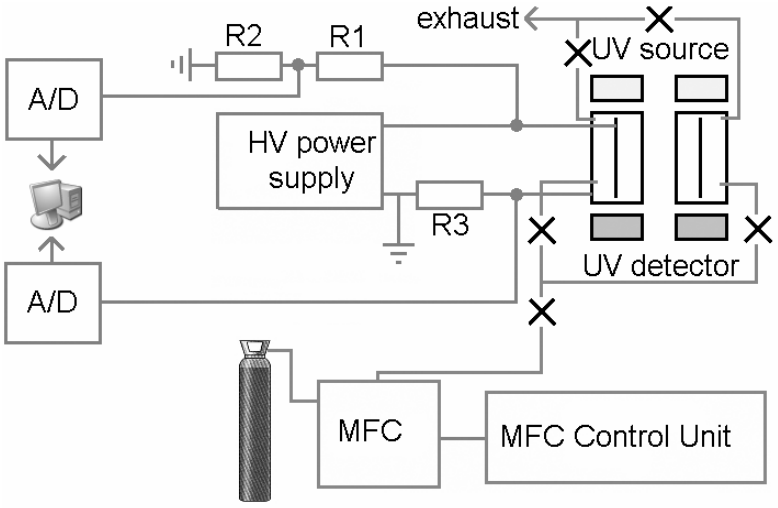

FIGURE 1. Experimental apparatus scheme.

3. EXPERIMENTAL RESULTS AND DISCUSSION

The ozone concentrations reached in the reactor for various gas flow rates and both polarities of the corona discharge are shown in the figure 2. Becker parameter is an average energy input into unit

volume of the discharge gap. If the flow rate is Q and the total discharge current at voltage U is I, the Becker parameter can be expressed as

$$\eta = \frac{I.U}{Q} = \frac{P}{Q}. \qquad \{1\}$$

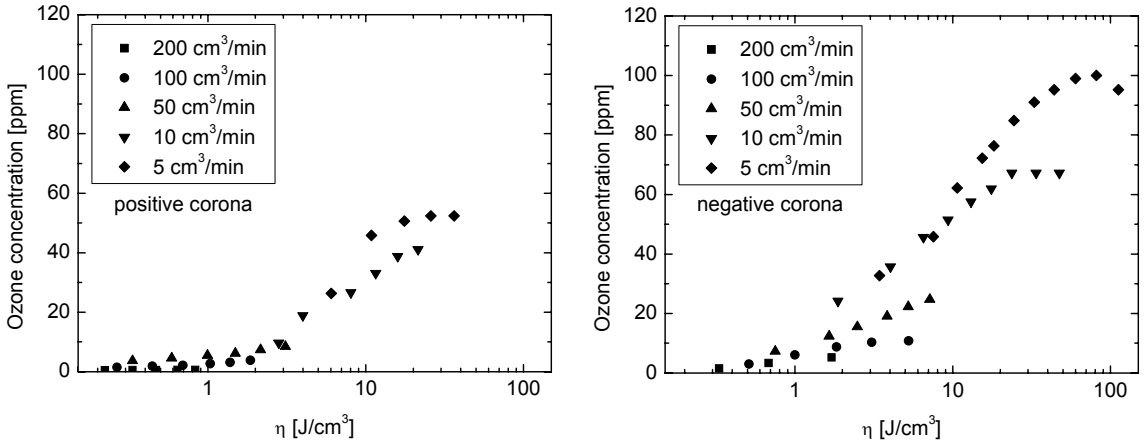

FIGURE 2. Ozone concentration dependence on Becker parameter for positive and negative corona discharge.

The concentration of ozone at the same value of Becker parameter is only slightly higher in negative corona discharge. The effect of different gas flow rate is similar in both positive and negative polarity. The ozone concentration is higher at lower flow rates as it can be expected.

The following reactions are responsible for ozone formation and decomposition in the volume of the reactor:

$e + CO_2 \rightarrow CO + O + e$ $\quad k_1 = f(E/N)$ (1) [5]

$O + O + CO_2 \rightarrow O_2 + CO_2$ $\quad k_2 = 1.04 \times 10^{-32}$ cm^{6}s^{-1} (2) [5]

$O + O_2 + M \rightarrow O_3 + M$ $\quad k_3 = 5.85 \times 10^{-34}$ cm^{6}s^{-1} (3) [5]

$e + O_3 \rightarrow O^- + O_2$ $\quad k_4 = f(E/N)$ (4) [5]

$e + O_3 \rightarrow O_2^- + O$ $\quad k_5 = f(E/N)$ (5) [5]

$O(^3P) + O_3 \rightarrow O_2 + O_2$ $\quad k_6 = 8.5 \times 10^{-15}$ cm^{3}s^{-1} (6) [5]

$O_3 + O_2(^1\Delta_g) \rightarrow O_2 + O_2 + O$ $\quad k_7 = 4 \times 10^{-15}$ cm^{3}s^{-1} (7) [5]

The onset voltage was found to be independent on the gas flow rate in both positive and negative corona discharge. In contrast to this, the breakdown voltage (transition of corona into spark) is decreasing with increasing gas flow rate in the negative corona. In positive corona the breakdown voltage has not been measured, as it was much higher then in the negative corona and the voltage of the power supply was limited.

The CV characteristics are shown in the figure 3. The effect of different gas flow rate in the positive corona is not significant. In contrast this effect is evident in the negative polarity. This is caused by the ability of ozone to capture electrons with low energy in the drift region of the discharge which cannot be attached to CO_2 because the threshold for this attachment is for electron energy approximately 4 eV. This is resulting into lowering the total discharge current. These processes are expressed by dissociative electron attachment reactions (4) and (5).

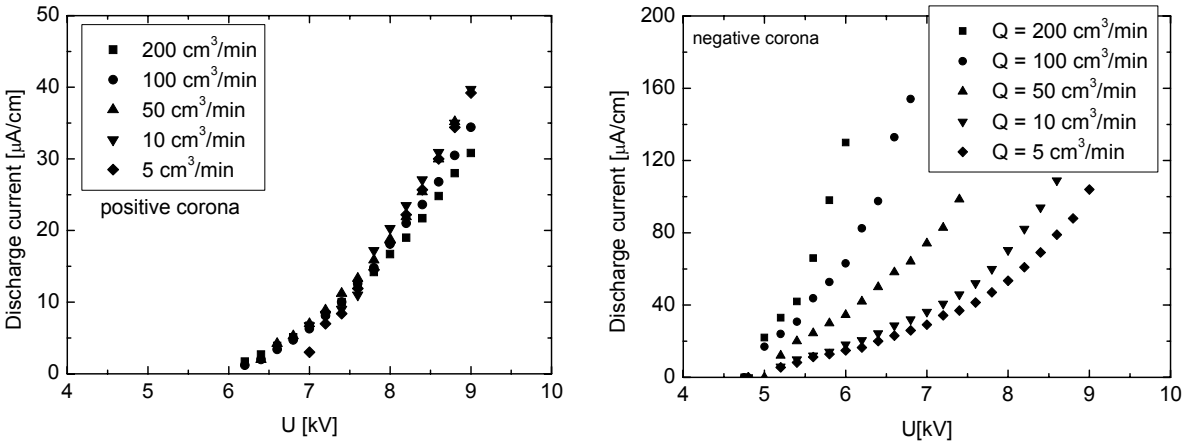

FIGURE 3. Current-voltage characteristics for both polarities of the corona discharge.

4. CONCLUSION

The ozone formation in DC corona discharge is apparently more effective in the negative polarity discharge. The influence of gas flow rate on CV characteristic of the discharge is evident just in negative polarity. This is caused by the role of dissociative electron attachment to ozone molecule in the drift region of the discharge volume.

ACKNOWLEDGMENTS

This research project was partially supported Slovak Grant Agency VEGA 1/1267/04, ESF projects COST P9 and EIPAM. One of authors, (A.S.), is grateful to program CEEPUS AT0063. This work was supported by Science and Technology Assistance Agency and the contract No. APVT-20-007504.

REFERENCES

[1] Batanov, G.M., Kossyi, I.A., Silakov, V.P.: *Plasma Phys. Reports*, 28**,** 2002, pp. 229.
[2] Toumi, R., Houston, P.L., Wodtke, A.M.: *J. Chem. Phys.* 104, 1996, pp. 775.
[3] Dinh, T.H.: Dissertation, Old Dominion University USA, 2002.
[4] Vuskovic, L., Ash, R.L., Shi, Z., Popovic, S., Dinh, T., *J. Aerospace*, 106, 1997, pp. 1041.
[5] Mikoviny, T., Kocan, M., Matejcik, S., Mason, N.J., Skalny, J.D.: *J. Phys. D.: Appl. Phys.*, 37, 2004, pp. 64-73.

Ozone Generating Method Using a Catalysis Electrode in Barrier Discharge

Akira Murai[1], Tsuyoshi Nakajima[2]
[1]Power Engineering R&D Center, The Kansai Electric Power Company Inc.
1-7 Seikacho, Sourakugun, Kyoto-prefecture, 619-0237, Japan
[2]Faculty of Engineering, Shinshu University
4-17-1 Wakasato, Nagano, 380-8553, Japan

Introduction

The manufacturing of ozone requires an extremely high amount of electrical energy 10 [kWh] in order to produce only 1 [kg] of ozone. Some ozone generators use an electrical discharge, while others utilize ultraviolet rays from normal air or oxygen gas to produce ozone. Until the 1980's, ozone was manufactured with dehydrated air, however recently it is manufactured from highly concentrated oxygen gas produced from a Pressure Swing Adsorption system. In the near future, most ozone will be produced from pure oxygen.

It is well known that the inert gases are important elements in efficient ozone production [1, 2]. Recently, several documents have explained the phenomena of the gradual decrease of ozone concentration after producing ozone for approximately 1 year under circumstances of supplied pure oxygen [3, 4]. We aimed to confirm that a third body, which presents at the interface between oxygen gas and a metal electrode, works to compose ozone from an oxygen molecule and an oxygen atom.

Outline of Equipment 1

Fig.1 shows the outline of the device used in the experiment. The parameter of the apparatus is shown from the left to the right of Fig.1. It is described in the ordered list below.

1) Oxygen gas cylinder: 99.5 [%] oxygen gas
2) Gas flow controller:
   Mass flow meter
   (maximum rate 2 [L/min] of oxygen)
   Mass flow meter
   (maximum rate 0.1 [L/min]of nitrogen)
3) High-voltage source:
   Produces a constant D/C
   (maximum of 7[μA]).
4) Ionization chamber:
   Fig.2 shows the electrode arrangement.
   A needle-cathode and a Cu plate-anode were placed in the cylinder. The gas flow was insulated, electrically from the main body, using a glass cylinder.
5) Gas-mixing chamber:
   A cylindrical SUS container 10 [cm] in diameter and 11.4 [cm] in length was used. The container has a capacity of 895 [mL]. A tube for the introduction of nitrogen and an ozone exhaust tube were connected to the container. Fig.3 shows the arrangement of the tubes.
7) Ozone concentration monitor:
   Type: EG2001R-NL made by Ebara Japan
8) Nitrogen gas cylinder: 99.9 [%] nitrogen gas

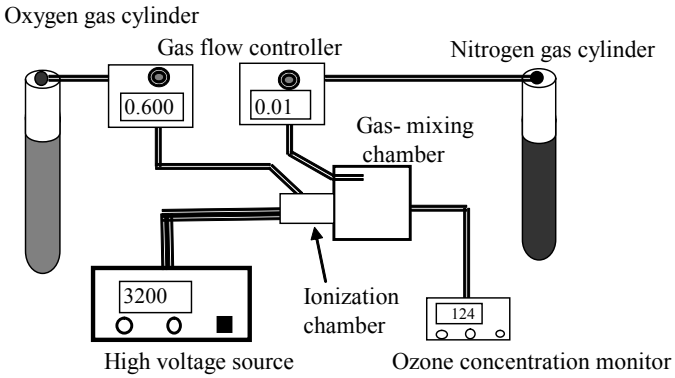

Fig. 1 Experiment device outline of equipment 1

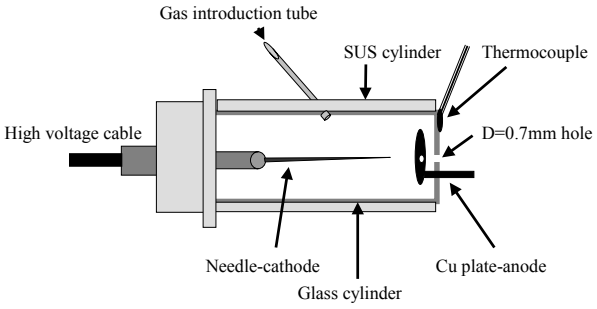

Fig. 2 Ionization chamber cross section

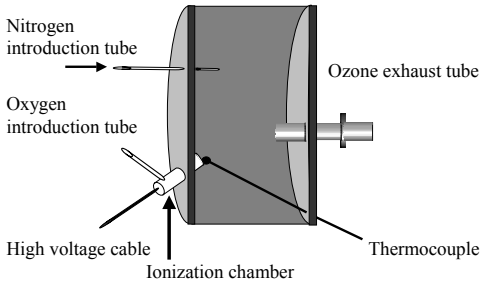

Fig. 3 Gas-mixing chamber cross section

Ozone Composition in Pure Oxygen Gas

While producing ozone for a long period of time using needle and plate electrodes and a direct current, in 99.5[%] oxygen, we were able to observe that the concentration of ozone decreased to 0 after several months in which the electrical discharge had produced ozone. As a result of experiments made using the same equipment, we were able to determine that ozone was composed temporarily by using the electrodes which had been inactive for one night in 99.5[%] oxygen. Then the concentration of ozone decreased to 0 as shown in Fig.4. The concentration of ozone increased due to the addition of nitrogen into a gas-mixing chamber located behind the electrical discharge as shown in Fig.5.

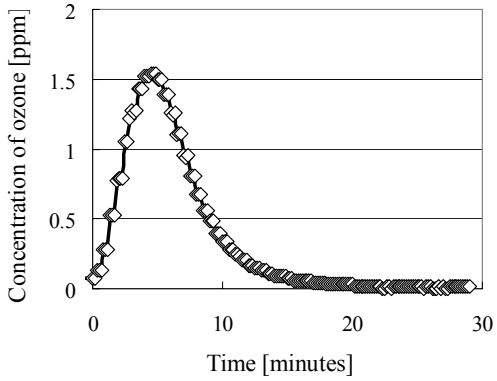

Fig.4 Characteristic of ozone concentration

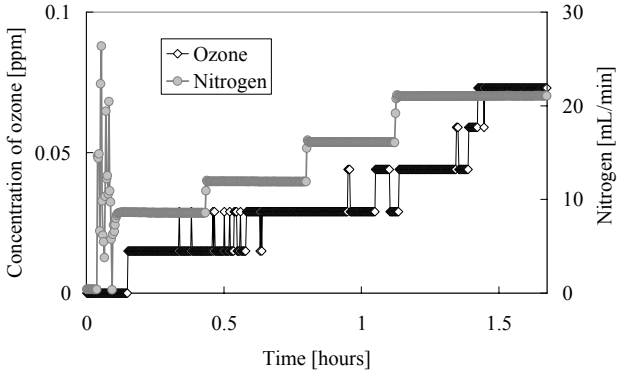

Fig.5 The characteristic of ozone concentration when nitrogen was added to the gas-mixing chamber

Theory of Ozone Generation

O_2^+, $O_2(E)$, $O_2(F)$, $O(^1D)$, O, $O_2(b^1\Sigma g^+)$, O^- $O_2(a^1\Delta g)$, and O_2^- are products in the oxygen gas released by an electrical discharge. When a nitrogen molecule is added as a third body, the difference between the energy of the oxygen molecule and the oxygen atom together, and that of the ozone molecule in the gas-mixing chamber, is adjusted. These are shown in the following expressions ((1) and (2)), where O_3 * shows an excited ozone and M shows a third body.

$$O_2 + O \rightleftharpoons O_3 * \quad (1)$$

$$O_3 * + M \longrightarrow O_3 + M \quad (2)$$

We presumed that the surfaces of the electrodes adsorbed the oxygen and nitrogen molecules. These molecules were struck by oxygen atoms. The probability of an oxygen atom striking an oxygen molecule, which was adjacent to a nitrogen molecule, could be expressed as a parabola curve. It is also shown in the following expression (5)

$$p_{N2}(x)=x \quad (3)$$

$$p_{O2}(x)=A_1(1-x) \quad (4)$$

$$p_{O3}(x)= p_{O2}(x)* p_{N2}(x)=A_1(1-x)*x \quad (5)$$

However, the distribution of oxygen and nitrogen molecules on the surface of the anode is not uniform. The probability of a collision between an oxygen atom and an oxygen molecule therefore obeys Bernoulli's law of distribution. It also closely resembles a Gauss distribution curve (expression (6)). The probability of an oxygen atom striking an oxygen molecule is proportional to the concentration of the ozone produced. In the Gauss curve, the standard deviation was calculated using Bernoulli's law of distribution. We presumed that the probability of collision between an oxygen atom and other molecules was the same; the population mean therefore became 0.5. We reduced the constant probability by 0.074693 so that the probability curve began and ended at 0.

$$f(x)= \frac{1}{\sigma\sqrt{2\pi}} \exp \frac{-(x-\mu)^2}{2\sigma^2} - C \quad (6)$$

where σ is the standard deviation (0.2); μ is the population mean (0.5);
C is the constant probability (0.074693).

The density of the third body at the interface decreases due to the electrical discharge following the exponential curve. We determined that the amount of composed ozone [$Y_{O3}(t)$], which was proportional to the probability of collision, could be calculated using the following expression (7):

$$Y_{O3}(t) = B\{ \frac{1}{\sigma\sqrt{2\pi}} \exp \frac{-(A\exp(-bt)-\mu)^2}{2\sigma^2} - C\} \quad (7)$$

Using the amounts shown in table 1, we calculated the amount of composed ozone as shown in Fig.6. To incorporate the effect of the mixing chamber and the tubes, we divided the time period in which ozone was composed into 500 parts, and then superimposed the results of supplying increasing and decreasing amounts of composed ozone. In this way, we were able to simulate the effect of the time delay caused by the mixing chamber and tubes on the result of composed ozone as shown in Fig.7. We evaluated the experiment data shown in Fig.4 with the results of our calculations. The results matched well, as shown in Fig.8.

Table 1 Coefficients of expression (7)

	A	B	b	τ (minutes)
Nitrogen	0.95	0.0303	0.24	4.17

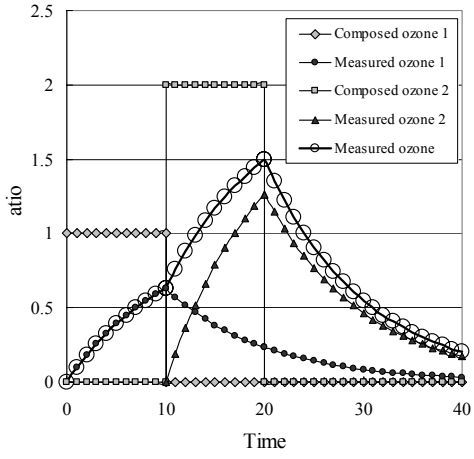

Fig.6 Method of superimposing in composed ozone

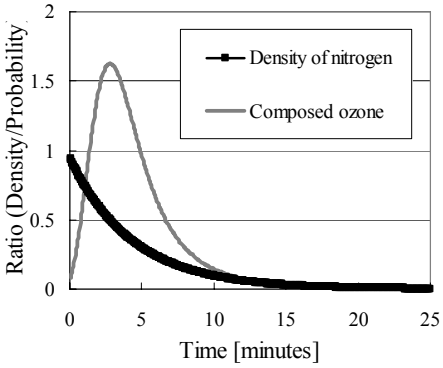

Fig.7 Composed ozone relating to nitrogen

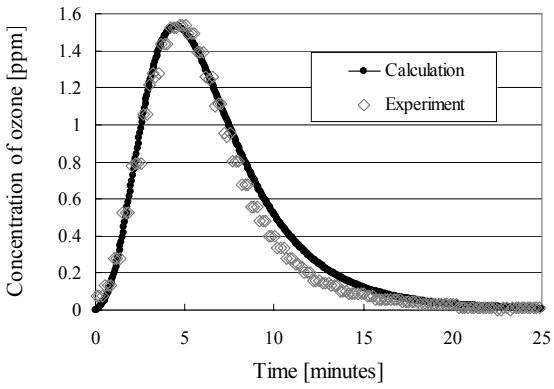

Fig.8 Results of calculations

Industrial Approach

In the next experiment, we used an industrial ozone generator, including ceramic dielectrics and a titanium expanded metal electrode, as shown in Fig.9. The production capacity is 10 [g]per hour by supplied 100 [W] electric power.

A change in the temperature of the cooling water led to a proportional increase in ozone concentration (Fig.10). It follows the formula of van't Hoff.

$$\log_e K = -dH / (R\,T) + C \quad (8)$$

where K is the pressure equilibrium constant;

H is the enthalpy; R is the gas constant; T is the temperature; and C is a constant.

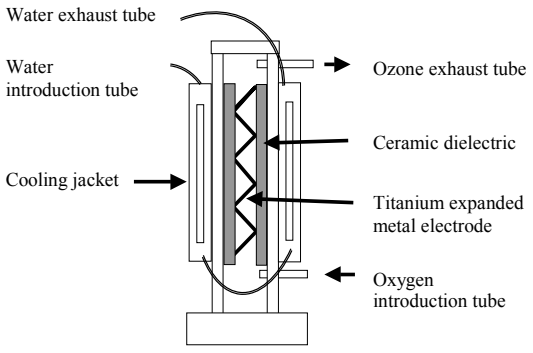

Fig.9 Cross section of the experimental device

The electrodes were spattered with argon gas. Afterwards, the generator was supplied with 99 [%] oxygen gas and produced ozone. The concentration of ozone increased from 98 [g/m^3] to 120 [g/m^3] under the same conditions (Fig.11). After reaching its peak, the concentration of ozone decreased to zero.

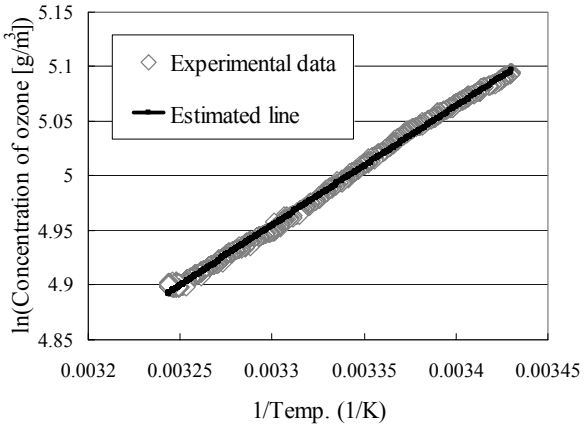

Fig.10 Characteristic of ozone concentration due to changing cooling water temperature

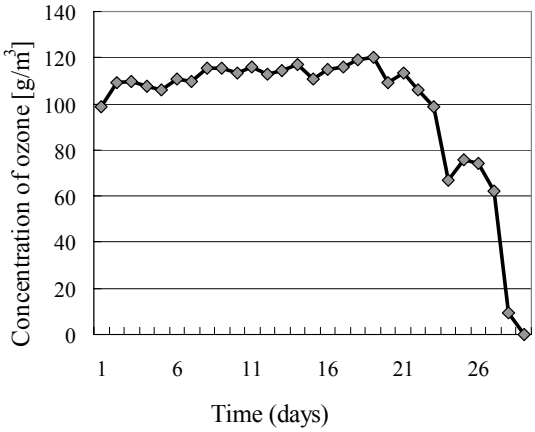

Fig.11 Changes in the concentration of ozone under the same conditions

Next, we changed the titanium electrode which released nitrogen to a titanium electrode covered with antimony. Antimony works better than nitrogen as a third body as shown in Fig.12. Due to the limitation of the ozone concentration monitor's ability to transfer data to a computer, we cannot now show data measuring higher than 200[g/m^3]. However during experimentation, a top reading of 230[g/m^3]was observed at 10[°C].

After changing from the titanium electrode to the antimony electrode and then doubling the oxygen flow rate, we were able to produce a higher concentration of ozone by increasing the temperature as shown in Fig.13.

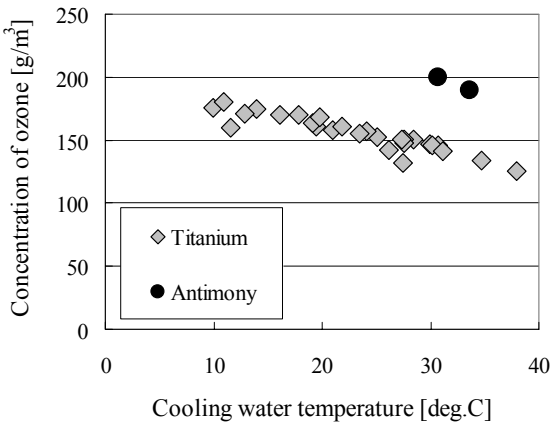

Fig.12 Comparison of ozone concentration between nitrogen and antimony

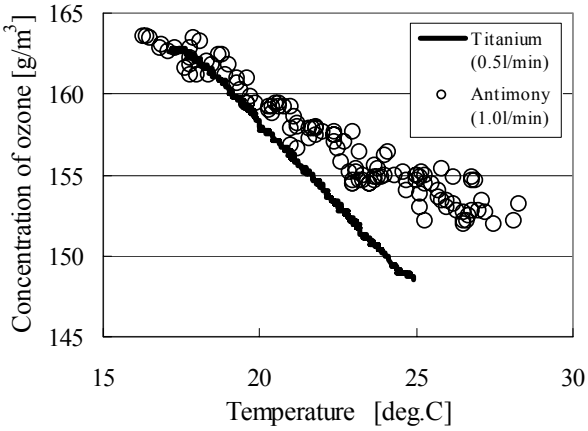

Fig.13 Results of the oxygen flow rate change

References

[1] R.G. Haverkamp, B.B. Miller, and K.W. Free, "Ozone Production in a High Frequency Dielectric Barrier Discharge Generator" Ozone Science & Engineering, Vol.24, No.5, pp.321-328, 2002

[2]M. J. Thomas, "Production Of Ozone in an Electrical Discharge Using Inert Gases as Catalysts", Ozone Science & Engineering, Vol.22, pp.53-64, 2000

[3] P. Uhlig, M. Haacke, and G. J. Pietsh, "On The Impact Of The Feed Gas Quality On The Efficiency Of Ozone Generation." 14th Ozone World Congress, Michigan, USA, pp.145-159, 1999

[4] H. V. Lang, G. Vezzu, and M. Suter: "Science and Experience based Improvements of industrial Ozone Generators." 17th Ozone World Congress, Strasbourg, France, pp.2.3 1-10, 2005

NARROW GAP DISCHARGE FOR OZONE GENERATION

N. Wada[1], Y. Tanimura[1], M. Tanaka[1] and M. Kuzumoto[2]

[1] *Advanced Technology R&D Center,*
Mitsubishi Electric Corporation
8-1-1, Tsukaguchi-Honmachi, Amagasaki, Hyogo 661-8661, JAPAN
[2] *Kobe Works,*
Mitsubishi Electric Corporation
1-1-2, Wadasaki-Cho, Hyogo-Ku, Kobe 652-8555, JAPAN

ABSTRACT. It is extremely important to examine a detailed mechanism of narrow gap discharge for development of the high performance and high density ozone generators. Authors have been researched the relationship between the ozone generation and the narrow gap discharge for high efficiency and high density ozone generation. In this paper, the mechanism of high density ozone generation is discussed according to the experimental results from the observation of the narrow gap discharge.

1. INTRODUCTION

Non-Equilibrium thermal plasmas have been in the limelight for the improvement of the global environment. Ozone generation by silent discharge is the most popular environmental technology in the application of the plasmas. Recently, ozone gas is developed with not only an environmental field but also the advanced technology such as the semiconductor and FPD (Flat Panel Display) manufacturing.

In ozone generators of low density, so-called, the large gap discharge of about 1.0mm, it is well known that many micro-discharge columns are randomly distributed in the discharge gap. Recently, the development of ultra-high density ozone generation of $400g/_Nm^3$ is achieved by the narrow gap discharge. But, the detailed mechanism of the narrow gap discharge has not been clarified yet. It has some possibilities that a peculiar mechanism of the narrow gap discharge that differs from the conventional discharge mechanism has acted on the ozone generation. It is extremely important to examine a detailed relationship between narrow gap discharge mechanism and ozone generation for development of the high performance and high density ozone generators.

2. HIGH EFFICIENCY AND HIGH DENSITY OZONE GENERATION

2.1. Ultra-high density ozone generation ~OZONE BLUE ~

Development of high density ozone generation has been accelerated by the application to the processes of the semiconductor and FPD processes of recent years. Generally, for CVD (Chemical Vapor Deposition) and the removal process of photo resists and so on, it has been required about $200g/_Nm^3$ of ozone density. But, in ALD (Atomic Layer Deposition) that is the process of next generation, it is demanded ultra-high density ozone of about $350g/_Nm^3$ or more.

It is well known that narrow discharge gap of about 0.1mm is extremely effective for generating of high density ozone [1]. Figure1 shows the photographs of the color of oxygen and ozone gases, respectively. At atmospheric pressure, the gases flow in the transparent glass vessel and are observed the color directly in the sight. By the photographs, it is understood that oxygen is colorless and transparent. And, it is realized that ozone colored in blue when ultra-high density ozone of 400g/$_N$m^3 is generated in the ozone generator by the discharge gap length of 0.05mm. Generally, ozone gases can be observed it is only transparent and colorlessness because of the low density. It is succeeded in the first time observation of "Ozone-Blue" in the world with the ultra-high density ozone gases.

(a)6N-grade oxygen (b)400g/$_N$m^3 ozone

FIGURE 1. The observation of the "Ozone-Blue".

2.2. Improvement of the ozone generation efficiency

Ozone generation efficiency has been discussed as oxygen atoms generation efficiency and the efficiency has been called "Maximum ozone generation efficiency". Figure2 shows the relationship between maximum ozone generation efficiency and reduced electric field (E/N). The experimental result and the calculation in oxygen are also shown in the figure. κ shows the electron current ratio here. For κ=1.0, the energy consumption in the plasma is originated only in the electrons drift between the electrodes, and the energy consumption with the ions is disregarded. By the figure, it is understood that the experimental results in various discharge gap length *d* corresponds for κ=0.55 of the calculation [2].

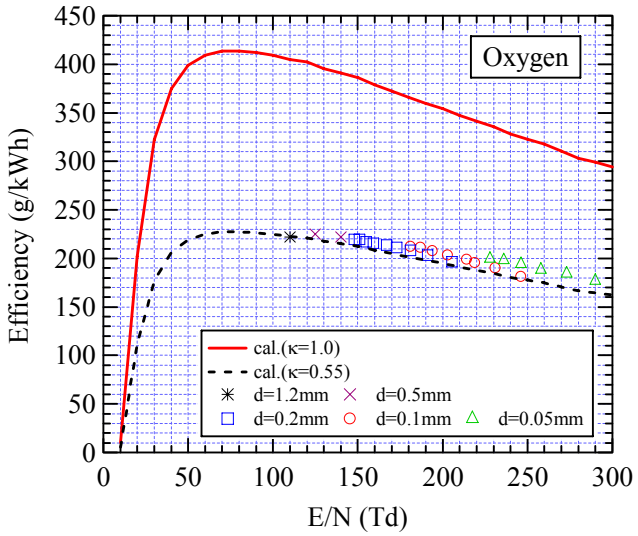

FIGURE 2. Maximum ozone generation efficiency.

In a word, this difference of the efficiency between κ=1.0 and the experimental result (κ=0.55) shows the energy consumption with the ions. For improvement of the high density

ozone generation efficiency, it is suggested that the improvement of the electron current ratio besides realizing a narrow gap length is extremely important.

3. OBSERVATION OF THE NARROW GAP DISCHARGE

3.1. Observation of the narrow gap discharge

Figure3 shows the results of the dependence of discharge gap length *d* on the micro-discharge. These figures are the results that observed the discharge space from the vertical direction by the un-gated mode of the Image Intensified CCD camera under the same conditions of ozone generation. The discharge space is observed through a transparent HV electrode. In this experimental ozone generator, the feed gases flow from the periphery of the electrode to the center gas outlet along the radial direction. The discharge gap length is formed by some spacers.

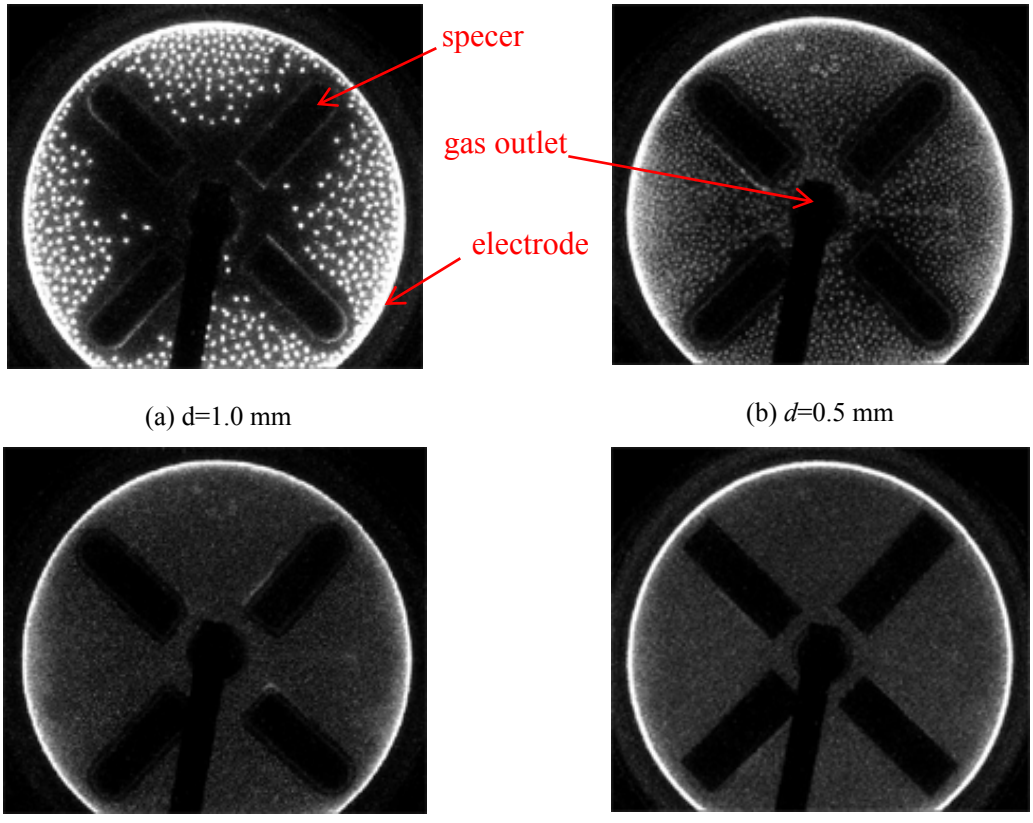

(a) d=1.0 mm (b) *d*=0.5 mm

(c) *d*=0.3 mm (d) *d*=0.1 mm

FIGURE 3. The observation of the narrow gap discharge.

In a case of *d*=1.0 mm, the discharge radiation can be distinguished each column individually. On the other hand, in cases of *d*=0.5 mm and *d*=0.3 mm, the diameters of the columns reduce and the area densities of the discharge columns increase suddenly. Finally, in extremely narrow gap (*d*=0.1 mm), micro-discharge columns can not be observed at all. Apparently, narrow gap discharge characteristic is very different from over 1.0mm gap in silent discharge.

3.2. Discussion

In extremely narrow discharge gap around 0.1mm or less, it is found that micro-discharge columns do not exist apparently by the observation of silent discharge. Figure4 shows the diameter of micro-discharge column by the Pd-product (P : gas pressure). In the case of *d*=0.1mm or less, it is assumed that the discharge would be formed by a swarm of super small diameter columns. Above this, in narrow gap discharge, it is not streamer-like discharge of silent discharge model in large gap length but maybe glow-like discharge.

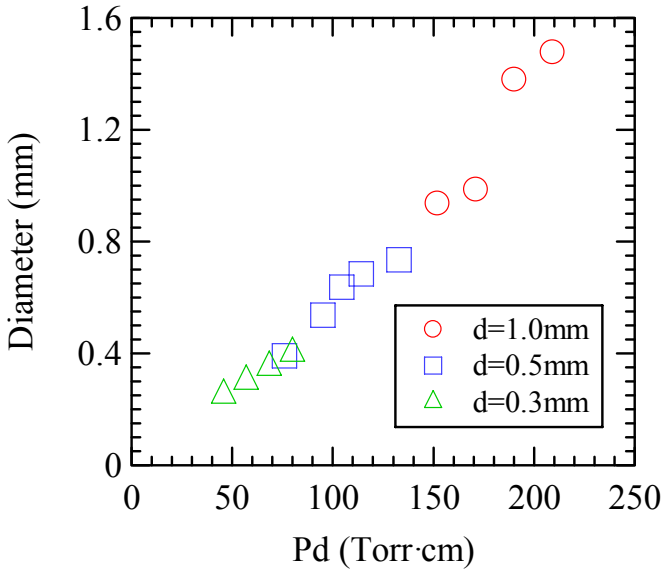

FIGURE 4. Diameter of the micro-discharge column

It is a possibility that electron current ratio changes greatly if the discharge form changes into glow-like discharge apparently. In the glow-like discharge, the useless charges are not necessary accumulated on the surface of the electrode, because the discharge columns do not exist. Therefore, the invalid energy consumption with the ions is decreased, and maybe, the electron current ratio is increased. Ozone generation efficiency will be improved by clarifying the difference of the discharge form between streamer-like and glow-like.

4. CONCLUTION

In narrow gap discharge, it was discussed the relationship between narrow gap discharge and ozone generation. In the gap length of 0.1mm or less, it is not streamer-like discharge of silent discharge in large gap length but maybe glow-like discharge. By a detailed examination of discharge form, it can be expected that electron current ratio and ozone generation efficiency is improved greatly.

REFERENCES

[1] M.Kuzumoto, J. Kitayama and Y.Tabata (1997). *Proceedings of 13th ozone world congress (Kyoto,Japan), Vol 2,* 815-820.
[2] J.Kitayama and M.Kuzumoto (1997). *J. Phys.D , 30,* 2453-2461.
[3] U.Kogelschatz and B.Eliasson. (1995). *Handbook of Electrostatic processes, Marcel Dekker Inc,* 581-603.

Paper number

ANALYSIS OF NON-EQUILIBRIUM PHENOMENA OCCURRING DURING AN OZONE GENERATION PROCESS

PART I. CONCEPTION OF EQUILIBRIUM PROCESSES ELECTROSINTHESIS OZONE

J. Ozonek[1] and S. Fijalkowski[2]

[1] *Institute of Environmental Protection Engineering*
Lublin University of Technology, POLAND
[2] *Department of Technical Thermodynamics,*
Lublin University of Technology, POLAND

ABSTRACT In the first part of the work the equilibrium phenomena model of ozone course synthesis is introduced. During modeling main process was considered electrosynthesis and concurrent processes thermodynamic-flow and thermal. It also showed the influence of coupling in real states on yield efficiency of industrial ozonizer.

The premise in result of analysis was formulated considerations to non-equilibrium process.

1. INTRODUCTION

Ozone generation processes belong to a group of processes that is characterized by high energy-consumption rate. A level of electrical energy consumption in ozone synthesis process does not exceed 20% and the remaining part of the energy is unproductively carried away to the environment. At the same time, when the process is conventionally run, the substrate gas thermal state gets elevated in the discharge zone. As experimental results show the elevated temperature of substrate gas at the ozonizer inlet as well as temperature rise in the reaction zone significantly reduce the ozone synthesis reaction advancement. It is also worth noting that a real ozone generation process is characterized by non-equilibrium in the physical, thermodynamic and thermal sense and its description within the frames of classical thermodynamics makes a model theoretical approximation of reality.

A new approach to describe of equilibrium process model ozone electrosynthesis in real condition is the aim of work.

2. THERMODYNAMICAL AND THERMAL ASPECTS OF THE OZONE GENERATION PROCESS

A discharge gap in the considered ozonizer is a space bounded by electrode surfaces and inlet and outlet cross-sections and it forms a natural area (limited zone) for the ozone synthesis reaction environment. It makes a particular kind of a chemical reactor where chemical processes run under the influence of silent discharges in a substrate gas (oxygen or air). Silent discharges form as a result of the presence of an electrical field of an adequately high potential difference level that surrounds the reaction area. Enthalpy of ozone formation out of oxygen according to a totaled reaction is 142.32 kJ/O_3 mole (the data concern a theoretical synthesis process that runs in a quasi-static - equilibrium way).

In reality, energy that is supplied to generate 1 mole of O_3 out of molecular oxygen contained in the air is much greater and it gets into a substrate gas with fluxes of charges accelerated in an electrical field that accompany silent discharges.

Part of the energy gets utilized directly for the ozone synthesis reaction (as an indispensable energy). Its remaining part (much greater than the former one) gets converted into heat in a dissipative process which follows from the properties of the process.

Heat released in a reactor (in a hypothetical extreme case the reactor is surrounded by adiabatic walls) with no possibility to perform any mechanical work, according to the 1st principle of thermodynamics, would increase the internal energy level which would be accompanied by a significant growth of gas temperature. The temperature growth can also be observed in the case of an insufficient heat abstraction from the reaction environment zone [1].

3. EQUILIBRIUM MODEL OF ENERGY CONVERSION IN THE OZONIZER GAP

The inquiry into the problem was been started with an analysis of energy conversion in the course of equilibrium electrosynthesis. To this end a behavior of a substrate gas elementary batch in the ozonizer reaction environment has been analyzed. The batch has been subdued to a physical-chemical change in electrical field. It has moved in the gap along the normal coordinate - x at a mean velocity - w_{av} with thermal and calorific parameters averaged along the gap height (fig. 1).

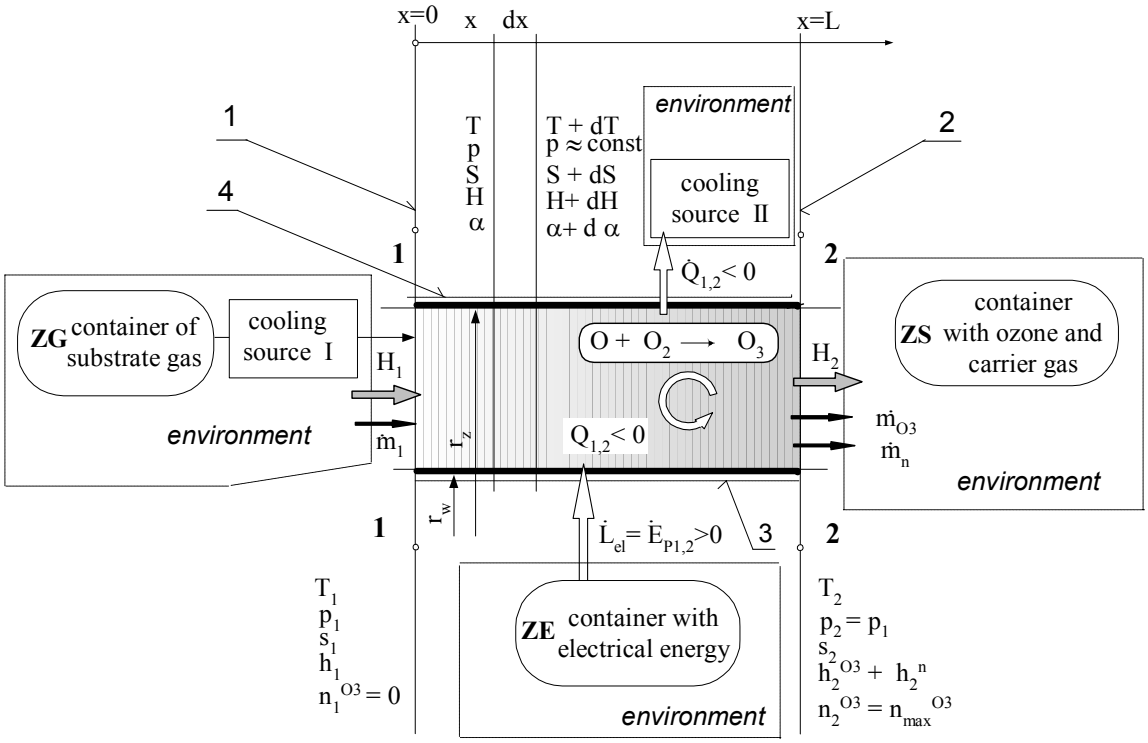

FIGURE 1. A model of an open thermodynamic process in the reaction environment (3)
1,2 - abstract walls that allow substance and energy flow; 3,4 - walls that are substance- impermeable and don't allow mechanical work exchange with the environment; 3 - adiabatic wall; 4 - heat motion to the walls allowed; 3 and 4 - considerable potential difference is applied.

From the viewpoint of classical thermodynamics the question of energy conversions of an elementary batch can be described by the following equation:

$$d\dot{H}_n + d\dot{H}_{O3} + d\dot{H}_r = d\dot{Q} + d\dot{L}_{el}, \qquad (1)$$

where: $d\dot{H}_n + d\dot{H}_{O3} = d\dot{H} > 0$ - elementary change in the substrate gas physical enthalpy flux and the generated ozone,

$d\dot{H}_r > 0$ - flux of ozone generation elementary enthalpy,

$d\dot{Q} < 0$ - flux of heat abstracted from the reaction zone,

$d\dot{L}$ - elementary flux of work transferred to the gas by electrical current in electrical field.

To take into account an effect of the generated ozone quantity on energy conversions within a specific environment of reactions proceeding with the participation of an electrical field has been introduced a notion of a modified relative rate of conversion (α) referred to the synthesis reaction.

With the application of the following notions: physical enthalpy of gas, formation enthalpy, heat penetration between the gas and the cooling agent and also of the function [2, 3] an explicit form of the equation of the I principle of thermodynamics has been obtained. The equation describes the course of an infinitesimal conversion of an infinitesimal gas batch that moves in the ozonizer gap and can be written as follows:

$$\begin{aligned}&\left[\dot{m}_s\, c_{pp} + \alpha \cdot \dot{n}^m_{O3}\, M_{O3}\left(c_{p0} - c_{pp}\right)\right]dT_x + \left[\dot{n}^m_{O3}\, M_{O3}\left(c_{p0} - c_{pp}\right)\left(T_x - T_{od}\right) + \dot{n}^m_{O3}\, M_{O3}\, \Delta h\right]d\alpha = \\ &= \left[\frac{E_v \cdot \dot{m}_s}{\rho_p \cdot L} - 2\pi \cdot r_z \cdot k\left(T_1 - T_{c1}\right) \cdot e^{\beta \cdot x}\right]dx\end{aligned} \tag{2}$$

where:

$k = \dfrac{2}{\pi}\dfrac{c_{pp}}{L} \cdot \dot{m}_s \cdot \dfrac{\dfrac{1}{2d}}{1 + \dfrac{\dot{m}_s}{\dot{m}_c}\dfrac{c_{pp}}{c_c}\dfrac{d_c}{d}} \cdot \varphi_s$ - coefficient of a heat transfer between gas in a discharge gap and a cooling medium

φ_s - coefficient characterizing an effect of a substrate gas flux on the heat-transfer coefficient k

$\beta = -\dfrac{2\pi \cdot r_z \cdot k}{\dot{m}_c \cdot c_c \cdot b}$ - coefficient characterizing changes in gas temperature resulting from a cooling action

$b = -\dfrac{1}{\dfrac{T_1}{T_{c2}} \cdot f_b + 1}$ - coefficient characterizing an effect of cooling medium temperature on β values $\qquad f_b = -\dfrac{T_2/T_1 - 1}{T_{c1}/T_{c21} - 1}$

A solution of the formula (2) has been presented in [4, 5], which allows to determine temperature distribution in the discharge gap.

$$T_x(x) = T_1 + \frac{E_v \cdot x}{\rho_p \cdot c_{pp} \cdot L} - \frac{\dot{m}_{O3}}{\dot{m}_s} \cdot \frac{\Delta h}{c_{pp}}\left(1 - exp\left(-\frac{k_1}{w_{śr}}x\right)\right) + \frac{2\pi \cdot r_z \cdot k \cdot \left(T_1 - T_{c1}\right)}{\dot{m}_s \cdot c_{pp} \cdot \beta}\left(1 - e^{\beta \cdot x}\right) \tag{3}$$

In the above equation coefficient k_1 reflects the rate constant of ozone decomposition counted in experimental investigations according to Vasilev equation [1]. Values this in the first order depend from the substrate gas temperature (the oxygen) on inlet to the discharges zone as well as the height of the discharge gap.

Equation (3) illustrates the effect of individual basic factors on the gas temperature distribution in the reaction environment, namely:

- the effect of the substrate gas temperature level at the ozonizer inlet- temperature T_1,
- the effect of the energy density, β,
- the effect of the gas cooling intensity level in the gap (the term that includes the heat penetration coefficient k).

4. RESULTS AND DISCUSSION

The presented research work includes theoretical analyses and experiments concerning ozone synthesis processes occurring in a non-equilibrium low-temperature plasma that forms in electrical discharges. The research is of fundamental character but it is also significant from the point of view of technologies of ozone production and its applications

The got formulae and the obtained observation have made a basis for formulating a set of assumptions for elaborating a model of irreversible and non-equilibrium phenomena of an ozone synthesis process (this means in the environment of the low temperature plasma).

The obtained results are basically of cognitive character although the obtained macro-kinetic relations as well as the proposed design solutions can also be applied in practice.

REFERENCES

[1] Lunin B.B., Popovith M.P., Tkaczenko C.N., *Fiziczeskaja chimia ozonu*, Izd. Moskovskogo Universiteta, Moskva 1998.

[2] Bejan A., *Avanced engineering thermodynamics*, New York, 1988.

[3] Ozonek J., Fijalkowski S., Pollo I., (1993). Energy distribution in a commercial ozone generating system, *Ozone Sci. Eng*, 15, 371-387.

[4] Ozonek J., Fijalkowski S., Warminska A., (2003). Thermal model of an ozonizer regarded as an exchanger operating at reduced temperatures, *Industrial Heat Engineering*, 25, 36-41.

[5] Fijalkowski S., Ozonek J., (2002). Thermodynamic analysis of the ozone synthesis process in a small-gap physical-chemical reactor, *Industrial Heat Engineering,* 24, 55-61.

List of more important symbols

c_p - specific heat at constant pressure, J/kg·K,
ρ - density, kg/m^3,
d - discharge gap size, mm,
H - enthalpy, J,
k_1 - reaction rate constant of ozone decomposition, m^3/s
L - discharge zone length, m
$\dot{m}$ - mass flow rate, kg/s
p - pressure, N/m^2
S - entropy, J
T - temperature, K,
w - rate of gas flow in ozonizer gap, m/s

subscript:

s - dry gas,
c - cooling liquid,
O_3 - ozone
pp - gas

Paper number

INFLUENCE OF OZONE GENERATION OF THE THICNESS OF DISCHARGE ELECTRODE AT SAW TOOTH PLATE ELECTRODE TYPE OF ELECTROSTATICS PRECIPITATOR

Y.Takagi[1], T. Takahashi[1], Y.Ehara[1], K.Yasumoto[2], A.Zukeran[2]

[1] *Musashi Institute of Technology*
1-28-1, Tamazutsumi, Setagaya-ku, Tokyo, 158-8557, Japan
[2] *Fuji Electric Co.Ltd.,*
1-11-2, Osaki, Shinagawa-ku, Tokyo, 141-0032, Japan

ABSTRACT. Electrostatic precipitator (ESP) is used to remove diesel exhaust particle in tunnel. However, ozone is generated because ESP used corona discharge. We conduct reducing ozone generation by changing the thickness of the saw tooth plate electrode. At the same time, collection efficiency is measured. In the same discharge current, ozone generation of the thin saw tooth plate electrode is lower than that of thick saw tooth plate electrode. In the same discharge current, the collection efficiency is almost same by changing the thickness of the saw tooth plate electrode.

1. INTRODUCTION

ESP has the advantage that collection efficiency is high, pressure drop is low, and maintenance is easy etc. In addition, ESP is widely used for industry and highway tunnel etc. ESP collects the particles by the corona discharge. Therefore, ESP generates harmful ozone in the human body and the environment without fail. The ozone exhausted from the tunnel causes oxidase smog. Recently, underground tunnel type expressways have been constructed in urban area. Therefore, the decrease of the ozone generated from ESP is requested. In past research, when high voltage electrode of thin plate used, ozone concentration of this electrode is lower than that of wire electrode [1]. In addition, when high voltage electrode of saw tooth plate used, ozone concentration of this electrode is lower than that of wire electrode. In this work, we force on reducing ozone generation by changing the thickness of the saw tooth plate electrode.

2. EXPERIMENT

2.1. Experimental system

The schematic diagram of the experimental system is shown in Figure.1. The gases exhausted from the diesel engine are diluted with air in the mixing chamber, then boosted by the fan and introduced into the ESP system. The gases cleaned by ESP pass through an absorbing fan, and then are exhausted. The gas velocity in the duct is approximately 7m/s. The particle concentration upstream and downstream ESP is measured by the particle counter (RION KC-01C). Ozone concentration behind ESP is measured by ozone monitor (EBARA JITSUGYOU EG-2001 R type)

2.2. Structure of electrodes

The structure of the saw-tooth type of ESP (ST type) is shown in Figure 2-a. The high voltage electrode used one saw-tooth electrode (made of stainless-steel, 70×160mm^2, pitch 5mm), the grounded electrode used two plates (made of stainless-steel, 70×180mm^2). These electrodes are set up for the gas flow in parallel and alternately. Thickness of ST electrode used four kinds of 0.8, 0.5, 0.2, and 0.1mm. The collecting section has a parallel-plate configuration and the spacing between the adjacent plates is 9mm. The structure of the wire type electrode of ESP (W type) is shown in Figure 2-b. The precharger consists of wires and plates. The diameter of a tungsten wire is 0.4mm, the plates are made of stainless steel (70×180mm^2). The collecting section used the same as ST type. Discharge current in the charging section was 0.02-0.08mA. DC 7.5kV was applied to high voltage electrode in the collecting section.

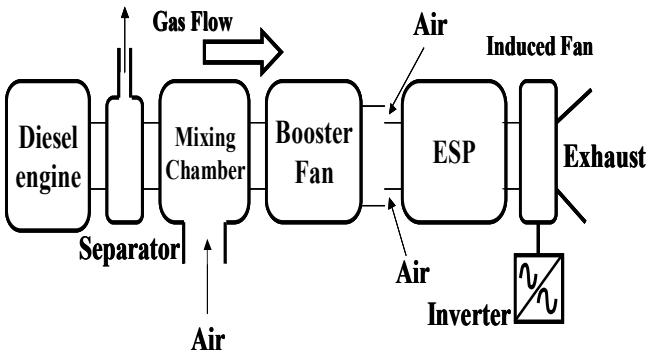

Figure 1. Schematic diagram of experimental system.

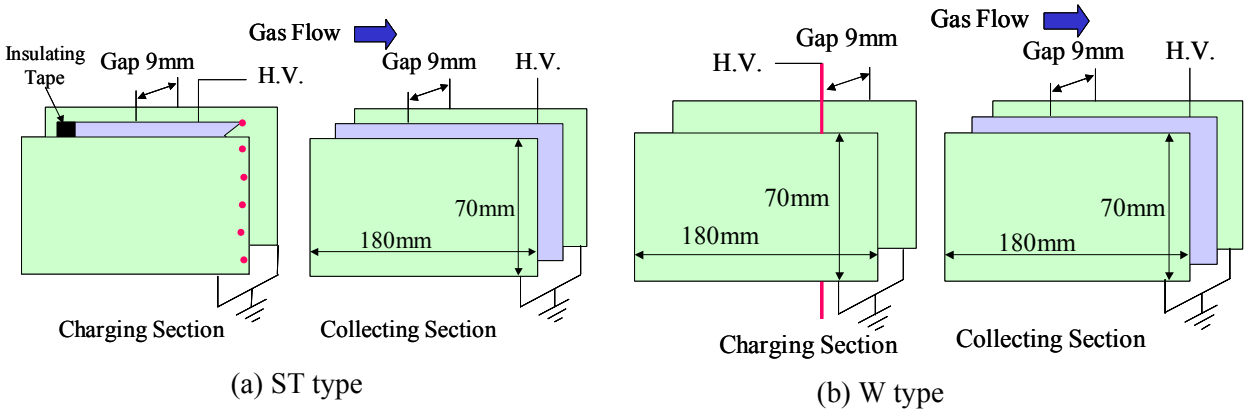

Figure 2. Structure of the electrode on ESP.

3. RESULT AND DISCUSSION

3.1. Characteristics of collection efficiency

Collection efficiency as a function of discharge current is shown in Figure 3. When the electrode thickness becomes 0.5mm or more, the collection efficiency decreases in the case of positive voltage. For this reason, it is considered that the discharge mode become streamer corona in the electrode thickness becomes 0.5mm or more. The collection efficiency of W type is higher than that of ST type in the positive voltage. ST type has the dead space that is not discharge. Collection efficiency in the negative voltage is almost same, when electrode thickness changes.

3.2. Characteristics of ozone concentration

Ozone concentration as a function of discharge current is shown in Figure 4. When the electrode thickness becomes 0.5mm or less, the ozone concentration decreases in the case of positive voltage. For this reason, it is considered that the discharge mode don't become streamer corona in the electrode thickness becomes 0.5mm or less. The ozone concentration of W type is almost as same as that of ST type of thickness 0.2 and 0.1mm.in the positive discharge. The ozone concentration of W type is higher than that of ST type in the negative voltage. Because ST type has the dead space that is not discharge. The ozone concentration decreases with thining down the thickness of the electrode in case of negative voltage. For the reason, area of oxygen dissociation is small. This is a area of ionization and of dissociation at high electric field on corona discharge. The ionizing energy of the oxygen molecule is 12.2eV and breakdown field strength is 30kV/cm in the atmosphere. Therefore, the electric field of

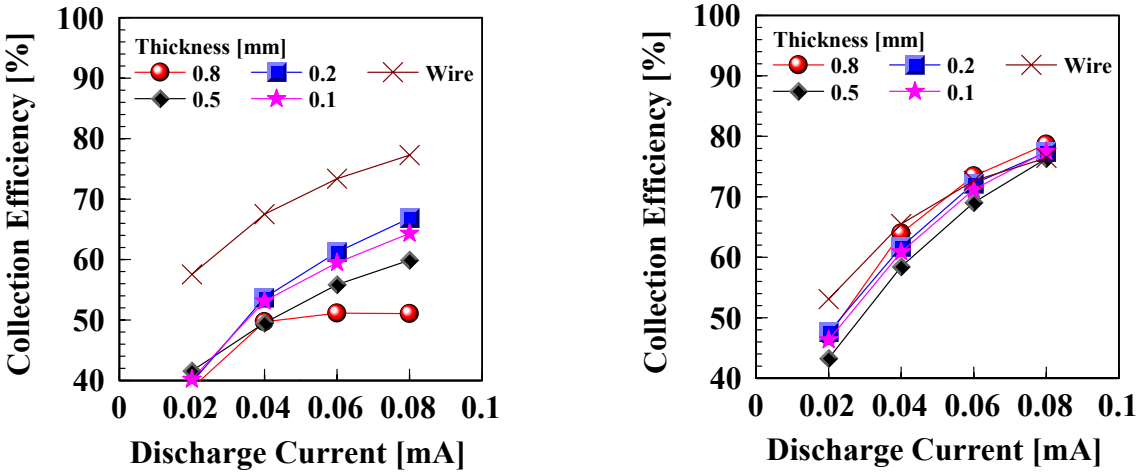

(a) Positive (b) Negative

Figure 3. Collection efficiency as a function of discharge current.

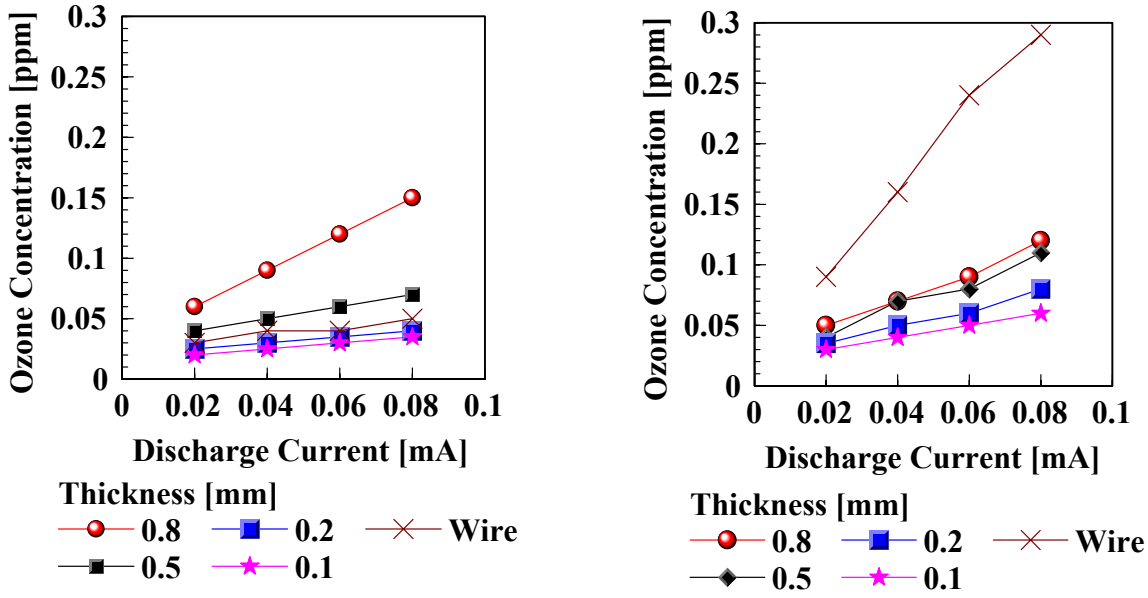

(a) Positive (b) Negative

Figure 4. Ozone concentration as a function of discharge current.

2.46kV/cm is necessary to have the energy of 1eV. The electric field of 12.5kV/cm or more need, because energy the oxygen molecule is 5.1eV[2]. The electric field analysis of the ST type used by this experiment was calculated by the finite element method.

The electrode thickness as a function of the area of dissociation as in case of 12.5kV/cm or more is shown in Figure 5. When electrode thickness is thin, area of dissociation decrease, and ozone concentration also decrease. Therefore, when the thickness of the electrode thin down as in case of negative voltage, ozone concentration decrease.

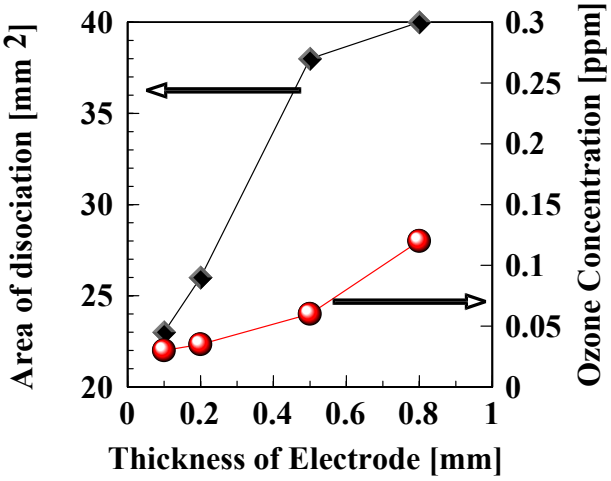

FIGURE 5. Area of dissociation as a function of thickness electrode.(Discharge current: 0.06mA)

4. CONCLUSIONS

In this work, we force on reducing ozone generation by changing the thickness of the saw tooth plate electrode.

(1) When the electrode thickness becomes 0.5mm or more, the collection efficiency decreases as in the case of positive voltage.
(2) Collection efficiency in the negative voltage is almost same, when electrode thickness changes.
(3) When the electrode thickness becomes 0.5mm or less, the ozone concentration decreases as in the case of positive voltage.
(4) When the thickness of the electrode thin down as in case of negative voltage, ozone concentration decreases.

REFERENCES

[1] Y.Ehara, K.Ito, Y.Takagi, A.Zukeran, K.Yasumoto. Reduction of ozone generation in electrostatic precipitator. International Society for Electrostatic Precipitator, 3C-1, (2006)

[2] K.Takakura, F.Kume, T. Kobayashi, M.Hayasaka, Y.Sekiya Consideration for the Characteristics of Ozone Generation by Positive and Negative Corona Discharges. J.Inst. Electrostat. Jpn., Vol.25, No.2, pp.101-104 (2001)

Paper number

ANALYSIS OF NON-EQUILIBRIUM PHENOMENA OCCURRING DURING AN OZONE GENERATION PROCESS

PART II. ANALYSIS OF ELECTROSYNTHESIS OF OZONE PROCESSES IN THE RANGE OF IRREVERSIBILITY AND NON-EQUILIBRIUM

S. Fijalkowski [1] and J. Ozonek [2]

[1] *Department of Technical Thermodynamics, Lublin University of Technology, POLAND*
[2] *Institute of Environmental Protection Engineering Lublin University of Technology, POLAND*

ABSTRACT. The main aim of this part of paper is to formulate the description bases of the model of irreversibility and non-equilibrium character of the processes during the real, silent discharge occurring in ozonizers.

The selection of the subject area is the result of the need of searching for the methods to use the electric driving energy during the ozone production on industrial scale more effectively. This aim was achieved by formulating the model of non-equilibrium character of electrosynthesis of ozone in real tubular ozonizers.

1. INTRODUCTION

The presented work deals with irreversibility and non-equilibrium of phenomena that accompany ozone generation in real reactors, described in [1]. The considerations aim at formulating a basis for the description of a model of irreversibility and non-equilibrium of processes that occur in the course of real silent discharges in an ozonizer reaction environment at ozone generation out of oxygen or atmospheric air.

The project includes an analysis of premises for the formulation of the mentioned model with taking into consideration conclusions that follow from the analyses of equilibrium energy conversions that occur in the reaction environment.

Fathoming of the subject range follows from need to find efficient ways of improving utilization of driving electrical energy in an industrial process of ozone generation [2 - 5].

2. CHARAKTERYSTYKA OBIEKTU MODELOWANIA I OGÓLNE PRZESŁANKI DO MODELU NIERÓWNOWAGOWOŚCI ELEKTROSYNTEZY

Gas that flows in the gap of a tubular ozonizer makes a material object of the modeling [1]. The gas is subdued to a non-equilibrium process of ozone electrosynthesis. Fig. 1 presents a diagram of a control element that travels over the zone of a hypothetic microdischarge channel (streamer) at the w velocity.

As real industrial ozonizers are tubular, a circularly symmetrical area of the reaction environment has been considered. The area is surrounded by two co-axial cylindrical surfaces (electrodes) separated by a gap of the d height. The internal surface is a high voltage electrode. Geometric properties of the area are determined by magnitude orders of the main dimensions of the area and namely: the discharge gap height $d \sim 10^{-3}$ m, while the length and width of the

area satisfy the relation $d/L << 1$. It makes possible to neglect the space curvature effect and treat the area as a space located between two plates (electrodes) of dimensions that are sufficiently bigger than a dimension of the discharge gap height d.

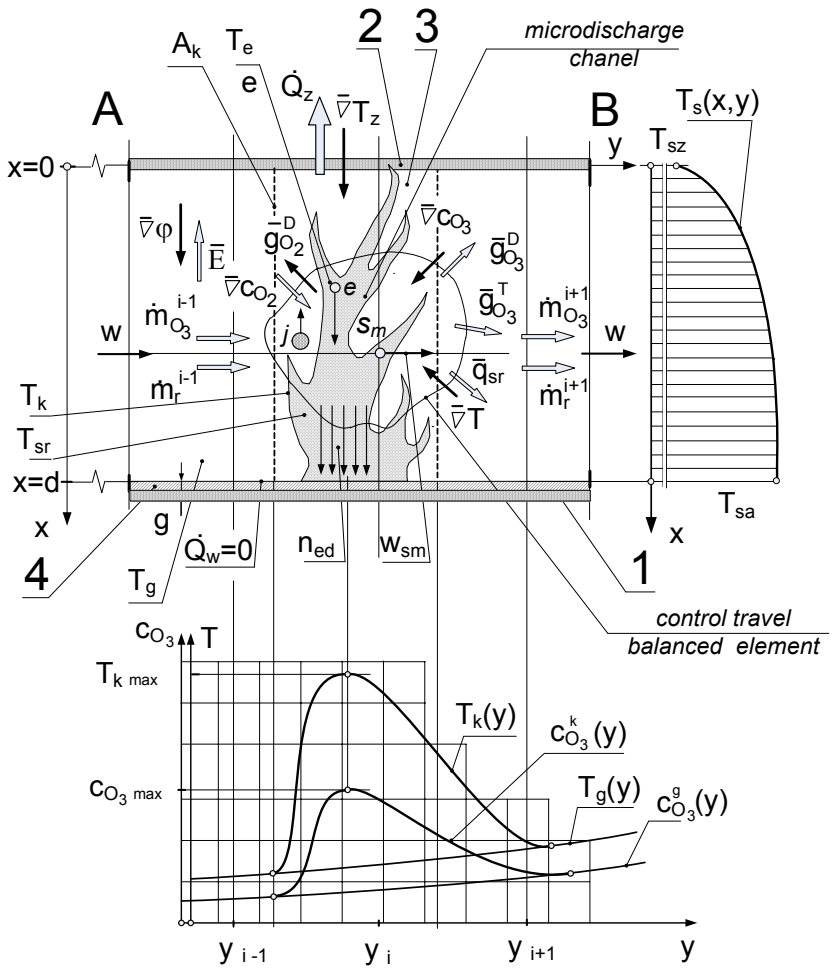

FIGURE 1. A diagram for the model of phenomena related to microdischarges in the reaction environment: A-cross-section of an inlet to the area with a discharge micro-channel B-cross-section of an outlet from the area; 1- high voltage electrode (instantaneous cathode - Kt), 2- grounded electrode (instantaneous anode - An) 3- discharge gap, 4- permanent dielectric layer

Entropy changes of the substrate gas and generated ozone in the reaction environment are influenced by entropy flux inflow and outflow from the gap environment - $\dot{S}_z$ as well as by entropy production in time within the environment - $\dot{S}_w$ (in internal sources), at the same time.

$$\dot{S}_w = \dot{S}_{EM} + \dot{S}_{EU} + \dot{S}_{qp} + \dot{S}\alpha_{2-3} + \dot{S}_{qw} + \dot{S}_{qz} + \dot{S}_{c2-3} + \dot{S}_{cT} \tag{1}$$

Principally, at assuming a phenomenological approach to the problem of a non-equilibrium nature of the phenomena, according to [5, 6] dissipation function in the following form used:

$$\Psi = T \cdot \frac{\partial^2 S_w}{\partial \tau \, \partial V} = T \cdot \frac{d\dot{S}_w}{dV} \geq 0 \tag{2}$$

This quantity is not a state function and its value depends on a quality of the characterized processes. Hence, for all elements that travel over the gap area the following equations are valid:

- equation of substantial balance of entropy in a control volume:

$$\rho \frac{ds}{d\tau} = - \overline{\nabla} \cdot \bar{J}_s + \Psi \frac{1}{T} \tag{3}$$

where: $\bar{J}_s$ - total entropy flux that flows out of individual elements to the gap environment,

- Gibbs equation of local equilibrium in a control volume:

$$\rho \frac{ds}{d\tau} = \frac{\rho}{T} \frac{di}{d\tau} - \frac{\rho}{T} \sum_{i=1}^{n} \mu_i \frac{dc_i}{d\tau} \tag{4}$$

Equations (2) and (3) make it possible to describe a dissipation function:

$$\Psi = \rho \frac{di}{d\tau} - \rho \sum_{i=1}^{n} \mu_i \frac{dc_i}{d\tau} + T \cdot \overline{\nabla} \bar{J}_s \tag{5}$$

Equation (5) makes a basis for the analysis of the non-equilibrium character of the considered ozone electrosynthesis process. Fig. 2 illustrates the nature of individual equation terms with respect to the irreversible process of electrosynthesis.

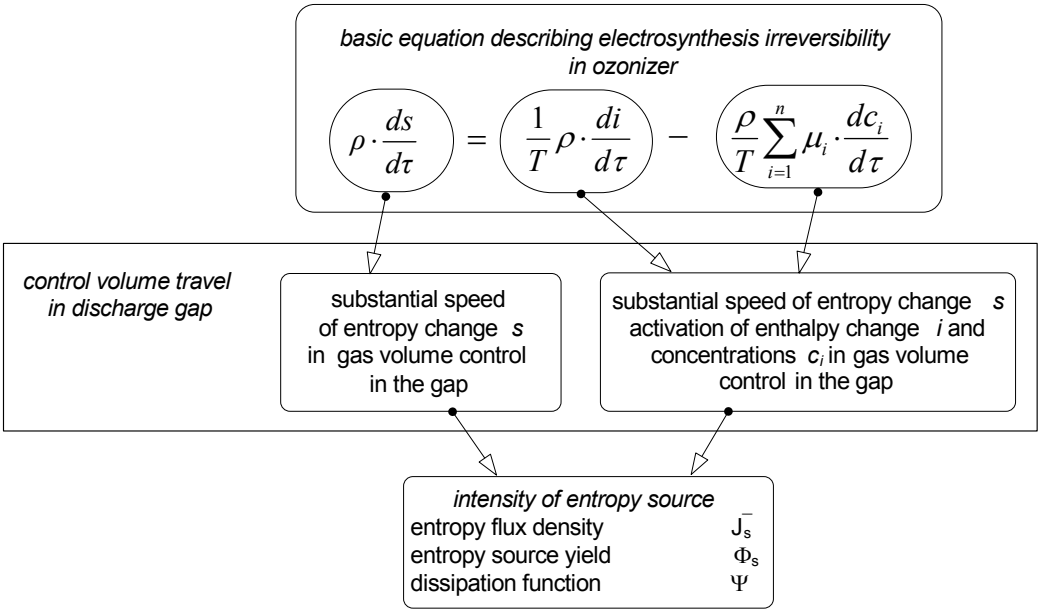

FIGURE 2. Schematic diagram to explain quantities of: entropy flux density, entropy source yield and dissipation function in reference to the Gibbs-Duhem equation.

Mathematical description of the non-equilibrium model of ozone electrosynthesis has been elaborated with a dissipation function described by the equation (5) taken into account. Such a way of describing the non-equilibrium character makes it possible to express the least temperature dependent phenomenological factors, which can be useful when analyzing the considered phenomena.

Individual components of the dissipation function Ψ_s for a non-equilibrium electrosynthesis of ozone can be expressed in the following sum form:

$$\Psi_s = \Psi_{EM} + \Psi_{EU} + \Psi_{qp} + \Psi\alpha_{2-3} + \Psi_{qw} + \Psi_{qz} + \Psi_c \tag{6}$$

- element that issues from the action of electrical field and electrons:

$$\Psi_E = \left(L_{ee} \frac{1}{e_e} \overline{\nabla} \mu_{ee} + L_{eq} \overline{\nabla}_x \ln T \right) \frac{\overline{\nabla} \mu_{ee}}{e_e} \tag{7}$$

- element that issues from the heat transfer by traveling electrons:

$$\Psi_{qp} = \left(L_{qq}^{P} \overline{\nabla}_x \ln T + L_{qe} \frac{1}{e_e} \overline{\nabla} \mu_{ee} \right) \overline{\nabla}_x \ln T \tag{8}$$

- element that issues from the reaction run of molecular oxygen O_2 decomposition into atoms and ozone synthesis O_3:

$$\Psi\alpha_{2-3} = T\left(J\alpha_2 \cdot A_{O2} + J\alpha_3 \cdot A_{O3}\right) \tag{9}$$

- element that issues from the heat transfer along the reactor :

$$\Psi_{qw} = \left[L_{qq}^{W}\,\overline{\nabla}_y \ln T + L_{qc}\cdot\overline{\nabla}_T\left(\mu_{O3}-\mu_{O2}\right)\right]\overline{\nabla}_y \ln T \tag{10}$$

- element that issues from the heat transfer from the gas to an external wall that surrounds the reaction environment:

$$\Psi_{qz} = \left(L_{qq}^{Z}\,\frac{\Delta T}{\delta_H \cdot T}\,\overline{n}_{0S}\right)\frac{\Delta T}{\delta_H \cdot T}\,\overline{n}_{0S} \tag{11}$$

- element that issues from an irreversible course of molecular oxygen O_2 decomposition into atoms and ozone synthesis O_3:

$$\Psi_c = \left[L_{cc}\,\overline{\nabla}_T\left(\mu_{O3}-\mu_{O2}\right)+L_{cq}\cdot\overline{\nabla}_y \ln T\right]\overline{\nabla}_T\left(\mu_{O3}-\mu_{O2}\right) \tag{12}$$

3. CONCLUSIONS

The presented considerations have made a basis for formulating a set of assumptions (causes and effects) for elaborating a model of irreversible and non-equilibrium phenomena that accompany an ozone synthesis process in steady states of an ozonizer operation and namely:

1. The main cause of a scalar nature is a thermodynamic physical-chemical stimulus described by chemical affinity of an ozone synthesis reaction.
2. Causes of the irreversibility and a non-equilibrium character of an ozone synthesis that exhibit properties of vector thermodynamic stimuli and follow from heterogeneity of the distributions in the gap region of the following factors: electrical and chemical potential of electrons, temperatures of gases inside the gap and in the region at a non-adiabatic surface that bounds the gap (T), ozone concentration in the gap (C).
3. To arrive at a full description of the discussed model it is necessary to formulate forms and relations of phenomenological factors in order to express generalized flows, conjugate and cross ones, and subsequently formulate the final form of the model description.

REFERENCES

[1] Ozonek J., Fijalkowski S., (2006). Analysis of non-equilibrium phenomena occurring during an ozone generation process, Part I. Conception of equilibrium processes, this proceeding

[2] Ozonek J., Fijałkowski S., Pollo I., (1997). Exergy identification of energy utilization efficiency in an industrial process of ozone generation *Ozone Sci. Eng*, 19,201-226.

[3] Fijałkowski S., Ozonek J., (2002). Thermodynamic analysis of the ozone synthesis process in a small-gap physical-chemical reactor, *Industrial Heat Engineering,* 24, 55-61.

[4] Filippov Y. V., Voblikova V.A., Panteleiev V.I., *Elektrosintez ozona*, Izd. Moskovskogo Universiteta*,* Moskva 1987.

[5] Lee H.M., Chang M.C., (2004). Kinetic modeling of ozone generation via dielectric barrier discharges, *Ozone Sci. Eng.* 26, 551-562.

[6] Bejan A., *Avanced engineering thermodynamics*, New York, 1988.

[7] Gyarmati I., *Non-equilibrium thermodynamics*, Springer Verlag, Berlin 1970.

AIR CREANING TEST BY CORONA REACTOR WITH WATER

K.Ohara[1], T.Fujii[1], Y. Arao[2] and M. Rea[3]

[1]*Department of Electrical engneering, Kobe City College of Technology,*
Gakuen Higashimachi 8-3, Nishiku,Kobe, 651-2194, Japan
[2]*Aero-Dynamic Machinery Division, Kawasaki Heavy Industries, Ltd.*
Higashi Kawasaki 3-1-1, Chuoku, 650-8670 Kobe, Japan
[3]*Department of Electrical Engineering, University of Padova,*
Via Gradenigo, 6/a, 35131 Padova, Italy

ABSTRACT. For application to contaminated air cleaning, we designed a combined system with two-stage electrostatic precipitator (ESP) and corona reactor with water. We carried out experiments on dust and NOx treatment with diesel engine exhaust gas under various conditions. The best treatment rate in the tests by the hybrid reactor model showed 75 % in NOx removal and 100 % in dust removal rates. On the polarity of applied DC voltage to the reactors, negative charging showed better removal rates in ESP for dust treatment and positive corona showed better NOx removal rate in the reactor with water.

1. INTRODUCTION

Recently, problem of air pollution has been widely discussed not only on big scale emission sources but also dispersed ones. It is focused in small scale emission sources with increasing of exhaust by cars and small boilers such as in house warming. The engine exhaust gas contains harmful substances including particle matter (PM), nitrogen oxide (NOx), sulfur oxide (SOx), carbon monoxide (CO) and carbon dioxide (CO_2). When human beings take in these substances, they get sicknesses of the bronchi system including asthma and chronic obstructive pulmonary disease (COPD). Therefore, to eliminate these substances in the exhaust gas or in the contaminated air is an important problem to maintain the fine living space.We have been researching mainly the treatment of dust and NOx by corona discharge reactors. Electrostatic precipitator (ESP) has already been widely used to mainly eliminate PM. ESP can eliminate PM almost in perfect, but can't remove NOx well. [1] We proposed a new method of simultaneous good removal of dust and NOx in the engine exhaust gas.

We have been researching on air cleaning reactor using a water-surface corona discharge with saw-edge electrodes. Water surface corona discharge is a corona discharge between discharge electrodes and water surface. This corona discharge provides more ozone and OH radical which are suitable radicals to proceed on the plasma chemical reactions for NOx treatment in engine exhaust gas. We confirmed the reactor provides good efficiently for NOx treatment by positive streamer corona discharge. We designed and carried out the treatment tests by the new model of hybrid system with two-stage ESP and water surface corona reactor.

2. EXPERIMENTAL SETUP

The hand-made water-surface reactor has 20 cm in width, a depth of 10 cm and 5 cm in height as shown in Fig.1. The reactor has three saw-edge discharge electrodes parallel placed 1.5 cm over the tap water surface. Fig.3 illustrates an experimental system. The hand-made two-stage ESP has 45 cm in width, a depth of 10 cm and 5 cm in height. The ESP and the reactor were connected with a plastic pipe of 1.5 cm diameter. The test gas was exhaust of diesel engine and supplied into the ESP by a plastic tube through a gas dry box after control of gas concentration. The test gas flow rate was 5l/min.

Concentration of dust particles was measured by piezobalance type dust monitor. NOx and

NO were measured separately by an ultraviolet absorbance type NOx analyzer. Positive and negative corona discharge characteristics of the ESP and the reactor were measured before the gas treatment tests. Removal rates were calculated by the measured dust and NOx concentrations when voltage was applied and not applied.

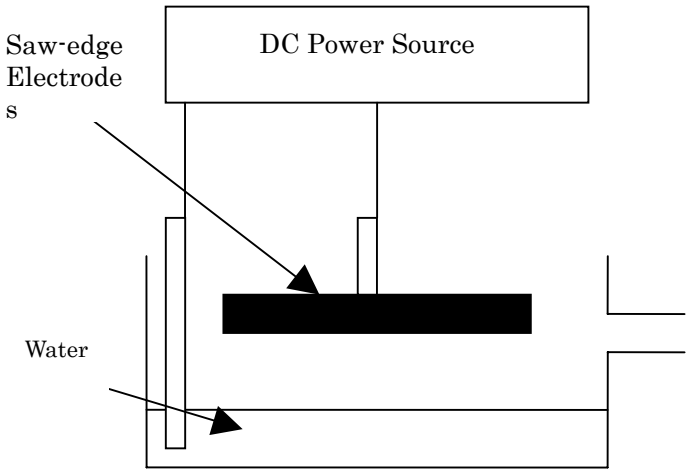

Fig.1 Corona Reactor with Water

Fig. 2 Saw-Edge Electrode

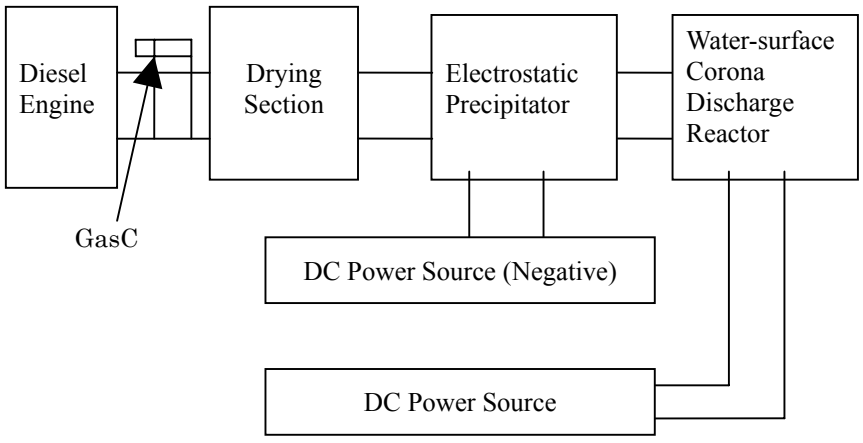

Fig.3 Experimental Layout

5. RESULTS AND DISCUSSION

Dust particles (SPM) in the diesel exhaust gas were well precipitated in the ESP by both positive and negative charging as shown in Fig.4. Positive and negative corona current over water in the reactor are shown in Fig.5. Maximum corona current was lower in positive than in negative. Fig.6 and Fig.7 show the NO and NOx removal rates by the hybrid treatment reactor system. The reactor system removed 100 % of NO and 80 % of NOx at 17 kV in positive corona but 38 % of NOx at 17 kV in negative corona discharge. The difference of NOx removal rates by applied voltage polarity is explained by ozone concentration generated in the corona space. Positive streamer corona produces more ozone than negative corona.

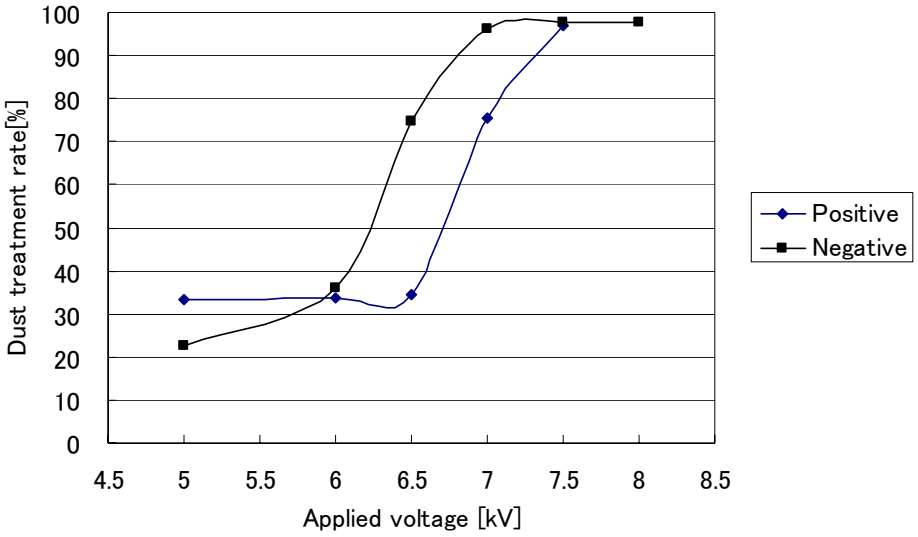

Fig.4 Dust Removal Rate by Two-stage ESP

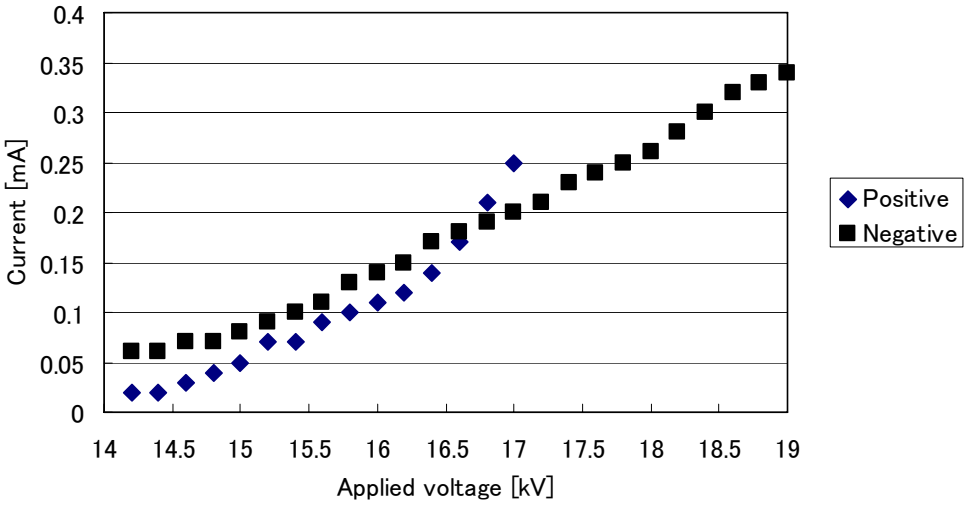

Fig.5 Corona Discharge Characteristics of Water-surface Corona Reactor

Estimated chemical reactions for NOx removal processes in the corona space in the reactor are,

Ozone produced by corona discharge oxidizes NO to NO_2 by reaction,

$$NO + O_3 \rightarrow NO_2 + O_2 \qquad (1)$$

NO_2 dissolves into water and changes into HNO_3 by following reactions,

$$3NO_2 + H_2O \rightarrow 2HNO_3 + NO \qquad (2)$$
$$2NO_2 + H_2O \rightarrow HNO_3 + HNO_2 \qquad (3)$$

These reactions are summarized as,

$$2NO + 3O_3 + H_2O \rightarrow 2HNO_3 + 3O_2 \qquad (4)$$

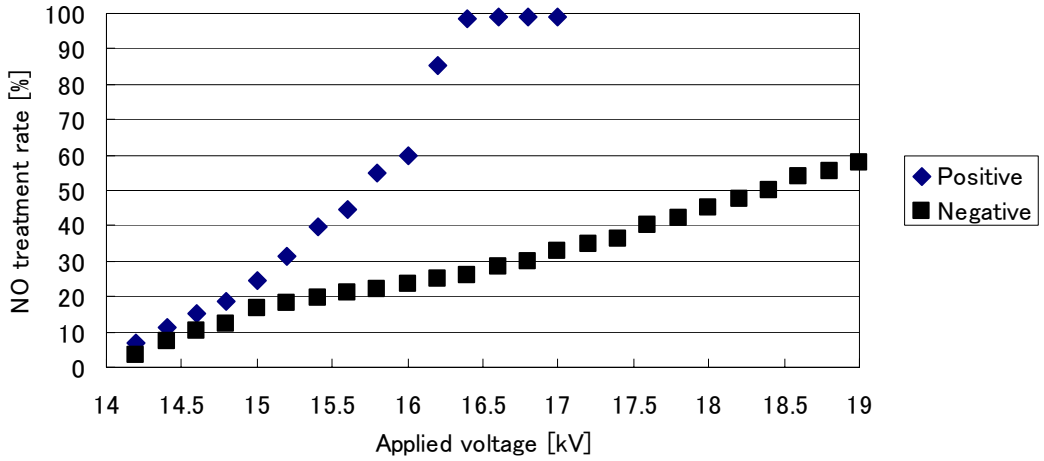

Fig.6. NO treatment rate by hybrid reactor system

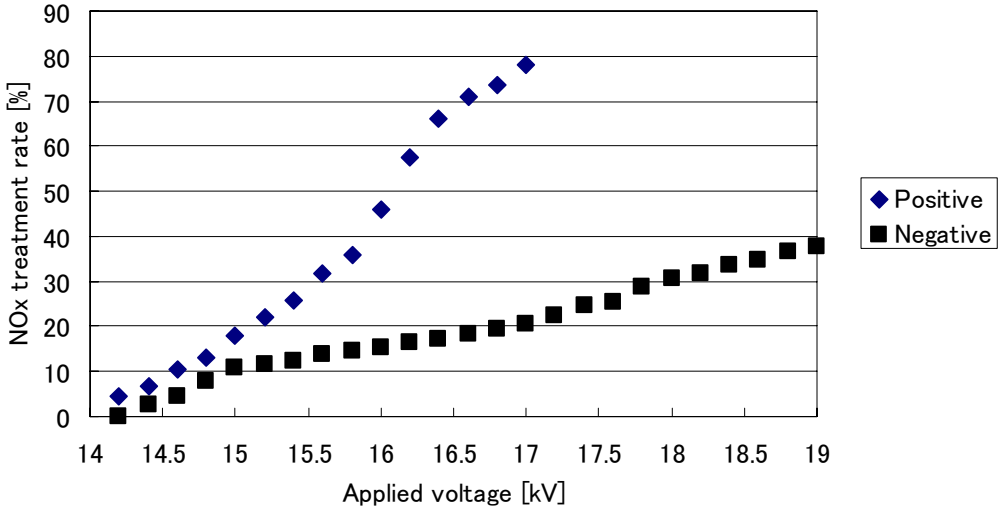

Fig.7. NOx removal rate by the hybrid reactor system

Positive streamer corona showed better NOx treatment than negative corona by our previous experiments with DC corona reactor with or without water. The hybrid system was confirmed to be effective to increase the NOx removal rate in the corona reactor by the reason of dust pre-cleaning in the two- stage ESP.

6 REFERENCES

[1] Tomio Fujii, Hiroshi Kitamura, Yasushi Arao. (2003). Development of Electrostatic Precipitator for Air Cleaning in Automobile Tunnel. 85-86

[2] The Institute of Electrostatics Japan. (1998). HANDBOOK OF ELECTROSTATICS 109-110

[3] Tomio Fujii, Yukio Aoki, Naoki Yoshioka, Massimo Rea. (2001). Removal of NOx by DC Corona Reactor with Water. Journal of Electrostatics, Vol.51-52, pp.8-

DEVELOPMENT OF OZONE GENERATOR USING PARALLEL DRIVING OF PIEZOELECTRIC TRANSFORMERS

K. Teranishi[1], S. Suzuki[2] and H. Itoh[2]

[1] *Department of Electrical and Computer Engineering, Ichinoseki National College of Technology*
Takanashi, Hagisho, Ichinoseki, Iwate 021-8511, JAPAN
[2] *Chiba Institute of Technology*
2-17-1 Tsudanuma, Narashino, Chiba 275-0016, JAPAN

ABSTRACT. Compact plasma reactors have been developed in our laboratory, which are construed by piezoelectric transformers (PTs) and are capable of generating glow discharges, corona discharges and dielectric barrier discharges (DBDs) in the wide gas pressure ranges from 10^{-3} to 10^{3} Torr. In particular, DBD-type ozone generator constructed by the PT could generate ozone with high yield efficiency up to 223 g/kWh. However, the maximum concentration and yield were obtained to be 20.3 g/Nm^3 and yield of 0.7 g/h, respectively, which may be hardly high enough in some ozone applications. In this study, a plasma reactor employing parallel driving of multiple PTs is investigated and applied to ozone generations in order to improve the power characteristics and to achieve higher ozone yield. By employing the parallel driving of six PTs, maximum ozone concentration is improved up to 44 g/Nm^3 and maximum yield is achieved to 3.5 g/h.

1. INTRODUCTION

A novel generation method of discharge plasma using piezoelectric transformers (PTs) has been developed and investigated to construct compact plasma reactors, aiming for the practical applications to plasma devices [1], [2]. By the present method, the mechanical vibration of the PT excites discharge plasmas on its ceramic surface that induces high-voltage due to the piezoelectric effect. This makes it possible to design compact plasma reactors and to generate various types of discharge plasmas, such as glow discharge, corona discharge and dielectric barrier discharge (DBD) at low-applied voltages in the wide range of gas pressure ranges from 10^{-2} to 10^{3} Torr. Therefore, the application of the DBD-plasma reactors constructed by the PT to the ozone generation has been attempted, which has been one of the important and successful applications of the DBD and has been also investigated by many researchers [3], [4]. Performance of the ozone generator based on our concept has been evaluated in the cases of feeding pure oxygen and air [1]. The result showed that the maximum yield efficiency was achieved up to 223 g/kWh by feeding oxygen; this value is very attractive compared to the DBD-type ozone generator reported by others [2]. However, the obtained maximum concentration and yield of 20.3 g/Nm^3 and 0.7 g/h are hardly high enough in some ozone applications. This is due to the compact configuration of the ozone generator, which is limited by the capacity of the reactor or power characteristics of a single PT operation. In this report, we will present some of the basic results for ozone generation by an ozone generator containing a single PT, characteristics of plasma reactor employing parallel driving of multiple PTs and the performance of the ozone generator employing the parallel driving of the six PTs.

2. EXPERIMENTAL

2.1. Ozone generator constructed by a single PT

Figure 1 shows the structure of the ozone generator that contains a single PT. A Rosen-type PT (60 x 13 x 2 mm) is used in this experiment. The PT is supported at its center and inserted in the rectangular duct framed by a couple of parallel glass plates. The distances between both sides of the PT surface and glass plates correspond to the gap length, which is maintained at 0.5 mm. The two glass plates are the dielectric electrodes and are covered with thin films of aluminium on their outer side as conductive back electrodes. A cooling water system is installed on both dielectric electrodes. When the PT is driven, the DBD plasma is generated at both gap spaces due to the high voltage induced on the ceramic surfaces of the PT. Sample gases, oxygen and air are provided from the gas inlet and pass through both of the gap spaces. The ozone concentrations are measured using an ozone monitor based on the UV absorption method. The generated ozone is finally exhausted in the atmosphere through an ozone decomposer. The discharge power is evaluated by the Lissajous figure method.

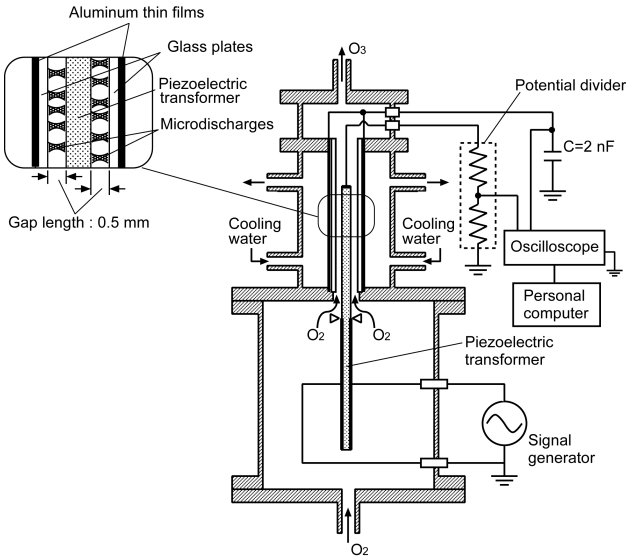

FIGURE 1. Ozone generator constructed by a single PT.

3. EXPERIMENTAL RESULTS AND DISCUSSIONS

3.1. Ozone production characteristics for the single operation of PT

The ozone concentration as a function of specific energy *W/Q* is shown in figure 2(a). Stable values of ozone concentration were obtained 5 min after starting operation of the ozone generator. By feeding oxygen into the ozone generator, the ozone concentration increases to a saturation level with increasing specific energy *W/Q*. The concentration is independent of the gas flow rate. The maximum ozone concentration is 20.3 g/Nm^3, achieved at a gas flow rate of *Q*=0.29 L/min.

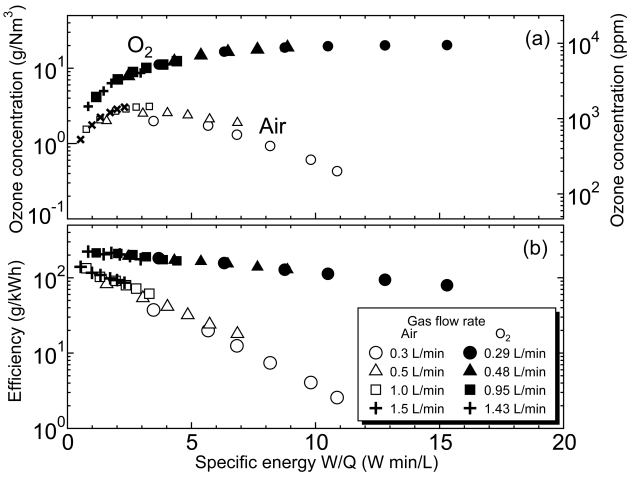

FIGURE 2. Ozone concentration and yield efficiency as a function of specific.

When air is supplied, the ozone concentration increases with increasing specific energy up to 3 W min/L, above which the concentration begins to decrease. In the higher specific-energy region, it is well known that nitrogen oxide (NOx) formation is enhanced, compared to ozone generation, and that the NOx molecules catalytically decompose ozone molecules [5]. Therefore, the decrease in ozone

concentration in air at specific energies higher than this threshold value is considered to be due to these previously identified reactions. The maximum ozone concentration in air is 3.38 g/Nm^3, achieved at a gas flow rate of Q=1.0 L/min. This concentration is six times lower than that achieved with pure oxygen supply.

Figure 2(b) shows the ozone yield efficiencies in oxygen and air as a function of specific energy. These values were determined from the results shown in figure2(a). The efficiency under both atmospheres decreases exponentially with increasing specific energy. The efficiency in oxygen is higher than that in air, and the negative gradient of efficiency with respect to specific energy in oxygen is fivefold lower than that in air. The maximum ozone yield efficiencies in air and oxygen were 139.6 and 222.7 g/kWh, respectively. Also, the maximum ozone yield is obtained to be 0.7 g/h at gas flow rate of 1.0 L/min.

3.2. Plasma reactor based on parallel-driven PTs

The PT-based ozone generator mentioned above consists of a single PT with discharge power of up to about 4 W at an applied voltage of 100 V. When higher power is injected into the PT, the device sometimes fractures due to the large amplitude of mechanical vibration. This remains a practical limitation of PT-based plasma reactors. To achieve higher power characteristics, the parallel driving of multiple PTs has been investigated. The electrode configuration of the plasma reactor with six parallel-driven PTs is shown in figure 3. The PTs are connected in parallel, wedged between a glass plate and the back electrode on a contact with spacers. DBD thus appears on both sides of the PT surface. Although individual voltage sources for each PT are shown in the schematic, the six PTs are connected in parallel and operated by a single signal generator via a voltage amplifier.

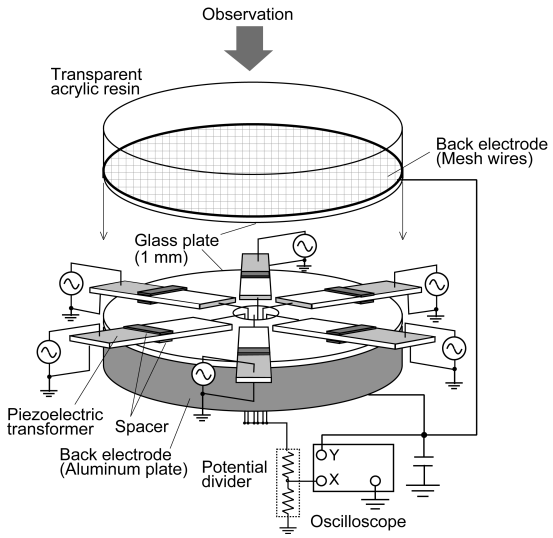

FIGURE 3. Configuration of plasma reactor employing parallel-driving of multiple PTs.

3.3. Observation of light patterns

Figure 4(a)-(f) shows typical light emission from this plasma reactor by changing number of the operated PTs. In this experiment, we use a back electrode that consists of a fine mesh (#152) of metal wires with a transparent acrylic body, allowing light patterns to be observed perpendicular to the electrode surface. The filamentary microdischarge is observed on each surface of the PT. The power achieved by this parallel configuration of six PTs is approximately 12 W that is thus 3 times that for single-PT operation. These results show that the discharge power is not proportional to the number of PTs connected, which may be due to a limitation of the voltage amplifier employed in this experiment.

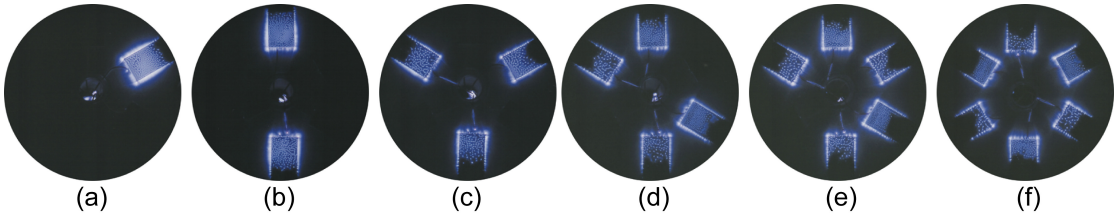

FIGURE 4. Observed light patterns of DBD by changing number of the operated PT.

3.4. Ozone production characteristics for parallel driving of Six PTs

Figure 5 shows the ozone concentration as a function of specific energy obtained by the ozone generator based on the parallel driving of the six PTs. Oxygen (99.9999%) was fed into the generator with gas flow rate of 0.5-3.0 L/min. The experimental results of the ozone generator constructed by a single PT that indicate in figure 2(a) are also plotted in the graph for the comparison.

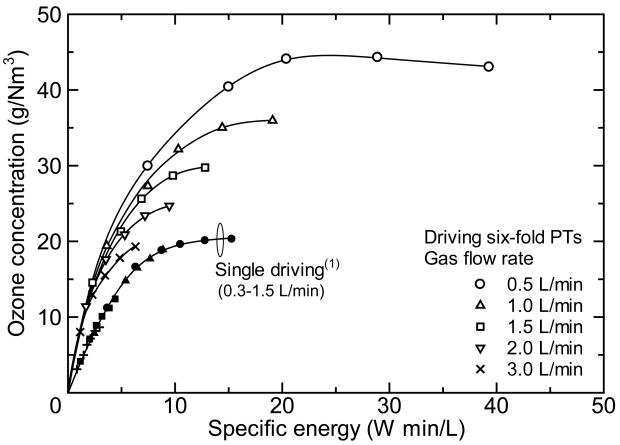

FIGURE 6. Ozone concentration characteristics for ozone generator based on the parallel driving of six PTs.

In the lower specific energy region below 3 W min/L, ozone concentration increases almost linearly, being independent of the gas flow rate. In this region, the slope of the curves is twice as large as that of the single-type ozone generator. However, increasing the specific energy, the ozone concentrations are saturated and depend on the gas flow rate. Although the saturations of the concentration are observed dominantly in the lower gas flow rate, the maximum ozone concentration of 44.3 g/Nm^3 is obtained at 0.5 L/min in gas flow rate. Therefore, the ozone concentration is improved by employing the parallel driving of the six PTs and the maximum concentration of the parallel-type ozone generator is about twice as large as that of the single-type one. The maximum ozone yield was also obtained to be 3.5 g/h at gas flow rate of 3.0 L/min, which is five times greater than that of single-type ozone generator.

4. CONCLUSIONS

The performance of two types of ozone generators constructed by a single PT and employing the parallel driving of the multiple PTs are investigated. The single-type ozone generator offers a compact system for ozone generation and small amount of ozone can be produced, in which the maximum ozone concentration and yield are about 20 g/Nm^3 and 0.7 g/h, respectively. By ozone generator employing parallel driving of the multiple PTs, the maximum ozone concentration and yield can be improved up to 44 g/Nm^3 and 3.5 g/h, which are twice and fivefold higher than those of the single-type ozone generator, respectively.

REFERENCES

[1] Teranishi, K., Suzuki, S. and Itoh, H. (2004). A Novel Generation Method of Dielectric Barrier Discharge and Ozone Production Using a Piezoelectric Transformer. *Jpn. J. Appl. Phys.,* 43, 6733-6739.

[2] Itoh, H., Teranishi, K. and Suzuki, S. (2005). Discharge Plasmas Generated by Piezoelectric Transformers and Their Applications. *Plasma Sources, Sci. Technol.*, 15, S51-S61.

[3] Kogelschatz, U. (2005). Non-Equilibrium Plasmas at about Atmospheric Pressure. Proc. 27th ICPIG, (CD-rom) W1-355

[4] Gibalov, V. I. and Pietsch, G. (2006). On the Performance of Ozone Generators Working with Dielectric Barrier Discharges. Ozone Science and Engineering, 28, 119-124.

[5] Yagi, S. and Tanaka, M. (1979). Mechanism of Ozone Generation in Air-Fed Ozonisers. J. Phys. D: Appl. Phys., 12, 1509.

RESEARCH ON THE POWER FACTOR CHRACTERISTCS OF OZONIZER

Liu Zhongjie, Quan zhaochun, Guan Genzhi, Zhang Yuanfang

Department Of Electrical Engineering
Faculty of Science and Engineering, Wuhan University
Wuhan, 430072, CHINA

ABSTRACT. At present, there are some problems needed to be settled for large power-middle frequency-high-voltage power supply. In this paper, on the basis of measurement of V-A characteristic and discharge power of a special middle-frequency (5~20 kHz) ozoner, its dynamic capacity value and discharge power factor while different frequency applied in the experiment have been detected. When middle-frequency voltage is added between the electrodes, the dynamic capacity of the reactor elevates several times, capacitive resistance and the capacity current also ascends largely. The power of the supply is not only very large but also changes sharply. Within the normal voltage domain (2 kV~30kV), the dynamic capacity have a peek value, which is meaningful for the research of the research on power supply which has a nonlinear load when discharging and on its power injection characteristic and discharge parameters optimization.

1. INTRODUCTION

There are lots of researches on DBD[1][2], the mechanics of ozone generating[3], power supply designs and their improvements. Ozone generating equipments as electrical loads have nonlinear characteristics, so researches about its dynamic electrical characteristics are important and meaningful to the design of ozonizer, optimization of the electrical parameters and the matching problem between the power supply and the reactor load.

2. DISCHARGE THEORIES AND EQUIVALENT CIRCUIT OF DBD OZONIZER

According to the theory of ozone generating, the equivalent circuit of the equipment is made up of the series of dielectric capacitance (C_d) and gas capacitance (C_g) when no transmit current is formed. Once the discharge between the electrodes happens, the gap can't be treated as capacitance anymore but a resistance, the voltage of whom is not ever changed, or it can act like a zener diode. The structure of the discharge tube and the equivalent circuit of reactor that often used as discharge model are shown in Figure 1.

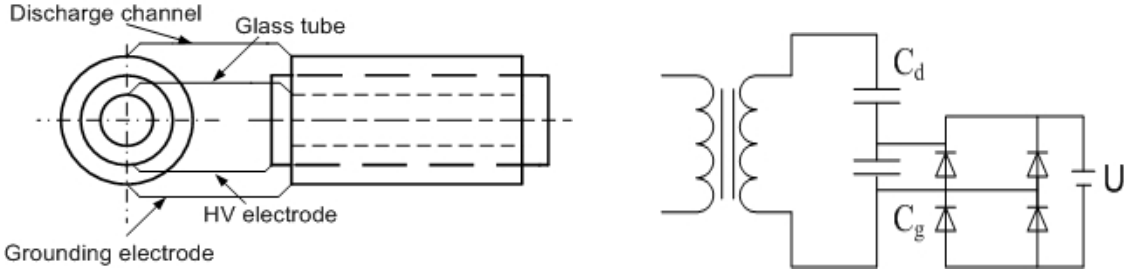

FIGURE 1 Equivalent circuit of ozone generator and the structure of the generating tube

Figure 2 is the structure the experimental install that used to detect the V-A characteristic of the reactor .Cylindrical structure is supposed as the discharge reactor, it is made up chiefly by insulate dielectric (Cylindrical class pipe) and discharge pipeline. When the voltage applied is less than the breakdown voltage(U_g), the ozonizer can be thought as series of the dielectric capacitance (C_d) and gas capacitance (C_g).The discharge channel capacitance remain invariable, while gas capacitance changes, the equivalent capacitance (C_t) of the total

ozonizer load and the transformer's inductance make up a series- resonance. Because the frequency of the equivalent series circuit is $\sqrt{LC}$, when the applied voltage exceeds U_z , the discharge enhances and leads to the increase of C_t but the value of $\sqrt{LC}$ decreases.

3. V-A CHARACTERISTICS OF THE REACTOR AND VOLTAGE-CURRENT AND DISCHARGE POWER WAVEFORM

To detect the characteristics of the loads and provide credible evident of design of power source, an ozone generating system is set up in the lab. Industrial oxygen is adopted as the gas supply, the discharge reactor is made up of a grounding electrode which is a stainless steel coaxial cylinder around which has the refrigeration pipe using cold water; a glass discharge tube as the discharge tube which has electric coat on the wall of it (the length is about 80 cm, outer diameter is 50 mm, inner diameter is 47 mm). An adjustable frequency power supply which has a regulating range from 50Hz to 2 kHz .A pulse current detector (TM63), pulse amplifier (TM501A), HV pulse detector and digital oscilloscope (Tek220) are used to detect the characteristics of voltage-current (as shown in Figure 2) and instantaneous discharging power.

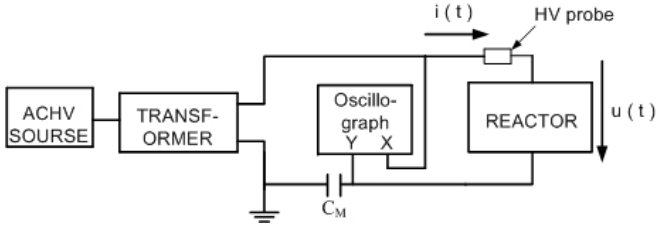

FIGURE 2 Sketch of measuring instantaneous by measuring Lissajou figure

C_M is used to measure the dynamic capacitance of the reactor. Figure 3 shows the waveform of the voltage, the current together with the instantaneous power during the discharge.

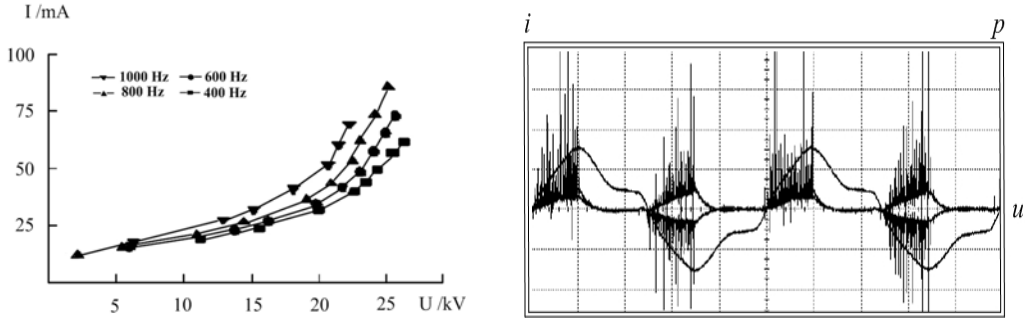

FIGURE 3 Typical V-A Characteristics and waveforms curve of instantaneous power

4. CHARACTERISTIC OF DYNAMIC CAPACITANCE OF THE REACTOR LOAD

The table of dynamic capacitance of the reactor can be gained by measuring the characteristic of voltage charge Lissajou figure, as show in table 1. The frequency of the applied voltage ranges from 50 Hz to 2 kHz. C_I is the capacitance of the reactor after the discharge ,which equals the value of the medium capacitance (C_d). C_{II} is the in-series-value of the medium capacitance (C_d) and the gas capacitance (C_g). The dynamic capacitance of the load changes largely during the discharge when different frequency voltages are applied because the ozone generator has special characteristic as a type of load of discharge. It can be seen that the capacitance of the reactor improves 3 or 4 times. Comparing the situation of discharge a conclusion can be drawn that once the gas medium is break, the conductivity of

the load enhances sharply.

TABLE 1. Dynamic load-capacitance of the reactor when applied different frequency voltage

f/Hz	V / kV	C_{I} / nF	C_{II} / nF
50	9.36	1.21	4.1
50	20.51	1.56	5.50
100	20	0.90	3.61
500	20	0.95	3.21
1000	20	0.91	3.25
1500	20	0.96	3.38
2000	20	0.81	3.51

5. REPRESENTATIONS AND CALCULATION OF DISCHARGE POWER AND THE POWER FACTOR

Discharge power and the power factor are important parameters, which reflect the working characteristic of ozone reactor in ozone generation research field. It is meaningful in the design of source and the matching of the source and the reactor and in the optimization of the electric parameters. Usually the discharge power can be measured by measuring the Lissajou figure or instantaneous power curve. The reactor is a kind of capacitive load and its power factor is no more than 1. To investigate the character of PF (ignore the influence of the temperature to the react) the analysis of the stationary working process of the ozonizer is necessary. Supposing U_m is the peak value of applied voltage; U_z is the break voltage; g, b are the character parameters, defining $k = U_m/U_z$, $b = C_g/C_d$, $g = U_d/U_z$.

The voltage formula is

$$U = -U_m \cos 2pft \tag{1}$$

The voltage of the gap is

$$U_g = \frac{1}{C_g}\int_0^t idt + U_g(0) = \frac{kU_z}{1+b}(1-\cos 2pft) + U_g(0) \tag{2}$$ [2]

When the voltage of the gas (U_g) exceeds the break voltage (U_z), the gas gap is break .So from formula (2) the following formula can be get:

$$q = \arccos[1-2(1+b)/k] - 2p \tag{3}$$

The active power consumed on the equivalent resistance of the reactor is:

$$P_0 = \frac{U_m^2}{2R_e} = 4fC_d^2U_z^2[k-(1+b)] \tag{4}$$ [2]

The effective current is:

$$I = \frac{\sqrt{p}fC_dkU_z}{1+b}\sqrt{2p(1+b)^2 + (1+2b)(\sin 2q - 2q)} \tag{5}$$ [1]

Then the apparent power is

$$S = I_g U_M / \sqrt{2} = \sqrt{p/2(1+b)} + C_a k^2 U_z^2 \sqrt{2p(1+b)^2 + (1+2b)(\sin 2q - 2q)} \tag{6}$$

so power factor is the ratio of active power and apparent power:

$$PF = \frac{P_0}{S} = \frac{4\sqrt{2}(1+b)[k-(1+b)]}{k^2\sqrt{2p^2(1+b)^2 + (1+2b)(\sin 2q - 2q)}} \tag{7}$$

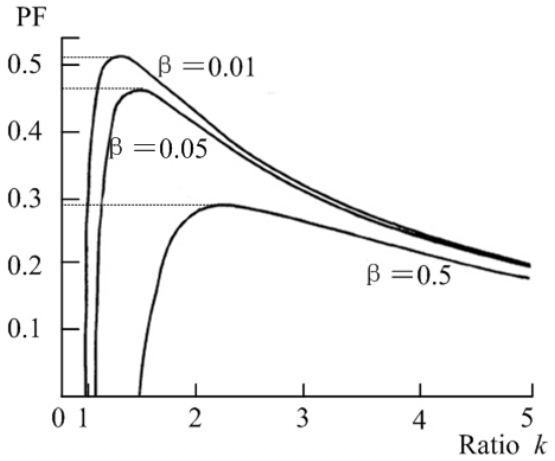

Figure 5 Curve of PF when β varies from0.01, 0.1 to 0.5 respectively

From figure5 it is seen that there are peak values of the power factor when b is evaluated several values respectively when k varies in the value rang from 0 to 5. There is a value rang of k, in which the equivalent resistance of the reactor has a minimum and the power factor has a maximum. According to figure6 it is known when the value of k is assigned from 1.21 to 3.75 the parameters of the ozonizer are matched most perfectly and the PF gains its maximum when the voltage is properly applied.

6. CONCLUSIONS

It is obvious that the power factor has a close relationship with the applied voltage and the frequency, but not simple linearity because the electric parameters of the discharge channel would change with the change of the frequency when the applied voltage is fixed. From the equal circuit it can be observed that the dynamic capacitance and the equal impedance of the reactor take on nonlinearly characteristics when applied deferent frequency AC voltage. According to the paper the value of power factor is influenced by not only the structure of the reactor and the distribution of the gas pressure, but also the peak value and waveform of the applied the voltage. It can also be concluded that in the certain voltage range there would be a peak value of the power factor.

REFERENCES

[1] S. Masuda, et al. (1999). A ceramic-based ozonizer using high frequency discharge. *IEEE Trans on Industry Application*, 24 (2).

[2] Wang Ninghui, et al. (2001) DBD Research on measurement of discharge power in DBD plasma reactor. *Journal of Scientific Instrument*, 22(3):78-79.

[3] Xu Xueji, Zhu Dingchang. (1996). Discharge Physics. Shanghai, *Fudan University Press*.

Improvement of ozone generation efficiency using parallel surface discharge type ozonizer

Kotaro Fujii , Satoshi Ihara , Chobei Yamabe

Department of Electrical and Electronic, Engineering,
Faculty of Science and Engineering, Saga University
1 Honjyo-machi,Saga 840-8502, Japan

Abstract. Recently, one of the most important content of ozone generation at atmospheric discharge is to improve the efficiency (ozone yield) for the discharge power. The parallel surface discharge ozoneizer was studied to improve the ozone yield. The parallel surface discharge ozonizer succeeded high the ozone yield compared with the single surface discharge ozoneizer.

1. Introduction

At the present time, one problem of the ozonizer operating at atmospheric discharge is lower the ozone yield than theoretical value. To increase the ozone yield, various studies were performed. The double-discharge-type ozonizer[(1)]is a method that the generated main discharge is triggered by the pre-discharge. It is able to get the high ozone yield of 400-450 [g/kWh] in the low ozone concentration. In other study, the method producing ozone is a polarization electric charge generated on the piezoelectric transformer with a mechanical vibration into the piezoelectric transformer. Therefore, the piezoelectric transformer is used as the ozonizer [(2)]. In recent years, surface discharge is attracting attention in ozone generation [(3)]. In comparison with a silent discharge used for industrial application, surface discharge can work at lower voltage. In addition, a surface discharge can be operated with high frequencies more than 10(kHz) at atmospheric pressure. In this study, as a method to raise the ozone yield, we devised the parallel surface discharge electrodes, which were arranged an electric discharge side of the surface discharge electrode of flat plate facing each other. Not only the surface discharge on one electrode but also volume discharge occurred between two electrodes arranged parallel. Since discharge occurred between two electrodes, the ozone concentration increased, and the ozone yield was higher than that of the single surface discharge ozonizer.

2. Experimental apparatus

2.1 Construction of electrode

The surface discharge type of ozonizer used for this study is constructed with the discharge

electrode, dielectric material and grounded electrode as shown in Fig.1. The discharge electrode is made of ruthenium oxide. The dielectric material is made of alumina ceramics. And the grounded electrode is made of alloy of silver and palladium. The dielectric is 37[mm] in length, 15[mm] in width, 0.8 [mm] in thickness. When high voltage is applied on a discharge electrode, non-uniform electric field occurs between the discharge electrode and the grounded electrode, the discharge occurs along the non-uniform electric field. Therefore, strength of discharge is in proportion to electric field strength, and the discharge area is almost identical to the area of the grounded electrode. The parallel surface discharge electrodes used in this study are shown in Fig.1. The left figure (a) shows a bird's-eye view, and the right one (b) shows a cross section of oblique lines in the left figure. Both electrode A and B are made of ruthenium tetroxide. In order to avoid arc discharge on those electrodes, horizontal distance between electrodes A and electrode B is set to 1.5[mm]. The vertical distance X between electrode A and B is set 0.5[mm] or 1[mm] in this study.

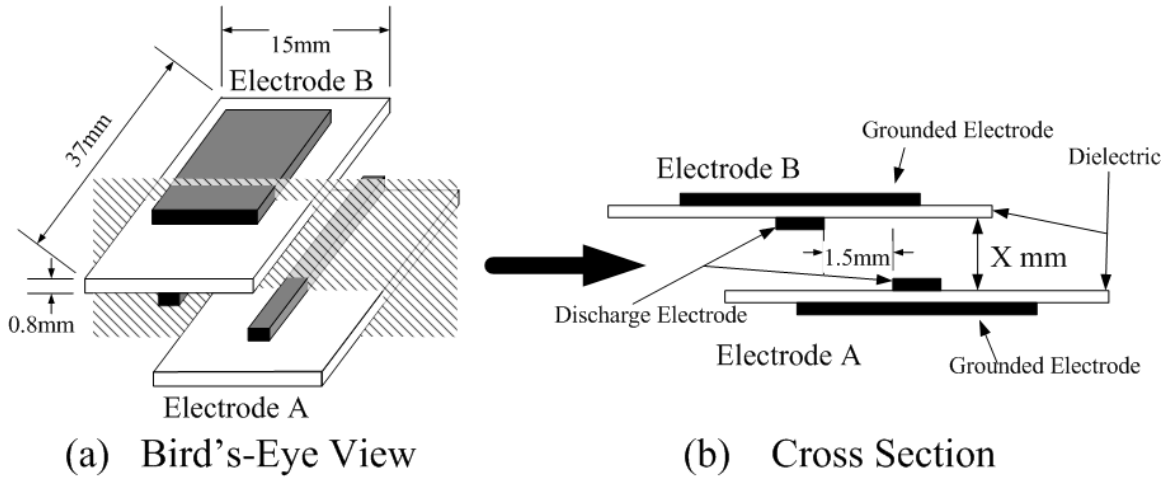

FIGURE 1. Structure of Parallel Electrodes

2.2 Experimental method

In this study, we prepared the same condition such as 30 [kHz] for high frequency power supply, and 5.0[kV_{PK-PK}] high voltage applied on the electrodes A and B. The phase difference between the voltage applied on electrodes A and B is change, from 10[deg] to 130[deg] with the barium capacitor. The discharge power was measured by V-Q Lissajou's figure. Where, the V is the applied voltage to the electrodes and Q is the electric charge for discharge measured by capacitor connected between the grounded electrode and earth. The 99[%] of oxygen gas are used for ozone generation. The oxygen gas flow controlled by the mass-flow controller is 1[liter/min]. The concentration of ozone was measured by the UV absorption ozone monitor (Ebara Jitsugyo Co.,Ltd., EG-2001). The ozone yield [g/kWh] was calculated by the following equation.

$$\textbf{Ozone Yield[g/kWh]} = \frac{\textbf{Ozone production per hour [g/h]}}{\textbf{Discharge power per second[W]}} \times \textbf{1000} \qquad (1)$$

3. Results and discussion

The applied voltage waveforms on electrodes A and B are shown in Fig.2 at the phase difference is 118[deg]. At a certain instant, the maximum potential difference on electrodes A and B was defined as V_M. When the phase difference is changed from 10[deg] to 130[deg], the influence of the ozone yield at X=1[mm] and X=0.5[mm] is indicated in Fig.3. The applied voltage to both electrodes A and B in this case is 5.0[kV_{PK-PK}] respectively. The ozone yield at X=0.5[mm] is higher than that of 1[mm]. Because two electrodes are parallel, the volume discharge occurred between two electrodes. It is assumed that the volume discharge is guided to the opposite surface discharge electrode which is grounded. Therefore, when gap space X is shorter, electric field strength in the gap becomes stronger, and it is thought that the volume discharge becomes stronger, thus the ozone yield increase. The ozone yield is improved when the phase difference of applied voltage becomes closer to 180[deg]. The ozone yields increase rapidly in particular in 10-30[deg] and 120-130[deg]. From 10[deg] to 30[deg] or from 120[deg] to 130[deg], the voltage of V_M in Fig.2 soars whenever the phase difference is changed. When V_M increases, an electric field between two electrodes becomes stronger and therefore an ozone yield increases.

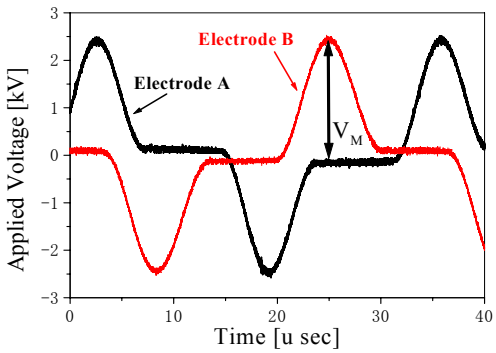

FIGURE. 2. Waveform of applied voltage. Phase difference is 118[deg].

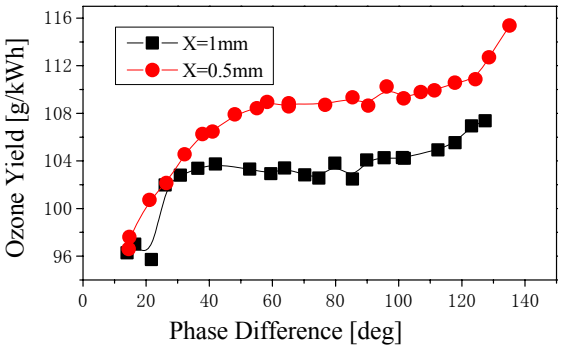

FIGURE. 3. Ozone Yield as a function of the phase difference.

To evaluate the ozone yield improvement for the parallel surface discharge electrodes used, we compared the value obtained by the parallel surface discharge electrodes with that of the single surface discharge electrode. The results are shown in Fig.4 and Fig.5. In Fig.4, the horizontal axis indicates the specific energy [W min/litter]. The vertical axis indicates the effect for the ozone concentration in Fig.4. And in Fig.5, the horizontal axis indicates the specific energy [W min/litter]. The vertical axis indicates the effect for the ozone yield is shown in Fig.5. In ozone generation with the single surface discharge electrode, only the electrode A used. In addition, the electrode B was changed into an acrylic wall. In the single surface electrode, in order to control specific energy, the applied voltage of electrode A changed from 4.5[kV_{PK-PK}] to 5.7[kV_{PK-PK}]. In comparison with the case of single surface discharge electrode, the parallel surface discharge electrodes increased the ozone

concentration maximum about 40% at both X=1[mm] and 0.5[mm]. In the ozone yield, the parallel surface discharge electrodes improved about maximum 40% at both X =1[mm] and 0.5[mm] compared with the case of single surface discharge electrode.

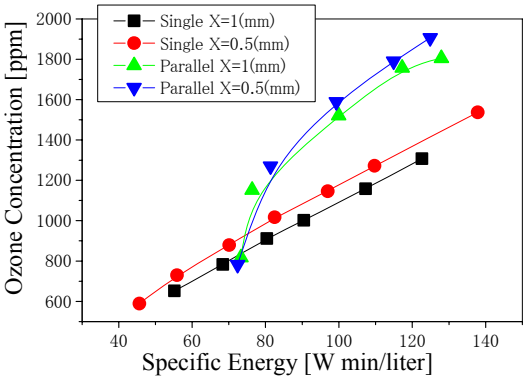

FIGURE. 4. Ozone concentration as a function of specific energy. In parallel, phase difference is 130[deg].

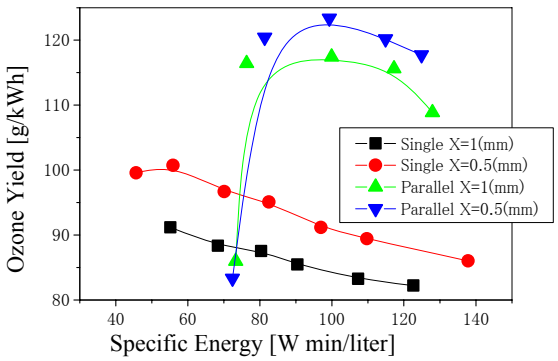

FIGURE. 5. Ozone yield as a function of specific energy. Phase difference is130 [deg].

4. Conclusion

The ozone yield increased rapidly with the parallel surface discharge electrodes when the phase difference of applied voltage became closer to 180[deg]. Compared to a single surface discharge electrode, the ozone concentration and yield increased about maximum 40%.

Acknowledgement

The author is grateful Dr.N.hayashi at Saga University for his discussion. The authors appreciate Mr.T.Tomari at Saga University for his collaboration.

References

(1)C.Yamabe, H.Akiyama, and K. Horii (1985) Proc, 7th Int. Symp. Plasma Chemistry, Eindhoven 327

(2) H.Itoh (2005) Discharge plasmas generated by piezoelectric transformer and their application. XXVIIth ICPIG ,Eindhoven , the Netherlands ,18-22

(3) S.MASUDA , K.AKUTSU, M.KURODA ,Y. AWATSU and Y. SHIBUYA(1988) A Ceramic-Based Ozonizer Using High-Frequency Discharge. IEEE Trans. IAS. VOL24, NO. 2 , 223-231

APPLICATION OF XeI EXCIMER RADIATION FOR EXCITATION OF PHOSPHORS

M. M. Guivan[1], A. Brablec[2*], J. Janca[2], P. St'ahel[2], P. Slavicek[2] and A. N. Malinin[1]

[1]*Department of Quantum Electronics,*
Faculty of Physics, Uzhgorod National University
Pidgirna 46, 88000 Uzhgorod, UKRAINE

[2] *Department of Physical Electronics,*
Faculty of Science, Masaryk University
Kotlarska 2, 61137 Brno, CZECH REPUBLIC

ABSTRACT. A diffuse coplanar surface discharge (DCSD), which generates in Xe/I_2 or $Ne(Kr)/Xe/I_2$ mixtures at pressures 1-100 kPa an intense narrow band ultraviolet excimer radiation at 253 nm (XeI^*), has been investigated. Spectral characteristics of the gas-discharge plasma as well as a composition of the working media have been studied in order to obtain the maximal yield of XeI excimer radiation. The experimental study of excitation of phosphors (green, red, and white component) by UV radiation has been carried out.

1. INTRODUCTION

Nowadays an active interest has been expressed to create efficient mercury-free gas discharge sources of spontaneous radiation in UV spectral range [1]. Dielectric barrier discharge (DBD) that excites rare gases and rare gas–halogen mixtures provides an efficient scheme for generating incoherent excimer radiation. Diffuse coplanar surface discharge (DCSD) is a type of the DBD generated on the surface of a dielectric barrier with embedded electrodes in planar design [2]. As to the creation of new light sources the great interest represents a xenon-iodine mixture because of effective formation of XeI* molecules. The wavelength of $B - X$ transition in XeI* excimer molecules (λ=253 nm) coincides with the brightest line of Hg at λ=253.6 nm. This is the reason why the phosphors developed for lamps based on mercury can be directly used in the mercury-free light sources emitting the radiation in the same wavelengths range as mercury tubes.

In this contribution the use of UV excimer radiation generated in diffuse coplanar surface discharge (DCSD) for excitation of green, red and white phosphors has been studied experimentally.

2. EXPERIMENTAL SET-UP

The experimental apparatus has been already described in [3]. The DCSD electrode module was manufactured on the glass plate as presented in [2]. Strip–like electrodes were 2

* Electronic address: abr92@elanor.sci.muni.cz

mm wide, the distance between strips was 1 mm. The thickness of a glass layer above electrodes was 0.14 mm. The plasma consists of numerous H-shaped elementary discharges with brighter streamer-like filamentary plasma that bridges two clouds of diffuse plasma formed over the embedded electrodes. The distance between the glass plate covered by phosphor and plasma sheet could change within the limits of 0.5-20 mm. The electrode system was mounted inside a chamber of 1.5 l in volume.

To excite working mixture the generator of high voltage AC pulses was used (peak-to-peak voltage up to 10 kV, frequency range from 1 to 100 kHz). The current/voltage measurements across the DCSD were performed for a discharge voltage up to 7 kV by current shunt and voltage probe Tektronix P6015A, respectively. Both quantities were registered by digital oscilloscope HP Infinium (500 MHz, 2 GSa/s). The total charge was measured with a non-inductive ceramic capacitor, used instead of the shunt. The average input electrical power was calculated using two methods: (a) directly by multiplying the voltage and current waveforms (Fig. 1,a), (b) from the charge-voltage Lissajous figure (Fig. 1,b). Typically, the charge-voltage figure is close to a parallelogram. The area of this figure is proportional to the energy dissipated during one period of the voltage. The average power is taken the area multiplied by a frequency.

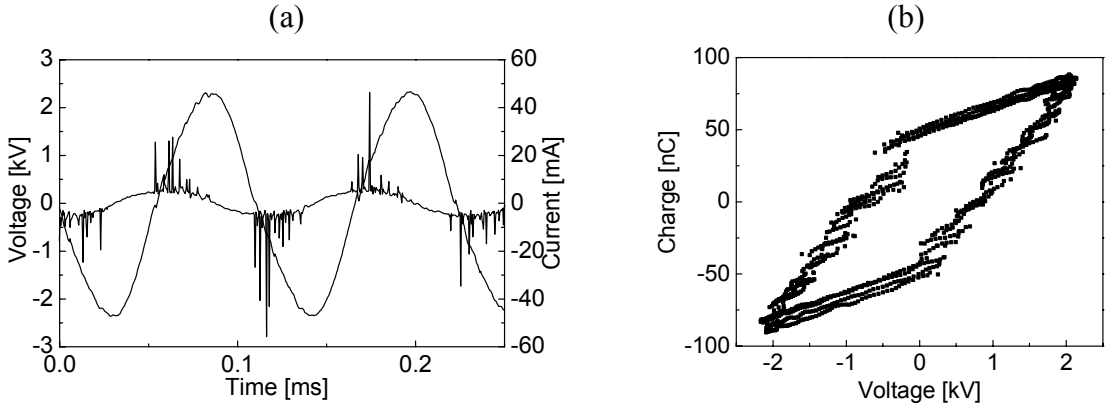

FIGURE 1. Typical voltage and current waveforms (a) and charge-voltage Lissajous figure of a DCSD (b) operated in the working mixture $Kr/Xe/I_2$ = 51 kPa / 4 kPa / 40 Pa.

Prior to filling of gases the chamber was pumped down below 10 Pa, iodine crystals were dried by means of resublimation cycles. The working mixture of rare gases with iodine vapors was prepared directly in the chamber.

The radiation was monitored perpendicularly to the surface of dielectrics through quartz window and it was analysed in spectral range 200-900 nm. The spectra were recorded by means of the Jobin - Yvon TRIAX 550 monochromator (grating 1200 grooves/mm, quartz optical fiber) equipped with high-speed CCD Spectrum ONE detector liquid nitrogen cooled. Spectral resolution of the system was about 0.05 nm. The registration system was calibrated within the wavelength regions 200 – 400 nm and 400 – 900 nm by means of the Deuterium lamp and Quartz Tungsten Halogen lamp emitting continuous spectra.

3. RESULTS AND DISCUSSION

The emission spectra of the DCSD operated in the Xe/I_2 or $Ne(Kr)/Xe/I_2$ mixtures were recorded and in UV range the molecular bands were observed such as XeI($B \rightarrow X$) - 253 nm,

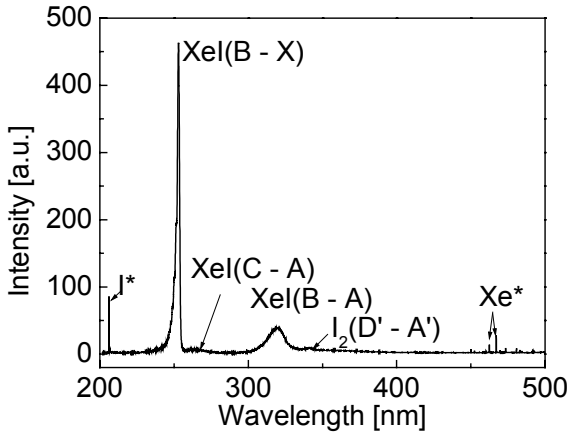

FIGURE 2. Emission spectrum of the DCSD in the working mixture Xe/I_2 = 15 kPa /40 Pa.

XeI($B \rightarrow A$) - 320 nm and $I_2(D' \rightarrow A')$ – 342 nm. The band XeI($B \rightarrow X$) has maximal brightness (Fig. 2).

The radiation brightness of molecular band was considered to be proportional to the area below corresponding curve in the spectrum. The full width at half maximum (FWHM) of XeI($B \rightarrow X$) band decreases from 2.6 to 1.5 nm within the pressure range 5 – 100 kPa. The optical emission at 206.2 nm has been realized due to atomic iodine transition ($^2P_{3/2} \rightarrow {}^2P_{1/2}$). A very low intensity emission was observed at 265 nm that correlates to XeI($C \rightarrow A$) while the wide molecular band in the range 350 - 400 nm with the maximum around 375 nm corresponds to Xe_2I^* excimer at pressure p(Xe)>25 kPa. Its brightness grows while the pressure increases. The low intensity atomic lines of Xe($7p \rightarrow 6s$) were revealed at 462 and 467 nm (Fig. 2).

The working mixtures were optimized for maximal yield of UV excimer radiation. Figure 3 shows the brightness of the XeI(B-X) band vs. frequency and xenon pressure in the Xe/I_2 mixture at fixed pressure I_2 $p(I_2)$=40 Pa. The XeI(B-X) band increased to its maximum value with gas pressure, and then decreased when the gas pressure p(Xe)>15 kPa was reached.

In the $Kr/Xe/I_2$ mixture the UV output initially increases with gas pressure, up to the maximum value in the range of 40-60 kPa, and then some decreases with pressure. Unlike to Xe/I_2 mixture, in the emission spectra of $Kr/Xe/I_2$ it was observed that the intensity of $I_2(D' \rightarrow A')$ band was more higher than intensity of XeI($B \rightarrow A$).

Using the different phosphors, the intense visible radiation was only observed in xenon-containing mixtures, such as Xe/I_2 or $Ne(Kr)/Xe/I_2$, capable to form the XeI excimer molecules (Fig. 4, 5). The best result was obtained when the $MgAl_{11}O_{19}$:(Ce, Tb) green phosphor (maximum intensity at 541 nm) was used (Fig. 5). Only weak fluorescence in visible range was registered when Ne/I_2 or Ar/I_2 mixtures was used. It was revealed that optimal distance between plasma and phosphor for obtaining intense homogeneous visible light was 3-5 mm.

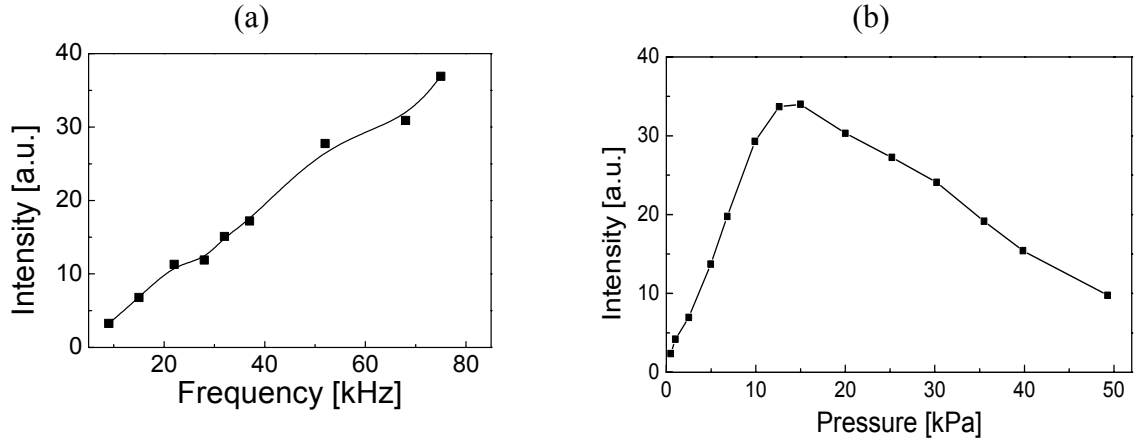

FIGURE 3. Brightness of the XeI(B-X) band vs. frequency (a) and xenon pressure (b), both in the mistureXe/I_2 at $p(I_2)$=40 Pa.

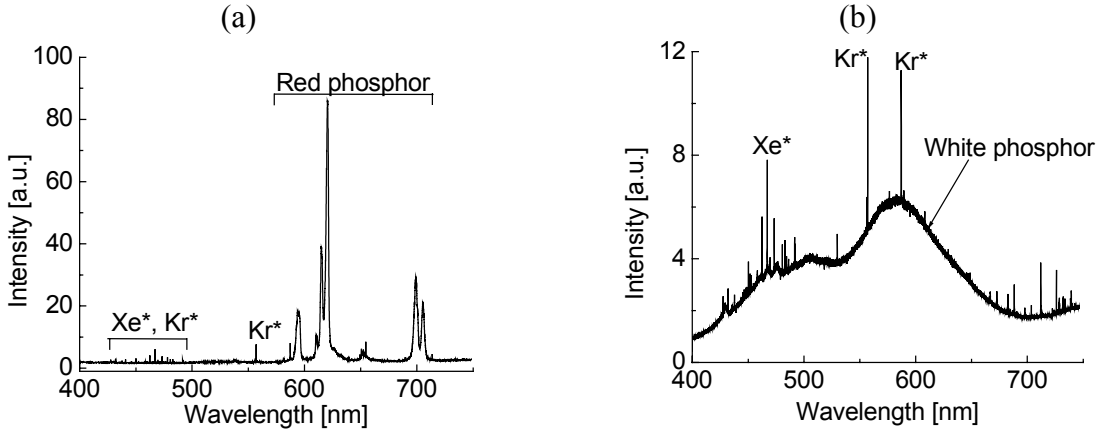

FIGURE 4. Emission spectra of the Y_2O_3:Eu red phosphor (a) and white phosphor (b) upon XeI* excitation (working mixture: $Kr/Xe/I_2$ = 51 kPa/4 kPa/40 Pa).

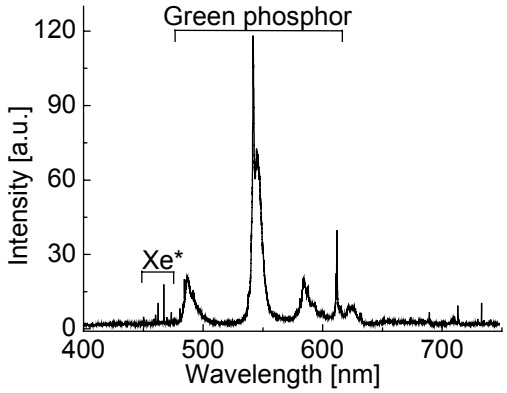

FIGURE 5. Emission spectrum of the $MgAl_{11}O_{19}$:(Ce, Tb) green phosphor upon XeI* excitation (working mixture: Xe/I_2 = 15 kPa/40 Pa).

The homogeneity was lower smaller distance of the phosphor and the DCSD while at big distance the intensity falls.

4. CONCLUSION

The excitation of phosphors by the XeI* excimer radiation generated by the DCSD was investigated. The working mixtures were optimized to obtain maximal output of the UV radiation. It was shown that Xe/I_2 or $Ne(Kr)/Xe/I_2$ discharges have the potential to be used in the mercury-free fluorescent lamps. The optimal distance between DCSD plasma sheet and phosphor needed for achievement the intense homogeneous luminescence in the visible range is 3-5 mm.

ACKNOWLEDGMENTS

This work has been financially supported by Czech Science Foundation, contract numbers 202/03/0708, 202/03/0011 and by the research intent MSM0021622411 funding by the Ministry of Education, Czech Republic.

REFERENCES

[1] Lomaev, M.I., Skakun, V.S., Sosnin, E.A., Tarasenko, V.F., Shitts, D.V., Erofeev, M.V. (2003). Excilamps: efficient sources of spontaneous UV and VUV radiation. *Phys. Usp.,* 46, 193-209.

[2] Simor, M., Rahel, J., Vojtek, P., Cernak, M., Brablec, A. (2002). Atmospheric - pressure diffuse coplanar surface discharge for surface treatments. *Appl. Phys. Lett.,* 81, 2716-2718.

[3] Guivan, N.N., Janca, J., Brablec, A., Stahel, P., Slavıcek, P., and Shimon, L.L. (2005). Planar UV excilamp excited by a surface barrier discharge. *J. Phys. D: Applied Physics*, 38(17), 3188–3193.

INVESTIGATION OF DBD POWER SUPPLIER OPTIMIZATION

G.Zvereva[1] , M.Maaspuro[2]

[1] *State Optical Institute, St-Petersburg, 199397, P.O. box 652, RUSSIA*
[2] *Espoo, 02760, Kirstinmaki 17-B34, FINLAND*

Rare gas dielectric barrier discharge (DBD) is an effective VUV light source. A VUV light source uses normally applied excitation voltage with an amplitude of several kilovolts and a frequency of 10-100 kHz. Optimization of the DBD power suppliers (PS) is an important task on the way for increasing efficiency of a VUV light sources. PS can be optimized for different aims: minimizing cost, size , weight and energy losses. In this work we analyzed various forms of energy loses in the PS.

Analysis shows that input power on the whole is lost in the transformer and in the driving transistors. The loses in the transformer occurs due to magnetic field dissipation, core heating, wire heating. In this study a transformer model was created to make calculation of the transformer used. The following parameters were used in the model: voltage conversion ratio of 1:1000, primary voltage max 10 V, secondary voltage max 10 kV with 1mA load current, nominal frequency 100 kHz and type of core was ferrite pot one. Calculations show that main power loses are connected with loses in the core.

CONCLUSIONS

Results show the importance of choosing applicable transformer parameters in order to reach high energy efficiency in a DBD power supply. One of the most important of parameters is the core material, which should be applicable to the frequency range of the excitation voltage.

Design and Development of the 1 kJ Nd:Glass Laser Facility for Basic Research on Quantum Engineering

S. K. Hong[1], K. H. Ko[1], K. T .Lee[1], J. T. Jin[1], M.S. Kim[1], D. H. Yun[1], J. J. Goo[1], L. Li[2] and C. H. Lim[1]

[1] *Laboratory for Quantum Optics, KAERI, Dukjin-Dong 150, Yusong, Daejon 305-353, Rep. of Korea*
[2] *Department of Applied Physics, The Paichai University*

ABSTRACT. The Korea Atomic Energy Research Institute (KAERI) is developing a high energy Nd:Glass laser facility for the basic research of quantum engineering. The system will deliver 4 beam lines with clear aperture of 100 mm and each beam will be more than 250 J at nanosecond regime. The laser system consists of an oscillator, two pre-amplifiers, four double-pass rod amplifiers and four phosphate glass disk amplifiers at the final stage. For a wide application of the system, we plan to build the laser system operated as a kilo-joule laser at nanosecond or a hundred TW at Pico-second.

1. INTRODUCTION

One of the purposes of high energy lasers, such as NIF, LMJ, Gekko XII and Shen-Guang III, is to investigate the principles of high energy density plasma science [1-5]. The high density plasma produced by the high energy lasers has received vast attention due to its fundamental sciences and variety of applications; laboratory astrophysics, the acceleration of high energy electron and proton, equation of state, and the fast ignition of inertial fusion research. The photo-nuclear radiation source by a high energy laser opens a new science field of quantum engineering. The Korea Atomic Energy Research Institute (KAERI) is developing a high energy Nd:Glass laser facility for basic research on quantum engineering. KAERI laser facility (KLF) is based on the laser components of Gekko IV [6] which was transferred from the Institute of Laser Engineering (ILE) Osaka University, December 2004. The system will deliver 4 beam lines with a clear aperture of 100 mm and each beam will be more than 250 J at the nanosecond regime. The laser system consists of an oscillator, two pre-amplifiers, four double-pass rod amplifiers and four phosphate glass disk amplifiers at the final stage. For a wide application of the system, we plan to build the laser system to be operated as a kilo-joule laser at a nano-second or a hundred TW at a pico-second.

The project is in collaboration with the ILE, Osaka University and LFRC, China. Combination of a nano-second high energy laser and a pico-second laser is expected to open a new physics area for a high energy density plasma.

2. OPTICAL LAYOUT

Re-modeling of the laser building started in June 2005. The building presents about 480 m^2 of floor space on the ground level, reserved for the laser system and implosion chamber. The rooms on the ground level are equipped with class 10,000 clean rooms. For the cleaning of an optical component and laser cavity assembly, a class 100 clean room, of about 30 m^2, is also

situated on the first floor of the building. The foundation is a 30 cm thick layer of concrete, which is separated from the building to avoid a vibration at the site. Capacitor bank and control room are located on the second floor of the building. A steel frame will serve to hold the optical components to provide a stable beam transport to the implosion chamber room. The building re-modeling was completed in March 2006. In parallel to the building re-modeling, preparation for a laser installation were made. The basic design of the main amplifier was provided by ILE, Osaka University, Japan. A schematic of the 4 beam KAERI laser facility including the implosion chamber is illustrated in Fig. 1.

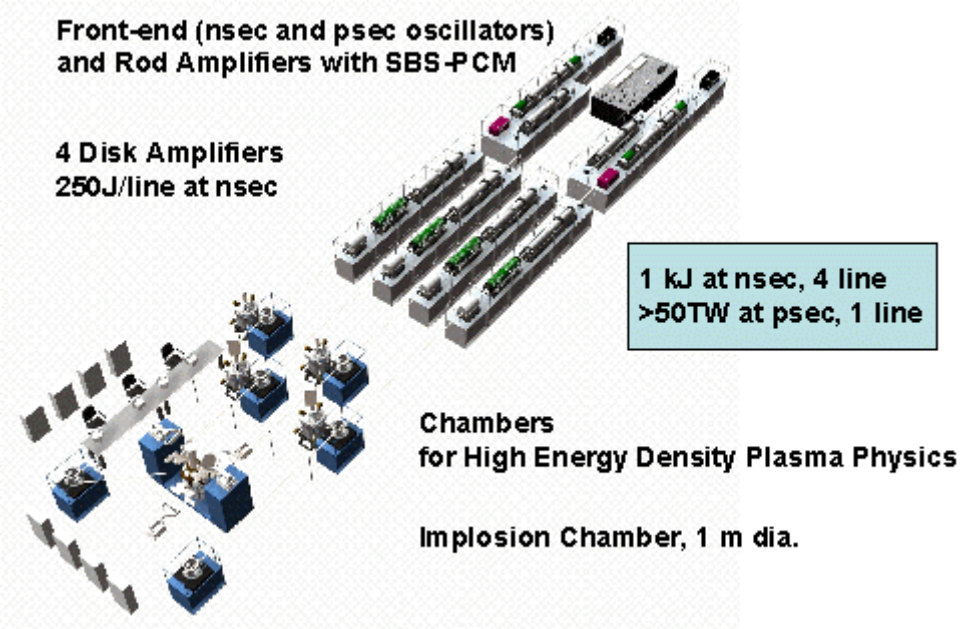

FIGURE 1. Sketch of KAERI laser facility (KLF).

The basic layout of KLF has been changed from the original single pass line to a SBS-PCM (Stimulated Brillouin Scattering - Phase Conjugated Mirror) double pass configuration. This change was motivated mainly by the recent experimental results of the preliminary co-work of KAERI and ILE. In contrast to the conventional folding mirror, SBS-PCM can compensate for the thermally induced phase distortion in a high energy laser system. The heavy fluorocarbon FC-75 was used as a SBS medium, because of its excellent optical quality; low absorption in a wide spectral regime from ultraviolet to infrared, high break down threshold (>100 GW/cm^2), good thermo-dynamic property and good chemical stability. The typical beam pattern reflected form the SBS mirror has been compare with the input beam, single pass beam, and double pass reflected beam from a conventional high reflection mirror. Near field burn pattern of each beam is illustrated in Fig 2. As shown in Fig. 2, the fidelity of SBS-PCM is much better than that of the conventional mirror.

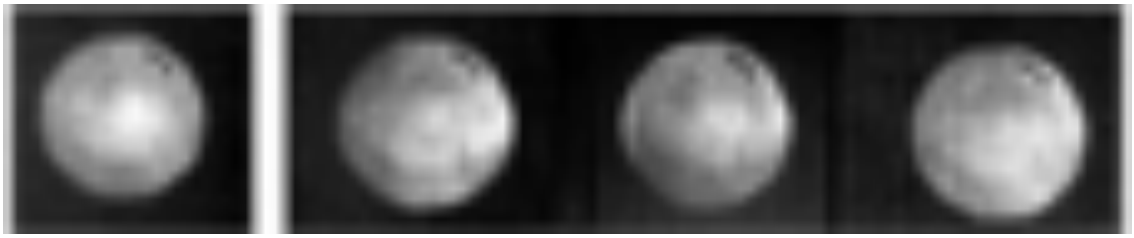

FIGURE 2. Near field patterns of laser beams (a) input beam, (b) double pass beam with SBS-PCM, (c) double pass beam with high reflectance mirror, (d) single pass beam.

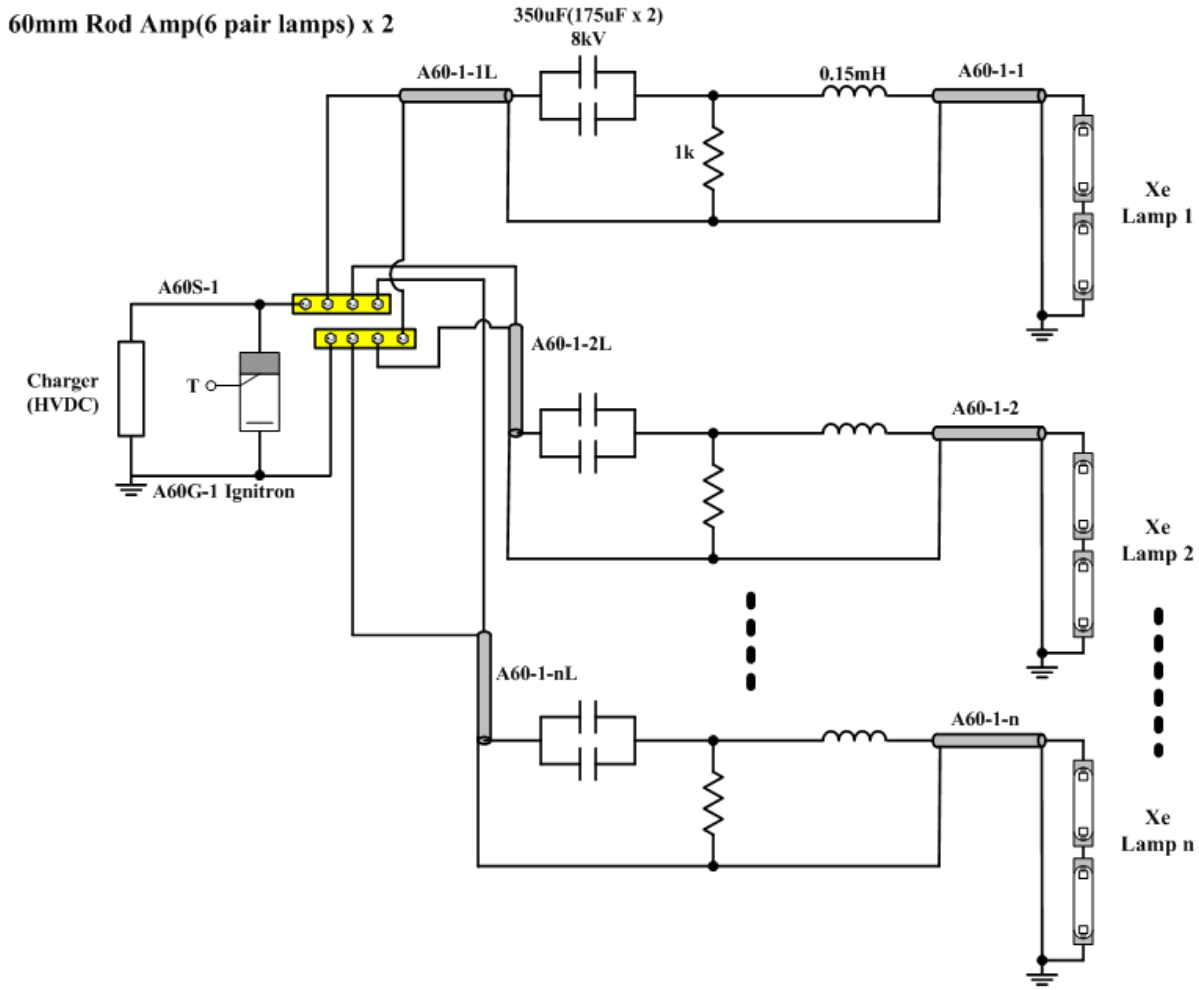

FIGURE 3. Pulse forming net work (PFN) for the discharge of flash lamp.

3. PULSE FORMING NET WORK AND CONTROLLERS

The test of the pulsed power system for the main amplifier was performed with the set-up of the capacitor bank and switching mode power supplies (SMPS). The pulse forming network for the flash-lamp discharge is illustrated in Fig. 3. RG217/U coaxial cables are used to connect the capacitor bank to the flash lamps. For energy storage, 175 F capacitors with a

nominal operation of 5 kV are used for the two serial UXL-S300 flash lamps, manufactured by Ushio Electric Co. We tested the integrity of the flash lamps and pulse forming network without a Nd:Glass gain medium to avoid a thermal shock. Current and voltage sensor was prepared to monitor the status of each flash lamp. New electronic modules based on the micro-processor, 16F74 Micro-chip, are developed to control the SMPS and ignitron switches and the monitoring of the flash-lamp discharge. These new modules allow a remote computer control of the power supply units, ignitron switches, and a monitoring of the current of lamp, gas/water flow, temperature and humidity. The control signals between the computer and micro-processor are delivered by an optical fiber to avoid electrical noise from the discharge. We replace the old laser controller into a small board with enhanced functions.

A restructuring of the implosion chamber with precision target alignment system is proceeding. The chamber is a 1 m diameter sphere with 16 flanges for lasers, a target injection, and diagnostics.

4. CONCLUSION

The Korea Atomic Energy Research Institute (KAERI) is developing a high energy Nd:Glass laser facility for basic research on quantum engineering. This laser consists of 4 beam lines with clear aperture of 108 mm and each beam will deliver more than 200 J at the nanosecond regime. SBS-PCM was studied to improve the beam quality and energy of the KAERI Laser Facility (KLF). All mechanical constructions of the target chamber will be finished in early 2006 and the installation of the optical components including the focusing mirror will be finished in the winter of 2006.

REFERENCES

[1] Wuest, C.R., “The National Ignition Facility; Laser Performance and First Experiments,” The 16th Technology of Fusion Energy Conference (Madison, WI, Sept. 14-16, 2004).

[2] Bigot, B., “Inertial Fusion Science and the Laser MegaJoule,” The 4th International Conference on Inertial Fusion Sciences and Applications (Biarritz, France Sept. 5-9, 2005)

[3] Miyanaga, N. “Progress in High Energy Laser Technology,” J. Plasma and Fusion Research Vol. 81, Suppl. (2005) 48-58.

[4] He, X.T., “The Status of Inertial Fusion Energy Research in China,” 2005 workshop on Ultra Density Plasma Production, Application and Theory for Laser Fusion (Nine Village Valley, Sichuan, China Oct 9-13, 2005)

[5] “Frontiers in High Energy Density Physics: The X-Games of Contemporary Science,” Committee on High Energy Density Plasma Physics, Plasma Science Committee, National Research Council, The National Academic Press, 2003.

[6] Annual progress report on laser fusion program September 1977-August 1978, Institute of Laser Engineering, Osaka University (1978); Annual progress report on fusion program 197 9 (1980).

ELECTRIC CHARACTERISTICS OF RARE GASES BARRIER DISCHARGES

G.Zvereva, G.Volkova, G.Gerasimov

State Optical Institute, ,Tuchkov per.-1, St-Petersburg, 199034, RUSSIA

ABSTRACT. In the work analysis of the current and VUV emission characteristics of dielectric barrier discharge (DBD) in different rare gases (Xe, Ar, Kr) were carried out (P=300 Torr, d=4 mm). DBD in Xe was found to have substantial differences compared with other rare gases: current amplitude 2-4 times higher and current duration 10 times shorter. This behavior is explained by different breakdown mechanism (streamer) compared with another rare gases (townsend). Experiments have shown a row of advantages of Ar DBD : lower breakdown voltage, bigger current pulse duration, higher energy quant of VUV emission, filaments with bigger diameter.

1.INTRODUCTION

Dielectric barrier discharge (DBD) in rare gases are known to be an effective VUV light sources . They have applications in different fields , such as: photocleaning of surfaces, deposition of dielectric materials, UV oxidation of semiconductors , printing machines [1]. More investigated and more used are Xe DBD's (λ=172 nm). Partially it is connected with more accessible lamp's windows material – quarts, while for the shorter wavelengths of Ar DBD (λ=126 nm) and Kr DBD (λ=147 nm) another, more expensive and complicate material should be used (MgF_2). In spite of the last fact investigation of DBD in different rare gases is important and able to give new perspectives for rare gases VUV light sources.

2.EXPERIMENTAL RESULTS AND DISCUSSION

In this work experiments with rectangular DBD excilamps were carried out. Lamps had discharge gap d=4 mm , were filled by different rare gases (Xe, Kr, Ar, Ne) at pressure P=300 Torr , were fed by sine voltage with frequency f=15 kHz and amplitude 5 kV. Lamps walls with 1.5 mm thickness served as the barriers. The aim of experiments was an investigation and a comparison of excilamps current and VUV emission values.

Expression for the current between excilamp's electrodes will be following [2]:

$$I = C \cdot dU/dt + I_g/(1+ C_g/C_d) = I_d + I_a$$

where C- excilamp capacity, C_g – gas gap capacity , C_d – capacity of dielectric barriers, U – applied voltage, I_d – displacement current, I_g- discharge current. Current I was measured with shunt , at the same time the displacement current I_d compensation was carried out.

In the Fig.1 oscillograms of the current in Ar, Kr and Xe DBD are shown. One can see current amplitude to grow from Ar to Xe , while current duration falls. Current duration is

defined by the time necessary for moving to barrier charge decreasing electric field E_{pl} in the gap below breakdown value. Electric field E_{pl} possible to express as [3]:

$$E_{pl}(z,t) = -\frac{\sigma_e(t)}{\varepsilon_0} + \frac{\sigma_B(t)}{\varepsilon_0} + \frac{\sigma_{pl}(z,t)}{\varepsilon_0}$$

where $\sigma_{pl}(z,t) = \int_{z_B}^{z} \rho(z,t)dz$, ρ(z,t) – volume charge density, σ_e and $\sigma_B = \int_0^T I_g(t)dt$ - surface charge density on electrodes and barriers .If with further voltage increasing electric field E_{pl} reaches breakdown value new current pulse appear. The lower the breakdown value, the higher the probability of the next current pulse appearing. Experiments (Fig.1) show new pulses to appear in Ar and Kr , while Xe having higher breakdown voltage has only one peak.

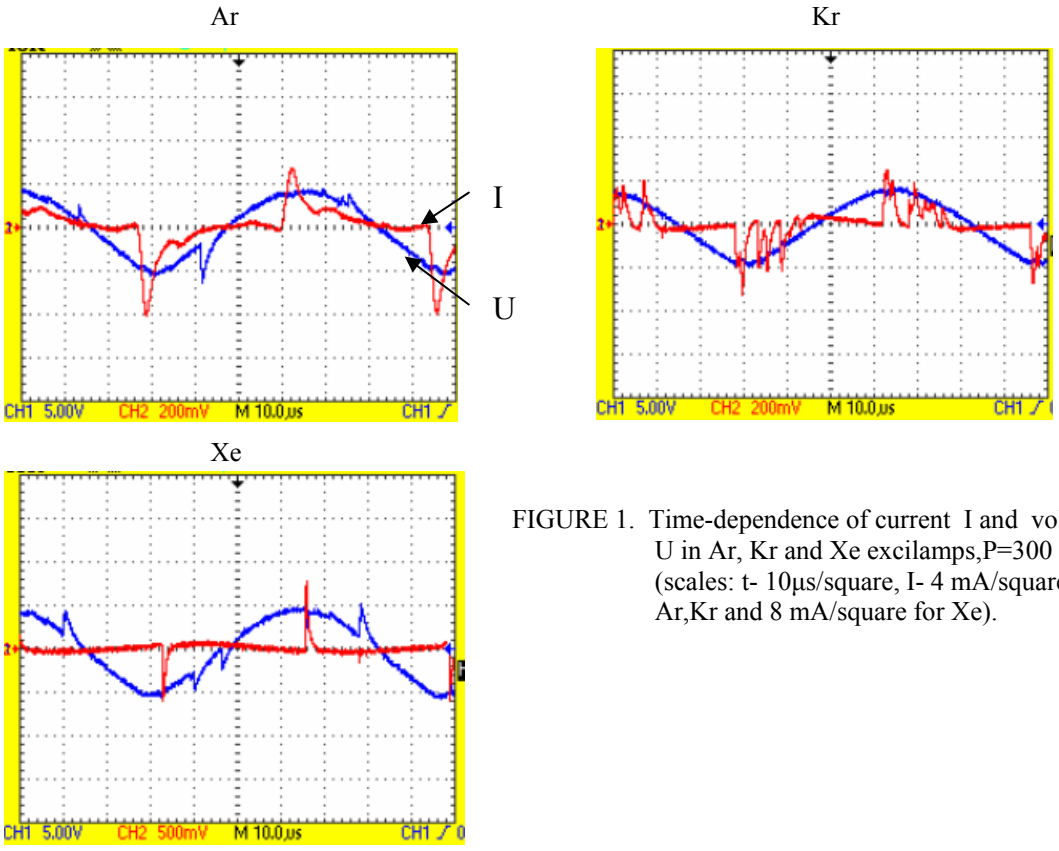

FIGURE 1. Time-dependence of current I and voltage U in Ar, Kr and Xe excilamps,P=300 Torr. (scales: t- 10µs/square, I- 4 mA/square for Ar,Kr and 8 mA/square for Xe).

Visually discharges were consisted of filaments. Xe filament radius was considerably lower (R=0.05 mm) than Ar (R=0.5 mm) one. This is possible to be explained by lower values of mobility (μ) and ionization coefficient (α) in Xe [4]:

$$R = \left(\frac{3e}{\alpha \cdot E_{pl}}\right)^{1/3} \exp(\alpha \cdot x), \text{ where } x=\mu E_{pl} t$$

Inside filaments with lower radius (Xe) volume discharge electric field E′ will be higher: $E' \sim \frac{1}{R^2}$ [4], providing higher ionization coefficient and current. Analysis shows E′ in Xe DBD to reach values comparable with external field one. This provides conditions for

development of streamer breakdown mechanism. Separation of Xe volt-ampere characteristics from Ne, Ar and Kr curves (Fig.2) can be explained by different breakdown mechanisms in Xe (streamer) compared with other rare gases (townsend).

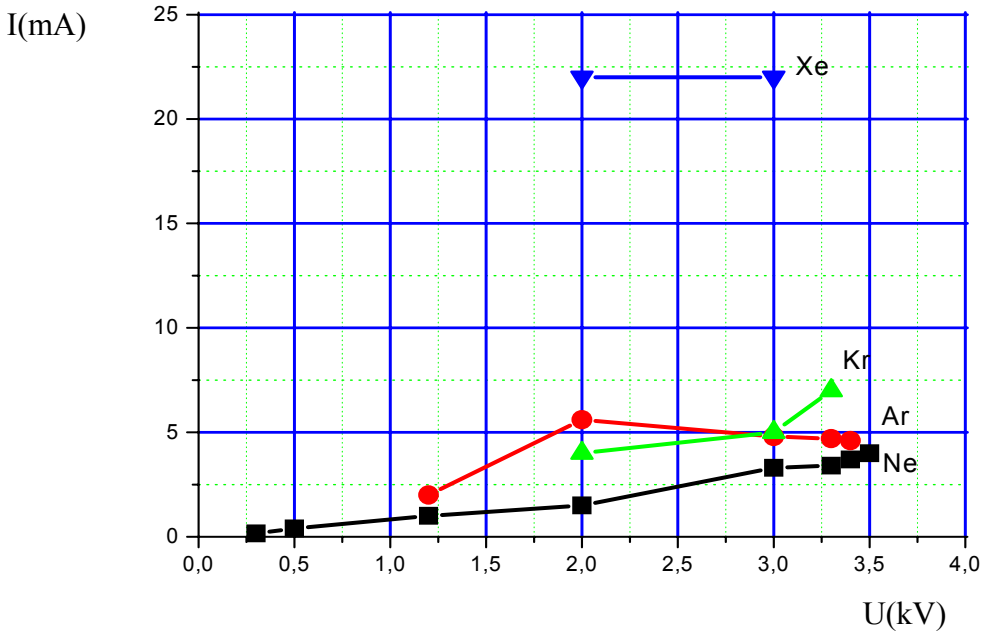

FIGURE 2. Volt-ampere characteristics of Ne, Ar, Kr and Xe excilamps (P=300 Torr), U-absolute voltage average value.

In Fig.3 Xe_2^*(λ=172 nm) and Ar_2^* (λ=126 nm) excimer emission dependences are shown. Bigger delay of Ar_2^* emission maximum towards current's peak is explained by lower velocity of Ar_2^* excimer formation ($k_{Ar}=1\ 10^{-32}$ cm^6/s) compared with Xe_2^* ($k_{Ar}=5\ 10^{-32}$ cm^6/s). Appropriate excimers formation times will be equal to $\tau_{Xe}=2\ 10^{-7}$ s, $\tau_{Ar}=1\ 10^{-6}$ s, which correspond to experimental results.

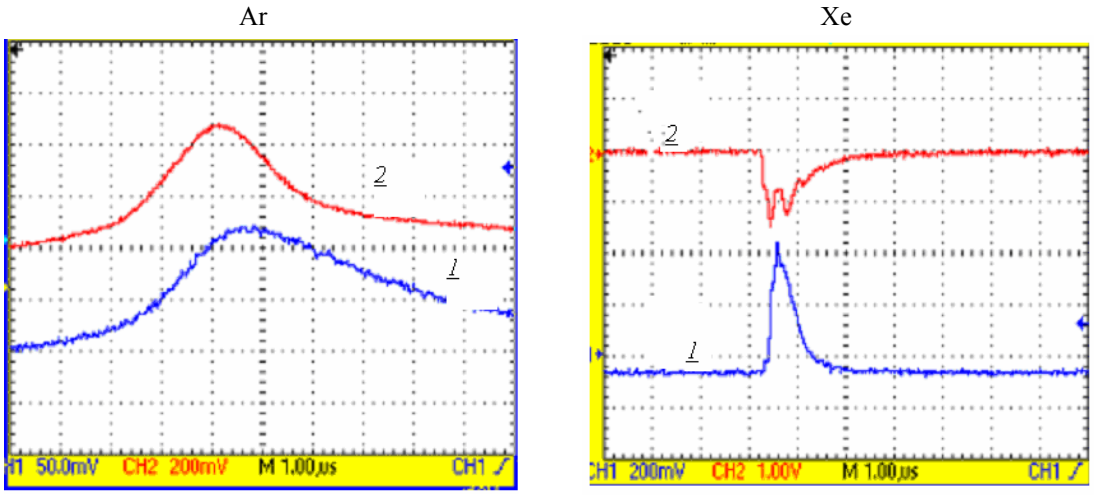

FIGURE 3. Oscillograms of excimer emission (1) and current (2) in Ar and Xe (scale: t- 1µs/square).

3.CONCLUSIONS

Comparative analysis of DBD in different rare gases : Ne, Ar, Kr and Xe shows DBD in Xe to have substantial differences compared with other rare gases: current amplitude 2-4 times higher and duration 10 times shorter. This is explained by different breakdown mechanism (streamer) compared with another rare gases one (townsend). Experiments have shown a number of advantages of Ar DBD : lower breakdown voltage, bigger current pulse duration, higher energy quant of VUV emission, filaments with bigger diameter.

ACKNOWLEDGMENTS

This work was supported by ISTC grant N3098.

REFERENCES

[1] Boyd] I.W., Zhang J.-Y. and Kogelschatz U. (2003). Development and applications of UV excimer lamps *Photo-Excited Processes, ed. by A.Peled,* Kluwer A.P., Boston, 161-197.
[2] Liu S. and Neiger M. (2001). Excitation of dielectric barrier discharges by unipolar submicrosecond square pulses. *J.Appl.Phys.*, 34, 1632-1638.
[3] High-effective methods of investigation and modelling of the barrier discharges for optimization of Plasma Display Panels and Excimer Lamps. (2006). *ISTC Report 3098*.
[4] RaizerYu.P. (1987). Gas Discharge Physics.

NON-THERMAL PLASMA REACTORS POWER SYSTEMS' DESIGNING AND EFFICIENCY

H. D. Stryczewska and T. Janowski

Institute of Electrical Engineering and Electrotechnologies,
Faculty of Electrical Engineering and Computer Science, Lublin University of Technology,
Lublin, 20-618, POLAND

ABSTRACT. Power systems of non-thermal plasma reactors depending on the discharges used for plasma generation require special methods of modelling and designing. Two kinds of plasma reactors from the point of view of electrical discharges used for plasma generation are taken into account in the paper: dielectric barrier discharge and gliding arc discharge reactor. In case of dielectric barrier discharges that present for power supply system the capacitive load, the characteristics of power system should permit to compensate relatively large reactive capacitive current component and to balance the single phase load, whereas the gliding arc discharge reactor represent active distorted load that has different requirements from power system. First of all, it should ignite the arc discharge and then to maintain its cyclic operation as well as to limit current after the arc is broken. Power requirements of both plasma reactors can be fulfil with the aid of specially constructed nonlinear transformers.

1. INTRODUCTION

Non-thermal plasma produced by electrical discharges is applied in many plasma-chemical processes, especially in the process of environment protection, toxic gas removal, liquid and solid wastes treatment. There are many various types of plasma reactors and they differ considerably from one another depending on their application, construction and kind of discharges used for plasma generation. In many applications, discharges in the presence of dielectric barrier, usually applied for ozone generation, and arc or quasi-arc discharges (gliding arc, plasma torches) are used, as they can generate non-thermal and non-equilibrium plasma at atmospheric pressure and their construction is not very complex.

Every plasma reactor represents rather an unusual load for its power system requiring supply voltage of 10 to 20kV, often of increased frequency with operating characteristics adapted to the reactor nature. Therefore every supply system should be equipped with transformers of special construction. As it is well known, the magnetic circuit of a transformer is non-linear, and under an applied sinusoidal voltage, the magnetic flux is distorted by odd harmonics. If the magnetic circuit construction created conditions for the higher harmonics of magnetic flux to have closed paths, achieve considerably large values. This phenomenon allows the construction of frequency converters known as magnetic frequency multipliers. The main disadvantage of this device is its inherently large magnetising current. They were often applied in power system until the seventies of last century when they were replaced by static semiconductor converters. But in some applications making use of higher magnetic flux harmonics still seems to be reasonable and advantageous. Power supply systems for non-thermal plasma reactors belong to these applications.

Electronic address:h.stryczewska@pollub.pl

In the paper the power supply systems of dielectric barrier discharge reactors (ozone generators) and arc discharge reactors are discussed from the point of view of their designing and efficiency.

2. PLASMA REACTORS POWER SYSTEM'S REQUIREMENTS

2.1. Ozone generator's power system

Although the idea of ozone generation by means of partial dielectric discharges was known 140 years ago, when Werner von Simens built the first ozone generator, the biggest progress in this domain have been made in XX century and still the investigations to increase the efficiency of ozone synthesis are carried out. Since 1906, when in Nice the first water treatment plant with ozone came into operation, the ozone production has grown several thousand times, the ozone generation systems have became more complicated and consume a lot of electrical energy. The electrical power installed in water treatment plant reaches value of MVA and still is growing up.

Industrial ozone generator consists of several hundred discharge elements connected in parallel and water cooled. The single discharge element is a tube capacitor with a laminar insulator of a glass dielectric and a gaseous gap, in which the barrier discharges occur when the voltage exceeds the ignition value. To power supply system ozone generator presents very specific load with relatively large capacitive component of distorted current and low power factor (PF=0.3-0.8). The productivity of the ozone generator depends on electrical parameters of the supplying circuit voltage, such as: value, frequency and shape. To obtain the high productivity of the ozone generator and to ensure its proper co-operation with the mains supply, the supply voltage frequency is often increased. Also, the reactive capacitive power should be compensated by series chokes. Unfortunately, the frequency conversion and additional chokes in the system cause increased power losses and the process of ozone generation as a whole is less efficient than at mains frequency.

Two types of power supply systems are most often used in the industrial O_3 production, i.e.: of mains frequency (50/60 Hz) and of medium (up to 1000 Hz) frequency. There are also reported systems operating at higher frequencies (10 kHz and more) or pulse power systems but up to now, they have not been applied in the water treatment practice.

The block diagrams of ozonizer's power systems applied in practice are given in Figure 1. Power systems operated at mains frequency usually consists of autotransformer, high voltage transformer and compensating choke (Fig. 1a).

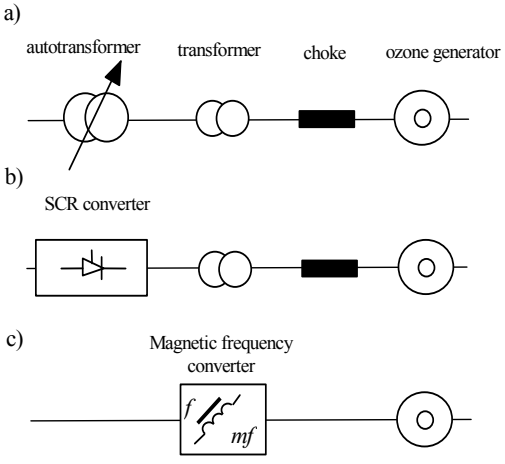

FIGURE 1. Block diagrams of the ozone generator power supply systems

The system of medium frequency is additionally equipped with frequency converter and most often it is a thyristor inverter. This system usually does not consist of individual voltage regulator as the value of output voltage can be regulated by the thyristor overlap, but, similar to mains frequency system, it should consist of choke and high voltage transformer (Fig. 1b).

Among systems of increased frequency, the magnetic frequency multipliers (m. f. m) are very suitable to supply ozonizers, unfortunately, not very often applied in practice [1]. In the system with magnetic frequency multiplier all functions required by ozonizer, i.e., the frequency increase, the voltage regulation and its transformation can be performed in one device.

Moreover, the magnetic frequency multiplier is stable and reliable power system, due to the fact that it consists of magnetic cores and cooper windings, like common use transformer.

Discussion and comparison of power losses and efficiency of three power systems operating at 50 Hz, 150 Hz and 600 Hz, from Figure 1, are presented in Table 1. Power losses were estimated at the assumption that all of the systems' components are designed to supply the ozone generator of the same nominal power (P_o=160 kW). As it can be seen, the least power losses, equal to 7% of nominal ozonizer's power and the highest efficiency (94%), are observed in the power system with magnetic frequency multiplier (Fig. 1c). Although its operation at increased frequency, the resultant magnitude of the magnetic flux density, responsible for power losses, is smaller than in the transformer of the same nominal power.

TABLE 1. Power losses in the supply systems of the ozone generator*

System element	Autotransformer/ frequency converter			Transformer/ Multiplier			Choke			Power, power losses and efficiency of the system				
System, accord. to Fig. No	S kVA	ΔP kW	ΔP %	S_T kVA	ΔP kW	ΔP %	S_{Ch} kVar	ΔP kW	%	P_o kW	ΔP kW	ΔP %	P_1 kW	η %
1a	200	6,0	3,0	200	10	5,0	200	6,0	3,0	160	22	14	182	88
1b	200	8,0	4,0	200	1,1	5,5	200	7,0	3,5	160	26	16	186	86
1c	-	-	-	200	11	5,5	-	-	-	160	11	7	171	94

The main reasons of the highest efficacy of the system with the magnetic frequency multiplier is that it combines all the functions required by the ozone generator and allows elimination of additional chokes, a frequency converter and an autotransformer, necessary in other systems Moreover, the secondary voltage can be efficiently controlled by an impedance connected in the multiplier neutral line.

The next, in turn, from the efficiency point of view is the system operating at mains frequency (Fig. 1a) in which power losses are equal to 14% of the nominal ozonizer's power.

The worst efficiency (86%) is presented by the system with SCR converter (Fig. 1b). Although the power losses in SCR converter are not very large (4%), the system still require high voltage transformer and chokes to compensate the reactive ozonizer's power.

2.2. Arc discharge reactor's power system

The plasma reactor with arc discharges requires a supply system in which the arc ignition occurs at high voltage, equal to (10-20) kV depending on the electrode distance at the ignition zone, while the arc discharges are maintained at several times lower voltage (1-2) kV. Like in the case of ozone generator, the arc discharge reactor can be energized from the systems operating at mains or increased frequency.

Block diagrams of power system of arc discharge reactors are presented in Fig. 2. A power transformer is the simplest system to energize the arc plasma reactor. It can transform the mains' voltage to the value required by the reactor but to limit the arc discharge current it should be equipped on its secondary with additional chokes connected in series with reactor's electrodes. To compensate the relatively large reactive power of the system the capacitor's bank is connected at the input of the power transformer (Fig. 2a). Similar operating conditions can be obtained in the leakage transformer (Fig. 2b) or in the systems with magnetic frequency multipliers (Fig. 2c). Both systems still require compensation of the large inductive component of the input current by capacitors' bank.

The discussed power systems are rather inefficient, because transformer is to be constructed for ignition voltage and operates at voltage which is several times smaller than

ignition voltage. Therefore, only about 10 % of the transformer power is transferred to the discharge and the efficiency of these systems is relatively low (61-76%, Table 2).

The integrated power supply system of arc discharge reactor [2] is free of these disadvantages. Its construction is based on specially connected nonlinear single phase transformers and combines the features of power transformer and magnetic frequency tripler.

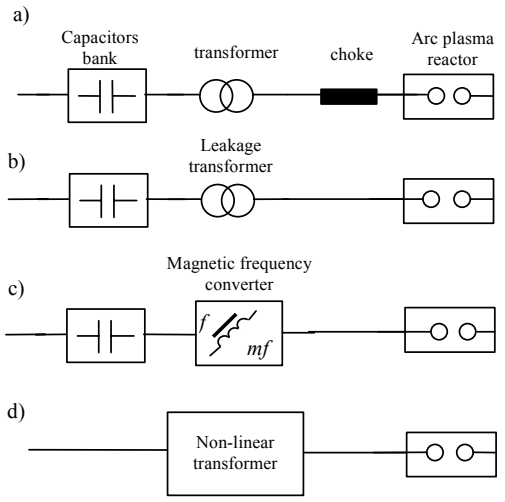

FIGURE 2. Block diagrams of arc discharge reactor's power systems

The arc ignition is performed by tripled frequency high voltage of very soft characteristic, while the power to the discharge is transferred at the much lower voltage and characteristics that allow to limit the discharge current [3, 4]. The most important feature of the system is that it integrates the function required by arc plasma reactor in one device, what means that number of power system elements can be considerably reduced and makes it much more efficient and reliable in contrast with other supply systems (91%). The main advantages of the proposed supply system are: the inherent capability to supply both ignition and operation electrodes circuits, the symmetrical load of the mains and the possibility of supplying the multielectrode and multistage arc plasma reactors

TABLE 2. Losses and efficiency of arc discharge plasma reactor's power systems*

System element	Capacitors' bank			Transformer			Limiting current choke			Power, power losses and efficiency of the system				
System from Fig. no	S	ΔP	ΔP	S_T	ΔP	ΔP	S_D	ΔP	ΔP	P_o	ΔP	ΔP	P_1	
	kVA	kW	%	kVA	kW	%	kVar	kW	%	KW	kW	%	kW	%
2a	360	3,6	1	400	18	4,5	360	11	3,0	50	32	62	82	61
2b	240	2,4	1	320	16	5,0	-	-	-	50	18,4	37	68,4	73
2c	160	1,6	1	240	14,4	6,0	-	-	-	50	16	32	66	76
2d	-	-	-	80	4,8	6,0	-	-	-	50	4,8	9,6	54,8	91

*Data presented in Table 1 and 2 were taken from catalogues of industrially produced transformers, chokes, capacitors and frequency converters of given power rating.

3. CONCLUSIONS

Independently on discharges applied for plasma generation, non-thermal plasma reactors require specially designed, efficient and reliable power systems. Taking advantage of the transformer's cores nonlinearity, simple, reliable, low cost and efficient power systems, especially suitable for industrial applications, can be constructed.

4. REFERENCES

[1]. Janowski, T., Stryczewska, H. (1992), *Ozone Science & Engineering*, vol. 14, pp. 139-152.
[2]. Janowski T., Stryczewska H. D. (1997), Plasmatron supplier to carry out chemical processes. *Polish Patent* No 172152, (in polish).
[3]. Janowski, T., Stryczewska, H. D,(1996) *Nonlinear Magnetic Systems*, A. J .Moses and A. Basak (eds.), *IOS Press*, pp. 31-34.
[4]. Stryczewska H.D, (1997), New Supply System of Non-thermal Plasma Reactor with Gliding Arc. Archives of Electrical Engineering, vol. XLVI, no 4, 379-399.

DILUTE TRICHLOROETHYLENE DECOMPOSITION IN AIR BY THE NONTHERMAL PLASMA, BYPRODUCTS AND CARBON BALANCE

T.Oda, K.Ono and R.Ono

Department of Electrical Engineering,
School of Engineering, the University of Tokyo
7-3-1 Hongo, Bunkyo-ku, Tokyo 113-8656, JAPAN

ABSTRACT. In order to improve the electric discharge energy efficiency to decompose dilute trichloroethylene (TCE) in the atmospheric pressure air by the nonthermal plasma, a new plasma reactor is examined with a short discharge gap and precise assembly. New manganese-dioxide supported alumina spheres of 3 mm in diameter are used as the ozone decomposer to enhance the TCE decomposition efficiency. Their results are very well. More than 95 % TCE is decomposed when the specific discharge energy density (SED) is only 11 J/L. Close to 100 % carbon balance from TCE to carbon oxide is also realized at SED of 90 J/L where that value was more than 400 J/L in the previous system.

1. INTRODUCTION

As the nonthermal plasma is very effective technology for environmental protection, especially decomposition of gaseous air contaminants in the air or the combustion flue gas, many researchers have engaged in investigating nonthermal plasma process. There are two main targets, that is how to decompose NOx or VOCs (volatile organic compounds)[1-12]. Recently many researchers would like to use the catalysts combined with the non-thermal plasma. It is also important matter how to remove toxic byproducts. The author's group has been working on the decomposition of trichloroethylene (TCE) as one good example of the halogenated hydrocarbons and also on the diagnosis of the high pressure nonthermal plasma by using the laser[13,14]. One main target of the authors' research is improving the energy efficiency of the process. In this paper, two kinds of experimental results are described. One is the improvement of the plasma reactor (optimization of the parameters: reactor size effect). Another approach is how to find the effective catalyst to enhance the TCE decomposition energy efficiency. As the catalyst has large surface area, the adsorption effect of TCE or some other VOCs by the catalyst is very large. Still now, their final performance (real catalytic effect) is not yet clear. The separation of the catalytic effect and the adsorption effect is not yet done enough.

The nonthermal plasma process of the dilute VOCs-contaminated air produces much amount of ozone which is toxic, and the exhausted air to the room should be ozone-free (the ozone concentration should be less than 0.1 ppm). The manganese oxide is very effective catalyst to decompose the ozone but that adsorption effect to the TCE is also very large generally. As the first try to improving the reactor, different discharge gap plasma reactors with different lengths are compared each other. As the new catalyst, manganese-dioxide supported alumina spheres of 3mm in diameter are fabricated and that catalytic performance is examined experimentally.

2. EXPERIMENTAL

2.1 Experimental System

The total experimental system is roughly the same as the former one[15] as shown in Fig. 1. As the VOCs (Volatile Organic Compounds), the dilute trichloroethylene (TCE) is used in this experiment. As shown in the Fig. 1, TCE concentration is adjusted by the injection of the TCE liquid with the ultra-slow injection syringe. The typical TCE concentration is 250 ppm which can be calculated from the injection volume of the TCE and the air gas flow rate where the air is synthesized air. GCMS is Shimadzu GCMS-QP55050A and FTIR is Presige 21 made by Shimadzu Co.

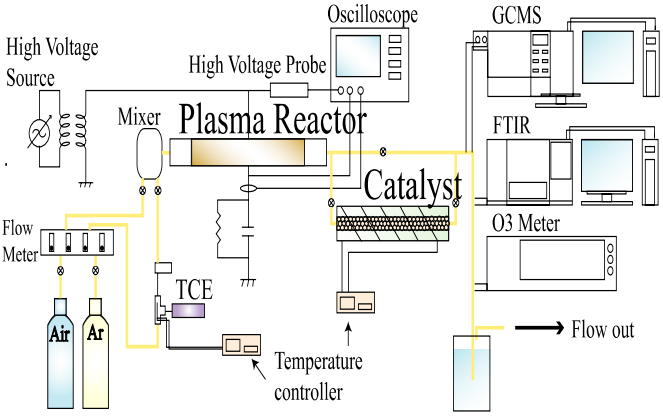

FIGURE 1 Experimental setup for the nonthermal plasma and gas flow.

2.2 Plasma Reactor

The plasma reactor used in this experiment is made of a 350 mm long Pyrex glass tube with a 255 mm long bolt-type discharge electrode coaxially located at the center of the tube. A wide thin cupper film is wound around the outside of the glass tube whose outer diameter is 19.2 mm and inner diameter is 16.8 mm. As the discharge gap is varied from 5.4 mm to 0.4 mm, the discharge areas are 49.3 cm^3, 36.5 cm^3, 27.7 cm^3, and 5.26 cm^3 where the residence times are 2.96 s (seconds), 2.19 s, 1.66 s, and 0.315 s, respectively. Figure 2 shows the discharge power versus the 50 Hz applied voltage. In the case of short gap, the discharge occurs at very low applied voltage but the increase of the electric power consumption versus the applied voltage is very small. On the other hand, the corona discharge occurs at high applied voltage but the discharge power is also increases greatly with the slight increase of the applied voltage.

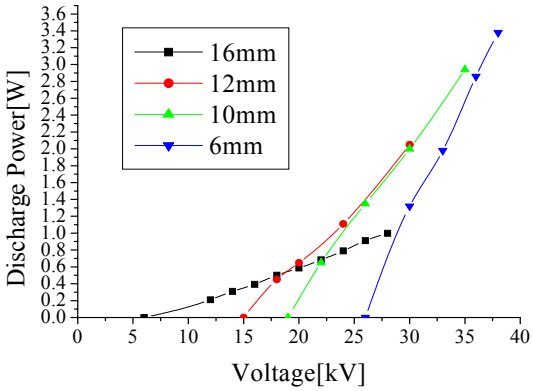

FIGURE 2 The discharge power versus the peak applied voltage for four reactors.

2.3 Catalyst Preparation

The authors found that the decomposition of the ozone by heating or catalyst also decompose VOCs. However, the catalyst powder adsorption effect to TCE is still pretty large and the adsorption saturation time of the TCE is larger than one hour if the ozone decomposition is enough. For that, a new catalyst was fabricated; that is the manganese-dioxide supported alumina spheres. Concentrations of the manganese-dioxide tested are 0.5 wt%, 1.0 wt% and 5.0 wt%. When degraded alumina spheres are heated, the desorption of nitric-dioxide from the manganese-dioxide supported alumina is detected by FTIR and the ozone decomposition performance recovers. The specific surface areas of them are compared each other with the ozone decomposition efficiency. The degradation

time constant for about 50 mg alumina is roughly one hour. However, that concentration is not enough to decompose the ozone perfectly. As TCE decomposition efficiency and the ozone decomposition are also strongly dependent on the catalyst amount, the authors use 1000 mg manganese-dioxide supported alumina which saturation time is less than 40 minutes and repeatability of the experiments is reasonable value.

3. EXPERIMENTAL RESULTS AND DISCUSSIONS

3.1 TCE Decomposition by the Direct Process without Catalyst

TCE decomposition efficiency by the Direct Process (TCE contaminated air passes through the plasma reactor) for different discharge gap reactors is shown in Fig. 3 where the size is the diameter of the discharge electrode (inner size is 16.8 mm in diameter corresponding to the gaps of 0.4 mm, 2.4 mm, 3.4 mm and 5.4 mm, respectively). The specific energy density (SED) is calculated as the discharge power (W = J/s) over flow rate (L/min) multiplied by 60 (second/minute). At SED of about 30 J/L, TCE decomposition is 80 % which value is the best value compared with the previous works. As shown in Fig.2, low power control is not easy for the large discharge gap reactor and exact comparison of the TCE decomposition performance among four different discharge gap reactors is not easy but Fig. 3 suggested the superiority of the short gap reactor.

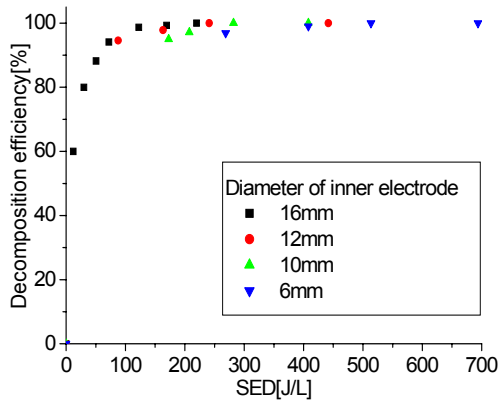

FIGURE 3 TCE decomposition efficiency versus SED where the gas flow rate is 0.5 L/m in this case(Direct).

That performance depending on the reactor length is also examined experimentally, suggesting that the longest reactor can remove largest amount of TCE among four different plasma-area length reactors, such as 100 mm, 150 mm, 250 mm or 300 mm long). There are no large differences among four reactors, especially, at low SED but the TCE decomposition energy efficiency of a longer reactor is better than shorter reactors at SED of more than 40 J/L. A long reactor may realize the uniform distribution of the TCE for long traveling and final result must be good. Another possibility is that dilute plasma can decompose more efficiently.

What kind of chemical reaction occurs in the plasma? For that, byproducts analysis was done as shown in Fig. 4. Main byproduct of TCE processed by the Plasma only, is DCAC (dichloroacetyl- chloride: CCl_2HCOCl) which increases with the increase of SED (SED < 60 J/L). At SED of 60 and 80 J/L, TCE decomposition is saturated and generation of DCAC is also saturated. DCAC is not decomposed by the plasma. On the other hand, the similar byproduct TCAA (trichloroacetaldehide: CCl_3COH the chemical

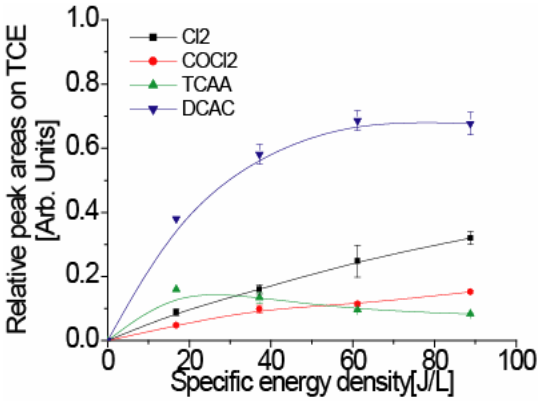

FIGURE 4 Byproducts versus specific discharge energy density for 255 mm long 0.4 mm gap reactor (Direct Process).

equation) increases till SED of 20 J/L. TCAA decreases with the increase of SED (from 20 to 90 J/L) indicating a slight decomposition by the plasma. Chlorine increases linearly with the increase of the SED and generation of phosgene ($COCl_2$) also increases with SED increase (a little bit saturates). Those results suggest that DCAC cannot be decomposed by the plasma (Direct Process) and final state of the Chlorine atom is chlorine molecule (Cl_2) or phosgene. TCAA is decomposed a little bit by the plasma.

3.2 TCE Decomposition by the Indirect Process with New Catalyst

By the Indirect Process only, TCE decomposition is very small (typically less than 10 %). The mixed air passes through the PTFE tube filled with the catalyst. That process named as the Indirect Process with the catalyst. By that method, TCE decomposition efficiency as shown in Fig.5 is much improved, more than the Direct Process (Fig. 3). At SED of 18 J/L, TCE decomposition efficiency is more than 95 %. If SED is more than 40 J/L where all TCE is decomposed at SED of 38 J/L, still the concentration of carbon dioxide, CO_2, increases with the increase of SED. On the other hand, the increase of carbon monoxide (CO) with the increase of SED is rather saturated. Maybe the oxidation of byproducts on the manganese-dioxide surface generates carbon-monoxide and carbon-dioxide. The carbon-monoxide is also oxidized to carbon-dioxide and the increase of the carbon-monoxide saturates. At SED of 20 J/L, TCE decomposition efficiency is more than 95% but carbon balance (from TCE to COx) is very poor (only 10 %). At SED of 90 J/L, carbon balance is only 45 % far from 100 %. The exact oxidation mechanism is not yet known but maybe the ozone decomposition produces much amount of atomic oxygen which has very strong oxidation. That atomic oxygen cannot oxidize DCAC.

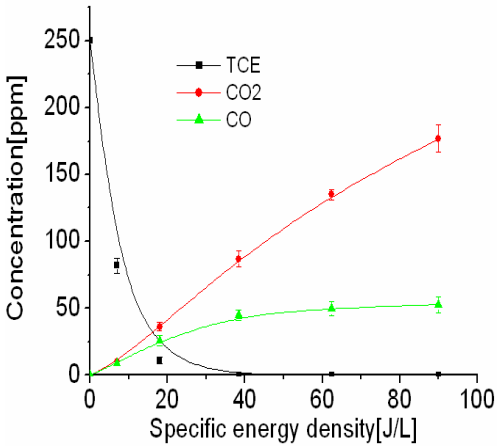

FIGURE 5 TCE, CO and CO_2 for different SED (Indirect method)

3.3 Direct Process with New Catalyst

TCE decomposition and CO_x production in the Direct Process with new catalysts are shown in Fig. 6. At SED of 11 J/L, TCE decomposition efficiency is about 95 %. The TCE decomposition efficiency is more than 99 % when the SED is only 15 J/L. Those values are energetically economical in practice. Concerning with carbon oxide (CO_x), the carbon-dioxide increases with the increase of the SED with good proportionality (a little bit saturates at SED of 90 J/L). The production of the carbon-monoxide is saturates above SED of 40 J/L in Fig. 6. At the SED of 15 J/L, there are many hydrocarbon byproducts which must be oxidized at higher SED than 15 J/L creating much amount of the carbon oxide (CO and CO_2). The saturation tendency of

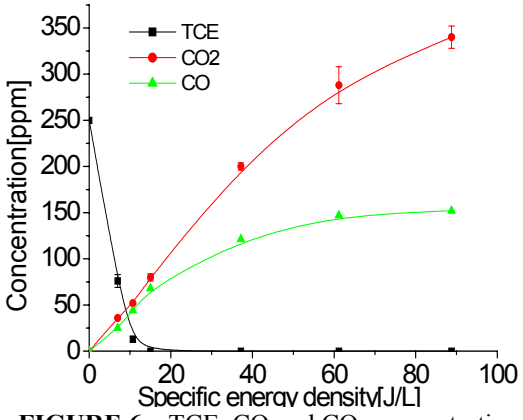

FIGURE 6 TCE, CO and CO_2 concentration variation versus the plasma energy; SED (Direct +MnO_2-supported alumina)

carbon-monoxide is due to the oxidation from carbon-monoxide to carbon-dioxide which reduces carbon-monoxide concentration. As the good indication of enough oxidation, carbon balance (carbon change ration typically from carbon of TCE to carbon of carbon oxide) is very well-known. At the SED of 15 J/L, TCE decomposition efficiency is more than 99 % but the carbon balance is only 30 %. If the SED is 90 J/L, the carbon balance is about 98 % which means that all hydrocarbons are fully oxidized and carbon component is oxidized. GCMS analysis suggested various kinds of organic compounds. Chlorine molecules (Cl_2) may be the final product of TCE and increases with the increase of the SED (this tendency is similar to the carbon-dioxide). The chlorine might be removed by the acid or basic solution. Another toxic byproduct is phosgene ($COCl_2$) whose concentration is saturated with the increase of the discharge power but does not decrease indicating that the phosgene does is not decomposed by the plasma or the atomic oxygen. The concentration of DCAC is very small. In other word, DCAC produced by the plasma is strongly oxidized by the new catalyst (manganese-oxide) and changes to carbon oxide, water and others. The generation of TCAA is more complicated in the figure. Maybe, residual TCE oxidized to TCAA on the catalyst surface. At the same time, some part of DCAC is also changed to TCAA on the catalyst surface till SED of 15 J/L. Further SED (more than 30 J/L), almost TCE is oxidized to DCAC in the plasma region (as shown in Fig. 4), TCAA generation is very small and residual TCAA is also oxidized on the catalyst surface or gaseous atomic oxygen.

4. SUMMARY

Dilute TCE (trichloroethylene) decomposition in air by the nonthermal plasma is experimentally tested for different size plasma reactors. The plasma process is also combined with newly manufactured manganese-dioxide supported alumina. Following results are obtained

(a) Short gap barrier discharge plasma reactor (0.4 mm discharge gap between the bolt type discharge electrode and glass tube insulator whose outside is wounded by the ground electrode plate).

(b) The long length plasma area reactor works well.

(c) If the plasma process is combined with new manganese-dioxide supported alumina spheres, TCE decomposition performance is greatly improved.

TCE decomposition efficiency is 80 % at SED of 30 J/L for Direct Process (no catalyst), 95 % at SED of 18 J/L for Indirect Process with the new catalyst, and 95 % at SED of 11 J/L for Direct Process with the new catalyst.

Carbon balance is also much improved by the combination of the catalyst. The carbon balance is 45 % at SED of 90 J/L for Indirect Process with the catalyst, more than 98 % at SED of 90 J/L. On the other hand, previous data suggested in Direct Process, carbon balance is only 10 % at SED of 60 J/L and 98 % at SED of 400 J/l.

(d) Still the chlorine molecule and the phosgene exist after the Direct Process with the catalyst and another post-chemical process must be done for purification.

ACKNOWLEDGMENTS

This work is partially supported by Scientific Grand in Aid from the Ministry of Education, Culture, Science and Technology. The authors are also thankful Profs. J.C.Chang, T.Yamamoto, A.Mizuno, Drs. K.Urashima and S.B.Han for their important advices in this work. The authors strongly appreciate Drs. A.Ogata and H.H.Kim for manufacturing new catalysts.

REFERENCES

[1] Masuda, S., H. Nakao, H. (1986). Control of NOx by positive and negative pulsed corona discharges. *Conference Records of the IEEE/IAS Annual Meeting*, 1173–1182.

[2] Mizuno, A., Clements, J.S., Davis, R.H. (1984). A device for the removal of sulfur dioxide from exhaust gas by pulsed energization of free electrons. *Conference Records of the IEEE/IAS Annual Meeting*, 1015–1020.

[3] Chang, J.S., Lawless, P.A., Yamamoto, T. (1991). Corona Discharge Processes. *IEEE Trans. Plasma Sci.*, 19, 1152-1166.

[4] Ohkubo, T., Kanazzawa, S., Nomoto, Y., Adachi, T., Yan, K.,. Chang, J.S. (1997). Effect of corona discharge modes on removal of NOx from air streams in a corona radical shower system. *Proceedings of the second Non-Thermal Plasma Technology and Gaseous Pollution of Control*, 70–73

[5] Shimizu, L., Oda, T. (2002). Nitrogen Oxides Removal by Using Plate Type Reactor Combined with Catalysts. *J.Adv.Oxid.Technol.,* 5, 217-222.

[6] Yoshioka, Y., K.Sano, K., Teshima, K. NOx removal from Diesel Engine Exhaust by Ozone Injection Method. *J.Adv.Oxid.Technol.*, 6, 143-149.

[7] Yamamoto, T., Ramanathan, K., Lawless, P.A., Ensor, D.S., Newsome, J.R. (1992). Control of volatile organic compounds by an AC energized ferroelectric pellet reactor and a pulsed corona reactor. *IEEE Trans. Ind. Appl.* 28, 528–534.

[8] Oda, T., Takahashi, T., Nakano, H., Masuda, S. (1993) Decomposition of fluorocarbon gaseous contaminants by surface discharge-induced plasma chemical processing I*EEE Trans. Ind. Appl.* 29, 787–792.

[9] Ogata, A., Shintani, N., Mizuno, K., Kushiyama, S. (1998). Effect of water on benze12512ne decomposition using packed-bed plasma reactor. *Proceedings of the Asia-Pacific Workshop on Advances in Oxidation Technology* 91–96.

[10] Einagar, H., Ibusuki, T., Futamura, S. (2000) Performance Evaluation of Hybrid Systems Comprising Silent Discharge Plasma and Catalysts for VOC Control. *IEEE Trans. Ind.Appl.*, 37 1476-1482.

[11] Urashima, K., Misaka, M., Ito, T., Chang, J.S. (2002). Destruction of Volatile Organic Compounds in Air by a Superimposed Barrier.5, 135-140.

[12] Oda, T., Yamaji, K., Takahashi, T. (2004) Decomposition of Dilute Trichloroethylene by Nonthermal Plasma Processing – Catalyst and Ozone Effect. *IEEE Trans.Ind.Appl*., l.40, .430-436.

[13] Ono, R., Oda, T. (2002). Dynamics and density estimation of hydroxyl radicals in a pulsed corona discharge. *J.Phys. D,* 35, 2133-2138

[14] Ono, R., Oda, T. (2004). Spatial distribution of ozone density in pulsed corona discharges observed by two-dimensional laser absorption method. *J.Phys. D,* 37, 730-735

[15] Han, S.B., Oda, T., Ono, R. (2005). Improvement of the Energy Efficiency in the Decomposition of Dilute Trichloroethylene by the Barrier Discharge Plasma Process. *IEEE Trans Ind.Appl.*, 41, 1343-1349

Paper number

THERMAL DECOMPOSITION OF MINERAL OXIDES TREATED IN AN IMMERSED ARC-PLASMA

Z. Kolacinski[1], L. Szymanski[2]

[1] *Faculty of Electrical, Electronic, Computer and Control Engineering,*
Institute of Electrical Apparatus, Technical University of Lodz
18/22 Stefanowskiego Street, 90-924 Lodz, POLAND
[2] *Academy of Humanities and Economics in Lodz,*
64 Rewolucji 1905r. Street, 90-922 Lodz, POLAND

ABSTRACT. Presently the economically viable solution applicable for most of the toxic mineral residues is the plasma-arc vitrification process. An immersed arc can be an effective tool for smelting of mineral waste compounds followed by their vitrification. This arc starts to burn in the working gas (i.e. argon) and then after melting of mineral compounds their gasification, thermal decomposition, ionization takes place. As an example of the of the solid mineral feed a fly ash has been used. It is discussed how the mineral gas works as a plasma medium.

1. INTRODUCTION

Increasing amount of mineral residues, produced by heavy industry plants such as mains, metal refining, chemical industry and incineration plants determine a potential environmental risk. The use of these residues as additives i.e. in cement industry is not always a proper solution as leaching of the concrete blocks can be not negligible and it may be increasing in time crossing over the regulatory limits. Now the economically viable solution applicable for most of the toxic mineral residues is the plasma-arc vitrification process. In the last twenty years a few different approaches for efficient minerals smelting and decomposition of organics were demonstrated. There were mostly experiments with plasma torches with steady and centrifugal crucibles [1] or with graphite open or shielded arc also with 2 electrodes in arc V-mode [2]. However, the most energy efficient system is such in which the electrode is immersed deeply in the feed allowing most of the heat generated by the arc to be transferred to the feed. In such a case the arc must be burning in mineral elements vapor and can not be shunted by the conducting current melt. In the paper some experimental results with the immersed arc are presented. As an example of the solid mineral feed is a fly ash. The feed thermal decomposition results in the production of a mineral gas. It is here discussed how this gas works as a plasma medium.

2. IMMERSED ELECTRODE ARC

The principle of this process is the arc submergence in the feed charge and also in its solution. Plasma utilization process might be a continuous one if the feeding of charge and collection of product are continuous.

Metallurgy [3-6] is the most developed branch of industry, where the electric arc is applied as a heat source. There are used mainly three-phase arc furnaces with three graphite electrodes, supplied with an alternating current. The hole in the electrodes allows inlet of a neutral gas like argon or nitrogen into the furnace, which also cools the electrodes. In this way, a thermal steady state of the furnace is reached. The following four typical metallurgical arc furnace types are to distinguish:

- an immersed electrode – Fig. 1.a),
- an open arc – Fig. 1.b),
- a shielded arc – Fig. 1.c),
- a submerged arc – Fig. 1.d).

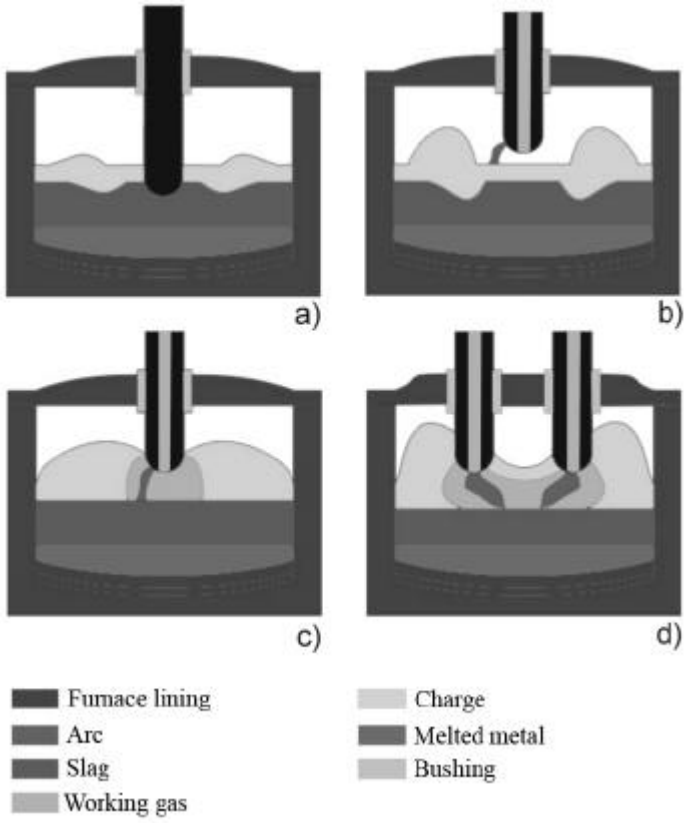

FIGURE 1. Examples of different configurations of metallurgical furnaces [7].

Differences between the above melting methods practically depend on position of electrodes in relation to the melted slag and to the position and depth of not melted charge-surrounding the electrodes.

In the immersed electrode system (Figure 1.a) the electrode tip is placed inside the slag solution. Energy is generated by Joule's heat only: $P=I^2R_{slag}$. Then heated slag transfers the heat to the charge. Energy efficiency of such process is at the level of 95%. Unfortunately, it is not any of arc regime in the furnace functioning. The typical state of the arc furnace running is the state with an arc generated above the charge – the open arc (Figure 1.b). In such

conditions, the large portion of energy is transferred to the external part of the furnace and then it is lost in water-cooled walls and the roof.

The most similar metallurgical arc furnace to our laboratory model is this with shielded arc (Figure 1. c). Though the arc is produced in between the electrode and the slag it burns in the atmosphere of gas flowing out from the electrode, so it is not the gas-mineral arc to such extend as in this work. In the arrangement with submerged arc (Figure 1.d) minimum 2 electrodes are required (if the power system is of the single-phase).

In our laboratory furnace the graphite electrode tip has been immersed in the mineral waste touching initially the graphite crucible bottom. After electrodes separation to a short gap (usually below 1 mm) a stable arc discharge named the idle arc was initiated using the ambient argon gas. The increase of the feed temperature effects in the gas coming from gradually evaporating compounds according to their boiling points. The gas enters the arc atmosphere. The arc discharge produces a gas sheath from the side of charge which is of mineral origin. The outer wall of the gas sheath is the melted mineral material layer. It has been proved that this layer is having electrical conductivity comparable to this of some metals. The resistance of fluid layer depends on its local resistivity, its effective cross section and the length. Is also probable, that resistivity of this layer near electrodes grows up sufficiently as a result of electrode cooling. It can prevent current shunting leading arc breaking. In every case however the arc voltage fall should be as high as possible so the arc can be elongated to the length assuring its stable regime called working arc regime. In this work experimental investigations it does not encounter any arc instability problems. However before working arc would be applied the idle arc had to be burning for the time up to 30s. After such "conditioning" of the system the arc could be elongated to maximum possible length and it was burning always steadily, until the tapping of the full charge.

3. THERMAL DECOMPOSITION OF SOME MINERAL WASTE MATERIALS

The calculation of thermal decomposition of the mineral feed materials had in view the qualification of gas fraction as an arc plasma environment, formed from the thermochemical transformation and vaporization of the mineral material. The ability of thermal ionization of these gases decide about the value of the arc heat potential. Material created in this way has got new structure. It becomes friendly for natural environment after cooling and vitrification. Thermochemical calculations were executed in commercial programs. The thermal decomposition of chosen waste materials was calculated in conditions of plasma pyrolysis. The materials representing feed were: fly ash from the heat and power generating plant Belchatow, asbestos - chryzotyle and sludge from municipality treatment plant. Some results are presented in Table 1.

The plasma creative gas of arc submerged in fly ash coming from the heat and power generating plant consists of atoms of such minerals as Al, Ca, Fe, K, Mg, Si and oxygen coming from breaking-up the mineral oxides. Effective forming of the mineral gas begins in temperature affirming the evaporation components of ash. It means, initiation of burning of arc has to proceed in material of electrodes vapor environment and residual gas surrounding electrodes. It seems to be necessary as quickly as possible supply of preliminary part of energy to the charge, which causes effective charge evaporation and generation of required amount of mineral gas. Utilization process of ash to temperature about 3000K is leaded without production of gas component as it is shown at Figure 2. Intensive evaporation of ash and forming gas compounds follows above this temperature.

TABLE 1. Chemical composition fly-ash from Heat and Power Generating Plant Belchatow used for computer simulation.

Element	Si	Ca	Al	Fe	Mg	Ti	K	P	Na	Mn	O	Total
Mass [g]	21,35	16,03	0,54	3,35	0,49	0,11	0,31	0,06	0,09	0,01	33,19	75,53

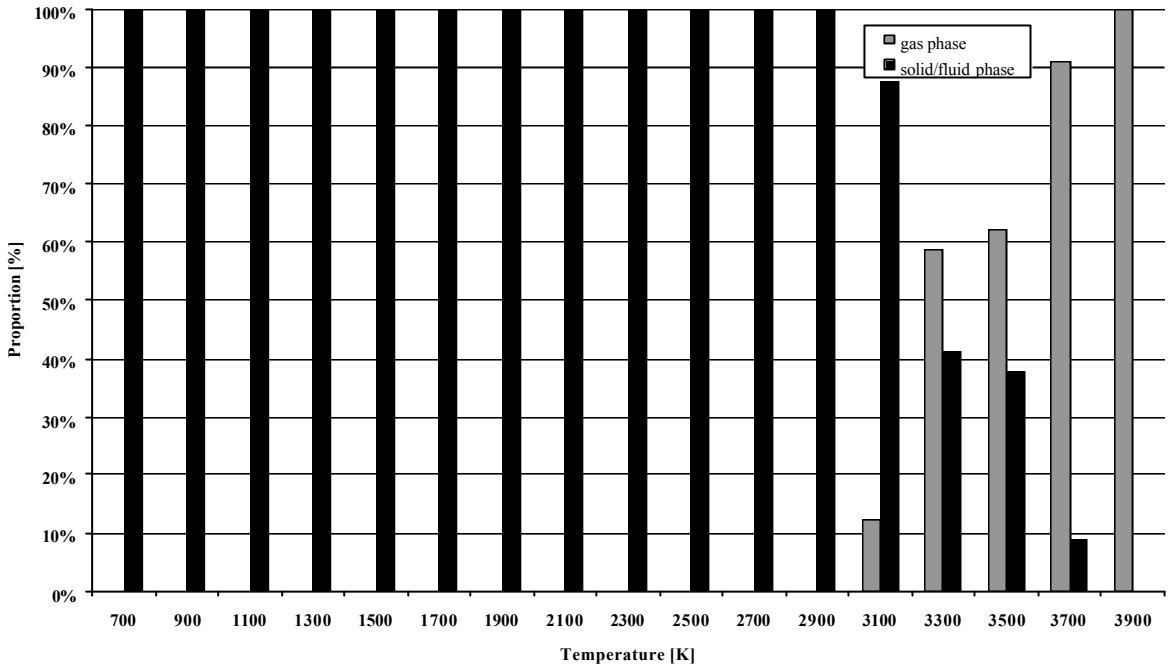

FIGURE 2. Percentage proportion mass of products during thermal decomposition of fly-ash.

Figure 3 presents the contents of magnesium compounds in gas phase in function of temperature.

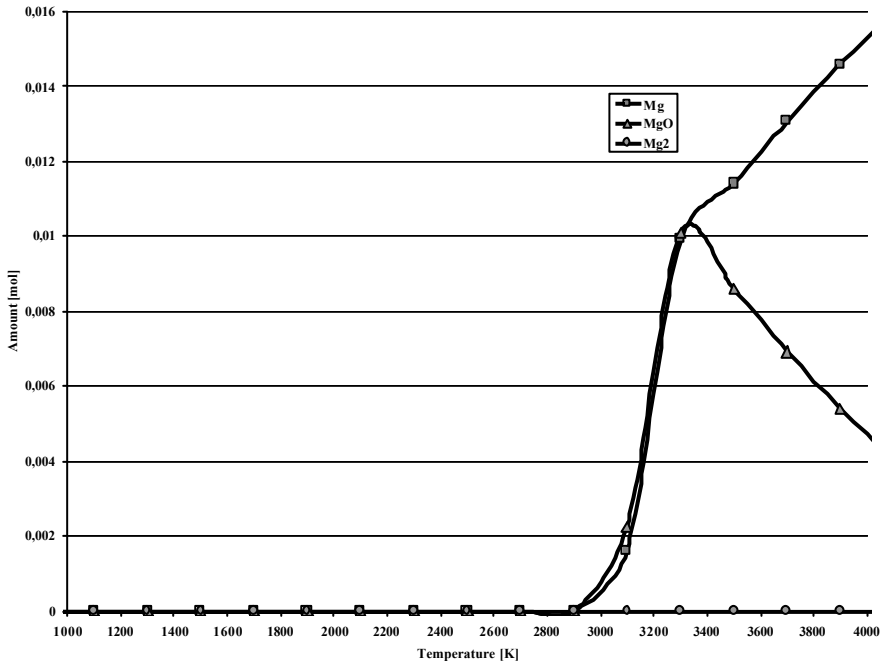

FIGURE 3. The relation between amount of Mg, MgO, Mg_2 in gas phase and the process temperature.

4. PROPERTIES OF THE VITRIFICATE

One of the most important features of the vitrificate is the leachability level of heavy metals. This property decides about wide use of the vitrificate and about possibility of returning it to the natural environment. Results of chosen investigations for leaching tests were placed in Table 2.

TABLE 2. Concentration of metals in aqueous solution produced from vitrificates.

	Medical ash without additions	Medical ash + 15%SiO_2	Fly-ash from heat and power generating plant Belchatow	Sludge from industrial treatment plant
Na	89	20	3,985	29,551
Ca	16,15	4,68	137,76	69,273
K	8,3	2,4	1,27	1,013
Zn	1,29	0,28	0,013	0,044
Mg	0,53	0,086	0,0127	0,034
Co	0,49	0,09	0,033	0,004
Fe	0,32	0,09	0,0198	0,015
Cu	0,178	0,054	0,026	0,006
Pb	0,166	0,0371	0,625	0,53
Ni	0,016	0,004	0,11	0,081
Cr	0,009	0,002	0	0
Cd	0,005	0	0,022	0,024
Mn	0,04	0,005	0,024	0,028

The next criterion determining an usefulness of the final product was the mass loss test. The results are presented in Table 3. It can be seen, the best effects have been reached for the vitrificate samples made of fly ash from heat and power generating plant Belchatow and the sludge from the municipality treatment plant.

TABLE 3. Mass loss in aqueous solution.

	Sample	Mass loss in aqueous solution [%]
1	Medical ash + 35% PCB	2,9
2	Fly-ash from heat and power generating plant Belchatow	1
3	Sludge from industrial treatment plant	9,28
4	Sludge from municipality treatment plant	1

Measured Vicker's hardness of the vitrificate is typical for usual kinds of glass. All these results show that that the vitrificate is safe and it suits well for producing building materials, road aggregate, etc.

5. CONCLUSIONS

The design and building of systems for thermal utilization of materials by the electric arc joins with qualification of the feed properties parameters as well as efficiency system. The laboratory tests proved that the use of the arc discharge generated inside the material among electrode submerged and crucible can be working well and effectively. The termochemical calculation allowed to define the best range of temperature of utilization. The properties of the vitrificate qualify it as an acceptable building material.

ACKNOWLEDGMENTS

This work has been supported by the Polish Ministry of Science and Education with Grant No. 1304/T10/2004/27.

REFERENCES

[1] (1999) Using the Centrifugal Method for the Plasma-Arc, *JOM Journal,* 51(10) pp.14-16.

[2] (1995) Plasma Treatment of Waste Materials – "*Pyrometallurgy*", Cambridge 1995.

[3] Barcza N.A., Curr T.R., and Jones R.T.(1990): Metallurgy of open-bath plasma processes, *Pure & Appl. Chem.,* Vol. 62, No.9, pp. 1761-1772.

[4] Jones R.T., Barcza N.A., Curr T.R. (1993): Plasma Developments in Africa, Originally published as Plasma Developments in Africa, *Second International Plasma Symposium: World progress in plasma applications,* organized by the CMP (Centre for Materials Production) of EPRI (Electric Power Research Institute).

[5] Barcza N.A., Curr T.R., Denton G.M., Hayman D.A. (1989): Mintek's Role in the development of plasma-arc technology based on a graphite cathode, *Thermal Plasma Workshop on Industrial Plasma Applications ISPC.*

[6] Bakken J.A., Jensen R., Monsen B., Raness O., Wrernes A.N. (1998): Thermal plasma process development in Norway, *Pure & Appl. Chem.,* Vol. 70, No. 6, pp. 1223-1228.

[7] Ma T., Bendzsak G.J., Perkins M. (2003): Power system design for high-power electric smelting and melting furnaces, *High Temp. Material Processes* 5, pp. 367-372.

PROPERTIES OF A HETEROGENEOUS SYSTEM OF SOLID PARTICLES IN GLIDING-DISCHARGE PLASMA

K. Schmidt-Szalowski, K. Krawczyk, M. Mlotek

Warsaw University of Technology, Faculty of Chemistry
ul. Noakowskiego 3, 00-664 Warszawa, POLAND

ABSTRACT. A gliding discharge reactor was developed for the methane conversion to C_2 hydrocarbons, operated with a spouted bed of solid particles (alumina-ceramics) within the plasma zone. The discharge conditions were influenced by the presence of the particles and the soot formation was reduced in gases of high methane content.

1. INTRODUCTION

A number of known reactions may be initiated through the action of energized electrons in non-equilibrium plasmas, by transferring reactant molecules into free radicals, opening a chain of successive reactant transformations. A variety of reaction paths may be initiated in this way resulting in the generation of miscellaneous products. Therefore, those processes are characterized by low selectivity. As one could expect, the efficiency of plasma chemical reactions might be improved by using suitable catalysts. A number of solid materials, expected catalysts, have been tested for different kind of hybrid processes, e.g. for removal of hydrocarbons, NO_x, soot etc. from engine exhaust and for cleaning industrial waste gases [1-6].

Taking into account the hitherto experiments an effort was made to develop a gliding discharge (GD) reactor for the gaseous reagent conversion, capable to operate with a spouted bed of solid catalyst particles being placed inside the plasma zone. As has been shown in a number of studies, GD can be effectively used for carrying out different chemical processes, both in homogeneous gas systems and in suspensions of powdered solids or liquid droplets in gases (e.g. for the partial fuels oxidation or the volatile pollutants destruction [7-12]). However, a novel solution is needed when particles of the solid should be kept for a longer time in the discharge zone, e.g. when the reaction involving the solid material proceeds slowly or when the solid plays the role of a catalyst for the reaction between gaseous reactants.

2. EXPERIMENTAL

A GD reactor of a special shape was designed aiming to use the spouted bed of solid particles, located within the discharge volume [7]. It is provided with a conic reaction chamber widening upwards to 50 mm in diameter and lined with a ceramic material, with two vertical electrodes for the generation of gliding discharges. Gaseous reactants, introduced at the bottom keep the particles moving within the inter-electrode space. The methane conversion to C_2 hydrocarbons was studied using a spouted bed of alumina-ceramics particles (0.16 – 0.5 mm) with a single batch packed to the reactor of 10 - 20 ml. Gas mixtures CH_4+H_2+Ar, were examined at atmospheric pressure. The reactor was powered by a 50 Hz system (Fig. 1) with the active power supplied being measured in a primary circuit (by means of an energy meter Pafal MOD A5). The electrical characteristics of the discharge course were recorded using

Electronic address: kss@ch.pw.edu.pl

oscilloscope Tektronix TDS 3032 equipped with Tektronix P6015 voltage probe and Tektronix TPC202 current probe. The temperature inside the reactor volume was measured with a thermocouple at the axis of reactor at the level of the upper end of electrodes.

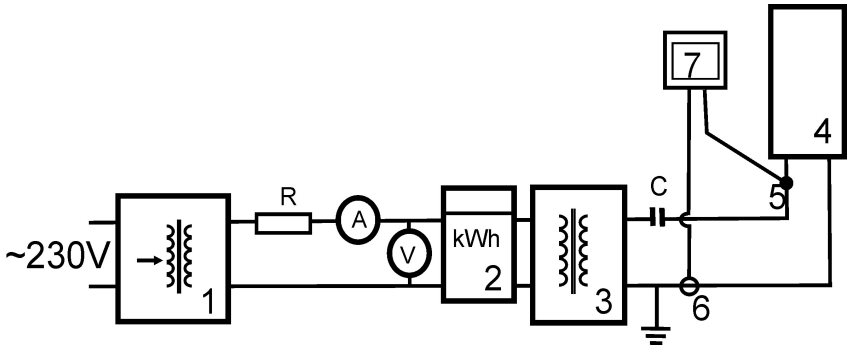

Figure 1. 1- Autotransformer, 2 – Energy counter, 3 – High voltage transformer, 4 – Reactor, 5 – Voltage probe, 6 – Current probe, 7 – Oscilloscope. R=3.1Ω, C=2μF.

The gases were analysed using Chrompak 9002 with a Carboxen 1000 column and a FID detector.

3. RESULTS AND DISCUSSION

The observed gas temperatures were low (120 - 320 °C) depending on the discharge power and the gas composition. This bears evidence of the high contribution of heat dissipated to the environment, amounting up to 70 - 80% of the energy supplied to the reactor. The discharge conditions were influenced by the presence of the spouted bed which resulted in an increase in voltage and decrease in current in the primary circuit (Fig. 2). At the same time, the effect of the spouted bed on the discharge feature was observed (Fig. 3-5).

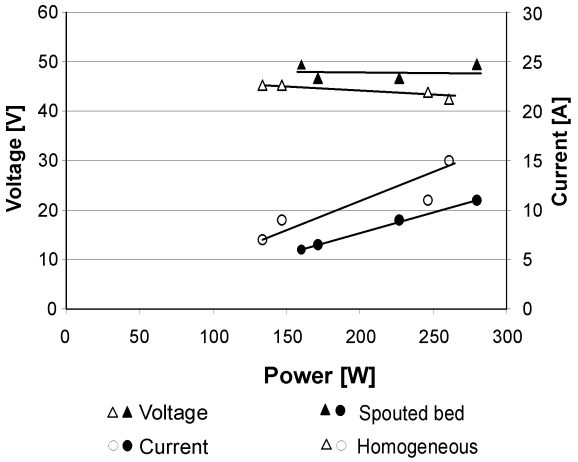

Figure 2. Effect of spouted bed on current and voltage (measured in a low voltage circuit). Overall gas flow 300Nl/h, gas composition: 0.4 CH_4 + 0.6 H_2

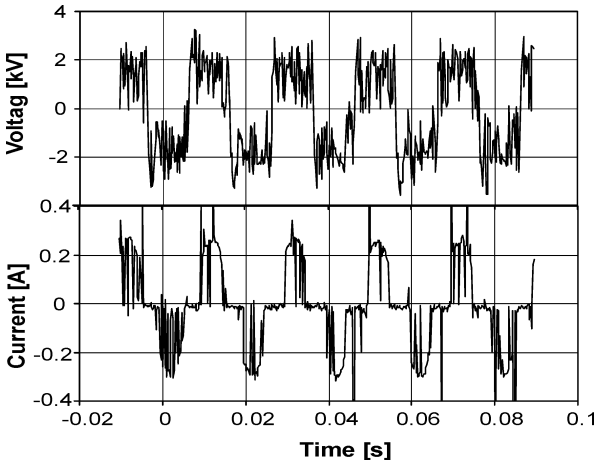

Figure 3. Voltage and current in the homogeneous process. Discharge power ~ 240W. Overall gas flow 300Nl/h, gas composition: 0.4 CH_4 + 0.6 H_2

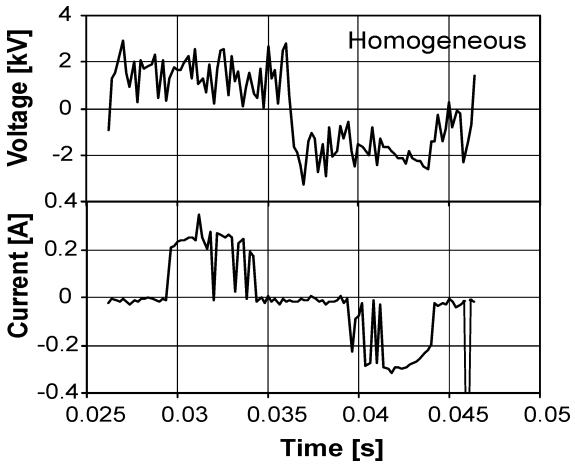

Figure 4. Voltage and current in the homogeneous process. Discharge power ~ 240W. Gas composition $0.6H_2 + 0.4CH_4$, gas flow 300Nl/h

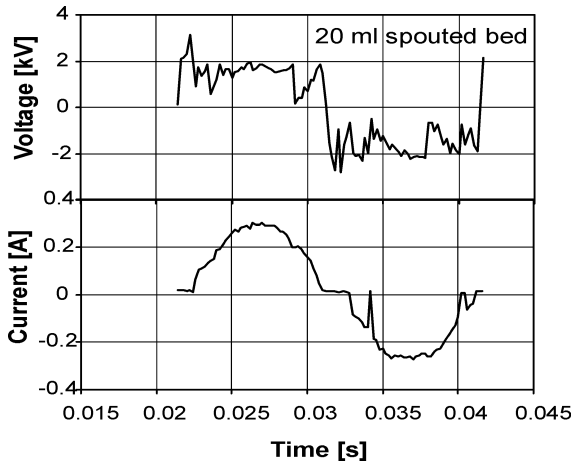

Figure 5. Voltage and current in a 20 ml spouted bed (0.16-0.315). Discharge power ~ 250W. Gas composition $0.6H_2 + 0.4CH_4$, gas flow 300Nl/h

The sawtooth shape of the voltage and current signals was the most distinguish for the discharges without the solid particles. When using a spouted bed, the shape of signals became more smooth, especially with the larger particles batch (20 ml). On the other hand, the time distance between the active parts of the discharge period increased due to the presence of the bed. Those findings illustrate the effect of solid particles on the discharge parameters with the recombination of ions and electrons on the particle surfaces being one of the possible reasons for that.

Acetylene was found to be the main product with a small admixture of ethylene. The overall methane conversion and the productivity of the methane conversion into C_2 hydrocarbons increased with the increasing discharge power and depended also on the gas composition (Fig. 6 and 7).

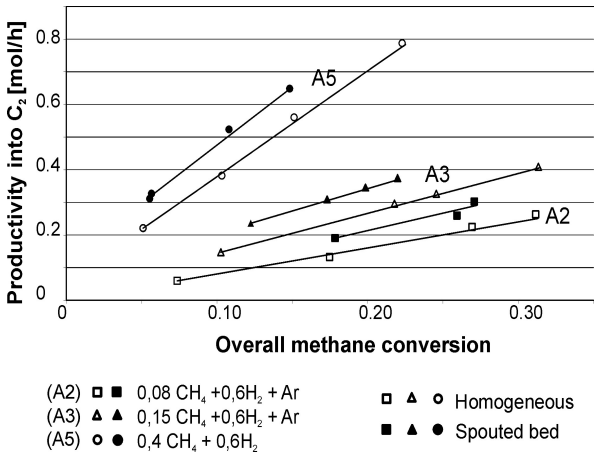

Figure. 6. Effect of the spouted bed (0.16-0.5) on C_2 productivity. Overall gas flow 300Nl\h

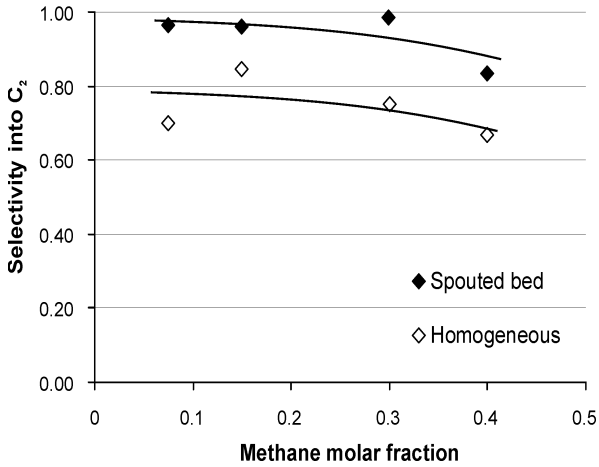

Figure. 7. Effect of the spouted bed (0.16-0.5) on C_2 selectivity. Overall gas flow 300Nl\h, gas composition: $0.6H_2+CH_4+Ar$. Discharge power 160W

The presence of the spouted bed of particles resulted to a minor degree in methane conversion into C_2 hydrocarbons, however, due to the significant reduction of the soot generation, the selectivity of conversion into C_2 was higher than without the bed. When using the methane rich mixture with hydrogen ($0.4\ CH_4+0.6\ H_2$), the selectivity into C_2 exceeded 80% in the

presence of particles. One can conclude that the heterogeneous processes of the active gas components on the particle surfaces resulted in the increase of selectivity of acetylene formation, however, mainly due to the lower reaction rate of soot generation. Summarizing those results it should be noticed that the presence of the spouted bed in the volume of the gliding discharge reactor may result in numerous changes of the process conditions, not only of the electrical parameters but also of the hydrodynamics of the gas flow. Moreover, the effects of the heterogeneous reactions on the particle surfaces, involving free radicals and excited molecules, cannot be excluded.

AKNOWLEDGMENT

This work was financially supported by Warsaw University of Technology.

REFERENCES

[1] Liu C-J., Eliasson B., Xue B., Li Y., Wang Y. (2001). Zeolite-enhanced plasma methane conversion directly to higher hydrocarbons using dielectric-barrier discharges. *React. Kinet. Catal. Lett.*, 74**,** 71-77

[2] Hammer Th., Kappes Th., Baldauf M. (2004). Plasma catalytic hybrid processes: gas discharge initiation and plasma activation of catalytic processes. *Catalysis Today*, 89**,** 5-14

[3] Song H.K., Choi J.-W., Yue S.H., Lee H., Na B.-K. (2004). Synthesis gas production via dielectric barrier discharge over Ni/γ-Al_2O_3 catalyst, *Catalysis Today,* 89**,** 27-33.

[4] Khassin A.A., Pietruszka B., Heintze M., Parmon V.N. (2004). The impact of a dielectric barrier discharge on the catalytic oxidation of methane over Ni-containing catalyst, *React. Kinet. Catal. Lett.*, 82(1), 131-137.

[5] Gordon C.L., Lobban L.L., Mallinson R.G. (2003). Ethylene production using a Pd and Ag-Pd-Y-zeolite catalyst in a DC plasma reactor, *Catalysis Today*, 84, 51-57

[6] Nagazoe H., Konuma M., Kobayashi M., Yamaguchi T., Onoe K. (2005). Development of new green process for methane reforming using microwave plasma / solid catalyst combined reactions, *ISPC 17, Toronto 2005*

[7] Schmidt-Szałowski K., Górska A., Młotek M. (in press) Plasma-catalytic Conversion of Methane by DBD and Gliding Discharges, *J. Advanced Oxidation Technol.*

[8] Czernichowski A. (1998), Electrically assisted conversion of natural gas into syngas, *Karboenergochmia-ekologia*, (11), 359-369

[9] Mutaf-Yardimci O., Saviliev A.V., Porshnev P.I., Fridman A.A., Kennedy L.A. (1999). Non-equilibrium effects in gliding arc discharges, *Ann. NY Academy Sci.* **891,** 304-308.

[10] Pellerin S., Cormier J-M., Richard F., Musiol K., Chapelle J. (1999). Determination of electrical parameters of a bi-dimentional d.c. Glidarc, *J. Phys. D: Appl. Phys.* **32**, 891-897

[11] Czernichowski P., Czernichowski A. (Dec. 28 1999). Electrically assisted partial oxidation of light hydrocarbons by oxygen, *US Patent 6 007 742.*

[12] Czernichowski A., Czernichowski M. (2005) Further development of plasma sources: the GlidArc-III, *ISPC 17, Toronto 2005*

Paper number

INCREASE OF NO REMOVAL EFFICIENCY BY GLOW LIKE DISCHARGE

Y.Yoshioka[1] and T. Shoyama[1]

[1] *Department of Electrical Engineering,*
Faculty of Engineering, Kanazawa Institute of Technology
7-1 Ohgigaoka, Nonoichi, Ishikawa, 921-8501 JAPAN

ABSTRACT. Theoretical prediction suggested that NO removal efficiency is higher in glow like discharge than in filamentary type discharge. In this paper, we report what factors are important to realize glow like discharge under atmospheric pressure and at a frequency less than 1kHz. After many experiments, we found that micro-discharges spread out in whole discharge space by elevating temperature of barrier material and/or by use of acrylic plate. NO removal efficiency of glow like discharge mode was improved more than 70% in comparison with that of glow like discharge mode.

1. INTRODUCTION

NO removal method by barrier discharge has a problem that energy efficiency is relatively low [(1)], and so various methods have been experimentally investigated [(2)]. Simulation of chemical reactions by a micro-discharge model was also carried out to know how NO was removed in barrier discharge. Our simulation studies showed that NO removal efficiency will increase considerably if filamentary barrier discharge mode changed to glow like discharge mode [(3)]. Recently, many studies have been carried out to realize an atmospheric glow discharge [(4)], it is still not so easy. However, a glow like discharge mode was found to be obtained easily by heating barrier to 60 ~ 80 C and/or by use of acrylic plate barrier [(5)]. In this paper, in chapter 2 we describe such a discharge mode change, and in chapter 3 we describe the result of NO removal experiment using glow like discharge mode.

2. CHANGE OF BARRIER DISCHARGE MODE [(5)]

2.1. Experimental set up

Figure1 shows our experimental discharge device, which has 100cm^2 of electrode area and two dielectric barriers. One of the barrier was pasted by aluminum electrode and other barrier was fitted by a glass with ITO coated electrode. As barrier discharge mode may be influenced by barrier material or surface condition of barrier, we used barrier materials shown in Table 1 and changed the temperature of barrier by setting the discharge device in a temperature controlled box. Air flow of 2.5Nm^3/h was sent to the discharge device, whose discharge gap is 1 ~ 3mm and high voltage of 200Hz was applied to the device. Barrier discharge was observed from ITO electrode side and from side of the device by a digital camera. In these experiments, the applied voltage and discharge current were measured. Q-V lissajous figure was measured.

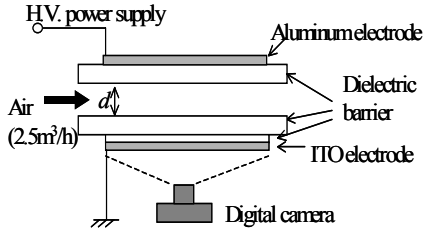

FIGURE 1 Barrier discharge device

2.2. Experimental result

Figure 2 (a)(b) shows the typical examples of barrier discharge taken with different barrier temperatures. It is seen that at room temperature, barrier discharge is a typical filamentary mode, but at higher barrier temperature (80C), the discharge spread out widely in whole discharge area and looks like glow discharge. When acrylic resin was used instead of soda glass, the similar discharge mode was observed as shown in figure 2 (c). It looks like glow discharge, but when we observe the discharge photographs carefully we can find that there are many small micro-discharges. Next, figure 3 shows records of discharge current, and it is seen that in both cases many pulse currents are observed, and magnitudes of current pulses are higher in case of acrylic resin barrier. However these current wave forms are same as the one observed in the typical barrier discharge. So we think that the discharge of figure 2(b)(c) looks like glow discharge, but it is not glow discharge but a glow like discharge.

TABLE 1 Barrier materials and their elative permittivity

NO	Barrier material	Relative permittivity
1	Soda glass	8.3
2	Pyrex glass	4.3
3	Acrylic resin	3.4
4	Frosted soda glass	8.3

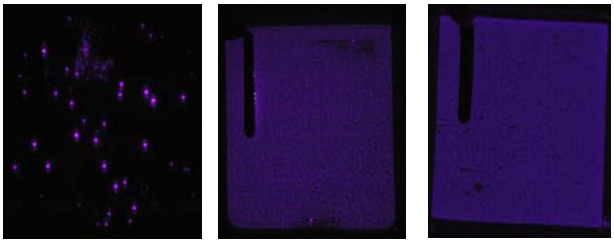

(a)glass, room (b)glass, 80C (c)acryl , 80C

FIGURE 2 Change of barrier discharge

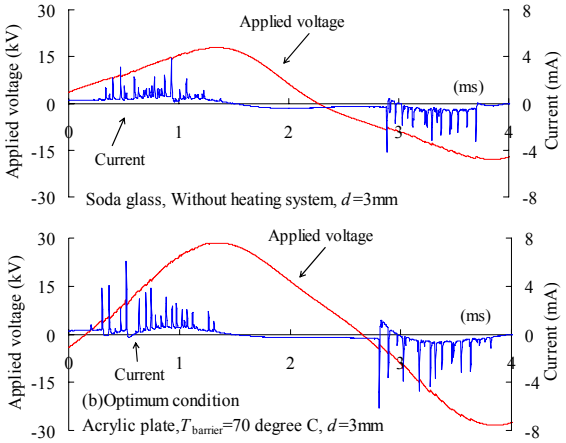

FIGURE 3 Discharge current measured on room temperature soda glass barrier and 70 C acrylic resin

3. NO REMOVAL EXPERIMENTS

3.1. Experimental set up and experimental conditions

In the previous chapter, we showed that a glow like wide spread discharge mode was obtained quite easily by heating the barrier and/or by use of acrylic resin barrier, and it is just the discharge mode that we expected to increase the NO removal efficiency. So in order to confirm whether this glow like discharge mode improves the efficiency or not, we carried out NO removal experiments. Figure 4 shows a NO removal system used in this experiment. Exhaust gases from a 2.4kVA diesel engine is cooled by a gas cooler down to about 40 C, and at a branch, exhaust gases are separated in two ways, and gas of 2.5Nm^3/h was led to a barrier discharge device. The

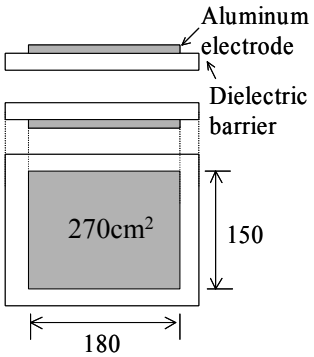

FIGURE 5 Discharge device used for NO removal experiments

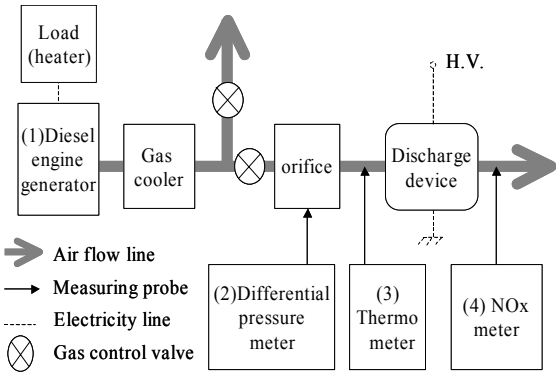

FIGURE 4 Experimental system of NO removal from diesel exhaust gases

flow rate was calculated by gas temperature and a pressure difference of both sides of an orifice set in the flow line. NOx was measured by a NOx meter (Testo Inc.), and discharge power was calculated from the area of Q-V lissajous figure. Figure 5 shows a discharge device, which is a parallel plate type with 1 ~3 mm gap and has an electrode size of 270cm^2. As for barrier material, we used soda glass, frosted soda glass, Pyrex glass and acrylic resin with 3mm thickness.

High voltage of 11 to 33kV, 200Hz sinusoidal wave was applied to the discharge device. Barrier discharge mode of a room temperature device was a typical filamentary type, but at a barrier temperature of 60 ~ 80 C and in case of acrylic resin barrier, the discharge changes from filamentary type to glow like mode as described in the previous chapter

.

3.2 NO removal performance on various barrier materials

Figure 6 shows the result of NO removal experiments on various barrier materials. NO concentration decreases with the increase of discharge power, but it is clearly seen that NO decreases faster with acrylic resin than with soda glass. Frosted glass has the lowest NO removal performance. Figure 7 shows the NO removal efficiency of three materials. The efficiency decreases with NO removal rate, so we compare the efficiency at 50% removal point. As it is seen in the graph NO removal efficiency of acrylic resin barrier attained to 28g/kWh. In case of soda glass, the efficiency is 19g/kWh and in case of frosted soda glass, it is 13g/kWh. There is a tendency that NO removal efficiency decreases with NO removal rate. It comes from the back reaction to produce NO from NO_2 by O radicals.

Usually NO removal efficiency of soda glass is around 20 g/kWh, so 28g/kWh obtained with acrylic resin barrier is a very high efficiency.

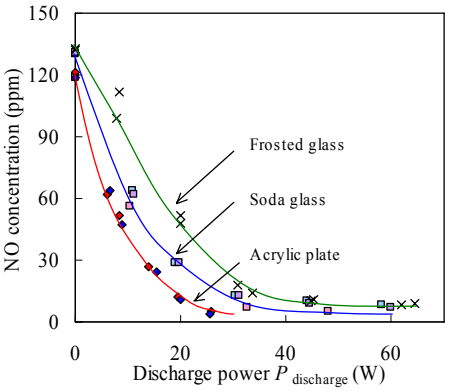

FIGURE 6 NO removal characteristics on barrier materials

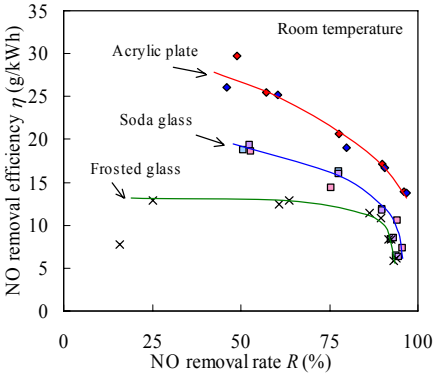

FIGURE 7 NO removal efficiency on various materials

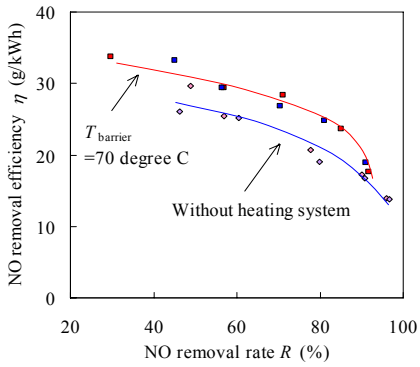

FIGURE 8 Temperature effect of NO removal efficiency

3.3 Effect of temperature of barrier material

At barrier temperature of 60 ~ 80 C, discharge mode changes from filamentary mode to glow like mode. So using acrylic resin barrier, we investigated the temperature effect on NO removal efficiency. Figure 8 shows the temperature effect of NO removal efficiency. As it is seen in the figure, the NO removal efficiency increased by 5 g/kWh at any NO removal rate. The highest efficiency is evaluated as 35g/kWh, and which is a very high value in comparison with the conventional efficiency of 20g/kWh.

In these experiments, the barrier temperature was 70 C and gas temperature was 37 C. After passing through the discharge space, temperature of gas was increased to 50 C. So in order to examine the effect of gas, we passed gas of 70 C to the discharge device, where barrier temperature was set as the same temperature. The result of NO removal experimnt

showed that there are almost no differences in NO removal efficiencies. So it is concluded that barrier temperature is more important than gas temperature.

TABLE 2 Barrier discharge parameters

Discharge channel radius r (mm)	0.05	0.1	0.2
Discharge current i (A)	0.08	0.31	1.26
Area of micro discharge dS (cm^2)	0.13	0.53	2.13
Parallel micro discharge m	5634	1409	352
Micro discharge energy W_1 (μJ)	1.41	5.65	22.6

4. DISCUSSION

In our simulation study, we made a micro-discharge model of barrier discharge, and taking one micro-discharge, we calculated at first the electron initiated radical formation reactions and reaction with NO in discharge channel, and then diffusion of these species to outside of discharge channel and reactions with NO were simultaneously calculated. As the result, the slow diffusion speed was found to be a critical factor to increase the energy efficiency. Besides, lower discharge current density, smaller micro-discharge diameter or random movement of micro-discharge location was expected to increase the NO removal efficiency [3]. Table 2 shows how the radius of micro-discharge channel influences the number of micro-discharges. The glow like discharge is consisted of many small discharges, and so it corresponds to the case of r = 0.05mm, because r = 0.1mm is known as the standard value of barrier discharge. Figure 9 shows result of calculation, and barrier discharge consisted of large number of micro-discharges has an efficiency of 35g/kWh at 50% removal rate, which is compared with the efficiency of 20g/kWh of conventional barrier discharge. This simulation result agrees well with experiments.

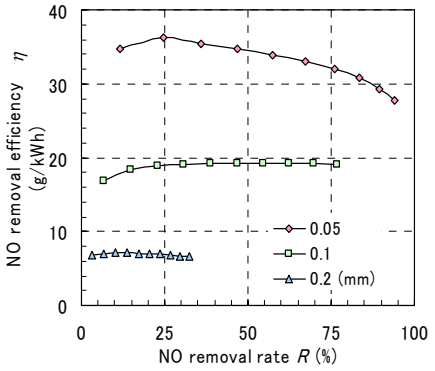

FIGURE 9 NO removal efficiency calculated by our simulation program

5. CONCLUSION

Glow like discharge was obtained at barrier temperature of 60 ~ 80 C and/or by use of acrylic resin barrier. NO removal experiments showed that the glow like discharge mode increases the NO removal efficiency by 1.7 times, in comparison with that of conventional barrier discharge. This result agrees well with the result of simulation study.

ACKNOWLEDGMENTS

The authors acknowledge the support of a Grand-in Aid for Scientific Research (C) of JSPS and also co-operation of experiments by Mr. T.Nishimura and Mr.A.Funato..

REFERENCES

[1] B.M.Penetrante; “Non-thermal Plasma Technologies for Pollution Control”, Part A, Springer-Verlag, Berlin (1994)

[2] J.S.Chang, “Recent Development of Plasma Pollution Control Technology; a critical Review”, Sci.& Technol. Adv.Materials, Vol.2, pp571-576, (2001)

[3]Y.Yoshioka, T.Shoyama : “Analysis of de-NOx process by barrier discharge using a chemical reaction model taking micro-discharge and diffusion into consideration”, 9th International symposium on High Pressure and Low Temperature Plasma Chemistry, HAKONE9, (2004)

[4] Peng Li, Manfred Lindmayer,”Influence of the barrier surface permittivity on the homogeneity of barrier discharges under atmospheric pressure”, Proc. XV GD2004 , Vol.1, pp223-226, (2004)

[5] T.Shoyama, Y.Yoshioka, “Changes of barrier discharge mode caused by elevation of barrier temperature, different dielectric material and surface structure”, to be presented at GD2006, Sep, (2006)

TREATMENT OF NOx BY THE BARRIER DISCHARGE REACTOR

M. Fujii and T. Fujii

Department of Electrical Engineering,
Kobe City College of Technology
Gakuen Higashimchit 8-3 , Nishiku, Kobe, 651-2194, JAPAN

ABSTRACT. Air pollutions caused by combustion gas emission are becoming one of the most serious problems particularly in the industrial areas. The research is focused on the treatment of NOx with lower cost performance by the plasma chemical reaction in barrier discharge space. Basic characteristics of AC barrier discharge were measured and discussed to find the best geometrical setting of electrodes for NOx treatment reactor. The optimal discharge conditions of the reactor were discussed by the result of NOx treatment test with the various frequency of applied AC voltage. One of the provisos is to find out the frequency for the best power performance. More than 95% of the NOx removal rate was confirmed by the experiment used of 10Hz of AC voltage by the diesel exhaust gas treatment test

1. INTRODUCTION

In applications of discharge plasma in the atmospheric pressure, some types of reactors for VOC or NOx treatment have been designed and investigated. The electron beam and the pulse corona reactors have been already constructed and tested at the boiler in the electric power station.[2] They reported well removal performance under specific conditions, but their construction and running costs were estimated too high in the economical balance. The DC corona and the AC barrier reactors were investigated for the application to NOx treatment in the smaller scale boiler or engines with lower cost performance. We designed the DC corona reactor with water for the application to both dust particle and NOx treatment, and got the better NOx removal results than the dry type. We confirmed that ozone and OH radical produced in the discharge plasma space were effective to proceed with the plasma chemical reactions for NOx removal processes. Much more discharge energy was needed for NOx treatment than precipitation of dust particle in this type of reactor. .[1],[2] Barrier discharge reactors have been developed for the application to ozone generator and tried to apply to the plasma chemical reactors for NOx or VOC treatment. We proposed the idea to combine the barrier discharge reactor with the DC corona reactor to improve the NOx removal rate for the combustion gas treatment use.

2. EXPERIMENTS

2.1. Stacked parallel plate reactor

A model reactor by AC barrier discharge with multi plate electrodes was designed and tested for the practical application to diesel exhaust gas treatment. The reactor model was handmade with 6~8 units of plate electrodes set in the plastic box of 20cm x 10cm x 8cm.

A unit of plate electrode was with a copper film on a glass plate as shown in FIGURE 1. The units were put together as layer separated by spacer. Space of each unit (discharge air

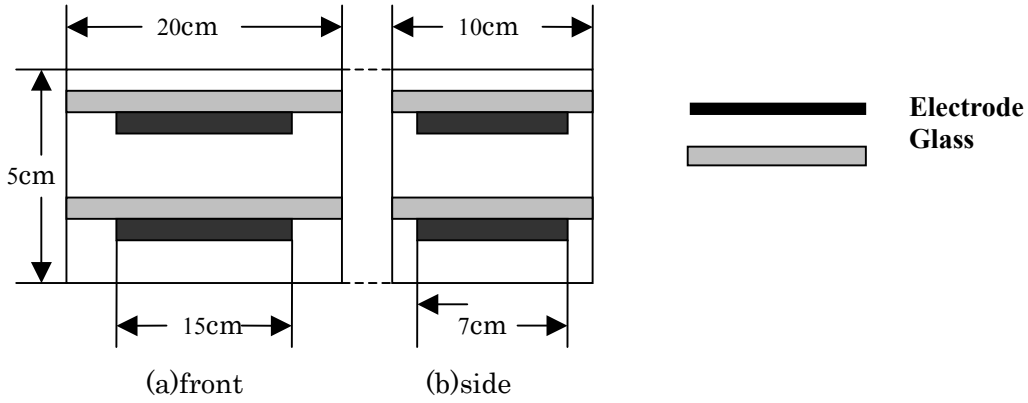

FIGURE 1. Barrier reactor model with layout of units of electrode

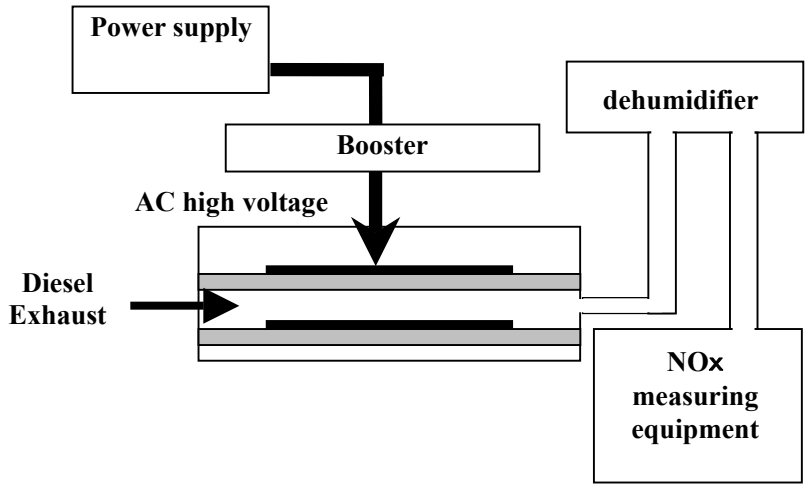

FIGURE 2. Experimental layout for NOx treatment test

gap) was 6mm (type A) and 8mm (type B) length

2.2. Experimental setup

FIGURE 2. shows the experimental layout for NOx treatment tests. AC voltage was generated by the oscillator with variable frequency and waveform and its output was linearly amplified up to high voltage to apply to the test reactor.

Basic characteristics of discharge current and ozone concentration were measured by changing the frequency of applied AC voltage. Temperature on the electrodes and discharge space were also measured. These experiments were carried out under room temperature and pure air flow. NOx treatment tests under various conditions were setup with diesel engine exhaust gas. Concentrations of NO and NOx were measured separately at the outlet of reactor by the NOx gas analyzer. Removal rate was calculated by the gas concentrations when voltage applied and did not applied to the test reactor.

3. RESULTS AND DISCUSSION

We show some typical results of barrier discharge characteristics and produced ozone concentrations for the applied AC voltage and frequency. By some results of NOx treatment test we discussed on the produced radicals and estimated chemical reactions in NOx removal processes in the reactor of type A

4.1 Barrier discharge characteristics

Characteristics of discharge current by parameter with frequency of applied AC voltage are shown in **FIGURE 3**. Discharge current increased as applied voltage increasing and saturated up to the maximum 13mA. Discharge current and the maximum saturated current depends on the frequency of applied AC voltage. Near the point of 500 Hz of applied AC voltage, characteristics of discharge current changed. In this case, the 2 kHz showed the maximum current as the increasing of applied voltage. These characteristics and fitting frequency should be changed by the geometry of layer of plate electrodes.

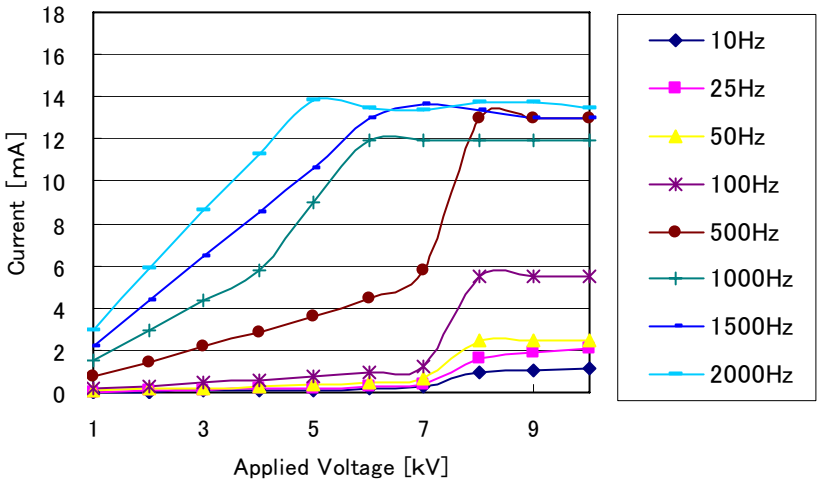

FIGURE 3. Discharge current characteristics with parameter of frequency

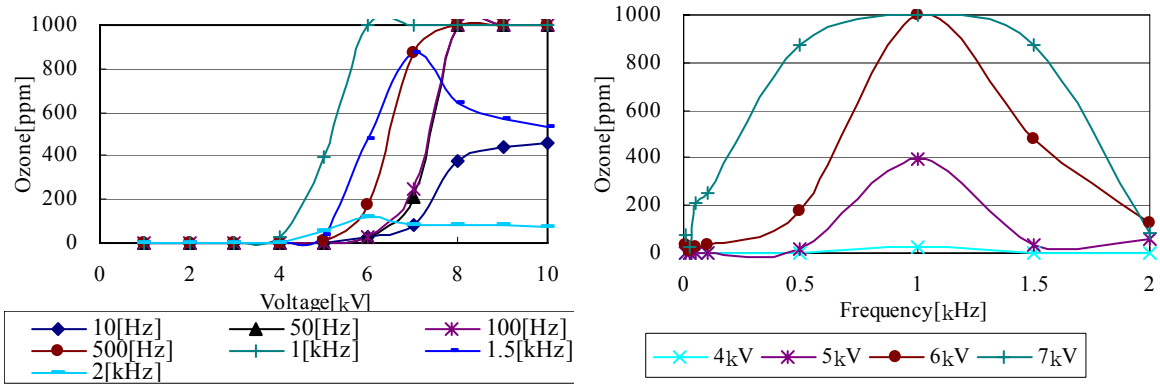

FIGURE 4. Ozone concentration vs. frequency of applied AC voltage

4.2 Ozone production

Concentrations of ozone produced by discharge were shown in **FIGURE 4**. They were measured at the outlet of the reactor with 5 litter/min clean air flow into the reactor. Ozone production was nearly direct proportional to discharge current at the middle frequency, but it decreased at lower or higher frequency. It showed the maximum concentration at the frequency of 1 kHz under various applied voltages. The frequency for maximum ozone concentration should be changed by the geometry and layout of electrodes in the reactor. Ozone concentration decreased in higher frequency over 1 kHz though discharge current increased. It may be by the reason of induction heating at the electrodes.

4.3 NOx treatment test

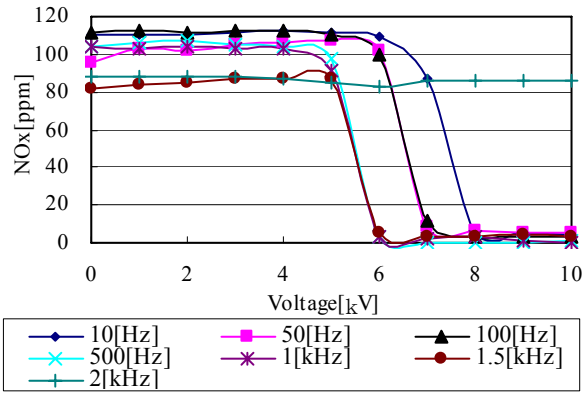

FIGURE 5. Concentration of NOx at the outlet of the barrier discharge reactor with parameter of frequency of applied AC voltage

The test was carried out by the reactor of type A with inlet NOx gas concentration of 80 ~110 ppm by diesel engine exhaust gas. Concentrations of NO and NOx were measured separately under various discharge conditions with 5 litter/m gas flow rate.

Concentrations of total NOx (NO + NO2) measured at the outlet of the reactor were shown in **FIGURE 5**. Almost of NOx in the diesel exhaust gas was treated in the reactor by applied voltage over 6 or 8 kV. But in case of the frequency of 2 kHz, NOx was not removed at all. It was because of less ozone presence in the reactor. The results of NOx removal tests indicate that it needs the ozone concentration of 400 ppm at least in the reactor to treat the total NOx concentration of about 100 ppm.

Fig.6 shows one of the best NOx removal results by lowest power input. 100% of NO and more than 95% of NOx removal rate was performed by the reactor for 80ppm of inlet NOx concentration. In this case the produced ozone concentration was needed at least 400ppm and the lowest discharge power was about 6W

REFERENCES

[1] T.Fujii, Y. Kaneda and M. Rea.(2000). NOx Treatment Test by Positive DC Corona Reactor with and without Water. Trans. Institute of Fluid-Flow Machinery, 107

[2] Tomio Fujii, Yukio Aoki, Naoki Yoshioka, Massimo Rea. (2001). Removal of NOx by DC Corona Reactor with Water. Journal of Electrostatics, Vol.51-52, pp.8-

Paper number

PHENOL OXIDATION BY PULSED STREAMER DISCHARGE IN WATER

M. Dors, E. Metel, M. Kocik, J. Mikielewicz, J. Mizeraczyk

Centre for Plasma and Laser Engineering
The Szewalski Institute of Fluid Flow Machinery, Polish Academy of Sciences
Fiszera 14, 80-231 Gdańsk, POLAND

The positive pulsed streamer discharge was generated between a stressed needle and a cylinder. Both electrodes were immersed in the distilled water contaminated with phenol (0.62 mM), to which $FeSO_4$ could be added. It was found that H_2 and H_2O_2 was produced during the streamer discharge in water with production rates of 0.021 mg/min and 0.55 mg/min, respectively. Increasing the discharge duration resulted in increased H_2O_2 concentration, phenol degradation rate, water conductivity and acidity. The oxidants produced by the streamer discharge oxidized up to 42% of phenol during 90 min processing of the water without $FeSO_4$. In the presence of $FeSO_4$ the phenol oxidation efficiency increased to 78%.

1. INTRODUCTION

It was already reported in [1-3] that addition of iron salts to the water processed by the pulsed streamer discharge enhanced degradation of several organic compounds. This was due to the known Fenton reaction which have been widely used to the degradation of a wide range of organic compounds.

In the presence of iron salts in the water, hydrogen peroxide, the most abundantly produced oxidant by the streamer discharge, is converted to hydroxyl radicals, which is much stronger oxidant than H_2O_2, through the Fenton reaction:

$$Fe^{2+} + H_2O_2 \rightarrow Fe^{3+} + OH^- + OH. \quad (1)$$

In the investigations [1-3] in the application of the pulsed streamer discharges in water for organic compound decomposition the relatively short pulses of several μs and of high peak current giving a pulse energy of several hundreds of mJ were used. This causes some problems with the power supplies, electromagnetic compatibility, intense electrode corrosion etc. In this paper, results of phenol decomposition in water by pulsed positive streamer discharge, using the pulses of similar energy, i.e in the hundreds mJ range, but longer in time (200 μs) and lower in the peak current (1A) are presented. The longer and weaker current pulses positively affected the processing performance without losses in the energy efficiency of the phenol removal if compared to the shorter and stronger current pulses used in [1-3].

Electronic address: mdors@imp.gda.pl

2. EXPERIMENTAL SET-UP

The experimental set-up is presented in Figure 1. The pulsed positive streamer discharge was generated between a stressed stainless steel needle electrode and a grounded brass cylinder electrode. The needle-cylinder spacing was 55 mm. The electrodes were placed in a glass cubical reactor (12,0 cm × 3,6 cm × 14,4 cm), which was filled with phenol-polluted water. Initial concentration of phenol was 0.62 mM. For studying an influence of Fenton reaction on phenol decomposition, Fe_2SO_4 was added to the water contaminated with phenol. Initial concentration of Fe_2SO_4 was 0.08 mM.

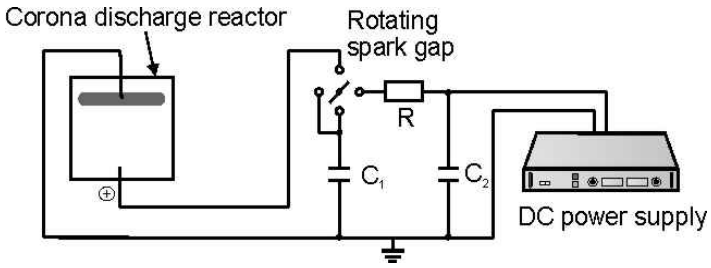

FIGURE 1. Experimental set-up.

The positive polarity high voltage pulses of 30 kV were applied to the needle electrode from a discharge capacitor C_1 (2 nF), which was charged from a DC power supply through a resistor R_p (10 kΩ) and a capacitor C_2 (22 nF). The repetition rate of the streamer pulses was 50 Hz and was determined by a rotation velocity of a rotary spark.

The concentration of phenol in the water was measured by a gas chromatograph before and after the streamer discharge processing. The water was analyzed also for the presence of hydrogen peroxide (pertitanic acid formation method). The acidity (pH) of the water was measured as well.

3. RESULTS AND DISCUSSION

When the phenol-polluted water without iron ions was processed by the pulsed streamer discharge the concentration of phenol in the water decreased with processing time from 0.62 mM to 0.36 mM, i.e. by 42% (Figure 2a). It means that phenol was oxidized by OH radicals produced only via electron reactions with water molecules [4]. Since the amount of oxidized phenol was such small we were not able to detect primary phenol oxidation products which are dihydroxyphenols (detection limit 1 $\mu g/cm^3$).

In the presence of iron ions phenol concentration decreased to 0.14 mM, i.e. by 78%, what resulted from enhanced OH radicals production via Fenton reaction. In this case, we detected dihydroxyphenols, the concentration of which was, however, much lower than expected. It is known that dihydroxyphenols are formed in oxidation reactions of phenol caused by OH radicals. On the other hand, the same species (OH radicals) react with dihydroxyphenols, converting them into organic aliphatic compounds, in particular into acids, such as muconic acid, oxalic acid etc. [1, 2].

Unfortunately, in our experiment we were not able to detect organic acids in water. However, if in our experiment organic acids were really formed, then we would have to observe an increase in acidity of the water. Indeed, the measurements of the water pH showed an increase in its acidity. The pH of the phenol-polluted water without and with iron ions decreased from 6.2 to 4.9 and 4.1, respectively. These results correspond to the amount of decomposed phenol. In the water with iron ions more phenol molecules were decomposed to organic acids and consequently pH was lower than in the water without iron ions.

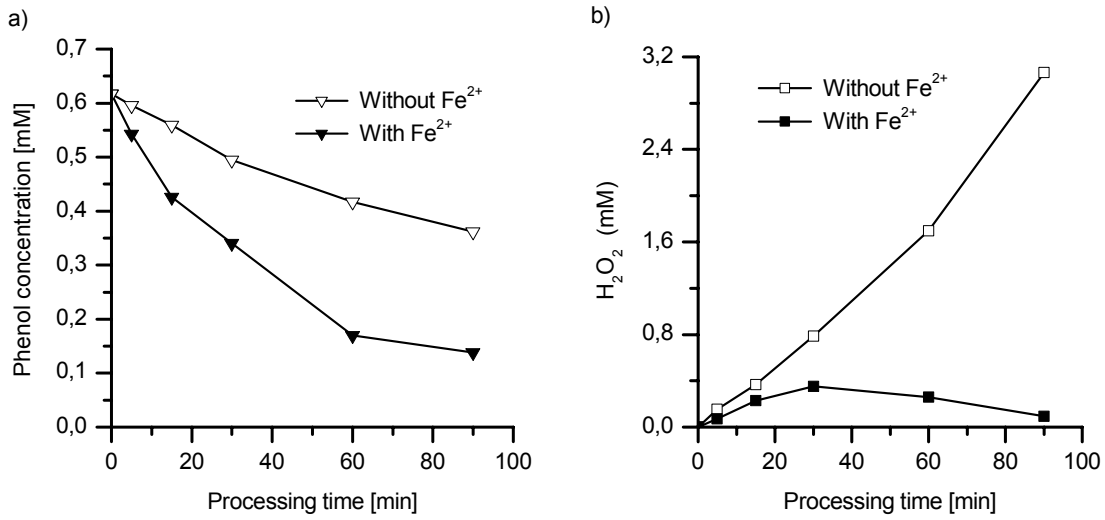

FIGURE 2. Concentration of phenol (a) and hydrogen peroxide (b) in water without and with iron ions after the pulsed positive streamer discharge processing. Initial phenol concentration 0.6 mM.

In the Fenton reaction most of H_2O_2 molecules formed during the discharge were converted into OH radicals which reacted with phenol. It is seen in Figure 2b that concentration of H_2O_2 in water containing iron ions after the streamer discharge processing is much lower than in the water without iron ions. In the water containing only phenol there was very small consumption of H_2O_2 in chemical reactions. As a result, H_2O_2 concentration increased linearly with a rate of 0.55 mg/min. When iron ions were present in the water, then concentration of H_2O_2 first increased up to 0.35 mM and then decreased with processing time below 0.1 mM. The explanation of the initial increase (before 30 min) and the following decrease (after 30 min) in H_2O_2 concentration is in the Fenton reaction. It is known that Fenton reaction rate is sensitive to the pH. The optimum pH is in the range 3-6 with maximum reaction rate at 4.2 [5]. Since dihydroxyphenols phenol were decomposed to organic acids, the pH of phenol-polluted water decreased with streamer discharge processing time. As was measured during the experiment in the presence of iron ions pH of the water decreased in 15 min. from initial value of 6.2 to 4.6 and after 30 min. slowly decreased to 4.1, which is optimum value for Fenton reaction rate. Thus, with processing time more organic acids were produced from phenol, what caused that the pH became lower and Fenton reaction rate increased consuming more H_2O_2 and giving more OH radicals, which oxidized next phenol molecules to organic acids. Very similar shape of pH curve, with rapid decrease at the beginning of the process, to the short period of stable value followed with the slow decrease, was predicted by the numerical model developed by Grymonpré et al. [2].

In order to compare the efficiency of all the experiments, a G_{50} yield value has been calculated, expressing the number of 50% converted phenol molecules divided by the energy input required [6]. In spite of using by us the longest streamer discharge pulse (200 μs) the energy of which was the lowest (337 mJ) comparing to others, G_{50} obtained in our experiment (4.6×10^{-9} mol/J) is more or less in the same range as that obtained by other researchers studying phenol degradation by pulse streamer discharge [1, 2, 7]. Using different length and energy of pulses and different additives, i.e. iron ions or gaseous oxygen, cause similar phenol degradation efficiency.

4. CONCLUSIONS

The results of phenol degradation in water with iron ions by pulsed positive streamer discharge showed that:

- additional production of OH radicals through Fenton reaction enhanced significantly phenol degradation rate from 42% to 78%;
- since the only role of Fenton reaction is to increase the production of O radicals, phenol degradation products are the same with and without iron ions in the water, i.e. dihydrohyphenols as primary phenol oxidation products, and organic acids as the following products;
- enhanced phenol degradation to organic acids results in lower pH, which reaches value optimal for Fenton reaction rate, i.e. 4.1;
- phenol degradation process, i.e. degradation rate, products and energy efficiency, does not depend on the streamer discharge pulse duration. Pulses of different duration but comparable energy cause similar effects in the phenol degradation process.

ACKNOWLEDGMENTS

This work was supported by the Ministry of Science and Information Society Technologies under programme PB 1280/T10/2004/27 and by the Institute of Fluid Flow Machinery, Polish Academy of Sciences under programme IMP PAN O3Z3T2.

REFERENCES

[1] Sunka, P., Babicky, V., Clupek, M., Lukes, P., Simek, M., Schmidt, J., Cernak, M. (1999). Generation of chemically active species by electrical discharges in water. *Plasma Sources Sci. Technol.*, 8, 258–265.

[2] Grymonpré. D.R., Sharma. A.K., Finney. W.C., Locke. B.R. (2001). The role of Fenton's reaction in aqueous phase pulsed streamer corona reactors. *Chemical Engineering Journal,* 82, 189–207.

[3] Koprivanac, N., Kušić, H., Vujević, D., Peternel, I., Locke, B.R. (2005). Influence of iron on degradation of organic dyes in corona. *Journal of Hazardous Materials*, B117, 113–119.

[4] Dors, M., Mizeraczyk, J., Mok, Y.S. (2006). Phenol oxidation in aqueous solution by gas phase corona discharge. *J. Adv. Oxid. Technol.*, 9, 2 /in print/.

[5] Reference Library: Peroxide Applications – Industrial Wastewater, US Peroxide, http://www.h2o2.com/applications/industrialwastewater/fentonsreagent.html.

[6] Hoeben. W.F.L.M., van Veldhuizen, E.M., Rutgers, W.R., Kroesen, G.M.W. (1999). Gas phase corona discharges for oxidation of phenol in an aqueous solution. *J. Phys. D: Apl. Phys.*, 32, L133–L137.

[7] Sun, B., Sato, M., Clements, J.S. (1999). Use of a pulsed high-voltage discharge for removal of organic compounds in aqueous solution. *J. Phys. D: Appl. Phys.*, 32, 1908-1915.

RESEARCH ON WASTE WATER PURIFICATION BY OZONE AND PHOTOCATALYST TREATMENT

Yoshiaki Suda, Hiroharu Kawasaki, Tamiko Ohshima and Yoshito Yagyu

Department of Electrical and Electronics Engineering, Sasebo National College of Technology, 1-1 Okishin, Sasebo, Nagasaki 857-1193, JAPAN

ABSTRACT. Ozone treatment and photocatalyst treatment have been performed to purify the waste water at several places of the sedimentation tanks in Sasebo city. Ozone treatment is not so effective for chemical oxygen demand (COD). Photocatalyst treatment is not so effective for both bacteria and COD. On the other hand, ozone treatment together with photocatalyst is effective for decrease not only bacteria count, but also COD. This may be due to the effect of ozone gas density and/or the hydroxyl radicals which have stronger oxidizing and bleaching effect than ozone.

1. INTRODUCTION

The water quality of river, lakes and marshes deteriorated by industrial waste water, domestic waste water and use of superfluous agricultural chemical [1]-[8]. Until now, the chlorine has been mainly used in the water purification. However, the chlorine reacts with organic substance in the water, and generates the trihalomethane, which is the carcinogen. The generation of the musty odor with the eutrophication of water source cannot be removed. On the other hand, ozone is one of the strongest oxidizing and bleaching agents that does not produce residues that could be harmful to the environment. For this chemical reaction, ozone has been used for a variety of applications such as bleaching, deodorization, and disinfection of water and atmospheric air. Recently, in the field of water purification, the use of ozonization has been regarded as important in eliminating the precursor of trihalogenated urethanes which are generated in chlorination process and are carcinogenic organic chlorides. In addition, photocatalyst (TiO_2) treatment was also used for the water purification. Photocatalyst treatment leads to the hydroxyl radicals (OH radicals) which have stronger oxidizing and bleaching effect than ozone. These physical effects may purify the waste water.

In this study, ozone and photocatalyst treatments for the waste water purification were applied at several places of the sedimentation tanks.

2. EXPERIMENTAL

Flowchart of the water purification in the waste water treatment plant in Sasebo city was shown elsewhere [9]. Generally, ozone treatment is carried out only in the final sedimentation tank exit, because the biochemical method with microorganisms, called

activated sludge is most widely adopted. In this experiment, the ozone treatment was applied at the primary sedimentation tank entrance (PSTEN), the primary sedimentation tank exit (PSTEX) and the final sedimentation tank exit (FSTEX).

A schematic diagram of the ozone generation system is shown in Fig. 1. Oxygen (O_2:99.5 %) gas was used for the source gas. The source gas was controlled at 0.5-1.5 LM by the mass flow controller (STEC: SEC-400), and fed into the discharge area. Ozone was generated by the silent discharge between the electrode and the dielectric surface. The sinusoidal ac voltage of 8 kV (10 kHz) was applied between the electrodes to occur the silent discharge in the gap. The generated ozone density was measured by gas phase ozone monitor (Ebara: EG-4000) used by UV absorption method. The ozone density for water purification was 10 g/m^3, and they were fed into the treatment reactor at 0.5-1.5 LM. The inside wall of the reactor was coated by titanium oxide (TiO_2) photocatalyst. The volume of waste water for treatment was 0.5 – 1.5 L, and the waste water was kept at ~300 K. An UV light of about 360 nm in wavelength was irradiated to the reactor wall to generate OH radicals. Treatment time was varied from 0 to 60 min.

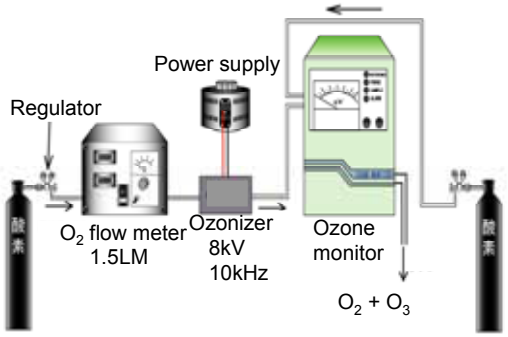

FIGURE 1. A schematic diagram of the ozone treatment system.

3. RESULTS AND DISCUSSIONS

3.1. Ozone treatment

Figure 2 shows temporal evolutions of the number of colon bacillus and the bacteria count at all places of the sedimentation tanks. Those values decreased drastically by ozone treatment, and the bacteria count decreased to almost zero after 10 min ozone treatment. These experimental results suggest that ozone treatment is effective for waste water purification in terms of turbidity, color unit, the number of colon bacillus and the bacteria count.

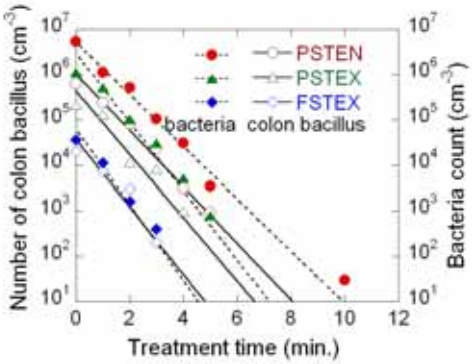

FIGURE 2. Temporal evolutions of the number of colon bacillus and the bacteria count.

Figure 3 shows the temporal evolutions of the turbidity with ozone treatment. The turbidity before ozone treatment was about 73% at PSTEN, 38% at PSTEX and 7% at FSTEX. These values are much higher than those of the service water. The turbidity decreased to the half value after 30 min ozone treatment, that is, about 40% at PSTEN, 21% at PSTEX, and 4% at FSTEX. After 30 min ozone treatment the turbidity was saturated. This tendency is almost same for the color unit for waste water, not

shown here.

Figure 4 shows the temporal evolutions of the chemical oxygen demand (COD) of the waste water before and after ozone treatment. The COD decreased slightly from 170 mg/1 to 130 mg/1 after 60 min ozone treatment at PSTEN. The COD also decreased from 120 mg/1 to 105 mg/1, and from 35 mg/1 to 20 mg/1 at PSTEX and FSTEX, respectively. These results suggest that ozone treatment is not so effective for decreasing COD.

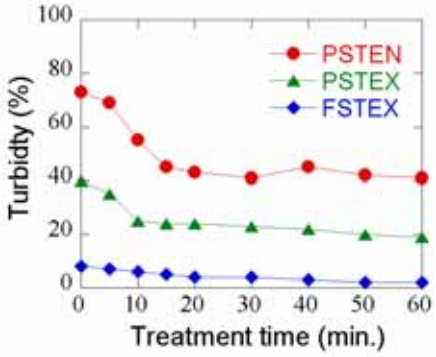

FIGURE 3. Temporal evolutions of the turbidity with ozone treatment.

3.2 Ozone treatment with photocatalyst

Photocatalyst treatment was used for the waste water purification. It was not very effective for decreasing COD and the bacteria count (not shown here). Both the ozone treatment and photocatalyst treatment cannot decrease the COD in the waste water. To decrease the COD, ozone treatment together with photocatalyst is applied to the same waste water simultaneously. In this measurement, the UV light of about 360 nm in wavelength was irradiated to the reactor wall with ozone gas.

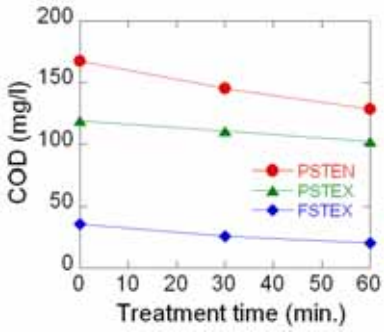

FIGURE 4. Temporal evolutions of the COD of the waste water.

Figure 5 shows the temporal evolutions of the number of colon bacillus and the bacteria count at PSTEN. The number of colon bacillus and the bacteria count decreased drastically by ozone treatment with photocatalyst, and the number of colon bacillus and the bacteria count decreased to zero after about 8 min ozone treatment together with photocatalyst. As the results, the decreasing rate is almost same of only ozone treatment.

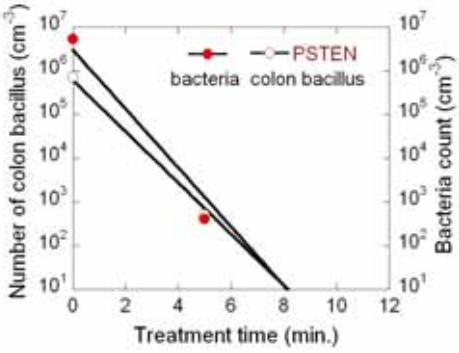

FIGURE 5. Temporal evolutions of the number of colon bacillus and the bacteria count.

Figure 6 shows the relation between the COD of the waste water and treatment time. The COD decreased from 170 mg/1 to 40 mg/1 after ozone treatment together with photocatalyst at PSTEN. This result suggests that only ozone treatment is not so effective for decreasing COD, but ozone treatment together with photocatalyst is effective for decreasing COD. The reason that ozone treatment with photocatalyst is effective for decreasing COD is not clear yet, but it may be due to hydroxyl radicals (OH radicals). In general, it is well known that OH radical generates at the surface of the photocatalyst with UV light irradiation. The OH radicals have stronger oxidizing and bleaching effect than

ozone. These results suggest that a kind of advanced oxidation processes (AOPs) can be applied effectively for the waste water treatment such as the ozone treatment together with photocatalyst.

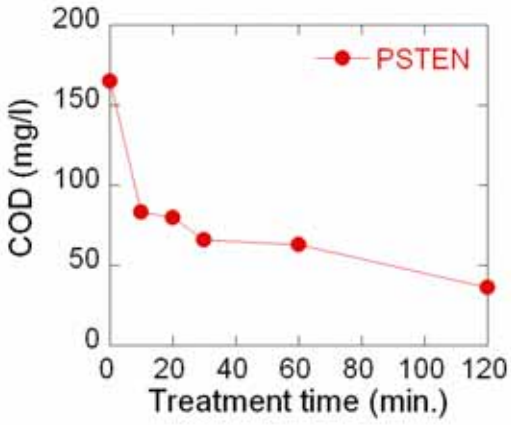

FIGURE 6. Temporal evolutions of the COD of the waste water.

4. CONCLUSION

The ozone treatment for the waste water purification was applied at all places of the sedimentation tanks. Experimental results suggest that ozone treatment is effective for decreasing the number of colon bacillus and the bacteria count, however, ozone treatment is not so effective for COD. Ozone treatment together with photocatalyst is effective for not only bacteria count, but also COD. This may be due to the effect of the hydroxyl radicals (OH radicals) that are one of the strongest oxidizing and bleaching agents. These results suggest that advanced oxidation processes (AOPs) can be applied effectively in the ozone treatment together with photocatalyst.

REFERENCES

[1] Gosho M., Ihara S., Ishimine M., Satoh S., Yamabe C., J. Inst. Elec. Eng. of Japan, ED-98-102, 1998, pp.49-52.

[2] Fukagawa M., Harada T., Takeuchi M., Murakami S., Proc. of 5th Japan/Korea Symposium on Water Environmental Engineering, 1996, pp.99-102.

[3] Murakami S., Takeuclu M., Fukagawa M., Proc. of ENSEARCH-JAWE Post-Conference Seminar on Industrial Wastewater Management, 1996, pp.37-42.

[4] Zimin Yu., Tnikhanova N., Rafikava G., Nasyrov I. , Bazhenov Y., Morozova S., Gerchikov A., J. Water Chem. Technol. 19, 1997, pp.31-35.

[5] Ihara S., Miyachi T., Hayashi N., Satoh S., Yamabe C., Jpn. J. Appl. Phys. , 38, 2000, p.4601-4605.

[6] Fukagawa M., Harada T., Takeuchi M., Murakami S., Proc. of 5th Japan/Korea Symposium on Water Environmental Engineering, 1996, p.99-104.

[7] Zimin Yu., Trulhanava N., Rafikava G., Nasyrov I., Bazhenov Y., Morozova S., Gerchikov A., J. Water Chem. Technol. , 1997, 19, p.31-37.

[8] Ikeda Y., Kawasaki H., Fujita I., Suda Y., Proc. of the 3rd International Symposium of Non-Thermal Plasma Technology for Pollution Control, 3, 2000, pp. 5-9.

[9] Suda Y., Kawasaki H., Ohshima T., J. Adv. Oxid. Technol. 2006, 9, pp. 1-4.

INACTIVATION OF *ESCHERICHIA COLI* BY PULSED CORONA DISCHARGE IN WATER

T. Vykouk[1], M. Clupek[2] and P. Lukes[2,a]

[1] *Department of Water Technology and Environmental Engineering, Institute of Chemical Technology, Prague Technicka 3, Prague 6, CZ-168 28, CZECH REPUBLIC*
[2] *Institute of Plasma Physics, Academy of Sciences of the Czech Republic Za Slovankou 3, Prague 8, CZ-182 00, CZECH REPUBLIC*

ABSTRACT. The decontamination effect of underwater pulsed corona discharge on bacteria *Escherichia coli* has been investigated. The reactor of needle-plate electrode geometry was used. The *E. coli* concentration decreased exponentially with increasing discharge treatment time and supplied energy input. The contribution of UV radiation and hydrogen peroxide in the overall bacterial inactivation efficiency of the discharge has been determined. UV light emitted from the discharge plasma channels was found to have significant effect on the inactivation of *E. coli* and its contribution was estimated to be about 30%. Effect of hydrogen peroxide was small, however, under influence of high electric field its lethal activity was greatly enhanced.

1. INTRODUCTION

Recently, the pulsed high voltage discharges generated directly in water have been demonstrated to initiate a variety of chemical and physical effects. These include ultraviolet radiation, overpressure shock waves, high electric field and, in particular, formation of chemically active species such as OH, H and O radicals and hydrogen peroxide H_2O_2 molecules. These physical and chemical processes in turn have been shown to be effective at degrading a variety of organic compounds and also in the inactivation and destruction of microorganisms in water. The mechanism of degradation of organic compounds was found to be attributed mainly to the oxidation by hydroxyl radicals produced directly by the discharge or indirectly from plasma chemically produced hydrogen peroxide (i.e. due to decomposition of H_2O_2 in the presence of iron ions) [1]. There is also evidence about contribution of reductive species HO_2 and H radicals in the removal of chemical compounds by the discharge in water [2]. On the other hand, less is known about mechanism of sterilization by means of electrical discharge in water. In general, it is expected that, in addition to the chemical effects, the physical processes such as high electric field and ultraviolet radiation from the discharge significantly contribute in the inactivation of microorganisms [3,4]. There are also possible synergistic effects of combined action of chemical and physical processes on the destructive efficiency of the discharge in water.

In this work the effects of pulsed corona discharge in water on inactivation of bacteria *Escherichia coli* are investigated. The role and contribution of ultraviolet radiation and hydrogen peroxide in the overall inactivation efficiency of the discharge is discussed.

[a] Electronic address: lukes@ipp.cas.cz

2. EXPERIMENTAL

The reactor used for generating of the pulsed corona discharge in water was described in detail in [5]. Briefly, electrode system of the needle-plate geometry immersed in a cylindrical glass vessel was used with the needle-plate distance of 28 mm. Needle electrode was made from conically shaped tungsten rod, which was almost totally insulated from surrounding water by Teflon insulator. A pulsed high voltage applied to the needle was provided by a pulse power supply. It consists of a variable voltage 0-30 kV DC source, a low inductance storage capacitor (C=7 nF) equipped with a high-frequency filter to reduce electromagnetic interference and a rotating double spark gap giving the maximum pulse repetition frequency of 100 Hz. In this work all experiments were conducted with fixed applied voltage of 23.3 kV of the positive polarity and pulse repetition frequency of 50 Hz. The electrical power (P=95 W) applied to the reactor was calculated from the applied voltage U, charging capacity C and pulse repetition frequency f as $P=f E_p$, where pulse energy E_p was evaluated as storage energy of the charged capacitor $E_p=½CU^2$ (E_p=1.9 J).

The discharge chamber was filled with a suspension of bacteria *Escherichia coli* that was circulated through the reactor using a peristaltic pump with the flow rate of 1 L/min. Total volume of bacterial suspension was 1600 mL with electrolytic conductivity of 200 μS/cm. Suspensions were prepared by preculturing the *E. coli* cells in the growth medium and then dispersed in sterile water. Number of cells in the suspension was assayed by counting colony forming units (CFUs) cultivated on agar plates. The initial amount of *E. coli* was about 10^5 CFU/mL in all experiments performed in this study. The concentration of H_2O_2 was determined colorimetrically using the reaction of H_2O_2 with titanyl ions. Absorbance of the yellow peroxotitanium (IV) complex at wavelength λ = 410 nm was measured.

3. RESULTS AND DISCUSSION

3.1. Inactivation of *E. coli* by the discharge

Fig. 1A shows the effect of pulsed corona discharge on viability of bacteria *E. coli* suspended in water. Plotted is the survival ratio between number of active colonies after and before applying of the discharge into the water versus discharge treatment time and supplied energy input, respectively. The *E. coli* concentration decreased exponentially with increasing time and for given electrical parameters the survival ratio declines four orders of magnitude in 15 min of corona discharge treatment (corresponding energy input of 54 J/mL).

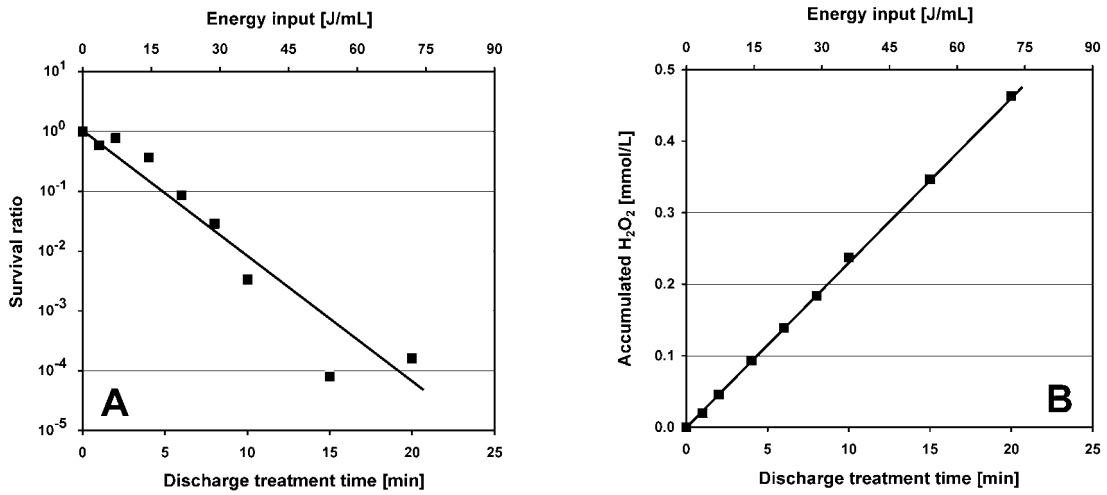

FIGURE 1. Kinetics of inactivation of *E. coli* (A) and production of H_2O_2 (B) by pulsed corona discharge in water as a function of applied energy input (U=23.3 kV, P=95 W, V=1600 mL, σ=200 μS/cm).

3.2. Effect of hydrogen peroxide

As it was mentioned decontamination effect of pulsed corona discharge on bacteria *E. coli* can be caused by combination of various physical and chemical effects. From chemical effects a role of H_2O_2 was further investigated. Fig. 1B shows the kinetics of accumulation of hydrogen peroxide in water produced by the discharge under the same experimental conditions as that used during inactivation of *E. coli* (Fig. 1A). It is apparent that amount of H_2O_2 in the solution increased linearly with the discharge treatment time (production rate $k_{H2O2} = 3.9\times10^{-7}$ mol/s). The concentration of H_2O_2 accumulated in the solution reached value about 0.35 mmol/L after 15 min of operation of the corona discharge reactor.

To assess lethal effect of such amount of H_2O_2 on 4-log reduction of *E. coli* by the discharge (Fig. 1A) hydrogen peroxide solutions of various concentration were prepared from commercial H_2O_2 reagent, mixed with bacterial suspension and the survival ratio as a function of H_2O_2 dosage was determined (i.e. without using discharge). Fig. 2A shows that survival ratio decreased exponentially with increasing H_2O_2 concentration. However, the amount of H_2O_2 required for reduction in concentration of *E. coli* by 4 orders of magnitude was significantly higher than the amount of H_2O_2 produced by the discharge (about 25 times). This would indicate that hydrogen peroxide does not play a significant role in the inactivation of *E. coli* by the discharge.

It should be, however, noted that there is also possibility of enhanced lethal activity of H_2O_2 under influence of high electric field that is produced in the corona discharge reactor. Although electric field generated by the discharge in water is highly inhomogeneous and, therefore, only qualitative estimation can be made, such synergy is apparent from Fig. 2B, which shows the results of inactivation of *E. coli* performed by means of homogenous pulsed electric field (PEF) generated in water using plane-to-plane electrode configuration [6]. As it was expected, PEF caused decrease in survival ratio of *E. coli,* which is in agreement with the lethal effect of PEF described in a number of papers [e.g. 7,8]. However, PEF effect was further improved by addition of H_2O_2 to the bacterial suspension in the amount of 1 mmol/L, for which only negligible effect of H_2O_2 on viability of *E. coli* was shown in Fig. 2A. This can be explained more likely by electroporation effect of electric field that can enhance penetration of H_2O_2 through the cell membrane and cause damage inside of the cell [9,10].

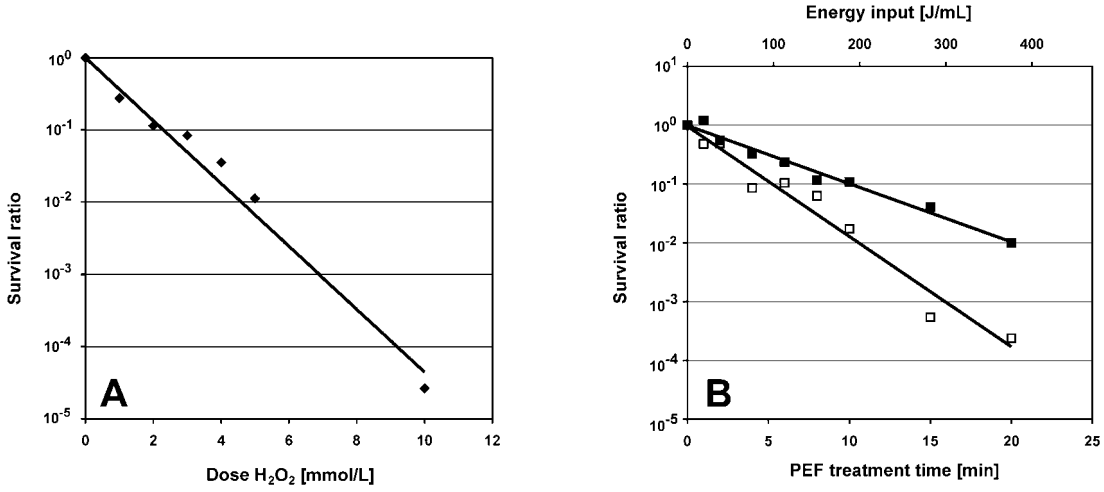

FIGURE 2. (A) Inactivation of *E. coli* as function of H_2O_2 dosage. (B) Inactivation of *E. coli* by pulsed electric field (■) and with addition of 1 mmol/L H_2O_2 (□) as a function of applied energy input (*E*=39 kV/cm, FWHM=200 ns, V=1000 mL, σ=5.9 mS/cm).

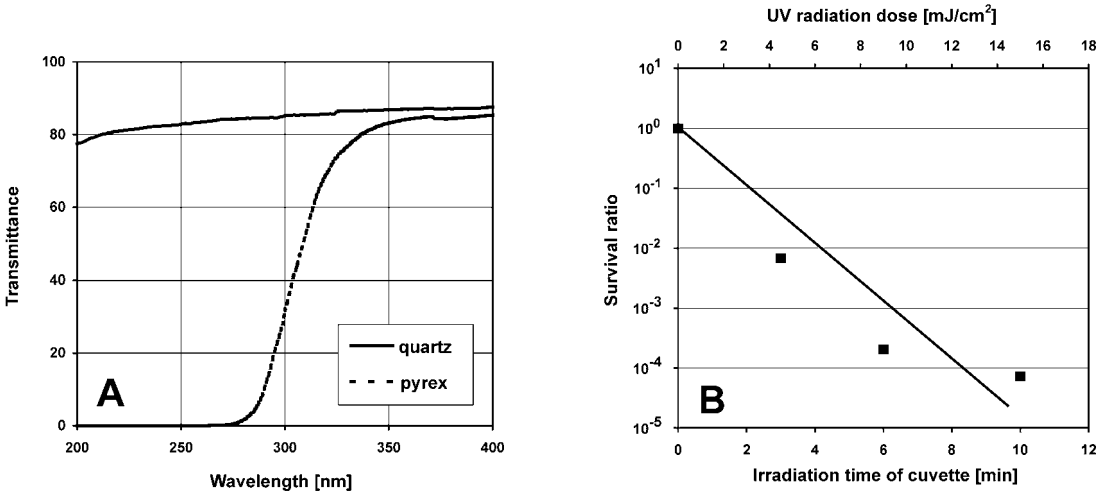

FIGURE 3. (A) Comparison of transmittance of pyrex and quartz cuvettes. (B) Inactivation of *E. coli* in quartz cuvette as function of exposure time to UV irradiation from the pulsed corona discharge in water (U=23.3 kV, P=95 W, σ=200 μS/cm).

3.3. Role of UV radiation from the discharge

The emission of UV light from the pulsed corona discharge in water has been demonstrated experimentally using chemical actinometry in previous work [11]. In order to investigate the role of UV radiation in the inactivation of *E. coli* by the discharge (Fig. 1A) two types of cuvettes of different transmittance made from pyrex glass and quartz were used (Fig. 3A). Cuvettes were filled with bacterial suspension, placed into the gap between discharge needle and grounded plate electrodes and irradiated by the light emitted from the discharge. The experimental conditions were the same as in previous experiments. When pyrex cuvette was used no change in viability of *E. coli* was observed after 20 min of irradiation by the discharge. On the other hand when the same experiment was performed in a quartz cuvette the number of cells decreased with increasing irradiation time (Fig. 3B).

Thus, since only difference in both experiments was the fraction of light emitted from the discharge (200-280 nm) this result can be attributed merely to the germicidal effects of UV radiation on *E. coli* [12]. Taking into account average residence time of bacterial suspension in the reactor and the volume of active discharge zone it can be further estimated that irradiation time of *E. coli* in cuvette was about 6.7 times higher than irradiation time of total volume of bacterial suspension treated in the reactor. Thus, from this about 30% contribution of UV radiation in the overall inactivation of *E. coli* by the discharge can be estimated.

4. CONCLUSIONS

The effects of pulsed corona discharge on microorganisms in water were investigated using bacteria *Escherichia coli*. The *E. coli* concentration decreased exponentially with increasing discharge treatment time and the survival ratio declines four orders of magnitude after providing the energy input of 54 J/mL. The contribution of ultraviolet radiation and hydrogen peroxide in overall inactivation efficiency of the discharge has been determined. Hydrogen peroxide itself did not play a significant role. However, under influence of high electric field its lethal activity was significantly enhanced. UV radiation from the discharge had significant effect and its contribution in the inactivation of *E. coli* by the discharge was estimated to be about 30%.

ACKNOWLEDGMENTS

Work was supported by the Academy of Sciences of the Czech Republic under contract No. K2043105.

REFERENCES

[1] Locke, B.R., Sato, M., Sunka, P., Hoffmann, M.R., Chang, J.-S. (2006). Electrohydraulic discharge and nonthermal plasma for water treatment. *Ind. Eng. Chem. Res*., 45, 882-905.

[2] Sahni, M., Locke, B.R. (2006). Quantification of reductive species produced by high voltage electrical discharges in water. *Plasma Process. Polym.*, 3, 342-354.

[3] Sato, M., Ohgiyama, T., Clements, J.S. (1996). Formation of chemical species and their effects on microorganisms using a pulsed high-voltage discharge in water. *IEEE Trans. Ind. Appl.,* 32, 106-112.

[4] Abou-Ghazala, A., Katsuki, S., Schoenbach, K.H., Dobbs, F.C., Moreira, K.R. (2002). Bacterial decontamination of water by means of pulsed-corona discharges. *IEEE Trans. Plasma Sci.,* 30, 1449-1453.

[5] Sunka, P., Babicky, V., Clupek, M., Lukes, P., Simek, M., Schmidt, J., Cernak, M. (1999). Generation of chemically active species by electrical discharges in water. *Plasma Sources Sci. Technol.*, 8, 258–265.

[6] Project K2043105 Institute of Plasma Physics AS CR.

[7] Sale, A.J.H., Hamilton, W.A. (1967). Effects of high electric fields on microorganisms. I. Killing of bacteria and yeasts. *Biochim. Biophys. Acta*, 148, 781-788.

[8] Schoenbach, K.H., Peterkin, F.E., Alden, R.W., Beebe S.J. (1997). The effect of pulsed electric fields on biological cells: Experiments and applications. *IEEE Trans. Plasma Sci.*, 25, 284-292.

[9] Juven, B.J., Pierson, M.D. (1996). Antibacterial effects of hydrogen peroxide and methods for its detection and quantification. *J. Food. Protect*., 59, 1233-1241.

[10] Brul, S., Coote, P. (1999). Preservative agents in foods: Mode of action and microbial resistance mechanisms – A Review. *Int. J. Food Microbiol.,* 50, 1–17.

[11] Lukes, P. (2001). *Water treatment by pulsed streamer corona discharge in water*. Institute of Plasma Physics AS CR: Prague, ISBN: 80-902724-6-0.

[12] U.S. Environmental Protection Agency (2003). *Ultraviolet disinfection guidance manual*, Washington, DC, USA.

PLASMA WATER TREATMENT BY MICRO DISCHARGE CHANNELS AT ATMOSPHERIC PRESSURE

K. Yasuoka, A. Yamatake, H. Katayama and S. Ishii

Department of Electrical and Electronic Engineering,
Tokyo Institute of Technology
2-12-1, Ookayama, Meguro-ku, Tokyo, 152-8552, JAPAN

ABSTRACT

Decomposition of a persistent material in water has been examined by using DC discharge cannels that are energized inside of small bubbles. The bubbles are successively formed in a hole of dielectric spacer that separates a high voltage electrode and treat water. The acetic acid of 10 ppm initial concentration, as a persistent material was decomposed and the decomposition rate showed no dependency on the feeding oxygen rate. In addition, the electric discharge was generated without feeding of oxygen because the bubbles can be formed by the electrolysis of treat water.

1. INTRODUCTION

OH radicals are expected to be used for decomposition of persistent chemical substances such as dioxin. The lifetime is quite short so that OH radicals have to be utilized where they are produced. The discharges generated in the bubbles [1,2] and on the surface of the treat water [3,4] have been reported. Generally, AC or pulsed voltage source was used to generate a high electric field inside of the bubbles or to generate energetic electrons for efficient dissociation of oxygen molecules. DC discharge can also decompose the persistent materials by combining a DC micro-hollow cathode discharge and fast flow of oxygen in treat water [5]. In that system, the generated oxygen atoms seemed to generate OH radicals in water by the reaction : $O + H_2O \rightarrow 2OH$. However, that DC system has drawbacks such that a large mount of oxygen gas is inevitable to produce a fast flow for utilizing short-lived oxygen atoms, the ballast resistors are need for parallel operation and the life of electrode is short due to the high thermal load.

In this report, we proposed a new DC electrode system that consists of high voltage metal electrode, dielectric spacer with a small hole and water electrode, and evaluated its discharge characteristics and the decomposition rate of acetic acid.

2. EXPERIMENTAL SETUP

The electrode system is similar to that of micro hollow cathode electrode, but the hole-configuration is different. The hole- diameter of the grounded electrode is around ten times larger than that of the dielectric spacer, while the high voltage electrode has no hole and installed by separating 0 or 0.1 mm from the dielectric spacer as shown in Figure 1(a), (b).

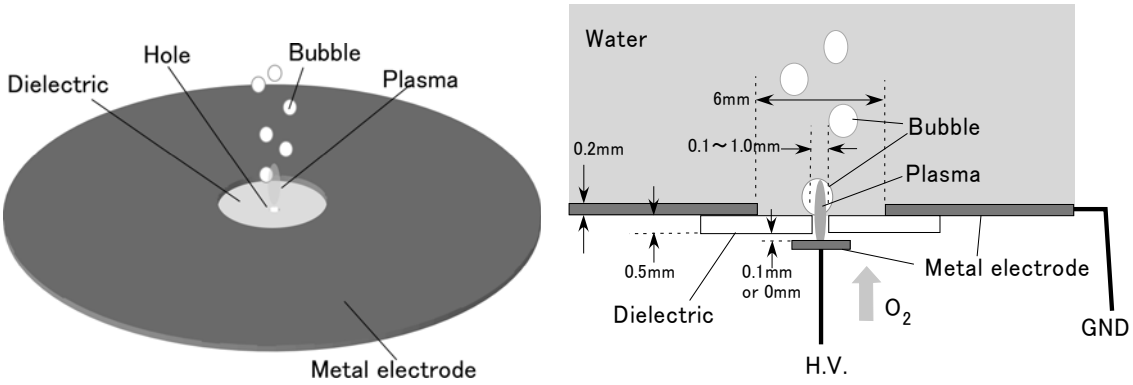

(a) (b)

FIGURE 1. Perspective (a) and cross sectional (b) illustrations of the electrode system.

The metal electrodes are made of 0.2 mm SUS plates. The thickness of alumina spacer is 0.5 mm and the hole- diameter of that is varied from 0.1 to 1.0 mm. Oxygen gas is fed through the hole of the spacer at flow rate of up to 300 sccm. Small bubbles are successively generated within and above the hole as illustrated in Fig. 1. When the high voltage electrode directly touches with the spacer, the gap length is 0 mm, so the oxygen can not be fed. Even in this case, babbles are generated through the electrolysis process by applying the voltage between the two metal electrodes. Acetic acid solution of 10 ppm initial concentration is used and its decomposition rate is evaluated by TOC (Total Organic Carbon) reduction using TOC analyzer (Sievers 810). The conductivity of 10 ppm solution is about 25 μS/cm.

3. RESULT AND DISCUSSION

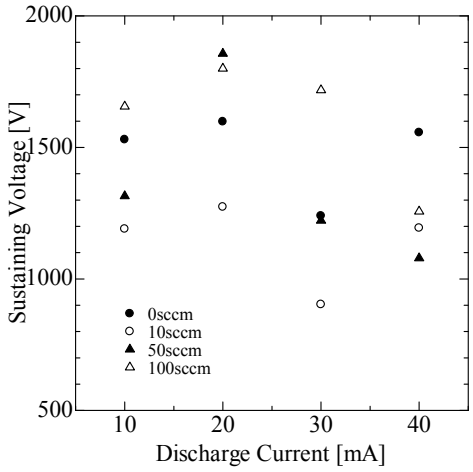

FIGURE 2. Sustaining voltage vs. current characteristics

By applying positive voltage to the high voltage electrode, micro channel discharges was generated inside of the bubbles and the light emission with the weak violet was observed. The averaged sustaining voltages of discharge versus currents are plotted as shown in Figure 2. The discharge current flows from the high voltage electrode to the grounded electrode through the discharge channel and the treat water. The voltages are measured between the metal electrodes, so that the voltage includes the voltage drop by the treat water. The value of sustaining voltage is around 1~2 kV and is higher than that of micro hollow discharge generated between the metal electrode. The positive slope of *VI* characteristics is obtained below 20 mA and consequently two or three parallel operation is possible in this setup. The sustaining voltage increases with increasing the gas flow rate form 10 to 100 sccm but the voltage at 0 sccm is higher than that at 10 or 50 sccm. This is because the extra voltage is need for bubble formation by electrolysis. Figure 3 shows the UV emission spectra observed from the water surface and that shows OH related band spectrum of around 308 nm.

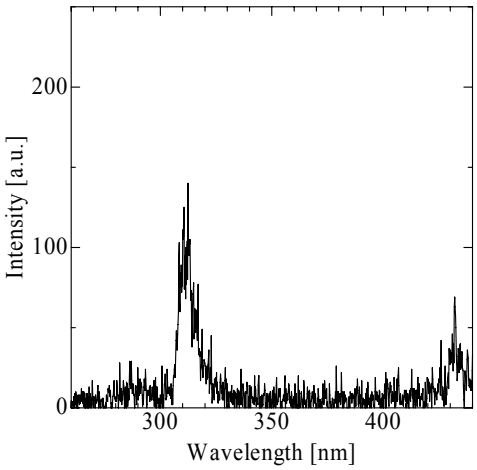

FIGURE 3. Emission spectra of discharge channels observed from water surface.

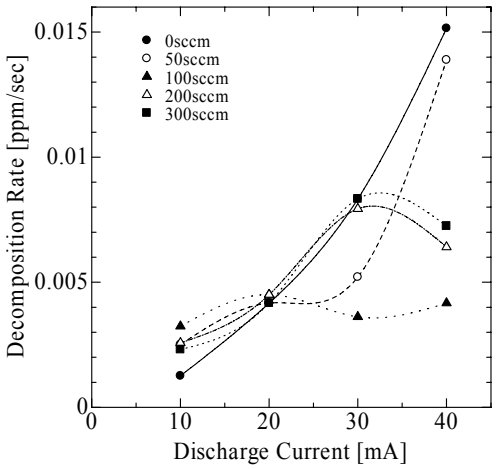

FIGURE 4. Decomposition rate of acetic acid vs. discharge current at different flow rates with 0.5mm hole- spacer.

Therefore, OH radicals seem to be generated by the reaction between DC discharge channels and treat water, such as $e+H_2O \rightarrow H+OH+e$, $e+O_2 \rightarrow O+O+e$, $O + H_2O \rightarrow 2OH$.

Figure 4 shows the current dependency of the decomposition using the spacer with 0.5 mm diameter hole. The decomposition rate is estimated by the following equation:

$$\frac{\Delta C}{\Delta t} = \frac{C_0 / 2}{t_{1/2}}, \qquad (1)$$

where C is the acetic acid concentration, t is the processing time and C_0 is the initial concentration. C_0 decreases by half within the time: $t_{1/2}$. The maximum decomposition rate was obtained at small rate of oxygen flow. This result is quite different from the characteristics obtained with micro hollow discharge system in that the fast gas flow was need to utilize atomic oxygen for decomposing persistent materials [5]. When the gas flow rate were 0 and 50 sccm in Figure 4, the decomposition rate increased with the current. While at 100, 200 and 300 sccm, the decomposition rate increased below certain current values, then saturated and decreased at higher discharge current. The saturation points on the discharge current depend on the gas flow rate. Such tendency was commonly observed with different diameters of spacer hole and was thought to be caused by the change of plasma- water reaction.

The energy efficiency of the acetic acid decomposition is also calculated using equation:

$$\eta = \frac{w(\Delta C / \Delta t) / m}{IV} \text{ [mol/J]}, \qquad (2)$$

where w is the weight of water, m is carbon mass in acetic acid (CH_3COOH), IV is the product of current and sustaining voltage. The results with the spacer having 0.5 mm hole are shown in Figure 5. The efficiency increased with current at flow rate of 0 or 50 sccm, but decreased or showed no dependency on current at higher flow rate over 100 sccm. The discharge- water contact area is proportional to the current at low flow rate, so the entire surface of the bubbles can be covered by discharge channels. At high flow rate, the bubble diameter increased with increasing the flow rate but the discharge channels became not to expand on the whole inner surface of the bubble even at the higher discharge current.

The advantage of this system is that one can operate without feeding the oxygen gas as shown in Figure 5. The optimum diameter of the spacer hole is not determined yet but the decomposition efficiency depends on the hole- diameter as shown in Figure 6. The efficiency

greatly changed with current and hole- diameters since the bubble shape was changed. The minimum diameter of the hole is limited by machining condition and the maximum diameter is determined to prevent the water leakage. From visible observation, the discharge was stable most with 0.1 mm hole within these conditions. The efficiency increased with current and saturated except for the case of 0.1 mm hole. In addition, no bubbles were formed in the high conductivity solution and it is because the condition of the electrolysis changed.

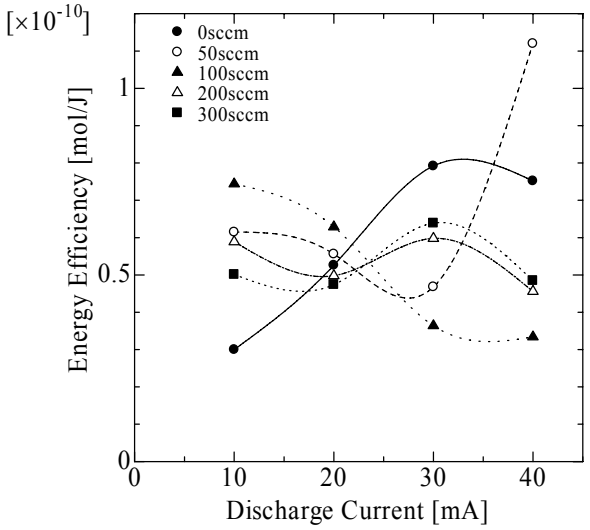

FIGURE 5. Energy efficiency for acetic acid decomposition as a function of discharge current with 0.5mm hole- spacer.

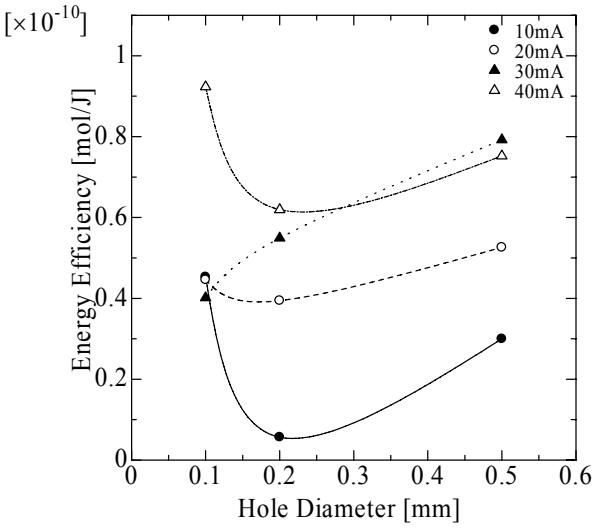

FIGURE 6. Energy efficiency for acetic acid decomposition as a function of hole diameter with no oxygen flow.

4. CONCLUSION

DC driven discharge channels are generated in water and utilized for the decomposition of persistent materials. The plasma channels are formed within the gas bubbles generated by external oxygen supply or electrolysis of treat water. The decomposition efficiency strongly depends on the reacting condition between the discharge channels and the bubble surface.

ACKNOWLEDGMENT

This work was supported by grant-in-aids for Scientific Research form the Ministry of Education, Culture, Sports, Science and Technology, Japan.

REFERENCES

[1] M. Kurahashi, S. Katsura, and A. Mizuno, *J. Electrostat*., 42, 93-105 (1997).

[2] T. Miichi, N. Hayashi, S. Ihara, S. Satoh, and C. Yamabe, *Ozone-Sci. Eng*., 24, 471-477 (2002).

[3] T. Iijima, Y. Okita, K. Kubo, R.Makise, and T. Murata, *Proc. World Ozone Congress*, IV.2.7, 1-11 (2005).

[4] F. Tochikubo, Y. Furuta, S. Uchida amd T. Watanabe, *JJAP*, 45, 2743-2748(2006).

[5] A. Yamatake, K. Yasuoka, and S. Ishii, *IEEJ Trans. FM*, 124, 1021-1026 (2004) (in Japanese).

THE EFFECTS OF PULSED STREAMER DISCHARGE ON A MARINE RED ALGAE, *PORPHYRA Y EZOENSIS*

Zi Li, Xiaofei Lin Takeshi Ohno, Takao Namihira, Sunao Katsuki, and Hidenori Akiyama

The Graduate School of Science and Technology of
Kumamoto University, 2-39-1 Kurokami,
Kumamoto 860-0862, JAPAN

ABSTRACT. *Porphyra yezoensis* has recently been recognized as a model plant for fundamental and applied study in marine biological science. In order to investigate of the gene expression of *Porphyra,* transcription activation is the first step. In this paper, we try to use pulsed streamer discharge in water to realize activated transcription of *Porphyra.* After applying 8 times streamer discharge, and 4 hours culture, the transcription activation investigation was carried out by using *Bromoporoxidase* (simplified as BOM) gene. From the results, it was found that transcription of BOM gene was activated after applying streamer discharge.

1. INTRODUCTION

Porphyra yezoensis is a genus of marine red algae and has recently been recognized as a model plant for fundamental and applied studies on the marine plants in biological research. *Porphyra* is used wildly in laboratory research because they complete their life cycle in culture within a few months and also because the haploid genome sizes in the gecus *porphyra* are of the same order of magnitude as those of *Arabidopsis thaliana* [1].

Transcription activation is the first step in eukaryotic gene expression. Gene regulation, which is about turning on and off expression of specific protein-coding genes in response to environmental changes, during development and in differentiated cells, widely occurs at the level of transcription activation. Usually, protoplast treatment, UV light, ozone and tissue culture were used as stress to realize transcription activation in biological research [2] [4].

It is well known, streamer discharge in water can cause four physical phenomena, such as the intense discharge current from the needle electrode to the ground, the free radical formation in the plasma, the ultraviolet radiation and the shockwave generation [3]. In this paper, we try to use pulsed streamer discharge in water to a stress of *Porphyra*. A stainless needle with 30 μm in diameter was employed as a point discharge electrode, 3cm apart from the ground, and applying a 1μs, 50kV pulse. A pulsed streamer discharge was obtained in the sterilizing water filled with *Porphyral* leaves (named sample water in this paper). After applying 8 times streamer discharge, and 4 hours culture, the transcription activation investigation was carried out by using *Bromoporoxidase* gene (simplified as BOM). From the results, it was found that transcription of BOM gene was activated after applying streamer discharge.

2. EXPERIMENT

2.1. Pulsed streamer discharge system

Figure 1 shows the schematic diagram of the pulsed power generator used in this work. The generator consisted of a positive dc source, the Blumlein type pulse forming network (B-PFN) and a pulse transformer (PT). A triggered spark gap switch (SGS) was used as a closing switch of B-PFN. B-PFN had 12 stages of LC ladder, which were composed with 20 nF of capacitor and 0.1 μH of inductor. The characteristic impedance ($2\sqrt{L/C}$) and the pulse width ($2N\sqrt{LC}$) of B-PFN, calculated from capacitance (C) and inductance (L) of LC ladder, and number (N) of LC ladder stages, were approximately 4.5 Ω and 1.1 μs, respectively. The FINEMET^{TM} was utilized as the core material of PT. PT had 5 of the winding ratio (windings: secondary windings = 1: 5). Therefore, the total characteristic impedance of the generator was computed at 112.5 Ω (4.5 Ω×5^2).

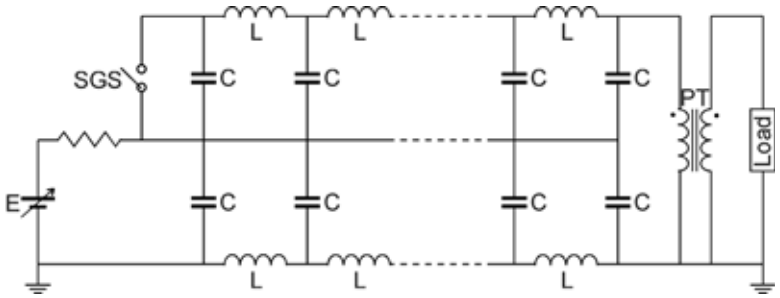

FIGURE 1. The circuit schematic of B-PFN

The positive polarity of pulsed voltage was applied to the needle electrode. For the utilization of the maximum flux swing of PT core, the reset current of 2 A was flown near the PT core.

2.2. Preparation of the red algae sample

Leafy gametophytes of *Porphyra yezoensis* were cultured in weekly renewed ESL medium containing 3.5 % Sealife power （Marinetech Co.,Ltd., Japan） and 1% (v/v)ESS2 stock solution (pH=8.0)in a 10 hours photoperiod of fluorescent illumination (50μmol·m-2·s-1) at 15°C with constant air bubbling for 4 weeks.

2.3. Discharge chamber and output waveform

Fig.2 shows the discharge chamber used in this experiment. The needle to plate electrode was utilized as the discharge chamber. The needle electrode with 30 μm in tip curvature was put concentrically into the cylinder wall with 6 mm in inner diameter and 2 mm in length. In the experiment, the discharge chamber was filled with the sterilizing water and objective red algae leaves. The output from the pulsed power generator was connected to the needle electrode and a piece of copper plate electrode was putted between the polyethylene insulator walls of the discharge chamber and was grounded. The charging voltage into B-PFN was fixed at +11.3 kV. The waveform of output voltage on the tip of the needle electrode is shown in figure 3.

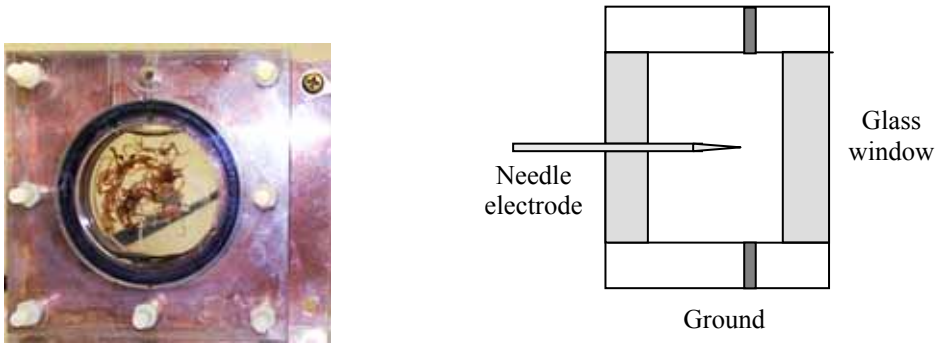

(a) (b)

FIGURE 2. (a) Discharge chamber appearance with sample water, (b) diagram of side view

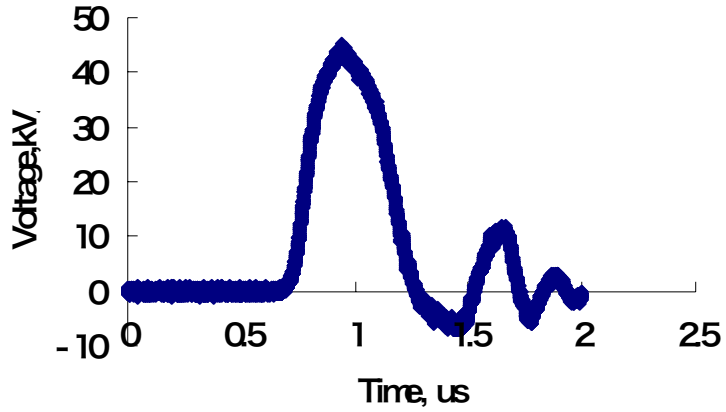

FIGURE 3.The waveform of output voltage of the needle electrode

3. INVESTIGATION OF TRANSCRIPTION ACTIVATION OF BOM GENE

After applying discharge, the Leafy gametophytes of *Porphyra yezoensis* were cultured in ESL medium for 4 hours with constant air bubbling for 4 weeks. The total RNA was extracted by the modified SDS/ phenol method. CDNA synthesis was carried out by reverse transcription followed by PCR amplification.

We use the PyEF gene as a control, which is a kind of gene with steady transcription level and is difficult to be affected by outside conditions.

3.1. BOM gene investigation

BOM gene is not easy to transcribe without applying stress. After PCR amplification of PyEF gene and BOM gene, electrophoresis was carried out. The results are showed in figure 4. From the result, transcription of BOM gene was activated after applying streamer discharge.

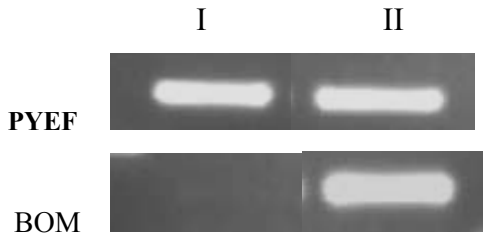

FIGURE 4. Electrophoresis results, where, I means without applying discharge, II means after applying discharge,

4. DISCUSSION

In this paper, we try to use pulsed streamer discharge in water to realize activated transcription of *Porphyra yezoensis*. From the results, it was confirmed that after applying 8 times streamer discharge in the sterilizing water with the leaves of *Porphyra*, the transcription of BOM gene was activated. Because streamer discharge in water can cause four physical phenomena, such as the intense discharge current from the needle electrode to the ground, the free radical formation in the plasma, the ultraviolet radiation and the shockwave generation. It is possible that streamer discharge can be used as a stress in biological research.

ACKNOWLEDGMENTS

We are very grateful to Prof. S.Takyuo(Graduate School of Science and Technology, Kumamoto University, Japan). He gave the valuable comments and discussions for this paper.

REFERENCES

[1] Itoshi NIKAIDO, Erika ASAMIZU, Maiko NAKAJIMA, Yasukazu NAKAMURA, Naotsune SAGA, and Satoshi TABATA, Generation of 10,154 Expressed Sequence Tags from a Leafy Gametophyte of a Marine Red Algae, *Porphyra yezoensis*, DNA Research 7,223-227 (2000).

[2] Lucia F. Franchini, Eric W. Ganko and John F. McDonald**.** Retrotransposon-Gene Associations Are Widespread Among D. melanogaster Populations *Mol. Biol. Evol.* 21(7):1323-1331. 2004

[3] H. Akiyama, “Streamer discharge in liquids and their applications”, IEEE Transactions on Dielectrics and Electrical Insulation, Vol.7, No.5, pp.646-653, 2000.

[4] Alcide Barberis, Micheal Petrascheck , “Transcription Activation in Eukaryotic Cells” , eEncyclopedia of life sciences, www.els.net.

ON THE HYDROGEN ENRICHMENT OF AN AIR-METHANE MIXTURE IN A ROTATING DISCHARGE REACTOR

E. El Ahmar*, A. Khacef and J. M. Cormier

GREMI - Polytech'Orleans, 14 rue d'Issoudun, B.P. 6744, 45067 Orléans Cedex 2, France
**elise.el-ahmar@univ-orleans.fr*

ABSTRACT. In this work, we propose a plasma treatment of air-methane (CH_4) mixture for hydrogen production applied to motor vehicles using a rotating discharge (RD). The RD reactor operating at atmospheric pressure was powered by a 50 Hz high voltage step-up transformer with leakage fluxes. Experimental results show that plasma treatment leads to the production of H_2 rich gas. For example, in a mixture with 20% CH_4 (total flow rate of 20 L/min, electrical power of 200 W), H_2 concentration is about 20%.

1. INTRODUCTION

Considering automotive pollution problems, researches have been focusing on the decreasing of fuel consumption and toxic products concentration such as nitrogen oxides (NO_x) and carbon dioxide (CO_2) by using hydrogen (pure or mixed with another fuel) as an alternative fuel.
In non-thermal plasma, an eventual acceleration of the chemical conversion and reforming reactions is due to the reactive species. The result is the production of H_2 rich gas. The addition of H_2 to a natural gas engine increases the flame speed, which reduces unburned hydrocarbons [1]. The H_2 would also displace carbon that would be available to produce carbon monoxide (CO) and carbon dioxide (CO_2) during combustion process. Due to the faster flame speed and broader flammability limits of hydrogen, addition of H_2 to natural gas results in a decrease of the maximum temperature leading to a low NO_x production [2, 3].
In this work, series of experiments using a rotating discharge (RD) for the treatment of air-CH_4 mixture applied to the internal combustion engine are presented.

2. EXPERIMENTAL SET-UP AND DIAGNOSTICS TOOLS

The experiments were carried out at atmospheric pressure and room temperature. Air-CH_4 experiments were conducted with CH_4 concentrations higher than the explosive limit (15%) i.e. ranging between 20% and 30% [4]. Mixtures with higher CH_4 concentration had been not studied because of carbon deposition phenomena (discharge instability, hampering of system functioning). Total flow rate used in these experiments is 20 $L.min^{-1}$.
The reactor consists of a quartz tube in which a conical central electrode and a cylindrical external one are laid out. The gas is injected into the reactor transversely with the axis of the system. The gas stream is guided by the cylindrical electrode. This reactor is powered with a 50 Hz high voltage step-up transformer, 220 V/10 kV, with leakage fluxes. The effect of leakage fluxes determines a reactance that produces a constant RMS value of the current in the discharge. When the system is under voltage, a discharge is produced between the electrodes at the place where those are closest. Then, the length of the discharge will grew up till it reaches the end of the electrode. At this place, the discharge will turn off and another one

will take place and so on …This type of reactor is very similar to the rotating discharge described in previous publications [5-7].

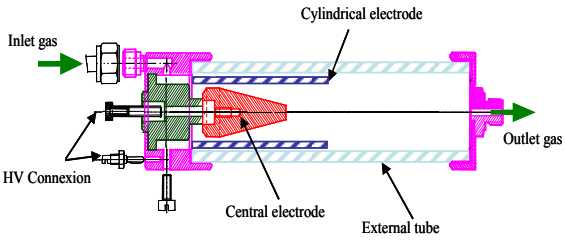

FIGURE 1. Schematic of the rotating discharge reactor.

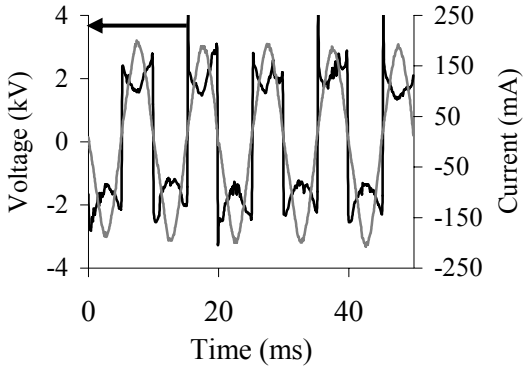

FIGURE 2. Typical current and voltage waveforms (20% CH_4, total flow rate= 20 $L.min^{-1}$).

Voltage and current were measured using a ST500 probe connected to a voltage divider (ratio: 0.01) and a Tektronix TCP 202 Hall effect probe, respectively. The signals from the probes were recorded on a Tektronix TDS 460A digital oscilloscope and processed in a PC.
Typical voltage and current waveforms are shown on figure 2. The electrical mean power is calculated from voltage-current recordings and determined by averaging the instantaneous power over a large number of discharges.
After plasma treatment, output gases were sampled and cooled in order to eliminate water. Dry output gases were analysed. Major components (O_2, N_2, H_2, CH_4, CO and CO_2) were quantified with Fourier Transform InfraRed spectroscopy-FTIR-(Nicolet Magna 550, equipped with a heated 10 m multiple pass absorption cell) and Gas Chromatography-GC-(Varian CP3800, equipped with Mole Sieve and Haysep N columns, a Thermal Conductivity Detectors (TCD), Flame Ionisation Detector (FID).)

3. EXPERIMENTAL RESULTS AND DISCUSSION

Analyses of formed species were carried out for two series of experimental conditions:

1) Input electrical power varying from 127 to 200 W while CH_4 and air concentrations remain constant (20% of CH_4 inlet);

2) CH_4 concentration varying from 20% and 30% while electrical power remains constant (200W).

3.1. Electrical power effect on CH_4 conversion and H_2 production

Analysis gas results at the outlet reactor are given on figure 3. The CH_4 and O_2 consumption are corresponding to the H_2, CO and CO_2 production. For the maximal power (200 W), CH_4 conversion is about 80% and H_2 production is about 20%. The CH_4 consumption is an increasing function of the power supplied to the plasma. The H_2 production seems to follow a similar behavior. The CO and CO_2 production seems to be independent of the power implanted to the plasma since this production is about 9.5 and 3.8%, respectively.
By-products such as C_2H_6, C_2H_4 and C_2H_2 were detected with concentrations less than 0.5% in all cases studied. These compounds could involve significant effects on the ignition process of the internal combustion engine.

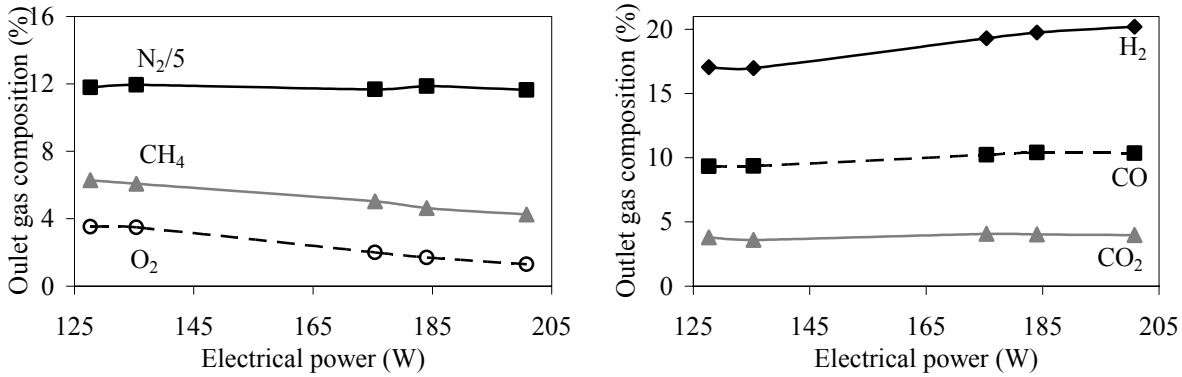

FIGURE 3. Experimental dry exhaust gas composition as function of electrical power (CH_4 inlet: 20%, total flow rate=20 $L.min^{-1}$).

3.2. Initial CH_4 mole fraction effect on CH_4 conversion and H_2 production

The experiments were done with a constant electrical power (200 W). As it can be seen from figure 4, the O_2 and CH_4 consumption are decreasing function of the CH_4 inlet. From these data, the CH_4 conversion rate is varying in the range [44-80%]. This conversion rate increases when the CH_4 inlet increases. The H_2, CO and CO_2 productions are also decreasing function. Between 25 and 30% of the CH_4 inlet, the H_2 production seems to be constant (17%).

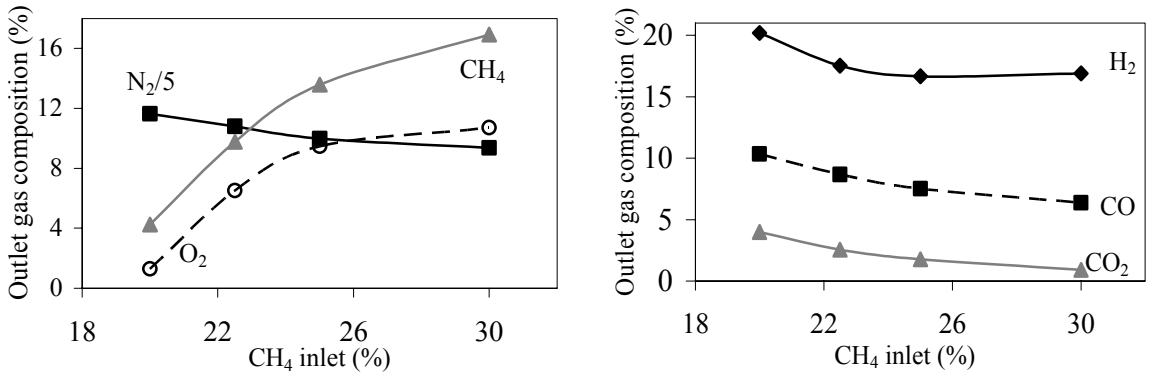

FIGURE 4. Experimental dry exhaust gas composition as function of CH_4 inlet (Electrical power=200W, total flow rate=20 $L.min^{-1}$).

3.3. Two reactions model

Taking into account the main products, concentrations parameters (such as selectivity) were calculated using the following main chemical reaction:

$$\begin{array}{lccccccc} & CH_4 & + & 1/2\ O_2 & \rightarrow & CO & + & 2\ H_2 \\ \text{Final state} & a\text{-}x & & b\text{-}1/2\ x & & x & & 2x \end{array} \qquad \Delta H_1 = -36\ kJ/mol \qquad (1)$$

$$\begin{array}{lccccccc} & CH_4 & + & 2\ O_2 & \rightarrow & CO_2 & + & 2\ H_2O \\ \text{Final state} & a\text{-}y & & b\text{-}2y & & y & & 2y \end{array} \qquad \Delta H_2 = -892\ kJ/mol \qquad (2)$$

a, b, x and y parameters represent the amounts of initial CH_4, initial O_2, CH_4 consumed via the partial oxidation reaction (1), CH_4 consumed via the complete oxidation reaction (2), respectively. These parameters could be calculated as function of the main products given by chromatography analysis. They led to the following equations:

$$x = \frac{a - [CH_4]}{1 + \frac{[CO_2]}{[CO]}}; \qquad y = \frac{[CO_2]}{[CO]};$$ where [i] represents the amount of the specie (i).

The selectivity is calculated from the following ratios:

Partial oxidation selectivity = x/(x+y);

Complete oxidation selectivity = y/(x+y).

These calculations show that the partial oxidation, in all the cases studied, is the dominant reaction. This selectivity increases from 72 to 88%, when CH_4 inlet increases from 20 to 30% and seems to be independent of the electrical power.

4. CONCLUSION

Two series of experiments using a RD were carried out. Plasma treatment results show an H_2 enrichment of the outlet gas in the range of (17-20%). An increase of the electrical power leads to an increase of CH_4 conversion. Contrarily, an increase of the CH_4 inlet leads to a decrease of CH_4 conversion. From our data and our calculations, the partial oxidation reaction seems to be the dominant reaction in such a process.
Therefore, works are in progress in order to optimize all the system parameters for reaching higher H_2 concentration such as the improvement of the discharge efficiency, using other hydrocarbons (propane, butane…) and adding new component to the inlet mixture.

5. REFERENCES

[1] El Ahmar, E., Khacef, A., Cormier, J.M. (2006). Plasma aided combustion of air-natural gas using an atmospheric pressure rotating discharge for vehicles applications. *Proc. Vth Non-Thermal Plasma Technology for Pollution control and sustainable Energy development, CD Rom ISNTPT 5.*

[2] Cohn, D.R., Rabinovich, A., Titus, C.H, Bromberg, L. (1997). Near term possibilities for extremely low emissions vehicles using on-board Plasmatron generation of hydrogen. *Int. J. hydrogen energy, 22, 715-723.*

[3] D'Andrea, T., Henshaw, P.F., Ting, D.S.K. (2004). The addition of hydrogen to a gasoline-fuelled S.I. engine. *Int. J. hydrogen energy, 29, 1541-1552.*

[4] El Ahmar, E., Met, C., Aubry, O., Khacef, A., Cormier, J.M. (2006). Hydrogen enrichment of a methane-air mixture by atmospheric pressure plasma for vehicles applications. *Chem. Eng. J., 116, 13-18.*

[5] Rusu, I., Cormier, J.M. (2003). On a possible mechanism of the methane steam reforming in a gliding arc reactor. *Chem. Eng. J., 91, 23-31.*

[6] Cormier, J. M., Rusu, I. (2001). Syngas production via methane steam reforming with oxygen: plasma reactors versus chemical reactions. *J. Phys. D: Appl. Phys., 34, 2798-2803.*

[7] Rusu, I., Cormier, J.M., (2003). Study of a rotarc plasma reactor stability by means of electric discharge frequency analysis. *Int. J. hydrogen energy, 28, 1039-1043.*

EFFECTS OF GLIDING ARC DISCHARGES ON *ERWINIA CAROTOVORA ATROSEPTICA* 1526

M. Moreau[1,2,3], N. Orange[2], J .-L. Brisset [1]

1 University of Rouen -Laboratoire d'Electrochimie (LEICA), F.76821-Mont-Saint-Aignan, (France)
2 University of Rouen- Laboratoire de Microbiologie du Froid (LMDF), Evreux,(France)
3 GIE Comité Nord, Paris, (France)

ABSTRACT : Decontamination of a phytopathogenic strain of bacteria *Erwinia carotovora atroseptica* 1526 *(Eca)* is achieved by means of gliding arc discharges in humid air. Cultures of *Eca* were exposed to the plasma in a gliding arc reactor prototype and were totally inactivated in a few minutes. The kinetic destruction of the bacteria is described and the biological mechanisms involved in the bacterial death are discussed.

1. INTRODUCTION

The electrical discharges are probably the most promising methods among the emerging decontamination techniques. The gliding discharges (or glidarc) draw industrial attention because of their low cost in equipment and working conditions, since they operate at ambient temperature and atmospheric pressure. Moreover their efficiency have been already established on other strains of bacteria [1-3]. The literature also report attempts to the use of non-thermal plasma for bio-decontamination [4]. However the mechanisms responsible for the bacterial destruction are poorly known.
We report here on the effects of glidarc on a selected strain of *Erwinia*. Many countries encounter serious problems with pectinolytic *Erwinia* which causes the loss of entire crops and very important financial damages for potatoes producers [5]. In E.C., *Erwinia* are among the major potato pathogens [6] and the producers are seeking for rapid and efficient decontamination techniques that can be applied both to the treatment of water and materials.

MATERIALS AND METHODS

Plasma reactor. The reactor used derived from the "glidarc" device previously [7] described (Fig. 1). It is basically a non-thermal quenched plasma system operated at atmospheric pressure and close to the ambient temperature. It consists of two metallic diverging electrodes raised to a high voltage fall (9 kV, 100 mA in open conditions) fitted with a feeding gas nozzle disposed along the axis of the reactor. An arc forms at the electrode minimum gap and moves along the electrodes pushed along by the gas flow until it breaks in a plasma plume and a new arc forms. The plasma plume then makes contact with the target and the activated species react at the liquid-gas interface. The plasma gas is a mixture of N_2-O_2 supplied by an air compressor and saturated with water by bubbling in a bubbling flask.

Bacterial strain and culture conditions. The strain of *Erwinia,* provided by the French Collection of Phytopathogenic Bacteria, *Erwinia carotovora atroseptica 1526* was exposed to the plasma for various treatment times (min). The strain was maintained as glycerol stocks and stored at – 80° C for further use. Before each treatment, the strain was re-suspended by

Corresponding author: Jean-Louis.Brisset@univ-rouen.fr

incubating at 28°C for 24 h in sterile LB broth in a stirred water bath. Then 25 mL of sterile LB were inoculated by 0.5 mL of these pre-cultures and grown for another 24 h at 28°C, and 20 mL samples were then exposed to the plasma, so that all the bacteria used for the study were in late stationary phase. Before and after each treatment viable counts of surviving cells were determined by the standard plating technique. The colony forming units (CFU) were counted after 48 h at 28°C.

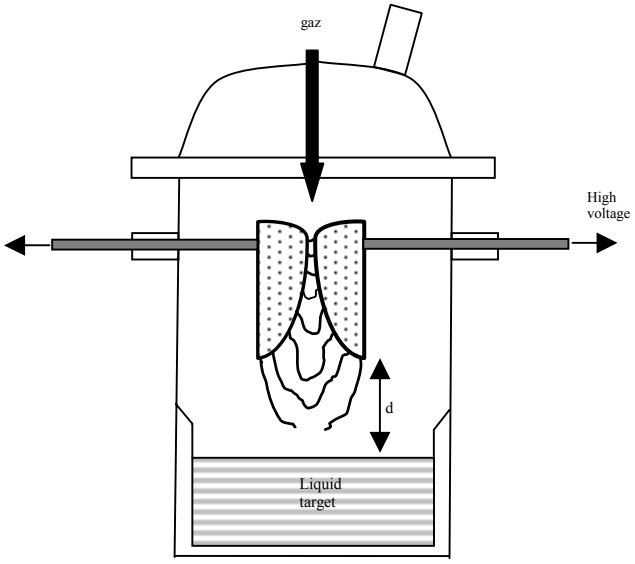

Figure 1: sketch of the reactor

Viability of bacteria. Viability of bacteria was assessed with the LIVE/DEAD *backlight* viability kit (molecular probes) based on the use of SYTO 9® and propidium iodide nucleic acid probes. Whereas SYTO 9® can easily enter bacteria membranes and labels all the population, propidium iodide only penetrates cells with damaged membranes. The SYTO 9® green labelled bacteria are thus considered as living cells while the red stained bacteria obtained with propidium iodide are actually dead cells. Observations were realised using an Axiovert S100 optical microscope (Zeiss, Oberkochen, Germany) equipped with an Olympus SC35 type 12 camera.

RESULTS

The effects of the gliding arc treatments were studied over a 15 min period, which is long enough to inactivate the whole bacterial population. The plot (Fig.2) illustrates the kinetics of the treatment on the growth potential of *Eca* after exposure to the discharge.
In our working conditions the total destruction of the bacterial culture is obtained in less than 5 minutes. The very short treatment time required is assigned to the energy dissipated by the discharge and consequently to the formation [10] of reactive species such as the OH and NO radicals which react at the liquid/plasma interface with the matter dispersed in the liquid target. During the plasma treatment, no variation of the suspension temperature is observed, which prevents from considering any direct thermal effect of the glidarc on the bacteria (data not shown).

The effects of the electric discharges and those of the plasma species on bacteria species are still poorly known and especially those concerning the gliding discharge. Various degradation mechanisms are proposed in the literature to explain the bacteria death:

- Alterations of the integrity of the membranes followed by irreparable damages of DNAs and RNAs [7-8],
- The photochemical effect and the UV light energy transferred to the surrounding gas (specially in low pressure discharges) [4]. However, the number of UV photons emitted by a gliding arc discharge is limited [9],
- The chemical action of the species induced in humid air plasma. Laroussi *et al*.[11] considered the respective roles of the plasma components on bacteria abatement.

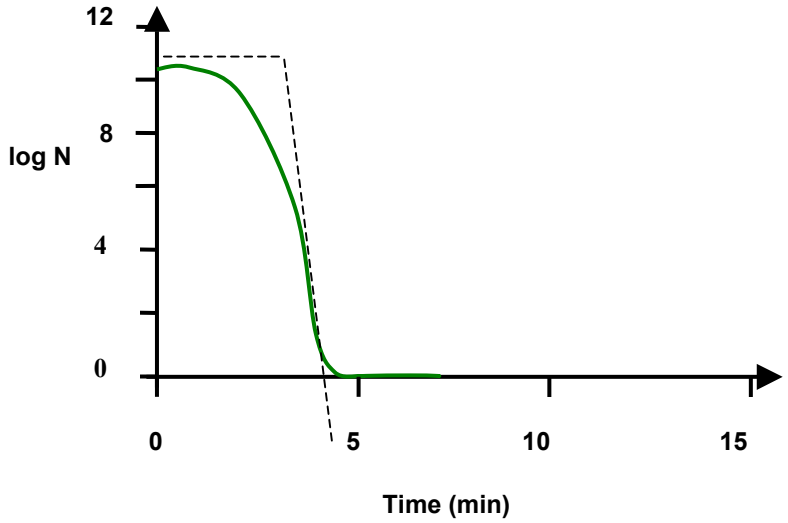

Figure 2: Destruction plots of *Eca* vs. exposure time. The dash lines show ideal 1st-order kinetics

Benstaali *et al*. [10] evidenced oxidising and acid effects in aqueous solutions of organic compounds exposed to the gliding discharge. These changes are respectively attributed to the occurrence of $HO^{\bullet}$ and $NO^{\bullet}$ radicals formed in the humid air plasma [10]. Our measurements confirm that $NO^{\bullet}$ is responsible for acid effects and for a pH lowering step of the medium by means of the formation of acids HNO_2/HNO_3 in solution. The relevant rapid pH fall can provokes a stress so violent that the bacteria have no time to adapt and die. $OH^{\bullet}$ is a still stronger oxidising agent which is probably associated with the rapid degradation of the organic matter [12]. In addition, it combines to yield H_2O_2 in aqueous medium and hydrogen peroxide is well known for its very high sterilization activity.

The result of bacterial destruction obtained by direct counting are consistent with those obtained by epifluorescence [2] (data not shown) and indicates that the plasma treatment does not generate viable but non culturable forms of *Eca*.

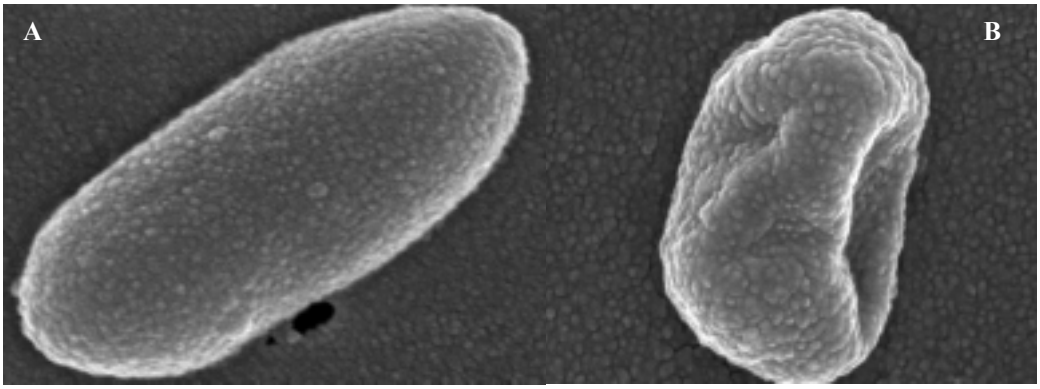

Figure 3: SEM photomicrographs of *Eca*. A) untreated and B) treated for t=2.5 min.(pictures UBHM)

The epifluorescence technique demonstrates that exposure to the plasma for a few minutes causes very important damages to the bacteria and suggests a loss of integrity of the bacterial membranes. This assumption is confirmed by SEM observations that show ruptures and/or disorganisation of the membrane (figures 3 A and B). Moreover, new results show that all the bacterial structure is disorganised after the treatment: both DNA (Desoxyribo Nucleic Acid) and LPS (Lipopolysaccharide) are degraded and outer membrane proteins are more easily extracted from the bacteria after a treatment by gliding arc (Data not shown).

CONCLUSION

The present study reports on the effects of a new decontamination technique, i.e., the gliding arc discharge at atmospheric pressure, on bacterial pathogen of industrial interest. The absence of formation of resistant forms of *Eca* even for very short exposure times to the gliding discharges makes this technique very interesting for industrial applications. These features strongly suggest that the decontamination process is related to the occurrence of the plasma formed species which cause deadly damages to the bacterial membrane that can not be repaired by the cells.

ACKNOWLEDGEMENTS

This work was performed with the financial support of GIE Comité Nord which is acknowledged for a grant (M.M.).
The SEM photographs were taken by UBHM- INRA (Massy, France).

REFERENCES

[1] H.Vitrac, J.Guespin-Michel and J.L Brisset, *Proc. Hakone VII*, **2**, (Greifswald, Ge 2000), 393-397.
[2] M. Moreau, M.G.J. Feuilloley, N. Orange and J.L. Brisset, *J. of Appl. Microbiol*., **98**, 1039-1046, 2005.
[3] Briandet, R., J.O. Kamgang, Y. Rutter, J.M. Herry, M.N. Bellon-Fontaine and J.L. Brisset, *Biofilms in Medicine*, (Elseneur, Dk, 2003).
[4] M. Moisan, J. Barbeau, S. Moreau, J. Pelletier, M. Tabrizian and L'H. Yahia, *Int. J. of Pharmaceutics*, **226**, 1-21, 2001.
[5] M.C.M. Pérombelon and G.P.C. Salmond,. In sight, U.S., R.P. Singh, and K. Kohmoto (eds.), *Pathogenesis and host specificity in plant disease*, Pergamon Press, Oxford, UK, vol. I, 1-20, 1995.
[6] Lesueur, H., A. Czernichowski and J. Chapelle, *Fr. Pat*. 2639172, 1988.
[7] Pelletier, *J. Agressologie*, **33,** 105-110, 1993
[8] Lerouge, S., M.R. Wertheimer, R. Marchand, M. Tabrizian and L'H. Yahia, *J. Biomed. Mat. Res.* , **51**, 128-135, 2000.
[9] Kuzmichev, A.I., I.A. Soloshenko, V.V. Tsiolko, V.I. Kryzhanovsky, V.Yu. Bazhenov, I.L. Mikhno and V.A. Khomomich, *Proc. Hakone VII*, **2**, (Greifswald, Ge., 2000), 402-406.
[10] Benstaali, B., D. Moussa, A. Addou et J.L. Brisset, *Eur. Phys. J. AP*, **4**, 171-179, 1998.
[11] Laroussi, M. and F. Leipold, *Int. J. of Mass Spectrometry*, 233, 81-86, 2004.
[12] Moussa, D., F. Abdelmalek, B. Benstaali, A. Addou, E. Hnatiuc and J-L. Brisset, *Eur. Phys. J. Appl. Phys*, 29, 189-199, 2005

EFFECTS OF THE GLIGING ARC DISCHARGES ON *ERWINIA CAROTOVORA ATROSEPTICA* 1526

M. Moreau[1,2,3], N. Orange[2], J .L. Brisset [1]

1 Université de Rouen -Laboratoire d'Electrochimie (LEICA), Mont-Saint-Aignan, (France)
2 Université de Rouen- Laboratoire de Microbiologie du Froid (LMDF), Evreux,(France)
3 GIE Comité Nord, Paris, (France)

Among the emerging techniques of decontamination, the gliding arc discharge is one of the most promising because of its low cost in equipment and energy and its good efficiency. However the mechanisms responsible for bacterial destruction are poorly known and the effects of this kind of discharge on micro-organisms have never been investigated.

In the present work, we investigate the effects of gliding arc treatment on a selected strain of *Erwinia: Erwinia carotovora atroseptica* 1526 (*Eca*), which is responsible for the "blackleg" disease of potatoes. Indeed, many world-wide countries encounter serious problems with pectinolytic *Erwinia* which cause the loss of entire crops and very important financial damage for potatoes producers. *Eca*, frequently encountered in production, was used to investigate the efficiency and reproducibility of the glidarc treatment and the mechanisms responsible for the death of the bacteria.

Cultures of *Eca*, taken in stationary phase were exposed to the plasma generated by electric discharges in a gliding arc reactor. The destruction kinetics of the bacteria were followed by direct platting. The destruction kinetics is characterised by an initial plateau accounting for a lag phase, during which the number of growing bacteria remains almost steady followed by a rapid decrease in the bacterial population, the rate of which reaches 10 logarithms units for 30 seconds, down to zero. An ultimate steady state close to zero plateau accounts for the reaction end. The number of bacteria able to generate colonies in Petri dishes is then close to zero, which suggests that an apparent sterilization occurs for 5 minute treatments.

The viability of the bacteria was determined by different techniques. First the LIVE/DEAD kit (Molecular Probes', USA), based on differences of fluorescence between bacteria which are dead or alive, suggests that all the bacteria in the population are dead after the glidarc treatment and not in a viable but non cultivable resistant forms; artificial inoculations of treated cultures of *Eca* in potatoes confirmed that *Eca* were actually dead.

Some physical-chemical mechanisms supposed to be responsible for bacterial destruction have been investigated. We studied the effects of the treatment on some components of the outer membrane of the bacteria (proteins and lipopolysaccharide) and the results suggest and important degradation of these components after a glidarc treatment. The feature is confirmed scanning electron microscopy which show ruptures and/or disorganisation of the membrane.

The results of the presented study demonstrate that exposure to the glidarc discharge allows a rapid and complete destruction of planctonic *Eca* without the formation of any resistant form and that the mechanisms responsible for the death of the bacteria are probably due to the reactive species created in the discharge (in particular the NO and OH radicals or their derivatives). The reduction rate of the bacterial population obtained by this technique suggests that it can be used for industrial sterilization.

SURFACE BIOLOGICAL DECONTAMINATION USING GLIDING DISCHARGES IN HUMID AIR AT ATMOSPHERIC PRESSURE : IMPACT OF THE TREATMENT DISTANCE

C. Bourgeois[1, 2], J.-M. Herry[2], D. Hilaire[3], J.-L. Brisset[1] and M. Naïtali[2]

[1] *Laboratoire d'Electrochimie (LEICA),*
University of Rouen. F-76821 Mont-Saint-Aignan, FRANCE
[2] *UMR Bioadhésion et Hygiène des Matériaux,*
ENSIA – INRA. F-91744 Massy, FRANCE
[3] *Centre d'Etude du Bouchet (CEB),*
Délégation Générale pour l'Armement. F-91710 Vert le Petit, FRANCE

ABSTRACT. The present study aims to optimize a new physical technology of microbial decontamination of surfaces using gliding electrical discharges operated at atmospheric pressure with humid air. We thus determined the influence of the treatment distance on the efficiency of decontamination of two non-pathogenic model Gram-positive microorganisms: *Staphylococcus epidermidis* and *Bacillus subtilis*. Contaminated supports were plasma treated for 30 minutes, and the bacterial destruction following plasma treatment was estimated at various distances between the tips of the electrodes and the surface of the sample (D). In the range of distance explored (D was comprised between 5 and 21.5 cm), we obtained a total destruction of 4.8 logarithm units of *S. epidermidis* cells for distances lower or equal to 13 cm, while only partial destruction was observed for *B. subtilis* spores.

1. INTRODUCTION

Sterilization is a physical or chemical process that destroys or eliminates all forms of life, i.e. microorganisms. Conventional sterilization techniques e.g. heat or biocides, rely on irreversible metabolic inactivation or on breakdown of vital structural components of microorganisms. Most of decontamination processes are time and energy consuming (thermal sterilisation cycles…) and can present adverse effects to the environment (use of chemical biocides). Moreover they can induce degradation of medical equipments (polymers accessories by heating treatments, steel by chemical biocides…)[1,2], so that an increased interest arose for the development of new methods for bacterial inactivation in the last decade. One solution is using electric discharges at atmospheric pressure and low temperature in wet air which generate active agents such as UV photons and reactive atomic and molecular radicals [3]. Among these non thermal plasma techniques, the gliding discharges technology is one of the most promising because of its low equipment and energy costs. Although its efficiency was showed on *Escherichia coli* [4], the mechanisms responsible for bacterial destruction are poorly known and the effects of this decontamination technique on pathogens of industrial and medical interest have just started.

We report here on the influence of the electrode to target distance D of the plasma device on the efficiency of decontamination of two non-pathogenic microorganisms, which are surrogate of pathogens of industrial interest, with different resistance capacity to classical decontamination processes. *S. epidermidis*, selected as model of vegetative cells, belongs to coagulase-negative *Staphylococcus* strains which are frequently associated with bacteremia

Corresponding author: naitali@ensia.fr

and hospital-acquired infections, particularly in patients with catheters or other plastic devices. Its well known adhesion capacity, biofilm production [5] and its increasing resistance to antibiotic treatments make *S. epidermidis* one of the most studied model microorganisms. In addition, *B. subtilis* was selected as a sporulated bacterial form. Indeed, bacterial spores are the most highly resistant entities against environmental stresses and decontamination processes, and therefore are used as biological indicators to evaluate the efficiency of different treatments. A number of mechanisms are responsible for the strong resistance of spores of *Bacillus* species to conventional decontamination techniques (specific cell wall biochemistry, low physiological activity….) which makes them an excellent experimental model. The necessity of safe, environmentally friendly, inert to material and effective treatments of cleaning and disinfection in food, cosmetic and medical industrial plants explains the need of developing researches to innovative biodecontamination techniques such as cold plasmas.

2. EXPERIMENTAL SECTION

The experimental plasma reactor used in this study derives from the "glidarc" device previously described [6]. It consists of two diverging electrodes raised to high voltage transformer (9 kV, 100 mA in open conditions) fitted with a feeding gas nozzle disposed along the axis of the reactor (Fig. 1). An electric arc forms at the electrodes minimum gap. This arc is pushed by the gas flow, moves to the tip of the electrodes, is then short-circuited by a new arc and finally breaks into a plasma plume. The active species of the plasma plume are potential sterilizing agents which can interact with the surface of the sample. In our operating conditions, the feeding gas was air saturated with water and its flow rate was controlled at 500 L h^{-1}.

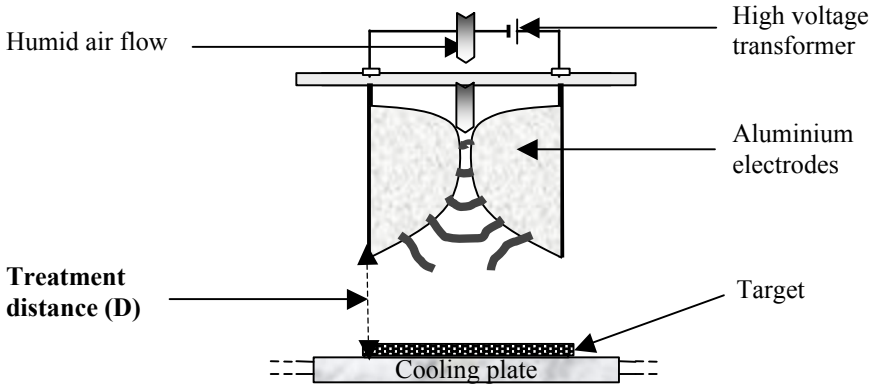

FIGURE 1. Experimental device

The microorganisms selected for this study were spores of *Bacillus subtilis* var *niger* (ATCC 9372) and vegetative cells of *Staphylococcus epidermidis* (ATCC 12228).

Conventionally stored and grown, the washed cultures were used to realize the adhesion on the 14 x 30 mm^2 solid support AISI 304 stainless steel by 100 µl microdrop deposition. Then, contaminated supports were plasma treated for 30 minutes at varying treatment distance D between the tips of the electrodes and the surface of the sample. To evaluate the effect of D on the decontamination efficiency of plasma, contaminated supports were treated at different distances ranging from 5 to 21.5 cm. In order to detach potential surviving adherent cells, treated supports were sonicated in physiological saline solution (NaCl 150 mM) at 28°C and 40 kHz for 2 minutes. Enumeration of viable surviving cells were determined by standard plating technique. The colonies forming units (CFU) were counted on Trypticase Soja Agar (TSA) after incubation of 48h at 30°C. When necessary, total destruction verification was

performed by direct deposition of the treated support in TSA to follow potential bacterial growth.

3. RESULTS

For studying the decontamination of adherent vegetative cells of *S. epidermidis*, each supports were contaminated with $6x10^4$ cells and then plasma treated. Figure 2 shows a total destruction of the plasma exposed vegetative cells, i.e., an abatement of 4.8 logarithm units for treatment distances lower than 13 cm. Beyond that, the destruction were only partial with 2.5 to 3.5 logarithm units of abatement. It is important to note that, for D value of 5, 9 and 13 cm, the analysis of treated supports directly deposited in agar did not show any bacterial development and thus confirm the total and complete decontamination of the material. It also allowed to eliminate the participation of sonication in this decontamination.

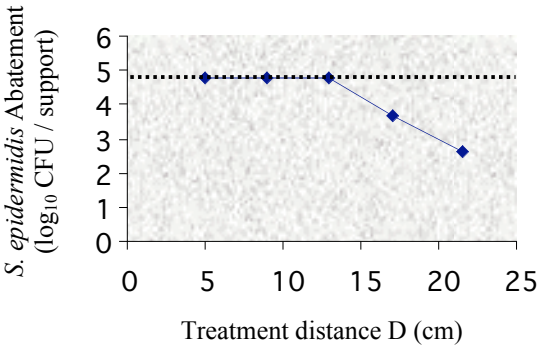

FIGURE 2. Effect of plasma treatment distance D on decontamination efficiency of adherent cells of *S. epidermidis* (····· initial contamination: 4.8 $\log_{10}$ units)

Regarding spores decontamination, the supports were contaminated by $3x10^5$ spores approximately and plasma treated. The results show only a partial destruction of plasma exposed spores with a maximum reduction of 4.5 logarithm units for a D value of 5 cm (Fig. 3). No total destruction was obtained under these conditions.

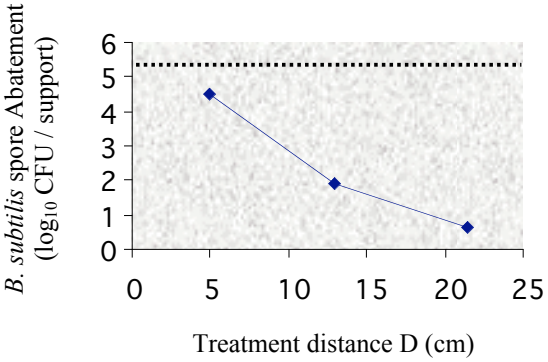

FIGURE 3. Effect of plasma treatment distance D on decontamination efficiency of adherent spores of *B. subtilis* (····· initial contamination: 5.46 $\log_{10}$ units)

This preliminary investigation shows that the destruction of adherent cells or spores greatly depends on the electrodes-target distance D. A total abatement was observed for *S.*

epidermidis vegetative cells, while survival adherent spores of *B. subtilis* exposed to the discharge in the same working conditions were detected. These results are consistent with the well-known increased resistance of the sporulated bacterial forms with respect to most of decontamination treatments [7, 8, 9].

4. CONCLUSION

Varying the plasma treatment distance allowed us to optimize one parameter of the system leading to a more effective biodecontamination. Another parameter which is out of control and influences the biodecontamination efficiency is the lifespan of the active species created in the plasma plume, which is probably very short (e.g., OH radical). Oppositely, an optimised biodecontamination requires that these species are created far enough from the target to be able to diffuse on a large surface (or characterized by a long lifespan, such as NO) and rather near the target to have time to act on the target adherent pathogens. This parameter has a very special importance because its control would make possible to draw up the effectiveness relationship between the distance treatment, the lifespan of the active species and their diffusion. Thus, it could evaluate plasma biodecontamination on supports of larger surfaces.

In conclusion, this study clearly shows that the gliding discharge treatment induces an important abatement of the bacterial populations and presents a great potential for surface biodecontamination. Although the mechanisms responsible for biological destruction are still poorly known, the promising effects of this technique on microbial pathogens represent a considerable industrial interest for microbiological safety.

ACKNOWLEDGEMENTS

This study was supported by a grant from the Délégation Générale pour l'Armement. We are grateful to R. Briandet and L. Guillier for large assistance and fruitful discussion.

REFERENCES

[1] Laroussi, M. (1996). Sterilisation of contaminated matter with an atmospheric pressure plasma. *IEEE Trans. Plasma Sci.* 24, 1189-1191.
[2] Whittaker, A.G., Graham, E.M., Baxter, R.L., Jones, A.C., Richardson, P.R., Meek, G., Campbell, G.A., Aitken, A., Baxter, H.C. (2004). Plasma cleaning of dental instruments. *J. Hosp. Infect.* 56, 37-41.
[3] Akitsu, T., Ohkawa, H., Tsuji, M., Kimura, H., Kogoma, M. (2005). Plasma sterilisation using glow discharge at atmospheric pressure. *Surface and Coatings Technology*. in press.
[4] Vitrac, H., Guespin-Michel, J., Brisset, J.L. (2000). A microbiological investigation of the gliding arc treatment of aqueous media. *Proc. "Hakone-7" Greifswald, Germany*. 2, 393-397.
[5] Donlan, R.M. and Costerton, J.W. (2002). Biofilms: survival mechanisms of clinically relevant microorganisms. *Clin. Microbiol. Rev.* 15, 167-193.
[6] Pelletier, J. (1993). La sterilisation par le procédé plasma. *J. Agressologie,* 33, 105-110.
[7] Kelly-Wintenberg, K., Montie, T.C., Brickman, C., Roth, J.R., Carr, A.K., Sorge, K., Wadsworth, L.C. and Tsai, P.P. (1998). Room temperature sterilization of surfaces and fabrics with a one atmosphere uniform glow discharge plasma. *J. Ind. Microbiol. Biotechnol.,* 20, 69-74.
[8] Mason, T.J., Paniwnyk, L., Chemat, F. (2003).Ultrasound as a preserving technology. In *Food preservation techniques* ed. Zeuthen P. and Bogh-Sorensen L., 303-337. Boca Raton, CRC Press.
[9] Picart, L. and Cheftel, J.C. (2003).Pulsed electric fields. In *Food preservation techniques* ed. Zeuthen P. and Bogh-Sorensen L., 360-427. Boca Raton, CRC Press.

HIGH DENSE OZONE GENERATION AND THE SUPPLY SYSTEM FOR AGRICULTURAL SOIL STERILIZATION

Kenji Ebihara[1], Tomoaki Ikegami[1], Masahiro Takayama[1], Hideki Ishida[1], Takamasa Sakai[2], Yutaka Gyoutoku[3], Henryka D.Stryczewska[4]

1 Department of Electrical and Computer Engineering and Graduate School of Science and Technology, Kumamoto University,

Kurokami 2-39-1, Kumamoto 860-8555 Japan

2 Kumamoto Technology and Industry Foundation,

Tabaru 2081-01, Mashiki, Kamimashiki,Kumamoto 861-2202, Japan

3 Kumamoto Prefecture Agricultural Research Center, Sakae 3801, Goshi, Kikuchi,Kumamoto 861-1113,Japan

4 Faculty of Electrical Engineering and Computer Science ,

Lublin University of Technology, Nadobystrzyccka street 38A,20-618 Lublin,Poland

ABSTRACT. We have developed high dense ozone technology aiming the application to soil treatment. High dense ozone up to 100 g/m^3 was continuously and steadily generated by high frequency dielectric barrier discharges at ozone generation efficiency of 120 g/kWh. Pulsed high frequency power operated at 1kHz -30 kHz was applied between a screw-type cylindrical electrode (outer dia. 10mm) and the gold electrode coated on the quartz tube(inner dia.12mm). The electrode of axial length of 250mm was water-cooled in order to decrease the dissociation of ozone. Multi-channel electrode system consisting of several electrode elements was used to supply a large volume of high dense ozone to the agricultural soil.

1.INTRODUCTION

Development of environmentally benign alternatives to methyl bromide for soil fumigation has been required. Soil sterilization is a physical or chemical process that destroys or eliminates microorganisms, especially bacteria and virus. Many sterilization methods such as autoclaving (moist heat), dry heat, microwave irradiation, and γ-ray irradiation are currently used to kill or inhibit microbial activities in soil. Ozone made from stable molecular oxygen(O_2) is a strong oxidative and germicidal agent. The ozone has a very short half-life of minutes or less in soil and decomposes in simple diatomic oxygen. Ozone sterilization has also many benefits based on on-site generation, minimum human toxicity, low persistent chemicals in the soil. Current technology in ozone generation utilizes several techniques including electrical discharges, UV light irradiation and electrochemical reactions. In the electrical discharge approach, ozone is generated by many types of electric discharges such as dielectric barrier discharge, pulsed discharge, corona discharge and surface discharge.

We have studied the high dense ozone by high frequency dielectric barrier discharge and

developed the agricultural soil sterilization system consisting of ozone generator and multi-injection pipe system[1-3].

2.EXPERIMENTAL

Figure 1 shows a schematic diagram of the experimental setup which consists of the ozone generator , a pulsed high frequency power supply, and an ozone supply system for soil sterilization. A pulsed electric power was generated by the high frequency oscillator which operates at the continuous mode and the interval mode (frequency range:1kHz-30kHz, pulse rise time:5 μs, Vp-p:15kV, 4kW, PHF-4K,HAIDEN). The dielectric barrier discharge was produced between a screw-type cylindrical electrode (outer dia. 10mm) and the gold electrode coated on the quartz tube(inner dia.12mm). The electrode of axial length of 250mm was water-cooled in order to decrease the dissociation of ozone. Multi-channel electrode system consisting of the 4-5electrodes elements was used to supply a large volume of high dense ozone to the agricultural soil. Oxygen gas was introduced to the electrode at various flow rates. Wide range ozone concentration was measured using the UV ozone monitor (0-500ppm,1.00-200g/m^3,OZM-7000G, Iwasaki Electric Co.,Ltd). The electric power was estimated using the measured wave forms of the voltage and the current.

High dense ozone in gas phase was directly injected into the soil at a depth of about 70mm. The treated soil was typical agricultural soil in Kumamoto area named as “KUROBOKU”. The pH and electrical conductivity of the soil were measured while the ozone was supplied. Sterilization effect of ozone was evaluated several conventional methods such as the CFU(colony forming unit) counting and the soil contamination with root-knot nematode(M.incognita). We also observed the effect of ozone treatment on the agricultural plant growth.

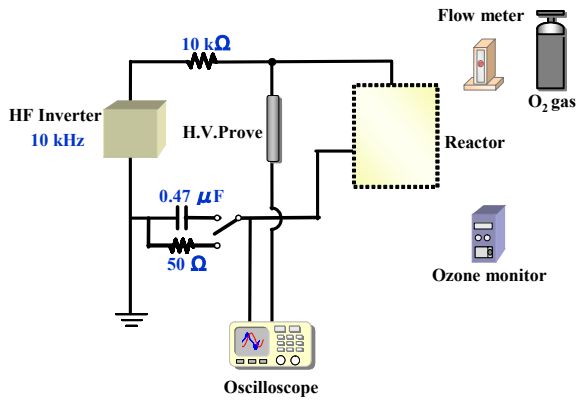

Figure 1.(a) Ozone generation system.

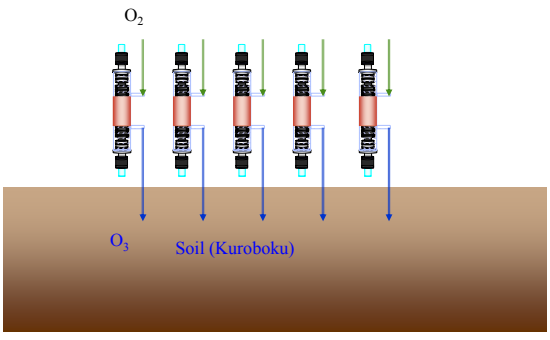

Figure 1.(b) Ozone supply reactor (multi-electrodes) for soil sterilization.

3.RESULTS AND DISCUSSION

Figure 2 shows ozone concentration as a function of applied voltages from 3.5 kV to 7kV at several O_2 flow rates. 10kHz continuous power was applied to a single electrode cooled at 15 °C. High dense ozone concentration of 106.1 g/m^3 was obtained at a low flow rate of 0.5 l/min. Ozone generation efficiency was a low value of 22.4g/kWh. When the flow rate is increased, the concentration decreases as known in many publications.

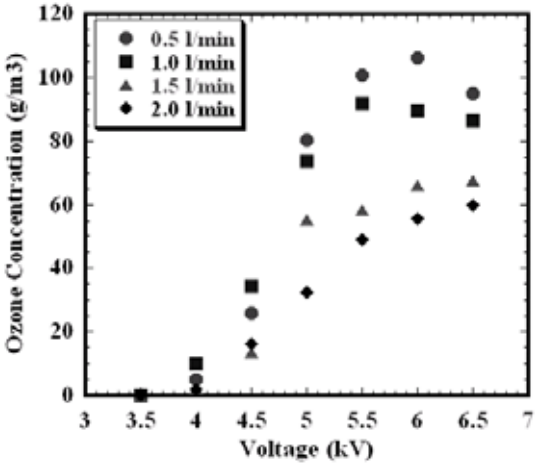

Figure 2. Ozone concentration of single electrode DBD at various O2 flow rate (10kHz).

Figure 3 shows the relationship between ozone generation efficiency and ozone concentration at various flow rates. Maximum efficiency of 53.5 g/kWh was obtained at 1.5 l/min. It is shown that the ozone generation efficiency decreases with decreasing flow rate.

In order to generate large volume of high dense ozone gas for soil sterilization, we used multi-electrode (four DBD tubes) in parallel connection as shown in Fig.1(b).

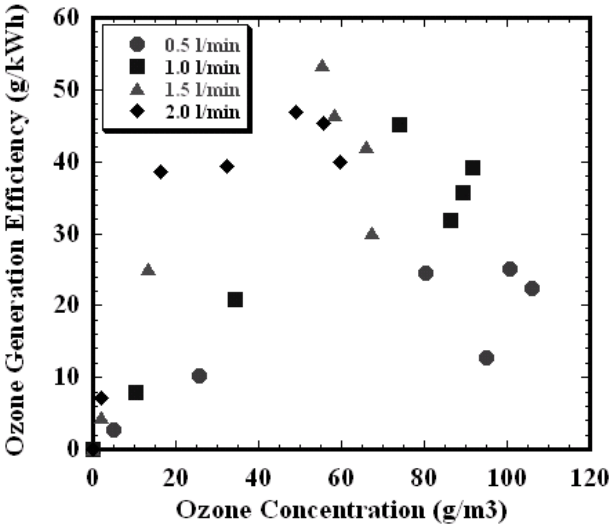

Figure 3. Relationship between ozone generation efficiency and ozone concentration for single DBD electrode. 10kHz.

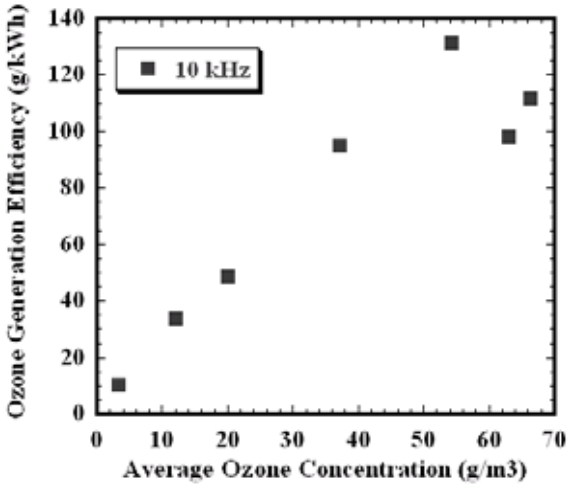

Figure 4. Relationship between ozone generation efficiency and ozone concentration for multi DBD electrodes. 10kHz.

Figure 4 shows total ozone generation efficiency as a function of averaged ozone concentration. The process conditions of 10kHz and 2 l/min (total 8 l/min) were used. When we operated each DBD electrode individually at same discharge conditions, maximum ozone concentration was in the range from 50.6 to 79.5 g/m^3. This figure indicates that the present four electrode parallel system can generate steadily a large volume of ozone gas of 8 liter/min containing around 60 g/m^3(0.3% O_3) .

This high dense ozone was injected into Kuroboku soil using multi-channel reactor (Fig.1b). The soil filled into the drain bed container (1200mmX900mmX500mm) was treated by ozone of concentration of 60 g/m^3 at a flow rate of 2.5 l/min. The young tomato seedlings were planted in the O_3 treated soil and the non-treated soil. We observed that the tomato stems planted in the O_3 treated soil can grow earlier than in the non-treated soil. The difference of the stem height became about 150mm after 35 days.

4. CONCLUSIONS

Ozone generation system suitable to soil sterilization was developed using pulsed high frequency power. High dense ozone of 100g/m^3 at 0.5 l/min and 60 g/m^3 at 2 l/min was attained for ozone treatment. Multi-channel DBD system can provide a large volume of high dense ozone(0.3% in O_2). The effect of ozone treatment on the plant growth was clearly confirmed.

ACKNOWLEDGMENT

This work have been supported by Research Project for utilizing Advanced Technologies in Agriculture, Forestry and Fisheries(the Ministry of Agriculture, Forest and Fisheries), and the Strategic Research Promotion Program of Information Technology of the Ministry of Internal Affairs and Communications.

REFERENCES

[1]Ebihara,E., Takayama,M.,Ikegami, T., Ogata,K. Stryczewska,H.D., Gyoutoku,Y., and Sakai,T.(2006),Development of agricultural soil sterilization using ozone generated by high frequency dielectric barrier discharge, J.Adv. Oxid. Technol. Vol.9,No.2(in print).

[2]Takayama, M.,Ebihara,E., Stryczewska,H.D., Ikegami,T., Gyoutoku,Y., Kubo,.K., Tachibana,M.(2005),Thin Solid Films,506-507,396-399.

[3]Ebihara,K., Takayama,M., Ikegami,T., Stryczewska,H.D., Gyoutoku,Y., Yokoyama,T., Gunjikake,N., Tachibana,M., Sakai,T.(2005), Proceedings of 17th International Symposium on Plasma Chemistry, Toronto, Canada,August 7th- 12th,CD(1201).

PLASMA WATER PURIFICATION BY DIELECTRIC BARRIER DISCHARGE IN MIXED STATE OF LIQUID AND GAS

H. Katayama, K. Yasuoka and S. Ishii

Department of Electrical and Electronic Engineering,
Tokyo Institute of Technology
2-12-1, Ookayama, Meguro-ku, Tokyo, 152-8552, JAPAN

ABSTRACT

Water treatment is studied using atmospheric dielectric barrier discharge in liquid-gas mixed states by bubbling the test water. In decolorization of Brilliant Blue, the maximum removal rate of 0.64 mg/min and removal efficiency of 9.0μg/J were obtained. The characteristic of color removal was strongly influenced by the volume balance of liquid and gas in the mixed state. In addition, the decomposition of acetic acid using pulsed barrier discharge was tested and the obtained removal efficiency was up to 7.4×10^{-10} mol/J.

1. INTRODUCTION

OH radicals have higher oxidation potential than that of ozone and are expected to be generated in water[1] for decomposition of persistent chemical substances such as dioxin.[2] As a candidate of plasma reactor for advanced oxidation system, we studied a DC driven micro hollow cathode discharge operated in water with fast flow of oxygen. The decomposition of the acetic acid that is a persistent substance as dioxin has been successfully demonstrated.[3] In this method, however, the area of contact surface between plasma and liquid is too small to treat a large amount of contaminated water. The OH radicals are generated in water by the following reaction : $O + H_2O \rightarrow 2OH$. The life time of OH radical is very short, so generated OH radicals need to be reacted with substances immediately. In this report, we proposed a new method using dielectric barrier discharge driven by pulsed power supply to enlarge the reaction area and to activate the reaction between plasma and treat water in a mixed state of liquid and gas generated by gas bubbles.

2. EXPERIMENTAL SETUP

The electrical circuit consists of a DC power supply, a thyratron switch, energy storage capacitor of 2nF and a plasma reactor. The pulse repetition rate is set at 200 Hz. The voltage applied to the reactor is measured using 1000:1 voltage probe (Tektronix P6015A) and the discharge current is measured using current transformer (Pearson Electronics Current Monitor 2100). The reactor schematics are shown in Fig.1. The reactors consist of an inner cylindrical glass which acts as electrode and bubbler (i.d. = 18 mm, o.d. = 22 mm) and an outer cylindrical glass which acts as electrode and vessel (i.d. = 26 mm, o.d. = 30 mm). One of two reactors has barriers with both sides of its electrodes (Fig.1 (a)) and the other has a barrier

only inside ground electrode. For convenience, we refer to each reactor in Fig.1 as double: D or single: S, respectively. The mixed state of liquid and gas is carried out by bubbling the treat water within the reactor.

Pure Oxygen gas (99.9 %) is fed through a mass flow controller into the treat water, dye aqueous solution colored by Brilliant Blue FCF ($C_{37}H_{34}N_2Na_2O_9S_3$) or acetic acid aqueous solution. Color removal is estimated from the concentration of Brilliant Blue FCF in water measured using the spectrophotometer, and the decomposition of acetic acid is obtained from TOC (Total Organic Carbon) reduction using TOC analyzer (Sievers 810).

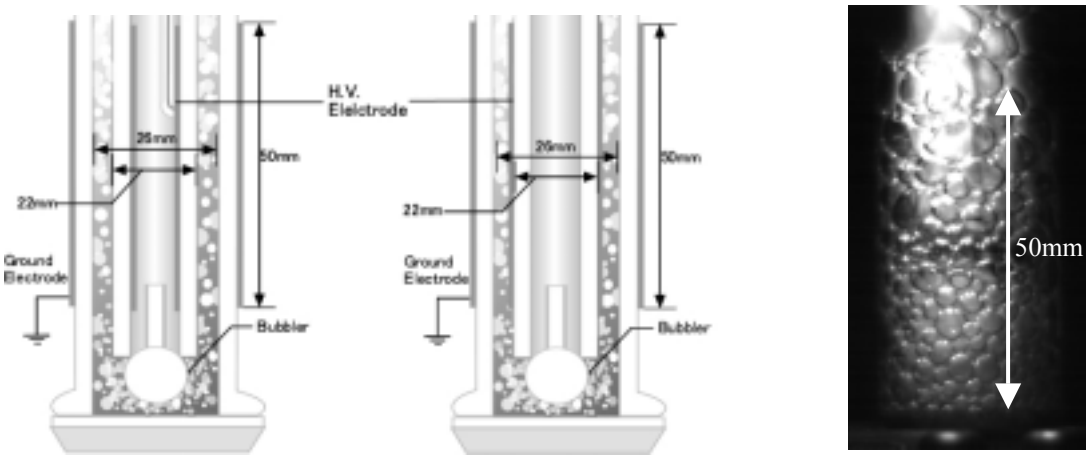

(a); Double barrier: D (b); Single barrier: S (c)

FIGURE 1. (a)**:** reactor D has barriers at both sides of the electrode and (b): reactor S has barrier only inside the ground electrode. Photograph (c) represents the aspect of bubble in the reactor taken by high speed camera.

3. RESULT AND DISCUSSION

Typical waveforms of discharge voltage and current in reactor D are shown in Fig.2. The applied voltage was changed from 16 kV to 22 kV. The total input energy in discharge was 3.8 ～ 7.8 mJ/pulse in reactor D, and 13.4 ～ 22.7 mJ/pulse in reactor S. The energy consumption in reactor S was larger than that in reactor D due to the larger discharge current: up to -40A at peak. That is because series capacitance of reactor S is larger than that of reactor D and the high voltage electrode is in contact with water.

Color removal characteristics and removal efficiency are shown in Fig.3. The initial concentration of Brilliant Blue FCF was 100mg/L, and the condition of liquid - gas mixed state was gas flow rate of 800sccm to test water amount of 10cc in each case. The decolorization percentage in reactor S was slightly higher than that in reactor D while the efficiency is higher in reactor D. This result suggests that a low-energy density operation with reactor D is suited for efficient decolorization.

The color removal and removal rate characteristics in different liquid-gas mixed states were shown in Fig.4. The gas flow rate against treat water amount was adjusted so that the bubbles covered the entire surface of electrode.

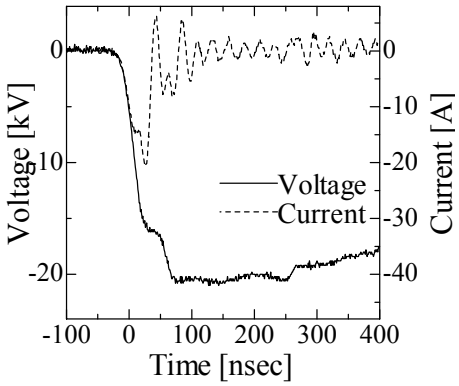

FIGURE 2. Typical wave form of voltage and current in case of reactor D. The gas flow rate is 800sccm to treat water amount of 10ml.

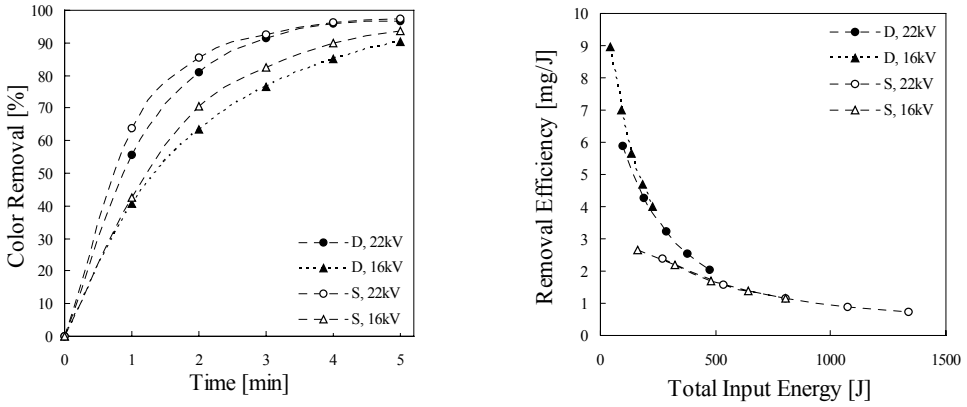

FIGURE 3. Comparison of Brilliant Blue FCF color removal characteristics (left) and removal efficiency (right) between reactor D and S in different voltages. The initial concentration of Brilliant Blue FCF is 100mg/L. The gas flow rate is 800sccm to treat water amount of 10cc in each case.

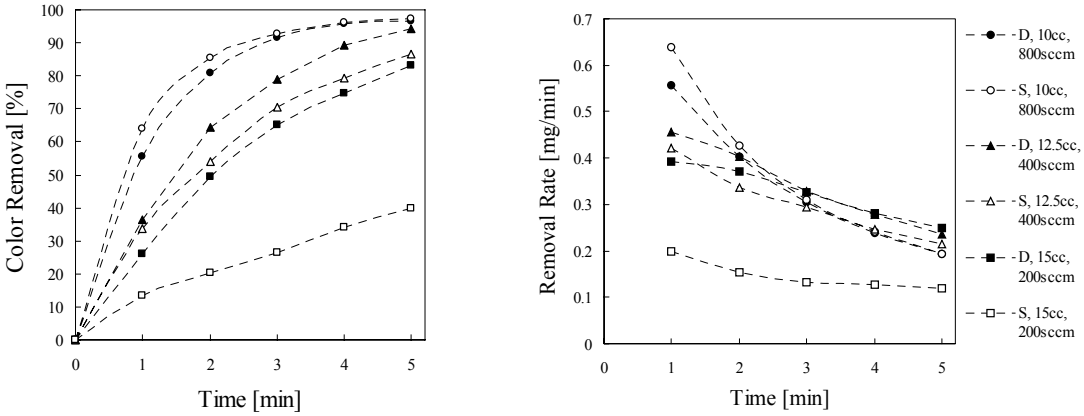

FIGURE 4. Comparison of color removal characteristics (left) and removal rate (right) in various liquid-gas mixed state. The initial concentration of Brilliant Blue FCF is 100 mg/L and the applied voltage is about 22 kV in each case.

For both reactors, the decolorization percentage decreased with increasing liquid volume to gas volume, especially at early stage of operations. This reduction was remarkable in reactor S at 15 cc, 200 sccm. At this condition, it seemed that gas breakdown didn't take place due to lack of successive bubbles or existence of liquid. Additionally, the major energy consumption in discharge was joule heating because the high voltage electrode directly contacted with water. Also color removal rate in reactor S became low along with increase of liquid volume while removal rate in reactor D showed similar characteristics in each condition. Consequently, it is possible to conclude that decolorization characteristics of reactor S depend on the volume balance between liquid and gas.

Fig.5 shows the decomposition characteristics of acetic acid at the conditions of applied voltage of 22 kV, the gas flow rate of 800sccm, treat water amount of 10cc. In this experiment, 50 % decomposition of acetic acid was achieved within 20 minutes using reactor S. As for the decolorization characteristics, higher decomposition was obtained with reactor S, but the efficiency was low. There were some differences between decomposition characteristics of acetic acid and organic dye. Especially, decomposition of acetic acid was only achieved when the gas volume was comparatively large against the liquid volume while color removal was confirmed in any conditions. For example, acetic acid was not decomposed at 400sccm to 12.5cc treat water. Take these results into consideration; it is supposed that the volume balance between liquid and gas has much effect on the decomposition characteristics of acetic acid. In other words, OH radical generation depends on the liquid-gas mixed state.

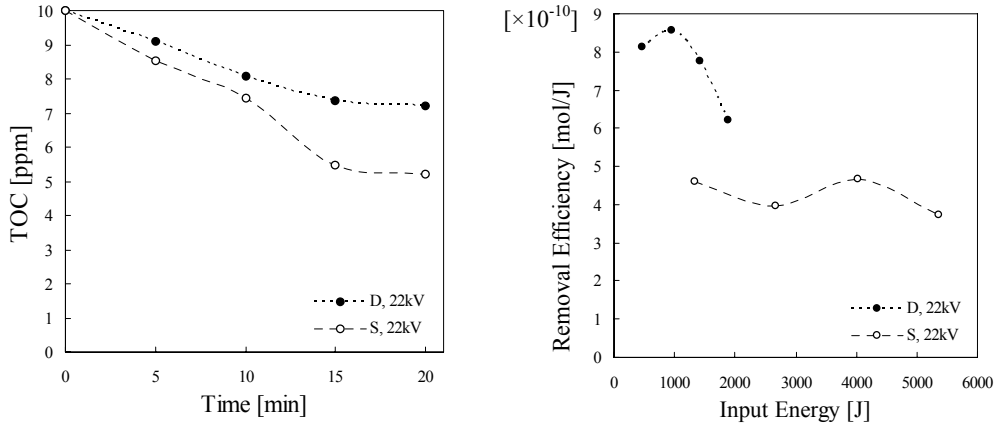

FIGURE 5. Decomposition characteristics of acetic acid (left) and removal efficiency (right) .The gas flow rate is 800sccm to treat water amount of 10cc in each case.

4. CONCLUSION

In this study, we have investigated the primary properties of a new method of water treatment using liquid and gas mixed state.

- The maximum decolorization efficiency was 9.0μg/J for Brilliant Blue FCF.
- 50% reduction of acetic acid solution of 10ppm was achieved at the removal efficiency of 7.4×10^{-10}mol/J.
- The removal efficiency of double barrier reactor D was higher than that of single barrier reactor S for all experimental conditions.
- The volume balance between liquid and gas is a crucial factor for the decomposition rate of acetic acid.

ACKNOWLEDGEMENT

This work was supported by grant-in-aids for Scientific Research form the Ministry of Education, Culture, Sports, Science and Technology, Japan.

REFERENCES

[1] T. Miichi, N. Hayashi, S. Ihara, S. Sato, and C. Yamabe, *Ozone - Sci. Eng.*, "Generation of Radicals using Discharge inside Bubbbles in Water for Waer Treatment", **24**, 471-477 (2002).

[2] F. Tochikubo, Y. Furuta, A. Uchida and T. Watanabe, *Jpn. J. App. Phys.,* "Study of Wastewater Treatment by OH radicals Using DC and Pulsed Corona Discharge over Water", **45**, 2743-2748 (2006).

[3] Atsushi Yamatake, Koichi Yasuoka, Shozo Ishii. *Jpn. J. Appl. Phys.,* "Ozone Generation by a DC Driven Micro-Hollow Cathode Discharge in Nitrogen-Mixed Oxygen Flow", **43**, 6381-6384 (2004)

SPME ANALYSIS OF VOC DESTRUCTION PRODUCTS – ATMOSPHERIC PRESSURE DISCHARGE

H. Grossmannova[1], M. Ciganek[2], J. Prochazkova[1] and F. Krcma[1]

[1] *Faculty of Chemistry, Brno University of Technology, Purkynova 118, Brno, CZECH REPUBLIC*
[2] *Veterinary Research Institute, Hudcova 70, Brno, CZECH REPUBLIC*

ABSTRACT. The aim of this experiment was to elaborate the issue of applicability of the solid phase microextraction (SPME) in the analysis of volatile organic compounds (VOCs) destruction products in the gliding arc discharge. Maximal conversion of 97 % was achieved at the oxygen content in carrier gas of 60 %. Tens of various high-molecular substances were observed, especially a large number of oxygenous compounds and further several nitrogenous and CH compounds. The concentrations of various generated species strongly depend on the gas mixture composition. Experimental data demonstrated that it is necessary to use several SPME fibers for full-scale high-molecular products analysis. The DVB/CAR/PDMS fiber is recommended especially when the destruction is done in the oxygen rich atmosphere. The plasma conditions during the destruction were monitored by the optical emission spectroscopy.

1. INTRODUCTION

VOCs are organic chemical compounds that have high enough vapour pressures under normal conditions to significantly vaporize and enter the atmosphere. VOCs are sometimes accidentally released from the exhaust of industrial processes and motor vehicles into the environment contribute strongly to air pollution causing photochemical smog, enhancement of the greenhouse effect and destruction of the ozone layer as well as they can become soil and groundwater contaminants. In recent years, insist on the quality of indoor environment as well. Common artificial sources of VOCs include paint thinners, strippers, wood preservatives and dry cleaning solvents. Regarding the medical risks, it is known that many VOCs are toxic, several of them are known as human carcinogens. Conventional techniques for the abatement of VOCs (volatile organic compounds), such as thermal and catalytic oxidation are widely spread techniques. They are known for their ability of total destruction but they suffer from low energy efficiency given the high operating temperatures. Technologies based on non-thermal plasmas could offer an alternative and they are capable of removal of various pollutants [1]. Moreover, undesirable toxic by-products can be formed. Gliding arc discharge (GlidArc) is an interesting possibility to generate a nonthermal plasma discharge at the atmospheric pressure [2]. Toluene is used for experiments as a model compound. By-products are sampled by SPME and analysed by gas chromatograph linked to mass spectrometer. The first part of our experiments was focused on the analysis of the high-molecular discharge products and secondarily on the optical emission spectroscopy measurements. We tested the SPME (solid phase microextraction) technique suitability for the discharge exhausts gas analysis and if this technique can be used efficiently in the field to extract VOCs by-products.

2. EXPERIMENT

The GlidArc is a well-known kind of the plasma discharge. Our plasma reactor consists of a single pair of diverging knife-shaped copper electrodes (thickness 1 mm, size 60 mm x 40 mm each), whose minimal distance is 0,6 mm. Electrodes are positioned in the fast gas flow. The applied DC voltage during our experiments was from 3,5 kV up to 4,5 kV with the discharge current of 35 mA. Gliding arc discharge was created in various gas mixtures of nitrogen, oxygen and argon at the atmospheric pressure. Just before entering the reactor, carrier gas was enriched by toluene, which was chosen as the model VOC. The gas mixture flow rate was 2 800ml/min. The details of the experimental setup are on the figure 1.

Samples were taken with SPME (Solid Phase Microextraction) fiber, in the concrete CW/DVB (Carbowax/divinylbenzene) recommended for alcohols and polar compounds and second CAR/PDMS/DVB (Carboxen/polydimethylsiloxane/divinylbenzene) used for low molecular compound sampling. SPME is a relatively new and attractive alternative sampling method [3]. The principle of SPME is an equilibrium partitioning of the analyte between the coating fiber and the solution or the headspace. This technique is powerful for trace analysis of organic pollutants in the environment. For quantitative analysis, it is very important to explore the dependence of the analyte mass in the fiber as a function of the extraction time. The GC/MS separation was performed in a CP-SELECT 624 CB fused silica capillary column. For the identification of reaction products an ion trap mass spectrometer (Saturn 2100, Varian) was used.

3. RESULTS

3.1. High-molecular products analysis

The areas of total absorbed high-molecular products of the toluene destruction in the nitrogen – oxygen gas mixture (21% O_2) are given in the fig. 2. We observed tens of various compounds, especially a large number of oxygenous compounds and further several nitrogenous and C_xH_y compounds. The main products of this treatment are benzaldehyde, phenol and benzyl alcohol. Increasing content of oxygen gives rise to the formation of oxidation products, the most abundant being benzaldehyde, obtained by many process, in all probability by oxidation of toluene, phenol - can be made from the partial oxidation of benzene, benzyl alcohol or benzeneacetaldehyde.

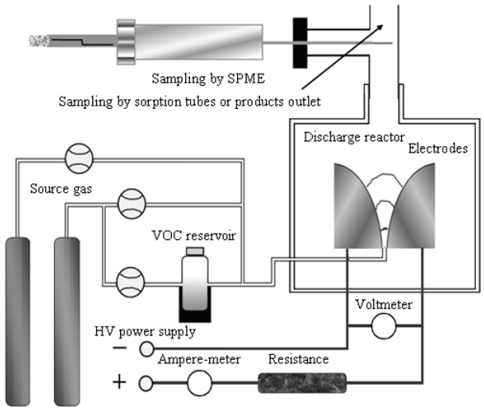

FIGURE 1. Schematic experimental setup of apparatus as configured for measurements and collection of exhaust products.

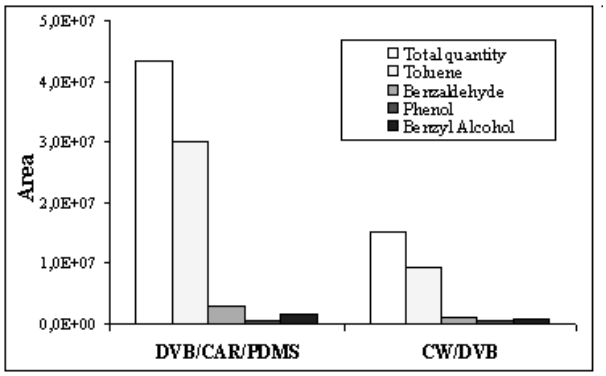

FIGURE 2. Carrier gas nitrogen, total gas flow 2800 ml/min, applied voltage 4 kV, current 35 mA, sampling time 2 min.

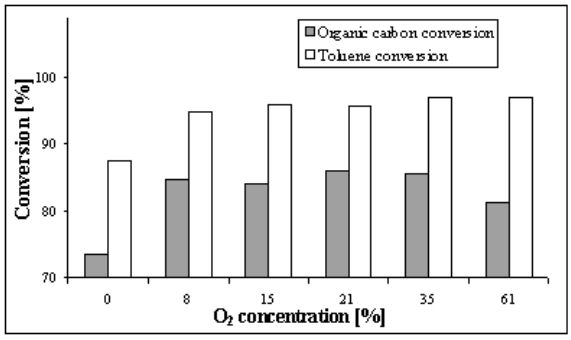

FIGURE 3. Conversion as the function of oxygen concentration, sampling time 5 min.

Apparently, almost 69 % of total absorbed amount on the fiber is still unexpanded toluene. The main nitrogenous products were nitropropanetriol and 1-nitro-2-methylpropane. We also remarked some significant C_xH_y products like ethylbenzene, which should be produced by combining the benzene and ethylene, styrene (commonly produced by catalytic dehydrogenation of the ethylbenzene) and bibenzyl, obviously the toluene dehydrocoupled product. Figure 3 presents the results of the final organic carbon conversion and toluene conversion, sampled by CW/DVB fiber. These results showed that the highest removal efficiency for toluene is obtained for the experiments with 61 % of oxygen in carrier gas. With raising concentration of O_2 in gas flow, toluene conversion is increasing up to 97 %. On the other side, if we assume that almost all organic by-products are extracted by the fiber, the highest organic carbon conversion is 87 %, it is achieved with the 21 % of O_2 in carrier gas.

3.2. Optical measurements

The spectrum of OH radical was used for the calculation of the discharge rotational temperature. The rotational line intensities from 0-0 transition of the OH (A-X) system (lines J = 5/2, 9/2, 11/2, 13/2) and the rotational constant given by NIST [4] were used for the rotational temperature calculation. Figure 4 presents dependencies of rotational temperature on O_2 flow for OH radicals measuring. It seems that the dependence obtained without toluene is almost independent on the O_2 flow, the other mixture with toluene gives the increasing character (rotational temperature increases with the increasing O_2 content). We also observed that relative emission intensity for NO radical with toluene and without toluene, respectively (see fig. 5). Both dependences of relative emission intensities on O_2 flow have the similar decreasing character.

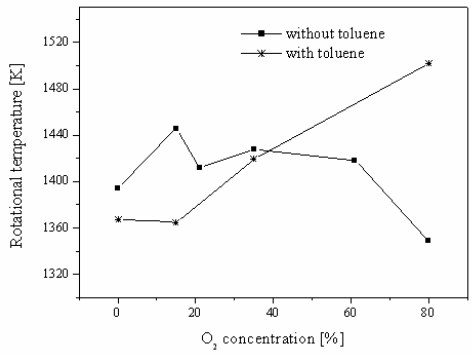

FIGURE 4. Rotational temperatures calculated from the OH radical spectrum.

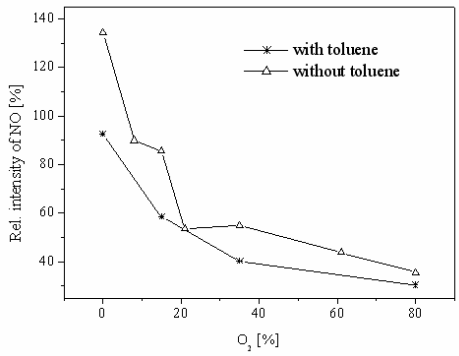

FIGURE 5. NO radical relative emission intensity

We also observed the influence of the input voltage (3,5 kV up to 4,5 kV) on the relative emission intensity of two OH and N_2 species. In both cases, the emission intensity slightly increased {44 a.u. - 46 a.u.} for N_2 and {134 a.u. - 147 a.u.} for OH with the increasing input voltage.

4. CONCLUSION

The presented work gives the results about applicability of the solid phase microextraction in the analysis of volatile organic compounds destruction in the non-thermal plasma. The concentrations of various generated compounds strongly depend on the gas mixture composition. The results showed that CW/DVB fiber can extract more products independently on the used VOC compound. With the insreasing ratio of oxygen in the carrier gas a slight decline of C_xH_y compounds amount, distinctive increasing of oxygenous compounds amount and exiguous growth of nitrogenous compounds have been observed. Optical emission spectroscopy measurements offer an interesting results dealing with plasma condition and active species created in plasma. Future experiments will be concerned with the low-molecular products analyses.

ACKNOWLEDGMENTS

This work was supported by Czech Ministry of Education, project No. 3218/2005, by the Czech Science Foundation, contract No. 202/03/H162 and partially by the Czech Ministry of Agriculture, grant No. MZE 0002716201.

REFERENCES

[1] Kim, H.H. (2004). Nonthermal plasma processing for Air-pollution control: A historical review. current issues, and future prospects. *Plasma Proc. Polymers,* 2, 91-110.
[2] Czernichowski, A., Ranaivosolarimanana, A. (1996). Zapping VOCs with a discontinuous electric arc. *Chem. Tech.,* 26, 45-49.
[3] Supelco. Bellefonte (1999). Solid Phase Microextraction. *Sigma-Aldrich Co.*, 923A.
[4] Talrose, V., Yermakov, A.N., Usov, A.A., et al., UV/Visible Spectra. In. Linstrom, P.J., W.G. Mallard, NIST Chemistry WebBook, (on-line).

REMOVAL OF COD AND COLOR USING ELECTRICAL DISCHARGE IN FOAMING COLUMN

J. Pawłat[1], S. Ihara[2]

[1]*Graduate School of IPS, Waseda University*
808-0135 Fukuoka ken, Kitakyushu-shi, Wakamatsu-ku, 2-7 Hibikino, Japan
[2]*School of Science and Engineering, Saga University*
840-8502 Saga ken, Saga-shi, 1 Honjo-machi, Japan

ABSTRACT. The influence of electrical discharge on the removal of ethyl violet and methylene blue in the foaming apparatus was observed. Discoloration was observed visually and concentration of pollutants was measured. Average 80 % removal efficiency was achieved after 30 min treatment in oxygen.

1. INTRODUCTION

In this paper, the experiments of removal of ethyl violet (EV) and methylene blue (MB) by the electrical discharge within foam are reported. Foam, in its dynamic flow state, consisting of the huge amount of gas in the liquid matrix might be formed with the addition of surface active components or without any foamable additives but in a strict gas flow regime using the diffusers. The theoretical aspects of foam formation and drainage are already widely known [1]. After first reports about the phenomenon of electrical discharge in foaming environment using the Blumlein pulse power source [2, 3], the possible applications and advantages for environmental techniques were suggested [4-7]. The electrical discharge in the foaming column caused formation of various oxidants, which can be directly applied to treat pollutants in gaseous or liquid phase introduced to the reactor. That allows to construct small, compact apparatus and to avoid loses of oxidants during the transportation process.

2. EXPERIMENTAL SET-UP

The main reactor of the foaming system, which is depicted in Fig. 1A, was a cylindrical, polyacrylate column. A ceramic diffuser was placed perpendicularly to the flow direction of media. The central HV electrode was placed inside the inner grounded electrode in homogenous foam zone, above the diffuser. The electrical circuit is shown in Fig. 1B. The pulse power source was operated at 30 Hz. The discharge voltage and current were measured using the high voltage probe and the Rogowski coil, respectively with an oscilloscope. The photo of apparatus filled with EV foam is presented in Fig. 1C. Average diameter of single bubble in foam ranged from 1 mm to 5 mm. It was not possible to obtain totally uniform discharge within foam.

[1]Electronic address: askmik@hotmail.com

The oscillograms of the discharge in EV foam are presented in Fig. 1D.

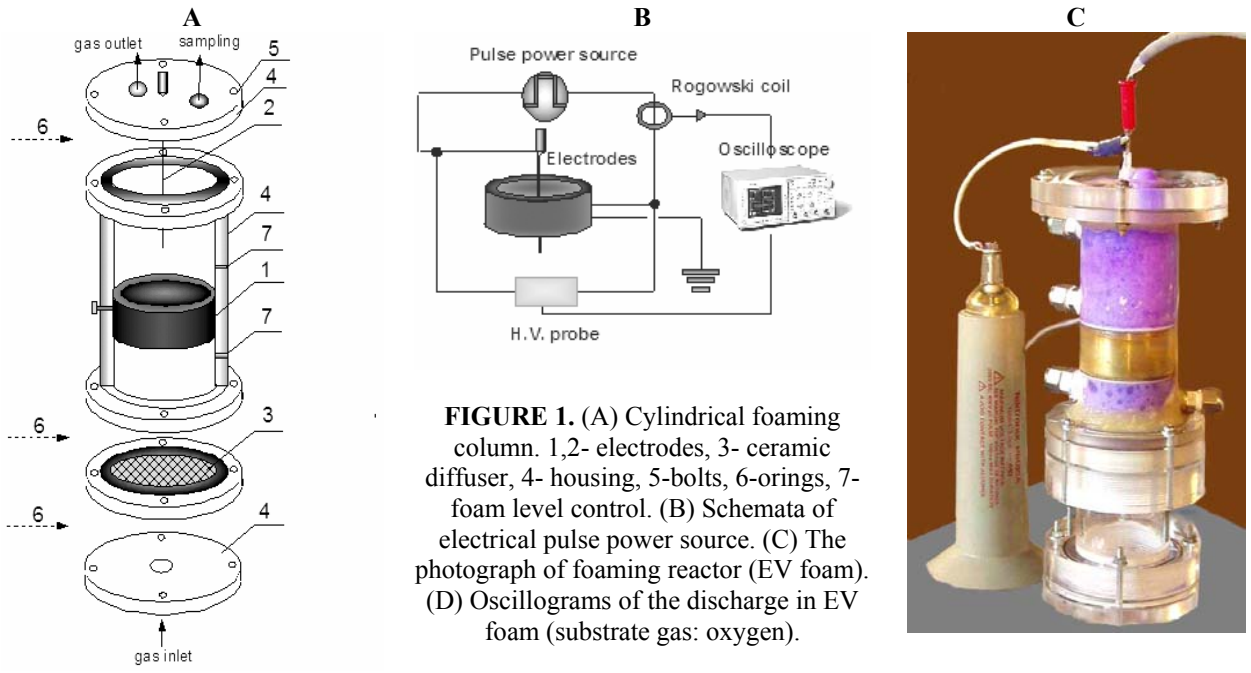

FIGURE 1. (A) Cylindrical foaming column. 1,2- electrodes, 3- ceramic diffuser, 4- housing, 5-bolts, 6-orings, 7- foam level control. (B) Schemata of electrical pulse power source. (C) The photograph of foaming reactor (EV foam). (D) Oscillograms of the discharge in EV foam (substrate gas: oxygen).

3. RESULTS AND DISCUSSION

Ethyl violet (basic violet 4, $C_{31}H_{42}N_3Cl$), which molecular stucture is presented in Fig. 2 has been recommended for inclusion in mixed dye solutions of the iron resorcin fuchsin type for demonstrating elastic fibers [8]. It is also used as an indicator in chemical and medical industry.

EV is a green crystalline powder, which colors water solutions in persistent, very deep purple. In the performed investigations pure water was mixed with EV to obtain 0.034 g/l solution.17 ml of this highly foamable substrate liquid was dosed to the reactor. The flow rate of substrate gases: oxygen and air ranged 0.3 l/min. The measurements of the UV absorbance to confirm EV removal were performed using HACH spectrometer. Typical absorbance curve of $C_{31}H_{42}N_3Cl$ is shown in Fig. 3. The highest light absorption peak of EV at the wavelength of 596 nm was analyzed for a various treatment times. The EV decomposition during the application of the

electrical discharge within foam was observed also visually. For 30 minutes treatment time ethyl violet removal rate ranged 81% and 71% in oxygen and air, respectively (Fig. 4). 58% reduction was observed after 30 min treatment of dodecyl surfactant and EV residues (Fig. 5) in oxygen.

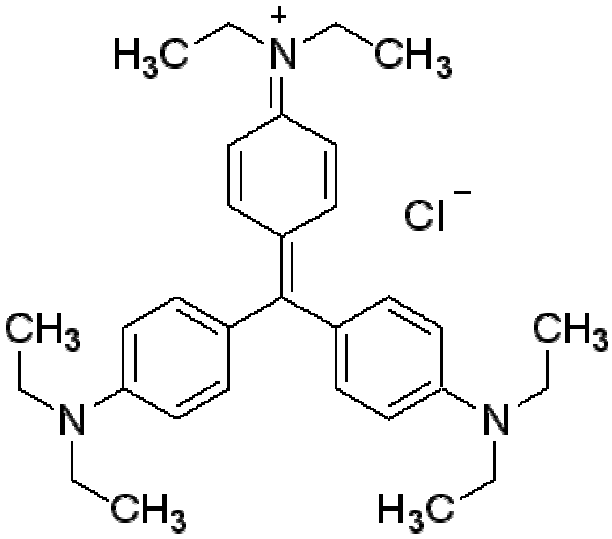

FIGURE 2. Ethyl violet.

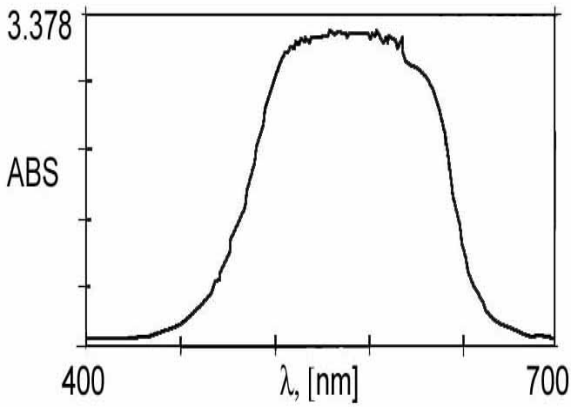

FIGURE 3. Absorbance of EV solution

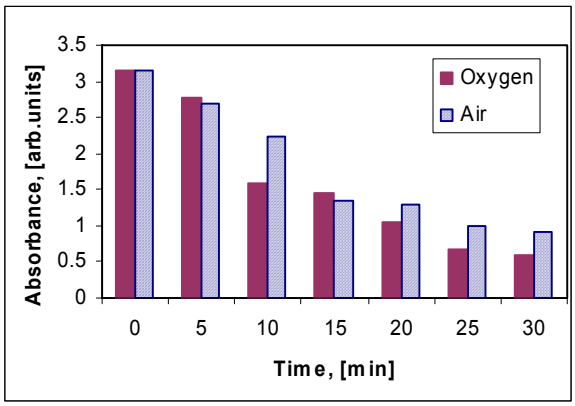

FIGURE 4. Removal of ethyl violet.

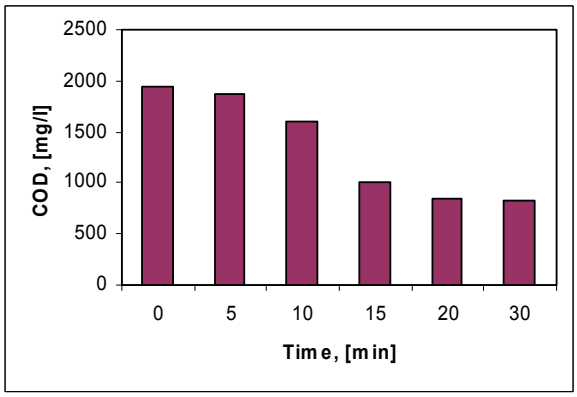

FIGURE 5. COD removal (dodecyl solution and ethyl violet, substrate gas- oxygen).

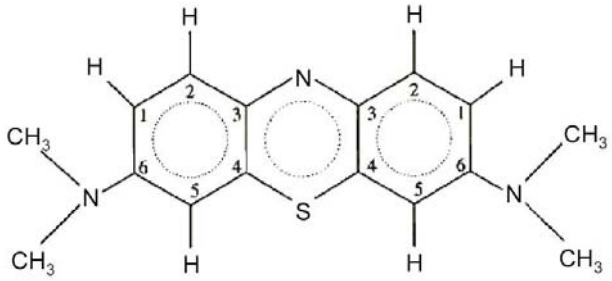

FIGURE 6. Methylene blue

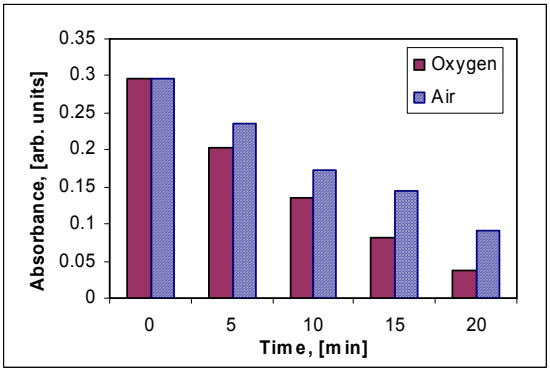

FIGURE 7. Removal of methylene blue.

The process of decomposition of methylene blue, toxic halogenated aromatic hydrocarbon was studied. MB ($C_{16}H_{18}N_3ClS$) is an odorless, green crystalline powder, soluble in water. This member of the thiazine dye group is often applied as a test model pollutant in semiconductor photocatalysis [9]. It participates in the transport of oxygen in blood and it is also used as a dye to stain certain parts of the body before or during surgery. The catalyst supported oxidization of the MB was found difficult, if only ozone was used [10]. The molecule of methylene blue is depicted in Fig.6. 60 ml of 35 mg/l solution was used as a substrate liquid. Gas flow rate was 4.5 l/min. Analyzed UV absorption (550-665 nm) decreased constantly with time as it is presented in Fig. 7. After 20 min treatment 88% removal efficiency was achieved in oxygen and 69% in air.
The color removal process took less time when the higher discharge frequencies were applied.

4. CONCLUSIONS

An apparatus based on the discharge in the foam was designed.
81% removal rate of ethyl violet was achieved after 30 min treatment in oxygen.
Removal rate of methylene blue ranged 88% in oxygen after 20 min treatment.

ACKNOWLEDGEMENT

Authors would like to thank to Professor Chobei Yamabe and Professor Toshitsugu Ueda for fruitful advices and help during research work.

REFERENCES

[1] Bistron S., Sarre P., Szymonik B. (1978). Nowy sposób prowadzenia procesów w pianie dynamicznej (in Polish). *Chemik 3,* 81-83.
[2] Pawłat J., Hayashi N., Yamabe C. (2001). Studies on electrical discharge effects in a foaming environment. *Jap. J. Appl. Phys., 40 (12),* 7061-7066.
[3] Pawłat J., Hayashi N., Ihara S., Yamabe C., Pollo I. (2003). Generation of Discharges in Dynamic Foam for Oxidants Formation Using Various Types of Electrodes. *J. Colloids A, 220,* 179-190.
[4] Pawłat J., Hensel K., Yamabe C. (2004). Discoloration of the Solutions in the Foaming Environment. *Czech. JPhys. 54 Suppl.C SPPT*, 332_1.
[5] Pawłat J., Ihara S., Yamabe C., Pollo I. (2005). Oxidant Formation and the Decomposition of Organic Compounds in Foaming Systems. *Plasma Process. Polym, 2(3),* 218–221.
[6] Pawłat J. (2005). Various Environmental Applications of the Cylindrical Foaming Column. *Przeglad Elektrotechniczny (Poland), 1.*
[7] Pawłat J., Hensel K., Ihara S. (2005). Decomposition of Humic Acid and Methylene Blue by Electric Discharge in Foam. *Acta Phys. Slovaca, 55(5),* 479-485.
[8] Adam B., Gorenc B., Gorenc D. (1988). Triphenylmethane dyes as reagents for extractive – spectrophotometric determination of anionic surfactants. *Acta Chimica Slovenica, 35*, 339-350.
[9] Lee S., Mills A. (2003). Novel photochemistry of leuco-Methylene Blue. *Chem. Commun. The Royal Society of Chemistry, 8*, 2366–2367,.
[10] Randorn C., Wongnawa S., Boonsin P. (2004). Bleaching of Methylene Blue by Hydrated Titanium Dioxide *Sci. Asia 30,* 149-156.

CONVERSION OF NITROUS OXIDE BY PULSED CORONA DISCHARGE

K. Schmidt-Szałowski and K. Krawczyk

Warsaw University of Technology, Faculty of Chemistry
ul. Noakowskiego 3, 00-664 Warszawa, POLAND

ABSTRACT. The conversion of nitrous oxide was examined applying pulsed corona discharges in N_2O+Ar+O_2 mixtures using two reactors with different length of the discharge zone. The highest overall conversion of nitrous oxide was 74.4%.

1. INTRODUCTION

In recent years attempts have been made to reduce the emission of particularly stable chemical compounds by the use of non-equilibrium plasma. The pulsed corona discharge (PCD) is used for one of those technologies based on non-equilibrium plasma. Compared to the DC and AC coronas as well as barrier discharges, pulsed corona discharge is more energy efficient because most of the energy supplied is consumed for initiating the chemical transformations and to a minor degree dissipated resulting in gas heating. It was found that the filling of the reaction space with plasma in PCD is higher than that in DC and AC coronas.

The corona discharge is formed in a system with a strongly inhomogeneous electric field. The ionic and excited atomic or molecular species produced in the discharge zone initiate chemical reactions. The main parameters of pulsed corona discharge are the time of the current rise and the maximum level of current and voltage. They strongly depend on the electrode geometry and on the kind of gas [1]. Plasmas of the pulsed corona discharges were used for the removal of a number of pollutants e.g. nitric oxide and sulphur dioxide [2-4], N_2O [5], volatile organic compounds [6,7], as well as for the dehydrogenation of ethane [8] and for water cleaning [9].

The aim of this work was to study of the efficiency of N_2O conversion to NO and to elements in pulsed corona discharges taking into account the effect of the reactor length on the plasma process. The experiments were carried out using N_2O+Ar+O_2 mixtures in a wide range of nitrous oxide concentrations.

2. EXPERIMENTAL

The conversion of nitrous oxide in the pulsed corona was studied using two reactors:

1. Stainless-steel corona reactor with the inner high voltage electrode made of metal wire. The stainless steal tube, 38 mm in diameter, was the outer electrode. The length of the active zone was 0.75 m.
2. Stainless-steel reactor like no. 1 with length of active zone 0.45 m.

The temperature of the gas inside the reactor was about 25-40 ^{o}C. Experiments were carried out at atmospheric pressure using the N_2O+Ar+O_2 mixtures with the initial concentration of nitrous oxide from 1 to 10% by vol. The overall gas flow rate was kept constant (20 Nl/h).

Electronic address: kraw@ch.pw.edu.pl

The reactors were powered by a pulsed electric system (Fig. 1). Electric parameters, (voltage and current) were measured using Tektronix TDS 3032 with a high voltage probe and Rogowsky's coil. The maximum power of the single pulse ($0.4\text{-}0.8*10^6$W) was calculated as a product of maximum voltage and current. Pulses of about 100 ns duration (current) of the frequency of 250-450 Hz, were applied. The discharge zone was recorded by camera. The contents of nitrous oxide in the inlet and outlet streams were determined by gas chromatography using a column filled with Porapak Q. The concentration of NO in the outlet gas was determined by the volumetric-gravimetric method.

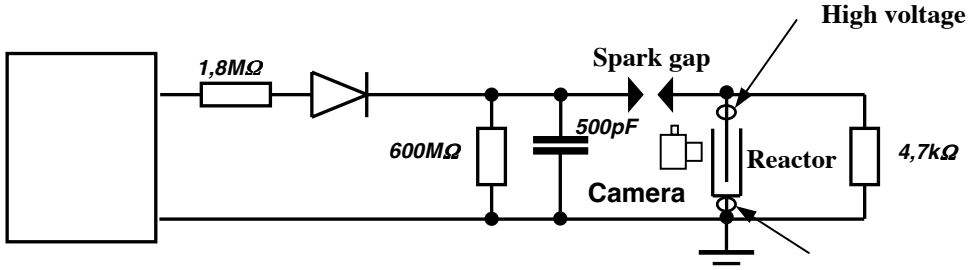

FIGURE 1. Experimental set-up

3. RESULTS AND DISCUSSION

A high overall conversion of nitrous oxide (to elements and to NO) up to 74.4% was observed in the gas mixture $Ar+O_2(5\%)+N_2O(1\%)$ using the reactor (1) (active zone 0.75 m) (Fig. 2, curve 1). For the N_2O concentration lower than 1%, the pulse corona discharge (Figs. 3A and 4A) was unstable and changes into a spark discharge (Figs. 3B and 4B). In the spark discharge the nitrous oxide conversion dropped to zero. The pulse frequency was about 5 sec^{-1}. In the reactor (2) (length of 0.45 m) in similar gas mixtures ($Ar+O_2(5\%)+N_2O$) the spark discharge appeared for higher nitrous oxide concentration than in reactor (1). The energy of single pulse and the pulse repetition were similar in both reactors, however, the density of energy in reactor (2) was higher than that in reactor (1).

A conclusion can be drawn that the pulsed corona discharge can be useful for the destruction of nitrous oxide in waste gases. As has been observed, the conversion of N_2O depends on its concentration in the inlet gas, and on the construction of the discharge zone. A high overall conversion of N_2O (to elements and NO) up to 74.4% was recorded, whereas the conversion into NO did not exceed 2.5%. However, the pulsed corona discharge may be unstable changing into a spark discharge when N_2O concentration is low.

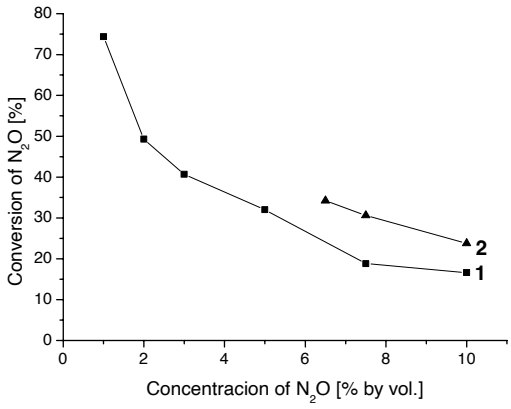

FIGURE 2. Influence of initial concentration of nitrous oxide on the conversion of N_2O. Carrier gas- argon + oxygen (5% by vol.). 1- reactor with the length of the active zone 0.75 m, 2 - reactor with the length of active

zone 0.45 m.

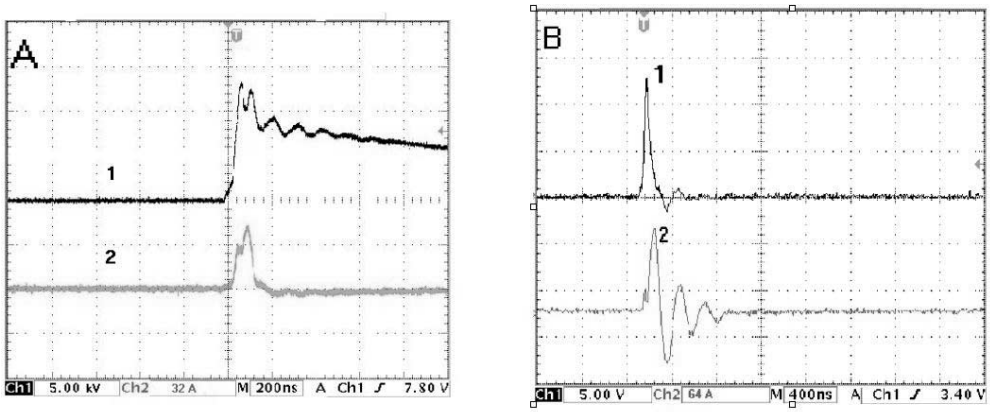

FIGURE 3. Typical waveform of voltage (1) and current (2) for pulsed corona discharge (A) and spark discharge (B)

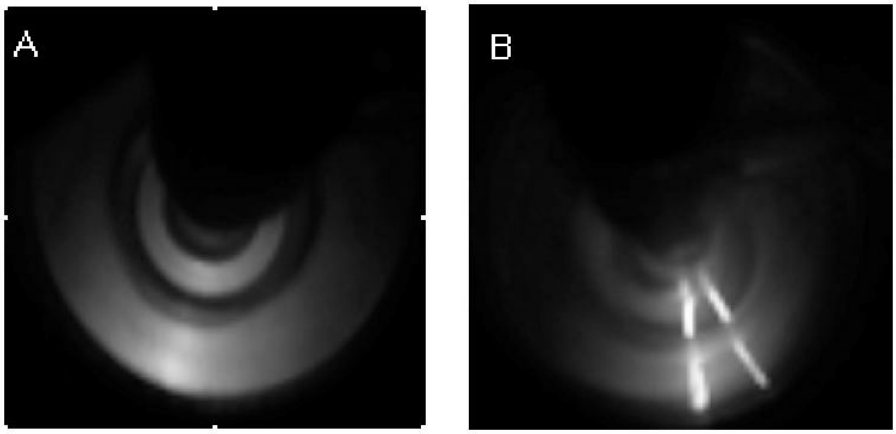

FIGURE 4. Examples of pulsed corona discharge (A) and spark discharge (B)

ACKNOWLEDGMENT

This work was supported by The Ministry of Scientific Research and Information Technology: grant No. 3 T09B 044 26.

REFERENCES

[1] Veldhuizen, E.M. (2003). Pulsed corona discharges: Fundamentals and environmental applications. *Proc. 16th Int. Symp. on Plasma Chemistry*. Pdf no. 821.

[2] Mok, Y.S., Nam, I-S. (2002). Modeling of pulsed discharge process for the removal of nitric oxide and sulphur dioxide. *Chem. Eng. J.*, 85, 87-97.

[3] Dors, M., Czech, T., Mizeraczyk, J., Cortiana A., Rea, M. (1996). NO_x removal from flue gases during corona discharge in a wet electrostatic precipitator. *Ochrona Środowiska*, 63, 7-12.

[4] Pollo, I., Rea, M., Wroński, M. (1996). Gaseous pollutants removal from waste gases using pulse corona discharges. *Chemia i inżynieria ekologiczna*, 3, 431-441.

[5] Hu, X., Nicholas, J., Zhang, J-J., Linjewile, T.M., Filippis, P., Agarwal, P.K. (2002). The destruction of N_2O in a pulsed corona discharge reactor. *Fuel*, 81, 1259-1268.

[6] Penetrante, B.M., Hsiao, M.C., Bardsley, J.N., Merritt, B.T., Vogtlin, G.E., Kuthi, A.,

Burkhart, C.P., Bayless, J.R. (1997). Decomposition of methylene chloride by electron beam and pulsed corona processing. *Physics Letters A*, 235, 76-82.
[7] Nifuku, M., Horvath, M., Bodnar, J., Zhang, G., Tanaka, T., Kiss, E., Woynarovich, G., Katoh, H. (1997). A study on the decomposition of volatile organic compounds by pulse corona. *J. of Electrostatics*, 40&41, 687-692.
[8] Zhang, X., Zhu, A., Li, X., Gong, W. (2004). Oxidative dehydrogenation of ethane with CO_2 over catalyst under pulse corona plasma. *Cat. Today*, 89, 83-89.
[9] Grabowski, L., Veldhuizen, E.M., Pemen, A. J. M., Rutgers, W.R. (2003). Water cleaning in a heterogeneous pulsed corona reactor. *Proc. 16th Int. Symp. on Plasma Chemistry*. Pdf no. 518.

CO OXIDATION USING ATMOSPHERIC NONTHERMAL PLASMA-DRIVEN CATALYSIS

H. H. Kim[1], S. Tsubota[2], M. Date[1], A. Ogata[1], and S. Futamura[1]

[1] *National Institute of Advanced Industrial Science and Technology (AIST)*

16-1 Onogawa, Tsukuba 305-8569, JAPAN

[2] *National Institute of Advanced Industrial Science and Technology (AIST)*

1-8-31Midorigaoka Ikeda, Osaka 563-8577, JAPAN

ABSTRACT. In this work, the oxidation of 1000 ppm CO was investigated using plasma-driven catalysis at atmospheric pressure and room temperature. We focused on the direct combination of nonthermal plasma with nanometer-sized gold (Au) catalyst supported on TiO_2 by a deposition-precipitation method. Application of nonthermal plasma greatly enhanced the CO oxidation using the used Au/TiO_2 catalysts, which have completely lost its catalytic activity. Oxygen plasma was found to be effective in the regeneration of the used Au/TiO_2 catalysts.

1. INTRODUCTION

There have been extensive research efforts on the application of nonthermal plasma (NTP) for the removal of various air pollutants such as NOx, SOx, odors, and volatile organic compounds (VOCs). The application fields of NTP for the control of air pollution include mobile source (i.e. cars) as well as small to large scale stationary sources. The combination of nonthermal with catalysts is currently the subject of increasing attention because this combination can achieve the enhancement of energy efficiency and the reduction of harmful byproduct formation at the same time [1, 2].

In this work, the oxidation of CO was investigated using nanometer-sized gold (Au) catalyst, which is well-known catalyst for the oxidation of CO at low temperature even below 0^oC [3-5]. The Au/TiO_2 catalysts were prepared by two different methods of deposition-precipitation and impregnation. The establishment of effective control method of CO has two important meanings in the NTP application for air pollution control. One is the abatement of CO simply as a toxic air pollutant. The other point is the control of product selectivity in the decomposition of VOCs using nonthermal plasma technology. Since the CO is hardly oxidized by gas-phase radical reactions, it is usually hard to remove CO via oxidation pathways to CO_2 using the NTP alone. One of the main purposes of this work is the influence of the NTP on the used Au/TiO_2 catalyst, which lost initial catalytic activity for the oxidation of CO. We also focused on the regeneration of the used Au/TiO_2 catalyst using oxygen plasma.

2. EXPERIMENTAL

2.1 Experimental Setup

Figure 1 shows the schematic diagram of the plasma-driven catalyst (PDC) reactor. The inner diameter and the effective length of the quartz tube were 1.3cm and 20cm, respectively.

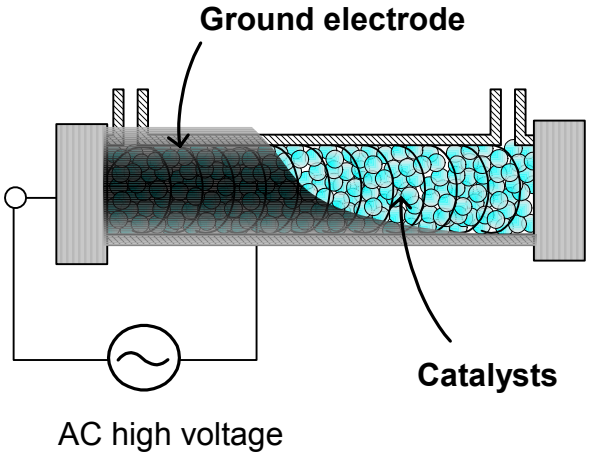

FIGURE 1. Plasma-driven catalyst (PDC) reactor.

A coil-type electrode made of stainless steel (0.45mm diameter) was set inside the tube as a high-voltage electrode, and silver paste was painted on the outside the quartz tube as a ground electrode. Gold catalysts were supported on TiO_2 pellets (anatase structure). The shape of the TiO_2 pellets was spherical with average diameter of about 1.8 mm. All the experiments were done at room temperature and atmospheric pressure. The preparation of Au/TiO_2 catalyst by the deposition-precipitation method is well described in the literature [4]. For reference, Au/TiO_2 catalyst was also prepared by the conventional impregnation method using $HAuCl_4$ standard solution. After several steps of drying processes, the Au/TiO_2 catalysts were calcined at 300^{o}C for 5 hours in air. The amount of Au catalysts on the TiO_2 were 2 wt% in both cases. The size of Au catalyst was determined by a high-resolution transmission electron microscopy (TEM, Hitachi H-9000NAR).

2.2 Gas and Electrical Measurements

Gas flow rates were regulated using mass flow controllers (KOFLOC, CR-300). The total gas flow rates were in the range of 4- 24 L/min, which corresponds to the gas hourly space velocity (GHSV) up to ~ 130,000h^{-1}. The initial CO concentration was set at 1000 ppm.

The PDC reactor was energized with an AC high voltage (~ 30 kV_{pk-pk}, ~ 1000 Hz) power supply (Trek, 20/20B). Discharge power and specific input energy (SIE) in the PDC reactor were measured using an automated V-Q Lissajous software [6]. The waveforms of the charge and the applied voltage were monitored with a digital oscilloscope (Tektronix, TDS3032B). The SIE, which is the ratio of discharge power (P_{dis}) to the gas flow rate (Q_f), was calculated with the following relations.

$$\text{Specific input energy (J/L)} = \frac{P_{dis}}{Q_f} \times 60 \qquad (1)$$

where the Q_f is in L/min.

3. RESULTS AND DISCUSSION

Figure 2 shows the TEM photographs of the Au/TiO_2 catalysts prepared by different methods. The sizes of the Au catalysts were about 3-7nm and 22-30nm for deposition-precipitation method and impregnation method, respectively. Since the smooth surface of Au does not adsorb CO at room temperature, the adsorption of CO mostly occurs

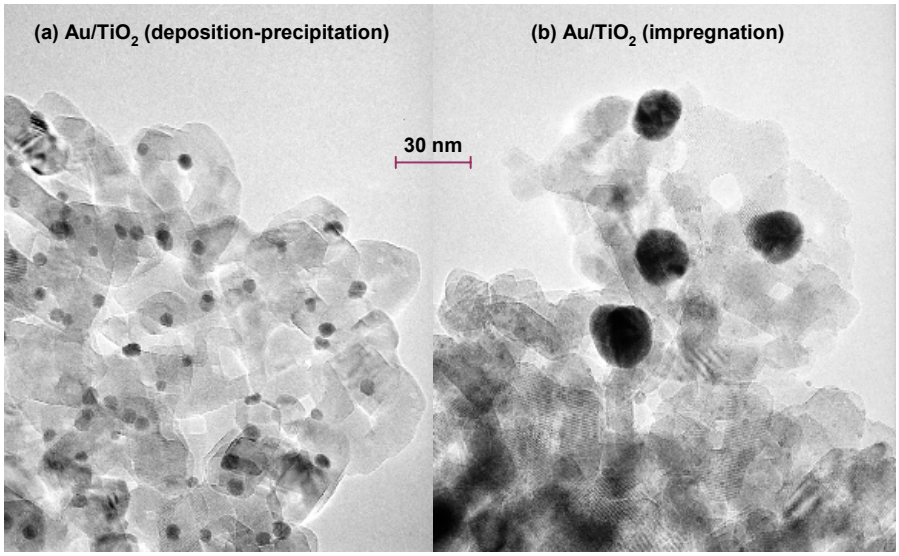

FIGURE 2. TEM photos of the Au/TiO_2 catalysts according to the preparation method; (a) Deposition-precipitation method, (b) Impregnation method.

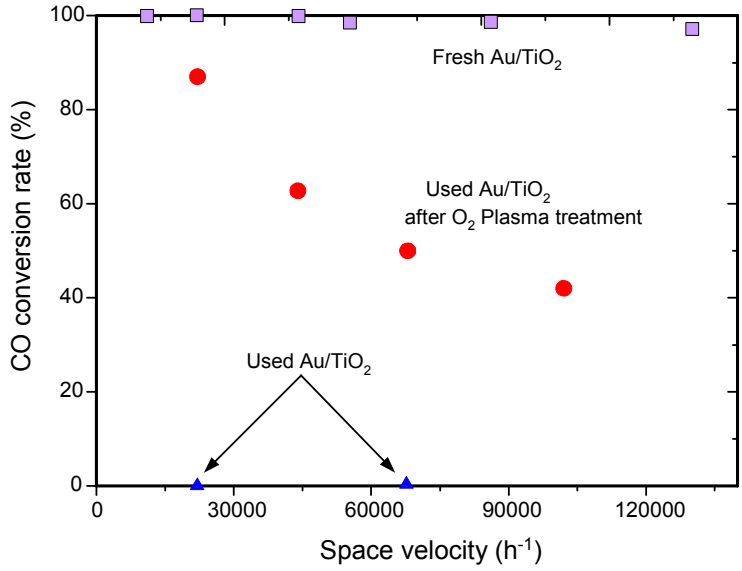

FIGURE 3. Ambient temperature CO oxidation using the 2.0wt% Au/TiO_2 catalyst prepared by deposition-precipitation method. Discharge power of the O_2 plasma for the regeneration of the used Au/TiO_2 was 10.9 W.

on steps, edges and corner sites of Au [7]. Therefore the smaller the Au size, the higher reactivity for CO oxidation. The Au/TiO_2 catalysts prepared by the impregnation method had no catalytic activity at room temperature, which is consistent with the reported data [8].

Figure 3 shows the CO oxidation over the Au/TiO_2 catalyst prepared by the deposition-precipitation method. Plasma was not applied during the CO oxidation reactions. Fresh Au/TiO_2 catalyst completely oxidized 1000 ppm CO to CO_2. The Au/TiO_2 catalyst maintained high catalytic activity even at high space velocity up to 130,000 h^{-1}. After the plasma-driven catalysis of benzene for about 10 hour, the activity toward CO oxidation was completely disappeared. When this deactivated catalyst was treated by O_2 plasma at a discharge power of 10.9 watt for about 30 min, the catalytic activity of CO oxidation recovered to about 88% at 22,000h^{-1}. The degree of the activity recovering can be further enhanced by treating the samples for longer time with higher energy input.

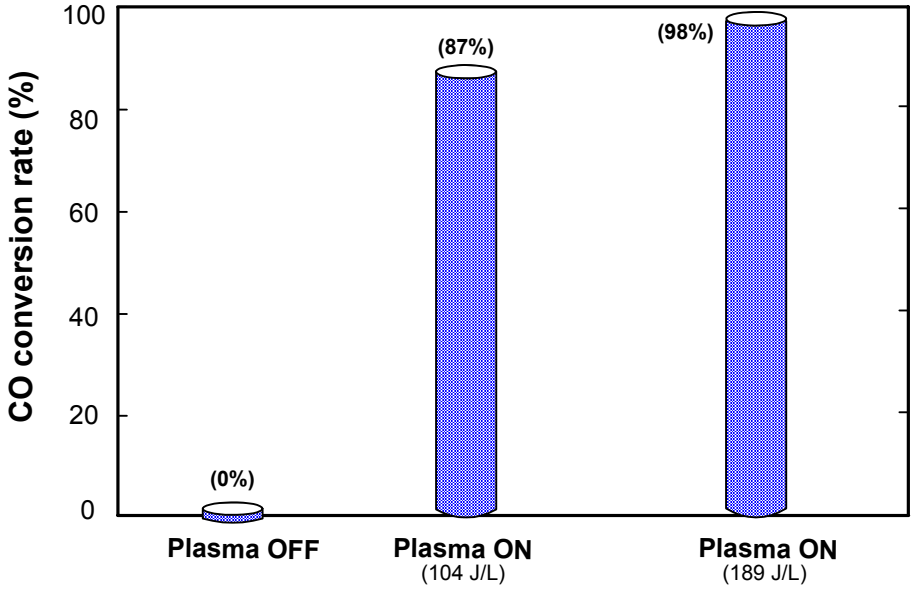

FIGURE 4. The effect of nonthermal plasma on the CO oxidation rate over the used Au/TiO_2 catalysts. (GHSV = 22,000h^{-1})

Figure 4 shows the CO oxidation using the plasma-driven catalyst reactor packed with the used Au/TiO_2 catalyst. The used Au/TiO_2 catalyst had no catalytic activity at ambient temperature without plasma application. Despite the zero activity of the used catalyst, the direct application of nonthermal plasma over the used Au/TiO_2 catalyst greatly enhanced the CO oxidation. The conversion rate of CO increased to 87% and 98% at specific input energies of 104 J/L and 189 J/L, respectively. There was no oxidation of CO using the plasma alone at these specific input energies. These results indicate that the plasma induced catalytic activity of CO oxidation originate different mechanism to those observed with the fresh Au/TiO_2 catalyst.

4. SUMMARY

The oxidation of CO using the nanometer-sized gold catalyst supported over TiO_2 catalysts was investigated. The Au/TiO_2 catalysts prepared by the deposition-precipitation method showed a good catalyst activity for the CO oxidation even at a high GHSV of 130,000 h^{-1}. Application of nonthermal plasma greatly enhanced the CO oxidation using the used Au/TiO_2 catalysts, which have completely lost its catalytic activity toward CO oxidation. Oxygen plasma was found to be effective in the regeneration of the used Au/TiO_2 catalysts.

REFERENCES

[1] Kim H H, Kobara H, Ogata A and Futamura S (2005). Comparative assessment of different non-thermal plasma reactors on energy efficiency and aerosol formation from decomposition of gas-phase benzene. *IEEE Trans. Ind. Applicat.*, 41, 206-14

[2] Kim H H (2004). Nonthermal plasma processing for air pollution control: A historical review, current issues, and future prospects. *Plasma Process. Polym.*, 1, 91-110

[3] Haruta M, Yamada N, Kobayashi T and Iijima S (1989). Gold catalysts prepared by coprecipitation for low-temperature oxidation of hydrogen and of carbon monoxide. *J.*

Catal., 115, 301-09

[4] Haruta M, Tsubota S, Kobayashi T, Kageyama H and Genet M H (1993). Low-temperature oxidation of CO over gold supported on TiO_2, α-Fe_2O_3, and Co_3O_4. *J. Catal.*, 144, 175-92

[5] Date M, Ichihashi Y, Yamashita T, Chiorino A, Boccuzzi F and Haruta M (2002). Performance of Au/TiO_2 catalyst under ambient conditions. *Catal. Today*, 72, 89-94

[6] Kim H H, Ogata A and Futamura S (2006). Effect of different catalysts on the decomposition of VOCs using flow-type plasma-driven catalysis. *IEEE Trans. Plasma Sci.*, 34, 984-95

[7] Haruta M and Date M (2001). Advances in the catalysis of Au nanoparticles. *Appl. Catal. A: General*, 222, 427-37

[8] Lopez N, Janssens T V W, Clausen B S, Xu Y, Mavrikakis M, Bligaard T and Norskov J K (2004). On the origin of the catalytic activity of gold nanoparticles for low-temperature CO oxidation. *J. Catal.*, 223, 232-35

Paper number

CONVERSION OF PROPANE BY PULSED DIELECTRIC BARRIER DISCHARGES IN AIR

O. Aubry, A. Khacef and J.M. Cormier

GREMI, Polytech'Orléans, 14 rue d'Issoudun, 45067 Orléans cedex 2, FRANCE

ABSTRACT. Dielectric barrier discharge reactor has been used to study the effect of voltage, pulse repetition rate and inlet mixture composition on propane conversion. The reactor is powered by a pulsed high voltage supply with amplitudes up to 30 kV and pulses repetition rate varied up to 200 Hz. Injected energy density and dry or wet air conditions play a major role on propane removal efficiency and the species produced (nature and concentrations).

1. INTRODUCTION

Non-thermal atmospheric pressure plasma processing is being actively studied for the effective removal of volatile organic compounds (VOCs') diluted in air [1-4]. Despite well-established implementations, fundamental knowledge of chemical processes need to be improved: products analysis, mass balance. Propane conversion results in a pulsed dielectric barrier discharge reactor (DBD) are reported in this paper. The aim is to characterize experimentally removal efficiency and the products by varying of voltages and pulse repetition rates.

2. EXPERIMENTAL

The experimental set-up used in this work was described previously [1,5-7]. The composition of the inlet gas mixture was controlled by mass flow controllers and the total flow rate was fixed at 1 $L.min^{-1}$. The inlet mixtures composition was dry or water saturated air with 1050 ppm of propane at room temperature and atmospheric pressure. The geometry of the DBD reactor was a wire to cylinder type.

The high-voltage generator is composed of two parts: the first one is a bank of ceramic knob storage and transfer capacitors of 4 nF. Each capacitor was connected in a Blumlein-type configuration. The second one was the cable transformer system. The storage capacitors were charged at a voltage (U_{ch}), and commuted with a fast switching element. Then, this high voltage fed the DBD through the cable transformer. A maximum open circuit voltage of six times the charging voltage of each cable was achieved. This pulse generator was able to deliver open circuit voltage up to 150 kV output into 80 ns (FWHM) pulses and short rise time (40 ns). In ours experiments, U_{ch} was between 3.5 and 5 kV and applied high voltage in the plasma reactor reached up to 30 kV (U_{appl}). The pulse repetition rate was adjustable, up to 200 Hz. Applied voltages and current measurements were displayed with an oscilloscope through high voltage and current probes.

Chemical analyses were performed by Fourier Transform Infra Red (FTIR, Nicolet Magna-IR 550 series II). Species quantified are only C_3H_8, CO_2 and CO. In addition of these main

products, by-products such as formaldehyde, acetaldehyde, formic acid, NO_x and $C_xH_yNO_z$ were observed.

3. RESULTS AND DISCUSSION

3.1. Propane conversion

The discharge pulse energy into the plasma was determined with a capacitive circuit and was given by: $Ed = \frac{(0.5\,C\,U_{ch}^2)\,f}{Q}$ where C is the transfer capacitance of the capacitors bank, U_{ch} the charging voltage, f the pulse repetition rate and Q the total flow rate. Charging voltages and pulse repetition rates range studied were the following: 3.5 kV, 15-200 Hz; 4.5 kV, 100-200 Hz; and 5 kV, 15-150 Hz. From these values, we reported species concentrations as functions of energy density (Ed). Ed range studied in this work is between 0 and 900 J/L.

In figure 1a, the effect of Ed on propane concentration in dry air is reported. Propane conversion rate increases significantly with increasing Ed. For a given charging voltage, a rise of the frequency implies an enhancement of the C_3H_8 consumption. This is observed too for a given f when U_{ch} increases. C_3H_8 is totally consumed when Ed is higher than 700 J/L. Ed is not the main parameter on the propane removal efficiency: for a given Ed, propane consumption depends on U_{ch} and f. For Ed=700 J/L, we have same conversion rates for U_{ch} equals to 4.5 and 5.0 kV and for pulse repetition rates of 200 and 125 Hz respectively.

Figures 1b and 1c show the influences of Ed and charging voltages on propane conversion rates in wet and dry air conditions. We can observe a similar effect of Ed on propane conversion rate in humid air and dry air: an increase of Ed leads to a rise of the conversion rate. Humid air conditions leads to a beneficial effect on the propane consumption with an increase of the propane conversion rate for the lowest U_{ch}. When the voltage rises, the effect decrease strongly: for 5 kV, a minor effect is observed when F<75 Hz.

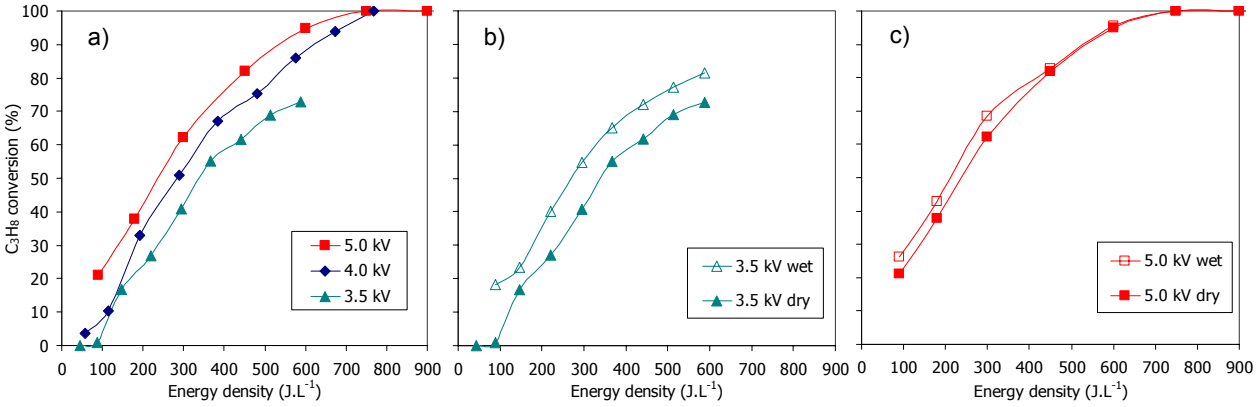

FIGURE 1. C_3H_8 conversion rates as functions of Ed and charging voltages in: a) dry air and b) wet air.

3.2. Species produced

Figures 2 display CO and CO_2 concentrations as functions of Ed for various U_{ch} and f values for propane diluted in dry air (full symbols). CO_x are the main carbon species produced when propane is consumed. An increase of Ed leads to a rise of CO and CO_2 concentrations. For a given Ed, there is a voltage effect between 3.5 and 4.5 kV, species concentrations increase. Between the highest voltages (4.5 and 5.0 kV), none effect of U_{ch} is observed at given Ed. In the lowest Ed range, CO_2 concentrations are higher than CO ones and this range

is varying with U_{ch}: 0-300 J/L for 3.5 kV and 0-180 J/L for 5 kV.

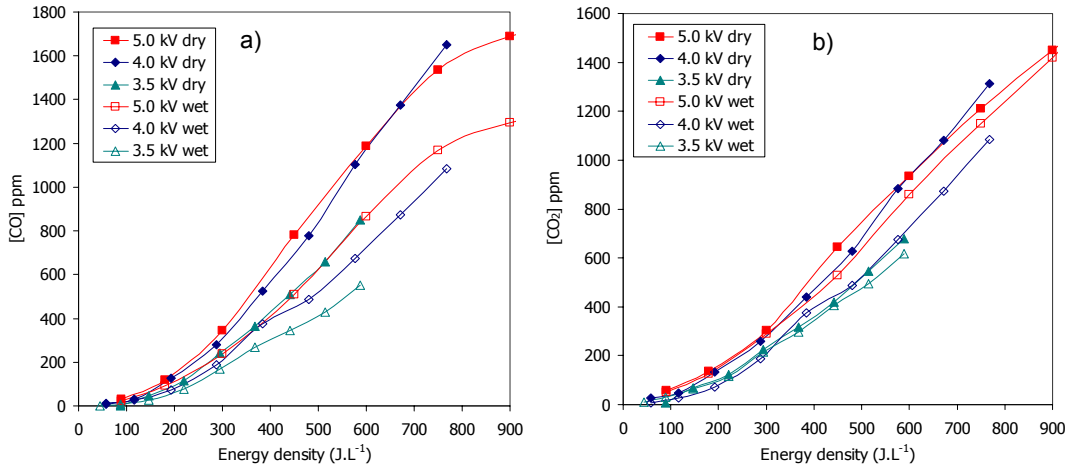

FIGURE 2. Effect of energy density on: a) CO, and b) CO_2 concentrations in dry and wet conditions.

In wet air conditions, CO and CO_2 concentrations increase when Ed rises (figures 2, open symbols). A comparison between results in dry and wet air shows that CO concentration strongly depends on the inlet mixture composition (up to 400 ppm for Ed=700 J/L). An increase of U_{ch} implies same effects on [CO] in dry or wet air conditions. Concerning CO_2 produced, humid air plays a minor role on [CO_2], a light decrease of CO_2 produced appears in wet air conditions (up to 200 ppm for U_{ch}=4 kV).

From non-consumed C_3H_8, CO and CO_2 concentrations, we calculated CO+CO_2 selectivity, S_{CO+CO2}, and measured carbon concentration, C_M, expressed by:
S_{CO+CO2}=([CO]+[CO_2])/(inlet total carbon) and [C_M]=3.[C_3H_8]+[CO]+[CO_2], respectively.

Effects of Ed on S_{CO+CO2} are reported in figure 3a and ones on [C_M] are shown in figures 3b and 3c. For the highest Ed (>700 J/L), CO and CO_2 are only the carbon species produced in dry air: S_{CO+CO2} is close to 100% and C_M is equal to the inlet carbon injected (3150 ppm). In wet air, maximum S_{CO+CO2} is only 80% at 900 J/L. C_M curves show effects of Ed on the species produced and influences of charging voltage.

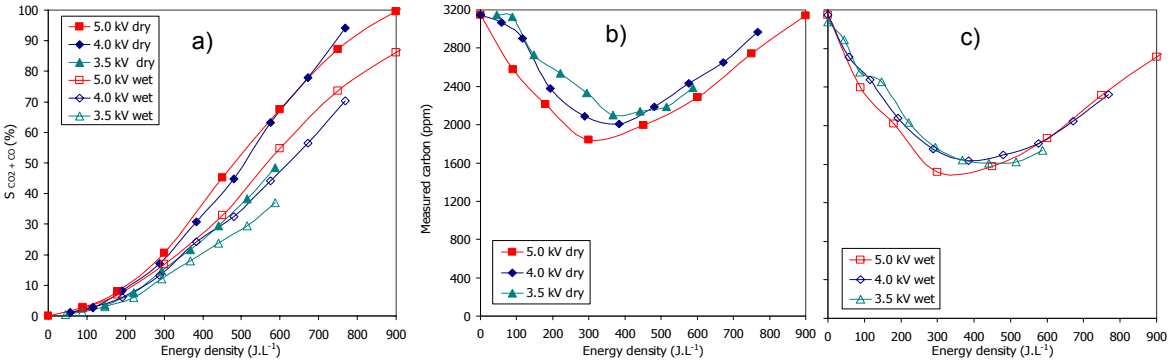

FIGURE 3. Effects of Ed on: a) CO+CO_2 selectivity, b) C_M in dry air and c) C_M in wet air.

ΔC is defined as the difference between C_M and the initial carbon injected. ΔC≠0 means that others carbon species are produced ($C_xH_yO_z$) and mainly between 150 and 800 J/L. The $C_xH_yO_z$ production is linked to the humidity in air and to U_{ch} for the lowest Ed values. Maximum carbon deficit, ΔC, in dry air is reached at 300 J/L for 5 kV, 350 J/L for 4.0 kV and 375 J/L for 3.5 kV and ΔC is 1300, 1160 and 1050 ppm, respectively. In wet air, ΔC increases

up to 1600 ppm for 5 kV.

CH_2O areas measured from experimental FTIR spectrum are reported in figures 4. Concentrations of formaldehyde are higher for dry conditions excepted for the lowest charging voltage studied where none influence of the air conditions are observed. In humid air, CH_2O is not promoted excepted for the higher Ed values where S_{CO+CO2} is lower. The trends of CH_2O correspond to the carbon deficit observed in figure 4b. Maximum CH_2O concentrations are reached between 300 and 400 J/L in function of U_{ch}. FTIR spectra show that others $C_xH_yN_wO_z$ species are promoted in wet air conditions.

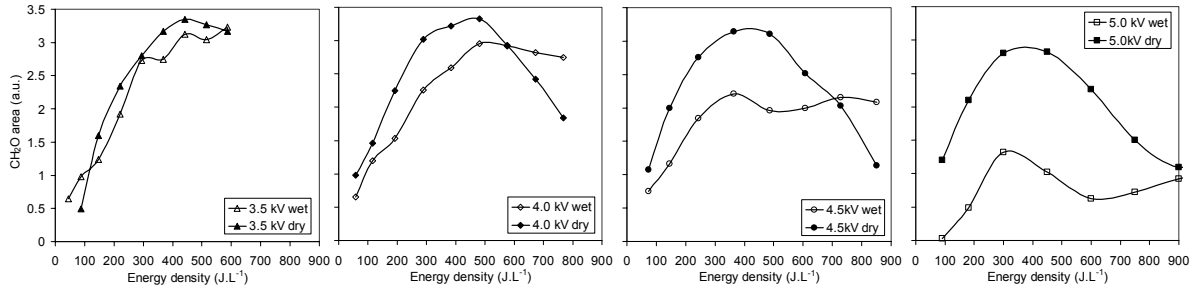

FIGURE 4. Effects of Ed, charging voltages and air conditions on CH_2O areas measured by FTIR.

CONCLUSION

This work shows that high propane conversion efficiency can be reached with an energy density equals to 700 J/L and main species produced are CO and CO_2. $CO+CO_2$ Selectivity reaches 100 % when propane is entirely consumed. Propane diluted in humid air implies a increase of the propane conversion for the lowest charging voltage studied and $CO+CO_2$ selectivity decreases in favor of $C_xH_yO_z$ species with $x > 2$.

REFERENCES

[1] Motret O., Aubry O., Thuillier C., Lascaud M., Met C., Cormier J.M. (2005). Conversion of Ethylene by Pulsed Dielectric Barrier Discharge in Dry and Wet - Parametrical Study. *Proc. 17th Int. Symp. Plasma Chemistry,* Toronto (Canada).

[2] McAdams R. (2001). Prospects for non-thermal atmospheric plasmas for pollution abatement. *J. Phys. D: Appl. Phys.*, 34, 2810-2821.

[3] Guo Y.F., Ye D.Q., Chen K.F., Tian Y.F. (2006). Humidity effect on Toluene Decomposition in a Wire-plat dielectric barrier discharge reactor. *Plasma Chem. Plasma Process*, 26, 237-249.

[4] Blin-Simiand N., Jorand J., Belhadj-Miled Z., Pasquiers S., Postel C. (2006). Influence of temperature on the removal of toluene by dielectric barrier discharge. *Proc. ISNTPT 5*, Oleron Island (France).

[5] Khacef, A., Viladrosa C., Cachoncinlle C., Robert E., Pouvesle J.M. (1997). High repetition rate compact source of nanosecond pulses of 5–100 keV x-ray photons, *Rev. Sci. Instrum.,* 68, 2292-2297.

[6] Khacef A., Cormier J.M., Pouvesle J.M. (2002). NOx remediation in oxygen-rich exhaust gas using atmospheric pressure non-thermal plasma generated by a pulsed nanosecond dielectric barrier discharge, *J. Phys. D: Appl. Phys.*, 35, 1491-1498.

[7] Aubry O., Khacef A., Cormier J.M. (2006). CO conversion by a dielectric barrier discharges using the water gas shift reaction. *Proc. ISNTPT 5*, Oleron Island (France).

OXYDATION OF SOOT PARTICULATES IN DIELECTRIC BARRIER DISCHARGES

J. Grundmann, S. Müller, R.-J. Zahn, A. Quade and H. Steffen

Institut für Niedertemperatur-Plasmaphysik,
Friedrich-Ludwig-Jahn-Str. 19
D-17489 Greifswald, GERMANY

ABSTRACT. The aim of the investigations is a better appreciation of oxidation mechanisms by ozone and NO_X for soot at low temperatures. We have estimated reaction rates, activation energies, oxygen and carbon ratios of the soot after processing.

1. EXPERIMENTAL

It was already shown in recent papers, that soot can be decomposed in different DBD configurations at low temperatures [1,2,3]. Because of the complex reaction mechanisms in a real system first the reaction of soot with ozone generated externally was investigated. The experiments were carried out in a cylindrical stainless steel vacuum vessel with ports/windows for diagnostic access and gas inlet/outlet.

A special DBD-configuration was installed within the vessel. A porous electrode served as a filter element and soot carrier [1,3].

All process diagnostics were done using an FTIR spectrometer (Ansyco Gasmet). Gas pipes and the DBD chamber were heated and the temperature controlled. XPS was used to investigate the change of the composition of soot. To verify the proposed reaction scheme, a

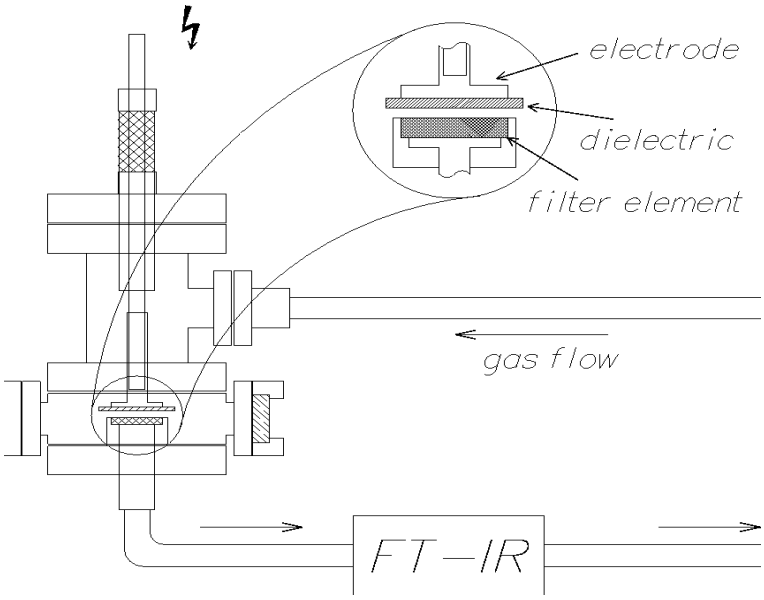

Figure 1. Schematic of the configuration [3].

simple simulation was done.

For special questions a simplified configuration was used. A commercial ozone generator which represents an ordinary DBD configuration served as ozonizer.

2. OXYGEN TREATMENT

In a first step soot was treated with a pure oxygen/ozone mixture. Several measurements at different temperatures of up to 350°C were done. The results suggests, that the decomposition process in oxygen is a three-stage process,

i. $HC + O_3 \rightarrow$ products

ii. $Soot + O_3 \rightarrow Soot\text{-}O + O_2$

iii. $Soot\text{-}O + O_3 \rightarrow Soot' + CO/CO_2$

Figure 2 ('circle'-points) shows the estimated reaction rates as an Arrhenius-plot. The activation energie was estimated to

$E_{O2} = 0.46$ eV.

In a next step soot was decomposed inside a DBD configuration. Again the carrier gas was oxygen. Now in addition to the previous measurements reactions with free radicals or excited atoms/ions are possible [4,5]. Furthermore a heating of a substrat by a plasma was reported [6] and should be taken into account.

The reaction rates at different temperatures in the range of 100...250°C were estimated (figure 2, 'cross'-points). The rates are significantly larger and the activation energies lower, respectively. The temperature dependence is similar to the results at pure ozone treatment but parallel shifted to higher reaction rates. This leads to the conclusion, that the plasma seems to reduce the activation energy. The activation energy was estimated to

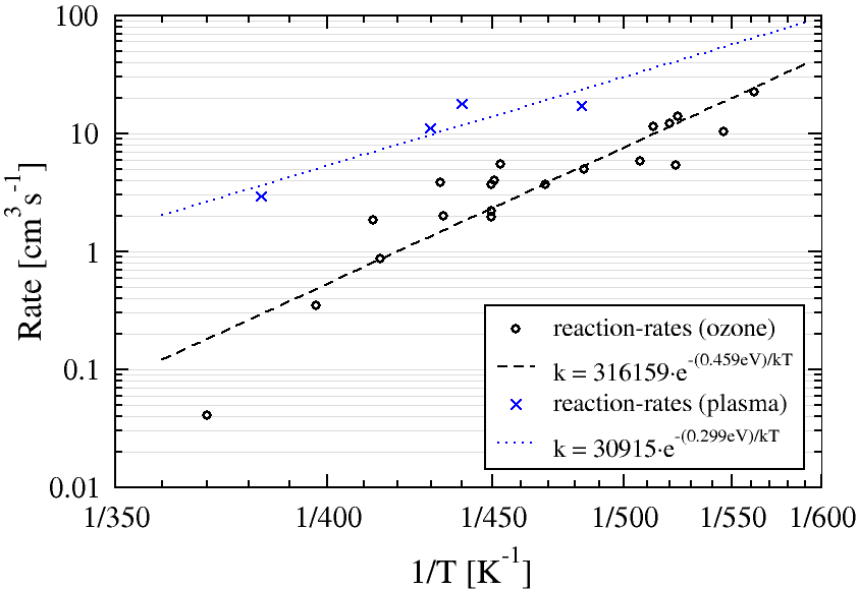

FIGURE 2. Plot of the estimated reaction rates versus 1/T. The circles mark the measurements with ozone externally generated, while the stars refer to the decomposition inside a discharge.

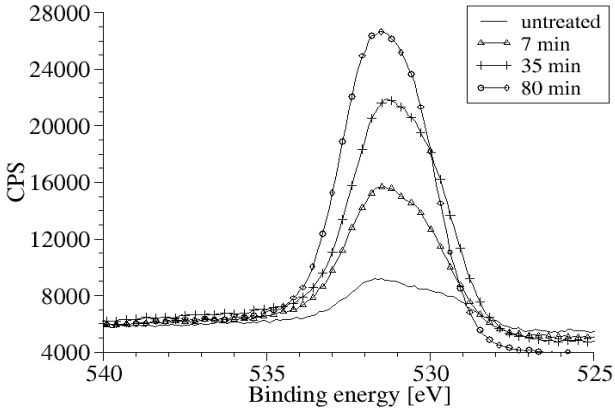

FIGURE 3. Oxygen ratio of the soot.

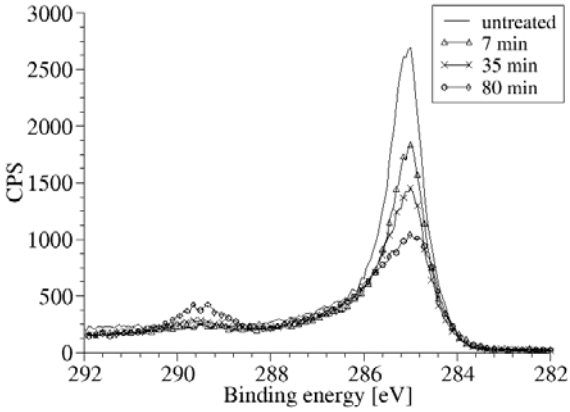

FIGURE 4. Carbon ratio of the soot.

$E_{O2,DBD} = 0.30$ eV

Furthermore the soot was analized using XPS. The decomposition temperature was chosen to 160°C. As expected from the equations above both, an increase of the oxygen bound into the soot surface (figure 3) and a decrase of the carbon fraction (figure 4) can be seen very clearly.

3. AIR TREATMENT

The main stable products of a DBD in air are ozone, nitrogen oxide and nitrogen dioxide. In addition to the reaction of soot with ozon reactions with nitrogen oxides are known [7,8,9].

iv. $Soot + NO_2 \rightarrow Soot\text{-}NO_2$

v. $Soot\text{-}NO_2 \rightarrow Soot\text{-}O + NO$

vi. $Soot\text{-}O + NO_2 \rightarrow Soot\text{-}NO + O_2$

vii. $Soot\text{-}O + NO \rightarrow Soot + NO_2$

The electric parameters of the DBD are chosen in such a way, that the discharge served as a source of NO_X. Under similar conditions the decomposition process was investigated using FTIR and XPS diagnostic again. The gas temperature was chosen to 160°C.

Figure 5 and 6 show the results of the XPS-measurement. The increase of the oxygen

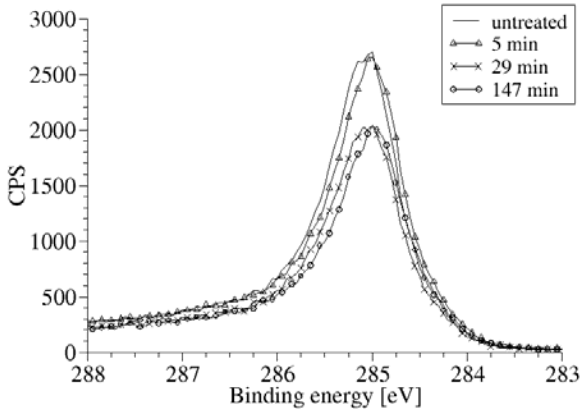

FIGURE 5: Proportion of carbon during the air treatment in the DBD.

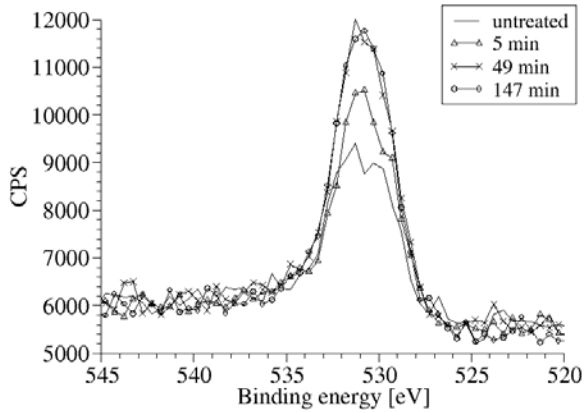

FIGURE 6. Proportion of oxygen during the air treatment in the DBD.

included into the soot-surface (figure 6) proves the reactions above. The concentration of carbon (figure 5) decreases slightly, which could be a result of the increasing oxygen. One consequence is that the decomposition of the soot-oxygen complex (soot-O), which corresponds to the decomposition of soot, without ozone is very slow at this low temperature. It suggests further, at least at this temperature range, that the reaction with ozone is the important process that decomposes the soot-oxygen complex.

REFERENCES

[1] Grundmann, J., Müller, S., Zahn, R.-J. (2005), Treatment of soot by dielectric barrier discharges and ozone. *Plasma Chemistry and Plasma Processes*, 25, 455-466

[2] Harano, A., Sadakata, M., Sato, M. (1991), Soot Oxidation in a Silent Discharge. *Journal of Chemical Engineering of Japan*, 24, 100-106

[3] Müller, S., Conrads, J., Best, W. (2000) Reactor for Decomposing Soot and Other Harmful Substances Contained in Flue Gas. *Hakone VII, Contr. Paper,* 2, 340-344

[4] Eliasson, B., Hirth, M., Kogelschatz, U. (1986), Ozone Synthesis from Oxygen in Dielectric Barrier Discharges. *J. Phys. D: Appl. Phys.*, 20, 1421-1437

[5] Braun, D., Gibalov, V., Pietsch, G. (1992), Two-Dimensional Modelling of the Dielectric Barrier Discharge in Air. *Plasma Sources Sci. Technol.*, 1, 166-174

[6] Kersten, H., Rohde, D., Steffen, H., Deutsch, H., Swinkels, G.H.P.M., Kroesen, G.M.W, Hippler, R. (2001). On the determination of energy fluxes at plasma-surface processes. *Appl. Phys. A*, 72, 531-540

[7] Kamm, S., Möhler, O., Naumann, K.-H., Saathoff, H., Schurath, U. (1998), Hetorogeneous Interaction of Ozone,NO2, and N2O5 with Soot Aerosol. *Proc. of the EUROTRAC Symposium, WIT press, Boston Southhampton 2000,* 1, 644-648

[8] Möhler, O., Naumann, K.-H., Saathoff, H., Schurath, U. (1997), The Influence of Soot Surface Reactions on the Ozone and NO_x Chemistry. *J. Aerosol Sci.*, 1997

[9] Chughtai, A. R., Welch, W. F., Smith, D. M. (1990) A Spectroscopic and Gravimetric Study of the Soot-NO_2/ N_2O_4 Reaction at various Temperatures. *Carbon*, 28, 411-421

BIOLOGICAL EFFECTS OF DC DISCHARGES IN ATMOSPHERIC AIR WITH WATER

Z. Machala[1], I. Jedlovsky[1], K. Hensel[1], V. Martisovits[1], V. Foltin[2]

[1]*Department of Astronomy, Earth Physics and Meteorology, Faculty of Mathematics, Physics and Informatics, Comenius University, Mlynska dolina, 84248 Bratislava, Slovakia (e-mail: machala@fmph.uniba.sk)*
[2]*Department of Experimental Physics, same address*

ABSTRACT. We tested biological effects of three types of DC electrical discharges in atmospheric air with one electrode submerged in water. The studied discharges were streamer corona, transient spark and glow discharge, operating in non-homogeneous electric field in the point-to-plane configuration, in both polarities of DC high voltage applied. They generate non-thermal plasmas with various gas temperatures and levels of thermal non-equilibrium. The discharge properties were investigated by means of electrical measurements and optical emission spectroscopy. Their biological effects were tested on selected Gram-negative and Gram-positive bacteria cultures (*S. typhimurium* and *B. subtilis*). The comparison of the effects of the three discharges indicates the major role of radicals and active species among other inactivation mechanisms.

1. INTRODUCTION

Non-thermal plasmas at atmospheric pressure are nowadays widely investigated for various chemical (flue gas and water cleaning) and bio-decontamination (sterilization) applications. [1, 2] Despite most related works use pulsed coronas and dielectric barrier discharges, we investigate three types of DC atmospheric discharges and test their biological effects on selected bacteria. In sterilization, it is very important to assess the importance of various effects involved. [2] We attempt to do so by employing emission spectroscopy of the investigated discharges.

2. INVESTIGATED DC DISCHARGES

2.1. Experimental-setup

The experimental setup for investigations of the DC discharges is shown in Figure 1. A homemade DC high voltage power supply (max. 25 kV/30 mA) sustains the discharges, enables mean voltage and current monitoring, and easy modification of the ballast resistance. The discharges were operated in the discharge chamber that allows their electrical, optical and spectroscopic diagnostics, working in various gases, with or without the plate electrode submerged in water, and changing the interelectrode distance. The stressed high voltage electrode was a hollow needle, opposite to the plate counter-electrode.

The discharge voltage was measured by the high voltage probe Tektronix P6015A (1000x). In the transient spark, the internal capacity of this high voltage probe was filtered by a small separating resistor *r* in order to minimize the capacity discharging in the spark pulse. A careful correction of the measured voltage on this *r* was then done. The interelectrode distance was varied between 2-10 mm. The discharge current was measured by: 1) mean DC current with

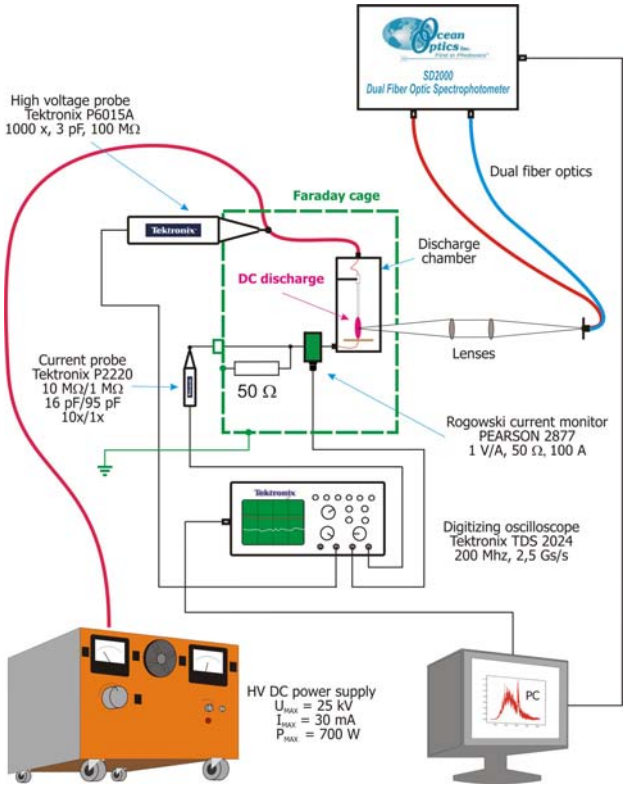

Figure 1. Experimental set-up for DC discharge experiments

milliamp meter; 2) time-dependent current waveform by the current probe on a 50 Ω resistor; and 3) by a Rogowski current monitor PEARSON 2877 (1 V/A). The current and voltage signals were processed by a digitizing oscilloscope Tektronix TDS 2024 (4 channels, 200 MHz, 1 GS/s) communicating with a PC. The entire chamber was placed in a Faraday cage to reduce induced noise signals and correctly measure voltage and current waveforms.

The light emission from the discharges was lead through the optical system consisting of a He-Ne laser for the alignment, an iris and two lenses, and focused on the entrance of the Y-type fiber optic leading into two-channel spectrometer Ocean Optics SD2000 (Master 200-500 nm, resolution 0.8; and Slave 500-1100 nm, resolution 1.7 nm) that was used for the optical emission diagnostics. The discharges were also photo-documented with a digital camera.

2.2. Electrical discharge characteristics

Three types of DC discharges in both polarities operating in atmospheric pressure air with or without water present in the discharge chamber were investigated: classical ***streamer corona (SC),*** and relatively novel ***transient spark (TS)*** and ***glow discharge (GD)***. These discharges generate nonequilibrium plasmas inducing various chemical end biological effects that are in the interest of chemical and bio-decontamination. Each discharge type generates plasma with specific properties, so each one was studied separately, both in the positive and the negative polarity. Testing discharges with an electrode immersed in water is important in order to adapt the conditions to the discharge action on biological media in water solution. The discharges have already been extensively studied previously. [3, 4] They are photo-documented in Figure 2.

Due to limited space we only show here the typical SC and TS pulses (Figure 3) of very short (~100 ns) duration. The discharge voltage remains fairly constant during the small streamer current pulses, while with TS it drops to zero during the high current pulses (~1A). The typical repetitive frequency of the streamer and spark pulses is 0.5-5 kHz, and 10-30 kHz, respectively. Thanks to very short pulse duration in TS (given by a small internal capacity of the discharge chamber), the plasma cannot reach LTE conditions. [3, 5]. On the other hand, the periodic streamer-to-spark transition provides nonequilibrium conditions with fast electrons that result in efficient chemical [3, 5] and biological cleaning effects. Pulseless high pressure DC glow discharges between two metal (or metal-liquid) electrodes and their chemical effects have been already described [3-6].

streamer corona transient spark glow discharge

Figure 2. Photographs of the discharges at various exposures, gap distance 4 mm.

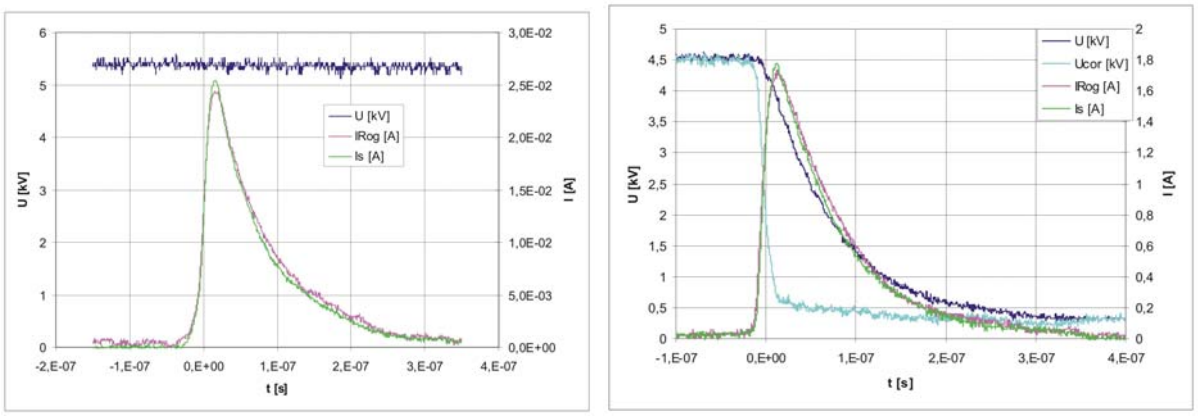

Figure 3. Streamer corona (left) and transient spark (right) – voltage and current pulses. U_{cor} is the voltage corrected for the value of the separating resistor r, I_{Rog} measured by the Rogowski current monitor, I_s measured by the current probe on a 50 Ω resistor.

2.3. Emission spectroscopy of DC discharges

Emission spectroscopy in UV-VIS region is a powerful technique of plasma diagnostics, because it gives valuable information on excited atomic and molecular states, enables to determine the rotational and vibrational temperatures and thus the level of nonequilibrium in the plasma, and, in addition, gives insight in an ongoing plasma chemistry [7].

Typical acquired spectra of the three discharges are shown in Figure 4. All discharges emit N_2 (2^{nd} and 1^{st} positive system), which indicates the excitation of N_2 molecules into $C^3\Pi_u$ state by the impact of electrons with relatively high energy (11 eV), and into $B^3\Pi_g$ state by electron impact or by C-B de-excitation. All discharges provide OH emission, thus indicating the presence of excited OH radicals formed from water molecules by dissociation.

GD emits the strongest OH and also emits NO γ system. NO is formed by the reaction N+O at high temperatures (~2000 K). Therefore, N and O radicals must be formed by the dissociation of air components. In addition, there is a strong water evaporation and consequent H_2O dissociation, thus leading to the large OH population. TS, besides N_2, emit N_2^+, which signifies high electron energy (19 eV is needed to excite N_2^+ into $B^2\Sigma_u^+$ state). High energy electrons leave

their fingerprints also in the VIS spectra as atomic lines of O, N and H radicals. These were not observed with other discharges. There is still a strong water dissociation and OH radical formation. SC only emits N_2 (2^{nd} and 1^{st} positive system) and some weak OH.

The measured spectra were used to determine the vibrational T_v and rotational T_r temperatures after fitting the experimental spectra with the simulated ones. We use Lifbase [8] (for OH) and Specair [9] (for N_2 a OH) simulation programs. Owing to fast collisional relaxation at atmospheric pressure, the gas temperature $T_g \approx T_r$. $T_v >> T_r$ indicates the nonequilibrium in the plasma. The preliminary results of temperature measurements are the following:

Streamer corona	$T_g \approx T_r = 500 \pm 200$ K,	$T_v = 6000 \pm 1000$ K
Transient spark	$T_g \approx T_r = 1000 \pm 500$ K,	$T_v = 8000 \pm 1000$ K
Glow discharge	$T_g \approx T_r = 2000 \pm 500$ K,	$T_v = 4000 \pm 1000$ K

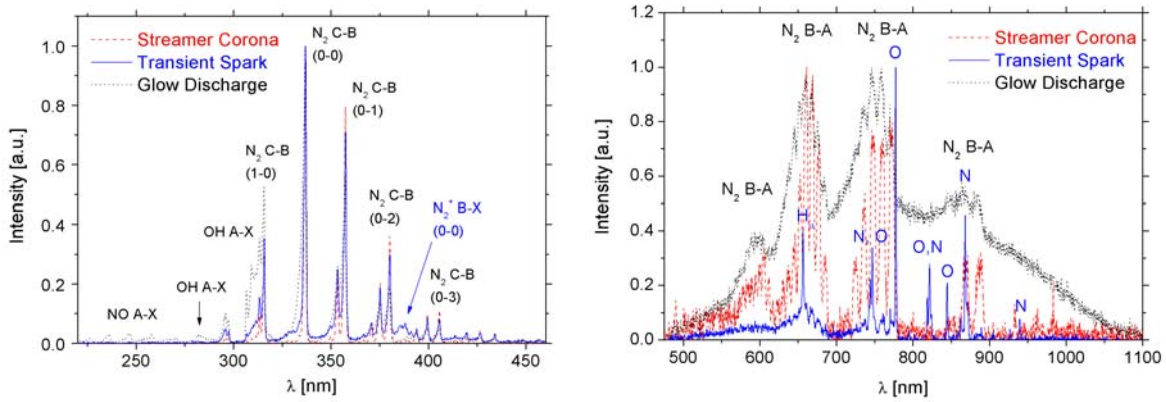

Figure 4. Emission spectra of DC discharges in UV and VIS.

3. BIOLOGICAL EFFECTS OF DC DISCHARGES

The biological effects of investigated DC discharges have been preliminarily tested on selected bacteria cultures:

1) *Salmonella typhimurium*, genetically modified strain (stem) TA 98, Gram-negative bacteria,

2) *Bacillus subtilis*, Gram-positive bacteria.

S. typhi is a pathogen causing typhus diseases, and so its sterilization is important from the viewpoint of drinking water decontamination. *B. subtilis* is not dangerous but belongs to the same group as extremely hazardous *B. anthracis* (Anthrax precursor), which nowadays represents one of the highest bio-terrorism risks. Besides the sterilizing effect of the non-thermal plasmas generated by the discharges, we partially investigated the roles of the involved bio-inactivation mechanisms, such as the thermal effect, the effect of radicals, charged particles, the electric field, and of the UV radiation.

3.1. Bacteria handling cultivation procedure

We used a standard microbiology procedure of bacteria handling and cultivation. The bacterial culture kept in the refrigerator was inoculated in the liquid nourishing medium. After pH adjustment it was placed in the overnight shaker at 37 °C where bacteria multiplied their

population. A diluted bacterial solution – inoculum – was then prepared with exactly set concentrations, typically measured in colony forming units (CFU) per ml, in the physiological medium. McFahrland turbidity scale standards were used to set the initial concentration. An exact volume (typically 10 µl) was then inoculated onto 4 Petri dishes with sterilized agar to make reference samples. The other part of inoculum (5 ml) was put in the discharge dish and treated by the specific discharge for a certain time (15, 30 or 60 s). After the discharge action, an exact volume of the treated inoculum was applied on other 4 Petri dishes with agar. All reference and treated samples on Petri dishes were incubated at 37 °C during 24 h to cultivate colonies (CFUs). Each living bacteria multiplies and gives rise to a colony observable by a naked eye. After the incubation, colonies on all Petri dishes were counted and statistically evaluated.

We developed a special discharge chamber for biological tests consisting of a 4-cm diameter Petri dish with a round copper plate counter-electrode on the bottom. The dish is placed in a glass vessel with a cover equipped with the needle electrode. The treated bacterial inoculum of the exact volume (typically 5 ml) is applied in the dish, onto the plate electrode. The discharge burns from the needle directly into the bacterial solution.

3.2. Results of bio-decontamination effects

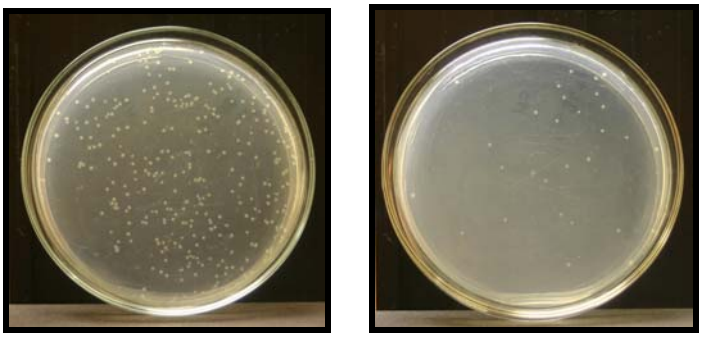

Figure 5. Cultivated bacteria on Petri dishes. Reference (left) and after-treatment (right) samples.

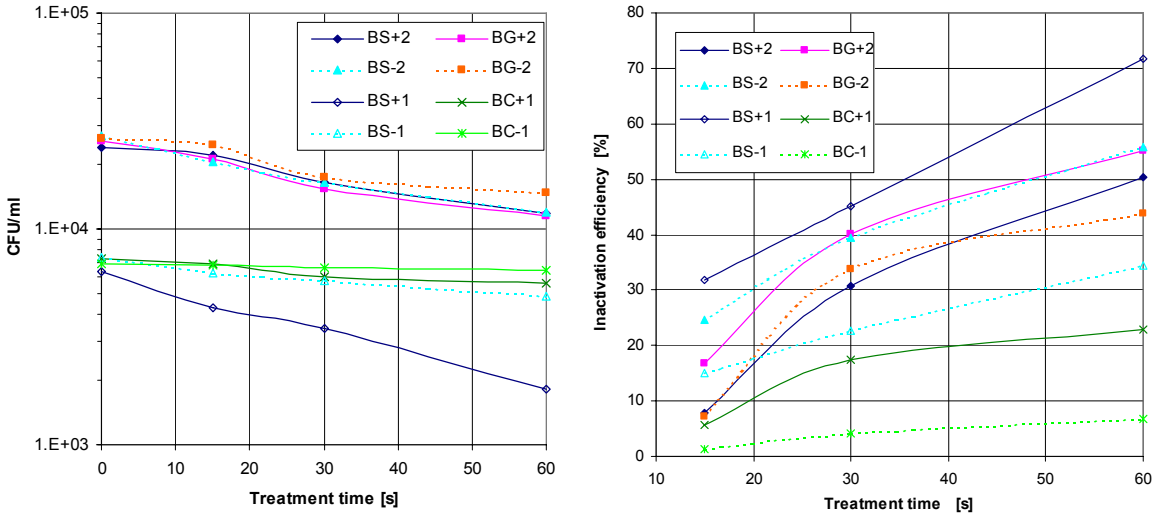

Figure 6. *S. typhi* survival curves in semi-logarithmic scale (left) and inactivation efficiency vs. treatment time (right). BS: transient spark, BG: glow discharge, BC: streamer corona, +: positive, -: negative polarity.

Several sets of bio-experiments have been performed. One set typically contained the treatment of the same inoculum by one discharge type in both polarities for treatment times of 15, 30, and 60 s, each combination per four samples, and 4 reference samples. The example of reference and treated cultivated samples is shown in photographs in Figure 5.

The survival curves of *S. typhi* are shown in Figure 6 in semi-logarithmic scale. The graph shows 4 experiment sets, two starting at lower (7000 CFU/ml – denoted 1) and two at higher (26,000 CFU/ml – denoted 2) initial bacterial concentrations. As expected, the number of CFUs decreased with the treatment time with all discharges. However, faster or slower inactivation can be observed with different discharges. In order to better compare the discharges we express the relative concentration decrease, i.e. the inactivation efficiency (Figure 6 right). The highest efficiencies were obtained in the positive TS, the lowest in the coronas; the GD gives fairly high efficiencies as well. All tested discharges were more efficient in the positive polarity.

Despite we performed several tests of inactivation of the Gram-positive spore-forming *B. subtilis* bacteria, so far we were not able to reasonably evaluate the survival curves and the efficiency. It is due to the problem with CFU counting after incubation of the tested and the reference samples. Although the initial concentrations were low, the incubated bacteria on the Petri dishes did not form nicely distinguished CFUs but continuous stains. However, a large decrease of their concentration was visually apparent which confirms that the method is applicable even for Gram-positive bacteria that are in general harder to inactivate.

3.3. Inactivation mechanisms

Bacteria inactivation (sterilization) mechanisms differ according to different authors. Most of them find that at atmospheric pressure, radicals and other active particles produced in the discharges play the dominant role. [2]

Our results obtained on inactivation of Gram-negative *S. typhi* demonstrate the highest efficiency in the positive TS. Spectroscopic characteristics of the TS described earlier showed that electrons with high energies are present in this discharge. These electrons initiate dissociations, ionizations and excitations of various species. The plasma is highly nonequilibrium, since $T_v >> T_r$. The atomic O, N and H radicals, and the N_2^+ ions have only been detected in this discharge, and there were a lot of OH radicals. O radicals may react with air O_2 and form ozone O_3. These results indicate that the role of radicals and other active species is very important. Energetic electrons themselves, directly interacting with bacteria may be important as well. High inactivation efficiencies were also reached in GD but at higher energy costs, due to the gas heating. The advantage of GD is a large number of OH radicals forming by dissociation of the vaporized water. It is hard to distinguish the temperature effect at this stage. SC was the least efficient discharge. This is partly because it is the least energetic and partly because the active region is in the proximity of the needle tip only, while most of the space is occupied by the drift region. Corona has the strongest electric field compared to other investigated discharges but this seems to have a minor effect.

At the present we are not able to distinguish the effect of UV radiation from the discharges. The most intense radiation comes from TS, mainly in UV A and VIS. On the other hand, GD emits more UV B germicide radiation due to NO γ system. This effect will be further investigated. We also plan experiments comparing direct and remote exposure of the micro-organisms in order to better separate the effects of active species from the effects of heat, UV, electric field and charges particles.

4. CONCLUSIONS

Three types of DC electrical discharges in atmospheric air with one electrode submerged in water (streamer corona, transient spark and glow discharge) were investigated by electrical measurements and optical emission spectroscopy. They generate non-thermal plasmas with various gas temperatures and properties. We performed the fist tests of their biological effects on selected Gram-negative and Gram-positive bacteria cultures (*S. typhimurium* and *B. subtilis*). The obtained bio-decontamination gives satisfactory results, although process optimization is necessary to reach higher inactivation efficiencies. In the synthesis with the spectroscopic discharge investigations we were able to determine some important mechanisms in the bio-decontamination process, especially the major role of radicals and active species. The preliminary results obtained are important from the standpoint of wastewater disinfection or bio-decontamination.

ACKNOWLEDGEMENTS

This work was supported by NATO EAP.RIG 981194, Slovak Grant Agency VEGA 1/2013/05, and Science and Technology Assistance Agency APVT-20-03240 grants.

REFERENCES

[1] H.-H. Kim, *Plasma Process. Polym.* 1 (2004), 91-110
[2] M. Laroussi, *IEEE Trans. Plasma Sci.* 30 (2002) 1409-1415
[3] Z. Machala: *„Continuous and transient electrical discharges, streamer triggered, at atmospheric pressure, for the removal of Volatile Organic Compounds (VOC)"*, Ph.D. thesis, University Paris-Sud XI, France, Comenius University Bratislava, Slovakia, 2000
[4] Z. Machala, E. Marode, C.O. Laux, C.H. Kruger, *J. Advanced Oxid. Technol.* 7 (2004), 133-137
[5] Z. Machala, M. Morvova, E. Marode, I. Morva, *J. Phys. D: Appl. Phys*. 33 (2000) 3198-3213
[6] Z. Machala, E. Marode, M. Morvova, P. Lukac, *Plasma Process. Polym.* 2 (2005) 152-161
[7] C.O. Laux, T.G. Spence, C.H. Kruger, and R.N. Zare, *Plasma Sources Sci. Technol.* 12 (2003) 125-138
[8] J. Luque and D.R. Crosley, SRI Report MP 99-009 (1999) 1
[9] C.O. Laux, *"Radiation and Nonequilibrium Collisional-Radiative models"* von Karman Institute for Fluid Dynamics, Lecture Series 2002-07, eds. D. Fletcher, T. Magin, J.-M. Charbonnier, G.S.R. Sarma, Rhode Saint-Genese, Belgium, June 4-7, 2002

Paper

PHENOL OXIDATION BY DC GAS PHASE CORONA DISCHARGE TO THE WATER SURFACE

M. Kocik, M. Dors, E. Metel, J. Mikielewicz, J. Mizeraczyk

Centre for Plasma and Laser Engineering
The Szewalski Institute of Fluid Flow Machinery, Polish Academy of Sciences
Fiszera 14, 80-231 Gdańsk, POLAND

Results of phenol degradation in water, induced by a DC positive corona discharge in an air-like gas mixture above the water surface are presented in this paper. A DC positive corona discharge was generated between a hollow needle, through which air with 1.5% CO_2 flowed, and the water surface. The water was artificially contaminated wit phenol (0.027 mM). The results showed that ozone produced by the corona discharge in the gas phase dissolved in water and oxidized phenol into dihydroxyphenols. Increasing the corona discharge duration results in an increased phenol degradation rate, water conductivity and acidity.

1. INTRODUCTION

Actually, the plasma treatment of drinking and waste water is not new. For a number of years tap water has been treated by ozone generated by various electrical discharges. This type of water treatment is called “the remote plasma method” [1] since the active species, like ozone, are generated by plasma aside the water system and then introduced into water. “The direct plasma method” of water treatment is the next generation method which generates plasma directly inside water or above the water surface, simultaneously oxidizing the inorganic and organic compounds in water and destroying the biological contaminants [2-7].

This paper is focused on the direct non-thermal plasma method of water treatment based on a DC positive corona discharge generated above the water surface.

2. EXPERIMENTAL SET-UP

The experimental set-up and the reactor are presented in Fig. 1. The positive DC corona discharge was generated between a stainless steel hollow needle electrode and the surface of pure water or water contaminated with phenol, which filled the reactor so that a grounded flat mesh electrode was 10 mm below the water surface. The mesh electrode was made of stainless steel. The outer and inner diameter of the hollow needle was 2 mm and 1.6 mm, respectively. The hollow needle-water surface spacing was 20 mm.

The positive polarity DC high voltage (18-23 kV) was applied through a 10 MΩ resistor to the hollow needle electrode. The time-averaged discharge current was 75 μA. The discharge pulse repetition rate was 50 kHz.

A dry air with CO_2(1.5%), stabilizing the corona discharge, was supplied through the

Electronic address: mdors@imp.gda.pl

hollow needle with a flow rate of 1 l/min. The pure water or water containing 0.027 mM of phenol was mixed continuously with a magnetic stirrer.

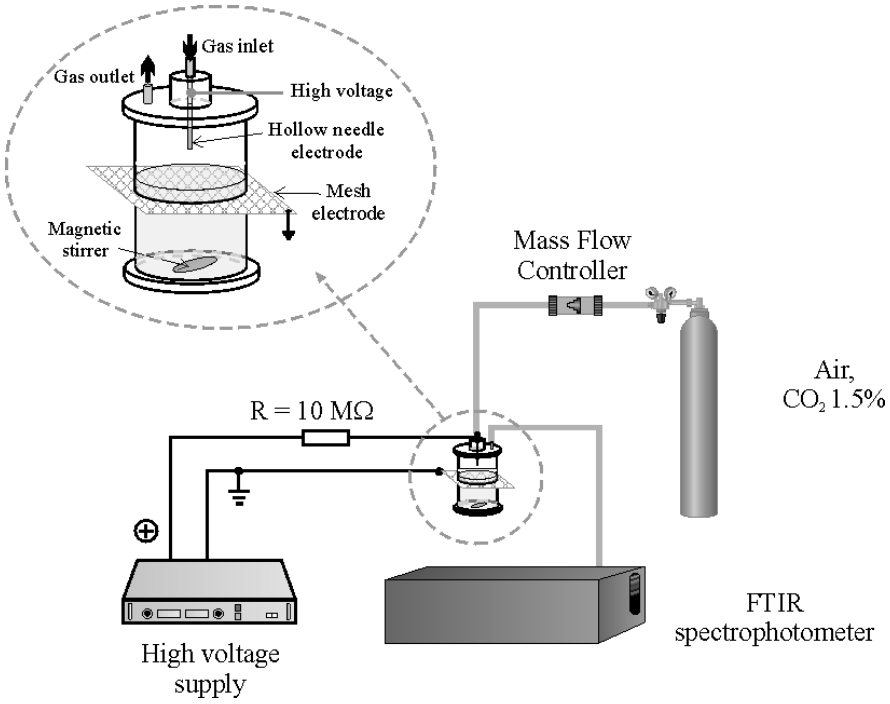

FIGURE 1. Experimental set-up.

The composition of the gas at the reactor outlet was analyzed by a FTIR spectrophotometer. The concentration of phenol in the water solution was measured by a gas chromatograph before and after the corona discharge processing. The water solution was analyzed also for the presence of ozone (iodometric method) and hydrogen peroxide (pertitanic acid formation method).

3. RESULTS AND DISCUSSION

As a result of the DC corona discharge processing, the concentration of phenol in water solution decreased with processing time from 0.027 mM to 0.002 mM (Figure 2a). The decrease in the phenol concentration was accompanied with the production of dihydroxyphenols, the concentration of which was, however, much lower than expected. It probably means that the phenol was converted also to other products not measured in this experiment.

As it is seen in Figure 2a, after 45 minutes of the DC corona processing the concentration of dihydroxyphenols decreased. It is known that dihydoxyphenols are formed in oxidation reactions of phenol caused by ozone and OH radicals, which can also react with dihydroxyphenols, resulting in organic aliphatic compounds, in particular acids, such as muconic acid, oxalic acid etc. [4-7].

The analysis of the gaseous phase composition after the DC corona processing of the pure water (without phenol), showed that the concentration of ozone produced by the corona discharge was 247 ppm and did not change during the processing (Figure 2b). The presence of phenol in the water caused a decrease in the concentration of gaseous ozone to 74 ppm.

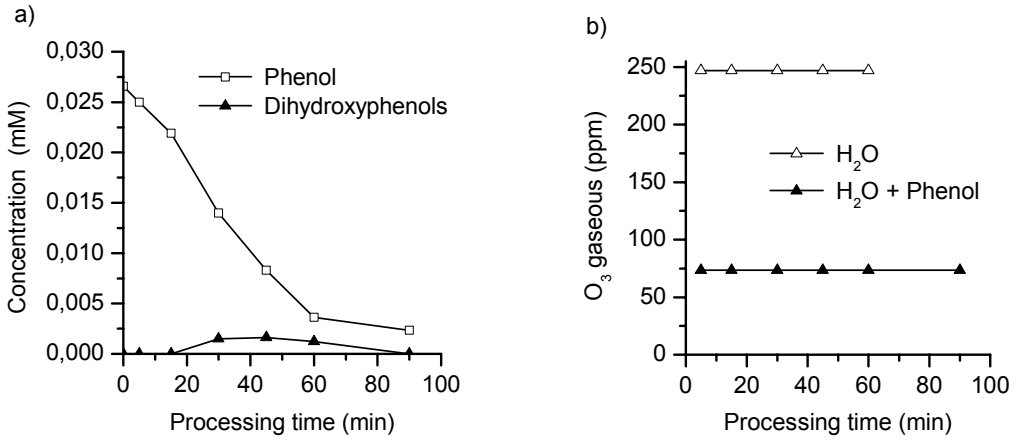

FIGURE 2. Concentrations of phenol and dihydroxyphenols in the aqueous phase (a) and ozone in gaseous phase (b) during the DC positive corona discharge processing. Discharge current 75 mA. Gas flow rate 1 l/min. Initial phenol concentration 0.027 mM.

The concentration of ozone in the aqueous phase increased when increasing processing time. Due to the reactions of ozone with phenols, the ozone concentration in the water containing phenol was lower of 0.03-0.06 mM than in the pure water (Figure 3a).

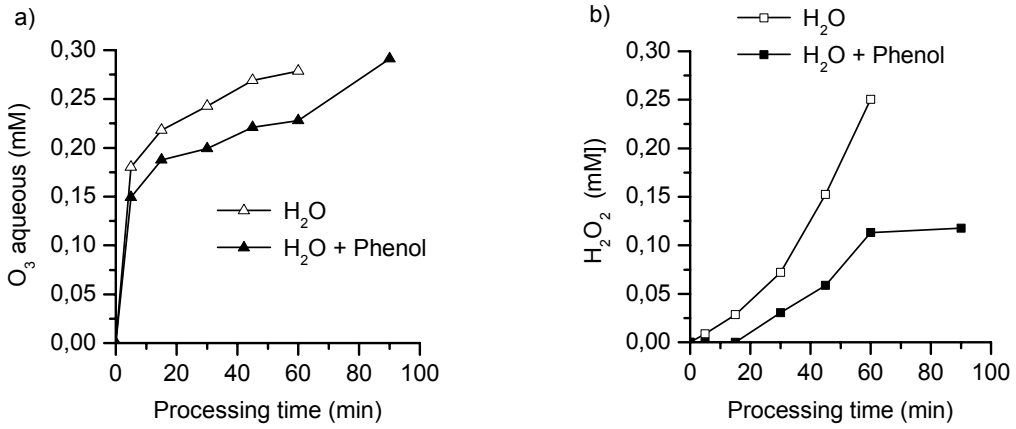

FIGURE 3. Concentration of ozone (a) and hydrogen peroxide (b) in the aqueous phase during the DC positive corona processing of pure water and water contaminated with phenol. Discharge current 75 μA. Gas flow rate 1 l/min. Initial phenol concentration 0.027 mM.

Changes in the concentration of H_2O_2 in the pure water and water contaminated with phenol are similar to those concerning ozone, i.e. H_2O_2 concentration, always higher in the pure water, increased with processing time (Figure 3b). Since H_2O_2 molecules are produced from OH radicals in reaction:

$$OH + OH \rightarrow H_2O_2, \quad (1)$$

the increased consumption of OH radicals when phenol is present in the water results in lower production of H_2O_2 and, therefore, in lower H_2O_2 concentration in the phenol contaminated water.

4. CONCLUSIONS

The results of gas phase DC positive corona discharge processing of water solution with phenol showed that:

- DC positive corona discharge produces OH radicals and ozone in gas phase. Both species dissolve in water and then oxidize phenol.
- Phenol is oxidized to dihydroxyphenols and aliphatic organic acids.
- The oxidants generated by DC positive corona discharge oxidize up to 91% of phenol during 90 min.
- The acidity and conductivity of the water increase with processing time mainly due to the presence of CO_2 in the gas phase (formation of CO_2^- and CO_3^- ions, which are precursors of carbonic acid). Organic acids formed from phenol slightly increase acidity.
- The energy efficiency of the phenol oxidation is up to 3.5×10^{-10} mol/J, and is comparable to the results obtained in pulsed corona discharge systems.

The main advantage of using DC corona discharge system is that it does not require matching the power supply to the corona discharge reactor, which is the problem in case of pulsed supply systems. Thus, energy loses and electromagnetic noise generated by the pulsed power supply can be avoided using DC corona discharge systems which are as efficient in phenol conversion as pulsed corona discharge installations.

ACKNOWLEDGMENTS

This work was supported by the Ministry of Science and Information Society Technologies under programme PB 1280/T10/2004/27 and by the Institute of Fluid Flow Machinery, Polish Academy of Sciences under programme IMP PAN O3Z3T2.

REFERENCES

[1] Locke, B.R., Sato, M., Sunka, P., Hoffmann, M.R., Chang, J.S. (2006). Electrohydraulic discharge and nonthermal plasma for water treatment. *Ind. Eng. Chem. Res.*, 45, 882-905.

[2] Sunka, P., Babicky, V., Clupek, M., Lukes, P., Simek, M., Schmidt, J., Cernak, M. (1999). Generation of chemically active species by electrical discharges in water. *Plasma Sources Sci. Technol.*, 8, 258–265.

[3] Joshi, A.A., Locke, B.R., Arce, P., Finney, W.C. (1995). Formation of hydroxyl radicals, hydrogen peroxide and aqueous electrons by pulsed streamer corona discharge in aqueous solution. *Journal of Hazardous Materials*, 41, 3-30.

[4] Hoeben. W.F.L.M., van Veldhuizen, E.M., Rutgers, W.R., Kroesen, G.M.W. (1999). Gas phase corona discharges for oxidation of phenol in an aqueous solution. *J. Phys. D: Apl. Phys.*, 32, L133–L137.

[5] Sun, B., Sato, M., Clements, J.S. (1999). Use of a pulsed high-voltage discharge for removal of organic compounds in aqueous solution. *J. Phys. D: Appl. Phys.*, 32, 1908-1915.

[6] Sugiarto, A.T., Sato, M. (2001). Pulsed plasma processing of organic compounds in aqueous solution. *Thin Solid Films*, 386, 295-299.

[7] Lukes, P., Appleton, A.T., Locke, B.R. (2004). Hydrogen peroxide and ozone formation in hybrid gas–liquid electrical discharge reactors. *IEEE Trans. Ind. Appl.*, 40, 1, 60-67.

Paper

THE ROLE OF IRON IONS IN THE PHENOL OXIDATION IN WATER BY GAS-PHASE DC CORONA DISCHARGE

J. Mizeraczyk, M. Dors, E. Metel, M. Kocik, J. Mikielewicz

Centre for Plasma and Laser Engineering
The Szewalski Institute of Fluid Flow Machinery, Polish Academy of Sciences
Fiszera 14, 80-231 Gdańsk, POLAND

The positive pulsed streamer discharge was generated between a stressed needle and a cylinder. Both electrodes were immersed in the distilled water contaminated with phenol (0.62 mM), to which $FeSO_4$ could be added. It was found that H_2 and H_2O_2 was produced during the streamer discharge in water with production rates of 0.021 mg/min and 0.55 mg/min, respectively. Increasing the discharge duration resulted in increased H_2O_2 concentration, phenol degradation rate, water conductivity and acidity. The oxidants produced by the streamer discharge oxidized up to 42% of phenol during 90 min processing of the water without $FeSO_4$. In the presence of $FeSO_4$ the phenol oxidation efficiency increased to 78%.

1. INTRODUCTION

Recently, pulsed-corona discharges have been intensively studied for the removal of hazardous organic pollutants from wastewater. A number of studies have utilized pulsed gas phase discharges generated over a water surface to produce in the gas or at the gas–liquid interface strongly oxidative species, such as OH radicals, O atoms, ozone (O_3) and hydrogen peroxide (H_2O_2). Due to the microsecond lifetime of radicals such as OH and O, only O_3 and H_2O_2, produced above the water surface (in the gaseous phase), can diffuse into the aqueous phase. Thus, organic pollutants are oxidized by radicals at the gas–liquid interface and by O_3 and H_2O_2 in the water bulk.

In the presence of iron, hydrogen peroxide produces large numbers of hydroxyl radicals through Fenton reaction:

$$Fe^{2+} + H_2O_2 \rightarrow Fe^{3+} + OH^- + OH. \quad (1)$$

It was already reported in [1-5] that addition of iron salts in the reactor of pulsed corona discharge in water enhance degradation of several organic compounds.

In previous reports [6] it was shown that gas phase DC corona discharge processing of water results in production of H_2O_2 in aqueous phase. Since Fenton reaction requires H_2O_2, one may expect that this reaction will run during corona discharge processing of water in the presence of iron ions. This report is aimed at studying the influence of the presence of Fe^{2+} ions on the efficiency of phenol oxidation in water processed with gas phase DC corona discharge.

Electronic address: mdors@imp.gda.pl

2. EXPERIMENTAL SET-UP

The experimental set-up and the reactor are presented in Figure 1. The positive DC corona discharge was generated between a stainless steel hollow needle electrode and the surface of pure water or water contaminated with phenol. A grounded flat stainless-steel mesh electrode was set 10 mm below the water surface. The outer and inner diameter of the hollow needle was 2 mm and 1.6 mm, respectively. The hollow needle-water surface spacing was 20 mm.

The positive polarity DC high voltage (18-23 kV) was applied through a 10 MΩ resistor to the hollow needle electrode. The time-averaged discharge current was 75 μA. The repetition rate of the corona pulses was 50 kHz.

Dry air with CO_2(1.5%), which stabilized the corona discharge, was supplied through the hollow needle with a flow rate of 1 l/min. The water containing 0.6 mM of phenol and 0.08 mM Fe_2SO_4 was mixed continuously with a magnetic stirrer.

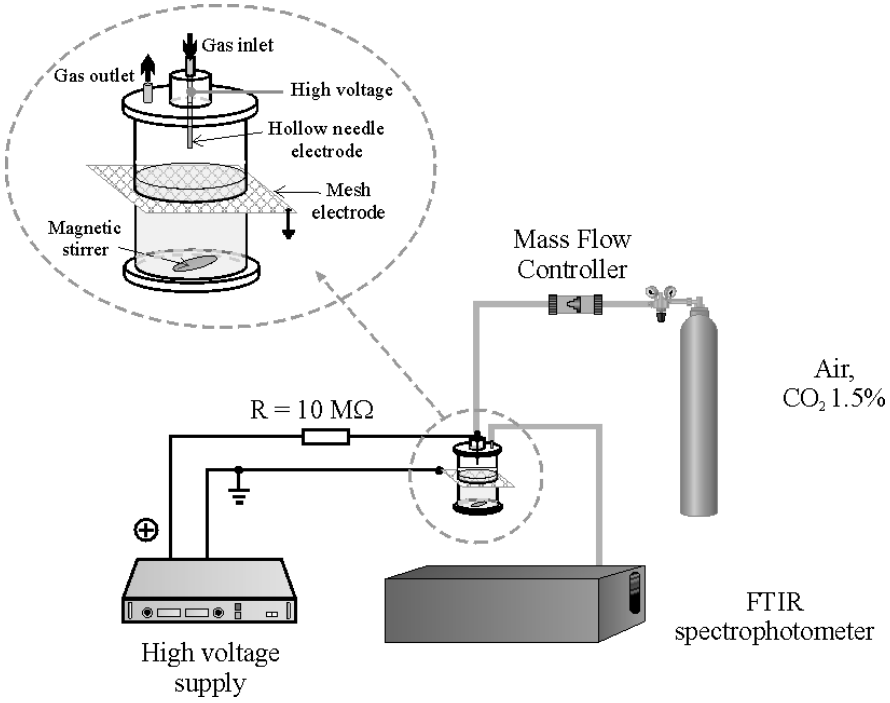

FIGURE 1. Experimental set-up.

The concentration of phenol in the water was measured by a gas chromatograph before and after the corona discharge processing. The water was analyzed also for the presence of ozone (iodometric method) and hydrogen peroxide (pertitanic acid formation method). The acidity (pH) and conductivity of the water were measured as well.

3. RESULTS AND DISCUSSION

When the phenol-polluted water was processed by the DC corona discharge the concentration of phenol in the water decreased with processing time from 0.61 mM to 0.23 mM, regardless the presence of iron ions (Figure 2a). It means that phenol was oxidized by ozone and OH radicals produced via electron reactions with water molecules and there was no additional production of OH radicals through Fenton reaction.

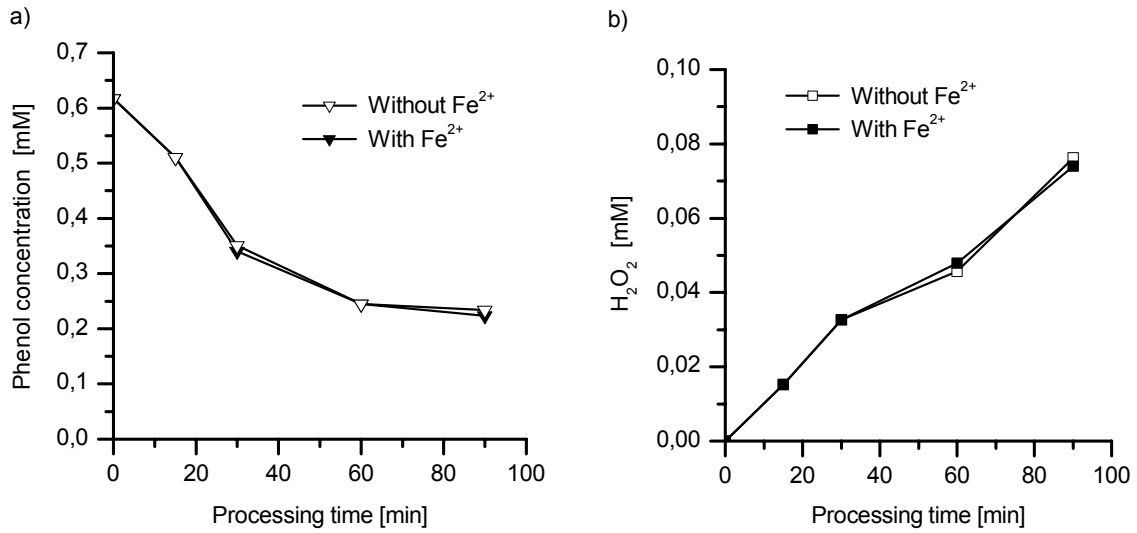

FIGURE 2. Concentration of phenol (a) and hydrogen peroxide (b) in aqueous phase without and with iron ions after the DC positive corona discharge processing. Discharge current 75 μA. Gas flow rate 1 l/min. Initial phenol concentration 0.6 mM.

Since phenol concentrations were the same after corona discharge processing of water with and without iron ions, a number of phenol oxidation products should be the same. Our previous studies [6] showed that phenol is oxidized into dihydroxyphenols and organic acids. In this experiment we have not detected dihydroxyphenols (detection limit 1 $\mu g/cm^3$), what suggests that the main products of phenol oxidation are organic acids and perhaps other simple, not aromatic, compounds. Unfortunately, we were not able to measure these simple organic compounds.

A lack of Fenton reaction was confirmed by the measurement of H_2O_2 concentration, which increased with processing time exactly the same way in water with and without iron ions (Figure 2b). Thus, there was no reaction between H_2O_2 molecules and iron ions.

However, iron ions were involved in some reactions, since the colour of the water contaminated with phenol and Fe_2SO_4 was changing with processing time from colourless through light yellow to dark yellow while there was no changes in colour when iron ions was not present in the phenol-polluted water. A most probable reaction of iron ions is the following one [7]:

$$Fe^{2+} + O_3 \rightarrow FeO^{2+} + O_2. \quad (2)$$

As it is seen in the reaction, the presence of ozone in the aqueous phase is required. It was reported in [6] that gas phase DC corona discharge produces ozone which dissolves in water and then oxidizes phenol. Concentration of ozone in aqueous phase measured in this experiment is presented in Figure 3. In the presence of iron ions in the phenol-polluted water ozone concentration is significantly lower comparing to the water with phenol only, what may be attributed to the reaction (2).

4. CONCLUSIONS

The results of phenol oxidation in water with iron ions by gas phase DC corona discharge showed that there was no additional production of OH radicals through Fenton reaction, in spite of significant production of hydrogen peroxide. Instead of going into Fenton reaction with hydrogen peroxide molecules, iron ions react with ozone which is produced in gas phase

and then dissolves in water. As a result phenol oxidation efficiency is the same in water with and without iron ions.

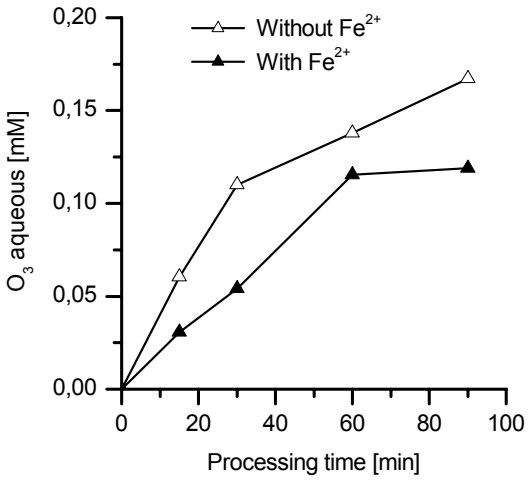

FIGURE 3. Concentration of ozone in aqueous phase without and with iron ions after the DC positive corona discharge processing of water polluted with phenol. Discharge current 75 μA. Gas flow rate 1 l/min. Initial phenol concentration 0.6 mM.

ACKNOWLEDGMENTS

This work was supported by the Ministry of Science and Information Society Technologies under programme PB 1280/T10/2004/27 and by the Institute of Fluid Flow Machinery, Polish Academy of Sciences under programme IMP PAN O3Z3T2.

REFERENCES

[1] Sunka, P., Babicky, V., Clupek, M., Lukes, P., Simek, M., Schmidt, J., Cernak, M. (1999). Generation of chemically active species by electrical discharges in water. *Plasma Sources Sci. Technol.*, 8, 258–265.

[2] D.R. Grymonpré, A.K. Sharma, W.C. Finney, B.C. Locke, The role of Fenton's reaction in aqueous phase pulsed streamer corona reactors, Chemical Engineering Journal, 82, 189–207, 2001

[3] N. Koprivanac, H. Kušić, D. Vujević, I. Peternel, B.R. Locke, Influence of iron on degradation of organic dyes in corona, Journal of Hazardous Materials, B117, 113–119, 2005

[4] Grymonpré. D.R., Sharma. A.K., Finney. W.C., Locke. B.R. (2001). The role of Fenton's reaction in aqueous phase pulsed streamer corona reactors. *Chemical Engineering Journal,* 82, 189–207.

[5] Koprivanac, N., Kušić, H., Vujević, D., Peternel, I., Locke, B.R. (2005). Influence of iron on degradation of organic dyes in corona. *Journal of Hazardous Materials*, B117, 113–119.

[6] Dors, M., Mizeraczyk, J., Mok, Y.S. (2006). Phenol oxidation in aqueous solution by gas phase corona discharge. *J. Adv. Oxid. Technol.*, 9, 2 /in print/.

[7] NIST Chemical Kinetics Database, http://kinetics.nist.gov/

A FUNDAMENTAL RESEARCH OF THE WATER TREATMENT USING A PULSED POWER TECHNOLOGY

Shou Nakazaki, Satoshi Ihara, and Chobei Yamabe

Department of Electrical and Electronic Engineering,
Faculty of Science and Engineering, Saga University

Abstract: Treatment of water including surfactants, Nonylphenolethoxylate(NPEO), using pulsed power discharge was tested experimentally. An electric discharge is formed at between needle electrodes and water surface using the pulse power with coaxial cable. Treatment of drainage including a surfactant is attempted by the free radicals that were generated by discharge. COD value was used for evaluation of treatment. The reduction of COD value was confirmed, and the successful treatment of the drainage was realized..

1. Introduction

A surfactant is a synthetic chemical, and it is widely used on water cleaning at the field of various industries, for example, a electronic parts, a machine part, fiber production and so on. Generally the surfactants are difficulty resolvability, and it has high COD value that is an index of water pollution.

Treatment of wastewater including surfactants, have been carried out using mainly combustion processes at industrial factory. However this processes takes a high cost because a large quantity of fuel (energy) is necessary to combustion, and also induce producing CO_2 that is origin of global warming.

Especially, the water pollution by Nonylphenolethoxylate (NPEO), which is often used for cleaning in various industries, is serious problem because Nonylphenol (NP), which induces endorine disruption in living body, is produced as a by-product due to the decomposition of NPEO.

In this study, treatment of water including surfactants, Nonylphenolethoxylate (NPEO), using pulsed power discharge was tested experimentally. A discharge is formed by applying the pulsed high voltage, and the free radicals is produced at inside of reactor. In our experimental, effectiveness of discharge on treatment of surfactants was evaluated from value of chemical oxygen demand(COD).

2. Experiment apparatus and method

The configuration of experimental apparatus is shown in Fig. 1. A pulsed power supply is consist of a step up transformer, matching resistance (50 Ω), a pulse transmission line (characteristic impedance is 50 Ω), a trigger less gap switch and discharge reactor for water treatment. The pulse width of output voltage was changed by changing the length of the pulse transmission line. After charging of transmission line, the gap switch is turned on and the output voltage is applied to rector.

The structure of a discharge reactor is shown in Fig. 2. The reactor has a cylindrical vessel with acrylic resin. The entrance and exit of raw gas for radical generation are installed to a reactor. The high voltage electrode is multi-needle consisting 91 stainless needles and a grounding electrode located at bottom of vessel is enamel coated metal. The electric discharge is formed between a tip of needle and a surface of the treatment water.

In this experiment, oxygen gas was flowed through the reactor at flow rate of 0.5 Liter/min, the discharge treatment was performed consecutively for 60 minutes. The voltage across the electrodes V_r and the discharge current I_r impressed on a reactor were measured with high voltage probe (Tektronix 6015A) and current probe (Pearson MODEL 2877), respectively. The discharge energy per one pulse (J/pulse) is calculated from applied voltage and discharge current waveforms. The average discharge power was calculated from the values of discharge energy and average frequency of discharge. COD (Chemical Oxygen Demand) is used for evaluation of discharge treatment. From COD values, which measured at before and after discharge, the reduction rate of COD is calculated by following equation.

$$\text{COD reduction rate (\%)} = \frac{COD_b - COD_a}{COD_b} \times 100 \qquad (1)$$

where, COD_b and COD_a are COD values at before and after discharge, respectively.

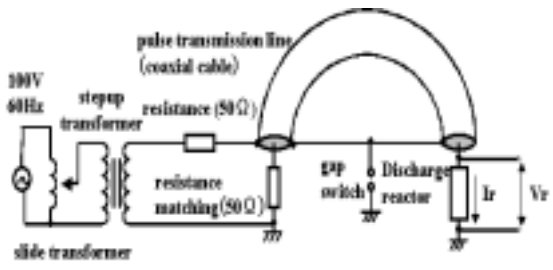

Fig.1 Configuration of experimental apparatus.

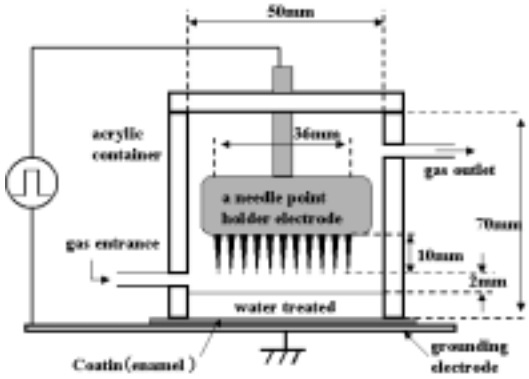

Fig.2 Structure of an electric discharge reactor.

In our experiment, industrial wastewater from factory and standard solution with NPEO were used as sample water. The components of wastewater are NPEO, resin, alcohol and SiO_2. The measured COD values of standard solution and wastewater were about 7600 mg/Liter and about 6400 mg/Liter, respectively. The standard solution also was treated by discharge, and COD reduction rate was measured. Two kinds of length of transmission line, 20m (pulse width T=120ns) and 40m (pulse width T=220ns) were used to examine the influence of pulse width.

3. Experimental Results

Figure 3 show the voltage and current waveforms, when the wastewater was treated. Figs. 3(a) and (b) are a voltage and current waveforms of T=120 ns and 220 ns, respectively. The peak values of applied voltage and current were about 10 kV and 80 A, respectively. The negative current which appeared at termination of voltage pulse is caused by capacitance of high voltage and grounded electrodes.

Figs. 4 and 5 are characteristics of COD reduction rate on discharge power, when standard solution and wastewater were treated, respectively. It can be seen that the both profiles have a peak values. The discharge power at the standard solution is lowers than at wastewater, because resistivity of wastewater water is higher than that of the standard solution.

It is found that the COD reduction rate decreases at higher discharge power. As discharge power increased, intensity of discharge emission becomes to be higher and the diameter of discharge path decreased. It may be suggest that the increase of gas temperature and the decrease of radical generation. It is possible that the decrease of COD reduction rate is because of decrease of radical generation.

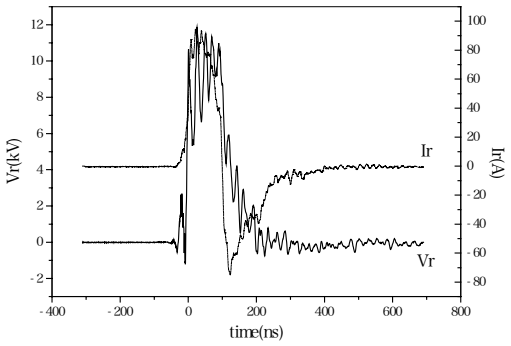

Fig. 3(a) Pulse width T =120 ns.

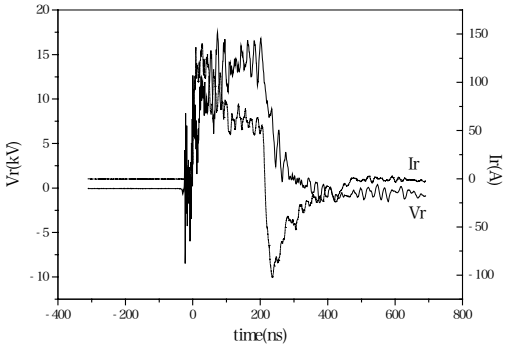

Fig. 3(b) Pulse width T =220 ns

Fig. 3 Voltage and current waveforms at different pulse width.

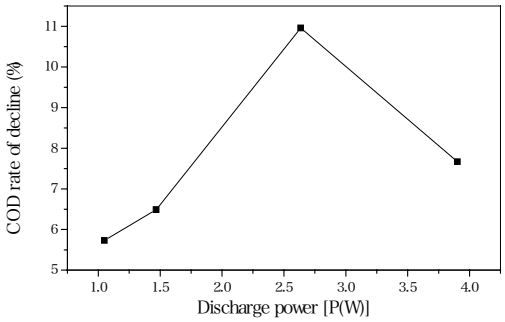

Fig. 4 COD rate of decline for discharge power (standard solution was treated)

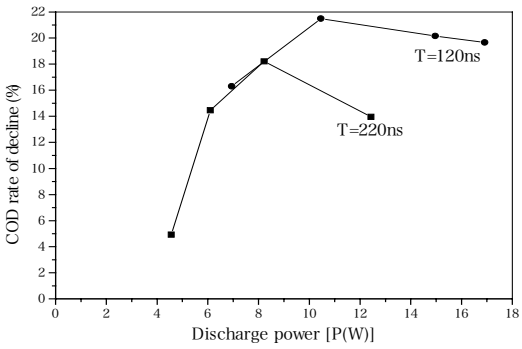

Fig. 5 Characteristics of COD reduction rate on discharge power (sample water was treated)

The COD reduction rate becomes to be higher at T=120 ns rather than T=220 ns as shown in Fig. 5. At the same discharge power, the energy per one pulse was larger at *T*=220 ns than *T*=120 ns. On the other hands, average discharge frequency was higher at *T*=120ns than *T*=220ns. It is found that low energy and high frequency suitable for reduction of COD.

4. Conclusion

Treatment of drainage including a surfactant was tried using the free radical that was generated by an electric discharge. The pulsed discharge was formed by the pulsed power generator. For standard solution including Nonylphenolethoxylate (NPEO), the maximum COD reduction rate of about 11% were obtained at initial COD value of about 7600 mg/Liter. On the other hand, for wastewater including NPEO and the other components, the maximum COD reduction rate of about 22% were obtained at pulse width of 120ns when the initial COD value of about 6400 mg/Liter. According to our results, it was found that the discharge is effective for treatment of water including surfactants.

Acknowledgements

We would like to thank Mr. Yasuo Suzuki, You Kawakita, Plasma Ion Assist Co., Ltd, Hisashi Nagaya, Techno Science Co., Ltd. for providing of samples, valuable discussions and comments.

POST-DISCHARGE PHENOMENA IN A GLIDING ARC TREATMENT OF AN AZO DYE

D. Moussa[(1)], G. Kamgang[(1)], J.L. Brisset[(1)], E. Hnatiuc[(2)]

[(1)]Laboratoire d'Electrochimie de l'Université de Rouen, 76821 MONT SAINT AIGNAN, FRANCE
[(2)]Technical University Gheorghe Asachi, Iasi, Romania, e-mail ehnatiuc@ee.tuiasi.ro

Gliding arc treatment of liquids has a great interest as it is very simple to use and quite cheap. A new area studied is the post-discharge self target evolving observed after gliding arc switching off as it permits to devise treatments with very short plasma running time. By that way, energy and time spends are reduced drastically, which fits to industrial purposes. We have focused on the oxidation of the acidic form of methyl orange (an azoic dye). Standard volumes of an acidic solution of methyl orange were treated by the wet air gliding arc during short times ranging from 0,5 to 3min and in each case, the evolving of main absorption band of the dye was monitored by spectroscopy as the appearance of a yellow new specie. This self post discharge evolving showed a typical first order kinetics both for the disappearance of the methyl orange red acidic form and for the appearance of the yellow product expected to be an nitroaromatic compound. Correlations between global constant of this kinetics process and some gliding arc treatment parameters were studied showing that such process is efficient even with only one minute of gliding arc exposure.

POST-DISCHARGE PHENOMENA IN GLIDING ARC TREATMENT OF AN AZO DYE

D. Moussa[1], G. Kamgang[1], J.L. Brisset[1] and E. Hnatiuc[2]

[1] *Laboratoire d'Electrochimie, University of Rouen, 76821MONT SAINT AIGNAN, FRANCE*
[2]*Technical University Gheorghe Asachi, IASI, ROMANIA*

ABSTRACT. Gliding discharge treatment of liquids has a great interest as it is very simple to use and quite cheap. A new area studied is the post-discharge self target evolving observed after gliding arc switching off as it permits to devise treatments with very short plasma running time. By that way, energy and time spends are reduced drastically, which fits to industrial purposes. We have focused on the oxidation of the acidic form of methyl orange (an azoic dye). Standard volumes of an acidic solution of methyl orange were treated by the wet air gliding arc during short times ranging from 0,5 to 3min and in each case, the evolving of main absorption band of the dye was monitored by spectroscopy as the appearance of 4-nitro-(N,N)-dimethylaniline (4-NDMA) as the major product. This self post discharge evolving showed a typical first order kinetics both for the disappearance of the methyl orange red acidic form and for the appearance of 4-NDMA. Correlations between global constant of this kinetics process and discharge exposure time were studied showing that such process is efficient even with only one minute of gliding arc exposure.

1. INTRODUCTION

The gliding discharge resulting by blowing an electrical discharge between divergent electrodes in a symmetrical configuration is a very interesting tool to make non thermal plasma at atmospheric pressure and near room temperature [1]. When blown, the discharge is quenched and breaks giving a non thermal plasma flow. The great interest of such tool is using quite cheap materials and equipment and being easy to use. It was used successfully in gas treatments [2], and more recently, liquids treatments [3-5]. A part of last works on aqueous solutions treatments focus on post-discharge effect, a chemical self evolving of the plasma exposed liquid target after switching off the discharge i.e without anymore plasma exposure. Such phenomenon was already observed in inorganic solutes oxidation by wet air gliding discharge [6]. It has a great interest for industrial purpose as it enables design of very short (i.e. flash) plasma treatments, the post-discharge effect completing the expected chemical treatment. In this present paper we have focused on oxidative cleavage of methyl orange (an azoic dye) as demonstrative illustration of post discharge oxidation of organic solutes.

2. EXPERIMENTAL SECTION

Gliding arc treatments were performed in a glass cylinder-shaped reactor fitted with magnetic stirring and water cooling jacket (Figure 1). The gliding discharge device mounted on the lid involves two diverging electrodes disposed symmetrically around a wet air nozzle.

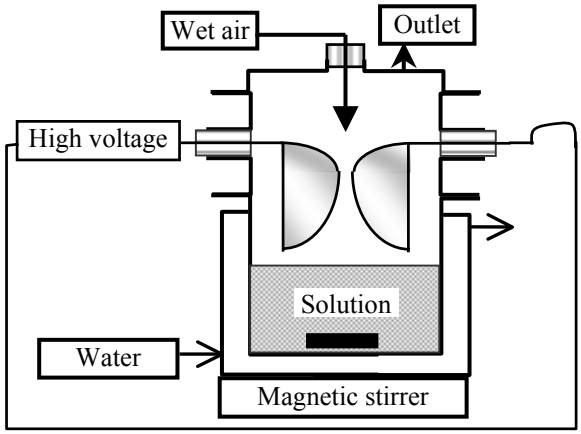

FIGURE 1. Experimental device

The electrodes are supplied in current by a transformer giving 10kV (open conditions) and a maximal current of 150mA. The nozzle is fed in wet air obtained by bubbling airflow (595L/h) through a Durant flask. The target consisting in 200mL of solution of methyl orange (25mg/L) and nitric acid (5.10^{-3}M) is exposed to the discharge for short time t* and just after, sampled in a closed spectrometry cell. The post-discharge solution evolving is monitored through both absorbency decrease of dye acidic form at 507,5nm and absorbency increase of yellow product at 420nm (different from basic form of the dye exhibiting absorption band at 465nm). Analysis of the final yellow product was performed with a Schimadzu LC20 AD HPLC chromatograph fitted with a UV cell detector (detection at 370nm) and a Inertsil ODS-3 C_{18} reverse phase column (length: 250mm, internal diameter: 4,6mm, granulometry: 5µm). Mobile phase (1mL/min) is consisted of acetonitrile and water with 70% (v/v) of acetonitrile during first 10 minute followed by a linear increase to 90% within 20min. Treated solution samples are alkalinized with any drops of ammonium hydroxide and directly injected (20µL loop). A standard of 4-nitro-N,N-dimethylaniline (4-NDMA) solution (20mg/L) is used for identification.

3. RESULTS AND DISCUSSION

The absorbency of the acidic red form of methyl orange (507,5nm) decreases after short treatment time t*. The kinetics (Figure 2, A) exhibits a typical global first order assessed by plots LnA vs time (Figure 2, B) for different discharge exposure times t*.

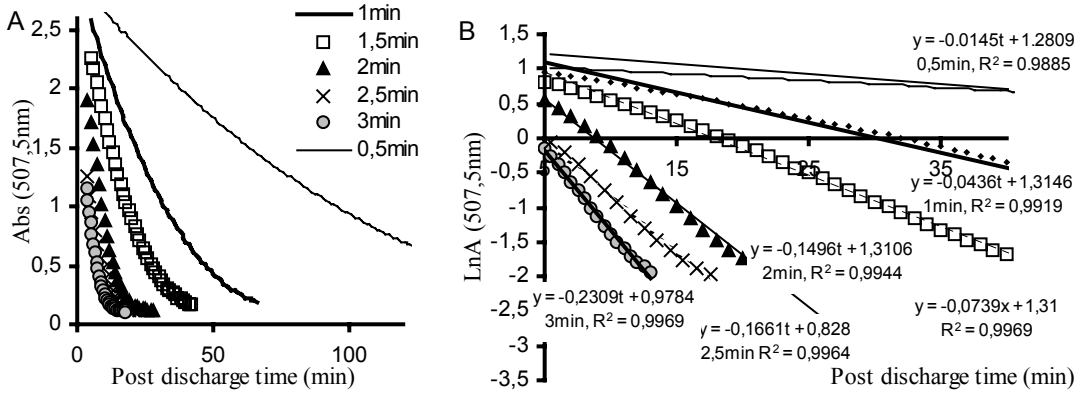

FIGURE 2. Kinetics of decrease of the acidic form of methyl orange for different exposure times

This favors the assumption that long life oxidizing species formed in the discharge have drifted to the liquid surface solution where their own oxidizing properties allow to degrade the dye target even after powering off the discharge. $HO^{\bullet}$ and $NO^{\bullet}$ radicals (shown in wet air gliding discharge [7]), O_2 and H_2O react together in the plasma to synthesize nitrous acid and hydrogen peroxide which drift into the solution. This last both species may react together to give peroxonitrous acid following [8].

$$HNO_2 + H_2O_2 \rightarrow ON\text{-}O_2H + H_2O$$

This last one is a powerful oxidizing agent. A yellow compound featured by an absorption peak at 420 nm concomitantly forms in post-discharge conditions. The relevant overall kinetics is first ordered with a rate constant k', obeying the expression

$$A_{420} = A_{f,420}\left(1 - e^{-k't}\right) \quad (1)$$

and assessed by the matching plot of the expression

$$Ln\left(A_{f,420} - A_{420}\right) = f(t) \quad (2)$$

versus the post-discharge time t (Figure 3).

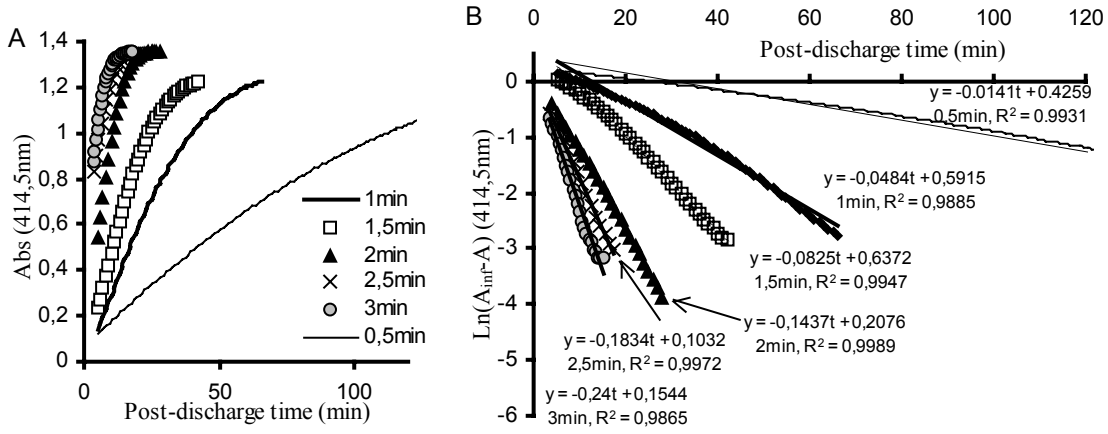

FIGURE 3. Kinetics of 4-NDMA (yellow) formation for different exposure times

The values of the constants k_o and k' for each treatment time are very close (Figures 2, 3, and 4).

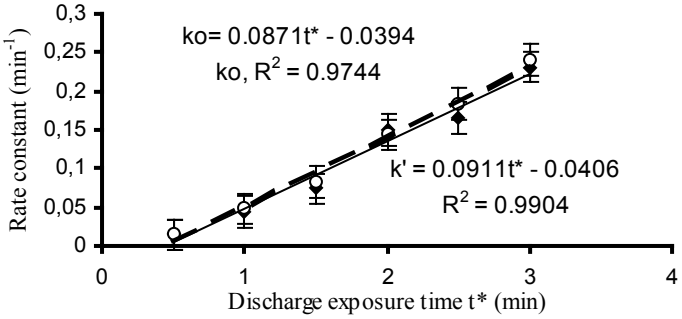

FIGURE 4. Correlation between discharge exposure t* and both rate constants k_o and k'

This suggests a nearly quantitative conversion of the dye to this yellow compound. HPLC analysis of the final solution (for t*=2,5min) by comparison with those of a standard sample assesses 4-nitro-N,N-dimethylaniline (4-NDMA) as yellow compound formed, and nearly

total disappearing of the dye. This leads us to thing that the post-discharge involves mainly an oxidation of the N=N bond in the dye by long life species inducing cleavage of this one. That leads to quantitative oxidative conversion of methyl orange to 4-NDMA. Plot of both rate constants k_o and k' vs discharge exposure time shows a relevant linear correlation. This feature may be explained as follows : the greater is the plasma exposure time t*, the greater is the total initial amount of active species formed in the gas phase and drifted into liquid target, and consequently the number of degraded dye molecules. On the basis of the correlation illustrated by figure 4, we can also guess that the amount of species drifted into the solution is too low to ensure the first-order kinetics process for a treatment time t* shorter than 0,5min. Oppositely, the kinetics plot for the 0,5 min treatment fits moderately with a first-order law compared with other plots and that feature confirms the considered assumption.

For a constant given flow we can write

$$k_o = k' = k(gt^* - l) = At^* - B \tag{3}$$

4. CONCLUSION

We have shown a post-discharge effect through self evolving of treated acidic solution of methyl orange. We have shown that such effect involves an oxidation of the diazo N=N bond of the dye by long life species such as HNO_2, H_2O_2 and perhaps peroxonitrous acid HOONO. The oxidation leads to cleavage of this diazo bond giving 4-nitro-N,N-dimethylaniline shown by HPLC. Works is in progress to identify other oxidation products among with 4-nitrosulfonic acid is expected and to assess HNO_2, H_2O_2 and peroxonitrous acid HOONO as species implicated in the post-discharge process.

REFERENCES

[1] Fridman,, A.A. Petrousov, A., Chapelle, J., Cormier, J.M., Czernichowski, A., Lesueur, H,. Stevefelt, J., (1994). *J. Phys. III France 4,* 1449-1465.

[2] Czernichowski A. (1994). *Pure Appl. Chem.,* 66(6), 1301-1310.

[3] Moussa, D., Brisset, J.L. (2003). *J. Hazardous Mater*., B102, 189-200.

[4] Benstaali, B., Moussa, D. Addou, A., Brisset, J.L. (1998). *Eur. Phys. J. AP*, 4, 171-179.

[5] Moussa, D., Abdelmalek, F., Benstaali, B., Addou, A., Hnatiuc, E., Brisset, J.L. (2005). *Eur. Phys. J. Appl. Phys*., 29,189-199.

[6] Doubla, A., Abdelmalek, F., Khélifa, K., Addou, A., Brisset, J.L. (2003). *J. Appl. Electrochem*., 33, 73-77.

[7] Benstaali, B., Boubert, P., Chéron,, B.G., Addou, A., Brisset, J.L. (2002). *Plasma Chem. Plasma Proc*., 22(4), 553-571.

[8] Halfpenny, E., Robinson, P.L., (1952). *J. Chem. Soc*, 928.

APPLICATION OF GLIDING ARC PLASMA IN HUMID AIR TO THE TREATMENT OF THIOUREA

E.B. Tsagou-Sobze[1,2], D. Moussa[2], A. Doubla[1], E. Hnatiuc[3], J.L. Brisset[2]

1 Department of inorganic Chemistry, Laboratory of mineral chemistry, University of Yaoundé, (Cameroon)
2 Department of chemistry, laboratory of electrochemical (L.E.I.A), University of Rouen (France)
3 Technical University " Gheorghe Asachi" IASI, Romania

ABSTRACT

Active species produced by humid air plasma and applied to aqueous solution of thiourea allowed us to confirm the efficiency of its degrading power. The major species NO and OH° highly contribute to the thiourea degradation. This molecule undergoes a double attack at the liquid surface by OH°, and in the solution by nitrosonium ions.

The treated solution was monitored by the barium titration of sulphate ions formed during the treatment. The solute concentration linearly increased as the target solution was exposed to the discharge. This feature evidenced that the pollutant molecule was broken according to a zero order kinetic scheme ($k° = 1{,}22.10^{-4}$ $mol.L^{-1}.min^{-1}$), for a degradation level 96,5 %

The analysis of the emitted gases show the presence of CO_2 (Dräger disposable test tubes) and a N_2 (spectre).

Keywords

Non-thermal plasma; gliding are discharge; atmospheric pressure; pollution abatement; aqueous solutions; degradation of thiourea

APPLICATION OF GLIDING ARC PLASMA IN HUMID AIR TO THE TREATMENT OF THIO-UREA

E.B. Tsagou-Sobze[1,2], D. Moussa[1], A. Doubla [2], E. Hnatiuc[3] and J.L. Brisset[1]

[1] *Laboratoire d'Electrochimie, University of Rouen, 76821-Mont Saint-Aignan, France*
[2]*Laboratoire de Chimie Minérale, University of Yaounde-I, Cameroon*
[3]*Technical University Gheorghe Asachi, Iasi, Romania*

ABSTRACT. Urea and Thio-urea molecules [$(NH_2)_2C=S$] dispersed in aqueous solutions are exposed to a gliding discharge in humid air. The major active species present in the plasma, i.e., mainly NO and OH° radicals react at the liquid surface and degrade the solute to CO_2 and N_2. The degradation mechanism for urea and thio-urea results from a double attack by OH° and nitrosonium ions. The overall degradation are zero-order with constants 5.28 10^{-6} s^{-1} or thio-urea and 2.03 10^{-6} s^{-1} for urea.

1. INTRODUCTION

The gliding discharge [1] is actually a quenched plasma operated at quasi ambient temperature and atmospheric pressure: it is a interesting tool to investigate the chemical properties of the active species and for various applications. Electric discharges in humid air induce acid and oxidising effects which are suitable to the treatment of liquids, i.e., the oxidation of organic pollutant solutes such as dyes [2], the removal of chlorinated organic solvents [3], of spent solvents (e.g., tributylphosphate [4]) or surfactans [5]. An example of S containing compound is considered: we selected thio-urea [$(NH_2)_2C=S$] and urea which are largely used in industrial applications.

The main species responsible for the chemical properties of a discharge were identified and quantified: OH and NO radicals [6,7] are known for their oxidising properties [8]. NO is also source of NO_2H and NO_3H with are essential to control the oxidation process of organic compounds. Other oxidising species (e.g., H_2O_2) are present in small concentrations in solution and can slightly affect the degradation kinetic rates.

1. EXPERIMENTAL SECTION

The gliding discharge (or gliding arc or glidarc) was proposed by Czernichowski *et al*. [1] as a plasma source at atmposheric pressure and quasi ambient temperature. An arc forms at the minimum gap between two diverging conductors connected to a HV (10 kV) source. A humid air flow (640 $L.h^{-1}$) directed through a nozzle disposed along the electrodes symmetry axis gently moves the arc feet to the tip of the electrodes, so that the arc length increases and breaks into a plasma plume. The resulting quenched plasma is a plume containing the active species formed in the discharge and able to react at the target surface. The reported treatments were performed in a batch reactor (Figure 1) fitted with magnetic stirring and water cooling jacket. The target consists of 200 mL of aqueous solutions of urea (5 mM) or thio-urea (20 mM). Samples of the treated solutions are readily analyzed by spectrometry, Total Organic Carbon measurements (Shimatsu TOC VE) or titrated for SO_4^{--} liberated.

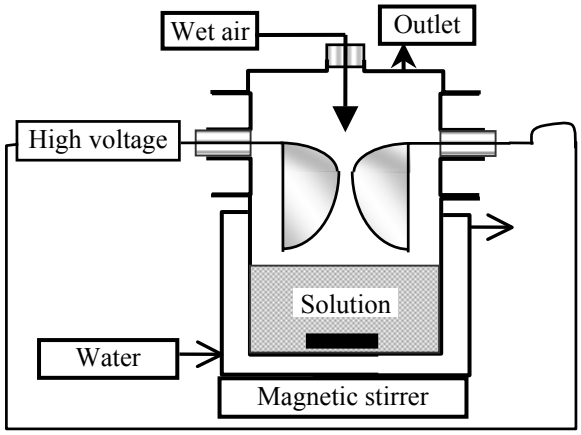

FIGURE 1. Experimental device

2. RESULTS AND DISCUSSION

The overall degradation reactions of thio-urea and urea are respectively

$$(NH_2)_2SO + 2\ O_2 + 2H_2O \rightarrow CO_2 + 2\ NH_4^+ + SO_4^{2-}$$

$$(NH_2)_2CO + 4\ O_2 \rightarrow CO_2 + H_2O + 2\ NO_3^- + 2\ H^+$$

The structures of these compounds are close to the amide functional group so that they are water sensitive via acid catalysed hydrolysis reactions. Matching reactions of degradation and hydrolysis should then be expected.

Degradation of urea

Spectral analysis of the plasma treated solutions shows a lack of absorbance of the blank urea solution in the UV-visible range and an increase around 240 nm for various increasing exposure times t* (min) to the discharge which is attributed to the formation of nitrite ions. Plasma degradation of urea is evidenced by means of TOC measurements. The concentration of the solution in Carbon, TOC (mgC L^{-1}), linearly decreases as t* increases. This zero order kinetic law is observed for t*<120 min ($k° = 0.317t* + 58.50$; $R^2 = 0.986$ or $k = 5.28\ 10^{-6}\ s^{-1}$ in the molar scale). For longer exposure times, the law changes to a 1st order diffusion controlled process, as observed in numerous examples.

Additional investigation on post-discharge phenomena [9,10] were successful. TOC abatement of plasma treated urea solutions was observed over 6 min and concerned more than 13 mg Carbon per liter (i.e., more than 30% of measured TOC); TOC post discharge evolution satisfactorily follows a pseudo first order kinetic law.

The reported results led us to consider matching reactions able to compete with the plasma treatment for degrading urea when the discharge is switched off. Adding HNO_2 to urea solutions not exposed to the discharge induced rapid TOC decreases with time. The solution also turns to greenish for a while and gas bubble form in the flask, which agrees with literature data relevant to the formation of a diazoic derivative and decarboxylation on mixing urea and NO_2^- ions in acidic medium (Fig. 2).The diazoic compound decomposes with N_2 emission. Oppositely, adding a mixture of $HNO_2$and H_2O_2 to urea showed no evolution of the solution. This is ascribed to the oxidation of nitrous acid by H_2O_2 in acid medium [9]:

$$HNO_2 + H_2O_2 \rightarrow HNO_3 + H_2O$$

We can conclude that nitrosonium ion NO^+ is involved in the reaction process. It may be either provided by the discharge or formed in the liquid phase from the action of H^+ on HNO_2, according to known reaction: $HNO_2 + H^+ \rightarrow H\text{-}O^+H - N{=}O \rightarrow H_2O + NO^+$

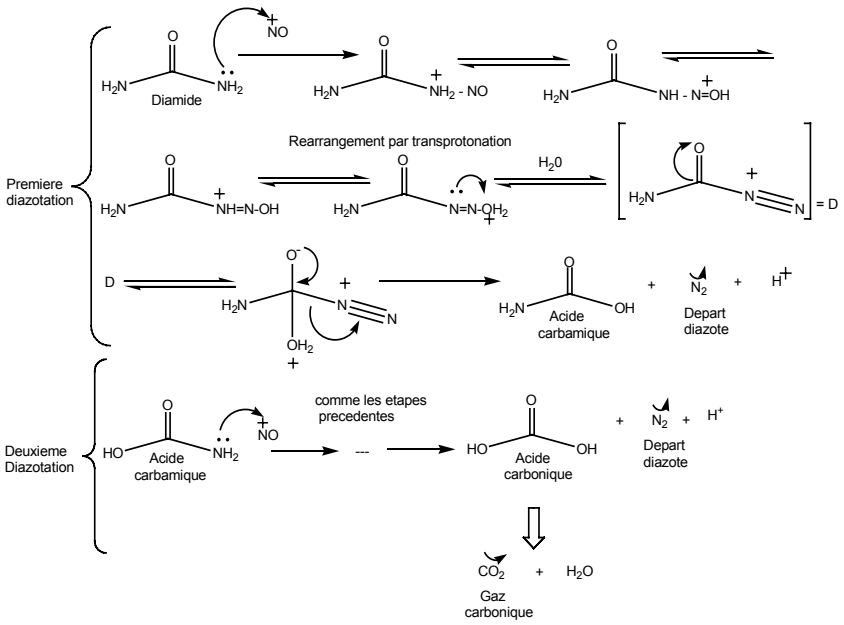

FIGURE 2- Proposed reaction scheme for the degradation if urea involving NO^+ [11]

The occurrence of a diazoic intermediate explains both the gas emission and the transient colour change of the solution. It also agrees with post-discharge phenomena since the various kinetic steps involved are less rapid than the action of the impinging radicals.

Degradation of thio-urea

The plasma treatment of thio-urea in similar conditions was undertaken to confirm that NO^+ occurs in the degradation mechanism of urea derivative molecule. No TOC measurements could be used because sulphur is poisonous for the catalyst. However noticeable changes in the colour of thio-urea solutions turning to pale yellow and an increase in turbidity resulted from the exposure to the plasma. Analysis of the output gases were positive to CO_2. The sulphate ions formed were followed by titration with $BaCl_2$ and conductometry measurements: the number of Ba^{2+} required was directly related with that of degraded thio-urea molecules. A kinetic plot was derived (Fig.3): after an induction time close to 15 min, the concentration of sulphate formed linearly increases with t* up to 150 min (end of reaction). The reaction obeys a pseudo zero order kinetic law with a kinetic constant k =2.03 10^{-6} s^{-1}.

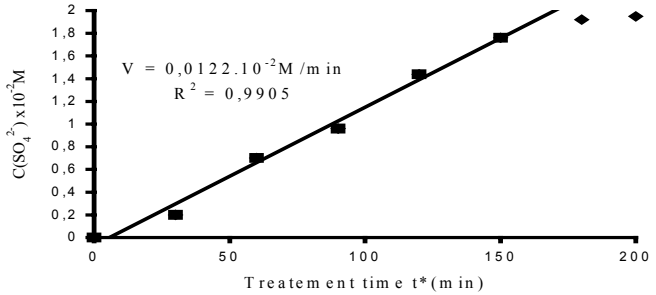

FIGURE 3 Formation of sulphate in thio-urea solutions exposed to the gliding arc [11].

The turbidity and the colour of the solution may be related to the formation of polymerized sulphur S_x an be consistent with the3% lack in the sulphate balance of the plasma treated solution (i.e., 10% for t*<30 min; 85% for 30<t*<150; and 1.5% for 150<t*<200).

A general reaction scheme (Fig. 4) involving S_x formation, as well as two competitive pathways involving respectively NO+ and OH° may be considered as a possible mechanism to account for the degradation process of thio-urea. The diazoic pathway is detailed in Fig.5.

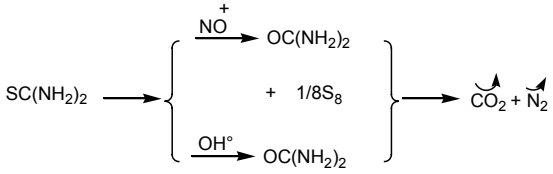

FIGURE 4 Parallel pathways for the plasmachemical degradation of thio-urea [11].

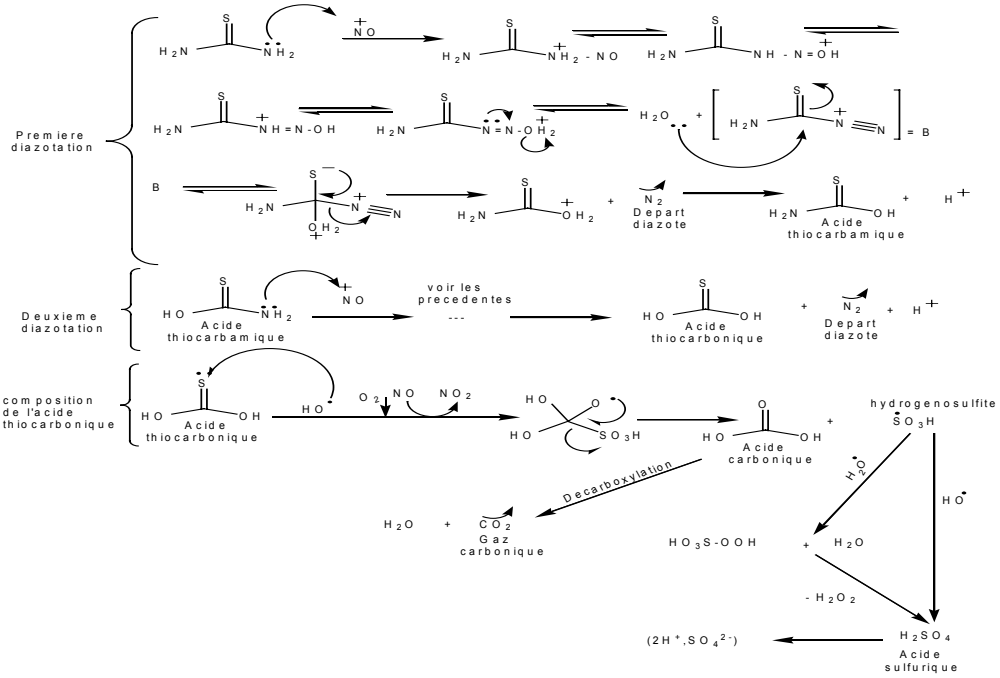

FIGURE 5. Detailed pathways for the degradationof thio-urea [11]

3. CONCLUSION

Urea and thio-urea dispersed in aqueous solution exposed to a gliding discharge in wet air are degraded. For both solutes, the kinetic law involves a 0-order step followed by a 1st-order kinetic step. The zero-order kinetic constants are resp. 2.03 10^{-6} s^{-1} and 5.28 10^{-6} s^{-1} for thio-urea and urea. Gas bubbles observed for both cases correspond to a mixture of N_2 and CO_2. The plasmachemical degradation of the solutes involves a diazoic intermediate induced by NO^+ which is unstable and yields N_2 gas. The occurrence and the influence of nitrosonium ion are clearly identified for the first time in the plasmachemical treatment of waste solutes.

LITERATURE CITED

[1] Czernichowski A. (1994). *Pure Appl. Chem.,* 66(6), 1301-1310.
[2] Fanmoe J., Kamgang J.-O., Moussa D., Brisset J.L. (2003) *Phys. Chem. News* 14, 1-4
[3] Abdelmalek F., Gharbi S., Benstaali B., Addou A., Brisset J.-L. (2004) *Wat. Res*. 38, 2339-2347
[4] Moussa, D., Brisset, J.L. (2003). *J. Hazardous Mater*.**,** B102, 189-200**.**
[5] Moussa D., Brisset J.L., Hnatiuc E., Decobert G. (2006). *J. Ind. Eng. Chem. Res*.45, 30-33
[6] Benstaali B., Boubert P., Cheron B.G., Addou A, Brisset J.-L. (2002) *Plasma Chem. Plasma Process*. 22, 553-571
[7] Benstaali B., Moussa, D. Addou, A., Brisset, J.-L. (1998). *Eur. Phys. J. AP*, 4, 171-179.
[8] Moussa, D., Abdelmalek, F., Benstaali, B., Addou, A., Hnatiuc, E., Brisset, J.L. (2005). *Eur. Phys. J. Appl. Phys.,* 29,189-199.
[9] Moussa D., Kamgang G., Brisset J.-L., Hnatiuc, E. (2006) *Proc. Hakone-10 Meeting, (Saga, Jpn. 2006),*
[10] Doubla, A., Abdelmalek, F., Khélifa, K., Addou, A., Brisset, J.L. (2003). *J. Appl. Electrochem*., 33, 73-77.
[11] Tragou-Sobze E. (2006). *Thesis, University of Rouen (France) and Yaounde I (Cameroon)* 170 p.

DECREASED OZONE CONCENTRATION DURING OZONE GENERATION USING 99.99% PURE OXYGEN AS THE FEED GAS

Masaki Taguchi[1], Tetsumi Takano[2], Haruo Itoh[3]

[1]Development Department
Environmental Systems Engineering Group,Fuji Electric Systems Co., Ltd.
7 Yawatakaigandori, Ichihara-shi, Chiba, 290-8511,JAPAN
[2]Material&Science Laboratory
Material Technology Group, Fuji Electric Advanced Technology Co., Ltd.
1 Fujimachi, Hino-shi, Tokyo, 191-8502,JAPAN
[3]Department of Electrical, Electronics and Computer Engineering
Faculty of Engineering, Chiba Institute of Technology,
2-17-1 Tsudanuma,Narashino-shi, Chiba, 275-0016, JAPAN

ABSTRACT

Ozone generated at ca.200 g/Nm^3 decreased to 1~5 g/Nm^3 in a few hours when 99.99% pure oxygen was used as the feed gas. Experimental equipment using two ozone generators in series with a gas feeding line between them was used to investigate this phenomenon. Based on the experimental results, it is suggested that NO_X on the surface of the electrode is essential for ozone generation and that the phenomenon of ozone decreasing during operation occurred because of the loss of NO_X from the electrodes by discharge when 99.99% pure oxygen was used as the feed gas.

1. INTRODUCTION

Ozone is second only to fluorine as the strongest known oxidant. Therefore, ozone is used in water treatment plants for disinfection, color removal, and odor removal. Ozone is often specifically used in drinking water treatment plants to suppress the formation of potentially carcinogenic trihalomethanes during chlorine disinfection. Ozone generators using oxygen as the feed gas generate ozone at much higher concentrations than generators using dry air. However, since around 1990, the phenomenon of rapid decrease in ozone concentration during ozone generation when using over 99.99% pure oxygen has been reported[1]-[3]. Hereinafter we will call this “the Phenomenon of Zero Ozone”, and use the abbreviation PZO. The details of PZO were investigated and are reported here.

2. EXPERIMENT

Two kinds of experiments were conducted.

① Supply of ozone to an ozone generator during PZO
② Adding gas to an ozone generator during PZO

A schematic of the ozone generating experiment is shown in Figure 1. Two generators were connected in series (The front and rear ozone generators are referred to as A and B,

respectively.). There were two ozone sampling points connected to ozone monitors to measure the input and output concentrations of ozone to and from B, respectively. There was a gas feed point between A and B. When PZO was observed in B, the aforementioned two experiments were conducted.

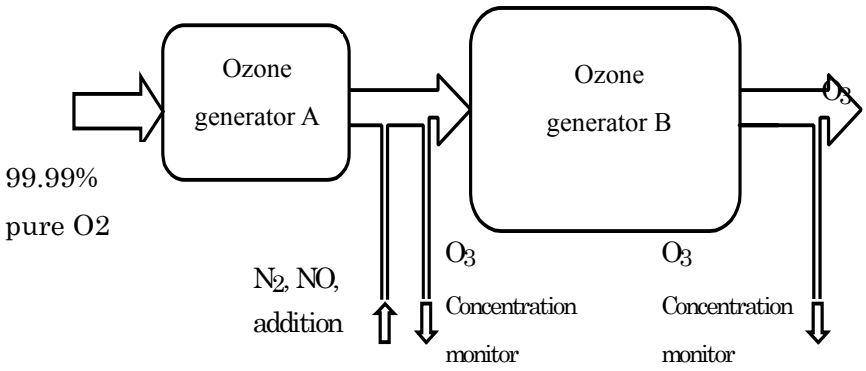

FIGURE 1. Schematic of ozone generator and system

3. RESULTS AND DISCUSSION

Figure 2 shows the PZO process in B. The initial concentration of ozone was ca.200 g/Nm^3. It was observed that the decrease in ozone concentration depended on the feed oxygen pure. More specifically, when 99.99% pure oxygen was used, the ozone concentration decreased in a few hours and reached almost zero (PZO). However, when 99.8% pure oxygen was used, the ozone concentration decreased by around 10% of the initial concentration in 10 hours.

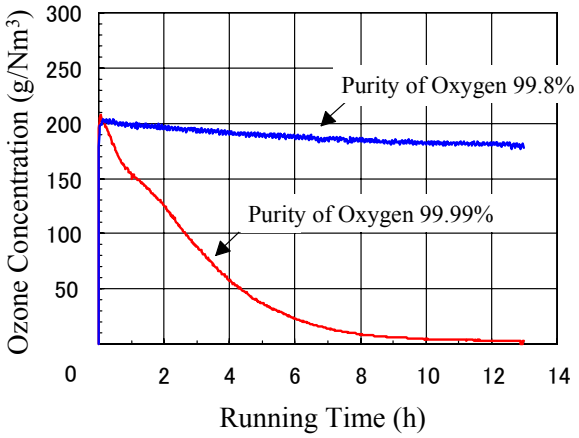

FIGURE 2. PZO Process

The experimental results are shown in Figure 3. Figure 4 shows the data in Fig.3 from 600 to 1080 minutes. Initially, generator B was started. After PZO was observed, generator A was started and the ozone generated was introduced into B. Soon after it was introduced, the concentration at B's outlet increased, however, it decreased immediately. When B stopped

running, its ozone concentration recovered to the same level as A. This suggests that ozone decomposition occurs when B is running.

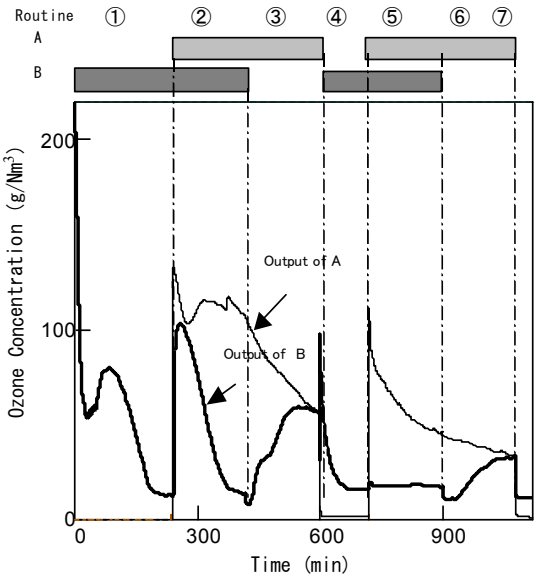

FIGURE 3. Operation Sequence of Ozone Generators (A&B) and Ozone Concentration (1)

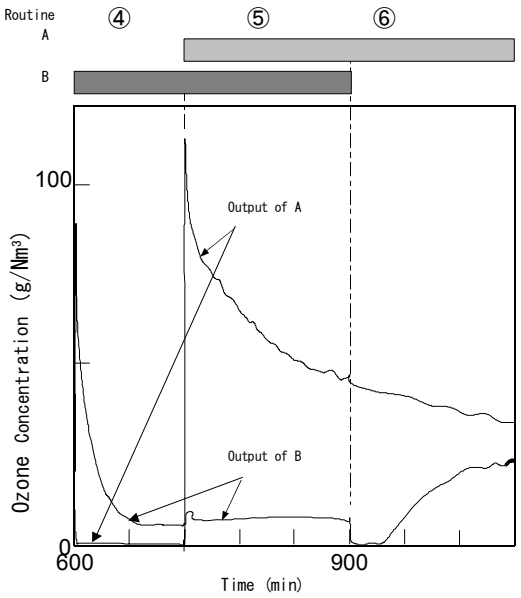

FIGURE 4. Operation Sequence of Ozone Generators (A&B) and Ozone Concentration (2)

Figure 5 shows the effect of the addition of N_2 on B's ozone generation. In this case, after B reached PZO, B was stopped. Then N_2 was introduced to B via the gas feed point. Generator B's ozone concentration recovered to the same level as the inlet's concentration, which was the same as A. However, when generator B was started again, the ozone concentration recovered rapidly to over 260g/Nm^3.

Because the ozone concentration recovered during N_2 feed and discharge between the electrodes, it is thought that NOx produced from N_2 by the discharge caused the recovery of the ozone concentration.

Figure 6 shows the effect of NO addition on ozone generation by B. Ozone was supplied to B from A. As shown in Fig.6, the increase in ozone concentration was triggered by the addition of NO and B's ozone concentration soon increased to slightly below the concentration of A. This means that only a small amount of ozone was consumed as NO became NO_X and NO_X caused the recovery of the concentration of B.

When the addition of NO was stopped, however, the ozone concentration remained constant. When B was discharged again, the ozone concentration increased to 300g/Nm^3. However, PZO was observed after a few hours.

Based on these results, it is suggested that NO_X on the surface of the electrode is essential for ozone generation, and that PZO occurred because of the loss of NO_X from the electrodes during electric discharge using 99.99% pure oxygen as the feed gas.

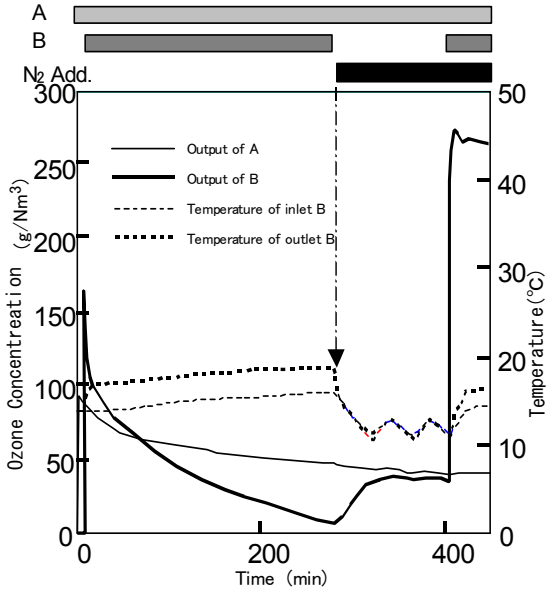

FIGURE 5. Effect of N_2 feed

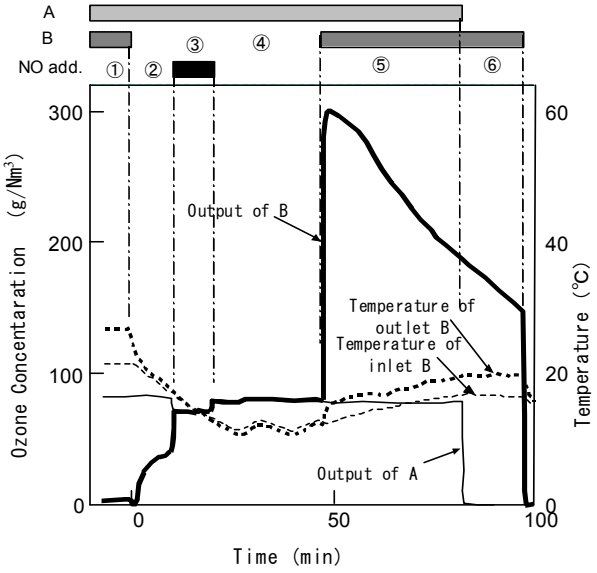

FIGURE 6. Effect of NO feed

4. CONCLUSION

The mechanism of the phenomenon of zero ozone (PZO) was investigated. The following is a summary of the results:

1) The phenomenon of zero ozone (PZO) was identified in our experimental ozone generating equipment. The concentration of ozone generated from the ozone generator using 99.99% pure oxygen as the feed gas decreased from approx. 200 g/Nm^3 to almost zero during operation.
2) The ozone concentration of the generator running during PZO was increased by feeding N_2.
3) When ozone was fed into the generator at PZO without discharge, the ozone concentration recovered rapidly when NO was fed into the generator.
4) The recovered ozone concentration remained constant without discharge.
5) Based on these results, it is suggested that NO_X on the electrode surface is essential for ozone generation and that PZO occurs because of the loss of NO_X from the electrodes by discharge when using 99.99% pure oxygen as the feed gas.

REFERENCES

[1] K Hashimoto, H Ishioka (2000). Ozone Generation Properties using High Purity Oxygen Gas, The Papers of Technical Meeting on Electrical Discharges IEE Japan ED-00-109

[2] M Taguchi, H Matsushita (2003). Properties of Ozone Generation using High Purity Oxygen Gas, The Papers of Technical Meeting on Electrical Discharges IEE Japan ED-03-153

[3] T Takano, K Yamashiro, H Itoh(2005). Extreme Decreasing of Ozone Product Using High Purity Oxygen, IEEJ Vol.125-A No.6 p508-514 (in Japanese)

DECOLORIZATION OF INDIGO CARMINE SOLUTION USING DISCHARGE ON SURFACE OF A GAS-LAYER IN WATER

T. Miichi[1]

[1] *Department of Electrical and Electronic Systems Engineering,*
Faculty of Engineering, OSAKA Institute of Technology
5-16-1 Omiya, Asahi-ku, Osaka 535-8585, JAPAN

ABSTRACT. A new method of a water treatment utilizing active species produced by the discharge on the surface of a gas-layer in water is proposed. Active species with short lifetime (e.g. OH radical) are used effectively for the water purification because active species react with water directly. The gas-layer (like a bubble) is formed when gas is supplied to the reactor. The indigo carmine solution was decolorized using this method. The volume and the concentration of indigo carmine solution were 500mL and 20mg/L respectively. The energy consumption of 1-pulse evaluated from waveforms of the applied voltage and the circuit current. When the total energy consumption was 6.41Wh, the decolorization rate of indigo solution was 96.9%.

1. INTRODUCTION

Recently, active species with the strong oxidizing potential are utilized for the water treatment. Active species such as OH radical and atomic oxygen with the short lifetime have very strong oxidization ability. We have proposed the new method of the water treatment utilizing radicals produced by the discharge on the surface of a gas-layer in water. The advantages of this method are as follows:

(1) The additional equipment for active species generation (active species generator) is not required.

(2) The short-life-time active species can be used effectively for the water purification because active species are generated on the surface of water by the gas discharge.

In our previous work, a discharge inside small bubbles (diameter: 1mm) was observed using plane electrodes[1]. In addition the generation of active species such as ozone and OH radical were confirmed. A new type reactor was developed to increase the volume of discharge region[2]. In the reactor, H. V. electrode is fixed on the inside of a gas-layer like a hemispherical bubble(diameter: 60mm) in water. The gas-layer is formed when gas is supplied to the reactor. A supply gas was argon. The indigo carmine solution was decolorized using the discharge on the surface of a gas-layer in water.

---

[1] Electronic address: miichi@ee.oit.ac.jp

2. EXPERIMENTAL APPARATUS

Figure 1 indicates the schematic diagram of the experimental apparatus. Electrodes for the discharge are immersed in water. The H. V. electrode is a cylindrical stainless steel mesh (32mesh/inch, wire diameter: 0.18mm). The H. V. electrode is fixed in an acrylic cylinder. The ground electrode is stainless steel plate with a size of 60mm × 60mm. When the high voltage is applied between electrodes, the point of the wire of the mesh electrode becomes a high electric field(Figure 2(a)). Therefore, the discharge is generated from the point of the wire of the mesh electrode. The discharge has the streamer shape and it is formed along the surface of a gas-layer.

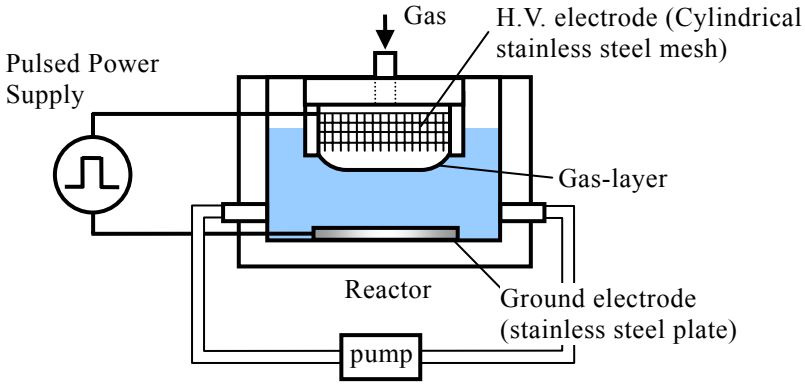

FIGURE 1. Schematic diagram of experimental apparatus.

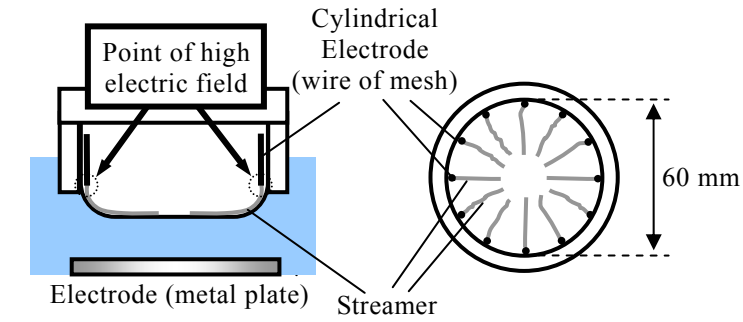

(a)Cross-sectional electrodes (b)Top view of electrode

FIGURE 2. Schematic diagram of electrodes for discharge.

The pulsed high voltage generated from a pulsed power supply is applied to the reactor. Table 1 shows the specification of the pulsed power supply. The applied voltage waveform between electrodes and the circuit current waveform were measured by the high voltage probe (EP-100K: Pulse Electronic Engineering Co. Ltd.) and the current transformer (2-0.1: Stangenes Industries Inc.), respectively.

TABLE 1. Specification of pulsed power supply.

Peaking capacitor	500pF
Peak of applied voltage	30~60kV
Rise time	50ns
Pulse width of applied voltage (without load)	Approximately 400ns (FWHM)

3. EXPERIMENTAL RESULT

Decolorization of indigo carmine solution using the discharge on the surface of a gas-layer in water was observed. Experimental conditions were as follows: the applied voltage peak was 22.2kV, the pulse repetition rate was 100pps, the volume of indigo carmine solution was 500ml, the concentration of solution was 20mg/l and the flow rate of the supply gas(argon) was 200ml/min. Figure 3 illustrates typical waveforms of the applied voltage between electrodes and the circuit current during a single operation. Waveforms of the voltage and the current varied as shown in Fig. 4 when the discharge period increases. It is thought that waveforms varied because the resistance of solution decreased by the discharge processing.

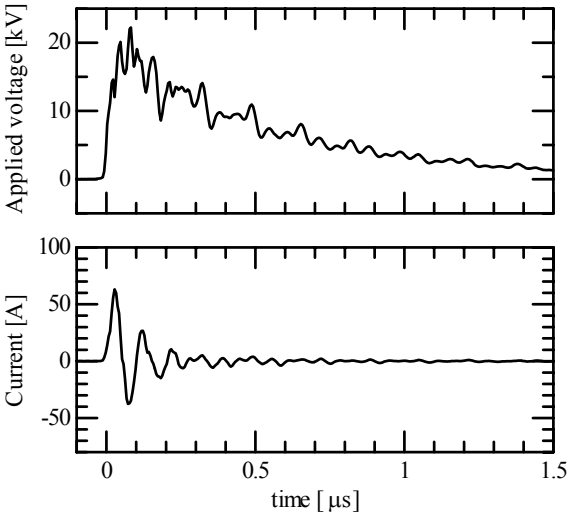

FIGURE 3. Typical waveforms of applied voltage between electrodes and circuit current during a single operation.

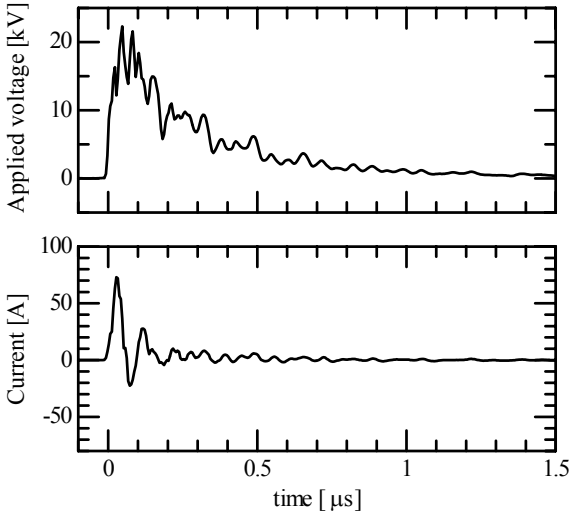

FIGURE 4. Waveforms of applied voltage between electrodes and circuit current after 90 minutes from discharge starting.

In order to clarify the treatment ability of this method, light absorption spectra of indigo solution after the discharge process were measured by a UV-VIS spectrophotometer (UVmini-1240: SHIMADZU CORPORATION). Figure 5 indicates the light absorption spectra of indigo solution for the different discharge period. The absorbance of 251nm, 287nm and 612nm decreases with increase of the discharge period because the structure of indigo is broken by generated OH radicals. It is thought that OH radicals are produced by the discharge on the surface of the gas-layer in water via the following reaction:

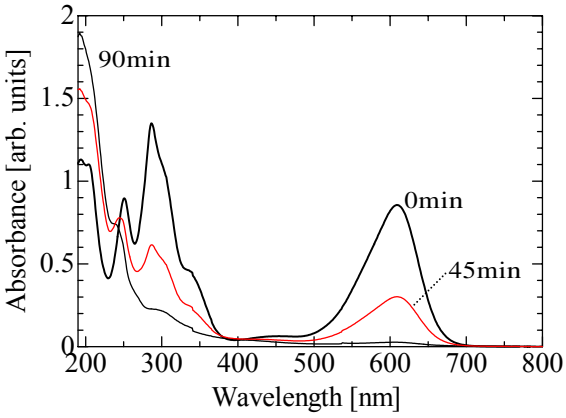

FIGURE 5. Light absorption spectra of indigo solution for different discharge period.

$$e + H_2O \longrightarrow e + H + OH\,. \qquad (1)$$

Since argon is used as the supply gas to the gas-layer, atomic oxygen and ozone are not

generated by the discharge. The absorbance of 200nm increases with the discharge period. OH radicals generated by the discharge combine to form hydrogen peroxide. Hydrogen peroxide has the light absorption peak in 200nm. Therefore, it is thought that the absorbance of 200nm increased because the amount of hydrogen peroxide increased.

The energy consumption of 1-pulse evaluated from waveforms of the applied voltage and the circuit current. When the total energy consumption was 6.41Wh, the decolorization rate of indigo solution was 96.9%.

4. CONCLUSION

In order to accomplish the efficient utilization of active species such as OH radical for water purification, we proposed a new method that uses the discharge on the surface of a gas-layer in water. The experimental result can be summarized as follows:

(1) The indigo carmine solution was decolorized using the discharge on the surface of an argon-gas-layer in water. When the total energy consumption was 6.41Wh, the decolorization rate of indigo solution was 96.9%.

(2) The absorbance of 251nm, 287nm and 612nm in solution decreases with increase of the discharge period because the structure of indigo is broken by generated OH radicals. On the other hand the absorbance of 200nm increases with the discharge period. It is thought that the hydrogen peroxide generated by the discharge influences an increase in this absorbance.

REFERENCES

[1] Miichi, T., Hayashi, N., Ihara, S., Satoh, S., Yamabe, C.(2002). Generation of Radicals using Discharge inside Bubbles in Water. *OZONE SCIENCE & ENGINEERING*, Vol.24, No.6, 471-477.

[2] Miichi, T., Hayashi, N., Ihara, S., Satoh, S., Yamabe, C.(2002). Generation of Radicals using Discharge inside Bubbles in Water(II). *Proc. 2002 Joint Conference of ACED & K-J Symposium on ED and HVE*, 1, 292-295.

Powder Treatments using Atmospheric Pressure Glow Plasma
＜Silica Coating on PLGA Powder for DDS＞

Masuhiro Kogoma, Kenichiro Yamaguchi and KunihitoTanaka

Department of Chemistry, Faculty of Science and Technology, Sophia University
7-1, Kioi-cho, Chiyoda-ku, Tokyo 102-8554, Japan

Abstract. PLGA (poly (DL-lactic - co - glycolic acid) micro capsules that sustain insulin in their polymer networks have been used as a drug delivery system for the diabetic patients. But the unexpected burst release of the medicine from the capsules sometimes occurred in the early stage just after the administration in the blood. Such burst release is attributed to the radical swelling of the capsule due to the water penetration. We tried to introduce a silica layer on the PLGA capsule surface by means of atmospheric pressure glow (APG) plasma to suppress the phenomenon. The ability to suppress the burst release was dependent on the discharge power and on the silicon atomic concentration introduced in the surface layer.

1. INTRODUCTION

PLGA (poly (DL-lactic - co - glycolic acid) micro capsule has been developed as a part of the injection materials for drug delivery systems because it can sustain many kinds of medicine such as insulin in its polymer network. After administration of PLGA micro capsule containing a medicine (insulin), the medicine will be released slowly from the capsule. At the final stage, the capsule will be dissolved into the blood.

The PLGA capsules, however, have a problem: the unexpected burst release of the medicine from the capsules sometimes occurred in the early stage just after the administration. Such burst release is attributed to the radical swelling of the capsule due to the water penetration. If we put a thin layer such as a silica film on the PLGA capsule surface to prevent rapid water penetration, we would be able to suppress the phenomenon. We tried to introduce the silica thin layer on the PLGA capsule surface by means of atmospheric pressure glow (APG) plasma to achieve this suppression.

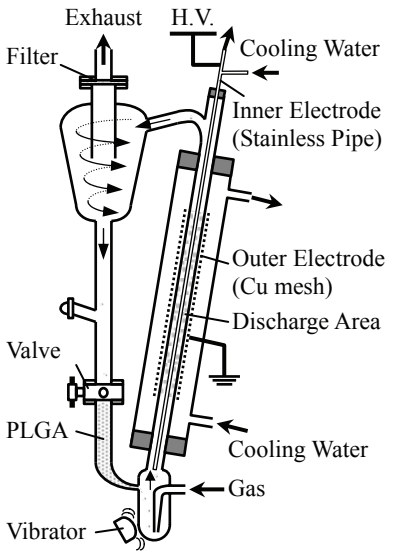

Fig. 1 Schematic diagram of the plasma reactor used for powder treatment.

2. EXPERIMENTAL

PLGA powder is prepared using solvent removal method; PLGA-50 (MW5000) is dissolved in dichloromethane mixed with zinc oxide and a small amount of insulin. The mean diameter of PLGA particles is about 30 μm. Figure 1 shows the discharge apparatus to treat PLGA powder. Discharge is maintained in atmospheric

Table 1 Discharge conditions.

Discharge frequency / MHz	13.56
Discharge power / W	100
Pulse duty ratio	0.5
He flow rate / sccm	2000
O_2 flow rate / sccm	20
CTMS flow rate / sccm	1.4

pressure He carrier gas that contained an organic silicone monomer such as CTMS (chlorotrimethylsilane) (Plasma-CVD method). The powder is introduced in the discharge zone by the gas flow; then the surfaces of particles are coated by a silicon-containing layer. The powder will be trapped in the filter. When we introduce oxygen gas with the monomer, we will have the silica layer on the PLGA surfaces.

We tried another method to make pre-coated powder by TEOS before oxidation in the plasma; that method is called semi-dry method. At first, TEOS vapor is adsorbed on the powder surface, and then the particle surfaces are oxidized in the plasma reactor. After the adsorbed TEOS-O_2 plasma treatment, the powder is treated again with CTMS-plasma deposition. Table 1 shows the discharge conditions. Due to the low melting temperature of PLGA (about 40 °C), both electrodes were cooled by water flow. To change the residence time of powder in the discharge zone, once-treated powder (first cycle) is introduced again to the discharge zone (second cycle). Powder recycling has been done by opening the powder stop bulb. RF discharge is controlled by pulse modulation to realize the high level dissociation of the monomer molecule in the application of low mean RF power. Treated powders are immersed in PBS (Phosphate Buffered Saline). Then the insulin released in the solution is measured by the BCA method using Albumin standard ampules and a photo-absorption meter for visible light.

3. RESULTS AND DISCUSSION

3.1 P-CVD

At first, we tried the silica deposition on the particles using P-CVD of CTMS-O_2 mixture in He flow. Figure 2 shows the insulin release rate to the saline from the powders as a function of immersion time in PBS measured by BCA.

In the figure, untreated powder exhibits the burst release in the early stage; but when we introduced CTMS with O_2, the maximum rate at burst peak was increased. An unexpected rate increasing compared with untreated one has occurred due to plasma treatment; this enhanced with increasing of the treatment cycle. It seemed that the treated surface is being destroyed by plasma attack before silica layer deposition can take place. Table 2 shows the XPS elemental analysis of the particle surfaces. Untreated particles do not show any Si atomic concentration. However, even in the treated particles, the Si atomic concentration is very small. On the other hand, increasing of oxygen and zinc concentrations are remarkable in the treated one. It is clear that the surface degradation will occur on the treated particles in the oxygen-containing plasma due to the attack of atomic oxygen.

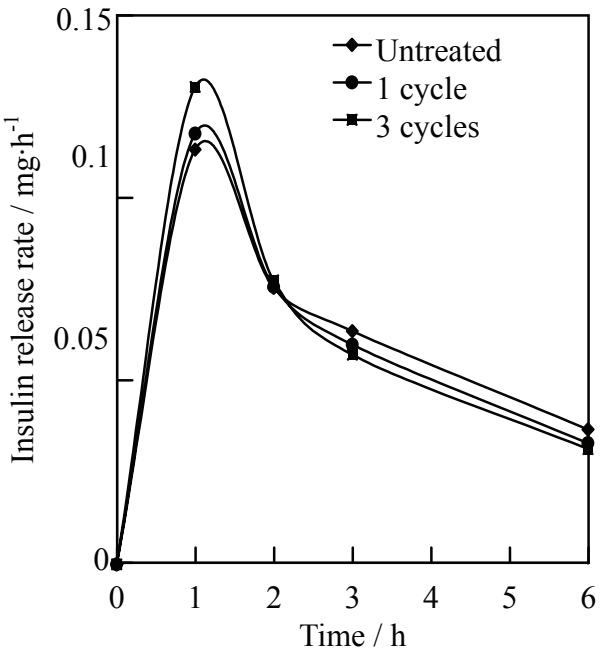

Fig. 2 The insulin release rate to the saline from the powders as a function of immersion time in PBS measured by BCA.

Table 2 Elemental analysis of the powders.

	C	O	Si	Cl	Zn
Untreated	70.64	29.36	0	0	0
1 cycle	56.09	41.82	0.98	0.59	0.52
3 cycles	56.92	40.46	0.94	0.82	0.86

3.2 CTMS deposition-plasma oxidation method

So we need some protection layer for the plasma oxidation on the particle surface before silica deposition. We tried to use the CTMS deposition without oxygen for the production of a protection layer on the powder surface. During one or more cycles, the powder was deposited with CTMS in the discharge zone; then the last deposited layer was oxidized using a He-O_2 system to produce the top silica layer. Table 3 shows the XPS elemental analysis of the surface treated with CTMS only and the surface after being oxidized with oxygen plasma.

In Table 3, Si atomic concentration is increased with increasing of the treating time(cycle number). The Zn atom peak was lost in the XPS spectrum. So the PLGA that was pretreated by CTMS plasma was not affected by destruction of the surface caused from oxygen plasma irradiation.

Table 3 Elemental analysis of the powders.

	C	O	Si	Cl	Zn
Untreated	70.64	29.36	0	0	0
1. CTMS/He 1 cycle	63.77	34.71	1.31	0.21	0
2. CTMS/He 3 cycle	58.19	36.96	4.01	0.84	0
3. After O_2/He plasma of 1.	61.82	36.36	1.7	0.12	0
4. After O_2/He plasma of 2.	54.13	41.3	4.33	0.24	0

Figure 3 shows the insulin release rate from the CTMS pretreated powders as a function of immersion time in PBS measured by BCA. In figure 3, the release rate curves of 1 cycle and 3 cycles were restrained compared with the untreated one.

Now, we will introduce the improvement factor as defined in the following equation to compare the suppression of insulin release rate at the concentration of the burst peak.

$$\text{Improvement Factor (IF)}(\%) = \frac{(\text{Release rate of untreated powder} - \text{Release rate of treated powder}) \times 100}{\text{Release rate of untreated powder}}$$

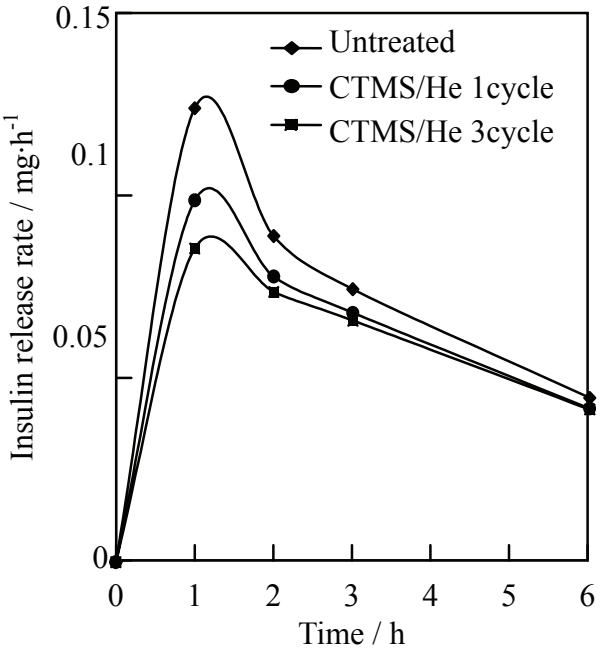

Fig.3 The insulin release rate from the CTMS pretreated powders as a function of immersion time in PBS measured by BCA.

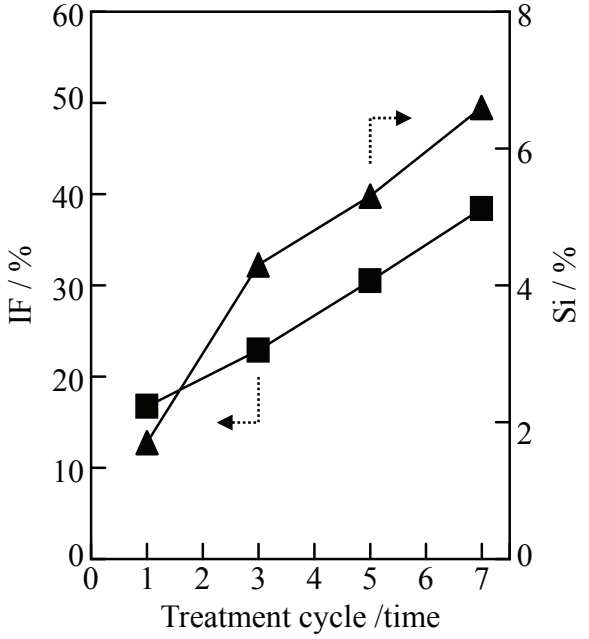

Fig.4 The improvement factor IF and the Si atomic concentration in the powders as a function of CTMS pretreatment cycle numbers.

Figure 4 shows the IF and the Si atomic concentration in the powders as a function of CTMS pretreatment cycle numbers. IF linearly increased with increasing of cycle numbers. The behavior is very similar to that of Si atomic concentration. The increasing of IF can be attributed to the increasing of the thickness of the Si-containing polymer layer.

3.3 Semi-dry method (TEOS adsorption – plasma oxidation then CTMS deposition)

In the case of CTMS deposition, treatment cycle numbers are a very important factor to improve the IF. But repeated cycle treatment in the apparatus decreases the powder yield. So we tried to obtain the silica-like layer as an inner layer instead of the CTMS polymer. In the Semi-dry method, PLGA powder is exposed once to TEOS vapor in a bottle. The amount of adsorbed TEOS was controlled by the vapor pressure. TEOS-adsorbed PLGA was oxidized in the O2 plasma. In this way, we will have a tight protection layer without direct plasma attack on the PLGA surface. Then TEOS-oxidized layers were covered with plasma polymer of CTMS to enhance the suppression of water penetration. Figure 5 shows IF as a function of the CTMS deposition cycles after the plasma oxidation of TEOS adsorption layer.

Even in one or two cycles, IF and Si-content in the layer are both increased more rapidly than in Figure 4 with increasing of the treatment cycle. The surface oxidation of polymer produced by CTMS plasma deposition (method 2) could not achieve dense enough material but the semi-dry method (method 3) could achieve such material. In fact, from FTIR absorption spectra of deposited samples that were obtained with the semi dry method, we found stronger Si-O-Si bond peaks than those obtained with CTMS deposition-plasma oxidation method at 1110 cm^{-1} and 800 cm^{-1}.

4. CONCLUSION

We attained the restriction of the early burst release of insulin in PLGA using two methods: the CTMS deposition-plasma oxidation and the TEOS adsorption-plasma oxidation followed by CTMS deposition. The second method could attain better results on the improvement factor than the first method. The difference between the methods will be attributed to the difference of the deposited silica density in the layers.

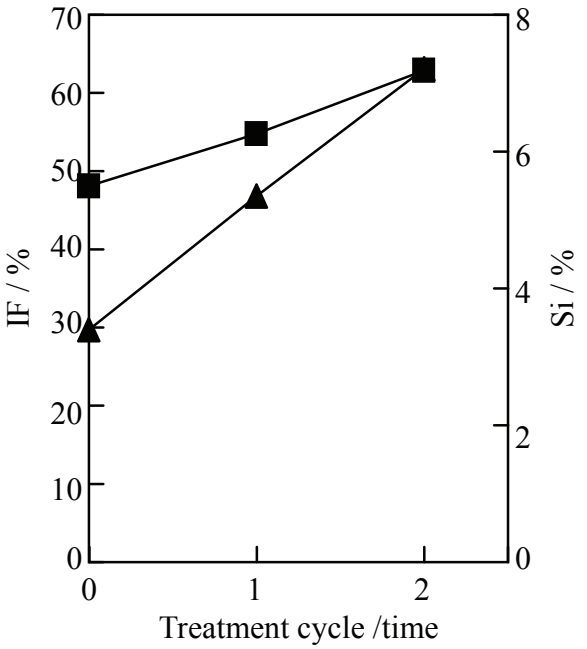

Fig. 5 IF as a function of the CTMS deposition cycles after the plasma oxidation of TEOS adsorption layer.

SILICON-FLUORIC FILMS DEPOSITED IN DBD UNDER ATMOSPHERIC PRESSURE

Z. Rżanek-Boroch[1], M. Wojucki[1], A. Ilik[2], A. Kosiński[3]

[1]*Faculty of Chemistry,*
Warsaw University of Technology,
00-664 Warsaw, Noakowskiego 3. Poland
[2] *Faculty of Physics and Chemistry,*
University of Lodz,
90-236 Lodz, Pomorska 149/153,Poland
[3]*Institute of Physical Chemistry*
Polish Academy of Sciences
01-224 Warsaw, 44-52 Kasprzaka, Poland

rzanek@ch.pw.edu.pl

ABSTRACT.

The aim of the work was to determine the influence of fluorine compound concentration in the gas mixture on composition of thin silicon-fluoric films deposited in dielectric barrier discharge (DBD) under atmospheric pressure. The films were deposited on single crystal silicon plates (100) from tetraethoxysilane (TEOS) mixtures with tetrafluoropropanol and argon at 400^{o}C in electric discharge of frequency about 3 kHz. The obtained films were analyzed by spectroscopic (IR, AES) and tribological methods and by atomic force microscope. The spectroscopic studies showed that the concentration of fluorine in the films did not exceed 2.3%. Films of low friction coefficient down to 0.11 were obtained from mixtures with the ratios of Si/F = 1/2 and Si/F = 1/6.

1. INTRODUCTION

In recent years an increasing interest is observed in plasma deposition of thin films under atmospheric pressure, with the use of silico-organic compounds as the precursors [1, 2]. The interest stems not only from economic reasons, as compared with the low pressure methods used up to now, but also from the stedily increasing role of surface and demand of new utility properties of materials, as well as from exhaustion of possibilities of the traditional technologies [3-5].

The aim the study was to obtain thin of low friction coefficient silicon surface by deposition of thin films composed of silicon and fluorine compounds

It should be expected that the silicon-fluoric films obtained by this method will find applications in Micro-electro-mechanical Systems (MEMS).

2. EXPERIMENTAL

The films were deposited in a reactor, supplied with a quartz dielectric barrier, in electric discharges of frequencies up to 3 kHz under atmospheric pressure. Argon was used as a carrier gas, and the precursor gas were mixtures of TEOS with tetrafluoropropanol with Si/F ratios of 1/2, 1/4 or 1/6. Total rate of gas mixture flow through the reactor was 12 dm^3/h. The deposition was carried out for 10 min at 400^{o}C. The obtained films were tested by:

- infrared spectroscopy with Fourier transformation (FT-IR)

- Auger electron spectroscopy (AES)
- determination of friction coefficient by means of a tribometer with a ¼" ball of ZrO_2 modified with Y_2O_3, under the loads of 40 mN-144 mN.
- surface topography determination by means of AFM

Table 1. Charactristics of thin films deposited at 400°C.

Sample	Si/F ratio in gas mixture	Thickness [nm]	Roughnes [nm]	Friction coefficient
F66	1/2	14	16	0.11
F65	1/4	27	12	0.16
F64	1/6	49	27	0.11
F77	1/0	40		0.14
Si				0.14

3. RESULTS AND DISCUSSION

3.1. FT-IR analysis

Fig. 1 shows the FT-IR spectra of films deposited at 400°C from gas mixtures with different contents of tetrafluoropropanol with the same content of TEOS.

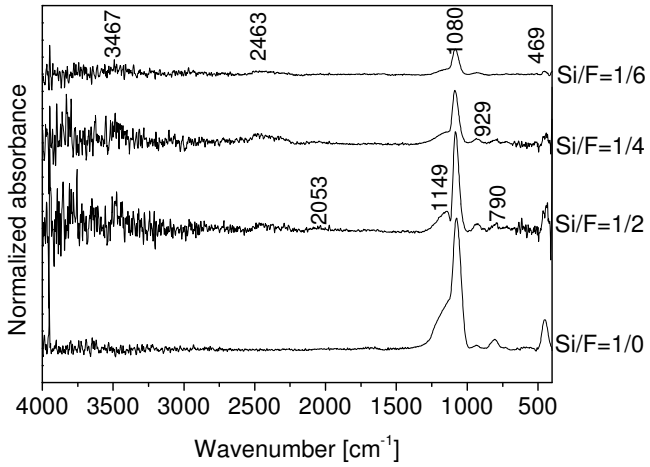

FIGURE 1. FTIR spectra of thin films deposited at 400°C

TABLE 2. Assignment of absorption bands in the FT-IR spectra [5]

Absorbance bands	
Wavenumber [cm^{-1}]	Bonds
469	Si-O-Si
790	Si-O-Si; Si-H
929	SiH_2
1080	Si-O-Si, CF
1149	Si-O-Si, CF
2053	Si-H
2463	?
3467	OH

For Si/F=1/2 the band corresponding to wavenumber 1149 cm^{-1} evidences the presence of Si-O-Si and possibly CF bonds. The band disappeared with increasing content of fluorine in the gas mixture and it was absent in the F77 film deposited from TEOS alone. Literature data [3] show that the band at 1080 cm^{-1} corresponding to oxide bonds (Si-O-Si) may also, in the presence of fluorine, be accounted for the CF bonds.

3.2. Auger electron spectroscopy (AES)

As results from the Auger spectroscopy studies there is a slight relationship between the fluorine content in the film and the content of tetrafluoropropanol in the gas mixture (Table

3). In general, however, only small amounts of fluorine might be incorporated in the films deposited at 400°C.

Table 3. Composition of thin films deposited at .400°C

Sample	Si/F	C [%]	F[%]	O[%]	Si [%]
F66	1/2	13.6	1.8	39.5	45.1
F65	1/4	20.6	2.3	36.4	40.7
F64	1/6	14.9	2.2	40.3	42.6

3.3. Friction coefficient

Tribological analyses showed (Table1), that friction coefficients of the films deposited at 400°C depended only slightly on composition of the gas mixture used. Small values of the coefficient (0.11) were obtained both for Si/F =1/2 and Si/F=1/6.

3.4. Surface morphology

In order to check the effect of gas mixture composition on surface topography of the films studies with the aid of atomic force microscope were performed. For the sake of comparison the surface of the silicon single crystal, used as substrate for the film deposition, is also shown in Fig. 2.

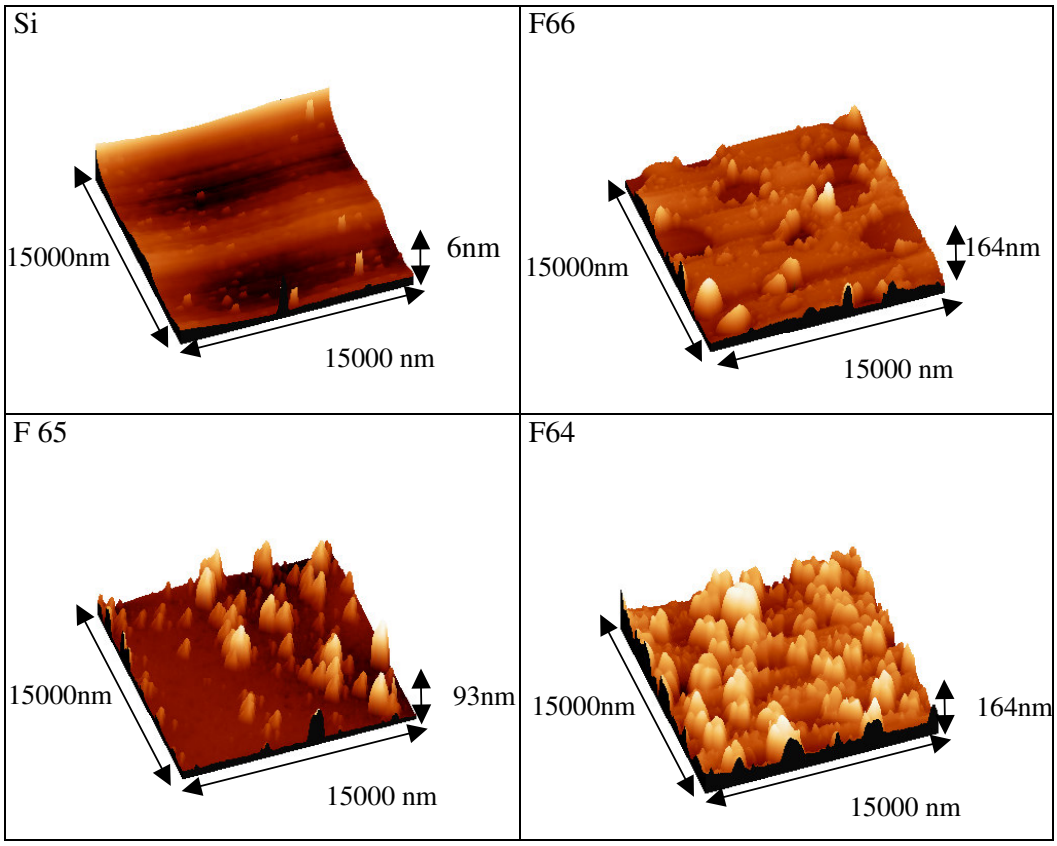

Fig.2 Topography of films surfaces.

It was found that the surface of the films changes with varying composition of the precursor mixture. The surface of the film F66 (Si/F=1/2) contains craters which are probably due to inhomogeneity of electric discharge obtained under these conditions. The friction coefficient of this film is 0.11, despite of considerable unevenness and 16 nm roughness of the surface.

The surface of the film F65 (Si/F = 1/4) having the friction coefficient 0.16 is not homogenous. A part of it is covered with excrescences and its roughness is 12 nm. The surface of the film F64 (Si/F=1/6) is not even, with both craters and excrescences, but it exhibits a low friction coefficient (0.11) despite of considerable roughness of 27 nm.

3. CONCLUSIONS

Thin films of low friction coefficient (0.11) were obtained in DBD discharge under atmospheric pressure from TEOS mixtures with tetrafluoropropanol and argon. Thin films deposited at 400^{o}C from gas mixtures with Si/F molar ratios of 1/2 or 1/6 were found to contain rather small amounts of fluorine, within 1.8 -2.3 %, as confirmed in spectroscopic studies (Table 3).It is to be guessed that fluorine is collected mainly on the surface of the films and, despite of considerable roughness, it affects favorably the friction coefficient, which is equal to 0.14 and lower than that of the F77 films, deposited under identical conditions from TEOS alone, in the absence of tetrafluoropropanol. The deposition of thin films from mixtures containing tetrafluoropropanol is accompanied by liberation of hydrogen fluoride [3] which may etch the silicon oxide layer

ACKNOWLEDGMENTS.

The work was supported by the Ministry of Science, Research, and Information Technology - Grant no. 3 T09B 008 27

REFERENCES

1. Schmidt-Szałowski, K.; Rżanek-Boroch, Z.; .Sentek, J.; Rymuza, Z.; Kusznierewicz, Z.; Misiak, M. (2000) Thin films deposition from Hexamethyldisiloxane and Hexamethyldisilazane under dielectric barrier discharge (DBD) conditions. *Plasmas and Polymers*, **5**, No.3/4, 173 –190
2. Rymuza, Z.; Misiak, M.; Rżanek-Boroch, Z.; Janowska, J. (2004). The effects of deposition and test conditions on nanomechanical behaviour of ultrathin films produced by plasma-enhanced chemical vapour deposition process at atmospheric pressure. *J. Thin Solid Films* 466,156-166
3. Durrant, S. F, Rangel, E.C, da Cruz, N.C., Castro, S.G.C, Bica de Moraes, M.A. (1966). Amorphous hydrogenated fluorinated carbon films produced by PECVD, Surface and Coatings Technology, 86-87,443-448
4. Nakamura, T., Ohana, T., Suzuki, M. Ishihara, M.,Tanaka, A., Koga,Y.(2005). Surface modification of diamond-like carbon films with perfluorooctyl functionalities and their surface properties. Surface Science 580,101-106.
5. Silverstein, R. M., Bassler, G.C. (1964). Spectroscopic identification of organic compounds, Willey, New York.

Paper number

PATTERNED DBD PRETREATMENT AT AMBIENT PRESSURE FOR LOW TEMPERATURE WAFER BONDING

M. Eichler[1], B. Michel[2], M. Thomas[1], C. Ruddy[3], H. Reinecke[3], M. Reiche[4], M. Gabriel[5] and C.-P. Klages[1,2]

[1] *Fraunhofer Institute for Surface Engineering and Thin Films IST, 38108 Braunschweig, Germany*
[2] *Technische Universität Braunschweig – Institut für Oberflächentechnik (IOT), 38108 Braunschweig, Germany*
[3] *HSG-IMIT, Institut für Mikro- und Informationstechnik der Hahn-Schickard-Gesellschaft e.V, 78052 Villingen-Schwenningen, Germany*
[4] *Max Planck Institute of Microstructure Physics, 06120 Halle, Germany*
[5] *Suss MicroTec Lithography GmbH, 85748 Garching, Germany*

ABSTRACT

Two new atmospheric-pressure plasma processes, Local Plasma Treatment (LPT) and Plasma Printing (PP), are described, which allow a localized dielectric barrier discharge (DBD) treatment at predefined areas of a semiconductor wafer. At LPT method an etched structure on the surface of the wafer defines the pattern for plasma activation, whereas the principle of PP is vice versa: the flat surface of a silicon wafer is locally treated with DBDs which are defined by a structured electrode.

1. INTRODUCTION

Silicon wafer bonding is widely used for applications like micro electro-mechanical systems (MEMS), silicon-on-insulator (SOI) and three-dimensional wafer level packaging. Conventional direct wafer bonding processes require high-temperature annealing steps (up to 1100 °C) in order to yield a reasonable bond strength. For wafers which already have electronic or mechanical components on them, low-temperature bonding is indispensable to prevent unwanted drift of device characteristics and degradation or damage of interconnects. It was shown recently, that high bond energies can also be achieved for annealing temperatures as low as 200 °C through surface activation by DBDs [1].

Atmospheric-pressure plasmas offer the unique opportunity to realize patterned surface modifications in a very easy way by localizing the discharge at specific substrate regions [2]. Furthermore, the equipment needed for surface treatment with DBDs is very simple and reliable. Compared to processes requiring vacuum, either, LPT and PP method, can be easily integrated even into existent production lines.

The LPT and the PP method are of considerable interest for the treatment of wafers on which surface modifications have to be limited to certain areas, e.g. for the production of MEMS containing elements such as membranes and valves. All of them suffer from the so called sticking effect, which comes from the unwanted adhesion of surfaces with high surface energy. One way to prevent sticking is an area-selective plasma treatment which can be applied not only to increase but also to decrease the free surface energy and thus bonding abilities.

After a short review of the uniform treatment of silicon wafers, as it is implemented now in industrial systems, the paper will explain the principles of the two new atmospheric-pressure

plasma processes, Local Plasma Treatment (LPT) and Plasma Printing (PP), which can be used to treat Si wafers and possibly other conductive substrates area-selectively in an easy way. Other potential applications of LPT and PP are presently under investigation in a joint research effort of several institutes and industrial partners [3-4].

2. UNIFORM PLASMA TREATMENT

A uniform treatment of silicon wafers can be achieved either in a dynamic mode with a moving substrate, or statically. Figure 1 shows the bond energies after dynamic DBD treatment in different gases as determined by crack opening measurements. Compared with the untreated (RCA-cleaned) reference, bond energies of DBD-treated wafers increase significantly beyond 200 °C annealing temperature.

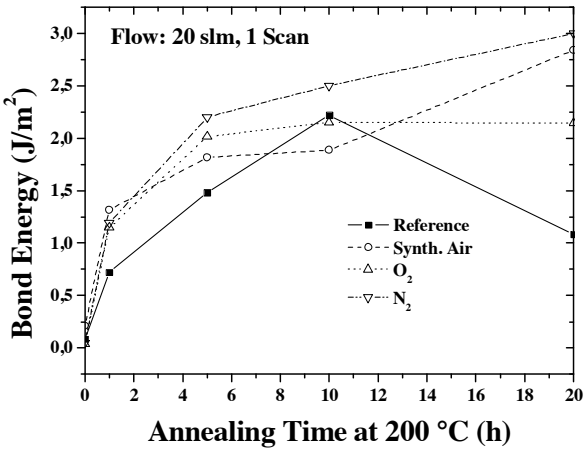

FIGURE 1. Effect of DBD on the bond energy.

In the static DBD treatment, the counter-electrode covers the whole wafer. The electrode can be made of glass with a transparent conductive film, e.g. indium tin oxide (ITO). This offers the opportunity to study the formation of the discharge and to influence the homogeneity of the discharge by adjusting the transparent electrode to the wafer. The gap distance and the gas in the gap can be easily controlled with the "plasma printing" setup built by the IST.

3. PATTERNED WAFER SURFACE MODIFICATION

The principles behind the Local Plasma Treatment (LPT) process for wafers carrying lithographically generated topographies and the Plasma Printing (PP) process for planar wafers will be explained in the following paragraph. Figure 2 shows a schematic drawing of the setup: the wafer is fixed on a grounded electrode, the transparent top electrode was sputtered on a glass substrate with dielectric constant ε_r and thickness t_b, the gap t_g between wafer and glass can be precisely adjusted. The high voltage V_0, which is applied to the electrodes leads to the Voltage V_g across the gap.

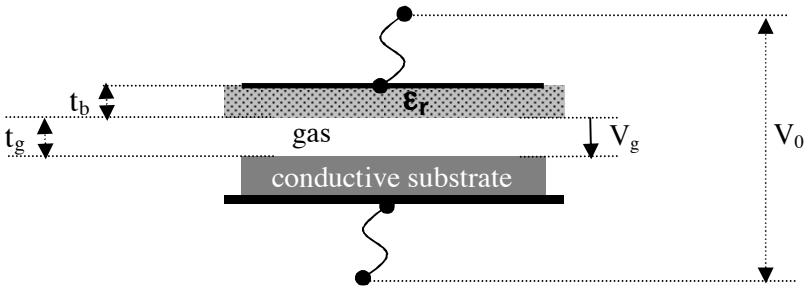

FIGURE 2. Principle of DBD treatment of conductive substrates, definition of parameters.

The voltage V_g is given by

$$V_g = V_0 \cdot \left(\frac{t_b}{\varepsilon_r \cdot t_g} + 1 \right)^{-1} \quad (1)$$

Together with Paschen's Law for the ignition voltage V_i of the discharge

$$V_i = (Bp) \cdot t_g \cdot \left(\ln \frac{(Ap) \cdot t_g}{\ln(1 + 1/\gamma)} \right)^{-1} \quad (2)$$

an equation for the required ignition voltage $V_{0,i}$ as a function of t_g can be derived.

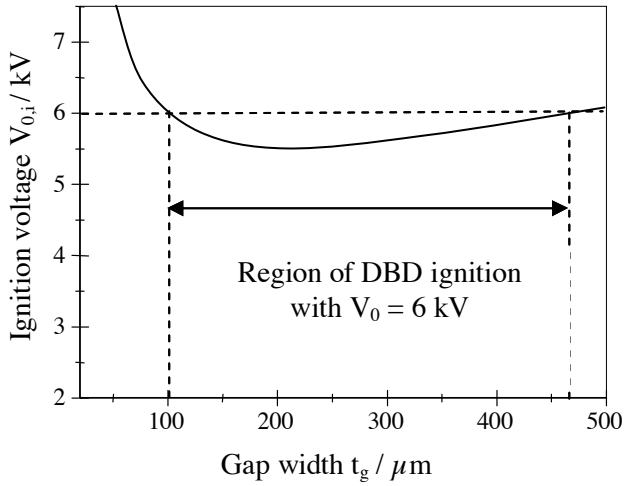

FIGURE 3. Dependence of the voltage required to ignite a nitrogen DBD in the arrangement shown in Figure 2; see text for parameters used.

Figure 3 shows this dependence for a borosilicate glass ($\varepsilon_r = 4.6$) of thickness $t_g = 2$ mm and nitrogen gas in the gap ($A \cdot p = 977\ mm^{-1}$, $B \cdot p = 25.5$ kV/mm [5]). For the expression $\ln(1+1/\gamma)$, which is strongly dependent on the electrode material, a typical value of 10 was assumed [5]. The graph in Figure 3 shows, that for an applied voltage, e.g. $V_0 = 6$ kV, the discharge will only be ignited for gap widths between 100 and 470 μm.

Figure 4 shows experimental ignition and extinguishing voltages measured for silicon wafers in nitrogen and oxygen DBDs, using an ITO electrode on a 2 mm borosilicate glass. At small gap widths for both gases the applied voltage must be increased in order to ignite the discharge. Quantitative deviations between the curves in Figures 3 and 4 are probably due to inappropriate parameters chosen for Paschen's Law. The characteristic gap width dependence of $V_{0,i}$ described above can be used for local plasma treatment of individual areas on an etched Si wafers with structures of feature sizes above 100 μm. Figure 5 shows the principle of the method: for distances beyond 150 μm (in nitrogen) between the upper parts of the surface and the surface of the glass electrode, the plasma ignites only on the raised areas, because the voltage is not sufficient to fulfil the $V_{0,i}$ condition in the recessed areas, where t_g is larger. However, for distances smaller than 150 μm, there is a strong increase of the ignition voltage for the raised parts and the plasma will cover only the recessed areas of etched structures with t_g being locally higher. The resolution for the patterned surface modification was found to be better than 50 μm for nitrogen as process gas [3].

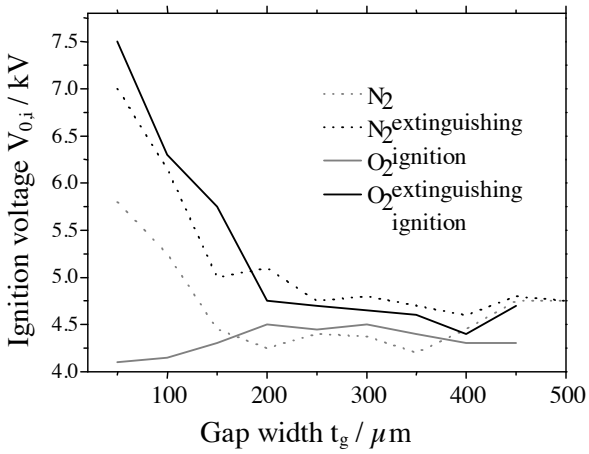

FIGURE 4. Ignition and extinguishing voltages as measured for nitrogen and oxygen at 55 kHz.

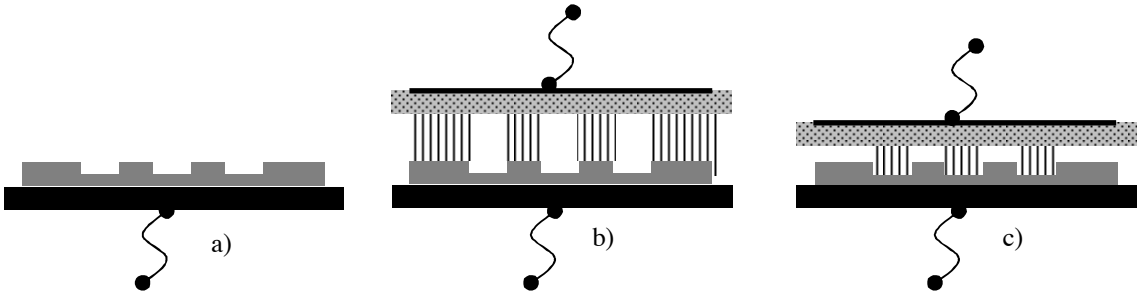

FIGURE 5. LPT treatment: a) structured wafer, b) large gap (> 150 μm), c) small gap (< 150 μm).

Unpatterned wafers can be treated area-selectively by the Plasma Printing (PP) method: An electrode with a structured dielectric mask on it is aligned to the wafer. By applying a voltage to the electrode, discharges are obtained in the cavities formed by the dielectric mask and the grounded wafer. The best resolution can be achieved by a good contact between dielectric mask and wafer. Resolutions down to 50 μm can be realized with standard techniques [4].

4. CONCLUSION

Patterned DBD treatment of conducting substrates, such as silicon, can be achieved by utilizing the effect that the voltage in the gap depends on gap width, while the necessary voltage for plasma ignition is fixed. The width of the gap is defined by the distance of the etched structures and the plane counter-electrode in the case of LPT, and the distance between the plane surface of the substrate and the structures of the dielectric mask on the counter-electrode in the case of PP, respectively.

ACKNOWLEDGMENTS

Financial support of the Arbeitsgemeinschaft industrieller Forschungsvereinigungen "Otto von Guericke" e.V. (AiF); contract no. FKZ 165 N, is gratefully acknowledged.

REFERENCES

[1] Gabriel, M., Johnson, B., Süss, R., Reiche, M. and Eichler, M. (2004). Low-temperature direct wafer bonding with ambient pressure plasma activation, *Proc. COMS 2004*, 353-357.

[2] Penache, C., Gessner, C., Betker, T., Bartels, V., Hollaender, A. and Klages, C.-P. (2004). Plasma printing – patterned surface functionalisation and coating at atmospheric pressure. *IEE Nanobiotechnology 151*, 139-144 (2004).

[3] Eichler, M., Thomas, M., Mewes, H., and Klages C.-P. (2005). Ortsselektive Atmosphärendruck-Plasmavorbehandlung für das Direkt-Wafer-Bonden bei niedrigen Temperaturen. *Proc. Mikrosystemtechnik Kongress 2005*, 115 – 118.

[4] Eichler, M., Mewes, H., Thomas, M., Klages, C.-P., Ruddy, C., Reinecke, H., Reiche M. and Gabriel, M. (2006). Patterned surface modification using ambient pressure plasma processes for enhanced wafer packaging by low temperature bonding. *Proc. SEMICON Europe 2006*.

[5] Küchler, A. Hochspannungstechnik, *Springer, Berlin, 2005*, p. 163-166.

Paper number

GERM REDUCTION OF HEAT SENSITIVE MATERIALS BY USING ATMOSPHERIC PRESSURE PLASMA SOURCES

R. Brandenburg[1,2], J. Ehlbeck[1], U. Krohmann[1], M. Stieber[1],
Th. von Woedtke[1], J. Zeymer[3], K. Rackow[1] and K.-D. Weltmann[1]

[1] *Institute of Low Temperature Plasma Physics, F.-L.-Jahn-Str. 19, D-17489 Greifswald, GERMANY*
Corresponding authors: brandenburg@inp-greifswald.de; ehlbeck@inp-greifswald.de
[2] *Vanguard Medical Services for Europe AG, Friedrichstr. 78, D-10117 Berlin, GERMANY*
[3] *Leibniz-Institute for Agricultural Engineering Potsdam, Max-Eyth-Allee 100, D-14469 Potsdam, GERMANY*

ABSTRACT. Two different atmospheric pressure plasma sources for the antimicrobial treatment of specific products containing heat sensitive materials are presented in this contribution. The propagating atmospheric microwave plasma has especially been developed for the treatment of all kinds of hollow compartments, e.g. bottles and other packaging. The rf-driven plasma jet is well suited for the treatment of complex 3-dimensional structures, e.g. medical products. The two plasma devices have been realized under the consideration of the strong needs for industrial use. The antimicrobial efficiency of these novel plasma devices is demonstrated on selected results.

1. INTRODUCTION

Numerous activities on the field of germ reduction of heat sensitive materials by means of non-thermal plasmas are known (see e.g. [1] and references therein). The plasma generation and the treatment method need to be adapted for each individual application. The properties of the product (material, dimensions, geometry etc.) as well as the requirements of the process (costs, inerrableness etc.) need to match with the plasma source and the process parameters. In this contribution we report about first attempts for the industrial applicability of atmospheric plasmas for antimicrobial treatment for medical devices and pharmaceutical products. According to the different tasks of the activities, two different kinds of plasma sources are used, namely a propagating atmospheric microwave plasma for the treatment of all kinds of hollow compartments (e.g. packaging) and a rf-driven plasma jet, which is predestined for modularisation and can be adapted to nearly any complex geometry [2], e.g. given by medical products. The plasma sources are realized under full consideration of the requirements for an industrial use. They are subsequently described in the chapters 2 and 3, respectively. The antimicrobial effect of the plasma is tested on selected test germs. Exemplary results will demonstrate the antimicrobial efficiency of the novel plasma devices.

2. RF-DRIVEN PLASMA JET

The plasma jet is operated in flowing argon and driven at a frequency f= 27.12 MHz. The set-up it is shown in fig. 1. The plasma jet consists of a nozzle made of ceramics (inner diameter of nozzle outlet about 7 mm). A needle electrode is mounted in the centre of the nozzle. The argon gas flows through the nozzle (Q= 20 slm) and the rf-voltage (P= 20 W) is coupled to the needle electrode via a matching network. The plasma is generated in the nozzle starting from the point of needle electrode and expands into the surrounding air outside the nozzle,

since the surrounding air as well as the substrate serves as “grounded electrode”. The plasma jet has a length of about 25 mm measured from the nozzle outlet and a diameter of about 8 mm for the conditions being considered. Plasma jets are especially suited for the treatment of complex 3D-structures, due to its compact design [2]. They are predestined for modularisation and therefore adaptable to nearly any geometry - such as given by medical products, which are in the scope of these studies.

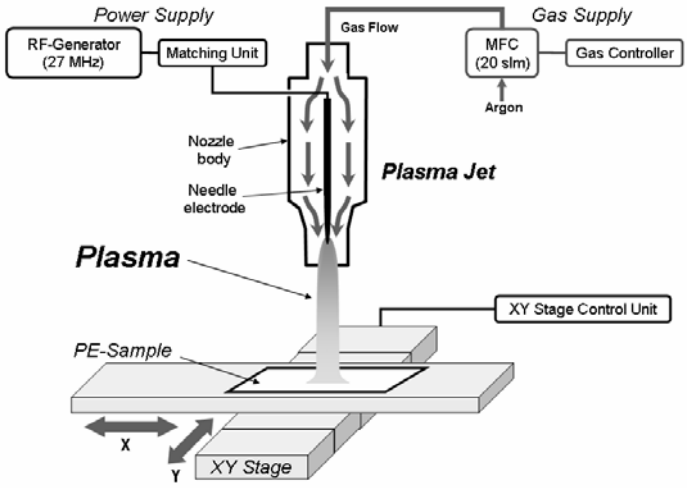

FIGURE 1. Experimental set-up of the plasma jet with gas and power supply and movable substrate holder.

The first step of the realization of an industrial process is the investigation on effects of antimicrobial treatment of samples made of polyethylene (PE) such is frequently used in medical devices (e.g. catheters). Therefore PE-strips inoculated for microbiological tests are treated by the plasma jet. The samples were inoculated punctually (diameter of area: 4-5 mm) with a use-dilution suspension of Escherichia coli or Bacillus atrophaeus spores respectively, and dried under aseptic conditions. As shown in fig. 1 the PE-samples are placed on a movable substrate holder. In the presented investigations of punctually inoculated strips the samples were not moved during the treatment. The antimicrobial efficacy of the different treatments is quantified by reduction factors for each single test strip. For this purpose the difference between the lg of the mean germ count per strip without treatment (control strips, lgN^0_{mean}) and the lg of germ count on single strips after treatment (lgN^t_{single}) was calculated.

$$\text{Reduction Factor} = lgN^0_{mean} - lgN^t_{single} \quad (1)$$

In the case of test strips without viable germs after treatment, the reduction factor was given by equation (2) as because of the microbiological detection limit for germ recovery of 100 cfu/strip. To summarize reduction factors, the median with minimum and maximum were given, because a Gaussian distribution of the results could not be assumed.

$$\text{Reduction Factor} = lgN^0_{mean} - 2 \quad (2)$$

The inoculated area was treated with the plasma jet for different times, while the plasma covered the inoculated region completely. Additionally, in order to study the effect of UV-radiation emitted by the jet (see [3]) the sample was shielded from the plasma jet with a quartz glass plate. To exclude an antimicrobial effect of heat produced by the jet, inoculated PE-samples were treated with a hot air stream with temperature as well as air flow conditions corresponding to the plasma treatment (ca. 80 °C). The results are presented in fig. 2.

Plasma jet treatment of B. atrophaeus spore strips resulted in an increasing time-dependent spore reduction up to a maximum reduction factor of 4.3 lg-steps (fig. 2a). Because of the

initial mean spore count $N^0_{mean}= 2 \cdot 10^6$ cfu/strip and the detection limit of germ recovery of 100 cfu/strip caused by the methods used in this study, this was the maximum reduction factor that could be proved experimentally if no surviving spores are detected after treatment (see [3] for details).

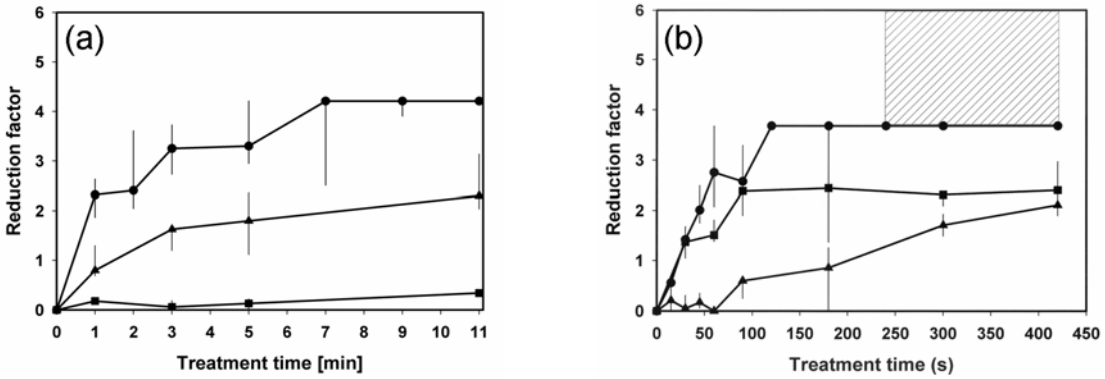

FIGURE 2. Median reduction factors after treatments with plasma jet (•), plasma jet shielded with quartz glass plate (▲), and hot air (■) of B. atrophaeus spore (a) and E. coli (b) test strip; ; error bars: spread between minimum and maximum reduction factor values; hatched area: all strips treated completely free of viable germs.

However, even if test strips without viable spores have been found after 5 and 7 min, already, also after 11 min, surviving germs could still be detected on two among five strips. That means that within the treatment time tested here, a maximum lethal effect of plasma treatment (i.e. all strips are free of viable spores) was not reached. In the experiments with the quartz glass plate positioned between strip and plasma, the antimicrobial efficacy was significantly lower with a maximum spore reduction of about 2 lg-steps only, after 11 min treatment time. After any treatment with hot air stream, no spore reduction could be detected. This is in correspondence with the high temperature resistance of B. atrophaeus spores. Different to bacterial spores, vegetative bacteria are usually much more sensitive. This could be shown also in this study where test strips contaminated with E. coli are used (fig. 2b). Four among five test strips without viable germs corresponding to a median reduction factor of 3.8 lg-steps, could be detected after 120 s plasma treatment, already. From 240 s plasma jet treatment all test strips were free of viable count. However, because of $N^0_{mean}= 6 \cdot 10^5$ cfu/strip and the detection limit of germ recovery of 100 cfu/strip, in this case it can be stated only an antibacterial efficacy of at least 3.8 lg-steps, even if the real effect could be much higher. This limitation of data evaluation is illustrated by the hatched area in the fig. 2b. Applying UV radiation alone, a germ reduction of about 2 lg-steps was found within 420 s, i.e. the effect was in the same range as found with B. atropheus spores. This result was surprising insofar as, the UV sensitivity of vegetative non-sporulating bacteria is generally considered to be much higher compared to bacterial spores. Thus the phenomenon of antimicrobial efficacy of the UV radiation of the plasma jet needs further investigation. Different to bacterial spores, a temperature effect has been found within the first 30 s of treatment where the plasma jet and the hot air curves are more or less identical. However, this effect became secondarily at longer treatment times.

All in all a reliable germ reduction on PE-samples was achieved, while the results demonstrate that the lethal effect of the plasma is based on a direct interaction of the plasma with the germs. To improve the antimicrobial effect the plasma jet parameters (power, gas flow rate and jet-sample distance) will be varied and other gases will be admixed to the argon gas. By the addition of air to argon, a higher production of “lethal” reactive oxygen species is expected. Further activities will be devoted to the technological adaptation of the plasma jet treatment of medical products.

3. PROPAGATING ATMOSPHERIC MICROWAVE PLASMA

The propagating microwave plasma source consists of multimode waveguide structure, which serves as the process chamber (see fig. 3, [4]). The plasma is driven in air by a magnetron (max. power of 1.8 kW). Pulsed microwave radiation (MW, f= 2.54 GHz) is coupled into the waveguide by an antenna. Discharge ignition is performed at the ignition point in the bottom of the chamber. After ignition, the plasma moves through the process chamber from bottom to top within less than a second. Therefore it is well suited to treat all kinds of hollow compartments. In these studies standard 200ml-bottles made of PET, and used as packaging for pharmaceutical products are treated. For microbiological test spore-containing dilution is sprayed into the plastic bottles and dried under aseptic conditions. Some preliminary results of microbiological tests are presented in fig. 4.

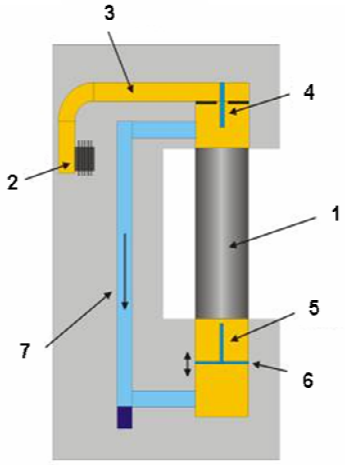

FIGURE 3. Basic scheme of the MW-plasma source; 1-process chamber, 2-magnetron, 3-wave guide, 4-coupling antenna, 5-ignition point, 6- short cut plunger, 7- gas circulation.

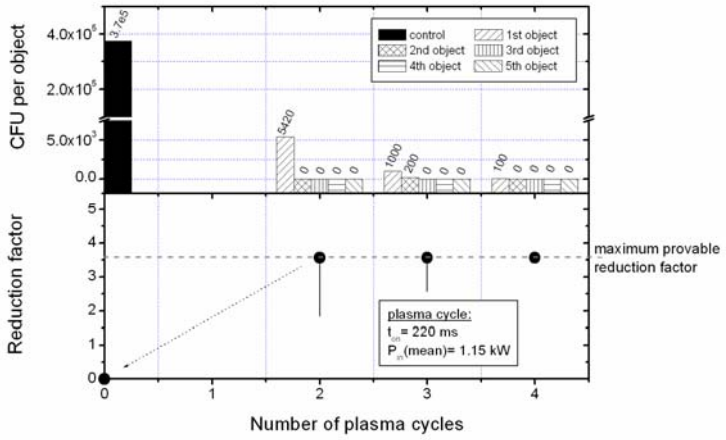

FIGURE 4. Colony forming units (cfu) per object (top) and resulting median reduction factors (bottom) after treatment of PET-bottles with MW-plasma, germs: B. atrophaeus spores; error bars in the bottom picture: spread between minimum and maximum reduction factor values.

MW-plasma treatment of PET-bottles inoculated with B. atrophaeus spores resulted in germ reductions within short treatment times. The maximal provable reduction factor of 3.6 lg-steps (N^0_{mean}= $3.7 \cdot 10^5$ cfu/bottle; detection limit of germ recovery= 100 cfu/bottle; see gray dashed line in fig. 4.) is reached even after 2 plasma cycles, i.e. total treatment time of 440 ms). Because of the limitation, it can be stated only an antibacterial efficiency of at least, but the real effect could be much higher. As higher is the number of plasma cycles as lower is the spread between the minimum and maximum reduction factor values. Since viable spores have been detected in all experiments, the maximum lethal effect of plasma treatment (i.e. all bottles free of germs) is not reached yet. This remains for future investigations. Furthermore, in single experiments local melting causing damage of bottles is observed. To avoid this, power input is needed to be optimized.

ACKNOWLEDGMENTS

This work is embedded in the network project "Plasmose" (FKZ 13N8666), funded by the Federal Ministry of Education and Research of Germany. The authors are grateful to Ch. Loesche (Vanguard AG) and B. Großjohann (Riemser Arzneimittel AG) for cooperation and fruitful discussions.

REFERENCES

[1] Laroussi M. et al. (2005). In: Non-Equilibrium air plasmas at atmospheric pressure, Series in Plasma Physics, Eds. K.H. Becker, U. Kogelschatz, K.H. Schoenbach and R.J. Barker (IoP Publishing LTD, 2005) p 537-672.
[2] Foest R. et al. (2005). *Plasma Phys. Control. Fusion*, **47**, B525-B536.
[3] Brandenburg R. (2006). submitted to *Contrib. Plasma Phys.*
[4] Ehlbeck J. et al. (2003). *Surf. Coat. Technol.*, 174-175, 793-497

DEPOSITION OF THIN FILMS AT HIGHER SUBSTRATE TEMPERATURES IN ATMOSPHERIC PRESSURE GLOW DISCHARGE

D. Trunec[a], M. Šíra, P. Stahel, V. Buršíková, D. Franta

Department of Physical Electronics, Faculty of Science,
Masaryk University, Kotlárská 2, 611 37 Brno, Czech Republic

ABSTRACT. The atmospheric pressure glow discharge was used for the deposition of thin organosilicon polymer films. The plasma was burning in pure nitrogen used as a carrier gas and a small admixture of organosilicons compounds such as hexamethyldisilazane (HMDSN) or hexamethyldisiloxane (HMDSO) was used as a monomer. The temperature of the substrate was elevated up to 120 °C to obtain harder thin films. The homogeneity of thin films was enhanced using movable upper electrode. Electrical measurements were used to distinguish between glow and filamentary regime. Mechanical properties of deposited films were characterised by depth sensing indentation technique. The films were polymer-like, transparent in visible range, with uniform thickness and without pinholes.

1. INTRODUCTION

Dielectric barrier discharges (DBD) are widely used for industrial purposes such as modification of polymer surface properties, e.g. wetability or adhesion, owing to the possibility of the atmospheric pressure processing and the on-line treatment. Although this method is very useful, the main disadvantage of DBDs is the lack of uniformity in filamentary regime. Under certain conditions homogeneous DBD can be obtained. Such homogeneous discharge is called atmospheric pressure glow discharge (APG discharge, APGD). The uniformity of the plasma favours this discharge type also for thin film deposition techniques. Sawada et al. [1] reported the organosilicon thin films deposition in APGD in helium with the admixture of tetraethoxysilane (TEOS) or hexamethyldisiloxane ($C_6H_{18}Si_2O$ - HMDSO) and oxygen, Prat et al. [2] reported the fluoro-polymer film deposition in helium APGD with admixture of hexafluoropropylene or tetrafluoroethylene, Gherardi et al. [3] used $N_2/SiH_4/N_2O$ APGD for SiO_2 deposition, Foest et al. [4] used APGD in helium with admixture of HMDSO for organosilicon thin film deposition. Trunec et al. [5] deposited thin films from HMDSO and hexamethyldisilazane (HMDSZ).

In the present paper we report the study of thin film deposition in APG discharge in nitrogen with small admixture of HMDSO. This monomer is widely used for the deposition of thin films [5]. The substrate was heated up to obtain thin films of better mechanical properties.

[a] Electronic address: trunec@physics.muni.cz

2. EXPERIMENTAL

The experiments were carried out in a plexi-glass discharge reactor with the dimensions 220 × 330 × 150 mm. The discharge burned between two plane metal electrodes, both covered with Simax glass, 2 mm thick (see figure 1). The diameter of the bottom circle electrode was 140 mm, the dimensions of the upper rectangle electrode was 65 × 40 mm. The top electrode was movable in one direction in the horizontal plane by a stepping motor to achieve better homogeneity of deposited films. The speed of the movement was 7 $cm.min^{-1}$. The space between the electrodes was set to 0.75 mm. The bottom electrode was equipped with the system of Peltier modules to heat up the substrate laying on the electrode. The highest achievable temperature 120 °C was limited by the construction of the Peltier modules. The temperature was measured by platinum temperature sensor placed below the substrate. The working gas with monomer was fetched through a system of holes so the gas was flowing in the plane of the electrodes from two sides. The gas mixture was pumped off in the corner of the reactor chamber. Before starting the experiments the discharge chamber was pumped down to 1 kPa and then filled by nitrogen to the pressure of 101 kPa. A nitrogen flow of 5.5 slpm was then added and the atmospheric pressure was maintained by slight pumping.

Thin films were deposited from hexamethyldisiloxane (HMDSO). The evaporated monomer was mixed into the nitrogen by means of the Bronkhorst Controlled Evaporator Mixer. The flow rate of the monomer was 1.25 g per hour, thus the concentration of the HMDSO in nitrogen was 3160 ppm. High voltage with the frequency 6.6 kHz was used for the discharge generation. The type of the discharge as concern a filamentary or a glow mode was determined from the discharge current measurements. The power density 5.3 $W.cm^{-3}$ was kept constant in all experiments presented in this paper. The power density was estimated from the input power to the electrical system. The discharge current and voltage were recorded by digital oscilloscope EZ DS-1080.

Thin films were deposited on the silicon wafer substrates with diameter of 14 cm. The total processing time was 60 min in all cases; the total deposition time was then only 30 min due to the movement of the substrate from and back to the discharge. The temperature of the substrate during the deposition varied between 25 °C to 120 °C.

The optical properties in the ultraviolet-visible range of the deposited thin films on the silicon substrates were investigated by means of ellipsometry. The UVISEL Jobin Yvon ellipsometer was used to measure the refractive index and the thickness of the thin film at five angles of incidence (55° - 75°) in the spectral range 240 – 830 nm.

The mechanical properties of thin films were investigated by means of the depth sensing

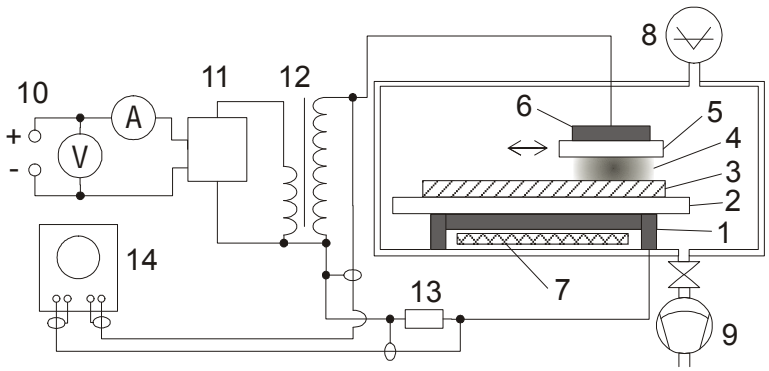

FIGURE 1. Experimental set-up: 1: bottom electrode, 2: glass dielectric, 3: Si sample, 4: APGD, 5: glass dielectric, 6: upper electrode, 7: heating system, 8: pressure gauge, 9: membrane pump, 10: direct current source, 11: high frequency generator, 12: high voltage transformer, 13: 120 O resistor, 14: oscilloscope.

indentation (DSI) technique using a Fischerscope H100 tester equipped with the Vickers indenter, microscope and CCD camera. This tester enables to register the load and the corresponding indentation depth as a function of time for the loading and unloading processes. The loading period of 20 s was followed by a hold time of 5 s, an unloading period of 20 s and finished after holding the minimum load for 5 s. Several tests were made at the different maximum indentation loads (i.e. several different indentation depths) to eliminate the influence of the substrate. Material mechanical parameters such as the universal hardness (microhardness) *HU* (DIN 50359-1), the elastic part, the plastic hardness HU_{pl}, etc. can be determined by means of the DSI method using the following relations:

$$HU = \frac{L}{A_{\mathrm{c}}} = \frac{L}{26.43h^2} \tag{1}$$

where *HU* is so called universal hardness giving information about the resistance of the material to the plastic and elastic deformation. L is the load applied on the indenter, h is the indentation depth, A_{c} is the contact area between the indenter and the studied material, 26.43 geometrical factor for the Vickers indenter. The plastic deformation can be determined using the following equation:

$$HU_{pl} = \frac{L_{\max}}{26.43h_r^2} \tag{2}$$

where HU_{pl} is the plastic hardness (resistance against the plastic deformation), h_{r} is the intercept of slope of unloading curve with the indentation depth axis at zero load.

3. RESULTS

The time course of discharge current is shown in the figure 2. Thin films were obviously deposited in a glow discharge regime [5].

Thin films were deposited at various temperatures of the substrate (25 °C, 45 °C, 60 °C, 85 °C and 116 °C). The microhardness of the thin film deposited at substrate temperature 25 °C showed out the same characteristics as in the previous work [5]: microhardness was about 0.5 GPa and the elastic modulus was about 15 GPa. The thin film deposited at the substrate temperature 60 °C showed out better mechanical properties: microhardness was 3.4 GPa and the plastic microhardness was 4.4 GPa. The load-penetration curves for the maximal load 2 mN are given in figure 3. The thin film deposited at the substrate temperatures 85 and 116 °C recorded the best mechanical properties: microhardness was

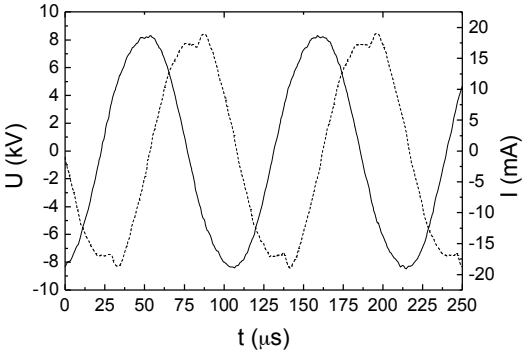

FIGURE 2. The time dependence of the discharge current and voltage (full line: voltage, dash line: current).

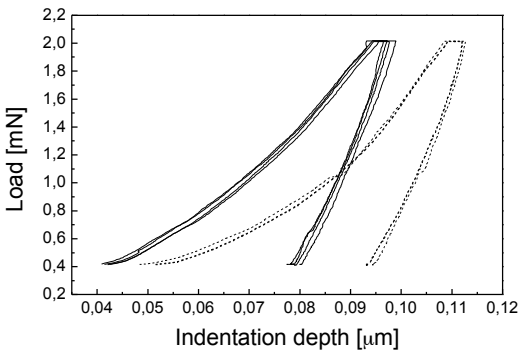

FIGURE 3. The load-penetration curves obtained by DSI technique (full lines: thin film deposited at substrate temperature 116 °C, dash lines: thin film deposited at substrate temperature 60 °C). Different curves shows the measurements on different places of the thin film.

TABLE 1. Universal hardness (*HU*) and plastic hardness (HU_{pl}) of thin films deposited at different substrate temperatures *T*.

T [°C]	25	45	60	85	116
HU [GPa]	0.50	3.37	3.37	4.74	4.16
HU_{pl} [GPa]	0.46	4.11	4.31	7.45	5.80

higher than 4 GPa and the plastic hardness was more than 5 GPa. Properies of deposited thin films are summerized in table 1. Thickness of thin films was not uniform across the silicon substrate. Thin films were thickest at rims (thickness about 300 nm) and thinnest in the central part of the film, creating plateau of almost uniform thickness (about 80 – 90 nm). The mechanical properties were measured at spots of the uniform thickness. The thickness was estimated from ellipsometry measurements. The refractive index at different samples was changing from 1.55 to 1.57 (measured at 500 nm). Thin films were transparent in visible range.

4. CONCLUSION

A deposition technique based on the atmospheric pressure glow discharge was studied. Thin films deposited at higher substrate temperature showed out better mechanical properties than thin films deposited at room temperature. The best-achieved universal hardness was 4.7 GPa for the thin film deposited at substrate temperature 85 °C, the plastic hardness was 7.45 GPa. The universal hardness was increased approximately eight times compared with the depositions at room temperature. Unfortunately thin films were not uniform in the thickness across the substrate. The distribution of the thickness is probably caused by the non-uniform flow of the monomer over the substrate.

ACKNOWLEDGMENTS

This research has been supported by the Czech Science Foundation under the contract 202/06/1473.

REFERENCES

[1] Sawada, Y., Ogawa, S., and Kogoma, M. (1995). *J. Phys. D: Appl Phys.,* 28, 1661.
[2] Prat, R., Koh, Y. J., Babukutty, Y., Kogoma, M., Okazaki, S., Kodama, M. (2000). *Polymer,* 41, 7355.
[3] Gherardi N, Martin, S., Massines, F. (2000). *J. Phys. D: Appl Phys.,* 33, L104.
[4] Foest, R., Adler, F., Sigeneger, F., and Schmidt, M. (2003). *Surf. Coating Technol.,* 163-164 323.
[5] Trunec, D., Navrátil, Z., Stahel, P., Zajícková, L., Buršíková, V., Cech, J. (2004). *J. Phys. D: Appl. Phys.,* 37, 2112.

Paper number

THICK FILM DEPOSITION OF PHOTO-CATALYTIC OXIDE FILMS BY TPCVD

Y. Ando[1], S. Tobe[2] and H. Tahara[3]

[1] *Department of Mechanical Engineering, Faculty of Engineering, Ashikaga Institute of Technology. 268-1 Omae, Ashikaga, Tochigi 326-8558, JAPAN*
[2] *Department of Mechanical Engineering, Faculty of Engineering, Ashikaga Institute of Technology. 268-1 Omae, Ashikaga, Tochigi 326-8558, JAPAN*
[3] *Department of Mechanical Science and Bioengineering, Graduate School of Engineering Science, Osaka University 1-3 Machikaneyama, Toyonaka, Osaka 560-8531, JAPAN*

ABSTRACT. To develop a functional film deposition process with high deposition rate, depositions of titanium oxide film and zinc oxide film by thermal plasma CVD in the air were carried out. Consequently, anatase/ rutile mixture and ZnO dominant films could be deposited. When the titanium oxide film was applied to photo-electronics device of dye sensitized solar cell, the cell could generate electromotive force of 49mV which was almost the half of that of the ready made one. From these results, this process was found to have high potential for high rate functional film deposition process conducted in the air.

1. INTRODUCTION

Oxide photo catalyst has been widely used in the various industrial fields. Especially, the needs of titanium oxide (TiO_2) film as photo-catalyst are increasing. As for the utility, this film has been used for not only an antibacterial coat but also dye sensitized solar cell. Although TiO_2 used as photo-catalyst was only anatase type with wide band gap until now, it was proved that rutile type, which has been used for the colorant, also had sufficient photo-catalytic property to dissociate water, recently. Moreover, though photo-catalytic property could appear by ultraviolet irradiation so far, the property could appear even on the condition of low intensity visible light irradiation by doping of some elements to titanium oxide. As another trendy oxide film, zinc oxide (ZnO) has been widely used as UV cut coating, arrester, piezo-electric device and so on for many years. Recently, since this material has excellent photo-electric property and electrical conductivity with transparency due to its width of band gap and high exciton binding energy, ZnO start to be used as LED and transparent electrode of dye-sensitized solar cell as well.

As the method of oxide film deposition, vapor deposition processes and sol-gel process have been mainly used. However, vapor deposition processes, such as sputtering and CVD, have some disadvantages such as necessity of vacuum equipment, low deposition rate, and sol-gel process also has some problems, for example difficulty of thick film deposition due to break down by internal stress occurred during deposition and so on. Although thermal spraying has been widely used as high rate film deposition process in the atmosphere environment, difficulty of film composition and structure control and high ingredient powder cost are disadvantages of this process. On the other hand, thermal plasma chemical vapor

deposition (TPCVD) is a CVD process using thermal plasma. Since thermal plasma has high energy, plasma chemical reaction with dense ions and radicals during deposition and high rate film deposition (over 10μm/min.) can be conducted. Therefore, this process is hoped to be not only a high rate functional film deposition process but also a coating process for structural materials like a thermal spraying. In case of TPCVD film, though non-oxide films such as SiC and diamond were mainly studied at the beginning, oxide films came to be studied after development of metal organic chemical vapor deposition (MOCVD) process.

In this study, in order to develop high rate film deposition process, deposition of TiO_2 and ZnO film was conducted as a basic study.

2. EXPERIMENTAL

Figure 1. shows schematic diagram of the TPCVD equipment. The equipment consisted of plasma torch, DC power supplying system, micro tube pump (feedstock supplying system) and working gas supplying system. The plasma torch has water cooled electrodes. The anode is made from copper, has alkoxide feeding port at the head and has a constrictor which is 6 mm in diameter. A cylindrical cathode made from 2 % thoriated tungsten has a diameter of 3 mm. Argon was used as the working gas. Mass flow rate of the gas was fixed at 20 SLM. As the feedstock for TiO_2 and ZnO film deposition, ethanol diluted titanium tetra butoxide (TTB, $Zn(OC_4H_9)_4$, TTB concentration 50%) and ethanol diluted zinc acetate ($(CH_3COO)_2Zn$) water solution (25%zinc acetate water solution) was used, respectively. Substrates were 15mm x 15mm x 1mm and 20mm x 40mm x 1mm copper plates with grit blasted surface. The substrate was set on the water cooled substrate holder and the central part of the sample was placed as the part was on the axial center of the plasma jet. The distance between the nozzle outlet of the plasma torch and the surface of the substrate was fixed at 100 mm. The deposition time was 5 min. The plasma discharge power was 25 V, 175 A. After film deposition, investigations of the microstructures of the films by X-ray diffraction (CuKa, 40 kV, 100 mA), photo galvanic test were conducted. **Table 1** shows deposition conditions.

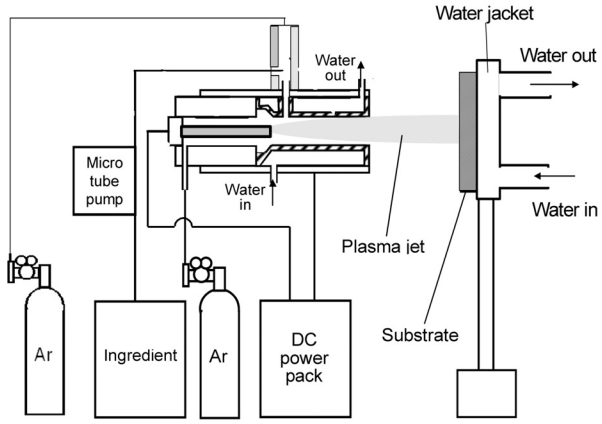

FIGURE 1. Schematic diagram of the TPCVD equipment.

TABLE 1. Experimental conditions.

Working gas	Ar
Working gas flow rate	20 l/min
Discharge current	175 A
Discharge voltage	25 V
Deposition distance (Nozzle outlet to Substrate)	100 mm
Ingredient	C_2H_5OH diluted TTB*1) Zinc acetate*2) solution
Substrate	Cu plate (15×15×1mm) Cu plate (40×20×1mm)

*1) Titanium tetra butoxide (TTB, $Ti(OC_4H_9)_4$)
*2) $(CH_3COO)_2Zn$)

3. RESULTS

3.1. Deposition of titanium oxide film

Figures 2-3. show appearance and XRD pattern of titanium oxide film deposited on the water cooled copper substrate. As the case of 430 stainless steel substrate [1], rigid titanium

oxide film could be obtained even in the case of copper substrate. Besides, as shown in Figure 3., anatase/ rutile mixture film could be deposited.

Figure 4. shows schematic diagrams of the conventional and present Dye sensitized solar cells (DSCs). In this study, though photo-galvanic test of the DSC using the deposited TiO_2 film was carried out in order to confirm photo catalytic property of the TiO_2 film, constitution of the DSC used in this test was different from the conventional one. That is, the cathode (photo catalytic electrode) was located under the anode in the present DSC though the cathode was located over the anode in the conventional one. In the case of present DSC type, DSC could be fabricated with lower cost since non-transparent electrode could be used a cathode.

FIGURE 2. Appearance of the titanium oxide film.

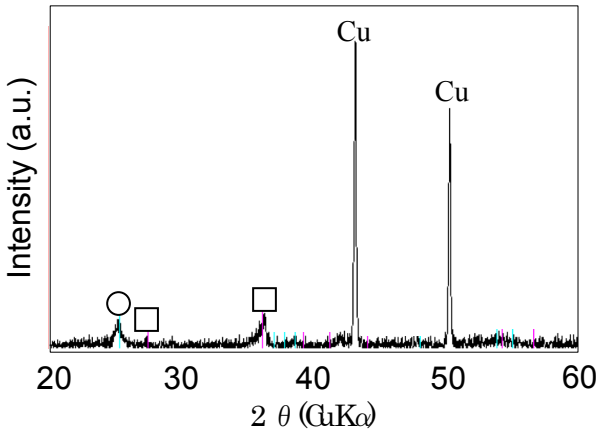

FIGURE 3. XRD patterns of the titanium oxide film (○ :Anatase, □ :Rutile)

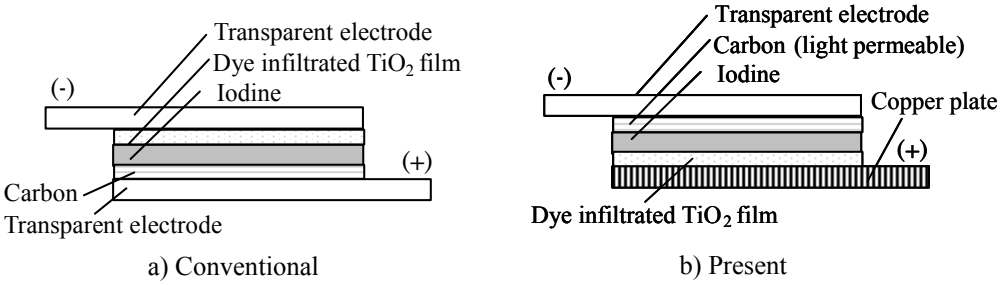

FIGURE 4. Schematic diagrams of dye sensitized solar cells.

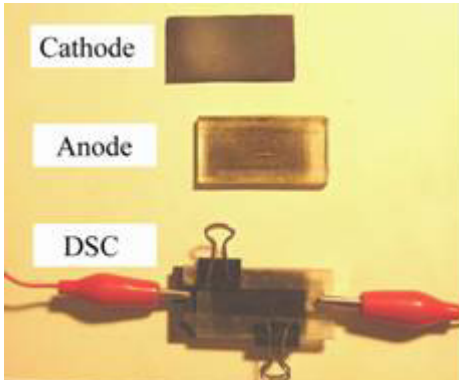

FIGURE 5. Appearance of dye sensitized solar cell.

TABLE 2. Results of photo galvanic test.

Cell	Electric light irradiation*2)	Dark room
Lower cathode commercial DSC*1)	105mV	0mV
Lower cathode DSC (with TPCVD film)	55mV	6mV

*1) Nishinoda denko "karyoku hatuden" kit
*2) Halogen light irradiation
(Irradiation distance: 150mm)

Figure 5. and **Table 2.** show appearance of the present DSC and the result of photo electronics test, respectively. Even in the case that the deposited TiO_2 film was utilized as photo electronics devise, the dye sensitized solar cell generated electromotive force of 49mV which was approximately the half of that of the ready made one (Nishinoda denko co., Ltd. "karyoku hatuden" kit) .

3.2. Deposition of zinc oxide film

In our previous study [2], it was proved that ZnO dominant film could be deposited on the non-cooled 430 stainless steel substrate. In this study, though zinc oxide film was deposited on the water-cooled copper substrate, according to the XRD pattern of the deposited zinc oxide film, ZnO dominant film could be deposited.

4. CONCLUSION

In order to develop a functional film deposition process with high deposition rate, depositions of titanium oxide film and zinc oxide film on copper substrate by thermal plasma CVD in the air were carried out. Consequently, the following information were obtained.

1) Even in the case of atmospheric TPCVD, ZnO and TiO_2 films could be deposited.
2) The DSC using the deposited titanium oxide film as photo-electronics device generated 49mV in electro motive force under a halogen light irradiation environment.

From these results, this process was found to have high potential for high rate photo-catalytic oxide film deposition process.

REFERENCES

[1] Ando Y., Tobe S., Tahara H. (2005). High Rate Deposition of Photo-Catalytic TiO_2 Film by Atmospheric TPCVD. *Advances in applied plasma science*, 5, 205- 210.

[2] Ando Y., Tobe S., Tahara H. (2006). Zinc Oxide Film Deposition by Atmospheric TPCVD. *Journal of Thermal Spraying* (Accepted).

ORGANIC THIN FILMS DEPOSITED BY PLD METHOD IN NITROGEN ATMOSPHERE

Takashi Tomemori[1], Sang-Moo Park[1], Kenji Ebihara[1,2], Tomoaki Ikegami[1,2]

[1]Department of Electrical and Computer Science,
Graduate School of Science and Technology, Kumamoto University
2-39-1 Kurokami,
Kumamoto 860-8555, Japan

[2]Department of Electrical and Computer Engineering
Faculty of Engineering, Kumamoto University
2-39-1 Kurokami,
Kumamoto 860-8555, Japan

ABSTRACT. Organic electroluminescence (EL) has been studied as next generation's flat-panel display because of high luminescence, wide viewing angle and low power consumption.

In this study, Alq_3, TPD and AZO films were deposited by the pulsed laser deposition. The optical transmittance of Alq_3 films deposited at laser fluence of 42 mJ/cm^2 and nitrogen pressure of 100 mTorr showed the highest absorption. The thin film deposited at O_2 pressure of 5mTorr showed lowest resistivity. The deposited Alq_3, TPD and AZO films were used to prepare for organic light emitting diode (OLED) structure of Al / Alq_3 / TPD / AZO.

1. INTRODUCTION

Organic light emitting diode (OLED) is expected as next generation's flat-panel display because of high luminescence, wide viewing angle and low power consumption. Organic materials are divided into two types of small organic molecules and polymers. For the small molecules, thin films for organic EL devices are commonly deposited by vacuum evaporation. The typical organic material is Tris-(8-hydroxyquinoline) aluminum(Alq_3) and N,N'-diphenyl-N,N'-(3-methyphenyl)-l,l'-bipheny-4-4'-diamine(TPD). Alq_3 has high electron mobility and stability of deposited thin film. The luminescence shows green at wave length of 520 nm. So it is used as electron transport layer and emission layer. TPD having high hole mobility can be used as hole transport layer. As glass transition temperature is very low with 60℃, it is weak for heat denaturation. Therefore, non-thermal deposited method becomes important[1][2]. The pulsed laser deposition (PLD) is a deposition method that prepares the thin films by the ion, atom, molecule and clusters generated by irradiating the laser to the surface of the target. Indium Tin Oxide (ITO) has been used as a transparent electrode of organic Electro Luminescence (EL). Now material of substitution is requested because indium that forms ITO is a very scarce material and expensive. Recently, impurity doped Zinc Oxide (ZnO) films have been investigated as alternate materials to ITO because zinc is a nontoxic and inexpensive material[3][4]. This is a II-VI semiconductor, highly

transparent in the visible region with a wide and direct band gap of about 3.37eV at room temperature and a high exciton binding energy of 60 meV. This material is very attractive because it has many applications such as transparent conductive contacts, solar cells, laser diodes, ultraviolet lasers and thin films transistors. In this work, Alq_3, TPD and Al-doped ZnO (AZO) deposited by PLD method. Nitrogen gas was used in the Alq_3 and TPD films preparation. Oxygen gas was used in the AZO films preparation.

TABLE 1. Experimental conditions

Target	Alq3, TPD	AZO
Ablation laser	KrF excimer laser Wavelength: 248 nm	
Ambient gas pressure	N_2(20,50,100mTorr)	O_2(1,5,10,50,100mTorr)
Substrate	Quartz glass, Si	Quartz glass
Temperature of substrate	Room temperature	500℃
Laser shots	6000shots	9000shots
Laser fluence	Alq_3 : 26, 42mJ/cm^2 TPD : 26, 54mJ/cm^2	2J/cm^2
Target to substrate distance	25mm	40mm

2. EXPERIMENTAL

2.1. Deposition of Alq_3 and TPD

Organic thin films were prepared on quartz glass and Si substrates at room temperature. Fig.1 and Fig.2 show structures of Alq_3 and TPD used here as targets. The targets were prepared by casting the Alq_3 power under high mechanical pressure. Fig.3 shows a schematic diagram of the PLD system. Ablation laser is KrF excimer laser (λ= 248 nm, 25 ns pulse width). All of the films were also deposited on quartz glass cleaned in an ultrasonic bath using acetone and then ethanol for 5min. The deposition chamber was initially evacuated to 4×10^{-5} Torr, and during deposition, nitrogen gas was introduced into the growth chamber. Nitrogen gas pressure was varied from 20 to 100 mTorr. Table1 shows experimental conditions.

The surface morphology was observed by atomic force microscopy (AFM : Seiko Instrument, SPI 3800N).The optical transmittance was observed by U-V visible spectrophotometer in the range of wavelength 200-800 nm.

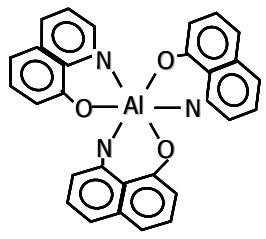

FIGURE 1. Structure of Alq_3.

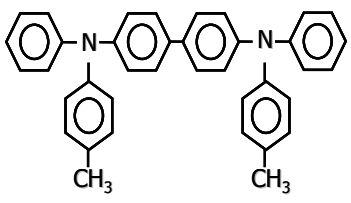

FIGURE 2. Structure of TPD.

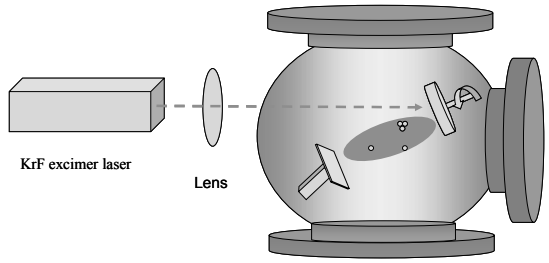

FIGURE 3. PLD equipment.

2.2. Deposition of AZO

AZO were prepared by PLD method on quartz glass substrates at substrate temperature 500°C. The pulsed laser was a KrF excimer laser with an energy fluence of 2 J/cm^2. The AZO films deposited using a ZnO target with an Al_2O_3 content of 2 wt %. During deposition, oxygen gas was introduced into the growth chamber where oxygen gas pressure was varied from 1 to 100 mTorr.

3. RESULTS AND DISCUSSION

3.1. Alq_3 thin films

Fig.4 shows optical transmittance of Alq_3 films prepared at laser fluence of 42 mJ/cm^2. The absorption of Alq_3 films deposited at nitrogen pressure of 100 mTorr shows the highest absorption at wavelength of 420 nm. In the other hand, the thin films deposited at nitrogen pressure of 20, 50 mTorr show low peak compared with nitrogen pressure conditions of 100 mTorr. The optimum gas pressure of 100 mTorr, when we use laser fluence of 42 mJ/cm^2, enhanced the nitrogen incorporation into the deposited films.

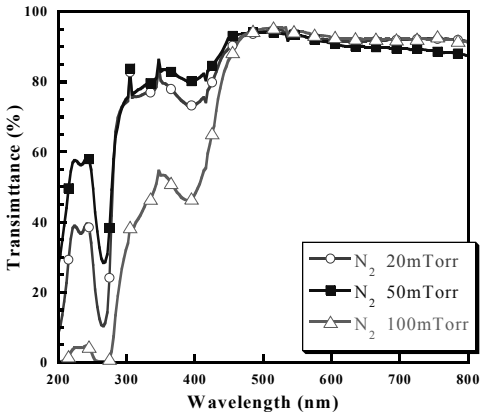

FIGURE 4. Optical transmittance of Alq_3 thin films deposited at 42 mJ/cm^2.

3.2. TPD thin films

Fig.5 shows optical transmittance of TPD films prepared at laser fluence of 26 mJ/cm^2. The absorption of TPD films deposited at nitrogen pressure of 20 mTorr showed the highest absorption at wavelength of 380 nm. But the thin film deposited at nitrogen pressure of 100 mTorr does not shown absorption peak. As a result, the optimum gas pressure is 20, 50 mTorr when we use laser fluence of 26 mJ/cm^2. Fig.6 shows the surface morphology of TPD thin films deposited at laser fluence of 26 mJ/cm^2. RMS of the thin film deposited with nitrogen pressure of 50 mTorr shows the lowest value of 1.43 nm. The thin film deposited by vacuum evaporation has a RMS of 11.24 nm. The thin film prepared by the PLD method showed smoother surface comparing with the thin film prepared by the vacuum evaporation method.

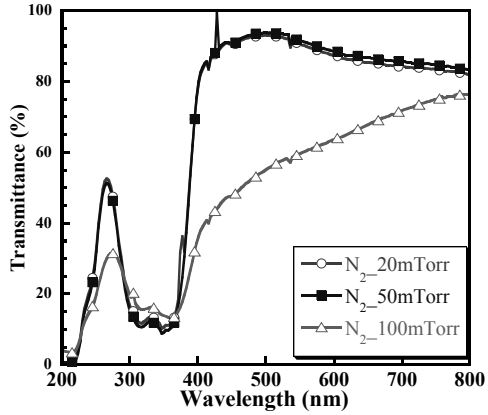

FIGURE 5. Optical transmittance of TPD thin films deposited at 26 mJ/cm^2.

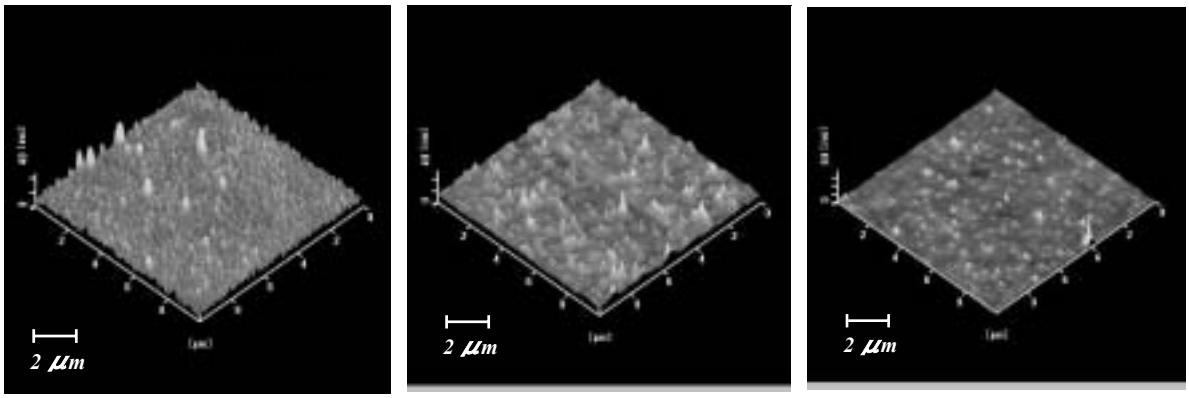

Vacuum evaporation | N_2 20mTorr | N_2 50mTorr

FIGURE 6. The surface of TPD thin films deposited at 26 mJ/cm^2.

3.3. AZO thin films

Fig.7 shows the optical transmittance of AZO films grown at a substrate temperature of 500°C under various oxygen pressures. We tried to prepare a transparent electrode with a high conductivity for optical applications where a film with a high transmittance in the visible range is very important. The averaged transmittance of all deposited films exceeds 80% in the visible range. Therefore, the AZO film obtained here would be a better transparent electrode for display applications. Fig.8 shows variations in resistivity as function of oxygen pressure for AZO deposited at substrate temperature of 500°C. The AZO film obtained O_2 pressure of 5 mTorr shows lowest resistivity films of 3.92×10^{-4} ω-cm. As a conventional ITO electrode has 2.0×10^{-4} ω-cm, present AZO can be used as transparent conductive film.

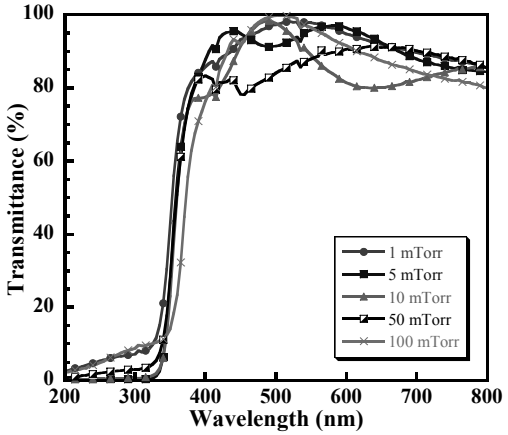

FIGURE 7. Optical transmittance of AZO film prepared at a substrate temperature of 500°C at various oxygen pressures.

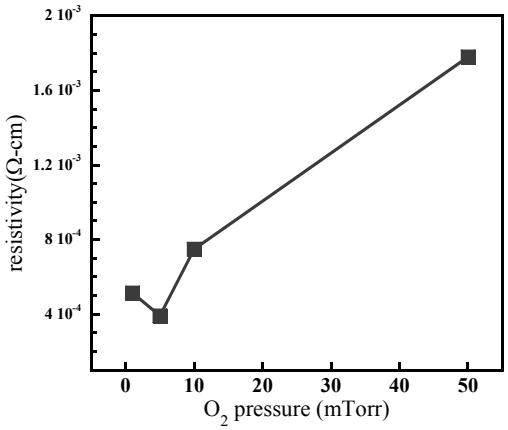

FIGURE 8. Variations in resistivity as function of oxygen pressure for AZO deposited a t substrate temperature of 500°C.

4. CONCLUSION

The optical transmittance of Alq_3 and TPD thin films deposited by PLD method in nitrogen atmosphere has been improved. As a result, PLD method in nitrogen atmosphere is a useful deposition method of organic material. Moreover, it was shown that optimum nitrogen gas pressure was different depending on laser fluence. High quality transparent and conductive AZO thin films were grown by PLD on quartz glass substrate. The growth was performed in the oxygen pressure range of 1-100 mTorr. The lowest resistivity of 3.92×10^{-4}(Ω-cm) was obtained at oxygen pressure of 5 mTorr.

5. REFERENCES

[1] X. Yang, Y. Tang, M. Yu, Q. Qin, Pulsed laser deposition of aluminum tris-8-hydroxyquinline thin films, Thin Solid Films 358 (2000)187-190.

[2] T.Tanaka, S.M.Park, T.Ikegami and K.Ebihara, Preparation of organic thin films by pulsed laser deposition in nitrogen atmosphere, Plasma Science Symposium 2005 / The 22nd Symposium on Plasma Processing (2005) 597-598.

[3] Sang-Moo Park, Tomoaki Ikegami, Kenji Ebihara, Effects of substrate temperature on the properties of Ga-doped ZnO by pulsed laser deposition, Thin Solid Films 513(2006)90-94.

[4] D.Xu, Z.Deng, Y.Xiao, C.Liang, Z.Pei, C.Sun, An anode with aluminum doped on zinc oxide thin films for organic light emitting devices, Physics Letters A 346(2005)148-152.

EFFECT OF ELECTRIC AND MAGNETIC FIELDS ON SEPARETED PLD METHOD

Shingo Yamaguchi[1], Sang-Moo Park[1], Kenji Ebihara[1,2], Tomoaki Ikegami[1,2]

[1]*Department of Electrical and Computer Science,*
Graduate School of Science and Technology, Kumamoto University
2-39-1 Kurokami,
Kumamoto 860-8555, Japan

[2]*Department of Electrical and Computer Engineering*
Faculty of Engineering, Kumamoto University
2-39-1 Kurokami,
Kumamoto 860-8555, Japan

ABSTRACT. We have developed the separated pulsed laser deposition (SPLD) technique to prepare high quality ZnO based films exhibiting uniform and droplet-free properties. This SPLD consists of an ablation chamber and a deposition chamber which can be independently evacuated under different ambient gases. ZnO thin films were deposited using both electric and magnetic fields in the SPLD method. ExB drift motion by an electric field (max: 71V/cm) and a magnetic field (0.1T, 0.27T) activated plasma plume to prepare smooth and droplet free ZnO film.

1. INTRODUCTION

As a wide band gap semiconductor with a large exitonic binding energy of 60meV, zinc oxide (ZnO) (E_g = 3.37eV) has been recognized as a promising material for use in ultraviolet(UV) light emission devices and laser diodes. Although the pulsed laser deposition (PLD) has been used to prepare ZnO films, PLD method has some problems such as deposition of droplets and small deposition area.

In this study, we developed a Separated Pulsed Laser Deposition (SPLD) method to solve the disadvantages of conventional PLD. The SPLD technique consists of an ablation chamber and a deposition chamber which are separated by a conic metallic wall with a small orifice. The pressures of an ablation chamber and a deposition chamber were controlled by the differential vacuum system. We deposited zinc oxide (ZnO) thin films by SPLD method to obtain high quality thin films [1-3]. ZnO thin films were deposited using both electric and magnetic fields in the SPLD method for high quality thin films.

2. EXPERIMENT

TABLE 1. Experimental conditions

Laser	**KrF Excimer Laser** **Wavelength : 248 nm** **Laser fluence : 3 J/cm²** **Repetition frequency : 5 Hz**
Laser shots	**30,000 shots (100 min)**
Target	**ZnO**
Substrate	**Quartz glass**
Distance of target and substrate	**11 cm**
Temperature of substrate	**400℃**
Orifice	**7 mm**
Ambient gas	**Ar Pa : 5 mTorr** **O_2 Pd : 10 mTorr**
Bias voltage	**V_b = 0~500 V, V_o = 0 V**
Magnet field	**0.27 T**

Figure 1 shows the experiment equipment used for the SPLD. The SPLD consists of an ablation chamber and a deposition chamber. These chambers were separated by conic metallic wall with a central orifice. We can independently control the ambient pressures of the ablation chamber(Pa) and the deposition chamber(Pd). The ablation chamber is a stainless steel globe with 300 mm diameter. The deposition chamber is made of a quartz tube of 100 mm diameter and a metallic conic wall with variable orifice diameters. The substrate is placed on a stainless steel base heated up to 400°C by IR lamp. The film is grown by applying variable voltage (V_b) between the conic wall and the substrate under the magnetic field. For the ablation process we used KrF excimer laser (λ=48nm, pulse duration=25ns). Table1 shows the deposition conditions of ZnO thin film. Figure 2 is the configuration of the components of the SPLD. The magnetic induction (***B***) is generated by the permanent magnet(Al-Ni-Co:Out.dia= 73.5mm,Inner dia=30mm,Max.flux=0.27T) in the deposition chamber. The positive electric field (***E***) between the substrate and the conical capsule becomes 71V/cm when V_b is 500V. Since the radial component of the magnetic induction (*Br*) crosses vertically with ***E***, the drift velocity of ions and electrons is given by

$$Vd=E/Br \quad \text{(m/s)[4] .}$$

This azimuthal averaged motion causes the plasma to flow by sweeping over the deposited film. The surface morphology of the deposited films was observed by using atomic force microscopy(AFM)(Seiko:SPI3800N). The optical transmittance was observed by U-V visible spectrophotometer in the range of wavelength 200-800 nm.

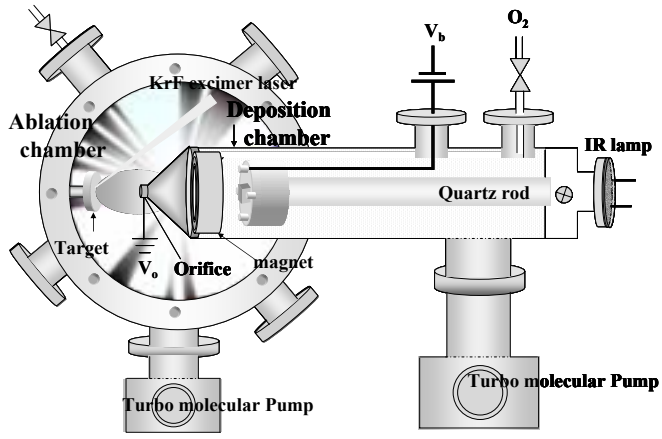

FIGURE 1. Separated PLD method

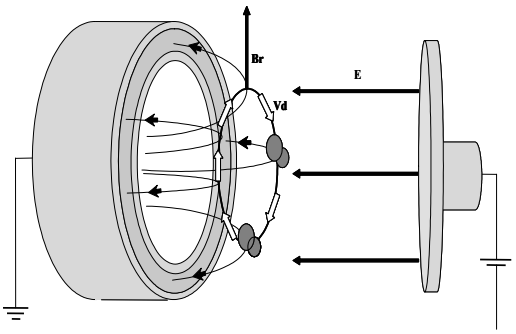

FIGURE 2. Drift motion of the electric and magnetic fields in the SPLD

3. RESULTS AND DISCUSSION

We deposited the ZnO films by changing the deposition conditions such as electric field (0V/cm, 71V/cm) and magnetic field (0.1T, 0.27T)

Figure 3 shows the AFM images of the films deposited at various conditions : (a) 71V/cm, (b) 0.1T, (c) 0.27T, (d)0.1T + 71V/cm, (e) 0.27T + 71V/cm. Table1 is the summary of RMS and grain size obtained. The small RMS of 0.84nm and the small grain size of 41nm were realized when electric field of 71V/cm and magnetic field of 0.1T were simultaneously applied. The drift velocity in these field conditions become 71km/s when Br = 0.1T. Higher magnetic field of 0.27T which gives Vd = 26km/s provides ZnO film with RMS of 4.16nm and grain size of 180nm. These results show that optimum drift velocity exists to deposit high quality ZnO films.

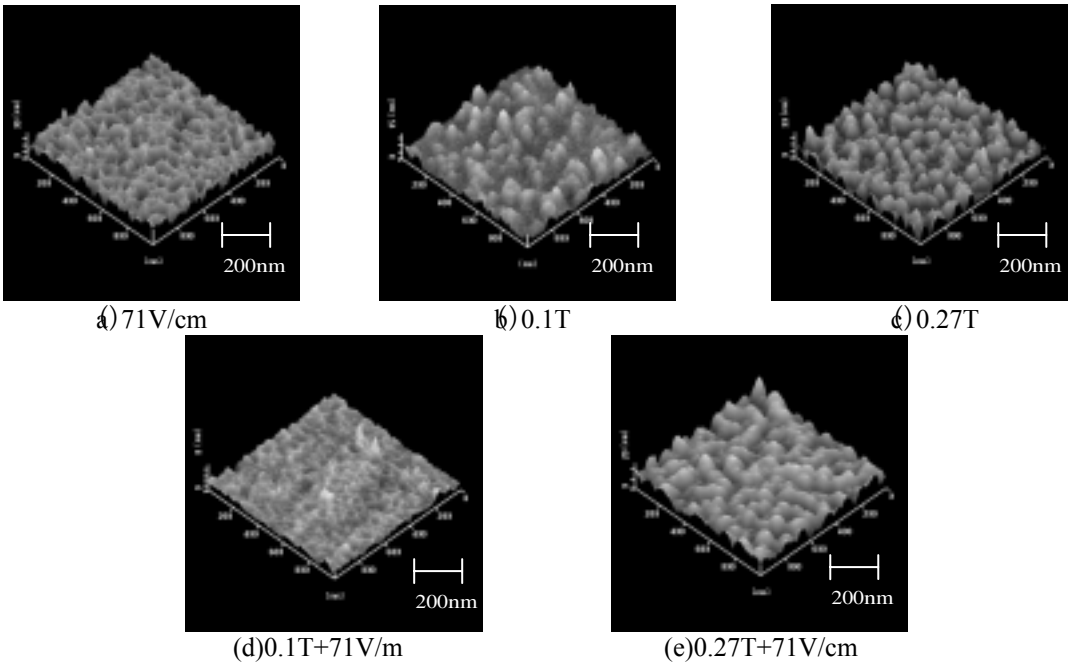

FIGURE 3. AFM image of ZnO films

TABLE 2. RMS and grain size of ZnO films prepared at various magnetic and electric fields

	(a)71V/cm	(b)0.1T	(c)0.27T	(d)0.1T+71V/cm	(e)0.27T+71V/cm
Drift speed	No drift	No drift	No drift	71km/s	26km/s
RMS	5.26nm	2.6nm	6.87nm	0.84nm	4.16nm
Grain size	61.27nm	101nm	128nm	41nm	180nm

The optical characteristics of ZnO thin films deposited on quartz glass at changing the magnetic field were investigated using a U-V visible spectrophotometer. The transmission spectra of the ZnO samples grown at different magnetic fields are presented in Figure 4. The transmittance is about 90% in the visible region for all the films. The optical band gap is 2.80eV at 0.1T+71V/cm, 2.78eV at 0.27T+71V/cm. Although the existence of the magnetic field can induce the azimuthal drift motion of the charged particles, their axial driving velocities toward the substrate are reduced to decrease the deposited energy on the film for migration and crystal growth. We can obtain higher optical band gap of 3.10eV when the bias voltage of 500V was only applied.

Figure 5 shows optical characteristics of ZnO thin films prepared at changing the electric field in magnetic field of 0.27T. The optical band gap becomes 2.61eV at 0.27T and 2.78eV at 0.27T+71V/cm. The better transmission is obtained with electric field of 71V/cm where the migration and crystal growth were enhanced due to higher electronic field.

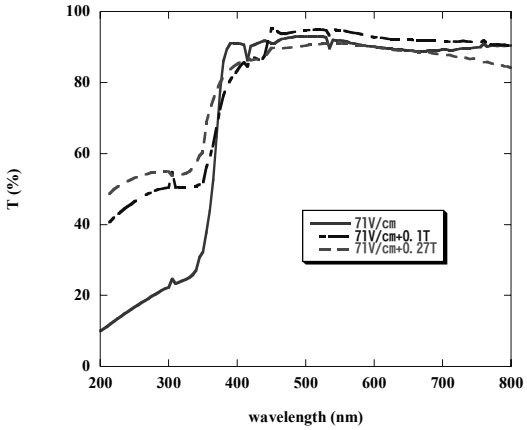

FIGURE 4. Optical transmittance spectra of ZnO films at different magnetic fields

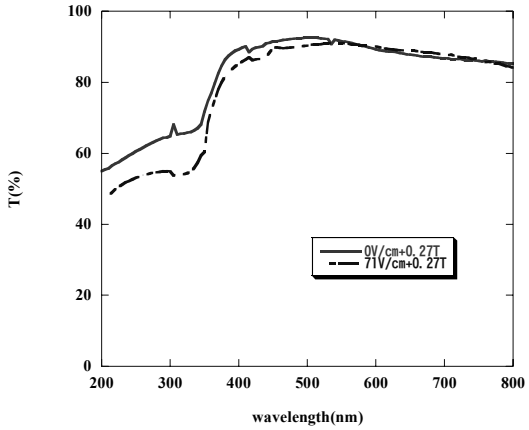

FIGURE 5. Optical transmittance spectra of ZnO Films at different electric filds

4. CONCLUSION

The ZnO thin films were deposited at different magnetic field and electric field by separated pulsed laser deposition (SPLD). As the result, the surface structure is very smooth (RMS=0.84nm, grain size=41nm) at electric field of 71V/cm and magnetic field of 0.1T. The ExB motion decreases the deposited energy on the film for migration and crystal growth.

5. REFERENCES

[1] Manuel Alonso, Kenji Ebihara, Kouji Fujii, Yuika Narita, Park Sang-Moo, Koudai Tokumasu, Tomoaki Ikegami, Proceedings of The 17th International Symposium on Plasma Chemistry, Canada, Toronto, 2005, p.543

[2] Kenji Ebihara, Sang-Moo Park, Koji Fujii, Tomoaki Ikegami, Diamond and Related Materials(in press , 2006)

[3] Sang-Moo Park, Tomoaki Ikegami and Kenji Ebihara, Jpn.J.Appl.Phys.44(2005)8027.

[4] J.R.Roth, Industrial Plasma Engineering (Vol.2): Application of Nonthermal Plasma Processing, Institute of Physics Publishing (Bristol, UK, 2001) p.214.

Paper number

APPLICATION OF SURFACE BARRIER DISCHARGE FOR DEPOSITION OF PROTECTIVE COATINGS AT ATMOSPHERIC PRESSURE

P. Sťahel, V. Buršíková , Z. Navrátil, P. Kloc, A. Brablec, M. Šíra and J. Janča

Department of Physical Electronics, Masaryk University,
Kotlarska 2, 611 37 Brno, Czech Republic

ABSTRACT. The technologies based on atmospheric pressure plasma sources become very promising tool for the control of surface properties of solids while the desirable bulk properties are kept. In this work the surface barrier discharge operated at atmospheric pressure was used for deposition of thin protective hydrophobic films from mixture of nitrogen with C_4F_8 on the paper substrate. The plasma was investigated by means of optical emission spectroscopy. Surface properties of the deposited films were studied by means of the contact angle measurements. The colorimetric parameters such as whiteness, yellowness or brightness of samples were measured in its deposited state and also in UV exposed states.

1. INTRODUCTION

Recently the technologies based on plasma technology become very promising. The majority of applications used to operate at reduced pressure [1, 2, 3] but the use of expensive vacuum systems that force batch processing has discouraged this application of low pressure plasmas in larger industrial scale for treatment of low-cost materials. The atmospheric pressure plasma processes offer several advantages for the modification of low-cost materials: costly vacuum equipment is not necessary, processing times are reduced, and the plasma modification of large surfaces is simpler than in low-pressure plasma reactor.

Barrier discharges can be used as a very attractive tool for the control of surface properties of solids while the desirable bulk properties are kept. Recently, mainly atmospheric corona or silent discharge devices are used for surface treatment of polymeric materials. In these cases the useful plasma conditions are achieved only in small volume plasma channels streamers developing perpendicularly to the material surface. As a consequence, the plasma is in a very limited contact with the surface, which results in low processing speeds, typically in the order of 1 m/min. Moreover, the localized arcing may result in the formation of pinholes in the material being treated. The disadvantages of corona and silent discharges can be eliminated using atmospheric pressure glow discharge (APGD) however APGD is very sensitive to gas purity and to optimisation of electrode arrangement and these facts limit its applicability [4]. In this work the surface barrier discharge operated at atmospheric pressure was used for deposition of thin protective hydrophobic films.

The aim of this work is to demonstrate the good protective properties of films deposited by means of this technique. Variation of colorimetric parameters of samples such as whiteness or

yellowness caused by plasma deposition and the behaviour of these parameters under intensive UV radiation is shown too.

2. EXPERIMENTAL

The surface discharge used for the deposition of teflon like films was created on the surface of the insulating mica plate, which was from one side fully covered with metal electrode while the reverse side the electrode was covered with moving paper sample pressed to mica with rod electrode consisting of 9 rotating rods 10 cm long, with 9 mm of spacing connected together [5]. Between each two rods electrodes 2 gas inlets were placed. The whole arrangement was placed into deposition chamber. The paper strips were drawn with controlled speed through the discharge chamber. The surface power density was varied from 0 to 1.0 W/cm2. In this study the deposition time was kept 90 s and the concentration of C_4F_8 in nitrogen was also kept constant in all cases i.e. 0.5 slm C_4F_8 in 10 slm of pure nitrogen. Filter paper was used as a substrate. The discharge was studied by means of the optical emission spectroscopy. Spectra of the discharge were recorded using the Jobin Yvon TRIAX 550 monochromator, equipped with the CCD detector, liquid nitrogen cooled. The total surface energy of samples γ^{TOT} and its components γ^{LW}, γ^{AB}, g^+, γ^- were investigated by means of the sessile drop technique using the Surface Energy Evaluation System (SEE System, http://www.seesystems.wz.cz). The contact angles were measured directly from the images of the solid /liquid meniscus of a liquid drop set on a solid, taken with CCD camera. The surface free energy and its components of samples were calculated according Lifshitz Van der Waals/acid base approach proposed in [6]. UV degradation tests were performed in device equipped by Hg high pressure lamp 300 W with 40 mW/cm^2. The temperature of sample during degradation experiment was kept constant (40 ^{o}C). The wetting properties were studied by means of industrial permeability tests consistent with the norm ISO 9073-8:1995. Chemical composition of deposited films was investigated by means of infrared spectroscopy.

3. EXPERIMENTAL

The fluorinated (teflon like) materials are widely used for their low surface energy and low wettability. In order to deposit highly hydrophobic natural polymeric surfaces, for example, CF_4 [7] or fluortrimethylsilane [8] can be used. (Besides the low pressure techniques, nowadays several attempts to deposit thin films at atmospheric pressure on several different cellulose based surfaces were done). In the past we reported on the formation of hydrophobic films enable to protect paper surfaces resistant against water penetration [9]. A typical spectrum of the discharge created in mixture of nitrogen and C_4F_8 is shown in Fig. 1. The spectrum is plotted in the range 300 - 500 nm, because above 500 nm only the second spectral order was registered. The spectra consist of the molecular bands, second positive system of nitrogen ($C\ ^3\Pi_u \rightarrow B\ ^3\Pi_g$). When octafluorbutane was admixed into nitrogen, intensive bands of CN violet system ($^2\Pi \rightarrow\ ^2\Sigma$) at 388 nm and 422 nm were observed. The vibrational temperature was calculated from the bands of second positive system of nitrogen N_2 0-2, N_2 1-3 and N_2 2-4. The value of the vibrational temperature varied only slightly with variation in power density and its value was evaluated at about 2 100 K in all cases.

Fig. 2 shows dependencies of the whiteness *W* and yellowness *Ye* samples in their as deposited state on the power density. Red lines is used as a guide of eyes. Yellowness of the sample increases and whiteness decreases with increasing power density. These colour

changes include not only changes caused by creation of film on the surface but also thermal and UV degradation of substrate during the deposition. The electrodes were heated by the discharge without external cooling, i.e. electrode temperature was different for different power densities. Therefore, the electrode temperature was higher at higher power density.

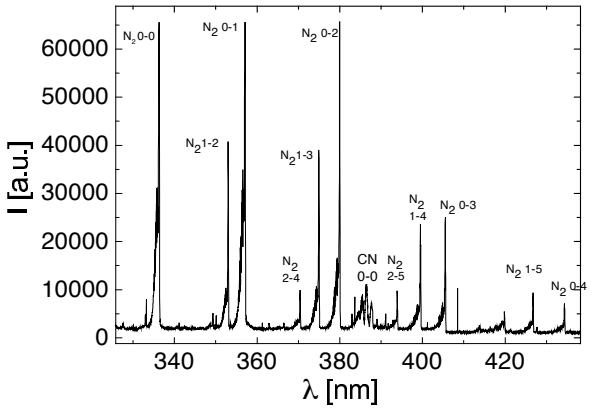

FIGURE 1. Emission spectrum of the surface discharge in nitrogen with admixture of C_4F_8.

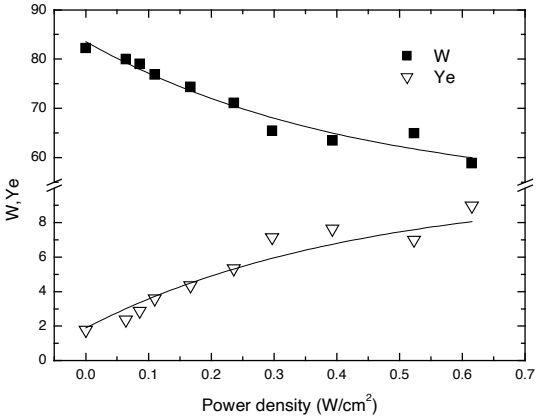

FIGURE 2.. Dependence of the whiteness *W* and yellowness *Ye* of as deposited samples on the power density. Red lines represent exponential increase resp. decrease fit.

In Fig. 3 the dependencies of total surface energy γ^{TOT} and its components γ^{LW}, γ^{AB}, g^+, γ^- are plotted as a function of power density. Samples deposited at power densities higher then 0.35 W/cm^2 show similar surface hydrophobic properties, however samples deposited at lower power density exhibit high surface energy.

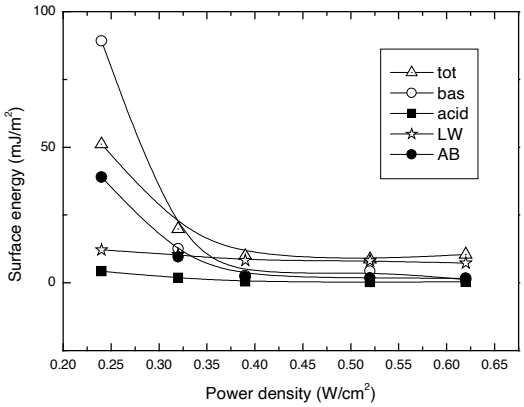

FIGURE 3. Dependence of total surface energy γ^{TOT} and its components γ^{LW}, γ^{AB}, g^+, γ^- are plotted as a function of power density

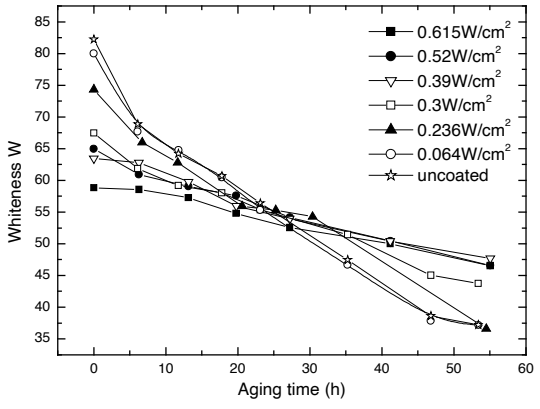

FIGURE 4. Whiteness vs time for different power density (aging effect).

In these cases surface properties are more in virtue of plasma treatment than deposition of teflon like surface layer. The total surface energy of untreated sample is shown as reference

and is rather different of samples after deposition. Surface of the sample deposited at the lowest power density is polar, however surface of uncoated sample is apolar.

In Fig. 4 the variation of colorimetric parameters under UV radiation is shown. For degradation test we used high pressure Hg source with 40 mW/cm^2. Whiteness of uncoated sample strongly decreases with increasing UV exposition. Samples coated with teflon like film exhibit significantly lower degradation than uncoated samples. Samples deposited at lower power density exhibit less protective properties than samples deposited at higher power density. Yellowness *Y e* shows also similar behaviour.

4. CONCLUSION

Highly hydrophobic thin films were prepared by a deposition technique based on the atmospheric pressure surface barrier discharge. The thin films were prepared from mixture of octafluorcyclobutane C_4F_8 with nitrogen at different power density.

Colorimetric parameters as whiteness and yellowness of samples were studied in as deposited state and also UV exposed states. Coated samples exhibited considerably higher UV radiation resistance than uncoated samples. Similar type of coating is possible to use as a highly effective transparent protection of solids against UV radiation and against humidity.

ACKNOWLEDGMENTS

This research has been supported by the grant No. 202/05/0777, Grant Agency of Czech Republic and the Long-term intent project No. MSM0021622411, Ministry of Education, Czech Republic.

REFERENCES

[1] Z. Q. Hua, R. Sitaru, F. Denes, R. A. Young: Plasmas and Polymers 2(3) (1998) 196.
[2] J. Behnisch, Plasma Processing of Polymers, In: R. d'Agostino, P. Favia, F. Fracassi (Eds.), *Plasma Processing of polymers, NATO ASI Series*. Vol. 346, (1996) p. 345.
[3] R. Mahlberg, H. E. M. Niemi, F. Denes, R. M. Rowell: *International Journal of Adhesion 62 Adhesives* 18 (1998) 283.
[4] R. Prat, Y. J. Koh, Y. Babukutty, M. Kogoma, S. Osakazaki, M. Kodama: *Polymer* 41 (2000) 7355.
[5] P. Sťahel, V. Buršíková, M. Šíra, Z. Navrátil, P. Kloc, J. Janča, *J. Adv. Oxid. Technol.*, 2,(2006) od p. 228
[6] M. N. Belgacem, A. Blayo, A. Gandini: Journal of Colloid and Interface Science 182 (1996) 431.
[7] H. T. Sahin, S. Monolache, R. A. Young, F. Denes: *Cellulose* 9 (2002) 171.
[8] F. Navarro, F. Davalos, F. Denes, L. E. Cruz, R. A. Young, J. Ramos: *Cellulose* 10 (2003) 411.
[9] V. Buršíková, P. Sťahel, J. Janča: *Czech. J. Phys.* 52 (2002) D866, Suppl. D.

Paper number

COATING ON THE INSIDE OF MICROFLUIDIC SYSTEMS WITH DBD BASED ATMOSPHERIC PRESSURE PA-CVD

M. Eichler, C. Berger, M. Thomas and C.-P. Klages

Fraunhofer Institute for Surface Engineering and Thin Films IST,
Bienroder Weg 54 E, 38108 Braunschweig, Germany

ABSTRACT

Dielectric barrier discharges at atmospheric pressure can be sustained in sub-mm cavities. These micro plasmas can be used for surface modifications of sealed microfluidic systems. With this technique coatings can be deposited and surface properties of microfluidics can be improved. Furthermore, the process allows to localize coatings to pre-selected narrow channel segments, so that different surface tensions can be generated area-selectively, e.g. for hydrophobic stops in hydrophilic channels.

1. INTRODUCTION

Injection molding of polymers is commonly used to produce microfluidic components with complex geometries. Since the usually hydrophobic polymer surface is not optimal for many applications, there is a strong demand for surface modifications or functional coatings deposited within the cavities. Low-pressure plasmas are well-known tools for polymer surface modification and coating. However, because of the large mean free paths of particles at low pressures, these discharges can only be sustained in relatively large volumes. At atmospheric pressure plasmas can be generated in the sub-mm-sized cavities themselves. Furthermore, plasmas can burn in already sealed channels and cavities, where only a gas inlet and outlet is needed.

2. UNIFORM COATINGS ALONG EXTENDED CHANNELS

In the experiments two electrodes attached to the microfluidic component drive the dielectric barrier discharge [1]. In order to make an optical observation of the plasma possible, one of the electrodes can be made from ITO or metal mesh. By applying a sufficiently high voltage on the electrodes the electrical field ignites a discharge in the channel (Figure 1). The required field strength is dependent on the used gas, the pressure as well as the channel profile and can be estimated using Paschen's Law. Based on the micro plasma process coatings can be achieved by chemical vapour deposition on the walls of the cavities. This opens a wide field of surface modifications such as the generation of chemical functional groups, deposition of barrier coatings and controlling the wetting behaviour.

For polymer components time-stable hydrophilicity provided by ultra thin SiO_2 layers is of special interest. These coatings were deposited from tetramethyl orthosilicate (TMOS). In long narrow channels the monomer depletion will cause a gradient in the coating thickness. This can be reduced by intermittent ignition of the discharge in order to allow a refilling of the channel with fresh monomer between the sinusoidal voltage trains.

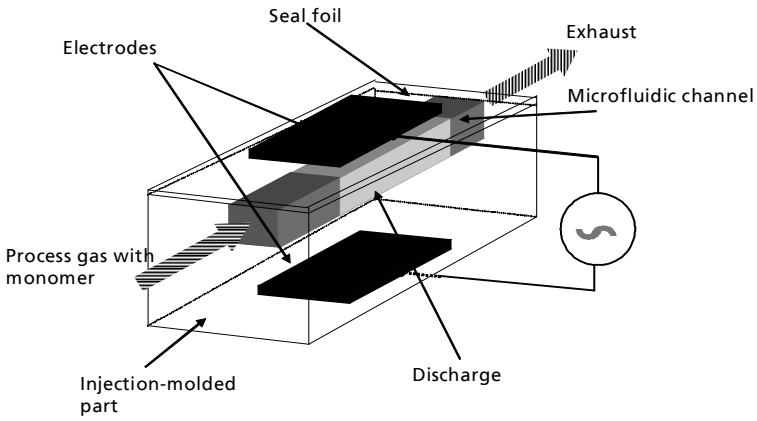

FIGURE 1. Experimental setup.

An unusually long (310 mm) meander-like channel with a cross section of 100 x 100 μm^2, generated by injection molding of cyclo-olefine polymer (COP) was used for a number of the coating experiments. The gas atmosphere was a mixture of helium with 2.5 vol-% oxygen and 0.85-vol-% TOMS. The plasma was ignited intermittently with pulse times of 100 ms and pause times of 500 ms. The residence time of the gas within the channel was calculated to be 310 ms at the overpressure used (200 mbar). Because of the ratio of length and cross section a treatment duration of 18 min was chosen, corresponding to a total "plasma on" duration of 3 min.

The coating thickness on the channel bottom was routinely characterized by microscopic infrared reflection spectroscopy using a Nicolet 5700 FTIR spectrometer. As a film thickness measure the relative reflection, defined as $R^* = (R_{peak}-R_{base})/R_{base}$, measured at the peak maximum of the strong Si-O-Si stretching vibration (1060-1070 cm^{-1}) was applied. Spectral simulations show a linear relation of this quantity with film thickness, as long as the thickness does not exceed a few 100 nm. Normalization to the baseline reflectivity was used in order to account for changes in the reflected intensity due to geometric effects. The thickness distribution is shown in Figure 2.

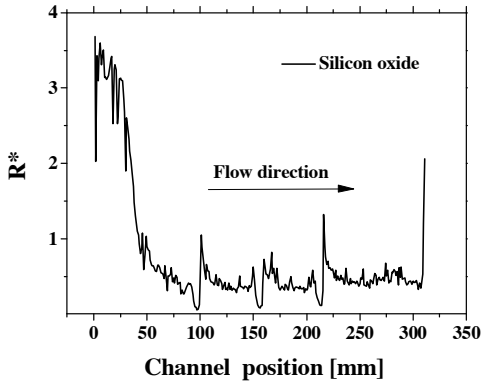

FIGURE 2. Coating thickness in an extended channel.

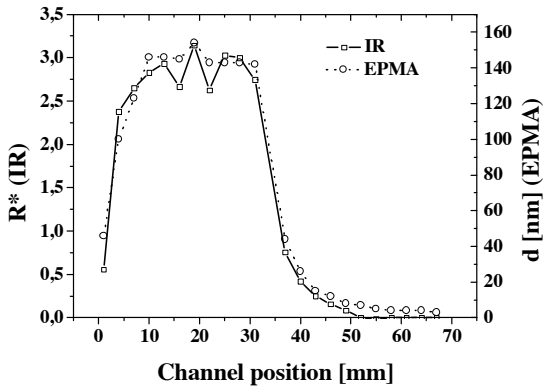

FIGURE 3. Correlation of IR and EPMA coating thickness measurements (300 x 500 μm channel).

The coating thickness near the entrance of the channel is clearly enhanced because of the continued supply of fresh monomer during the 100 ms pulse. Beyond 75 mm the monomer is virtually completely depleted and only during the pause fresh monomer can enter beyond this length. The sharp bends in the curve at 100 mm, 160 mm, 220 mm and the outlet are due to the electrode shape which ends in these parts close to the channel. This causes locally inhomogeneous, higher and lower electrical fields, respectively.

In order to determine absolute coating thickness, FTIR measurements were correlated with electron probe micro-analytical (EPMA) data. In Figure 3 both graphs are plotted in the same diagram for SiO_2 in a 300 x 500 μm^2 channel. The overall agreement of the curves is satisfying. Up to 150 nm for SiO_2 the following correlation was found: 1 R* ≈ 50 nm. (Additional measurements on thicker coatings showed different correlation coefficients between EPMA and IR spectroscopic results.)

Coatings thicknesses from 20 to 100 nm show a sufficient performance for a multiplicity of applications, e.g. time-stable surface functionalization. Thicker coatings can advantageously be used for barrier applications.

3. LOCAL TREATMENT

Surface modifications on selected areas in fluidic structures can improve the function of microfluidic systems. This has been realized by deposition of a hydrophobic stop in a hydrophilic channel. The principle is shown in Figure 4. Driven by capillary force water will wet a hydrophilic channel (water contact angle < 90°) and stops at the begin of a region with smaller free surface energy (hydrophobic stop). Driven by a pressure impulse on the channel inlet the water can get over the hydrophobic part and continue flowing driven by capillary force.

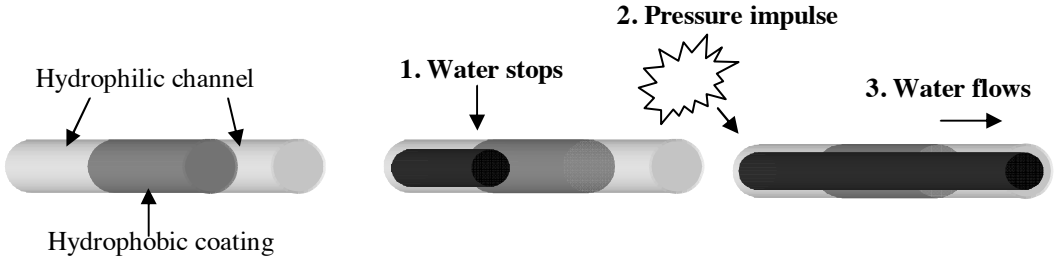

FIGURE 4. Hydrophobic stop for aqueous fluids.

The area-selective surface modification was achieved by using small electrodes which will establish a localized electrical field sufficient to ignite the plasma locally. The dimension of the plasma-treated area can be influenced by the shape and the size of the electrodes as well as the composition of the process gas.

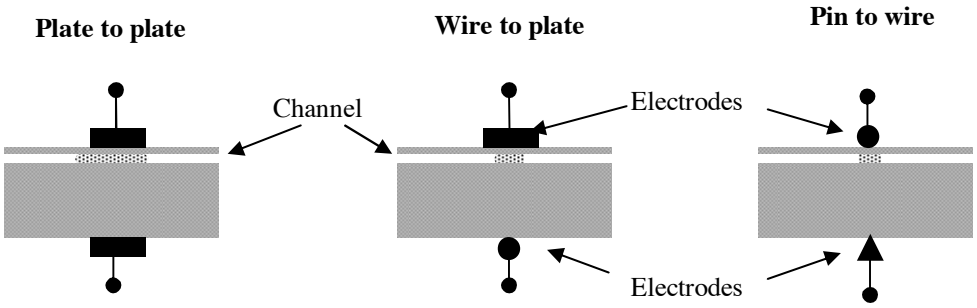

FIGURE 5. Different electrode configurations.

In Figure 5 three different electrode configurations and the resulting plasma zones are shown. For the experiments plates with a width of 2 mm and wires with a diameter of 0.2 mm were used. The pins were made from the same 0.2 mm wires, the radius of the top was not defined. For the “wire to plate” and the “pin to plate” configuration it would be helpful for a localized ignition to set the smaller electrodes closer to the seal foil. Because of limitations in

the set up we used the shown configuration. The experiments were done in COP channels with a width of 500 μm and a depth of 300 μm.

TABLE 1. Treatment parameters.

	He [vol%]	N_2 [vol%]	HMDSO [vol%]	Voltage [V]	Treatment time [s]
Plate to plate	99.8	0.0	0.20	5.2	30
Wire to plate	92.3	7.5	0.22	7.5	60
Pin to wire	39.5	60.0	0.44	16.5	20

Due to its small breakdown voltage helium is a favored process gas. However, due to the formation of jet-like "plasma tails", extending into the low-field regions beyond the electrodes, the localization of the discharge in pure helium is difficult. Addition of molecular gases, e.g. nitrogen or oxygen, is necessary, which will enlarge the breakdown voltages. For hydrophobic coatings the monomer hexamethyl disiloxane (HMDSO) was used. Process gases and process parameter are shown in Table 1.

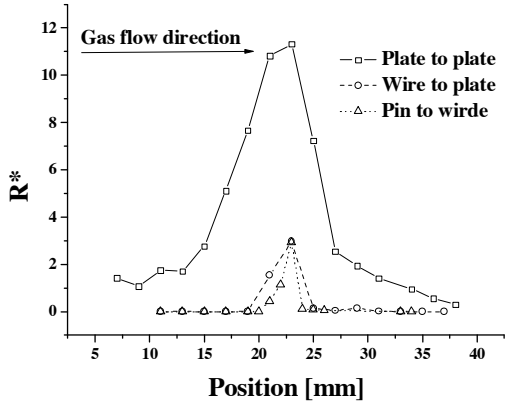

FIGURE 6. HMDSO coating thicknesses.

Thickness distributions of HMDSO coatings are shown in Figure 6, as measured by IR-spectroscopy. The coating areas agree with the plasma ignition areas. Surprisingly the thickness profiles are highly symmetric, in spite of the large gas velocities used; i.e., there is no deposition in the afterglow region, a fact which might be attributed to missing surface activation in zones without plasma contact.

4. CONCLUSION

Microplasmas generated in cavities offer the possibility to improve the surface properties and even more the function of sealed microfluidic systems. This new technique allows modifying extended channels as well as defined areas. By the use of different monomers and process gases the surface properties can be chosen to conform to a wide range of requirements.

ACKNOWLEDGMENTS

Financial support of the Bundesministerium für Wirtschaft und Arbeit (BMWA) and eight industrial partners of the InnoNet project MicroPlas, contract no. 16INO272., is gratefully acknowledged. We also acknowledge the help of Cornelia Steinberg, Fraunhofer IST, with EPMA measurements and analysis.

REFERENCES

[1] Klages, C.-P. and Thyen, R. (2000). Verfahren zur plasmagestuetzten Behandlung der Innenflaeche eines Hohlkoerpers, *German Patent DE 100 35 177 C2*.

[2] Eichler, M., Thomas, M., Hacker, J., and Klages, C.-P., Functional coatings deposition in microfluidic systems by DBD-based PA-CVD. *Proc. CAPPSA 2005*, pp. 138 – 142.

SILICON BASED THIN FILM DEPOSITED FROM HEXAMETHYLDISILOXANE IN AN ATMOSPHERIC PRESSURE TOWNSEND DISCHARGE

T. Paulmier, N. Gherardi*, L. Maechler, I. Enache, H. Caquineau, F. Massines

Laboratoire de Génie Electrique de Toulouse, Université Paul Sabatier,
118 route de Narbonne, 31062 Toulouse Cedex 9, France

ABSTRACT. The aim of this work is to determine the growth mechanisms of silicon deposit produced by Atmospheric Pressure Townsend Discharges using a mixture of nitrogen (N_2), nitrous oxide (N_2O) and hexamethyldisiloxane (HMDSO). The surface is characterized by profilometry, spectroscopic ellipsometry and Infra-Red absorption spectroscopy. Experiments have been done as a function of the dissipated power for different [N_2O]/[HMDSO] ratios. A wide range of silicon coatings is obtained from $SiO_xN_yC_zH_w$ polymeric like materials to SiO_2 like films. The dissociation and transport mechanisms have been analysed from the different deposition rate profiles.

1. INTRODUCTION

Dielectric barrier discharge working at atmospheric pressure is a useful material technology used for the production of a wide range of polymer, carbon, silicon and oxide coatings on glass, metal foils, polymer tissues or semi-conductor wafers [1-6]. Due to their low toxicity, their chemical stability and low flammability, organosilicon compounds such as hexamethyldisiloxane (HMDSO) are very advantageous precursors for the production of silicon thin films. Our study deals with the production of silica coatings by atmospheric pressure Townsend discharge [2, 3] and the understanding of the dissociation and deposition mechanisms. The approach consists in analyzing the chemical composition and evolution as well as the deposition profile as a function of the reactive gas composition, the oxidant ratio and the dissipated power in the discharge.

2. EXPERIMENTAL SET-UP

The experimental set-up has already been described in previous publications [2]. In our study, nitrogen is used as vector gas with a flow of 4.5 $l.min^{-1}$. It is mixed with a small quantity (10 to 44 ppm) of hexamethyldisiloxane (HMDSO), and with N_2O as oxidant agent. The [N_2O] / [HMDSO] ratio varies from 0 to 100. All the films have been deposited on a 2 inches diameter silicium wafer during 15 minutes and analyzed after treatment by Fourier-Transform Infrared Spectroscopy (FT-IR), profilometry and spectroscopic ellipsometry. The power in the discharge is calculated through measurements on discharge current and voltages [3].

* Electronic address : gherardi@lget.ups-tlse.fr

3. RESULTS AND DISCUSSION

3.1. Influence of [N_2O] / |HMDSO] ratio on composition and structure of the coatings

In a first step, we have studied the influence of N_2O / HMDSO ratio on the chemical composition and structure of the deposited coating. When this ratio R varies from 0 to 100, keeping constant the dissipated power at 0.5 W.cm^{-2} and the HMDSO concentration at 4 ppm, we can notice by FT-IR spectroscopy that the deposited coating evolves from a smooth $SiO_xN_yC_zH_w$ like material at R lower than 6 to a dense SiO_2-like material, with a significant concentration of Si-OH functionalities at higher R. The nature of the different peaks is indicated on the figure below.

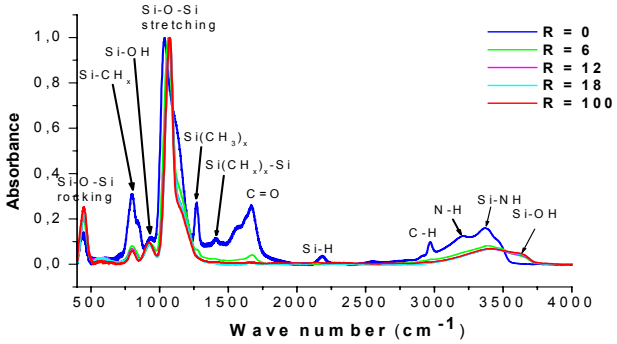

FIGURE 1. FT-IR spectra (normalized to Si-O-Si peak) for different R ratio at: HMDSO: 4 ppm, dissipated power: 0.5 W.cm^{-2}

When present, Carbon is in the form of Si-CH_x, Si-O-C, C=O, CH_x. The gradual shift toward higher wave number of Si-O-Si peak when R increases is linked to the decrease of disorder and stress in the film. An interesting feature is the decrease of the Si-NH group with the increasing R ratio which has to be opposed with the increase of the silanol groups Si-OH. This trend suggests a substitution of N with O in the film. The evolution of the deposition rate in regard of the dissipated power and the gas residence time can give some information on the dissociation and deposition phenomena.

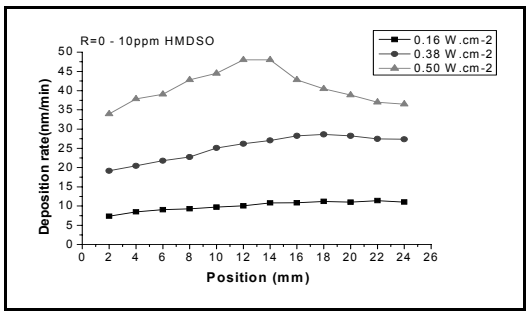

FIGURE 1. Profile of deposition rate in regard of the dissipated power for R = 0 and [HMDSO] = 10 ppm

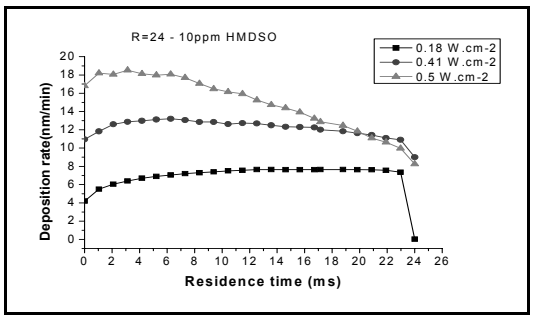

FIGURE 2. Profile of deposition rate in regard of the dissipated power for R = 24 and [HMDSO] = 10 ppm

For a nil R ratio (figure 2), and for a given dissipated power, the increase of the dissociation rate as a function of the residence time is very slow comparing to R equal to 24 (figure 3). The maximum thickness is indeed placed in the middle or close by the outlet of the plasma area. At 0.16 W.cm^{-2}, the deposition rate does not even reach a maximum point (figure 2) which means that HMDSO is not completely consumed. We can explain this slow deposition rate by the absence of oxygenated species in the discharge. The dissociation is then only ruled

by the concentration of nitrogen metastable $N_2(A_3\Sigma_u^+)$ which varies slowly as a function of the residence time. At elevated power, once the maximum deposition rate is reached, we can notice a rapid decrease of this rate with a significant slope being the feature of precursor depletion. We can deduce from this behaviour, which is very different from what is observed at R = 24, that the active species coming from the dissociation of HMDSO are transported by a strong driving force. The assumption is that some ionic species are produced within the plasma area, accelerated and rapidly stuck to the substrate. For R = 24, we can observe a rapid increase of the deposition rate with a maximum placed close by the entrance for both frequencies. This features a rapid dissociation of HMDSO by the plasma discharge explained by the presence of several reactive species: the metastable $N_2(A_3\Sigma_u^+)$ coming from nitrogen and the active species NO and O coming from N_2O. The decreasing section is rather slow revealing a slow diffusion of the active species to the surface. The slope of the decreasing part rises with the increasing injected power: this trend is due to the higher production of reactive species which enhance dramatically the HMDSO dissociation rate.

3.2. Deposition kinetics in regard of HMDSO concentration and dissipated power

In a second step, we have studied the influence of the initial HMDSO concentration and of the dissipated power on the deposition kinetics of this process for an R ratio equal to 24 (figures 4 and 5).

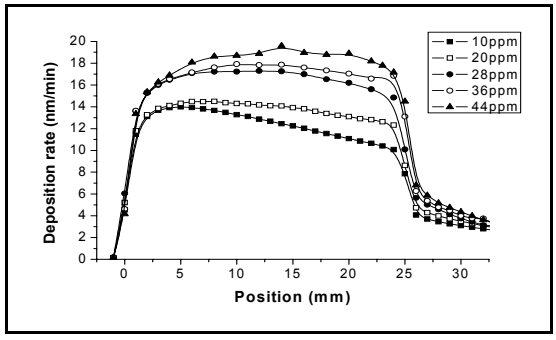

FIGURE 3. Profile of deposition rate for a dissipated power equal to 0.5 W.cm^{-2}

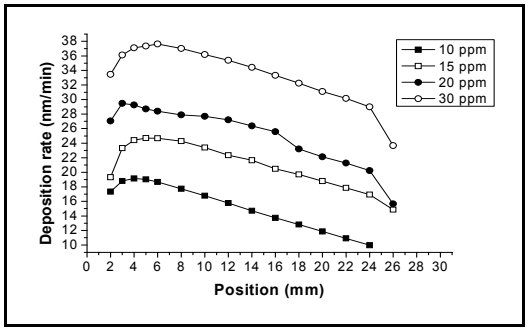

FIGURE 4. Profile of deposition rate for a dissipated power equal to 0.65 W.cm^{-2}

From figure 4, we can notice an increase of the deposition rate with the HMDSO initial concentration. Whereas the thickness rapidly drops down along the gas path at low HMDSO rate, the deposition rate profile gets almost constant at higher HMDSO concentration. From this, we can deduce that, for the same dissipated power, the quantity of dissociative species (metastables and oxygen species) is not sufficient at elevated HMDSO concentration to consume a large amount of monomer. This trend is not observed at higher dissipated power (see figure 5) where the dissociation rate increases rapidly and in the same way for each concentration. The maximum deposition rate is then located at the entrance of the plasma zone and remains almost at the same position when HMDSO concentration changes. On the other hand, at lower dissipated power (figure 4), this maximum moves gradually from the entrance to the outlet of the plasma area which confirms that HMDSO dissociation kinetics falls down steadily. From Figure 6, we can notice a flat evolution of the maximum deposition rate at 0.5 W.cm^{-2}. This is also in accordance with a lack of nitrogen and oxygenated active species at this power level, which tends then to saturate the deposition rate. The second possibility is that the metastable or ionic oxygenated species formed from N_2O would sputter the deposited coating and then impinge on the deposit growth. If we increase the dissipated power, the maximum deposition rate increases significantly and evolves almost proportionally to HMDSO concentration. We can thus assert that the production of oxygenated active

species and nitrogen metastables is a limiting factor in the dissociation and deposition mechanism when the dissipated power is not sufficient. However, the maximum thickness is not perfectly proportional to HMDSO concentration which suggests that we may reach a threshold in the creation of HMDSO active species or that we have an additional constraint in the transport or deposition mechanisms.

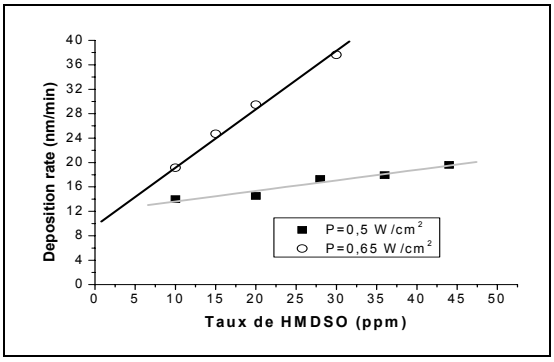

FIGURE 5. Evolution of the maximum deposition rate in regard of HMDSO concentration and dissipated power

4. CONCLUSION

This paper aimed to understand more clearly the dissociation and deposition mechanisms leading to the formation of silicon thin films produced by dielectric barrier discharge at atmospheric pressure. This Townsend discharge working at temperature lower than 50°C allows the production of a wide range of coatings from $SiO_xN_yC_zH_w$ materials to dense SiO_2 like films with a significant quantity of Si-OH functionalities. We have demonstrated that the deposition rate profile as a function of the dissipated power, HMDSO concentration and R ratio allows getting a good knowledge on the dissociation mechanisms and kinetics. The evolution and concentration of the nitrogen metastable and oxygenated species has especially a strong influence on the deposition profile and uniformity of the coating.

REFERENCES

[1] Sawada Y., Ogawa S. and Kogoma M. (1995). Synthesis of plasma-polymerized tetraethoxysilane and hexamethyldisiloxane films prepared by atmospheric pressure glow discharge. *J. Phys. D: Appl. Phys.*, 28, 1661-1669.

[2] Massines F., Gherardi N., Fornelli A. And Martin S. (2005). Atmospheric pressure plasma deposition of thin films by Townsend dielectric barrier discharge. *Surf. Coat. Technol.*, 200, 1855-1861.

[3] Massines F., Ségur P., Gherardi N., Khamphan C., Ricard A., (2003). Physics and chemistry in a glow dielectric barrier discharge at atmospheric pressure: diagnostics and modelling, *Surf. Coat. Technol.*, 174-175, 8-14.

[4] Sonnenfeld A., Tun T.M., Zajickova L., Kozlov K.V., Wagner H.E., Behnke J.F. and Hippler R. (2001). Deposition process based on organosilicon precursors in Dielectric Barrier Discharges at atmospheric pressure – A comparison. *Plasmas and Polymers*, 6(4), 237-266.

[5] Vinogradov I.P., Dinkelmann A., Lunk A. (2003). Deposition of fluorocarbon polymer films in a dielectric barrier discharge (DBD). *Surface and Coatings Technology*, 174-175, 509-514.

[6] Foest R., Adler F., Sigeneger F., Schmidt M. (2003). Study of an atmospheric pressure glow discharge (APG) for thin film deposition. *Surface and Coatings Technology*, 163-164, pp. 323-330.

PBG FIBER FOR LOW GAS CONCENTRATION MEASUREMENT

J. Pawłat[1], T. Sugiyama[2], T. Matsuo[1], T. Ueda[1]

Graduate School of IPS, Waseda University
808-0135 Fukuoka ken, Kitakyushu-shi, Wakamatsu-ku, 2-7 Hibikino, Japan
Yokogawa Electric Corporation, 180-8750, Tokyo, 2-9-32 Naka-cho, Musashino-shi, Japan

ABSTRACT. An idea of high-sensitivity gas concentration measuring system basing on Photonic Bandgap fiber (PBG fiber) was studied. Several types of PBG fibers of various parameters were designed. Core diameters ranged from 10.9 to 26.25 μm. Capillary gas flow rate within the fiber was simulated and measured. Attenuation of newly produced fibers was investigated and concentration of ammonia gas was measured using the new type sensing system.

1. INTRODUCTION

Development of semiconductor manufacturing industry, constant tendency to miniaturize the products and need for cheap and simple measurements of traces of various compounds encouraged our research group to engage in the development of a new measurement system. The results of preliminary research on in-situ measurement using tunable laser and glass or metal tanks [1-3] and the perforated optic fiber (to guide light while filled with gas) [4] as the gas cells were very promising. In this paper the analysis of the micro-capillary gas flow phenomenon inside fiber, examination of properties of photonic crystal fiber, the design of the proper fibers for our device and study on the low concentration gas measurement system for the semiconductor manufacturing industry are presented. First results of ammonia concentration measurements are shown.

2. EXPERIMENTAL SET UP

The main goal of the experiment was to measure low concentration of ammonia where few ppm- concentration gas could be diluted with high purity nitrogen even to ppb level. Gas was dosed into the gas cell of special design and it passed throughout the optic fiber for proper measurement of light absorption. The gas- providing system is presented in Fig. 1. 1550 nm emission wavelength tunable laser was chosen for the optical measurement system using commonly produced PBG fiber. Light passed objective lens, the zero-order waveplate and was spitted using cube beam splitter. The output light was guided inside the optic fiber from and to the gas cells, and passed objective lens with the zero-order waveplate. Finally, both: measurement light wave front and reference light wavefront (adjusted using mirror) were received by two photodetectors New Focus 2011-S. The coupling of the light depends on the light source and fiber bandwidth. For measurement of newly designed fibres' properties at 1.5 and 1.9 μm, the set-ups with LED lamps and Oriel Fiber Illuminator with xenon lamp were used. The photo and working scheme of optical sub-system with lamp is depicted in Fig. 2. Light, which was emitted by above sources, passed through chopper unit, focusing lenses and was guided to MS 260i Oriel monochrometer. Light of certain wavelenght was detected

[1]Electronic address: askmik@hotmail.com

using wide-wavelength GaInAs pin photodiode. Signals from photodiode and chopper were adjusted and amplified by Lock-In amplifier and observed using digital oscilloscope and digital multimeter. The emitted light, which wavelength corresponded to the absorption of ammonia molecule should be partly absorbed by the gas within the optical fiber. The absorption would be then strictly related to the concentration of NH_3 in the carrying gas (high-purity nitrogen).

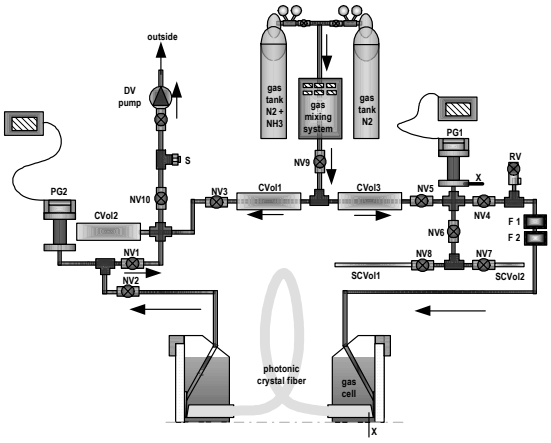

FIGURE 1. Scheme of gas-providing sub-system. PG1, PG2- pressure control, NV1-NV10- control valves, RF- relief valve, F1, F2- filters, CVol1-CVol3- control volumes, SmallCVol1, SmallCVol2- small control volumes, S1- spare connection.

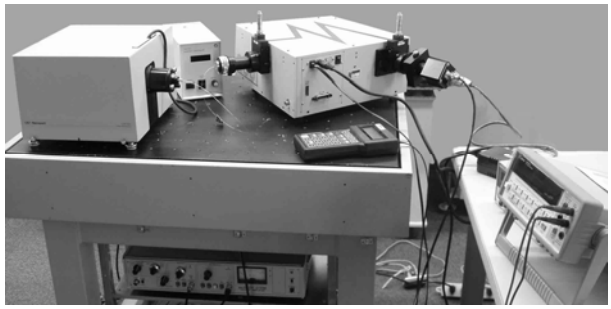

FIGURE 2. Photo of optical subsystem with lamp.

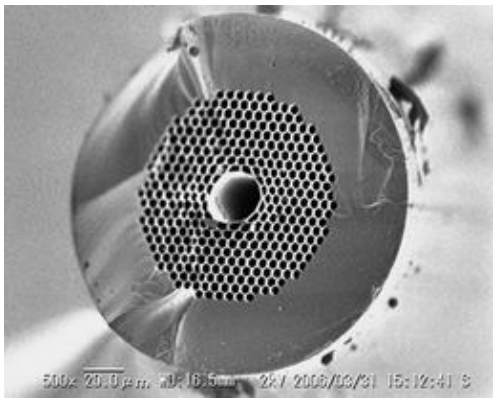

FIGURE 3. SEM photos of photonic crystal fiber: core 26.25. μm after cutting using adjustable fiber cutter, Resolution: 500.

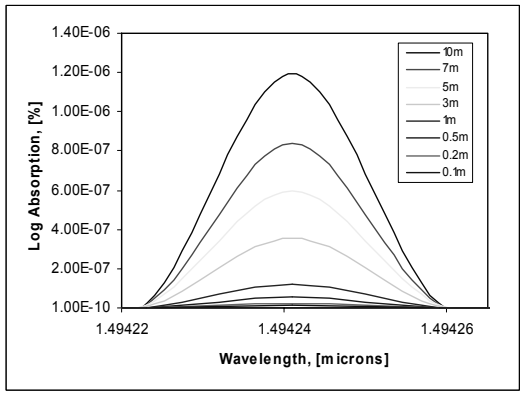

FIGURE 4. HITRAN simulation of light absorption in dependence on on the length of optic fiber (sub-ppb ammonia concentration, 0.1 atm).

At first, HC-1550-02 fiber of 10.9 μm core was tested. Then, new PBG fibers of 1960 nm center operating wavelength were developed particularly for the research purpose. The core diameters of new fibers used in the experiment were: 15.2 μm, 16.2 μm, 19.4 μm, and 19.6 μm and 26.25. μm. The microscope photo of the 26.25 μm photonic band gap fiber is shown in Fig. 3. According to HITRAN simulations (Fig. 4) to measure the ppb level of ammonia, several meters of fiber are required, to ppm level- less than 1 meter would be enough. Lowering the pressure below the atmospheric one enables sharpening of absorption peaks. Thus, peaks caused by the molecules of chosen pollutant can be distinguished from the other eventual contaminants. In the presented collision-broadening simulation wall collisions were not considered.

3. RESULTS AND DISCUSSION

Microcapillary nitrogen gas flow simulations were performed employing the standard mathematical software. All presented results were obtained assuming gas flow within the core and 20°C temperature. Velocity of the gas was calculated from the pressure difference $\Delta p = p_1 - p_2$. The known flow equation of Darcy-Weisbach (1), widely used in sanitary engineering was applied to experimental conditions:

$$\Delta p = \lambda \, (l / d) \, (\rho v^2 / 2), \, [Pa] \qquad (1)$$

Where Δp is pressure difference on both ends of the optical fiber, l - length of the reactor, d - core diameter, ρ - gas density at certain pressure, v - gas velocity, μ - dynamic (absolute) viscosity, λ - coefficient, which depends on Reynolds number, for laminar flow ($Re < 2300$):

$$\lambda = 64/Re, \, [-] \qquad (2)$$

The result of gas velocity simulation is presented in Fig. 5(A). Velocity was calculated from the equation (1) for 26.25. μm core PBG fiber and various lengths from 10 cm to 1 m.

(A)

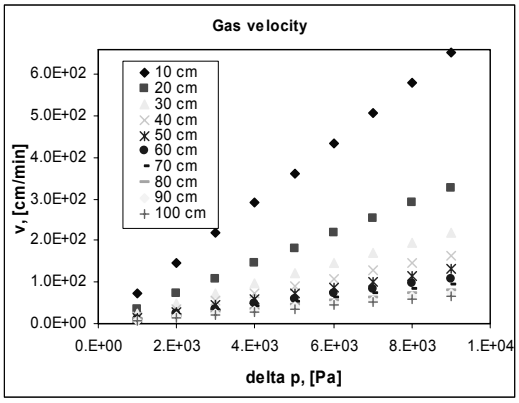

(B)

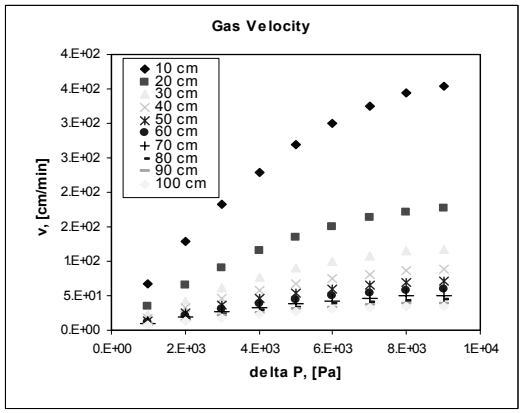

FIGURE 5. Simulation of gas velocity in dependence on the pressure difference for non-compressible (A) and for compressible (B) flow.

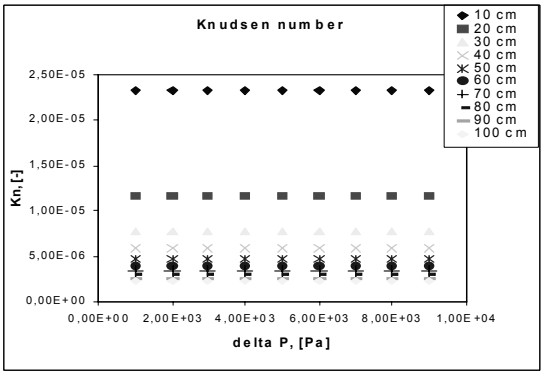

FIGURE 6. Knudsen number for compressible flows within fibers.

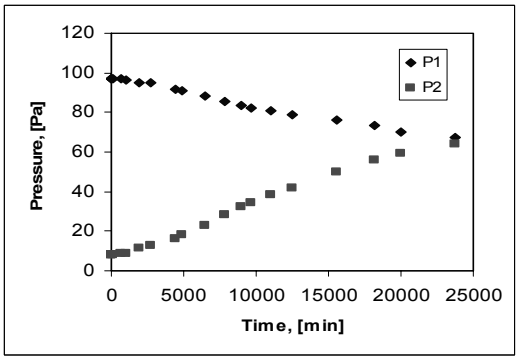

FIGURE 7. The experimental result of the gas flow measurement, 26.25. μm core PBG fiber.

Darcy-Weisbach equation does not take the compressibility into an account and obtained values for gas are different from the real case. Therefore, quasi-Panhandle equation (5), for modelling of the compressible fluid flow was also taken unto account.

$$p_1^2 - p_2^2 = G^2 RT / F^2 \, (\lambda \, (l/d) + 2\log_e (v_2/v_1)), \, [Pa] \qquad (3)$$

Gas flow rate was calculated according the equations (3) and (2). The results of modeling process are shown in Fig. 5(B). To ensure that it was proper to use continuum mechanics formulation of fluid dynamics instead of statistical mechanics for our capillary flow, Knudsen

numbers were calculated according to equations (4).

$$Kn = \lambda_{fp} / l = (k_B T)/(2^{(1/2)} \sigma^2 P l), [-] \quad (4)$$

Where λ_{fp} is mean free path, l - representative physical length scale, k_B - Boltzmann's constant, T – temperature, σ – diameter, p_1 - total initial pressure, [Pa]. Results of simulations for tested fibers in the case of compressible flow are shown in Fig. 6. Knudsen number was much lower than one. Thus, the mean free path of a molecule was much smaller than a length scale of the problem so the continuum assumption of fluid mechanics was a good approximation.

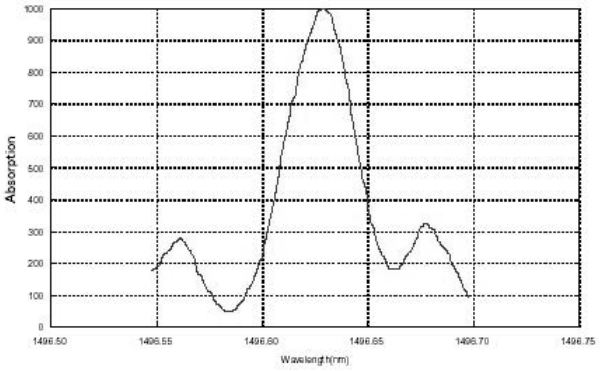

FIGURE 8. Measured 10 ppm ammonian peak.

Predicted gas flows were confirmed by the experimental results. It was possible to measure the flow rate of the nitrogen gas inside the PBG fiber with various pressure differences on the opposite ends. Average velocity on P1 side ranged 228 cm/min at 91 kPa pressure differences for 20 cm of 26.25 μm core PBG fiber. That was in the order range between compressible (177 cm/min) and non-compressible (326 cm/min) flow simulation results for the same parameters. The example of long running experiment on time of pressure balancing for such a fiber is depicted in Fig. 7. The result of NH_3 concentration measurement using short length PBG fiber of 10.9 μm core is shown in Fig. 8. According to our estimations it will be possible to measure 0.5 ppb/m in this case. Besides, the larger core PBG fibers will be further developed, what practically can solve the problems related to gas velocity. Adsorption and desorption phenomena within silica fiber walls will be also studied as presently only pure nitrogen purging system was applied .

4. CONCLUSIONS.

The set-up for measuring of ppb concentration of ammonia was designed.
New types PBG fibers were produced. Simulations of mass flow rate of gas and of gas velocity in dependence on applied pressure were performed.
Gas flow rate in the experimental condition was corresponding to the simulated one. It was sufficient for fast ppm-order measurement using short optic fibers as a gas cells. First experiments of measurement NH_3 concentrations were performed.

ACKNOWLEDGEMENT

This research was supported by the Grant-in-Aid of Japanese Ministry of Ecology and Natural Resources. Authors would like to thank to Professor Lev Zimin and Mr. Tatsuhiko Saitoh for fruitful advices and help during research work.

REFERENCES

[1] Ueda T., OkamotoY. (1998). In Situ Status Measurement Technology. *Proc. 1st Symp. . Adv. Photon Proces. Meas. Technol.*, 25-28.
[2] Sugiyama T., Wada M., Nakajima S., Ueda T. (2001). High sensitivity In-situ Gas Measurement. *Proc. 4th Workshop on Adv. Photon Proces. and Meas.t Technol.*, 63-66.
[3] Sugiyama T., Ueda T. (2003). In-situ Measurement for the Gas Concentrations Using Tunable Lasers. *Proc. of Tech. Meeting on Sensors and Micromachines*, CHS-03-56, 1-4.
[4] Pawlat J., Matsuo T., Sugiyama T., Ueda T. (2006) Measurement of Low Gas Concentration Using Photonic Bandgap Fiber. *J. Adv. Oxid. Technol.* 9(2),150-155.

DEVELOPMENT OF A TYPE OF COMPACT NANOSECOND PULSE GENERATOR

Quan Zhaochun, Liu Zhongjie, Li Zhi, Gao Yanhui, Xie Xiongjie, Zhang Yuanfang, Guan Genzhi

Department Of Electrical Engineering
Faculty of Science and Engineering, Wuhan University
Wuhan, 430072, CHINA

ABSTRACT. This paper presents a type of nanosecond pulse generator. We have gained ideal nanosecond pulse by shaping technique, reshaping technique and pulse truncation technique. We use a cable to shape, design a specific switch to reshape and obtain truncation waveform on basis of the refraction and reflection theory. The equipment holds the following virtues: 1) It has compact structure with high-power; 2) single nanosecond pulse has been gained 3) Lots of short-width pulses with ultra short front-time and behind-time have been got; 4) It has sharp high peak value and high stability. It is very important to develop the equipment because it is a great progress on the research of generating nanosecond pulse and application in plasma scientific research.

1. INTRODUCTION

The high-power pulse technique is of vital significance to modern science. It has been widely used in high voltage insulation experiments and microwave technology of power system. The key points and advancing front of the pulse power research are: 1) miniaturized device of high power and high efficiency; 2) obtaining a single pulse; 3) obtaining a pulse of steep front edge，steep back edge and short-width. This device is a type of high voltage energy-stored capacity nanosecond pulse generator and of simple structure, high peak-to-peak amplitude, steep front edge and high stability.

2. EXPERIMENTAL CIRCUIT AND OBTAINING THE PULSE WAVE

The experimental circuit of this equipment is showed in figure 1.

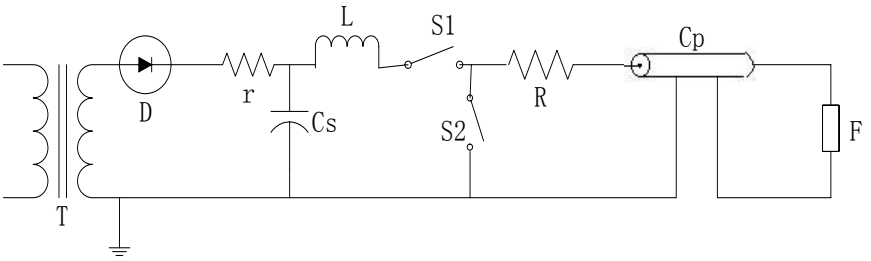

T: step-up transformer, D: rectifier cell, r : charging resistor, C_S : pulse capacitor, L : loop inductance, S_1, S_2: switches, R : loop resistance, including the switch resistance, load resistance and loop stray resistance, C_p: capacitance of transmission line, F: load.

FIGURE 1. The experimental circuit of the equipment

2.1. Shaping and reshaping of the front edge

In figure 1, the discharge loop is composed of C_S, L, S_1, R, C_P and F. When the voltage over C_S gets to U_0, switch S_1 has a breakdown and C_S discharges through L, R, C_p and F. Because the C_P we chose is very small, so we can get a steep rise of voltage. And S_1 is the specific switch designed for reshaping, so the front edge is both formed and reshaped in the discharge loop.

The discharge loop's equivalent circuit is showed in figure 2.

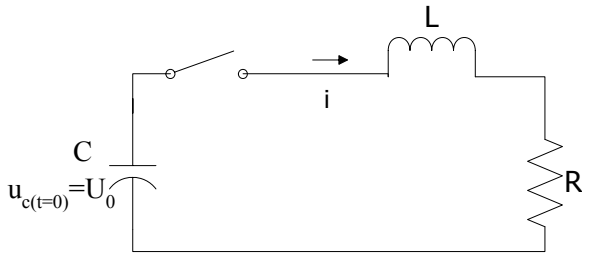

C: a capacitor that stores energy, L: sum of inductance of the transmission line, the isolation gap and the load, R: sum of resistance of the transmission line, the isolation gap and the load.

FIGURE 2. The discharge loop's equivalent circuit

From the circuit theoretical analysis we can obtain:

$$i = c\frac{du_c}{dt} \tag{1}$$

$$u_c = L\frac{di}{dt} + iR \tag{2}$$

$$LC\frac{d^2u_c}{dt^2} + RC\frac{du_c}{dt} - u_c = 0 \tag{3}$$

Solve the differential equation, we get:

$$u_c(t) = U_0[\frac{1}{a-b}(ae^{at} - be^{bt}) + \frac{R}{L}(e^{at} - e^{bt})] \tag{4}$$

And $a = \dfrac{-R/L + \sqrt{R^2/L^2 + 4/LC}}{2}$, $b = \dfrac{-R/L - \sqrt{R^2/L^2 + 4/LC}}{2}$

$$\text{So } i = C\frac{du}{dt} = \frac{CU_0}{a-b}[(a^2 + \frac{R}{L}a)ae^{at} - (b^2 + \frac{R}{L}b)e^{bt}] \tag{5}$$

When $t = 0$, and the R is neglected, there is:

$$(\frac{di}{dt})_m = \frac{U_0}{L} \tag{6}$$

As shown in equation (6), the bigger L is, the smaller $(\frac{di}{dt})_m$ is. It is because that the voltage over L won't jump. Therefore, reducing the loop inductance is vital to get a steep nanosecond current pulse. So when we design the reshaping switch S_1, we should reduce its inductance to get a pulse we want.

2.2. Pulse truncation

In figure 1 we know that when S_1 has a breakdown, the wave transmits to the load F along the electric cable. And the load F in our experiment is actually a gap, so the terminal of the transmission line is open circuit. According to the wave refraction and reflection theory, when the wave transmits to the terminal of the transmission line, a total reflection occurs. And the reflection wave will cause the entrance voltage to rise to two times of the forward wave voltage U_0. So the voltage over S_2 is $2U_0$, which is higher than its breakdown voltage. Thus the truncation switch S_2 acts and has a breakdown. Then the circuit turns short-circuit so the input voltage is truncated.

3. THE EXPERIMENTAL DEVICE

In order to obtain a nanosecond pulse, reducing the pulse width is the most important. Therefore the inductance of the spark gap is requested to be small, namely, the gap should be narrow as far as possible, and the spark should have passages to pass through as many as possible, moreover, the spark resistance must be small as far as possible. According to the theoretical analysis above, using a high-pressure gas-filled reshaping switch can meet the needs above. The specific structure of the reshaping switch S_1 is shown in figure 3.

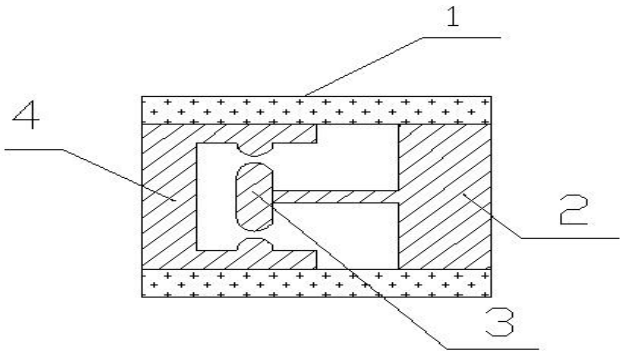

1.Insulator, 2. Lower voltage electrode, 3. Lower voltage ball, 4. High voltage electrode.

FIGURE 3. Configuration and structure of the reshaping switch S_1.

There is an arc inside, its surface is spherical, and the low voltage electrode is a ball impression. Designing like this makes the entire discharge passage equal to that of a series of face-to-face spherical electrodes, thus the discharge passage changes from line to plane and the inductance of the switch is reduced. And the trigger of S_1 is a piezo-electricity ceram electronic ignitor. It is safe and of high stability.

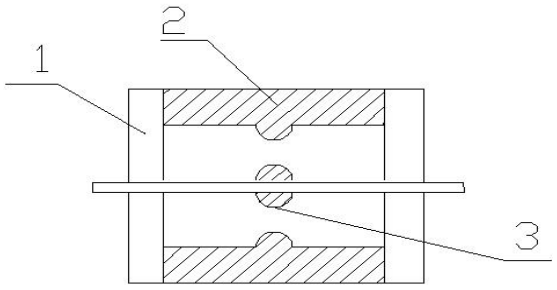

1.Insulator, 2. Lower voltage electrode, 3. High voltage electrode **.**

FIGURE 4. Configuration and structure of the truncation switch S_2.

According to the assessment of nanosecond pulse output width, current and inductance, the parameters of pulse capacitor are as follows: The charging voltage was 50kV, the capacitance was 5nF consists of six coaxial parallel capacitors.

According to the pulse width and the existing conditions, we chose a cable of 110kV, length of 2.5m,capacitance of 750 pF .

4. EXPERIMENTAL RESULT AND CONCLUSIONS

The experimental result is shown in figure 5. It shows the output current waveform and pulse width of the device. The pulse width that we obtained is 18ns and the current is 2.5kA.

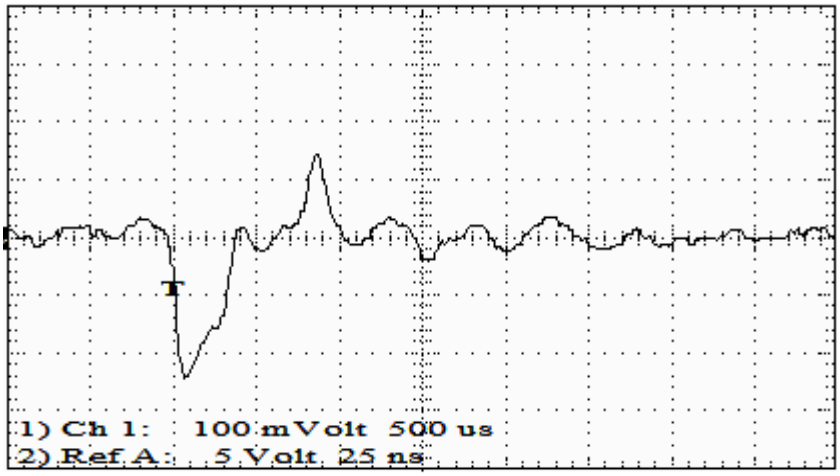

FIGURE 5. The waveform of output current in experiment

(1) This device can generate a predetermined nanosecond single pulse, and it has sharp high peak value and it is of high stability.
(2) Adopted a piezo-electricity ceram trigger in reshaping switch and it is safe and of high stability.
(3) Realized the pulse truncation on basis of the wave refraction and reflection theory.
(4) This device has realized the prospective purpose, obtained a requested nanosecond pulse, and had an output of a single high-power pulse wave.

REFERENCES

[1] Liu Ji, HeYuanji, Yang Jiaxiang. Numerical Analysis on Pulse Capacitive Energy Stored Circuit With High-current. *Journal Harbin University of Sci. & Tech.* Vol.4 No.5 90-94
[2] Fan Kuanjun, Feng Guangyao, Pei Yuanji, Wang Xiang qi, Zhong Guojian. Design of Fast Current Pulse Generator. *Atomic Energy Science and Technology* Vol.35, No.40 305-309
[3] Zhou Zecun, Chief Editor. (1988). High voltage technology. Beijing: *Water conservation electric power publishing house.*

Breaking of Ice Using Pulsed Power

S. Ihara[1], C. Yamabe[1] and S. Ushio[2]

[1] *Saga University, Honjo-machi, Saga, Japan*
[2] *National Institute of Polar Reasearch, Koga 1-chome, Itabashi-ku, Tokyo, Japan*

Abstract

The breaking of ice using shock waves produced by a pulsed power generator is suggested as a new method for navigation of icebreakers in order to realize the safe and quick navigation in icebound sea. Shock waves can be produced by applying a voltage between electrodes in contact with an ice sample. The ice breaking by the pulsed power was demonstrated in tap water experimentally. During the experiments, the ice sample was artificially made from pure water. In the salt water with a salinity of 3.5%, the ice sample was not broken according to the results obtained using the cylindrical electrode with a flat tip. By using the conical electrode with the pointed tip, the above ice sample was broken. The shock waves caused by the ionized region formed at the tip of the conical electrode and the localized intense stress at the crack seem to be the important factors behind the ice breaking in the salt water.

1. Introduction

The development of navigation systems for icebreakers on icebound sea has been important for the advancement of natural resources production. For example, in the Northern Sakhalin in the Sea of Okhotsk, the commercial production of crude oil and gas began. At present, production during the winter season is not carried out. On year-round production during the winter season, including the winter season, the Sea of Okhotsk is covered by sea ice[1-3].

To make possible the navigation in icebound sea, an icebreaker crushes the sea ice using the force generated by the ship's mass. As the ship advances into an unbroken ice field, the crushing of ice begins to occur at the point of contact, shown in Fig. 1. A specially shaped hull made of high-strength material is required for the design of the icebreaker. Furthermore, in the regions where thick ice sheets exist, the navigation time is prolonged because continuous crushing is difficult or even impossible. If worse comes to worst, it is possible that the navigation is impossible. Realizing a new method of icebreaking to minimize the disadvantages mentioned above is beneficial to marine transport and shipbuilding.

The ice breaking using pulsed power has been proposed as a new method for the operation of icebreakers in the icebound sea[4]. The ice is broken by shock waves produced by the pulsed power. The reasons for using pulsed power are as follows:

(1) The degree of damage to the hull can be significantly decreased.
(2) Continuous breaking can be realized because the pulsed power generator can be operated repetitively.

An overview of the navigation in icebound sea using the pulsed power is shown in Fig. 2. The pulsed power generator is loaded on the ship, and the electrodes connected to the generator are guided to the ice surface from the bow using an insulated rod with several joints.

The fundamental studies on the destruction of solid materials using the pulsed power were carried out for the development of new drilling and demolition technologies[5, 6].

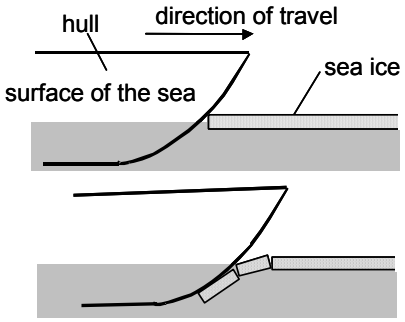

Fig. 1. Navigation in icebound sea.

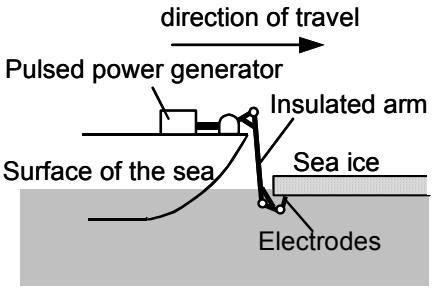

Fig. 2. Navigation in icebound sea.

In the studies described in ref. 6, the Marx generator was employed as an energy source, and granite was used as the sample of solid material. The rod electrodes were allowed to contact the surface of sample, which was immersed in water. Although the destruction of solid materials such as rocks using the pulsed power has been tested in detail until now, there is a lack of experimental results for the ice breaking. Thus, demonstrating the breaking of ice and obtaining fundamental data are necessary.

The final purposes of this research are to evaluate the efficiency of ice breaking by pulsed power, and to discuss the usefulness of this method. In order to do that, the demonstration of ice breaking and the discussion of the breaking mechanisms are required. In this research, experiments on ice breaking are carried out using the pulsed power generator and an ice sample. In these experiments, ice

samples were made from pure water, placed into a plastic vessel, which was filled with water or salt water. Also, the shape of the electrode was tested. In this paper, experimental results and mechanisms of breaking are described and discussed.

2. Experimental apparatus and Method

Figure 3 shows a schematic diagram of the experimental apparatus. A Marx generator, with six capacitors with a capacitance of 0.2 μF, was used as a pulsed power generator. The capacitors of the generator were charged to a negative high voltage, and triggered by an external signal to a gap switch. The circuit parameters R_s and circuit inductance including L_s were estimated to be approximately 20 Ω and 1.5 μH, respectively, assuming that C_s is 33nF. The ice

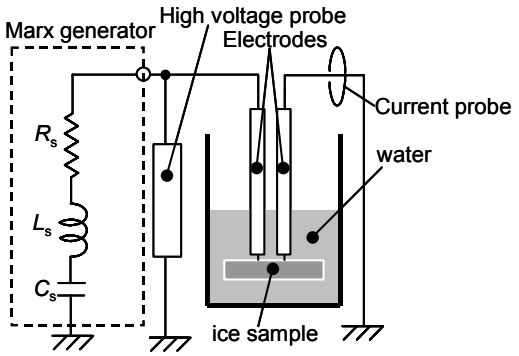

Fig. 3. Schematic diagram of the experimental apparatus.

sample was placed in a plastic vessel, which was filled with water. At first, tap water was used. In the next step, salt water with a salinity of 3.5% was used to simulate the actual condition. Ice samples were made from pure water. The electrodes were made of a dielectric material (polyethylene) and metal (copper).

Figure 4 shows the set-up of the electrode system and the dimensions of the electrodes. The tips of the electrodes contacted the surface of the ice sample. In these experiments, two kinds of electrode shapes, cylindrical and conical (shown

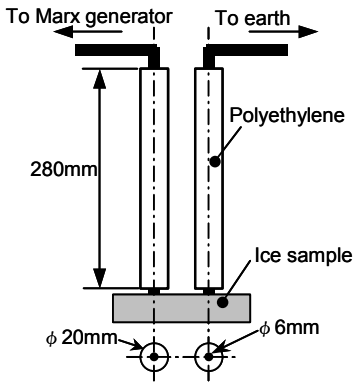

Fig. 4. Set-up of the electrode system and the dimensions of the electrodes.

in Fig. 5), were tested to investigate the electrode shape effects, particularly in the case of using salt water.

In the experiments, the voltage between the electrodes was measured using a high-voltage probe (EP-50K: Pulse Electric Engineering Co., Ltd.), and the current was measured using a current probe (Model 110A: Pearson Electronics, Inc). A digital oscilloscope (DS4374: IWATSU) was used to observe the waveforms.

3. Experimental Results

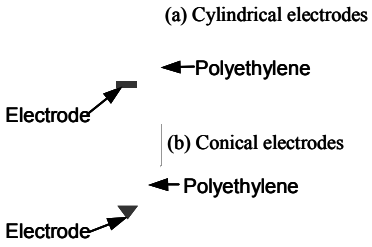

Fig. 5. Electrode shapes(cylindrical and conical).

3.1 Results in the case of using tap water

The experiments in the case of using the tap water were carried out. In these experiments, the cylindrical electrodes were used, and the dimensions of the ice sample were 95×82×28 mm (thickness of 28 mm). The experimental results are shown in Fig. 6. At t=0, a voltage of 50 kV was applied to the electrodes, and after 30 μs, the discharge current started to rise. Figure 7 shows photographs of the ice sample before and after discharge. It can be seen from this photograph that the ice sheet was broken by discharge. When the discharge current was not observed, the ice sheets were not broken. Therefore it is clear that the discharge across the electrodes results in breakage of the ice sheet. A photograph of the discharge between the electrodes was taken. It was confirmed from this photograph that the discharge occurred on the surface between the electrodes.

The power was calculated from the current and voltage

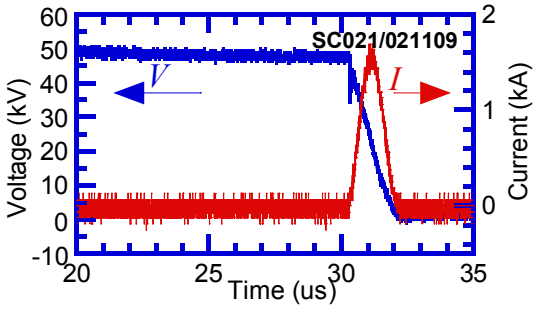

Fig. 6. Experimental results (Voltage and current waveforms).

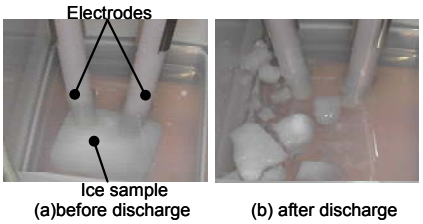

Fig. 7. Ice sample before and after discharge.

waveforms, and the energy was calculated from the integral of the power. The inductance of the discharge region was

neglected. It can be seen that the maximum power and energy were 40 MW and 33 J, respectively. At that time, the charging energy of the power supply, which was calculated from the measured voltage just before the discharge started, was 36 J. Therefore, almost all charging energy was consumed by the discharge between the electrodes; the discharge led to the breaking of the ice.

The *V-I* characteristics obtained from voltage and current waveforms had two regions, which had negative and positive slopes (shown in ref. 4). The negative slope denoted the formation of the arc discharge, and the positive slope denoted the decrease in the discharge current during a time constant for the parameters of the electric circuit including the discharge region. The resistance evaluated from the positive slope in the *V-I* characteristic was approximately 9 Ω at a current of less than 1 kA.

3.2 Results in the case of using salt water

In practice, sea ice exists in seawater or in water with higher conductivity than tap water. Thus, the experiments using salt water with a salinity of 3.5% were carried out in order to simulate the actual conditions. In the case of cylindrical electrode, ice breaking was not confirmed. Also, the discharge emission could be observed only at the tip of the electrodes. The total charging energy of the pulsed power generator was 60 J. On the other hand, by using the conical electrodes, the ice sample was successfully broken, with the same total charging energy. In this case, the discharge emission could also be observed only at the tip of electrodes. Although the voltage waveforms were decreased at a certain time constant after the peak value in both cases, a clear difference was shown in the current waveforms. A higher peak current was observed using the conical electrodes than using the cylindrical electrodes. Fig. 8 shows the waveform of the discharge power calculated from the voltage and current waveforms in both cases. The peak value of discharge power increased from 25 MW to 40 MW by changing the electrode shape from cylindrical to conical. From the experimental results, it was found that the conical electrode with the sharp-pointed tip was effective for the breaking of ice.

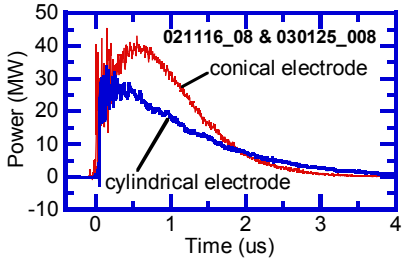

Fig. 8. Waveform of the discharge power in cases of (a) cylindrical and (b) conical electrodes.

Figure 9 shows the *V-I* characteristics obtained from voltage and current waveforms. It can be seen from this figure that in the case of the cylindrical electrode the *V-I* characteristics had an almost constant positive slope, which indicated that the current observed here was caused by the ions contained in the salt water. The resistance evaluated from this positive slope shown in Fig. 9 was approximately 63 Ω. In other words, this current could be regarded as a leakage current because it did not contribute to the breaking of the ice sample. Such a leakage current was consumed as a joule loss. In the case of the conical electrode, the negative slope region was observed at voltage of 50 kV to 40 kV, and then the positive slope region appeared at less then 30 kV. The resistance evaluated from this positive slope was approximately 30 Ω.

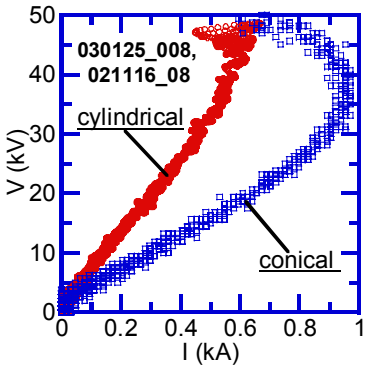

Fig. 9. *VI* characteristics in cases of cylindrical and conical electrodes.

4. Discussion

In the case of tap water, the formation of arc discharge between the electrodes was clearly observed, and the ice sample was broken using the cylindrical electrodes. The negative slope region in *V-I* characteristics (shown in Fig. 7 of ref. 4) indicates the formation of arc discharge. From these results, the main phenomena for the discharge and ice breaking in the tap water were presumed as follows.

(1) By applying voltage across the electrodes, the arc discharge starts to be formed at the surface of the ice sample. This step corresponds to the negative slope region in *V-I* characteristics.

(2) Starting the arc discharge forms the shock wave. Local intense stress occurs in the cracks inside the ice during propagation of the shock wave, resulting in the breaking of the ice.

By using the conical electrodes the pointed tip of the electrode got into the ice sample, and the ice breaking occurred in the salt water; while using the cylindrical electrode, it did not take place. The main effects of using the conical electrode were as follows:

(1) The energy loss by leakage current decreased because the tip of the electrode got into the ice sample.

(2) The region with intense electric field was formed inside the ice.

By considering the above effects, the following phenomena were assumed to be the mechanisms behind the ice breaking.

(1) Ionized regions are formed by the high electric field at the tip of the conical electrode. This step corresponds to the negative slope region in *V-I* characteristics shown in Fig. 9.

(2) The shock wave is induced by the formation of ionized regions.

(3) Local intense stress occurs in the cracks inside the ice during the propagation of the shock wave, resulting in the breaking of the ice.

The difference in the above phenomena between the cases of tap water and salt water is caused by the resistivity of the water. In the case of salt water, no arc discharge path was observed between the electrodes because of the leakage current caused by the low resistivity of salt water. It suggests that the shock wave with sufficient pressure for ice breaking can not be generated in the case of salt water and cylindrical electrodes. By using the conical electrodes, the leakage current was decreased and the ionized region was formed inside the ice sample. The formation of the ionized region results in the formation of the negative slope region in the *V-I* characteristics. The maximum value of discharge power increases rather than in the case of cylindrical electrodes. It seems that the ionized region promotes the formation of the shock wave with high pressure and realizes the ice breaking. In the medium with low resistivity, the following points are important for ice breaking:

(1) To decrease leakage current flow through the medium.
(2) To create a source of shock wave inside the ice sample, for example, by using an electrode with a pointed tip.

Fulfilling the above conditions causes the maximum value of the discharge power to increase, and the formation of shock wave is promoted. In Fig. 8, the higher peak power, obtained using the conical electrode, is caused by the above conditions. In our results, the threshold value of discharge power for ice breaking was unknown. In order to determine the threshold value, experiments in which the charging energy is changed are necessary.

Sea ice contains brine, which is seawater with high salinity. The brine is confined in microscopic regions inside the sea ice. It is known that brine strongly affects the mechanical strength of ice. Reference 7 showed the empirical equation indicating the relationship of mechanical strength and relative brine volume, as follows.

$$\frac{\sigma_f}{\sigma_0} = 1 - A\sqrt{V_b} \qquad (1)$$

Here, V_b is relative brine volume, A is a constant, σ_f and σ_0 are mechanical strengths of sea ice with brine and pure ice without brine, respectively. According to the above equation, the increase in the relative brine volume results in the decrease in strength as a function of $V_b^{1/2}$. Therefore, it seemed that the energy required for breaking of sea ice is lower than that of the experiment described here.

The relative brine volume depends on the ice salinity, ice temperature and other factors[8]. The crystal size and orientation also affect the mechanical strength of the ice. It is difficult to evaluate the mechanical strength of the ice quantitatively because the properties described above complexly change due to the manner of freezing of the water, its quality, and other factors. In our experiment, all the ice samples were made in the same freezer and under the same conditions. Therefore each experimental data obtained here could be compared. In future studies, the experiments that consider the properties of ice, and experiments using natural sea ice are planned.

5. Conclusion

In this research, ice breaking using pulsed power was proposed as a new method for the operation of icebreakers in icebound sea. In this research, breaking of the ice sample artificially made from pure water by pulsed power was demonstrated in tap water experimentally. In order to simulate actual conditions, the ice sample in the salt water with a salinity of 3.5% was tested. Results using the cylindrical electrode with a flat tip show that the ice sample was not broken. By using the conical electrode with the pointed tip, the ice sample was successfully broken. It was found from the results that the conical electrode is effective for ice breaking in medium with low resistivity. It seemed that the shock wave caused by the ionized region at the tip of the conical electrode and the localized intense stress at crack are the important factors behind the ice breaking in salt water.

Experiments that consider the various properties of ice, and those using natural sea ice should be carried out in order to evaluate the efficiency of ice breaking.

References

[1] K. Izumiya, A. Konno and S. Sakai: *Proc. 17th Int. Symposium Okhotsk Sea & Sea Ice*, Hokkaido, 2002, p. 267.
[2] A. Konno and K. Izumiya: *Proc. 17th Int. Symp. Okhotsk Sea & Sea Ice*, Hokkaido, 2002, p. 275.
[3] K. Ogiwara, N. Otsuka, K. Kanaami, S. Takahashi, K. Maida and H. Saeki: *Proc. 17th Int. Symp. Okhotsk Sea & Sea Ice*, Hokkaido, 2002, p. 290.
[4] S. Ihara and C. Yamabe: *Jpn. J. Appl. Phys*. **42** (2003) L489.
[5] I. V. Lisitsyn, H. Inoue, I. Nishizawa, S. Katsuki and H. Akiyama: *J. Appl. Phys*. **84** (1998) No. 11, 6262.
[6] I. V. Lisitsyn, H. Inoue, S. Katsuki and H. Akiyama: *IEEE Trans. Dielectr. Electr. Insulation* **6** (1999) 105.
[7] Schwarz, J. and Week, W. F.: *J. Glaciol*. **19** (1977) 499.
[8] Frankenstein, G. and Garner, R.: *J. Glaciol*. **6** (1967) 943.

Author Index

A

A. B. Saveliev ---------- 4O-02
A. Brablec ---------- 6O-02 2O-07 2P-06 8P-07
A. Doubla---------- 7P-14
A. Goldman ---------- IL-01
A. Ilik ---------- 8O-03
A. Khacef ---------- 4P-03 7O-13 7P-07
A. Kosinski ---------- 8O-03
A. Mizuno ---------- 1O-07
A. N. Malinin ---------- 6O-02
A. Ogata ---------- 7P-06
A. Quade ---------- 7P-08
A. Stoica ---------- 5O-01
A. Yamatake ---------- 7O-10
A. Zukeran ---------- 5P-01
A. Murai ---------- 5O-02

B

B. Dodet ---------- 4O-01 IL-01
B. Michel ---------- 8O-04
B. Polednik ---------- 4P-05

C

C. Berger ---------- 8P-08
C. H. Lim ---------- 6P-03
C. Postel ---------- 7O-12
C. Ruddy ---------- 8O-04
C. Yamabe ---------- 2P-11 5P-06 7P-12 9P-03
C.-P. Klages ---------- 8O-04 8P-08
C. Cixuan ---------- 1P-04
C. Shixiu ---------- 1P-04
C. Xuegou ---------- 1P-04
C. Honda ---------- 8P-01

D

D. Franta ---------- 8P-03
D. H. Yun ---------- 6P-03
D. Moussa ---------- 7P-13 7P-14
D. Trunec ---------- 2O-05 8P-03
D. Wang ---------- 1O-05 4P-04
D. Sasahara ---------- 2P-04

E

E. El Ahmar ---------- 7O-13
E. Hnatiuc ---------- 7P-13 7P-14
E. Metel ---------- 2P-01 7O-07 7P-10 7P-11
E. Odic ---------- IL-01 4O-01
E.B. Tsagou-Sobze ---------- 7P-14
Et. Es-sebbar ---------- 1O-06

F

F. Jorand ---------- 7O-12
F. Krcma ---------- 2P-03 7P-02
F. Massines ---------- 8P-09 1O-06
F. Mitsugi ---------- 2O-03 2P-09
F. Ouni ---------- 4P-03
F. Tochikubo ---------- 2O-04

G

G. Genzhi ---------- 5P-05 9P-02
G. J. Pietsch ---------- 4O-02
G. Kamgang ---------- 7P-13
G. Komarzyniec ---------- 2P-07
G.S. Fedoseev ---------- 4O-01
G. Gerasimov ---------- 6P-04
G. Volkova ---------- 6P-04
G. Zvereva ---------- 6P-02 6P-04
G. Yanhui ---------- 9P-02

H

H. Akashi ---------- 1P-07
H. Akiyama ---------- 1O-05 4P-04 7O-11
H. Caquineau ---------- 8P-09 1O-06
H. D. Stryczewska ---------- 2P-07 7O-01 7O-16
H. Grossmannova ---------- 7P-02
H. H. Kim ---------- 7P-06
H. Imaizumi ---------- 1P-07
H. Ishida ---------- 7O-16
H. Itoh ---------- 1P-03 4P-02 5P-04 7P-15
H. Katayama ---------- 7O-10 7P-01
H. Kawasaki ---------- 7O-08
H. Matsuura ---------- 2O-08
H. Ogawa ---------- IL-02
H. Reinecke ---------- 8O-04
H. Steffen ---------- 7P-08
H. Sugiyama ---------- IL-02

H. Tahara ---------- 8P-04
H. Tamaribuchi ---------- 1O-05
H.-E. Wagner ---------- 2O-05 2O-06 2P-10

I

I. Enache ---------- 1O-06 8P-09
I. Jedlovsky ---------- 7P-09

J

J .L. Brisset ---------- 7O-14
J. Aarik ---------- 1O-03
J. Azuma ---------- IL-02
J. Čech ---------- 2O-07
J. Christopher Whitehead --- 1P-02
J. D. Skalný ---------- 5O-01
J. Ehlbeck ---------- 8O-05
J. Grundmann ---------- 7P-08
J. J. Goo ---------- 6P-03
J. Janča ---------- 6O-02 8P-07
J. Jaroszyńska-Wolińska ---- 2P-08
J. Kadlecova ---------- 2P-06
J. M. Cormier ---------- 4P-03 7O-13
J. Mikielewicz ---------- 2P-01 7O-07 7P-10 7P-11
J. Mizeraczyk ---------- 2O-03 2P-01 7O-07 7P-10 7P-11 2P-09
J. Országh ---------- 5O-01
J. Ozonek ---------- 2P-05 5O-04 5P-02
J. Pawłat ---------- 7P-03 9O-02
J. Podliński ---------- 2P-01
J. Prochazkova ---------- 2P-03 7P-02
J. Raud ---------- 1O-03
J. T. Jin ---------- 6P-03
J. Zeymer ---------- 8O-05
J.L. Brisset ---------- 7P-13 7P-14
J.M. Cormier ---------- 7P-07
J.P. Borra ---------- 2O-01
J.-S. Chang ---------- 2O-03 2P-09

K

K. Ebihara ---------- 2P-04 7O-16 8P-05 8P-06
K. Fujii ---------- 5P-06
K. H. Ko ---------- 6P-03
K. Hensel ---------- 1O-07 7P-09
K. Jaholkowski ---------- 2P-05
K. Krawczyk ---------- 7O-04 7P-04

K. Rackow ---------- 8O-05
K. Sasaki ---------- 2O-02
K. Schmidt-Szalowski -------- 7O-04 7P-04
K. T. Lee ---------- 6P-03
K. Takahashi ---------- IL-02
K. Tanaka ---------- 2P-02 8O-01
K. Teranishi ---------- 5P-04
K. Toda ---------- 4P-04
K. Yamaguchi ---------- 8O-01
K. Yasuoka ---------- 7O-10 7P-01
K. Zhang ---------- 1P-02
K.-D. Weltmann ---------- 8O-05
K. Ohara ---------- 5P-03
K. Okamoto ---------- 4P-04
K. Ono ---------- 7O-02
K.V. Kozlov ---------- 1O-04 1P-06 2O-06 2P-10 4O-01
K.Yasumoto ---------- 5P-01

L

L. Li ---------- 6P-03
L. Maechler ---------- 8P-09
L. Magne ---------- 7O-12
L. Szymanski ---------- 7O-03
L. Zhi ---------- 9P-02
L. Zhongjie ---------- 5P-05 9P-02

M

M. Černák ---------- 2O-07
M. Ciganek ---------- 7P-02
M. Clupek ---------- 7O-09
M. Date ---------- 7P-06
M. Dors ---------- 2P-01 7O-07 7P-10 7P-11
M. Eichler ---------- 8O-04 8P-08
M. Fujii ---------- 7O-06
M. Gabriel ---------- 8O-04
M. Ganciu ---------- 4O-01
M. Goldman ---------- IL-01
M. Janda ---------- 1O-07
M. Kamada ---------- IL-02
M. Kocik ---------- 2O-03 2P-01 7O-07 7P-10 7P-11 2P-09
M. Kogoma ---------- 2P-02 8O-01
M. Kuzumoto ---------- 5O-03
M. Laan ---------- 1O-03
M. Lestinsky ---------- 1O-07

M. M. Guivan ---------- 6O-02
M. Mlotek ---------- 7O-04
M. Moreau ---------- 7O-14
M. Otsubo ---------- 8P-01
M. Rea ---------- 5P-03
M. Reiche ---------- 8O-04
M. Šíra ---------- 8P-03 8P-07
M. Stieber ---------- 8O-05
M. Taguchi ---------- 7P-15
M. Takayama ---------- 7O-16
M. Tanaka ---------- 5O-03
M. Thomas ---------- 8O-04 8P-08
M. Wojucki ---------- 8O-03
M.J. Kirkpatrick ---------- 4O-01
M. Maaspuro ---------- 6P-02
M.S. Kim ---------- 6P-03
M.V. Sokolova ---------- 1O-04
M. Wronski ---------- 4P-05

N

N. Gherardi ---------- 1O-06 8O-02
N. J. Mason ---------- 5O-01
N. Naudé ---------- 1O-06
N. Okayama ---------- 1P-01
N. Orange ---------- 7O-14
N. Takada ---------- 2O-02
N. Teshima ---------- 4P-04
N. Wada ---------- 5O-03

O

O. Aubry ---------- 7P-07
O. Sarroukh ---------- 7O-12

P

P. A. Tatarenko ---------- 1O-04 1P-06 4O-01
P. Kloc ---------- 8P-07
P. Lukes ---------- 7O-09
P. Slavicek ---------- 2P-06 6O-02
P. Smekal ---------- 2P-06
P. St'ahel ---------- 2O-07 8P-03 6O-02 8P-07
P. Tardiveau ---------- 1O-07
P. Vanek ---------- 2P-06

Q

Q. Zhaochun ----------
Q. Zhaochun ---------- 5P-05 9P-02

R

R. Brandenburg ---------- 2O-06 2P-10 8O-05
R. Tuda ---------- 2P-04
R.-J. Zahn ---------- 7P-08
R. Ono ---------- 7O-02

S

S. Fijalkowski ---------- 2P-05 5O-04 5P-02
S. Futamura ---------- 7P-06
S. Ihara ---------- 7P-03 2P-11 5P-06 7P-12 9P-03
S. Ishii ---------- 7O-10 7P-01
S. K. Hong ---------- 6P-03
S. Kanazawa ---------- 2P-09 2O-03
S. Katsuki ---------- 1O-05 7O-11
S. L. Hill ---------- 1P-02
Š. Matejčík ---------- 5O-01
S. Müller ---------- 7P-08
S. Nakazaki ---------- 7P-12
S. Ono ---------- 1P-01
S. Pasquiers ---------- 7O-12
S. Sakai ---------- 4P-04
S. Salamitou ---------- IL-01
S. Suzuki ---------- 4P-02 5P-04
S. Tobe ---------- 8P-04
S. Tokudomi ---------- IL-02
S. Tsubota ---------- 7P-06
S. Uchida ---------- 2O-04
S. Ushio ---------- 9P-03
S. Yamaguchi ---------- 8P-06
S. Youlin ---------- 1P-04
S.A.Krivov ---------- 1O-04
Sang-Moo Park ---------- 8P-05 8P-06

T

T. Fujii ---------- 5P-03 7O-06
T. Hoder ---------- 2O-06 2P-10
T. Ikegami ---------- 2P-04 7O-16 8P-05 8P-06
T. Janowski ---------- 2P-07 7O-01
T. Kitajima ---------- 1P-07

T. Kiyan ---------- 4P-04
T. Matsuo ---------- 9O-02
T. Miichi ---------- 7P-16
T. Nakajima ---------- 5O-02
T. Nakamiya ---------- 2P-04
T. Nakano ---------- 1P-07
T. Namihira ---------- 1O-05 4P-04 7O-11
T. Ohkubo ---------- 2O-03 2P-09
T. Ohno ---------- 7O-11
T. Ohshima ---------- 7O-08
T. Paulmier ---------- 8P-09
T. Sakai ---------- 7O-16
T. Shoyama ---------- 7O-05
T. Sugiyama ---------- 9O-02
T. Suzuki ---------- 4P-02
T. Takahashi ---------- 5P-01
T. Takano ---------- 7P-15
T. Tanaka ---------- IL-02
T. Tokuichi ---------- 1O-05
T. Tomemori ---------- 8P-05
T. Ueda ---------- 9O-02
T. Vykouk ---------- 7O-09
T. Yoshida ---------- 2O-02
T. Oda ---------- 7O-02
Th. von Woedtke ---------- 8O-05

U

U. Kogelschatz ---------- 1O-01
U. Krohmann ---------- 8O-05

V

V. Buršíková ---------- 8P-03 8P-07
V. Foltin ---------- 7P-09
V. Martisovits ---------- 1O-07 7P-09
V.G. Samoilovich ---------- 1O-04 1P-06 4O-01

W

W. Guan ---------- 2P-11

X

X. Guangrun ---------- 1P-04
X. Lin ---------- 7O-11
X. Xiongjie ---------- 9P-02

Y

Y. Ando ---------- 8P-04

Y. Arao ---------- 5P-03
Y. Gyoutoku ---------- 7O-16
Y. Kashiwagi ---------- 1P-03
Y. Matsushita ---------- 2O-04
Y. Miyazaki ---------- 9P-03
Y. Nakamura ---------- IL-03
Y. Nomoto ---------- 2O-03 2P-09
Y. Sasada ---------- 2O-08
Y. Suda ---------- 7O-08
Y. Tanimura ---------- 5O-03
Y. Yagyu ---------- 7O-08
Y. Yanagawa ---------- 2P-02
Y. Yoshioka ---------- 7O-05
Y. Zhu ---------- 8P-01
Y. Ehara ---------- 5P-01
Y.Takagi ---------- 5P-01
Youl-Moon Sung ---------- 8P-01 8P-02

Z

Z. Kolacinski ---------- 7O-03
Z. Li ---------- 7O-11
Z. Machala ---------- 1O-07
Z. Machala ---------- 7P-09
Z. Navrátil ---------- 2O-05 8P-07
Z. R anek-Boroch ---------- 8O-03
Z. Stara ---------- 2P-03
Z. Yuanfang ---------- 5P-05 9P-02